Proceedings of the Sixth International Workshop on

Relativistic Aspects of Nuclear Physics

Editors

T. Kodama
C. E. Aguiar
H.-T. Elze
F. Grassi
Y. Hama
G. Krein

World Scientific

Proceedings of the Sixth International Workshop on

Relativistic Aspects of Nuclear Physics

This page is intentionally left blank

Proceedings of the Sixth International Workshop on

Relativistic Aspects of Nuclear Physics

Caraguatatuba, São Paulo, Brazil 17–20 October 2000

Editors

Takeshi Kodama
Carlos Eduardo Aguiar
Hans Thomas Elze
Federal University of Rio de Janeiro, Brazil

Frederique Grassi and Yogiro Hama
University of São Paulo, Brazil

Gastão Krein
State University of São Paulo, Brazil

World Scientific
Singapore • New Jersey • London • Hong Kong

Published by

World Scientific Publishing Co. Pte. Ltd.

P O Box 128, Farrer Road, Singapore 912805

USA office: Suite 1B, 1060 Main Street, River Edge, NJ 07661

UK office: 57 Shelton Street, Covent Garden, London WC2H 9HE

British Library Cataloguing-in-Publication Data
A catalogue record for this book is available from the British Library.

RELATIVISTIC ASPECTS OF NUCLEAR PHYSICS
RANP2000

ISBN 981-02-4715-X

Printed in Singapore by Uto-Print

PREFACE

It is our pleasure to present the Proceedings of the VI International Workshop on Relativistic Aspects of Nuclear Physics (*RANP 2000*). This time, the meeting took place in Tabatinga, a pleasant beach on the southern coast of Brazil, for the first time out of the city of Rio de Janeiro. This series of workshops started in 1989, aiming to stimulate Brazilian scientific activities on Relativistic Nuclear Physics, especially among young researchers and graduate students. The VI Workshop, held in October 2000, reflected the excitement created in the field by the start of operations of Brookhaven's Relativistic Heavy Ion Collider just four months earlier, in June. The new frontiers of investigation opened by RHIC, among other topics, were actively discussed by the 100 participants of the Workshop, which came from all parts of Brazil and abroad.

RANP 2000 kept the format of the previous meetings, somewhat in the way between a specialist's workshop and an advanced graduate school. The invited speakers did a remarkable job in presenting the most recent and important developments in Relativistic Nuclear Physics in a didactical manner. They have also kindly contributed the manuscripts which form part of this volume. Members of the organizing committee express their sincere thanks to those invited speakers who always warmly contributed to the success of the meeting. In addition, many interesting contributed papers were presented in a poster session which are also included in the book. Note that the number of contributed works increased steadily and this time we had more than twice compared to the earlier meetings of this series. We are happy for this fact which shows the growth of the young researchers of the area in Brazil.

It is worth to mention that we had a really exciting round-table debate entitled, "QGP - Observed or not yet observed ? That is the question." In spite of the hottest discussion on a very controversial subject at the moment, the discussion leader transformed skillfully the fatal collision into a Happy-Hour, by the help of lubricating fluid, called "caipirinha". We regret that we failed to record this historically interesting debate.

As usual, Ms. Dilza Barros again helped us the organization as Conference Secretary. We thank her dedication and professional work. The organization of *RANP 2000* was supported from several Institutions to which we would like to express our thanks: CNPq, FAPESP, FAPERJ, CAPES, CLAF, PRONEX, CBPF, UFRJ, UERJ.

On April the 22nd of this year in Tokyo, Prof. Mituo Taketani deceased. He was not only one of the great leaders of modern Japanese physics but also left big footsteps in the Brazilian Physics community as is described in the article of Prof. Afredo Marques included in this volume[1]. We thus dedicate this book to the memory of Prof. M. Taketani.

[1] Prof. Alfredo Marques, the ex-director of CBPF, has been an important member of the Brazil-Japan collaboration in Cosmic Ray Experiment, which discovered the well-known Centauro events.

This page is intentionally left blank

CONTENTS

Contributed Papers

MITUO TAKETANI

In Memoriam

Alfredo Marques
Centro Brasileiro de Pesquisas Físicas, R. Xavier Sigaud 150,
22290-180, Rio de Janeiro, RJ, Brazil

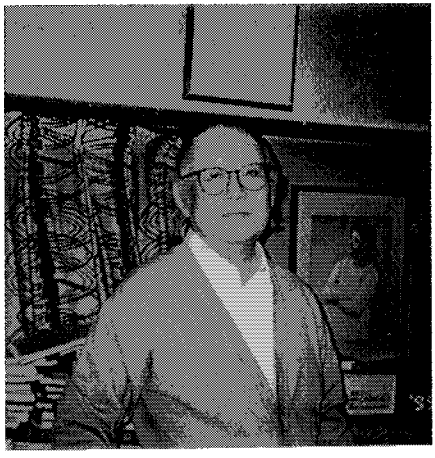

At early hours in the morning, on April the 22nd, Mituo Taketani, 88 passed away after a long disease. Japanese press noticed the event with wide coverage: deceased one of the great leaders of modern Japanese physics.

Mituo Taketani was born in Ohmuta, county of Fukuoka. Graduated in 1934 from the Imperial University of Kyoto and developed most of his scientific life as a professor at Rikkyo University. Soon after graduation joined the group of H. Yukawa, where, with S. Sakata and others, played prominent role in the pioneering developments of meson theory. He shares, with Yukawa, Tomonaga and Sakata, the reputation for setting the grounds of modern theoretical physics in Japan.

Taketani was more than a talented physicist. Endowed with wide intellectual interests and deep social commitment, the borderlines separating his work as a physicist from the philosophical thinking and social engagement are by no means neat. He himself traced a splendid portrait of his intellectual polymorphism in his paper: *Methodological Approaches in the Development of the Meson Theory of Yukawa in Japan*, in the Supplement of the Progress of Theoretical Physics **50**, 12 (1971); three entangled discourses run alternately along the paper: one on the scientific backgrounds of the original proposal and further development in early pion physics, another one on dialectics of the nature and a third one on his political engagement, by editing, with other young intellectuals in Kyoto, the journal World Culture, whose positions against fascism took all of them into jail under the charge of defending ideas favorable to the Communist Party of Japan. According to the Yomiuri Shinbun of 14th May, Yukawa, referring to him, commented: " joined our group the frustrated man named Taketani,

responsible for all agitation among us. Our work would never have developed properly if not for him ". With the word "frustrated", he meant, his political commitments and philosophical mood, as he inserted philosophical and political issues in the discussions on physics. His graduation thesis was on methodology of science whereby he presented his "three level" method characteristics of all natural knowledge: first comes the *substantial* stage, whereby the composition of the subject is assessed; next comes the *essential* stage, whereby the behavior of the substance and action is recognized, and finally the *fundamental* stage where theory is finished and articulated with other knowledge. This idea was present on every development of early pion physics in Japan and in the hands of Sakata and Tanikawa, in 1942, led to the two particle model in pion decay. Idiomatic difficulties and the advent of World War II kept all those findings far from the reach of most physicists in occident; the discovery of pion decay in 1947 with mass and disintegration mode in agreement with their predictions turned attention of the whole world towards those original, creative work. Many people found it quite a surprise the inventiveness of Japanese group, postulating new, unobserved particles to get through nuclear problems, while most authorities in the occident - no less than N. Bohr in the front line - claimed that quantum mechanics had to be modified to be used in nuclear dimensions. Certainly all those achievements owed a lot to the "frustrated" young man that joined the group.

Physics in Brazil has remarkable connections with Taketani and Yukawa group . First of all, Lattes and Occhialini were at the University of S. Paulo when they left to Bristol and, in association with Powell, discovered the pion decay. This outstanding experiment removed all suspicion yet remaining about Yukawa's particle and paved the way to the Noble Prize in Physics that he received in 1949. By that time the members of *nisei* community in S.Paulo - Brazilians with Japanese ascendants - had split into two factions, one of which did not believe the war was over and Japan had been defeated, causing many trouble to all group. The opposing party decided to collect money in the community to invite Yukawa to come over, expecting to convince all the rest, with the help of his respectful word, that the war was over. Yukawa, however, could not come owing to health problems. The money was then sent to Japan to help scientific work under Yukawa, for buying equipment, support people with grants, etc, as the conditions for research work at the time were really poor. In 1953 Taketani took a leave from Rikkyo to accept an invitation from the Institute of Theoretical Physics of S. Paulo; in the occasion he mentioned how helpful was that money and that, if not for other reasons, he would have come in gratitude to the generosity of the Japanese community.

He came over a second occasion in the early sixties, now to the Department of Physics of the University of S. Paulo. Charming, cheerful character, he made many acquaintances within and outside scientific community and left, as he went back to Japan, a handful of new friends and grateful students that worked under his direction. At this occasion he helped in the final negotiations initiated by Lattes and Yukawa, in Kyoto, during the International Conference of Cosmic Rays, shaping what would be the Brazil-Japan Collaboration in high energy interactions in cosmic rays. Beginning the year '62, when most cosmic ray physicists left to set experiments in satellites and many of them had the opinion that the days of cosmic ray physics were over, Brazil-Japan Collaboration on high energy interactions in cosmic rays stays alive after nearly forty years of productive life, perhaps a record in duration of collaborative work. Taketani's views were also important to the groups in Japan that joined this work: his authoritative word as a member of the scientific board that decided upon the funds to build a 40 GeV accelerator (presently

the Tsukuba 12 GeV machine) was decisive to allocate 10% of the project's budget to cosmic ray research. This attitude cost him many complaints and bitter criticism from the part of accelerator physicists that wanted to have all money. Taketani argued that Cosmic Ray Physics was a tradition in Japan, initiated by Nishina, that was worth to be continued because it would work better and faster than accelerators to disclose the physics of strong interactions at very high energies. In fact it took more than two decades before accelerators entered in closer competition with the new findings of Brazil-Japan Collaboration.

M. Taketani left behind a voluminous scientific bibliography. Thanks to his versatile mind he also left many contributions on social issues, as the essays: Nuclear Ashes, Social Responsibility of Scientists, and others, having published this year a last one headed Dangerous Scientific Technologies. He was also very fond of pop music and even acknowledged as an expert on the theme: his apartment in the neighborhood of Tokyo was crowded with stacks of CD's and tapes some of them sent by young musicians and distributors looking for a word of criticism and advice.

Mituo Taketani was a sensible, passionate character who devoted his life to the cause of Truth, Equality and Freedom. In Japan or abroad, physicists or not, all of us feel like orphans: a significant portion of the immaterial beliefs on the values of work, intellectual independence, courage, endurance, sincerity, altruism, that build the human faith in a better future, disappear with him.

I am indebted to Drs. A. Ohsawa, T. Kodama and E.H. Shibuya for kindly making available to me valuable information on Professor Taketani.

This page is intentionally left blank

Invited Talks

John Harris

FIRST PHYSICS RESULTS FROM STAR

JOHN W. HARRIS FOR THE STAR COLLABORATION
Physics Department, Yale University,
P.O. Box 208124, New Haven CT, U.S.A. 06520-8124
E-mail: John.Harris@Yale.edu

The Relativistic Heavy Ion Collider (RHIC) commenced operation for physics in the Summer of 2000. Initial results on collider performance, detector performance of the STAR experiment, and preliminary physics results on hadron production from STAR will be reported.

1 Introduction

The primary motivation for the field of relativistic heavy ion physics is to study and understand Quantum Chromodynamics (QCD) at high energy densities, greater than a few GeV/fm^3. At sufficiently high energy densities, a phase transition to a quark-gluon plasma, a deconfined state of quarks and gluons,[1] is expected. Formation of a quark-gluon plasma, which has implications for nuclear physics, astrophysics, cosmology and particle physics, is the major focus of relativistic heavy ion experiments. Collisions of heavy ions at RHIC are expected to exceed the energy densities required for this transition. With the start of operations of the Relativistic Heavy Ion Collider (RHIC)[2] the field has entered a new realm of heavy ion collider physics, where perturbative QCD effects become important. Hard scattering processes are expected as well as increased energy and particle densities. A new round of collider experiments at RHIC is aimed at identifying the deconfinement phase transition and the effects of chiral symmetry restoration,[3] and characterizing the properties of each.

In this paper, results will be reported from the inaugural run at RHIC, which was just completed one month prior to this Workshop. This paper will be divided into three main sections. Following the introduction, a brief overview of the RHIC collider and experiments will be presented. The remainder of this paper will focus on the STAR experiment[4] and the first physics results from the Summer 2000 run. The data-taking and event triggering in STAR will be described along with information on the performance of the detector. Preliminary results on the multiplicity, pseudorapidity, and transverse momentum distributions of negative hadrons from RHIC collisions will be presented, as will measurements of two-particle interferometry, anti-proton to proton ratios, and elliptic flow. First reconstruction of strange particles at

RHIC will also be presented. A concluding statement will be made on the physics that is anticipated from STAR in the future.

2 The Relativistic Heavy Ion Collider and Its First Run

The first physics run at the Relativistic Heavy Ion Collider (RHIC) took place in the Summer of 2000. The RHIC accelerator-collider complex at Brookhaven is displayed in a schematic diagram in Fig.1. During the Summer 2000 run, Au beams were accelerated from the tandem Van de Graaff accelerator through a transfer line into the AGS Booster synchrotron and then into the AGS before injection into RHIC. RHIC was designed to accelerate and collide ions from protons up to the heaviest nuclei over a range of energies, up to 250 GeV for protons and 100 A-GeV for Au nuclei, as shown in Fig. 2. Beam energies during this first run were kept to a moderate 65 A-GeV. RHIC attained its goal of ten percent of design luminosity by the end of the Summer 2000 run at the collision center-of-mass energy of $\sqrt{s_{NN}} = 130$ GeV.

There are four experiments at RHIC. These experiments have various approaches to search for the deconfinement phase transition to the quark gluon plasma (QGP). The STAR experiment[4] concentrates on measurements of hadron production over a large solid angle in order to measure single- and multi-particle spectra and to study global observables on an event-by-event basis. The PHENIX experiment[5] focuses on measurements of lepton and photon production and has the capability of measuring hadrons in a limited range of pseudorapidity. The two smaller experiments BRAHMS (a forward and midrapidity hadron spectrometer)[6] and PHOBOS (a compact multiparticle spectrometer)[7] focus on single- and multi-particle spectra. The collaborations, which have constructed these detector systems and which will exploit their physics capabilities, consist of approximately 900 scientists from over 80 institutions internationally. In addition to colliding heavy ion beams, RHIC will collide polarized protons to study the spin content of the proton.[8] STAR and PHENIX are actively involved in the spin physics program planned for RHIC.

3 The STAR Experiment

STAR will investigate the behavior of strongly interacting matter at high energy density and search for signatures of QGP formation and chiral symmetry restoration in collisions of relativistic nuclei at RHIC. The STAR detector measures simultaneously many experimental observables to study possible signatures of the QGP phase transition as well as the space-time evolution of

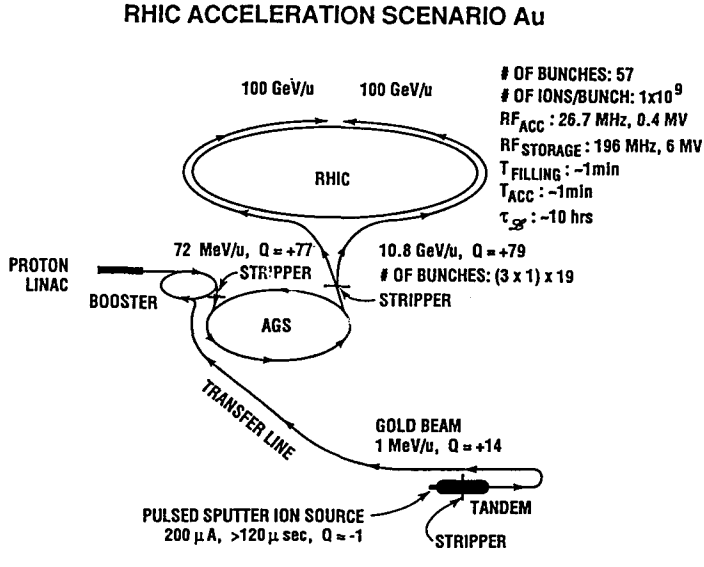

Figure 1. The Relativistic Heavy Ion Collider (RHIC) accelerator complex at Brookhaven National Laboratory. Nuclear beams are accelerated from the tandem Van de Graaff, through the transfer line into the AGS Booster and AGS prior to injection into RHIC. Details of the characteristics of proton and Au beams are also indicated after acceleration in each phase.

the collision process over a variety of colliding nuclear systems.[4] STAR also measures ultra-peripheral collisions of relativistic nuclei to study photon and pomeron interactions resulting from the intense electromagnetic fields of the colliding ions and colorless strong interactions, respectively.[9] STAR will also study proton-proton interactions and proton-nucleus interactions in order to understand the initial parton distribution functions of the incident nuclei and for reference data for the heavy ion data. A physics program to determine the contribution of the gluon spin to the spin structure function of the proton by colliding polarized protons is planned.

The layout of the STAR (Solenoidal Tracker At RHIC) experiment[4] is shown in Fig.3. The initial configuration of STAR in 2000 consists of a large

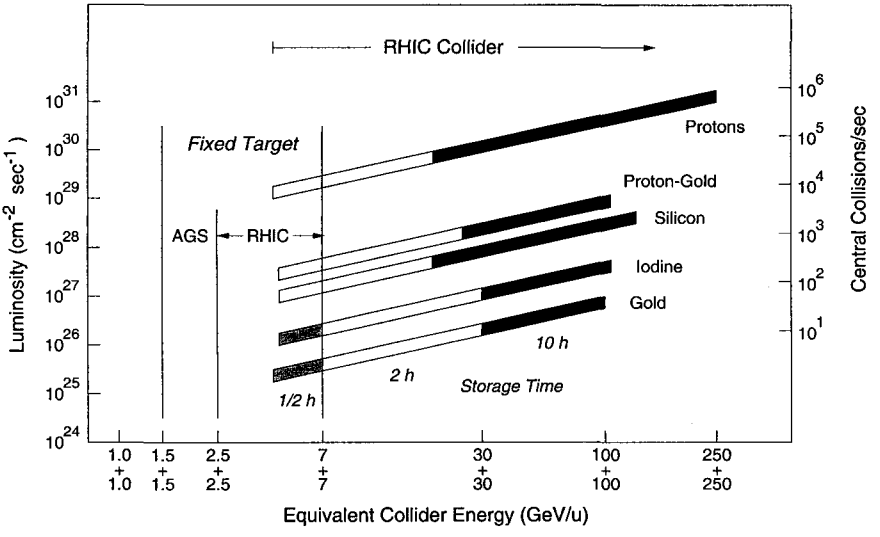

Figure 2. Operating parameters for the Relativistic Heavy Ion Collider (RHIC). Displayed are the design luminosities (left) and number of central collisions per second (right) as a function of collider energy for various combinations of nuclear beams. The anticipated average storage time before refilling the collider rings is shown for each beam combination.

time projection chamber (TPC) covering $\mid \eta \mid < 2$, a ring imaging Cherenkov detector[10] covering $\mid \eta \mid < 0.3$ and $\Delta\phi = 0.1\pi$ (not shown in Fig.3), and trigger detectors inside a room temperature solenoidal magnet with 0.25 T magnetic field. The solenoid provides a uniform magnetic field of maximum strength 0.5 T allowing for tracking, momentum analysis and particle identification via ionization energy loss measurements in the TPC. Measurements in the TPC were carried out at mid-rapidity with full azimuthal coverage ($\Delta\phi = 2\pi$) and symmetry.

3.1 STAR Trigger

STAR utilizes a central trigger barrel (CTB) to trigger on collision centrality. The CTB, shown in Fig.3, surrounds the outer cylinder of the TPC, and triggers on the flux of charged-particles in the $\mid \eta \mid < 1$ region. In addition, zero-degree calorimeters (ZDC) located at $\theta < 2$ mrad, and not shown in Fig.3, are used for determining the amount of energy in neutral particles remaining in the forward directions. Each experiment at RHIC has a com-

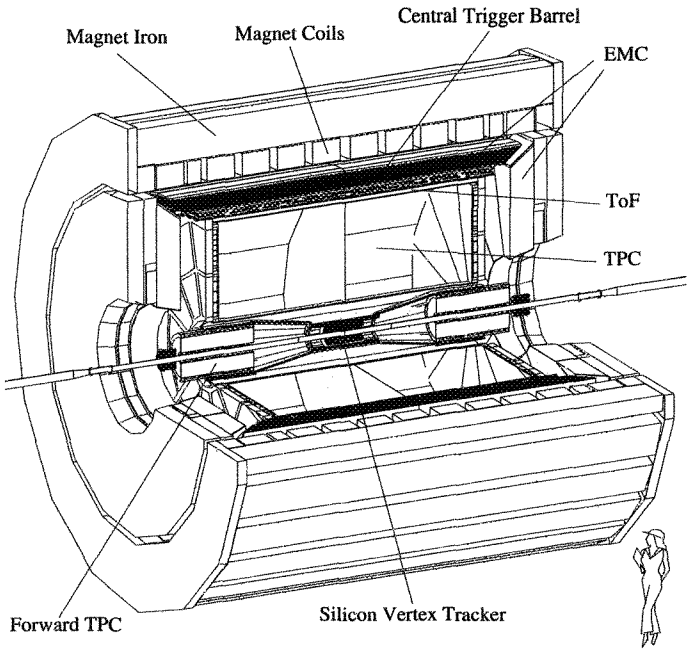

Figure 3. Layout of the STAR experiment at RHIC.

plement of ZDC's for triggering and cross-calibrating the centrality triggering between experiments[11]. Displayed in Fig.4 is the correlation between the summed ZDC pulse height and that of the CTB for events with a primary collision vertex that was successfully reconstructed from tracks in the TPC. The largest number of events occurs for large ZDC values and small CTB values (gray region of the plot). From simulations this corresponds to collisions at large impact parameters, which occur most frequently and which characteristically leave a large amount of energy in the forward direction (toward and into the ZDC) and a small amount of energy and particles sideward into the CTB. Collisions at progressively smaller impact parameters occur less frequently and result in less energy in the forward direction (resulting in lower pulse heights in the ZDC, which detects neutrons at $\theta < 2$ mrad) and more energy in the sideward direction (resulting in larger pulse heights in the CTB). Thus, the correlation between the ZDC and CTB is a monotonic

function that is used in the experiment to provide a trigger for centrality of the collision.[a]

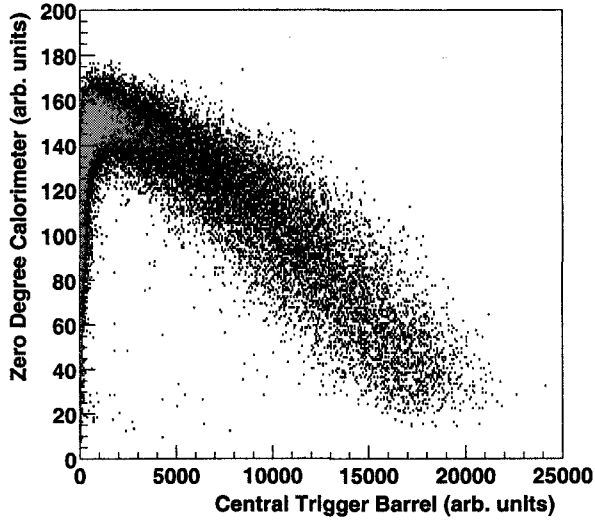

Figure 4. Correlation between the summed pulse heights from the Zero Degree Calorimeters (ZDC) and those of the Central Trigger Barrel (CTB) for events with a primary collision vertex, that was successfully reconstructed from tracks in the Time Projection Chamber. The largest concentration of events in this minimum bias trigger is (represented as the gray region) at low CTB values and large ZDC values around 150. See text for details.

A minimum bias trigger was obtained by selecting events with a pulse height representing at least one neutron in each of the forward ZDC's, which corresponds to 95 percent of the geometrical cross section. Triggers corresponding to smaller impact parameter were implemented by selecting events with less energy in the forward ZDCs, but with sufficient CTB signal to eliminate the second branch at low CTB values shown in Fig.4.

[a]The ZDC is, in fact, double-valued since collisions at either small or large impact parameter (corresponding to a large or small particle flux sideward into the CTB) can result in a small amount of energy in the forward ZDC direction.

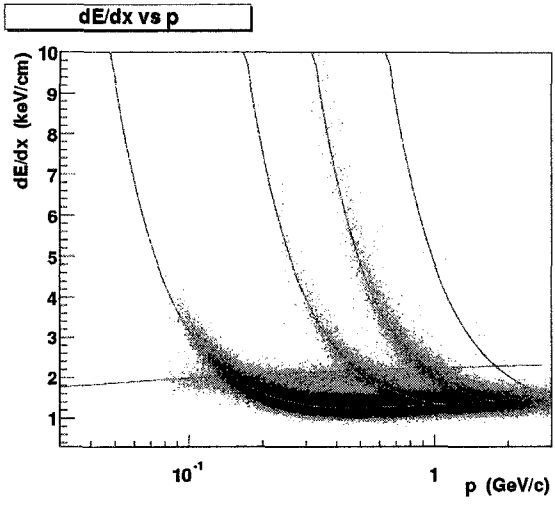

Figure 5. Preliminary distribution of the ionization energy loss for charged-particles measured in the STAR Time Projection Chamber as a function of the momentum of the particle. Also drawn are curves corresponding to the Bethe-Bloch formula for charged e, π, K, p, and d.

3.2 STAR Detector Performance

The performance of RHIC and the STAR detector systems was analyzed prior to embarking upon measurements for physics and analysis. The root mean square deviation of the collision vertices of the beams from RHIC was determined from tracking in STAR to be approximately 1.5 mm in the direction transverse to the beam. The longitudinal distribution of beam collision points in STAR was found to be rather broad with a root mean square deviation of approximately 70 cm.[b] The standard deviation of the position resolution for track points measured in the TPC at mid-rapidity was found to be approximately 0.5 mm. The momentum resolution was determined to be $\delta p/p < 2$ percent for a majority of the tracks in the TPC. The $\delta p/p$ was found to decrease with the number of hit points along the track and increase with particle momentum, as expected. The ionization energy loss (dE/dx)

[b]This is expected to decrease by a factor of 4 in the next run with the inclusion of additional RHIC collider components.

resolution was found to reach 8 percent for tracks measured over the entire radial extension of the TPC. All of these performance factors are consistent with the original design specifications for performance of the TPC in STAR. [4] For reference, the measured energy loss (dE/dx) of charged particles detected in the TPC is displayed in Fig.5. Predictions of the Bethe-Bloch formula for electrons, pions, kaons, protons and deuterons are illustrated as curves on the figure. The measured dE/dx contours as a function of momentum are used in STAR to distinguish electrons, pions, kaons, protons and deuterons at sufficiently low momenta.

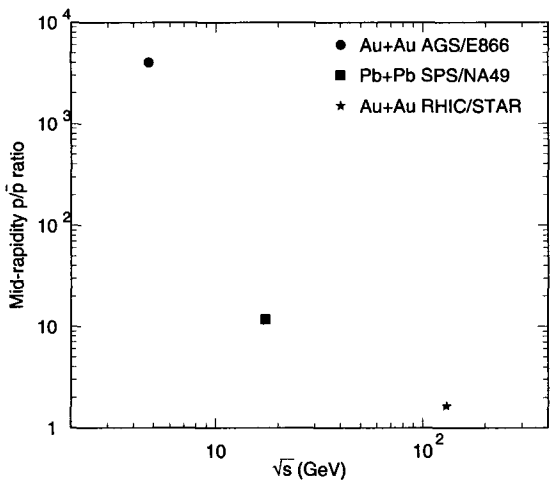

Figure 6. The mid-rapidity proton to anti-proton ratio as a function of $\sqrt{s_{NN}}$ from central collisions at the AGS, [12] SPS, [13] and preliminary data from STAR.

3.3 STAR Proton to Anti-Proton Ratios

The ratio of the yields of protons relative to anti-protons yields information on baryon transport in the collision process and the net baryon number

at mid-rapidity. This is one of the first measurements that can be made in STAR with only minor corrections. This can be attributed to STAR's large tracking efficiency over its 2π azimuthal acceptance, and its complete symmetry about the magnetic field direction. The corrections are concentrated at low momentum in the form of additional protons from secondary interactions in detector materials and anti-proton absorption in these materials. Monte Carlo simulations were employed to estimate the yield of protons from background processes and to determine the degree of absorption for anti-protons in STAR. The corrections for background protons were found to be $< 10\%$ and those for anti-proton absorption $< 5\%$ for transverse momenta p_t >0.4 GeV/c. The particle identification efficiencies for protons and anti-protons in STAR are high for $p_t < 1.0$ GeV/c, as can be seen in Fig.5. The proton to anti-proton ratio measured at mid-rapidity as a function of $\sqrt{s_{NN}}$ is shown in Fig.6 for central collision data from the AGS,[12] SPS[13] and preliminary data from STAR at RHIC. The proton to anti-proton ratio decreases by over two orders of magnitude from the AGS to the SPS, and by another order of magnitude to the preliminary value measured in STAR. The decrease in the observed proton to anti-proton ratio as a function of $\sqrt{s_{NN}}$ reflects an increase in the proton - anti-proton pair production at higher energies. However, since the ratio is larger than unity, a significant positive net baryon density is still observed at mid-rapidity even at this RHIC energy.

3.4 Particle Multiplicities and Spectra from STAR

Measurements of the particle multiplicity, and pseudorapidity and transverse momentum distributions provide important information on the kinetic freeze-out stage of the reaction process. This can be used to constrain theoretical descriptions of the evolution of the system from the initial hot, dense phase of the collision through chemical freeze-out and eventual kinetic decoupling. Shown in Fig.7 are preliminary results on the multiplicity distribution of negative hadrons for collisions of Au + Au at $\sqrt{s_{NN}} = 130$ GeV measured in a minimum bias trigger in STAR. The transverse momentum and pseudorapidity acceptance are listed in the figure. Also shown in gray is the distribution for the 5 % most central collisions, and a solid curve depicts the predictions of a HIJING calculation.[14] The shape of the minimum bias distribution is typical of the shapes measured at lower energies and represents the geometry of the collisions. The large impact parameter collisions, which have large cross sections, produce low multiplicities. As the impact parameters decrease, the cross sections decrease and extend out to the largest multiplicities for the smallest impact parameters. Note that the highest negative hadron

multiplicities reach 335 per unit rapidity at mid-rapidity and with $p_t > 0.1$ GeV/c.

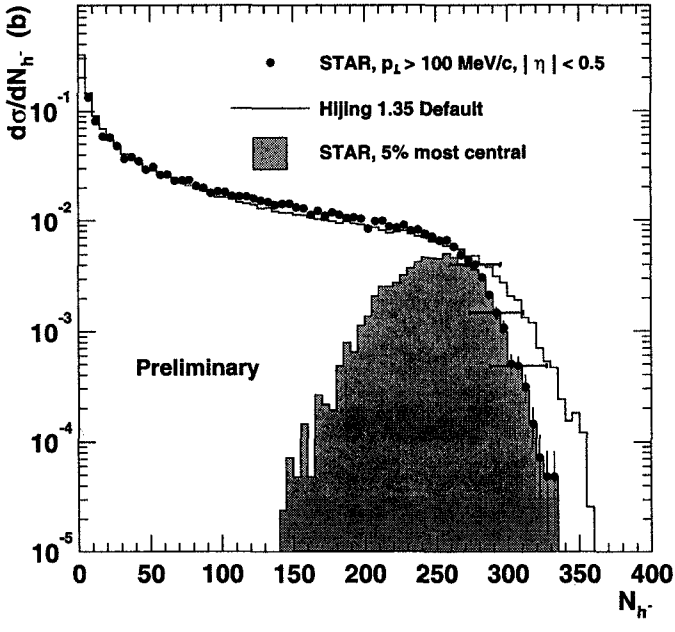

Figure 7. Preliminary multiplicity distributions of negative hadrons at mid-rapidity for collisions of Au + Au measured in STAR. The data points are the result for a minimum bias trigger, and the gray region is the distribution for the most central 5 % of the collision events. Also shown is a curve for the prediction of the HIJING model.[14]

Displayed in Fig.8 is the transverse momentum distribution of negative hadrons measured at mid-rapidity in central Au + Au collisions in STAR at $\sqrt{s_{NN}} = 130$ GeV. The data from central collisions of Pb + Pb measured at mid-rapidity in NA49 at $\sqrt{s_{NN}} = 17$ GeV are also displayed in Fig.8.[15] For comparison, the transverse momentum distributions for the average of the negative plus positive hadrons in anti-proton plus proton collisions measured in UA1 at $\sqrt{s} = 200$ GeV are also displayed.[16] All of the distributions follow a simple power-law formulation and, as seen in the figure, the data from STAR is harder (flatter) than the other two distributions in the figure.

The pseudorapidity distribution for negative hadrons measured in STAR

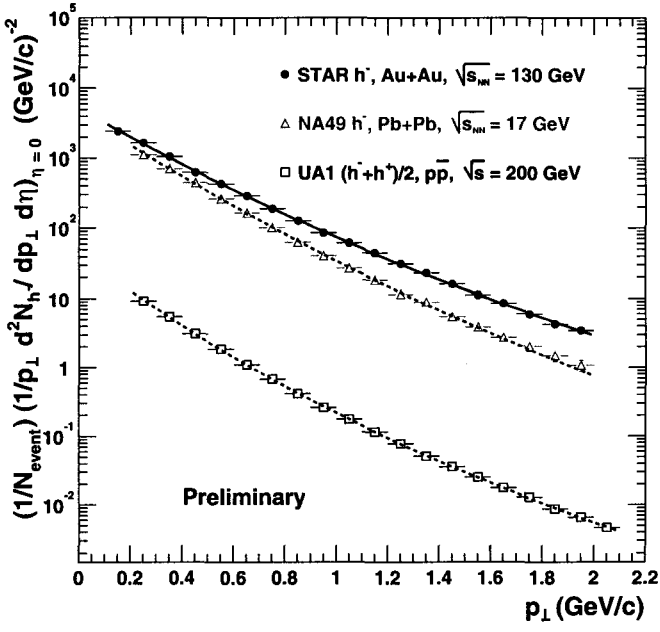

Figure 8. Negative hadron transverse momentum distributions measured at mid-rapidity in central Au + Au collisions in STAR (preliminary) at RHIC, and in central Pb + Pb collisions in NA49 at the CERN SPS. Also shown are the average of the negative plus positive hadron transverse momentum distributions in proton + anti-proton collisions in UA1.

is displayed in Fig.9 for the 5 % most central collisions. The solid dots represent the distribution for $p_t > 0.1$ GeV/c and the open squares represent the same data extrapolated for $p_t > 0$. Also shown in Fig.9 for comparison are the data published by the PHOBOS Collaboration[17] for the average charged particle multiplicity measured over the range $-1.0 < \eta < 1.0$ and as depicted by the dashed line. There is good agreement bewteen the measurements for the average multiplicities. Pseudorapidity distributions like those measured in Fig.9 should constrain some of the important ingredients used in model calculations, particularly the initial gluon distributions and possibly the evolution in the early phase of the collisions, both of which are expected to significantly influence the particle production.

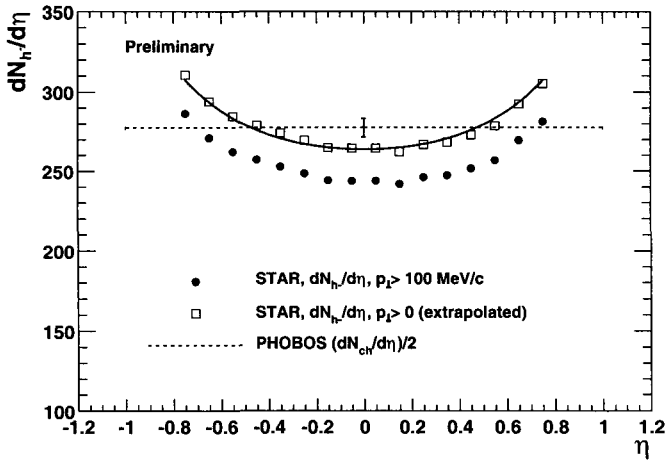

Figure 9. Preliminary pseudorapidity distribution for negative hadrons measured in STAR for the most central 5 % of the collisions. The solid dots are the distribution for $p_t > 0.1$ GeV/c and the open squares are the same data extrapolated for $p_t > 0$. See text for more details.

Using ionization energy loss as displayed in Fig.5, the spectra of identified particles can be measured. Displayed in Fig.10 is a preliminary spectrum of negative pions measured in STAR as a function of transverse mass (less the pion rest mass). These data are measured for the 5 % most central collisions at mid-rapidity. Clearly, the spectrum is not exponential over the entire mass range shown. However for reference, fitting only the upper end of this spectrum yields an inverse slope of 190 ± 15 MeV. More detailed analyses of the spectra for other identified particles and comparisons as a function of centrality are in progress and are needed prior to drawing serious conclusions.

3.5 STAR Strangeness Measurements

To gain access to the high density phase and information on its strangeness content, strange mesons (K^+, K^-, K^o, K^{*o}, $\bar{K}^{*o}$, ϕ) and baryons ($\bar{\Lambda}, \Lambda, \Xi^-, \bar{\Xi}^+$, $\Omega^-, \bar{\Omega}^+$) can be measured in STAR at mid-rapidity. An enhancement in the production of strange particles resulting from chemical equilibrium of a system of quarks and gluons was one of the first predictions for a signature of QGP formation.[18] Preliminary invariant mass spectra recon-

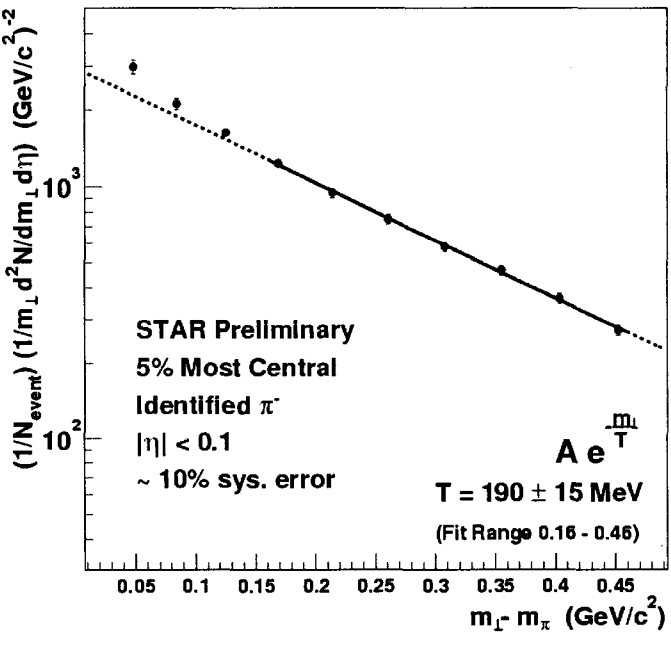

Figure 10. Transverse mass spectrum for negative pions at mid-rapidity in central Au + Au collisions.

structed from measurements of the secondary decays of Λ and Ξ^- in STAR are shown in Fig.11 and Fig.12, respectively. Determination of the efficiencies for detecting and reconstructing these secondary decay vertices in STAR is presently underway. Once the efficiency for identifying and measuring the decay of each particle is known, then its production cross section and momentum spectrum can be extracted from the data, and a chemical equilibrium analysis applied to the resultant particle yields to determine characteristics (the baryochemical potential, temperature and degree of saturation in strangeness) of the emitting system. An enhancement in the strange antibaryon content[19,20] and an increased enhancement of multiply-strange baryons ($\Xi^-, \bar{\Xi}^+$, Ω) compared to singly-strange hadrons[19] have been predicted to signify the presence of a QGP.

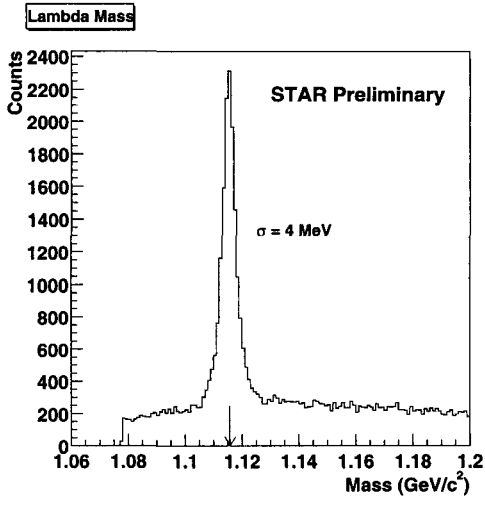

Figure 11. Preliminary invariant mass distributions reconstructed from the secondary decay products of the Λ in STAR.

3.6 STAR Elliptic Flow Measurements

As in the case for the proton to anti-proton ratio, STAR's inherent geometrical symmetry has allowed us to make an early determination of the elliptic flow in collisions at RHIC.[21] Elliptic flow represents the second harmonic Fourier coefficient of the azimuthal particle distribution relative to the reaction plane. It is represented by $v_2 = \langle (p_x^2 - p_y^2)/(p_x^2 + p_y^2) \rangle$, where the x and y directions are transverse to that of the colliding beams. Elliptic flow is a consequence of and, in turn, reflects the transverse pressure gradient that develops in the early part of the collision. The pressure gradient and the elliptic flow are inherently azimuthally asymmetric due to the anisotropic collision geometry for non-zero impact parameters. The magnitude of the elliptic flow is a product of the strength of the transverse pressure gradient and the ability of the system to convert this original spatial anisotropy into momentum space anisotropy. Predictions of hydrodynamic models[22] and transport models[23] show that elliptic flow is sensitive to the early dynamics of the collision process.

The result of the first STAR elliptic flow measurement is shown in Fig.13. Plotted is the value of the peak elliptic flow v_2 measured in STAR (data

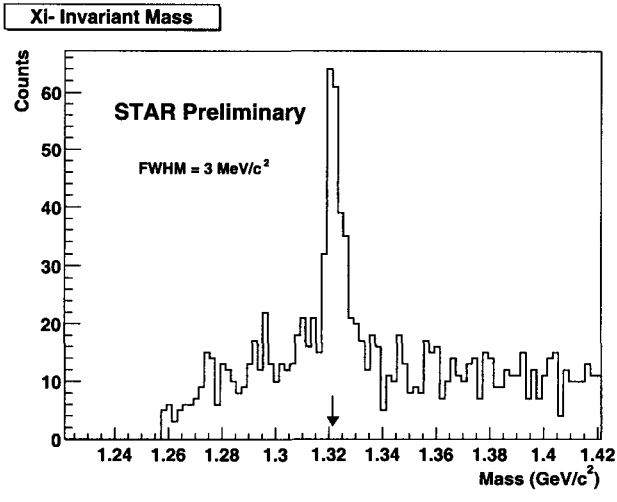

Figure 12. Preliminary invariant mass distributions reconstructed from the secondary decay products of the Ξ^- in STAR.

points) as a function of the centrality of the collision as represented by the fraction of the maximum charged particle multiplicity (n_{ch}/n_{max}) observed. Thus in Fig.13, the collision centrality increases (or the impact parameter decreases) for larger values of n_{ch}/n_{max} along the abscissa. Also presented are the range of values of v_2 (open rectangles) in the hydrodynamic limit for the various spatial configurations of the initial geometrical eccentricity. An overall scale factor, of 0.19 for the lower edge of the rectangle and 0.25 for the upper edge, was applied for normalization. These results suggest that the hydrodynamic limit is reached in the most central collisions (large n_{ch}/n_{max}) and that less central collisions (towards lower values of n_{ch}/n_{max}) produce less elliptic flow than predicted from hydrodynamics. Also of interest is the large value of v_2 relative to that measured at the AGS and at the SPS. The peak elliptic flow measured at this RHIC energy in STAR reaches 6 %, while the values measured at the AGS and SPS are 2 % [24] and 3.5 %,[25] respectively. This suggests that there is more significant early thermalization at RHIC than at the lower energies. In particular, at RHIC the most central collisions appear to approach the hydrodynamic limit where complete thermalization would be expected.

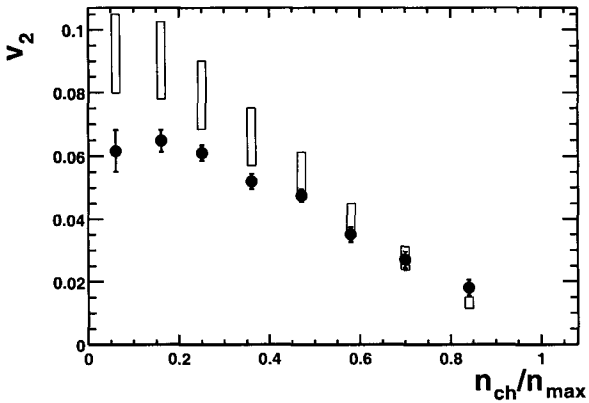

Figure 13. Data points represent the peak elliptic flow v_2 measured in STAR as a function of the ratio n_{ch}/n_{max}. Open rectangles exhibit the hydrodynamic limits for v_2. See text for details.

3.7 Two-Pion Correlations from STAR

Correlations between identical bosons provide information on the freeze-out geometry, the expansion dynamics and possibly the existence of a QGP.[26] The dependence of the pion-emitting source parameters on the transverse momentum components of the particle pairs, and as a function of the various types of particle pairs can be measured with high statistics in STAR. In the present study a multi-dimensional analysis is made using the standard Pratt-Bertsch decomposition[26,27] into outward, sideward, and longitudinal momentum differences and radius parameters. The data are analyzed in the longitudinally co-moving source frame, in which the total longitudinal momentum of the pair (collinear with the colliding beams) is zero. As expected, larger sizes of the pion-emitting source are found for the more central (i.e. decreasing impact parameter) events, which in turn have higher pion multiplicities. This source size is observed to decrease with increasing transverse momentum of the pion pair. This dependence is similar to what has been observed at lower energies and is an effect of collective transverse flow. Shown in Fig.14 are preliminary results from STAR for the coherence parameter λ and the radius parameters R_{out}, R_{side}, and R_{long} extracted in the analysis. Also shown are values of these parameters extracted from similar analyses at

lower energies. All analyses are for low transverse momentum ($\sim$ 170 MeV/c) negative pion pairs at midrapidity for central collisions of Au + Au or Pb + Pb. From Fig.14 the values of λ, R_{out}, R_{side}, and R_{long} extend smoothly from the dependence at lower energies and do not reflect significant changes in the source from those observed at the CERN SPS energy. The anomalously large source sizes or source lifetimes predicted for a long-lived mixed phase[28] have not been observed in this study.

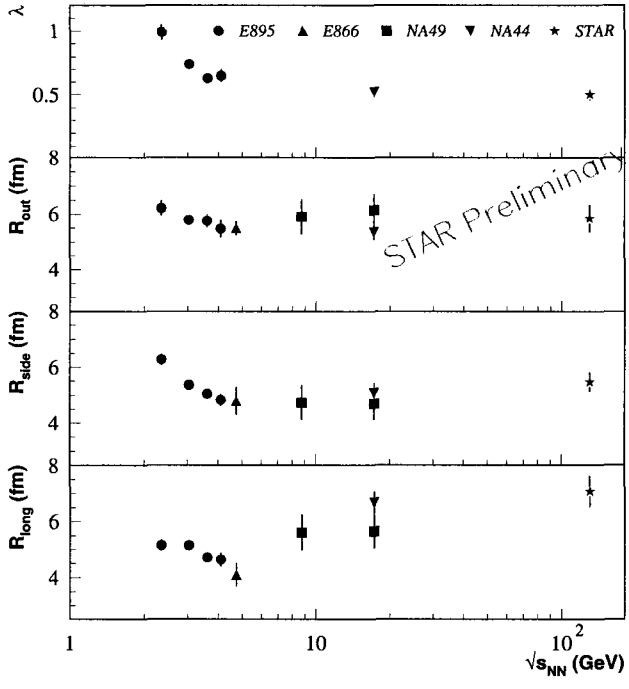

Figure 14. Compilation of results on two-particle correlation (HBT) parameters from measurements using central collisions of Au + Au at the BNL-AGS, Pb + Pb at the CERN-SPS and new preliminary Au + Au data from the STAR experiment at RHIC. Plotted are the coherence parameter λ, R_{out}, R_{side}, and $R_{longitudinal}$. See text for details.

3.8 Future Results from STAR

Inclusive p_t distributions of charged particles will be extended to high p_t ($\sim$ 10 GeV/c) to study parton energy loss.[29] To determine the degree of equilibration of the system and to investigate fluctuations, STAR will measure triple differential cross sections for production of various types of particles as a function of transverse momentum (p_t), pseudo-rapidity (η) and azimuthal angle (ϕ).

As a consequence of the high multiplicities in central collision events and the large acceptance of STAR, various measurements can be made on an event-by-event basis. These include: the slope of the transverse momentum (p_t) distribution for pions, the $\langle p_t \rangle$ for pions and kaons; the flow of different types of particles as a function of p_t, rapidity, and azimuthal angle; and the fluctuations in particle ratios, energy density, and entropy density.

Additional tracking detectors will be added for the run in 2001. These are a silicon vertex tracker (SVT) covering $| \eta | < 1$, and a forward radial-drift TPC (FTPC) covering $2.5 < | \eta | < 4$. For the next run the electromagnetic calorimeter (EMC) will reach approximately 20% of its eventual $-1 < \eta < 2$ and $\Delta\phi = 2\pi$ coverage and will allow measurement of the transverse energy of events, and trigger on and measure high transverse momentum photons and particles. The remainder of the EMC, which includes one endcap, will be constructed and installed over the next 2 - 3 years. A time-of-flight (TOF) patch covering $0 < \eta < 1$ and $\Delta\phi = 0.04\pi$ will also be installed for 2001 operation to extend the particle identification for single particle spectra at midrapidity in STAR. A larger barrel TOF covering $| \eta | < 1$ and $\Delta\phi = 2\pi$ is being proposed for installation after completion of the EMC.

4 Conclusions

The RHIC collider and experiments have successfully commenced operation. The experiments have started to investigate a new realm of physics. The first results from STAR indicate that the baryon density at mid-rapidity is lower than observed in previous heavy ion experiments at lower energies indicating an expected increase in particle - anti-particle production. The particle production is large as exhibited by the measured charged particle multiplicities. The negative hadron transverse momentum distributions exhibit a power-law dependence and are observed to be harder than their counterparts at the CERN SPS and in proton + anti-proton collisions at slightly higher energy. The elliptic flow measured in STAR is larger than observed at lower energies. This suggests that there is significant early thermalization at RHIC,

greater than observed at lower energies. Two-particle corrrelation measurements exhibit source sizes similar to those measured at the CERN SPS with heavy ions. Other measurements such as identified particle spectra, strange particle yields, and event-by-event measurements are anticipated from this first RHIC run.

Acknowledgements

We thank the RHIC Operations Group at Brookhaven National Laboratory for their support and for providing collisions for the experiment. This work was supported by the Division of Nuclear Physics and the Division of High Energy Physics of the Office of Science of the U.S. Department of Energy, the U.S. National Science Foundation, the Bundesministerium fuer Bildung und Forschung of Germany, the Insitut National de la Physique Nucleaire et de la Physique des Particules of France, the United Kingdom Engineering and Physical Sciences Research Council, and the Russian Ministry of Science and Technology.

References

1. J.C. Collins and M.J. Perry, Phys. Rev. Lett. 34, 1353 (1975); G. Chapline and L. Susskind, Phys. Rev. D 20, 2610 (1979).
2. Conceptual Design of the Relativistic Heavy Ion Collider (Report BNL 52195, 1989).
3. see Nucl. Phys. A661 (1999) and references therein.
4. Conceptual Design Report for the Solenoidal Tracker At RHIC, The STAR Collaboration, PUB-5347 (1992); J.W. Harris et al, Nucl. Phys. A 566, 277c (1994).
5. PHENIX Experiment at RHIC - Preliminary Conceptual Design Report, PHENIX Collaboration Report (1992).
6. Interim Design Report for the BRAHMS Experiment at RHIC, BNL Report, (1994).
7. RHIC Letter of Intent to Study Very Low pt Phenomena at RHIC, PHOBOS Collaboration (1991).
8. Proposal on Spin Physics Using the RHIC Polarized Collider, RHIC Spin Collaboration (1992).
9. S. Klein and E. Scannapieco in Proceedings on Intersections Between Particle and Nuclear Physics: 6th Conference, ed. T.W. Donnelly, LBNL Report LBNL-40495, (AIP Press, 1997); J. Nystrand and S. Klein in Proceedings of Hadron '97, (LBNL Report LBNL-41111, BNL, 1997).

10. A Ring Imaging Cherenkov Detector for STAR, STARnote 349, STAR/ALICE RICH Collaboration (1998); ALICE Collaboration, Technical Design and Report, Detector for High Momentum PID, CERN/LHCC 98-19.
11. C. Adler, A. Denisov, E. Garcia, M. Murray, H. Stroebele, and S. White, pre-print nucl-ex/0008005 (2000).
12. L. Ahle et al (E802 Collaboration), Phys. Rev. Lett. 81 (1998) 2650.
13. F. Sikler et al (NA49 Collaboration), Nucl. Phys. A661 (1999) 45c.
14. X. N. Wang and M. Gyulassy, Phys. Rev. D44 (1991) 3501; Comput. Phys. Commun. 83 (1994) 307; and private communication.
15. H. Appelhaeuser et al., Phys. Rev. Lett. 82 (1999) 2471.
16. C. Albajar et al., Nucl. Phys. B355 (1990) 261.
17. B.B. Back et al., Phys. Rev. Lett. 85 (2000) 3100.
18. J. Rafelski and B. Müller, Phys. Rev. Lett. 48, 1066 (1982). [Erratum: *ibid.* 56, 2334 (1986).]
19. J. Rafelski, Phys. Rep. 88, 331 (1982).
20. P. Koch, B. Müller and J. Rafelski, Phys. Rep. 142, 167 (1986).
21. K.H, Ackermann et al (STAR Collaboration), Phys. Rev. Lett. 86 (2001) 402.
22. P.F. Kolb, J. Sollfrank, and U. Heinz, pre-print hep-ph/0006129 v2 (2000).
23. B. Zhang, M. Gyulassy, C.M. Ko, Phys. Lett. B455 (1999) 45.
24. J. Barrette et al (E877 Collaboration), Phys. Rev. C55 (1997) 1420.
25. A.M. Poskanzer and S.A. Voloshin for the NA49 Collaboration, Nucl. Phys. A661 (1999) 341c.
26. S. Pratt, Phys. Rev. D **33**, 1314 (1986); G. Bertsch, M. Gong and M. Tohyama, Phys. Rev. C **37**, 1896 (1988); and G. Bertsch, Nucl. Phys. A **498**, 151c (1989).
27. S. Pratt et al., Phys. Rev. C42 (1990) 2646.
28. D. H. Rischke, Nucl. Phys. A610 (1996) 88c; D.H. Rischke and M. Gyulassy, Nucl. Phys. A608 (1996) 479.
29. M. Gyulassy and M. Pluemmer, Phys. Lett. B 243, 432 (1990)2; X.N. Wang and M. Gyulassy, Phys. Rev. Lett. 68, 1480 (1992).

Grazyna Odyniec

Was a New Phase of Nuclear Matter Observed at CERN SPS ...?

G.Odyniec [a]

[a]Nuclear Science Division, Lawrence Berkeley National Laboratory,
Berkeley, CA 94720, USA

The enhanced production of strange particles, that was predicted as a consequence of the formation of quark-gluon plasma, was observed in CERN SPS heavy ion experiments. As data matured, the emphasis on theory and interpretation of experimental results has increased. In this presentation the hadronic yields and their ratios, as well as the role of strangeness production in the search for a new phase of matter, in both experiment and theory, are discussed.

1. Introduction

The search for the quark-gluon plasma in man-made collisions was motivated by results of lattice-QCD calculations which show the disappearance of the hadronic phase of matter once the energy density exceeds a critical value of $\sim$ 1 to 1.5 GeV/fm^3. In its place a new, partially deconfined QCD state, governed by the rules of elementary collisions between quarks and gluons, is supposed to be formed [1,2]. To make a quark-gluon plasma in the laboratory it is necessary to collide two nuclei head on (e.g. RHIC collider experiments), or to direct a high-energy nuclear beam at a solid target (like SPS, AGS fixed target experiments). The challenge is to achieve the high enough energy density over a large volume and perhaps more dificult, to have reliable methods of identifying and probing the resulting quark-gluon plasma.The direct comparison between experiment and theory is neither simple nor straightforward due to number of reasons, both theoretical and experimental. On the theory side one needs to remember that basic assumptions of QCD are not fully satisfied by the experiment. Whereas the majority of experimental difficulties arise from the fact that detectors look at the collisions after freeze-out.

2. Strangeness at CERN

The first results from the CERN Pb+Pb collisions at the top SPS energy of 158 GeV/c per nucleon demonstrated [3] that the average energy density, calculated within Bjorken formulation, significantly exceeds ($\sim$2-3 times) the lattice QCD estimated critical value, thus satisfying the prerequisite conditions needed for the QGP formation. And, indeed, the early measurements of strangeness and J/ψ production show that the experimental data do not allow for the the interpretation within the hadronic scenario [4]. The J/ψ suppression is discussed broadly elsewhere (*e.g.*[5,6]). This paper's emphasis is on strangeness.

Strangeness, in general, is very interesting. There is no strangeness in the initial state of the collision - the strangeness (which is created during the collision) thus provides information on the reaction dynamics. Moreover, it presents a link between the partonic and the hadronic phase because the signal interpolates. Most interestingly, strangeness is expected to serve as a distinct observable of QGP formation [7,8]. The lower threshold for $s\bar{s}$ pair production in QGP, compare to the hadron gas, favors strangeness production. The abundant presence of gluons in the plasma is a source of additional strangeness productions via $gg \rightarrow s\bar{s}$. Due to Pauli blocking, at large baryon density production of $s\bar{s}$ might be favored if lowest available u, d quark energy levels are larger than $2m_s$. Finally, the equilibration time in plasma is much shorter (and comparable to the time needed for two colliding nuclei to traverse each other at this energy) than in hadronic gas (~20-30 times).

If plasma is created, the yields of multi-strange baryons will be particularly sensitive to the density of s (and $\bar{s}$) quarks. In hadronic processes the suppression of strange particle production increases with the growth of strangeness content (strongly affecting Ξs and Ωs), while in the QGP scenario they can be easily created due to copious production of strange quark pairs from gluons. Consequently, an unusually high yield of multi-strange hyperons (compared to the ones observed in elementary collisions) is very much expected in the plasma scenario.

The very first measurement of strangeness enhancement at SPS' top energy ($\sqrt{s} = 17$ GeV) came from the NA35 experiment (S+S, S+Ag collisions) [28,29], and it was limited to strange particle yields (Λ, $\bar{\Lambda}$,K^0) with |S=1|. It was anticipated that some discontinuity between pp, pA and central AA collisions, would show up and, indeed, data demonstrated this behavior. Fig. 1 shows K/π ratio for pp, pA and AA collisions as a function of the number of participants (~ centrality). Note, that kaons account for about 70% of overall strangeness production. The enhancement in K/π from pp, pA to AA is very distinct (factor ~2). More interestingly, strangeness/entropy ratio stays the same for all three systems (S+S, S+Ag and Pb+Pb). This suggests that the system reached some kind of saturation in the s and $\bar{s}$ quarks yields already in S+S reaction. This seems to rule out the possible interpretation of strangeness enhancement as a consequence of hadronic re-interactions. For a detailed discussion see [9]. The generalization of K/π study to the global analysis of strange to non-strange quarks in central Pb+Pb, S+Ag and S+S in SPS and p+p, p+A, e^+e^-, and $p + \bar{p}$ [10] confirmed the results presented in Fig.1.

3. Multi-Strange Hyperons

While the AGS strangeness production can be understood in terms of independent nucleon-nucleon collisions and hadronic re-interactions, this is not the case at the SPS [9]. The precise measurements of strange hyperons and their anti-particles reveal a systematic increase with respect to p+Pb (Λ, Ξ, Ω - WA97 data [30,31]) and with respect to p+p (Ξ - NA49 data [25]). The excess is larger for particles of higher strangeness content, becoming most dramatic for $\Omega+\bar{\Omega}$ (up to factor ~ 20). Figure 2 shows WA97 data [11] on particle yields expressed in units of the corresponding yields per p+Pb in four centrality bins of Pb+Pb collisions. The solid line drawn through the p+Pb point and proportional to the number of participants (N^G_{part}) estimated using multiplicity measurements and the Glauber

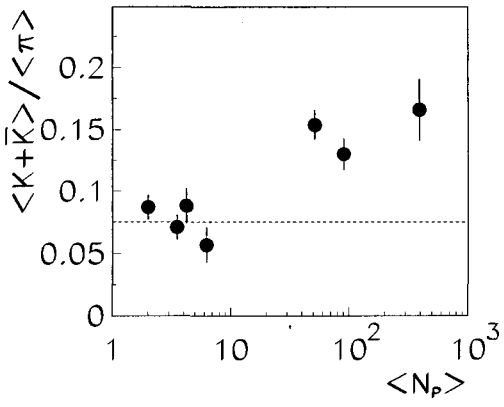

Figure 1. Multiplicity ratio $\langle K+\bar{K}\rangle/\langle\pi^-\rangle$ in full phase space for pp, pA and AA collisions plotted versus the average number of participating nucleons.

model, increases from p+Pb to Pb+Pb. The dashed lines represent linear fits ($\sim N_{part}^{\beta}$) to the experimental points. Values of exponent β, plotted on the right side, are consistent with 1. All Pb+Pb points (negative particles, $\Lambda+\bar{\Lambda}$, $\Xi+\bar{\Xi}$ and $\Omega+\bar{\Omega}$) lie above the solid line, suggesting a presence of centrality range where yields grow faster than linear with N_{part}^{G} somewhere between the p+Pb and the Pb+Pb points. With the centralities covered by WA97 acceptance the yields per participant are already quite constant which implies a proportionality to the volume, mainly. This hints that all the reported enhancements saturate at some value of N_{part}^{G} below the lower limit of the covered centrality interval, and that the mechanism responsible for the strangeness enhancement in Pb+Pb collisions may be independent of the centrality when the number of participants exceeds 100. It is clearly important to explore the smaller systems and/or more peripheral collisions as well as lower energies to determine where this effect sets in. If the result survives further detailed investigations - it will become a very strong evidence of strangeness saturation phenomenon as discussed in the previous chapter. In contrast, the non-strange yields per participant exhibit only a minor increase (π/N_{part} and $(\rho+\omega)/N_{part}$ by ~ 20 %, $\bar{p}/N_{part} \approx$ const).

Note, that negative particle yields for all centrality intervals are significantly above the "pA line", what is expected for QGP formation models due to the increase of the number of degrees of freedom in the plasma phase [12].

In summary, the CERN SPS heavy ion data on strangeness production demonstrates that the system of hadronic yield ratios undergoes a dramatic change when going from p+p, p+A to central Pb+Pb. The changeover occurs at the semi-central Pb+Pb collisions and below the central S+A. However, the experimental data on S+A is less comprehensive. This concludes the experimental part of this paper. The following chapters will dwell on

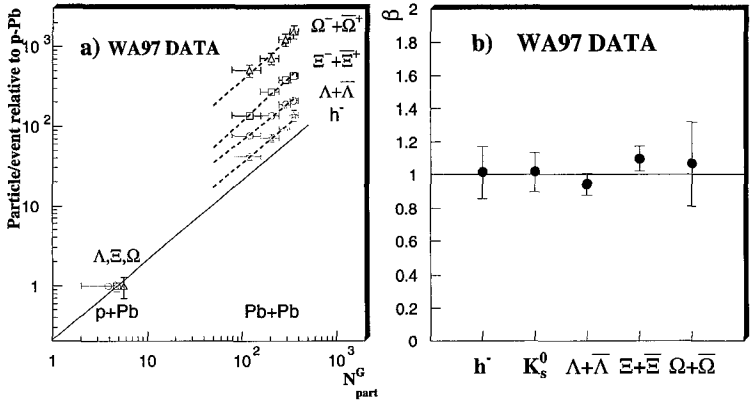

Figure 2. a) The h^-, Λ, Ξ, and Ω yields in Pb+Pb collisions expressed in units of yields observed in p+Pb as a function of number of participants for WA97 data. b) The fitted values of the exponent β.

the possible interpretation of these extremely interesting and intriguing results and how they influenced our basic understanding of primordial conditions of parton to hadron phase transition (the critical temperature and energy density estimates, and most importantly, the flavor composition at the end of the partonic phase).

4. Useful Lesson from LEP

To understand the above data, it might be helpful to make a short detour to the high energy physics territory.

Analysis of hadron production in LEP experiments ($e^+e^- \rightarrow Z^0 \rightarrow$ hadrons at $\sqrt{s}$=91 GeV) with partonic transport model VNI, based on perturbative QCD, has shown a remarkable lack of sensitivity to the details of assumed non-perturbative hadronization scenario (Geiger at al. [13]). It appears that the statistical phase space weights overwhelm all other macroscopic influences. The final state multi-hadronic population, thus, represents the most probable maximum entropy stage. Note, that this excellent agreement with the data (up to hyperons) was obtained without including re-scattering. A similar conclusion was reached using hadro-chemical equilibrium models of Hagedorn type e.g. Becattini et al.[14] describes successfully the the same very broad range of LEP data (including all 25 species from π to Ω) over four orders of magnitude. Since there is essentially no hadronic re-scattering in e^+e^- collisions, the apparent equilibrium state can not result from interactions between a couple of tenths of hadrons in the event, but it came "from above", i.e., from higher energy density prevailing at the onset of hadronization at the critical energy density.

Both types of models were extended to the SPS energy with similar results. The

partonic transport model VNI, after modifications appropriate for very heavy systems [15], was able to fit well the NA49 data (p, K and π yields and rapidity distributions) without any consideration of secondary hadronic cascading. The dominant fraction of the hadron yields (near midrapidity) did indeed originate, according to VNI, from parton to hadron phase transition.

The hadro-chemical (thermal) models (Becattini et al.[16] and Braun-Munzinger et al.[17]) reflect the differences between e^+e^- and Pb+Pb in their proper parameters, particularly the chemical potential μ_B ($\approx$0 in e^+e^-) became significant in the larger system. While both calculations are grand canonical based, they differ significantly in their treatment of the excluded volume, and in their specific approach to the strangeness saturation. In both cases there is a rather good agreement with the data, however both models use different data sets to compare with. Temperatures obtained in both calculations are very similar to each other (Becattini: T=176 $\pm$9 MeV, Braun-Munzinger: T=168$\pm$2.4 MeV) and to T_{e+e-}=165 MeV. Thus, contrary to the expectations, the large Pb+Pb hadronic system did not "cool" the hadronic population. The SPS data totally eliminated the scenario of hadronic re-scattering as a plausible reason of final state termalization. The state created at hadronization stays essentially unchanged through the entire post interaction space-time evolution of the system until its arrival at the detectors. This explains why S+S, S+Ag and Pb+Pb ratios of "strange to non-strange" remains the same for all three systems (see Fig.1 and discussion in Chapter 2).

Taking for granted such indications of the "order from above" (resulting from the explosive character of the expansion) allows us to interpret the observed hadronic yields as the one established at the critical point of hadronization, and they therefore serve as a messenger from the close of partonic phase.

However, one needs to be careful when relying on the interpretation within thermal models alone since their assumption are usually not fully satisfied by the experimental data. For the discussion - see[18].

5. More on Models ...

Recently, Dumitru [19] and Bass[20] proposed a new approach combining hydrodynamical description which is the most accurate for the very dense (close to equilibrium) systems with a microscopic transport model which is well suited to study the more diluted space-time regions of the collision. They assume formation of QGP which expands as an ideal relativistic fluid and goes through a mixed phase where it coexists with hadronic matter. After hadronization, the system evolution is followed with an UrQMD model formalism [21] until it completely freezes-out. Figure 3 (taken from [19]) compares the m_T spectra on the hadronization hypersurface (thin lines) and those of freeze-out (thick lines) with the experimental points. The squares and diamonds represent the WA97 and NA49 data, respectively. Consistent with our previous conclusion, the spectra of Ω's and Ξ's with $m_T \geq$1.6 GeV are practically unaffected by the hadronic stage and closely resemble those at hadronization. This is due to the fact that the scattering rates for Ξ and Ω in a pion-rich hadron gas are very small. On average the baryons which finally emerge as Ξ's and Ω's suffer even less interactions than the final-state $\bar{p}$'s and $\bar{\Lambda}$'s (so called "early freeze-out" [22]). Within this model the hadronic gas emerging from the hadronization of QGP is

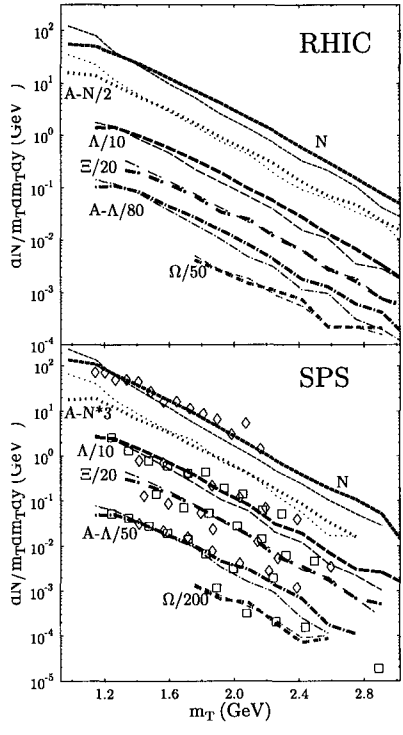

Figure 3. Transverse mass spectra of N, $\bar{N}$, Λ, Ξ, and Ω at $y_{c.m.}$=0 in central Pb+Pb collisions at SPS (lower panel) and Au+Au at RHIC (upper panel). For description see text.

"transparent" for the multi-strange hyperons and therefore it is reasonable to assume that these particles deliver unaltered information about the conditions on the hadronization hypersurface. Note, that the contribution from the re-scattering significantly increases the transverse flow of Λ's and N's.

The inverse slope analysis [23] revealed the "departure" of Ω's from the linear increase of T with the hadron mass which would result if all hadrons freeze-out simultaneously from the common radial velocity field. This provided a prospect of determining the transverse flow associated directly with the stage of primordial hadrosynthesis, at which the true temperature is $\sim$ 170-180 MeV. The observed temperature parameter T_Ω=230 MeV would then give an estimate of the "primordial flow" from the partonic phase, amounting to $\beta = 0.27$ [24].

6. Φ Mesons

Next to Ω, the Φ meson, which contains a strange and a non-strange quark, would be the most interesting in this regard. However, the NA49 and NA50 (the only two CERN experiments which could address Φ meson production) report significant discrepancy in measured m_T slope. The NA49 number T=305±15 MeV [32,26] is consistent with the overall systematics leaving Ω alone in the category of outliers, whereas the NA50 number, T=225±6 MeV [27], is significantly bellow the studied systematics, which might mean that both Ω and Φ decouple earlier. Differences in the experimental procedure, analysis, and in the decay channels (leptons in case of NA50 and kaons in NA49) cannot account for this discrepancy. Hopefully, the new high statistics CERN experiment NA6i will resolve this ambiguity soon.

Very interestingly, the NA49 4π integrated Φ yields are the same as the corresponding 4π integrated Ξ yields, about 8 per central Pb+Pb collision; whereas the $\langle\Phi\rangle/\langle\pi\rangle$ ratio changes between pp and Pb+Pb by factor of 2.8. Note, that for double strange Ξ hyperons an enhancement factor of about one order of magnitude was reported when comparing p+p with the central Pb+Pb collisions [25].

7. Summary and What Next ?

While there is still ultimate hope that a definite conclusion on the formation of QGP will eventually emerge from the analysis of direct lepton signals, the strangeness results already now point well beyond the hadronic scenario.

The discussed above dramatic change (enhancement) with respect to pp and pA in strangeness production in the central A+A collisions resulted from two independent analysis performed by two, very different CERN heavy ion experiments: WA97/NA57 and NA49. The reported changeover occurs below the central Pb+Pb and S+A collisions, probably in Pb+Pb peripheral reactions. The enhancement increases with the strangeness content reaching a factor of about 10-20 for multi-strange hyperons. Moreover, the strangeness enhancement appears to be the same for the light (S+S), medium (S+A) and heavy (Pb+Pb) colliding system. The observed saturation, expressed, e.g. by the strangeness suppression factor λ_s [10], may imply a scenario in which quark flavor is already saturated in the pre-hadronic phase of collision for both light and heavy systems. Assuming that the hadronization process preserve this information, one would indeed expect similar values of strangeness suppression factor λ_s in the hadronic phase. Interestingly enough, it appears that secondary hadron scattering, expected to be much more abundant in Pb+Pb collisions, is of minor importance for the strangeness production.

Note that contrary to the NA50 findings which seem to indicate possible QGP formation only in Pb+Pb collisions, strangeness production (NA49) suggests that the flavor equilibrium in the partonic phase takes place already in the light system of S+S.

Further measurements are urgently needed to understand the strangeness evolution from pp/p+A to central the A+A collisions. The data on strangeness production as a function of centrality (in range of number of participants, from a few to a 100) would likely pin down some kind of critical point. The answer to the fundamental question regarding phase transition is close, but not yet in hand.

So far there is no real theory of strangeness production at these energies. A number of

models applied to some aspects of strangeness suggest that the strangeness content in the final state of A+A is in agreement with that calculated for the equilibrated partonic system. Moreover, the multi-strange hyperons were shown to provide direct information on the hadronization stage of collision; there seems to be no rearrangement after hadronization. Whether it is the only plausible interpretation, and whether this interpretation will survive a confrontation with the newly acquired data at 40 GeV/c (and possible in the future, at 80 GeV/c) remains to be seen. Clearly, further theoretical work is needed to understand the observed results on strangeness production at CERN SPS.

The additional information, of fundamental importance, will become available shortly from the RHIC collider experiments running at much higher effective collision energies, where the symmetry between quark and antiquark production should be considerably better then at the SPS. These new experimental results, will be in a position to confirm the existance of quark deconfinment and disclose the properties of quark-gluon plasma.

REFERENCES

1. A.Ukawa, Nucl.Phys. A638 (1998) 339c.
2. E.Laermann, Nucl.Phys. A610 (1996) 1c. Phase Separation in Glass, North-Holland, Amsterdam, 1984.
3. T.Albert et al., Phys.Rev.Lett. 75 (1995) 3814.
4. e.g. Quark Matter 99 Conf. Proc., Nucl.Phys. A661 (1999).
5. C.Cicalo et al., Nucl.Phys. A661 (1999) 93c.
6. H.Satz, Nucl.Phys. A661 (1999) 104c.
7. J.Rafelski, B.Müller, Phys.Rev.Lett. 48 (1982) 1066.
8. P.Koch, B.Müller, J.Rafelski, Phys.Rep. 142 (1986) 165.
9. G.Odyniec, Nucl.Phys. A638 (1998) 135c.
10. F.Beccatini, M.Gazdzicki, J.Sollfrank, Nucl.Phys. A638 (1998) 403c.
11. F.Antinori et al., Eur.Phys.J. C11 (1999) 79.
12. M.Gazdzicki, M.I.Gorenstein, Acta Phys. Polon. B30 (1999) 2705 and references therein.
13. J.Ellis, K.Geiger, Phys.Rev. D54 (1996) 1967.
14. F.Becattini, Z.Phys. C69 (1996) 485.
15. K.Geiger, D.K.Srivastava, Phys.Rev. C56 (1997) 2718.
16. F.Becattini, M.Gazdzicki, J.Sollfrank, Euro.Phys. J.C1 (1998) 143.
17. P.Braun-Munzinger, I Heppe, J.Stachel, Nucl.Phys. A638 (1998) 3c, nucl-th/9903010v2.
18. U.Heinz Nucl.Phys. A661 (1999) 140c.
19. A.Dumitru et al., nucl-th/9901046v2.
20. S.A.Bass and A.Dumitru, nucl-th/0001033.
21. S.A.Bass et al., Prog.Part.Nucl.Phys. 41, 225 (1998).
22. H.van Hecke, H.Sorge, N.Xu, Phys.Rev.Lett. 81 (1998) 5798.
23. Quark Matter 97 Conference Proc., Nucl.Phys. A638 (1998).
24. R.Stock, Nucl.Phys. A661 (1999) 282c.
25. H.Appelshauser et al., Phys.Lett. B444 (1998) 523.
26. C.Hohne and the NA49 Coll., Nucl.Phys. A661 (1999) 485c.

27. N.Willis and the NA50 Coll., Nucl. Phys. A661 (1999) 534c.
28. M.Gazdzicki and the NA35 Coll., Nucl. Phys. A498 (1989) 375c.
29. A.Bamberger et al., Nucl.Phys. A498 (1989) 133c.
30. R.A.Fini and the WA97 Coll., Nucl.Phys.A - in print.
31. T.Virgili and the NA57 Coll., Nucl.Phys.A - in print.
32. J.Bachler et al., Phys.Lett. B - in print.

Angela V. Olinto

The Origin of the Highest Energy Cosmic Rays

A. V. OLINTO
Department of Astronomy & Astrophysics,
& Enrico Fermi Institute,
The University of Chicago, Chicago, IL 60637, USA
E-mail: olinto@oddjob.uchicago.edu

Contrary to expectations, several cosmic ray events with energies above 10^{20} eV have been observed. The flux of such events is well above the predicted Greisen-Zatsepin-Kuzmin cutoff due to the pion production (via the Δ resonace) of extragalactic cosmic ray protons off the cosmic microwave background. In addition to the relatively high flux of events, the isotropic distribution of arrival directions and an indication of hadronic primaries strongly challenge all models proposed to resolve this puzzle. Models based on astrophysical accelerators need to invoke strong Galactic and extragalactic magnetic fields with specific properties which are yet to be observed, while models based on physics beyond the standard model of particle physics generally predict photon primaries contrary to experimental indications. The resolution of this puzzle awaits a significant increase in the data at these energies which will be provided by future experiments.

1 Introduction

The role of cosmic rays in the discovery of fundamental properties of nature dates back to the early 1900's. Over the last century, Brazilian physicists have actively contributed to these discoveries with the most notable example of Prof. Cesar Lattes and the discovery of the π meson decay in Chacaltaya.[1] After a century of direct and indirect cosmic ray detections, the data now spans 12 orders of magnitude in energy and about 32 in flux as shown in Figure 1.[2] A strikingly simple power law spectrum over these many decades in energy is observed: up to energies $\sim 10^{15}$ eV the spectrum is $J(E) \propto E^{-\gamma}$ with $\gamma \simeq 2.7$ and becomes steeper for higher energies, $\gamma \simeq 3$. Most of these cosmic rays are believed to be accelerated in Galactic Supernovae shocks via Fermi acceleration and to propagate diffusively in Galactic magnetic fields. This hypothesis is yet to be confirmed from direct observations of Supernova remnants. In addition, the energetic requirements at the highest energies call for alternative sources which are expected to originate from extragalactic sources since proton Larmor radii become larger than Galactic dimensions at these extreme energies.

Once extragalactic sources of protons are considered, their spectrum should not continue as a simple power law due to the effect of the cosmic background radiation along their path. In the rest frame of 10^{20} eV protons the cosmic microwave background corresponds to gamma rays with energies above the Δ

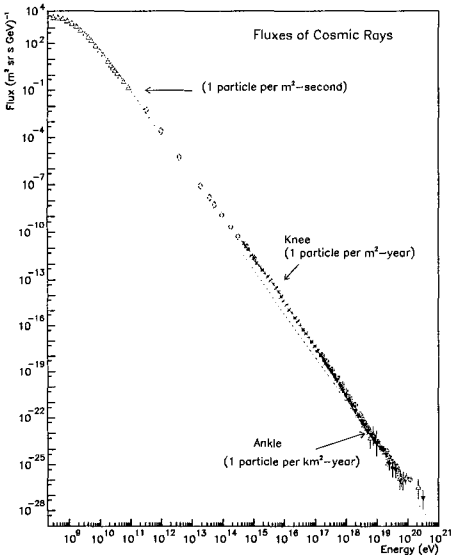

Figure 1: *Cosmic ray spectrum compiled by S. Swordy [2].*

resonance. Once protons reach these energies, they lose energy very efficiently through the production of pions. As ultra-high energy protons travel across intergalactic space, the pion photo-production process off the cosmic microwave background quickly reduces their energy to below $\sim 7 \times 10^{19}$ eV as seen in Figure 2.[3] If protons of 10^{20} eV are observed, their sources are limited to distances of less than about 50 Mpc from Earth. This threshold energy loss process should introduce a clear feature and a cutoff around $\sim 10^{19-20}$ eV in the spectrum of extragalactic protons even if the injection spectrum at the source is a power law. This photopion production gives rise to the well-known Greisen-Zatsepin-Kuzmin[4] (GZK) cutoff which is shown in Figure 3 by the dashed line for a uniform distribution of sources.

Figure 3[5] shows the expected spectrum (flux multiplied by E^3 versus energy) for extragalactic proton sources (dashed line) and the flux observed by the Akeno Giant Air Shower Array (AGASA). AGASA has accumulated many hundreds of events (728) with energies above 10^{19} eV and 8 events above 10^{20} eV.[5] As can be seen from the figure, the data shows no indication of a cutoff. This surprise has triggered considerable interest and the proposal of a number of exotic scenarios designed to explain these data. In addition to the ultra-

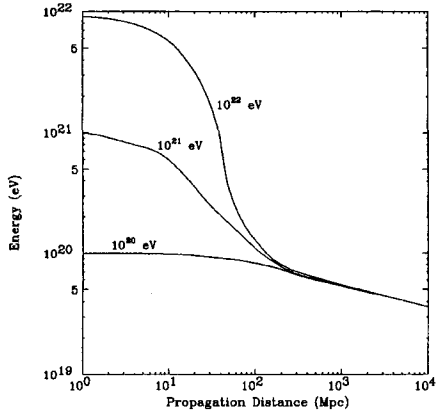

Figure 2: *Proton energy vs. propagation distance through the 2.7-K cosmic background radiation for the indicated initial energies from [2].*

high energy events detected by AGASA, other experiments such as Fly's Eye, Haverah Park, Yakutsk, and Volcano Ranch, have reported a number of events at the highest energies (see, e.g., [6] for reviews).

These observations are surprising because not only the propagation of particles at these energies is prone to large energy losses, but the energy requirements for astrophysical sources to accelerate particles to $> 10^{20}$ eV are extraordinary. Different primaries do not ease the difficulty. Ultra-high energy nuclei are photodisintegrated on shorter distances due to the infrared background [7] while the radio background constrains photons to originate from even closer systems.[8]

The shape of the GZK cutoff depends on the source input spectrum and the distribution of sources in space as well as in the intergalactic magnetic field. In Figure 4, we contrast the flux observed by AGASA with a monte-carlo of the expected flux for proton sources distributed homogeneously (shaded region) or distributed like galaxies (hatched region) with injection spectrum $J(E) \propto E^{-\gamma}$ and $\gamma = 3$.[9] We modeled the distribution of ultra-high energy cosmic ray (UHECR) sources by using the galaxy distribution measured by the recent IRAS redshift survey know as PSCz.[10] As can be seen from the figure, even allowing for the local overdensity the observations are consistently above the theoretical expectation. In fact, when we normalize our simulations by requiring that the number of events with $E \geq 10^{19}$ eV equals the AGASA observations (728), we find that the number of expected events for $E \geq 10^{20}$

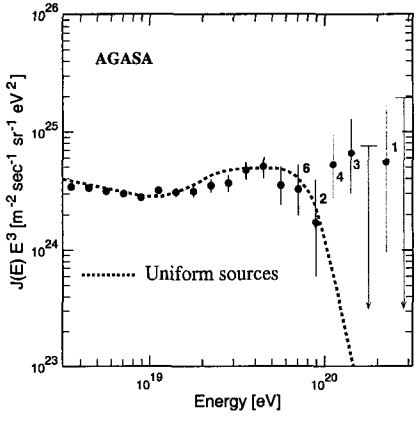

Figure 3: $E^3J(E)$ *versus* E *observed by AGASA and expected flux for a uniform extragalactic source distribution [4].*

eV is only 1.2 ± 1.0 for the PSCz case, i.e., "6 σ" away from the observed 8 events.

The gap between observed flux and model predictions narrows as the injection spectrum of the UHECR sources becomes much harder than $\gamma = 3$. For $\gamma = 2.1$ (shown in Figure 3), the number of expected events above 10^{20} eV reaches 3.3 ± 1.6 for a homogeneous distribution while for the PSCz catalog it is 3.7 ± 2.0. This trend can be seen also in Figure 6, where mean fluxes for $\gamma = 1.5, 2.1$ and 2.7 are shown.

In addition to the presence of events past the GZK cutoff, there has been no clear counterparts identified in the arrival direction of the highest energy events. If these events are protons or photons, these observations should be astronomical, i.e., their arrival directions should be the angular position of sources. At these high energies the Galactic and extragalactic magnetic fields should not affect proton orbits significantly so that even protons would point back to their sources within a few degrees. Protons at 10^{20} eV propagate mainly in straight lines as they traverse the Galaxy since their gyroradii are $\sim$ 100 kpc in μG fields which is typical in the Galactic disk. Extragalactic fields are expected to be $\ll \mu$G,[11,12] and induce at most $\sim 1^o$ deviation from the source. Even if the Local Supercluster has relatively strong fields, the highest energy events may deviate at most $\sim 10^o$.[13,14] At present, no correlations between arrival directions and plausible optical counterparts such as sources in the Galactic plane, the Local Group, or the Local Supercluster have been

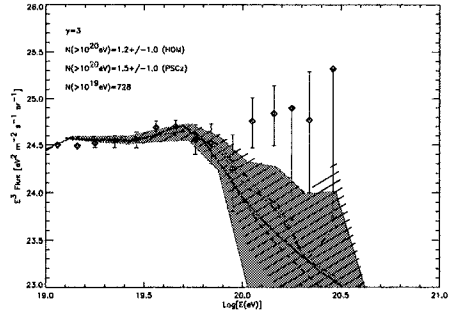

Figure 4: *Simulated fluxes for the AGASA statistics of 728 events above* 10^{19} *eV, and* $\gamma = 3$, *using a homogeneous source distribution (\ hatches) and the PSCz distribution (dense / hatches). The solid and dashed lines are the results of the analytical calculations for the same two cases. The dash-dotted and dash-dot-dot-dotted lines trace the mean simulated fluxes for the homogeneous and the PSCz cases. (see [9]).*

clearly identified. Ultra high energy cosmic ray data are consistent with an isotropic distribution of sources in sharp contrast to the anisotropic distribution of light within 50 Mpc from Earth.

The absence of a GZK cutoff and the isotropy of arrival directions are two of the many challenges that models for the origin of UHECRs face. This is an exciting open field, with many scenarios being proposed but no clear resolution. Not only the origin of these particles may be due to physics beyond the standard model of particle physics, but their existence can be used to constrain extensions of the standard model such as violations of Lorentz invariance.[15]

In the next section, we discuss the issues involved in the propagation of UHECRs from source to Earth. We then summarize the astrophysical Zevatron proposals followed by the models that involve new physics. To conclude, future observational tests of UHECR models and their implications are discussed. Fore recent reviews see [16-19].

2 Propagation - Losses and Magnetic Fields

Before contrasting plausible candidates for UHECR sources with the observed spectrum and arrival direction distribution, we discuss the effects of propagation from source to Earth. Propagation studies involve both the study of losses along the primaries' path, such as the photopion production responsible for the GZK cutoff, as well as the structure and magnitude of cosmic magnetic fields that determine the trajectories of charged primaries and influence the

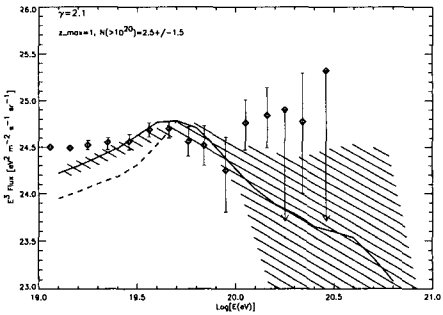

Figure 5: *Simulated fluxes for the AGASA statistics of 728 events above* 10^{19} *eV, and* $\gamma = 2.1$, *using a homogeneous source distribution with* $z_{max} = 0.1$ *(/ hatches), the PSCz distribution with* $z_{max} = 0.1$ *(horizontal hatches), and a homogeneous source distribution with* $z_{max} = 1$ *(\ hatches) (see [9]).*

development of the associated electromagnetic cascade.[20]

For primary protons the main loss processes are photopion production off the CMB that gives rise to the GZK cutoff[4] and pair production.[21] For straight line propagation, the cutoff should be present at $\sim 5 \times 10^{19}$ eV and a significant number of hard sources should be located within $\sim$ 50 Mpc from us. As we discussed above, even with the small number of accumulated events at the highest energies, the AGASA spectrum is incompatible with a GZK cutoff for a homogeneous extragalactic source distribution. The shape of the cutoff can be modified if the distribution of sources is not homogeneous[9,22,23] and if the particle trajectories are not rectilinear (e.g., the case of sizeable intergalactic magnetic fields).[24–28,14]

Charged particles of energies up to 10^{20} eV can be deflected significantly in cosmic magnetic fields. In a constant magnetic field of strength $B = B_6 \mu$G, particles of energy $E = E_{20} 10^{20}$eV and charge Ze have Larmor radii of $r_L \simeq$ 110 kpc $(E_{20}/B_6 Z)$. If the UHECR primaries are protons, only large scale intergalactic magnetic fields affect their propagation significantly unless the Galactic halo has extended fields.[25] For higher Z, the Galactic magnetic field can strongly affect the trajectories of primaries.[29,30]

Whereas Galactic magnetic fields are reasonably well studied, extragalactic fields are still very ill understood.[11] Faraday rotation measures show large magnitude fields ($\gtrsim \mu$G) in the central regions of clusters of galaxies. In regions between clusters, the presence of magnetic fields is evidenced by synchrotron emission but the strength and structure are yet to be determined. On the largest scales, limits can be imposed by the observed isotropy of the CMB

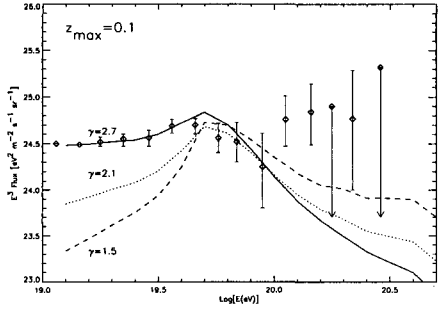

Figure 6: *Propagated spectrum for source spectral index of* γ *= 1.5, 2.1, 2.7.*

and by a statistical interpretation of Faraday rotation measures of light from distant quasars. The isotropy of the CMB can constrain the present horizon scale fields $B_{H_0^{-1}} \lesssim 3 \times 10^{-9}$ G.[31] Although the distribution of Faraday rotation measures have large non-gaussian tails, a reasonable limit can be derived using the median of the distribution in an inhomogeneous universe: for fields assumed to be constant on the present horizon scale, $B_{H_0^{-1}} \lesssim 10^{-9}$ G; for fields with 50 Mpc coherence length, $B_{50\mathrm{Mpc}} \lesssim 6 \times 10^{-9}$ G; while for 1 Mpc coherence length, $B_{Mpc} \lesssim 10^{-8}$ G.[12] These limits apply to a $\Omega_b h^2 = 0.02$ universe and use quasars up to redshift $z = 2.5$. Local structures can have fields above these upper limits as long as they are not common along random lines of site between $z = 0$ and 2.5.[13,12]

Of particular interest is the field in the local 10 Mpc volume around us. If the Local Supercluster has fields of about 10^{-8} G or larger, the propagation of ultra high energy protons could become diffusive and the spectrum and angular distribution at the highest energies would be significantly modified.[13,28,32] For example, in Figure 7,[28] a source with spectral index $\gamma \gtrsim 2$ that can reach $E_{max} \gtrsim 10^{20}$ eV is constrained by the overproduction of lower energy events around 1 to 10 EeV (EeV $\equiv 10^{18}$ eV). Furthermore, the structure and magnitude of magnetic fields in the Galactic halo[25,30] or in a possible Galactic wind can also affect the observed UHECRs. In particular, if our Galaxy has a strong magnetized wind, what appears to be an isotropic distribution in arrival directions may have originated on a small region of the sky such as the Virgo cluster.[33] In the future, as sources of UHECRs are identified, large scale magnetic fields will be better constrained.[34]

If cosmic rays are heavier nuclei, the attenuation length is shorter than that for protons due to photodisintegration on the infrared background.[7] However,

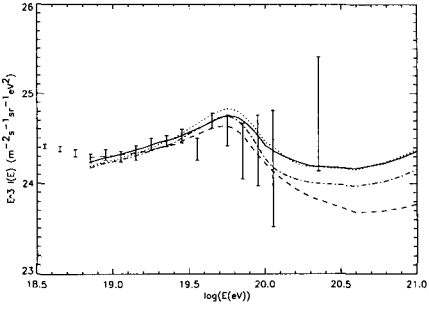

Figure 7: Flux vs. Energy with $E_{max} = 10^{21}$ eV at source. Choices of source distance r(Mpc), spectral index γ, proton luminosity L_p(erg/s), and LSC field B(μG) are: solid line (13 Mpc, 2.1, 2.2×10^{43} erg/s, 0.05 μG); dotted line (10 Mpc, 2.1, 10^{43} erg/s, 0.1 μG); dashed line (10 Mpc, 2.4, 3.2×10^{43} erg/s, 0.1 μG); and dashed-dotted line (17 Mpc, 2.1, 3.3×10^{43} erg/s, 0.05 μG).

UHE nuclei may be of Galactic origin. For large enough charge, the trajectories of UHE nuclei are significantly affected by the Galactic magnetic field[30] such that a Galactic origin can appear isotropic.[29] The magnetically induced distortion of the flux map of UHE events can give rise to some higher flux regions where caustics form and some much lower flux regions (blind spots).[30] Such propagation effects are one of the reasons why full-sky coverage is necessary for resolving the UHECR puzzle.

The trajectories of photon primaries are not affected by magnetic fields, but energy losses due to the radio background constrain photons to originate from systems at $\lesssim$10 Mpc.[35] If associated with luminous systems, sources of UHE photons should point back to their nearby sources. The lack of counterpart identifications suggests that if the primaries are photons, their origin involves physics beyond the standard model.

3 Astrophysical Zevatrons

The puzzle presented by the observations of cosmic rays above 10^{20} eV have generated a number of proposals that we divide here as *Astrophysical Zevatrons* and *New Physics* models. Astrophysical Zevatrons are also referred to as bottom-up models and involve searching for acceleration sites in known astrophysical objects that can reach ZeV energies. New Physics proposals can be either hybrid or pure top-down models. Hybrid models involve Zevatrons and extensions of the particle physics standard model while top-down models

involve the decay of very high mass relics from the early universe and physics way beyond the standard model. Here we discuss astrophysical Zevatrons while new physics models are discussed in the next section.

Cosmic rays can be accelerated in astrophysical plasmas when large-scale macroscopic motions, such as shocks, winds, and turbulent flows, are transferred to individual particles. The maximum energy of accelerated particles, $E_{\rm max}$, can be estimated by requiring that the gyroradius of the particle be contained in the acceleration region: $E_{\rm max} = Ze\,B\,L$, where Ze is the charge of the particle, B is the strength and L the coherence length of the magnetic field embedded in the plasma. For $E_{\rm max} \gtrsim 10^{20}$ eV and $Z \sim 1$, the only known astrophysical sources with reasonable BL products are neutron stars ($B \sim 10^{13}$ G, $L \sim 10$ km), active galactic nuclei (AGNs) ($B \sim 10^4$ G, $L \sim 10$ AU), radio lobes of AGNs ($B \sim 0.1\mu$G, $L \sim 10$ kpc), and clusters of galaxies ($B \sim \mu$G, $L \sim 100$ kpc). In Figure 8, we highlight the B vs. L for objects that can reach $E_{max} = 10^{20}$ eV with $Z = 1$ (dashed line) and $Z = 26$ (solid line). We discuss each of these candidates below.

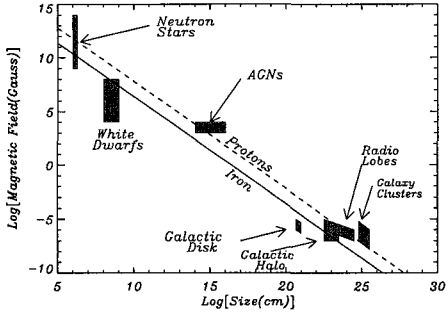

Figure 8: *B vs. L, for* $E_{max} = 10^{20}$ *eV,* $Z = 1$ *(dashed line) and* $Z = 26$ *(solid line) from [16].*

Clusters of Galaxies: Cluster shocks are reasonable sites to consider for UHECR acceleration, since particles with energy up to $E_{\rm max}$ can be contained by cluster fields. However, efficient losses due to photopion production off the CMB during the propagation inside the cluster limit UHECRs in cluster shocks to reach at most ~ 10 EeV.[36]

AGN Radio Lobes: Next on the list of plausible Zevatrons are extremely powerful radio galaxies.[37] Jets from the central black-hole of an active galaxy end at a termination shock where the interaction of the jet with the intergalactic medium forms radio lobes and 'hot spots'. Of special interest are the most powerful AGNs where shocks can accelerate particles to energies well above an

EeV via the first-order Fermi mechanism. These sources may be responsible for the flux of UHECRs up to the GZK cutoff.[38]

A nearby specially powerful source may be able to reach energies past the cutoff. However, extremely powerful AGNs with radio lobes and hot spots are rare and far apart. The closest known object is M87 in the Virgo cluster ($\sim$ 18 Mpc away) and could be a main source of UHECRs. Although a single nearby source with especially hard spectra may fit the spectrum for a given strength and structure of the intergalactic magnetic field,[28] it is unlikely to match the observed arrival direction distribution. If M87 is the primary source of UHECRs a concentration of events in the direction of M87 or the Virgo cluster should be seen in arrival directions. No such hot spot is observed (*Hot spot* in Table 1). The next known nearby source after M87 is NGC315 which is already too far at a distance of $\sim$ 80 Mpc. Any unknown source between M87 and NGC315 would likely contribute a second hot spot, not an isotropic distribution. The very distant radio lobes will contribute a GZK cut spectrum which is not observed.

The lack of a clear hot spot in the direction of M87 has encouraged the idea that a strong Galactic magnetic wind may exist that could help isotropize the arrival directions of UHECRs. A Galactic wind with a strongly magnetized azimuthal component[33] (*GalacticWind* in Table 1) can significantly alter the paths of UHECRs such that the observed arrival directions of events above 10^{20} eV would trace back to the North Galactic Pole which is close to the Virgo where M87 resides. If our Galaxy has such a wind is yet to be determined. The proposed wind would focus most observed events into the northern Galactic pole and render point source identification fruitless.[39] Future observations of UHECRs from the Southern Hemisphere by the Southern Auger Observatory will provide precious data on previously unobserved parts of the sky and help distinguish plausible proposals for the effect of local magnetic fields on arrival directions. Full sky coverage is a key discriminator of such proposals.

AGN - Central Regions: The powerful engines that give rise to the observed jets and radio lobes are located in the central regions of active galaxies and are powered by the accretion of matter onto supermassive black holes. It is reasonable to consider the central engines themselves as the likely accelerators.[40] In principle, the nuclei of generic active galaxies (not only the ones with radio lobes) can accelerate particles via a unipolar inductor not unlike the one operating in pulsars. In the case of AGNs, the magnetic field may be provided by the infalling matter and the spinning black hole horizon provides the imperfect conductor for the unipolar induction.

The problem with AGNs as UHECR sources is two-fold: first, UHE particles face debilitating losses in the acceleration region due to the intense ra-

diation field present in AGNs, and second, the spatial distribution of objects should give rise to a GZK cutoff of the observed spectrum. In the central regions of AGNs, loss processes are expected to downgrade particle energies well below the maximum achievable energy. This limitation has led to the proposal that quasar remnants, supermassive black holes in centers of inactive galaxies, are more effective UHECR accelerators.[41] In this case, losses at the source are not as significant but the propagation from source to us should still lead to a clear GZK cutoff since sources would be associated with the large scale structure of the galaxy distribution (*LSS* in Table 1). From Figure 4–6, these models can only succeed if the source spectrum is fairly hard ($\gamma \lesssim 2$).[9]

Table 1: Zevatrons

	Radio Lobes	AGN Center	YNSWs	GRBs
Composition	Proton	Proton	Iron	Proton
Source γ	2–3	2–3	1	$\Delta E/E \sim 1$
Sky Distrib.	M87(1 spot)	LSS	Galaxy	Hot Spot
B Needs	Galactic Wind	–	B_{gal}	B_{IGM}
Difficulties	Hot Spot	GZK	Iron	flux, B_{IGM}

Neutron Stars: Another astrophysical system capable of accelerating UHECRs is a neutron star. In addition to having the ability to confine $10^{20} eV$ protons (Figure 8), the rotation energy of young neutron stars is more than sufficient to match the observed UHECR fluxes.[42] However, acceleration processes inside the neutron star light cylinder are bound to fail much like the AGN central region case: ambient magnetic and radiation fields induce significant losses. However, the plasma that expands beyond the light cylinder is free from the main loss processes and may be accelerated to ultra high energies.

One possible source of UHECR past the GZK cutoff is the early evolution of neutron stars. In particular, newly formed, rapidly rotating neutron stars may accelerate iron nuclei to UHEs through relativistic MHD winds beyond their light cylinders.[43] This mechanism naturally leads to very hard injection spectra ($\gamma \simeq 1$) (see Table 1). As seen in Figure 6, $\gamma \sim 1$ improves the agreement between predicted flux and observations for energies above 10^{20} eV. In this case, UHECRs originate mostly in the Galaxy and the arrival directions require that the primaries be heavier nuclei. Depending on the structure of Galactic magnetic fields, the trajectories of iron nuclei from Galactic neutron stars may be consistent with the observed arrival directions of the highest energy events.[29] Moreover, if cosmic rays of a few times 10^{18} eV are protons of Galactic origin, the isotropic distribution observed at these energies is indicative of the diffusive

effect of the Galactic magnetic fields on iron at $\sim 10^{20}$ eV. This proposal should be constrained once the primary composition is clearly determined (see *Iron* in Table 1).

It has also been suggested that young extragalactic highly magnetized neutron stars (magnetars) may be sources of UHE protons which are accelerated by reconnection events.[44] These would be prone to a GZK cut spectrum and would need a very hard injection spectrum to become viable explanations.

Gamma-Ray Bursts: Transient high energy phenomena such as gamma-ray bursts (GRBs) may also be a source of ultra-high energies protons.[45] In addition to both phenomena having unknown origins, GRBs and UHECRs have other similarities that may argue for a common source. Like UHECRs, GRBs are distributed isotropically in the sky, and the average rate of γ-ray energy emitted by GRBs is comparable to the energy generation rate of UHECRs of energy $> 10^{19}$ eV in a redshift independent cosmological distribution of sources, both have $\approx 10^{44}$erg /Mpc^3/yr.

However, recent GRB counterpart identifications argue for a strong cosmological evolution for GRBs. The redshift dependence of GRB distribution is such that the flux of UHECR associated with nearby GRBs would be too small to fit the UHECR observations.[46] In addition, the distribution of UHECR arrival directions and arrival times argues against the GRB–UHECR common origin. Events past the GZK cutoff require that only GRBs from $\lesssim$50 Mpc contribute. Since less than about *one* burst is expected to have occurred within this region over a period of 100 yr, the unique source would appear as a concentration of UHECR events in a small part of the sky (a *Hot spot* in Table 1). In addition, the signal would be very narrow in energy $\Delta E/E \sim 1$. Again, a strong intergalactic magnetic field can ease some of these difficulties giving a very large dispersion in the arrival time and direction of protons produced in a single burst (*large* B_{IGM} in Table 1).[45] Finally, if the observed small scale clustering of arrival directions is confirmed by future experiments with clusters having some lower energy events clearly precede higher energy ones, bursts would be invalidated.[27]

4 New Physics Models

The UHECR puzzle has inspired a number of different models that involve physics beyond the standard model of particle physics. New Physics proposals can be top-down models or a hybrid of astrophysical Zevatrons with new particles. Top-down models involve the decay of very high mass relics that could have been formed in the early universe.

The most economical among hybrid proposals involves a familiar exten-

sion of the standard model, namely, neutrino masses. If some flavor of neutrinos have mass (e.g., $\sim 0.1eV$), the relic neutrino background is a target for extremely high energy neutrinos to interact and generate other particles by forming a Z-boson that subsequently decays[47] (see ν *Z burst* in Table 2). If the universe has very luminous sources (Zevatrons) of extremely high energy neutrinos ($\gg 10^{21}$ eV), these neutrinos would traverse very large distances before annihilating with neutrinos in the smooth cosmic neutrino background. UHE neutrino Zevatrons can be much further than the GZK limited volume, since neutrinos do not suffer the GZK losses. But if the interaction occurs throughout a large volume, the GZK feature should also be observed. For plausible neutrino masses $\sim 0.1eV$, the neutrino background is very unclustered, so the arrival direction for events should be isotropic and small scale clustering may be a strong challenge for this proposal. The weakest link in this proposal is the nature of a Zevatron powerful enough to accelerate protons above tens of ZeVs that can produce neutrinos as secondaries with $\gtrsim$ ZeV. This Zevatron is quite spectacular, requiring an energy generation in excess of presently known highest energy sources (referred to as *ZeV ν's* in Table 2).

Another suggestion is that the UHECR primary is a new hadronic particle that is also accelerated in Zevatrons. The mass of a hypothetical hadronic primary can be limited by the shower development of the Fly's Eye highest energy event to be below $\lesssim$50 GeV.[48] As in the Z-burst proposal, a neutral particle is usually harder to accelerate and are usually created as secondaries of even higher energy charged primaries. But once formed these can traverse large distances without being affected by cosmic magnetic fields. Thus, a signature for future experiments of hybrid models that invoke new particles as primaries is a clear correlation between the position of powerful Zevatrons in the sky such as distant compact radio quasars and the arrival direction of UHE events.[49] Preliminary evidence for such a correlation has been recently reported.[50]

Another exotic primary that can be accelerated to ultra high energies by astrophysical systems is the vorton. Vortons are small loops of superconducting cosmic string stabilized by the angular momentum of charge carriers.[51] Vortons can be a component of the dark matter in galactic halos and be accelerated by astrophysical magnetic fields.[52] Vortons as primaries can be constrained by the observed shower development profile.

It is possible that none of the astrophysical scenarios or the hybrid new physics models are able to explain present and future UHECR data. In that case, the alternative is to consider top-down models. Top-down models involve the decay of monopole-antimonoploe pairs,[53] ordinary and superconducting cosmic strings, cosmic necklaces, and superheavy long-lived relic particles. The

idea behind these models is that relics of the very early universe, topological defects (TDs) or superheavy relic (SHR) particles, produced after or at the end of inflation, can decay today and generate UHECRs. Defects, such as cosmic strings, domain walls, and magnetic monopoles, can be generated through the Kibble mechanism as symmetries are broken with the expansion and cooling of the universe. Topologically stable defects can survive to the present and decompose into their constituent fields as they collapse, annihilate, or reach critical current in the case of superconducting cosmic strings. The decay products, superheavy gauge and higgs bosons, decay into jets of hadrons, mostly pions. Pions in the jets subsequently decay into γ-rays, electrons, and neutrinos. Only a few percent of the hadrons are expected to be nucleons. Typical features of these scenarios are a predominant release of γ-rays and neutrinos and a QCD fragmentation spectrum which is considerably harder than the case of Zevatron shock acceleration.

ZeV energies are not a challenge for top-down models since symmetry breaking scales at the end of inflation typically are $\gg 10^{21}$ eV (typical X-particle masses vary between $\sim 10^{22-25}$ eV). Fitting the observed flux of UHECRs is the real challenge since the typical distances between TDs is the Horizon scale, i. e., about several Gpc. The low flux hurts proposals based on ordinary and superconducting cosmic strings which are distributed throughout space (*Extragal. TD* in Table 2). Monopoles usually suffer the opposite problem, they would in general be too numerous. Inflation succeeds in diluting the number density of monopoles and makes them too rare for UHECR production. To reach the observed UHECR flux, monopole models usually involve some degree of fine tuning. If enough monopoles and antimonopoles survive from the early universe, they may form a bound state, named monopolonium, that can decay generating UHECRs. The lifetime of monopolonia may be too short for this scenario to succeed unless they are connected by strings.[54]

Once two symmetry breaking scales are invoked, a combination of horizon scales gives room to reasonable number densities. This can be arranged for cosmic strings that end in monopoles making a monopole string network or even more clearly for cosmic necklaces.[55] Cosmic necklaces are hybrid defects where each monopole is connected to two strings resembling beads on a cosmic string necklace. Necklace networks may evolve to configurations that can fit the UHECR flux which is ultimately generated by the annihilation of monopoles with antimonopoles trapped in the string.[55,56] In these scenarios, protons dominate the flux in the lower energy side of the GZK cutoff while photons tend to dominate at higher energies depending on the radio background (see Figure 9 and *Extragal. TD* in Table 2). If future data can settle the composition of UHECRs from 0.01 to 1 ZeV, these models can be well

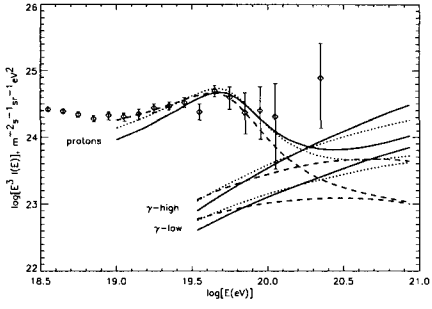

Figure 9: *Proton and γ-ray fluxes from necklaces for $m_X = 10^{14}$ GeV (dashed lines), 10^{15} GeV (dotted lines), and 10^{16} GeV (solid lines) normalized to the observed data. γ-high and γ-low correspond to two extreme cases of γ-ray absorption (see, [56]).*

constrained. In addition to fitting the UHECR flux, topological defect models are constrained by limits on the flux of high energy photons, from 10 MeV to 100 GeV, observed by EGRET.

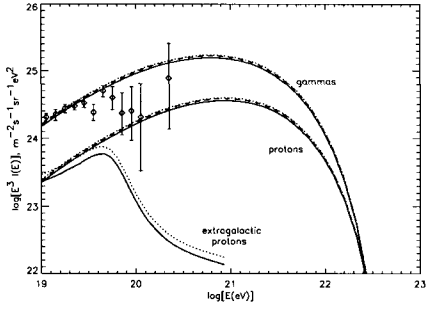

Figure 10: *SHRs or monopolia decay fluxes (for $m_X = 10^{14}$ GeV): nucleons from the halo (protons), γ-rays from the halo (gammas) and extragalactic protons. Solid, dotted and dashed curves correspond to different model parameters (see [56]).*

Another interesting possibility is the recent proposal that UHECRs are produced by the decay of unstable superheavy relics that live much longer than the age of the universe.[57] SHRs may be produced at the end of inflation by non-thermal effects such as a varying gravitational field, parametric resonances during preheating, instant preheating, or the decay of topological defects. These models need to invoke special symmetries to insure unusually

long lifetimes for SHRs and that a sufficiently small percentage decays today producing UHECRs.[57,58] As in the topological defects case, the decay of these relics also generates jets of hadrons. These particles behave like cold dark matter and could constitute a fair fraction of the halo of our Galaxy. Therefore, their halo decay products would not be limited by the GZK cutoff allowing for a large flux at UHEs (see Figure 10 and *SHRs* in Table 2). Similar signatures can occur if topological defects are microscopic, such as monopolonia and vortons, and decay in the Halo of our Galaxy (*Halo TD* in Table 2). In both cases (*SHRs* and *Halo TD*) the composition of the primary would be a good discriminant since the decay products are usually dominated by photons.

Table 2: NEW PHYSICS

	ν Z burst	Extragal TD	Halo TD	SHRs
Composition	Photon	Pho+GZK p	Photon	Photon
Source γ	Z frag	QCD frag	QCD frag	QCD frag
Sky Distrib.	Isotropic	Isotropic	Gal Halo	Gal Halo
Problem:Pho+	ZeV ν's	flux	origin	lifetime

Future experiments should be able to probe these hypotheses. For instance, in the case of SHR and monopolonium decays, the arrival direction distribution should be close to isotropic but show an asymmetry due to the position of the Earth in the Galactic Halo[56] and the clustering due to small scale dark matter inhomogeneities.[59] Studying plausible halo models for their expected asymmetry and inhomogeneitis will help constrain halo distributions especially when larger data sets are available in the future. High energy gamma ray experiments such as GLAST will also help constrain SHR models via the electromagnetic decay products.[60]

5 Conclusion

Next generation experiments such as the High Resolution Fly's Eye which recently started operating, the Pierre Auger Project which is now under construction, the proposed Telescope Array, and the EUSO and OWL satellites will significantly improve the data at the extremely-high end of the cosmic ray spectrum.[6] With these observatories a clear determination of the spectrum and spatial distribution of UHECR sources is within reach.

The lack of a GZK cutoff should become clear with HiRes and Auger and most extragalactic Zevatrons may be ruled out. The observed spectrum will distinguish Zevatrons from new physics models by testing the hardness of the

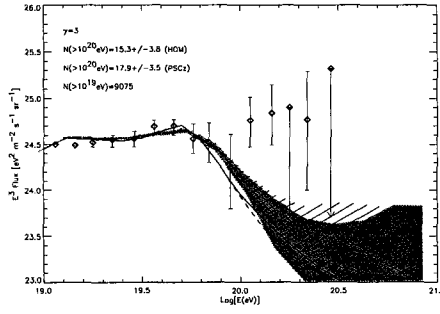

Figure 11: *Simulated fluxes for the Auger projected statistics of 9075 events above* 10^{19} *eV, and* $\gamma = 3$*, using a homogeneous source distribution (\ hatches) and the PSCz distribution (/ hatches). The solid and dashed lines are the results of the analytical calculations for the same two cases. The dash-dotted and dash-dot-dot-dotted lines trace the mean simulated fluxes for the homogeneous and the PSCz cases. (see [7]).*

spectrum and the effect of propagation. Figure 11 shows how clearly Auger will test the spectrum in spite of their clustering properties. The cosmography of sources should also become clear and able to discriminate between plausible populations for UHECR sources. The correlation of arrival directions for events with energies above 10^{20} eV with some known structure such as the Galaxy, the Galactic halo, the Local Group or the Local Supercluster would be key in differentiating between different models. For instance, a correlation with the Galactic center and disk should become apparent at extremely high energies for the case of young neutron star winds, while a correlation with the large scale galaxy distribution should become clear for the case of quasar remnants. If SHRs or monopolonia are responsible for UHECR production, the arrival directions should correlate with the dark matter distribution and show the halo asymmetry. For these signatures to be tested, full sky coverage is essential. Finally, an excellent discriminator would be an unambiguous composition determination of the primaries. In general, Galactic disk models invoke iron nuclei to be consistent with the isotropic distribution, extragalactic Zevatrons tend to favor proton primaries, while photon primaries are more common for early universe relics. The hybrid detector of the Auger Project should help determine the composition by measuring the depth of shower maximum and the muon content of the same shower. The prospect of testing extremely high energy physics as well as solving the UHECR mystery awaits improved observations that should be coming in the next decade with experiments under construction such as Auger[61] or in the planning stages such as the Telescope

Array,[62] EUSO,[63] and OWL.[64]

6 Acknowledgment

I thank the organizers of the Relativistic Aspects of Nuclear Physics 2000 meeting, in particular, T. Kodama for his hospitality. This work was supported by NSF through grant AST-0071235 and DOE grant DE-FG0291 ER40606.

1. C.M.G. Lattes, G.P.S. Occhialini & C.F. Powell, Nature, Vol. 160, 453, 1947.
2. S. Swordy, private communication. The data represent published results of the LEAP, Proton, Akeno, AGASA, Fly's Eye, Haverah Park, and Yakutsk experiments.
3. J. W. Cronin, Reviews of Modern Physics, Vol. 71, No. 2, S165 1999
4. K. Greisen, *Phys. Rev. Lett.* 16 (1966) 748; G. T. Zatsepin and V. A. Kuzmin, *Sov. Phys. JETP Lett.* 4 (1966) 78.
5. N. Hayashida et al., astro-ph/0008102, appendix for *Astrophys. J.* 522 (1999) 225.
6. G. Medina-Tanco, in this volume; M. Nagano, A.A. Watson, Reviews of Modern Physics 72 (2000) 689; A. A. Watson, Phys. Rept. 333-334 (2000) 309.
7. J. L. Puget, F. W. Stecker, and J. H. Bredekamp, *Astrophys. J.* 205 (1976) 638; F. W. Stecker and M. H. Salamon, *Astrophys. J.* 512 (1999) 521.
8. V. S. Berezinsky, Yad. Fiz. 11 (1970) 339; R. J. Protheroe and P. L. Biermann, *Astropart. Phys.* 6 (1996) 45; erratum ibid. 7 (1997) 181.
9. M. Blanton, P. Blasi, & A. V. Olinto, astro-ph/0009466.
10. W. Saunders et al., (astro-ph/0001117).
11. P. P. Kronberg, Rep. Prog. Phys., 57 (1994) 325; J. P. Vallée, *Fundamentals of Cosmic Physics*, 19 (1997) 1.
12. P. Blasi, S. Burles, and A. V. Olinto, *Astrophys. J.* 514 (1999) L79.
13. D. Ryu, H. Kang and P. L. Bierman, *Astron. Astrophys.* 335 (1998) 19.
14. G. Sigl, M. Lemoine, and P. Biermann, *Astropart. Phys.* 10 (1999) 141.
15. see e.g., L. Gonzalez-Mestres, *Nucl. Phys. B (Proc. Suppl.)* 48 (1996) 131; S. Coleman and S. L. Glashow, *Phys. Rev. D* 59 (1999) 116008; R. Aloisio, P. Blasi, P Ghia, and A. Grillo, preprint INFN/AE-99/24.
16. A. V. Olinto, *Phys. Rept.* 333-334 (2000) 329.
17. P. Bhattacharjee and G. Sigl, *Phys. Rept.* 327 (2000) 109.
18. V. S. Berezinsky, *Nucl.Phys. (Proc.Suppl.)* 70 (1999) 41.
19. R. D. Blandford, *Particle Physics and the Universe*, eds. Bergstrom, Carlson and Fransson (World Scientific, 1999).

20. S. Lee, A. V. Olinto, and G. Sigl, Astrophys. J. 455 (1995) L21; R. J. Protheroe and P. A. Johnson, Astropart. Phys. 4 (1996) 253; erratum, ibid 5 (1996) 215.
21. G. B. Blumenthal, Phys. Rev. D 1 (1970) 1596.
22. V. S. Berezinsky, S.V. Bulanov, V. A. Dogiel, V. L. Ginzburg, and V. S. Ptuskin, Astrophysics of Cosmic Rays, (Amsterdam: North Holland, 1990).
23. J. N. Bahcall and E. Waxman, Astrophys.J. 542 (2000) 542-547.
24. E. Waxman and J. Miralda-Escude, Astrophys. J. 472 (1996) L89.
25. T. Stanev, Astrophys. J. 479 (1997) 290.
26. G. A. Medina Tanco, E. M. de Gouveia Dal Pino, and J. E. Horvath, Astropart. Phys. 6 (1997) 337.
27. G. Sigl, M. Lemoine, and A. V. Olinto, Phys. Rev. 56 (1997) 4470.
28. P. Blasi and A. V. Olinto, *Phys. Rev.* D **59** (1999) 023001.
29. V. N. Zirakashvili, D. N. Pochepkin, V. S. Ptuskin, and S. I. Rogovaya, Astron. Lett. 24 (1998) 139.
30. D. Harari, S. Mollerach, and E. Roulet, (1999) astro-ph/9906309
31. J. D. Barrow, P. G. Ferreira, and J. Silk, Phys. Rev. Lett. 78 (1997) 3610.
32. J. Wdowczyk and A. W. Wofendale, Nature 281 (1979) 356; M. Giler, J. Wdowczyk, and A. W. Wolfendale, J. Phys. G.: Nucl. Phys. 6 (1980) 1561; V.S. Berezinsky, S.I. Grigorieva, and V.A. Dogiel 1989, Sov. Phys. JETP 69, 453; ibid. Astronomy and Astrophysics 232 (1990) 582.
33. E. J. Ahn, G. Medina-Tanco, P. Biermann, T. Stanev, astro-ph/9911123 (1999).
34. M. Lemoine, G. Sigl, A. V. Olinto, and D. Schramm, Astropart. Phys. 486 (1997) L115.
35. F. W. Stecker, Astrophys. J. 157 (1969) 507; G. G. Fazio and F. W. Stecker, Nature 226 (1970) 135; V. S. Berezinsky, Yad. Fiz. 11 (1970) 339; R. J. Protheroe and P. L. Biermann, Astropart. Phys. 6 (1996) 45; erratum ibid. 7 (1997) 181.
36. H. Kang, D. Ryu, T.W. Jones, *Astropart. Phys.* 456 (1996) 422.
37. P.L. Biermann and P. Strittmatter, *Astropart. Phys.* **322** (1987) 643.
38. J. P. Rachen and P. L. Biermann, *Astron. Astrophys.* **272** (1993) 161.
39. P. Billoir and A Letessier-Selvon, astroph/000142 (2000).
40. K.S. Thorne, R. Price, & D. MacDonals, *Black Holes: The Membrane Paradigm* (New Haven: Yale Press) (1986).
41. E. Boldt and P. Ghosh, *Mon. Not. R. Astron. Soc.*, in press (1999).
42. A. Venkatesan, M. C. Miller, and A. V. Olinto, *Astrophys. J.* 484 (1997) 323.

43. A. V. Olinto, R. I. Epstein, and P. Blasi, *Proceedings of 26th ICRC*, Salt Lake City, **4**, 361 (1999); P. Blasi, R. I. Epstein, and A. V. Olinto, *Astrophys. J. Letters* 533 (2000) L123.
44. E.M. de Gouveia Dal Pino, A. Lazarian, *Astrophys. J.* 536 (2000) L31-L34.
45. E. Waxman, *Phys. Rev. Lett.* 75 (1995) 386; M. Vietri, *Ap. J.* 453 (1995) 883.
46. F. W. Stecker, *Astropart. Phys.* 14 (2000) 207.
47. D. Fargion, B. Mele, and A. Salis, Astrophys.J. 517 (1999) 725-733; T. Weiler, *Astropar. Phys.* **11** (1999) 303.
48. I. F. Albuquerque, G. Farrar, and E. Kolb, *Phys. Rev.* D **59** (1999) 015021.
49. G. R. Farrar and P. L. Biermann, *Phys. Rev. Lett.* **81** (1998) 3579.
50. A. Virmani, et al., astro-ph/0010235
51. R. L. Davis and E. P. S. Shellard, *Nucl. Phys.* B 323 (1989) 209.
52. S. Bonazzola and P. Peter, *Astropart. Phys.* **7**, 161 (1997).
53. C. T. Hill, *Nucl. Phys.* B **224** (1983) 469; D. N. Schramm and C.T. Hill, Proc. 18th ICRC (Bangalore) **2** (1983) 393.
54. J. J. Blanco-Pillado and K. D. Olum, Phys.Rev. D60 (1999) 083001.
55. V. Berezinsky and A. Vilenkin, *Phys. Rev. Lett.* **79** (1997) 5202.
56. V. Berezinsky, P. Blasi, and A. Vilenkin, *Phys. Rev.* D **58** (1998) 103515-1.
57. V. Berezinsky, M. Kachelrieß and A. Vilenkin, *Phys. Rev. Lett.* **79** (1997) 4302; V. Kuzmin and V. Rubakov, Yad. Fisika **61** (1998) 1122.
58. D. J. H. Chung, E. W. Kolb, and A. Riotto, *Phys. Rev. Lett.* **81** (1998) 4048; V. Kuzmin and I. Tkachev, *Phys. Rev.* D **59** (1999) 123006.
59. P. Blasi & R. K. Seth, *Phys. Lett.* B 486 (2000) 233-238.
60. P. Blasi, *Phys. Rev.* D **60** (1999) 023514.
61. J. W. Cronin, *Nucl. Phys. B. (Proc. Suppl.)* 28 (1992) 213.
62. M. Teshima et al., *Nucl. Phys. B (Proc. Suppl.)* 28B (1992) 169.
63. L. Scarsi, in the proceedings of the International Workshop on Observing Ultra High Energy Cosmic Rays From Space and Earth, Metepec, Puebla, Mexico (2000).
64. R. E. Streitmatter, Proc. of *Workshop on Observing Giant Cosmic Ray Air Showers from* $> 10^{20}$ *eV Particles from Space*, eds. J. F. Krizmanic, J. F. Ormes, and R. E. Streitmatter (AIP Conference Proceedings 433, 1997).

Gustavo M. Tanco

Ultra-high energy cosmic rays: current data and propagation scenarios

Gustavo Medina Tanco
Instituto Astronômico e Geofísico, Universidade de São Paulo, Brazil
gustavo@iagusp.usp.br

Abstract

The available data on Ultra High Energy Cosmic Ray (UHECR), defined here as particles arriving from outer space at total energies above $\sim 10^{18}$ eV, are briefly reviewed with an eye on constraints imposed by propagation. Since UHECR are most likely charged particles, the intervening galactic and intergalactic magnetic fields, have the potential to affect propagation at energies of hundreds of EeV in a significant way and, therefore, our present knowledge of this subject is also sketched. In fact, provided enough data is collected by new experiments, like Auger and the planned EUSO, UHECR will be in the future an invaluable diagnostic tool for cosmic magnetic fields up to distances of ~ 100 Mpc.

1 Introduction

Cosmic rays (CR), relativistic particles that continuously strike the upper layers of the Earth's atmosphere, span an enormous interval in energy: more than 11 orders of magnitude. Several are the production, acceleration and propagation mechanisms involved over this huge energy range, in which the particle flux goes down from 10^4 m^{-2} s^{-1} at ~ 1 GeV to 1 (100 km^2)$^{-1}$ yr^{-1} at > 100 EeV, the highest energies detected so far.

The spectrum is remarkably regular over this energy interval (see 1), and can be described by a succession of power laws separated by a few breaks: the knee at a few PeV, the second knee at ~ 0.75 EeV and the ankle at $\sim 5 - 10$ EeV. Of particular relevance to the study UHECR is the expected GZK cut-off at $\gtrsim 40$ EeV (Greisen, 1966; Zatsepin and Kuzmin, 1966), apparently absent in the current data.

UHECR lay at the very tail of the CR spectrum. At the risk of arbitrariness, one can use the second knee as the energy frontier separating them from the lower-energy cosmic rays.

A simple way of getting an insight into the general characteristics of CR, and on the physical meaning of the selection of the second knee for the definition of UHECR, is to compare the expected gyroradii of charged nuclei with the dimensions of the relevant propagation regions:

$$\left(\frac{r_g}{100\text{kpc}}\right) = \frac{1}{Z}\frac{E_{20}}{B_{\mu\text{G}}} \tag{1}$$

where E_{20} is the energy, in units of 10^{20} eV, of a nucleus of charge Z, propagating in a magnetic field of intensity $B_{\mu\text{G}}$ in μG. Two characteristic values for the latter, representative of the galactic magnetic field (GMF) and intergalactic magnetic field (IGMF), are 10^{-6} and 10^{-9} Gauss respectively.

At energies below 10^{18} eV, CR particles have gyroradii much smaller than the thickness of the galactic disk, ~ 1 kpc; therefore, they propagate diffusively and are effectively confined inside the disk. However, at energies above $\sim 10^{18}$ eV, the gyroradii are much larger than

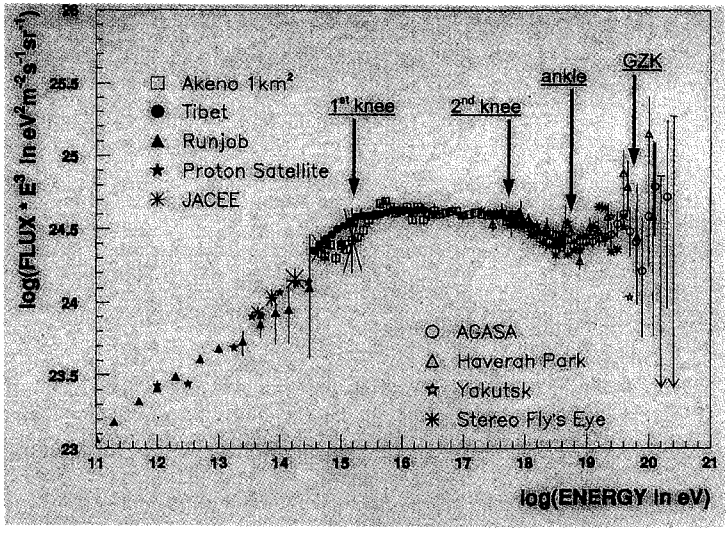

Figure 1: Differential energy spectrum of primary cosmic rays. Adapted from Nagano and Watson (2000)

the typical Galaxy thickness, and the diffusive approximation breaks down. Furthermore, for an average IGMF of $\sim 10^{-9}$ Gauss (Kronberg, 1994a) the gyroradius of the lightest nuclei in the intergalactic medium are in excess of 100 Mpc at $E > 10^{20}$ eV.

Up to energies around the knee, CR are galactic and, very likely, accelerated by first order Fermi processes at galactic supernova remnant (SNR) shock waves (Drury, 1983; Moraal and Axford, 1983; Völk and Biermann, 1988; Markiewicz et al., 1990; Medina Tanco and Opher, 1993). At energies between the knee and the ankle the origin of the particles is more uncertain though still galactic. SNR propagating through the wind of its progenitor star could play an important role in accelerating these nuclei, and in explaining the observed gradual change to a heavier component (Biermann, 1988).

The acceleration mechanism of UHECR is essentially unknown. However, several mechanisms have been proposed. At the most general level, they can be classified into two large groups: bottom-up and top-down mechanisms. Bottom-up mechanisms, although more conservative, imply the stretching of rather well known acceleration processes to their theoretical limits (and sometimes beyond). They involve, among others, particle acceleration in the accretion flows of cosmological structures (Norman et al., 1995; Kang et al., 1996), galaxy collisions (Cesarsky and Ptuskin, 1993; Al-Dargazelli et al., 1997), galactic wind shocks (Jokipii and Morfill, 1987), pulsars (Hillas, 1984; Shemi, 1995), active galactic nuclei (Biermann and Strittmatter, 1987), powerful radio galaxies (Rawlings and Saunders, 1991; Biermann, 1998), gamma ray bursts (Vietry, 1995; Vietry, 1998; Waxman, 1995; Stanev et al., 1996), etc.. Top-down mechanisms, on the other hand, escape from the acceleration problems at the expense of exoticism. They already form the particles at high energies and involve the most interesting Physics, for example: the decay of topological defects into superheavy gauge and Higgs bosons, which then decay into high energy neutrinos, gamma rays and nucleons with energies up to the GUT scale ($\sim 10^{25}$ eV) (Bhattacharge et al., 1992; Sigl et al., 1994; Berezinsky et al., 1997; Berezinsky, 1998; Birkel and Sarkar, 1998) , high energy neutrino annihilation on relic neutrinos (Waxman, 1998), etc.

In general, the distribution of sources of UHECR particles in bottom-up mechanisms should be related to the distribution of luminous matter in the Universe. In contrast, for top-down mechanisms, either an isotropic distribution of sources or a spatial distribution resembling dark matter should be expected in most of the models (Hillas, 1998; Dubovsky and Tinyakov, 1998; Medina Tanco, 2000a). Ideally, these distributions should produce distinguishable signatures in the arrival angular distribution of events.

2 Composition

Beyond the ankle, the increase in the maximum depth of air showers points to a change back to a lighter (proton dominated?) component (Nagano and Watson, 2000). At the same time, the arrival directions of UHECR seem remarkably isotropic (Takeda, 1999a; Hayashida, 1999a), showing no evidence of correlation with either the galactic or the supergalactic planes (Uchihori, 1996). As light nuclei don't propagate diffusively inside the galactic plane at these energies, the previous observations point strongly to particle sources outside the galactic disk, either located in an extended galactic halo or extragalactic.

As for the identity of the UHECR particles and their sources, a wide spectrum of possibilities is allowed by the scarce available data. Deeply penetrating primaries seem to be ruled out by Fly's Eye (Baltrusaitis et al., 1985)and AGASA (Inoue, 1999) data with an upper limit (at the 90% CL) 10 times smaller than the observed UHECR flux above $10^{19.5}$ eV (Nagano and Watson, 2000). There is no indication either in the AGASA, Haverah Park (Hinton, 1999) or Fly's Eye (Halzen et al., 1995) data set, that the primaries above 10^{20} eV are gamma-rays, as generally favored by top-down UHECR production mechanisms. Therefore, so far, observations leave hadrons as the most likely primaries.

Neutrons, even at the highest energies detected, have a Lorentz factor $\Gamma \sim 10^{11}$ and, therefore, decay into protons after a free fly of only ~ 1 Mpc. Thus, UHECR are probably charged hadrons. Heavy nuclei, on the other hand, interact strongly with the infrared background (IRB) and photodisintegrate, which severely limit their travel distance. Although definite conclusions are critically dependent on the IRB flux assumed (Puget et al., 1976; Malkan and Stecker, 1998; Stecker, 1998; Epele and Roulet, 1998), it is likely that UHECR are mainly light nuclei, possibly protons.

3 Propagation

Intergalactic space is host to a bath of photons covering the whole electromagnetic spectrum. The intensity of this radiation background field peaks at microwave frequencies, with still considerable photon densities at both infrared and radio frequencies. UHECR interact strongly with photons in this energy range.

Protons interact with the all-pervading cosmic microwave background radiation (CMBR) via pair production and photo-pion production interactions. The attenuation length for pair production is ~ 1 Mpc with a threshold at $E \sim 10^{18}$ eV, and inelasticity of only $\Delta E \sim 0.1$ % per interaction. The attenuation length for photo-pion production, on the other hand, is ~ 6 Mpc at the threshold of $E \sim 10^{19.6}$ eV, with an inelasticity $\Delta E \sim 20$ % per interaction (Berezinsky and Grigor'eva, 1988a; Yoshida and Teshima, 1993a; Protheroe and Johnson, 1996). Therefore, the latter is the dominant energy loss mechanism. Unless the particles have unreasonably high energy at the sources, the flux at Earth should originate in a relatively small volume of nearby universe, the GZK-sphere, with a radius of the order of $50 - 100$ Mpc (Medina Tanco et al., 1997; Hillas, 1998). Furthermore, the energy spectrum resulting from a homogeneous distribution of sources should present a distinguishable GZK-cut-off at $E > 10^{19.5}$ eV (Berezinsky and Grigor'eva, 1988a; Yoshida and Teshima, 1993a; Medina-Tanco, 1999). Since the latter cut-off is apparently not present in the available data (Takeda, 1998; Takeda, 1999b) there is probably some kind of clustering or even a local enhancement in the UHECR source density distribution. At any rate, this remains a very much debated and open topic in the area.

For heavy nuclei, photodisintegration and pair production processes are important (Puget et al., 1976). The dominant energy loss channel is single-nucleon emission: $A+\gamma_{2.7K} \rightarrow (A-1)+N$, where N is a nucleon. The energy loss due to interactions with IR photons is effective below 5×10^{19} eV while the interaction with CMB photons is more prominent above 2×10^{20} eV. Pair production energy losses by heavy nuclei are stronger for $5 \times 10^{19} < E < 2 \times 10^{20}$eV.

Gamma rays experience strong energy losses due to electron-positron pair creation in interactions with the CMBR at energies $> 4 \times 10^{14}$eV and with the radio background at $> 2 \times 10^{19}$eV. Consequently, the universe is very opaque to high energy photons, with attenuation lengths that vary from $\sim$ 3 Mpc at 10^{18}eV to $\sim$ 10 Mpc at 10^{20}eV. From that point on, however, the attenuation length grows steadily, reaching $\sim 10^2$ Mpc at 10^{21}eV (Bhattacharjee and Sigl, 2000).

In any case, whether hadrons or photons, UHECR are not able to travel cosmological distances unless one claims unreasonably high energies at the sources.

Besides radiation backgrounds, the intergalactic and galactic media are host to magnetic fields too. It is likely the UHECR are charged hadrons, which means that the particle trajectories are coupled, in principle, to an unknown extent to the intervening magnetic fields. Unfortunately, our knowledge of the topology and intensity of the large scale magnetic fields in the local universe and galactic halo is limited; it resumes, mainly, to upper limits or rotation measurement constraints to the product of the magnetic field intensity times the square root of the correlation length averaged along some few lines of sight (Kronberg, 1994a).

The implicit assumption of a particular field model with rather low IGMF intensities, combined with the high energy of particles beyond the GZK cut-off, has led to the notion of a random walk propagation scenario (Waxman and Miralda-Escudé, 1996; Medina Tanco et al., 1997; Lemoine et al., 1997b; Sigl et al., 1997) where small particle deflections:

$$\delta\theta(E) = 0.025 \times \left(\frac{D}{L_c}\right)^{1/2} \times \left(\frac{L_c}{10\mathrm{Mpc}}\right) \times \left(\frac{B}{10^{-11}\mathrm{G}}\right) \times \left(\frac{E}{10^{20}\mathrm{eV}}\right) \qquad (2)$$

allow for an easy identification of the sources. Nevertheless, the propagation character of UHECR can be strongly dependent on the model assumed for the magnetic fields inside the propagation region, the GZK-sphere.

4 Magnetic scenarios

In broad terms, the propagation region comprises: (a) the source and its immediate, probably magnetized, environment, (b) the intergalactic medium, (c) the galactic halo, (d) the galactic disk, (e) the heliosphere and (f) the magnetosphere.

The sources and their environments are essentially unknown. Magnetic fields, if present, are probably relevant to the acceleration mechanism and/or escape probability of the particles. However, we can always redefine the size of the source to include this environment and, consequently, we will not make such a distinction in what follows.

The heliosphere and magnetosphere, despite their relatively large coherent magnetic fields, have length scales small enough to produce only minute deflections and, from the point of view of propagation can be neglected. The latter does not mean, however, that these magnetic fields cannot play a relevant role in other phenomena related to UHECR (Stanev and Vankov, 1997; Medina-Tanco and Watson, 1999).

The main components of the problem are then, at least from the point of view of the magnetic field, the IGMF and GMF (both halo and disk field).

4.1 The galactic magnetic field

The grand design of the Galactic magnetic field is difficult to observe from our position inside the system. However, a global picture exists, particularly reliable within $2-3$ kpc from the Sun (Beck et al., 1996), based on Zeeman splitting of radio and maser lines, and Faraday

rotation measurements from pulsars and extragalactic sources, complemented with frequency dependent time delay measurements of pulsar signals.

Several parametrizations are available (Vallee, 1991; Han and Qiao, 1994) for the regular component of the GMF . Radio polarization observations of other phase-on and edge-on spiral galaxies confirm the existence of such a large scale ordered magnetic component, encompassing the visible spiral disk structure, and possibly extending into the galaxy halo. These polarization observations of other spiral galaxies represent an important test, since rotation measures of the GMF sample mainly the warm component of the interstellar medium, which has a filling factor of only $\sim$ 20 %, rising doubts about the global relevance of the latter results.

Furthermore, the large scale magnetic field structures in the few tens of spiral galaxies studied so far, present a narrow spectrum of topologies. Basically, in the plane of the galaxy the field is either axisymmetric or bisymmetric while in the direction perpendicular to the galaxy plane the horizontal component has either quadrupolar (horizontal field even in z and perpendicular field odd in z) or dipolar (horizontal field odd in z and perpendicular field even in z) symmetry, and mode mixing can also occur (Beck et al., 1996). It is not clear which of these symmetries actually applies to our own galaxy. Some authors favor an axisymmetric model (Rand and Kulkarni, 1989; Rand and Lyne, 1994), while others prefer a bisymmetric one (Sofue and Fujimoto, 1983; Han and Qiao, 1994). The symmetry of the horizontal component with respect to the midplane is somehow masked by local fluctuations in the vicinity of the Sun, therefore, claims exist for both, odd and even symmetries, although the latter probably agrees better with the observations. The perpendicular component is very small near the midplane and is difficult to disentangle from local inhomogeneities. At least one reversal in the field direction exist internal to the Solar circle at $0.2 - 0.3$ kpc in the direction of the Sagitarius arm and there is widespread controversy regarding the existence of either one or two additional inner and one outer reversals. In any case, the Sun is too close to a reversal and, therefore, the local GMF intensity may not be representative of the Galaxy as a whole, where typical values might run as high as 4–6 μG.

Superimposed on the regular component is a random component of comparable, or even larger intensity. Its origin and maintenance mechanism are poorly known. The strength of the rms random magnetic field, however, seems to reflect equipartition with the kinetic energy in the turbulence. A comprehensive study of rotation measurements differences between pairs of pulsars points to an rms amplitude of $4 - 6$ μG and correlation length between 10 and 100 pc (Ohno and Shibata, 1993). A plausible mechanism to produce the random field component is the small scale dynamo, which would produce magnetic flux ropes with a length of about 50–100 pc, thickness of $\sim$ 5–10 pc and a filling factor of $\sim$ 1% embedded in the warm phase of the ISM (Shukurov, 2000). Some kind of consensus seems to exist around a model in which the strength of the regular field is 1.8 ± 0.3 μG and the total local field is ~ 5 μG probably increasing towards the Galactic center (Han, 2000).

Therefore, even if the present uncertainties preclude the exact knowledge of the GMF, a limited spectrum of possible configurations exists which can be used to check different UHECR propagation scenarios. Furthermore, in the future, whenever better statistics on UHECR are available, these data could be used to further improve our knowledge on the GMF.

Given a parameterization for the GMF, particles arriving at Earth from any direction in the sky can be back-tracked through the galactic disk and halo to the border of the halo where the IGMF starts. This procedure defines a mapping between the arrival directions at the border of the halo and the arrival directions at the position of the Earth inside the Galaxy. In this way, the intrinsic angular error boxes due to the existence of a GMF can be estimated as a function of arrival direction. For example, for an axisymmetric, quadrupolar, without a z (perpendicular to the galactic plane) component (ASS-S) model of GMF, and incoming UHECR nuclei at 2.5×10^{20} eV, it can be shown that (Medina Tanco, 1997a; Medina Tanco et al., 1998): (a) for protons, the intrinsic error boxes due to the GMF are $< 1^o$ for most of the sky; the exception are those lines of sight that cross the central region of the Galaxy and first quadrant at low galactic latitudes, where the angular uncertainty can grow rapidly

beyond 4°; (b) iron nuclei, on the other hand, suffer very large deflections over most of the observable sky even at energies as high as 2.5×10^{20} eV.

Better UHECR statistics, on the other hand, could be used as a tool to study the large scale geometry of the GMF. If the Galaxy were immersed in an isotropic extragalactic UHECR flux, the distinction between ASS-S and BSS-S GMF models should be possible by the soon to be built Auger observatory after approximately five years of exposure (Medina Tanco, 2001).

4.2 The intergalactic magnetic field

Luminous matter, as traced by galaxies, as well as dark matter, as traced by galaxies and clusters large scale velocity fields, is distributed inhomogeneously in the universe. Groups, clusters, superclusters, walls, filaments and voids are known to exist at all observed distances and are very well mapped in the local universe. Hence, the distribution of matter inside the GZK-sphere is highly inhomogeneous and so is, very likely, the distribution of UHECR sources.

Synchrotron emission and multi-wavelength radio polarization measurements show that magnetic fields are widespread in the Universe. But how do they encompass the structure seen in the distribution of matter we do not yet know (Kronberg, 1994b).

The available limits on the IGMF come from rotation measurements in clusters of galaxies and suggest that $B_{IGM} \times L_c^{1/2} < 10^{-9}$ G $\times$ Mpc$^{1/2}$ (Kronberg, 1994b), where L_c is the field reversal scale. Note, however, that this kind of measurement doesn't set an actual limit to the intensity of the magnetic field unless the reversal scale is known along a particular line of sight. The latter means that, depending on the structure of the IGMF, substantially different scenarios can be envisioned that are able satisfy the rotation measurement constraints.

Unfortunately, we do not know what is the actual large scale structure of the IGMF. Nevertheless, we can imagine two extreme scenarios that are likely to bound the true IGMF structure.

In one scenario (Ryu et al., 1998), by $z = 0$, the magnetic field has been convected together with the accretion flows into walls, filaments and clusters, depleting the voids from field. According to these large scale structure calculations, the magnetic field is confined in high density, small filling factor regions, bounded by a rather thin skin of rapidly decreasing intensity, surrounded by large volumes of negligible IGMF. The resulting IGMF inside structures is highly correlated in scales of up to tens of Mpc. Furthermore, in order to comply with the rotation measurement constraints mentioned before, the intensity of the magnetic field inside the density structures must be correspondingly high, 0.1–1 μG, which is comparable with GMF values within the interstellar medium. We will call the latter scenario *laminar-structure* .

In the second model, that we will call *cellular-structure* , we imagine the space divided into adjacent cells, each one with a uniform magnetic field randomly oriented. We identify the size of a cell with the magnitude of the local reversal scale. Furthermore, one can assume that the intensity of the magnetic field scales as some power of the local matter (electron) density and, consequently, the rotation measurement constraint $B_{IGM} \times L_c^{1/2} < 10^{-9}$ G $\times$ Mpc$^{1/2}$ tells how the reversal scale, i.e., the size of the cells, should be scaled. A convenient reference, such as the IGMF in the Virgo (Arp, 1988) or Comma (Kim et al., 1989) cluster can be used for normalization. The cellular-structure scenario leads to a more widespread IGMF, filling even the voids. The observational constraints imply then that the IGMF varies much more smoothly, from 10^{-10}G inside voids to a few times 10^{-9}–10^{-8}G inside walls and filaments, only reaching high values, $0.1 - 1$ μG, inside and around clusters of galaxies.

Observations are not enough at present to distinguish between these two scenarios, but we can still try to asses what are their implications for UHECR propagation.

4.3 UHECR propagation in a laminar-IGMF

This is the most difficult scenario to dealt with because it does not accept a statistical treatment and results are very dependent on details about the exact magnetic field configuration inside the GZK-sphere, which is beyond our present knowledge.

A simpler approach is to study the UHECR emissivity of a single wall surrounded by a void (Medina Tanco, 1999; Medina Tanco, 1998b).

Under general condition, that could be consider as representative of the system supergalactic plane-Milky Way, simulations show that the UHECR flux measured can vary by three orders of magnitude depending of the relative orientation between the wall, the field and the observer. At the same time, almost all directional information is lost, and the strength of the GZK-cut-off would vary considerably as a function of orientation (Medina Tanco, 1998b).

In this case, there is nothing like a random walk: particles tend to be trapped inside the walls and move in a systematic way. Most of the particles drift perpendicularly to the regular field while their guiding centers bounce along the field, while the gyroradii decrease as the particles lose energy in interactions with the radiation backgrounds. Even the few particles that do escape from the wall, do so in an non-isotropic way.

The laminar IGMF model is, actually, the worst scenario for doing some kind of astronomy with UHECR. It would be very difficult to interpret the UHECR angular data and to identify individual particle sources. Furthermore, the significance of any statistical analysis would be greatly impaired due to systematics.

4.4 UHECR propagation in a cellular-IGMF

The cellular model is the easiest scenario to deal with numerically and, by far, the most promising from the point of view of the astrophysics of UHECR. This is also the IGMF model that has been used probably more frequently in the literature (Auger Design Report, 1996; Waxman and J., 1996; Lemoine et al., 1997a; G. et al., 1997; Medina Tanco, 1997b; Medina Tanco et al., 1997; Medina Tanco, 1997c; Medina Tanco, 1998a; Medina-Tanco, 1999; Medina Tanco, 2000b; Medina Tanco and Enßlin , 2001).

The main assumption here, is that the intensity of the magnetic field scales with density. Indeed, for those spatial scales where measurements are available, the intensity of the magnetic fields seem to correlate remarkably well with the density of thermal gas in the medium. This is valid at least at galactic and smaller scales (Vallee, 1997; Medina Tanco, 2000c). It is apparent that B can be reasonably well fitted by a single power law over ~ 14 orders of magnitude in thermal gas density at sub-galactic scales. A power law correlation, though with a different power law index, is also suggested at very large scales (c.f. figure 5 in Medina Tanco 2000b), from galactic halos to the environments outside galaxy clusters, over ~ 4 orders of magnitude in thermal gas density. This view (Vallee, 1997) is, however, still controversial (Kronberg, 1994b). In fact, magnetic fields in galaxy clusters are roughly ~ 1 μG, which is of the order of interstellar magnetic fields; furthermore, supracluster emission around the Coma cluster suggests μG fields in extended regions beyond cluster cores. The latter could indicate that the IGMF cares little about the density of the associated thermal gas density, having everywhere an intensity close to the microwave background-equivalent magnetic field strength, $B_{BGE} \simeq 3 \times 10^{-6}$ G.

Taking the view that a power law scaling exist, a model can be devised in which the IGMF correlates with the distribution of matter as traced, for example, by the distribution of galaxies. A high degree of non-homogeneity should then be expected, with relatively high values of B_{IGMF} over small regions (< 1 Mpc) of high matter density. These systems should be immersed in vast low density/low B_{IGMF} regions with $B_{IGMF} < 10^{-9}$ G. Furthermore, in accordance with rotation measurements, the topology of the field should be such that it is structured coherently on scales of the order of the correlation length L_c which, in turn, scales with IGMF intensity: $L_c \propto B^{-2}_{IGMF}(r)$. $\vec{B}_{IGMF}$ should be independently oriented at distances $> L_c$. Therefore, a 3D ensemble of cells can be constructed, with cell size given by the correlation length, L_c, and such that: $L_c \propto B^{-2}_{IGMF}(r)$, while $B_{IGMF} \propto \rho^{0.35}_{gal}(r)$ (Vallee,

1997) or $\propto \rho_{gal}^{2/3}(r)$ (for frozen-in field compression), where ρ_{gal} is the galaxy density, and the IGMF is uniform inside cells of size L_c and randomly oriented with respect to adjacent cells (Medina Tanco, 1997c; Medina Tanco and Enßlin , 2001). The observed IGMF value at some given point, like the Virgo cluster, can be used as the normalization condition for the magnetic field intensity. The density of galaxies, ρ_{gal}, is estimated using either redshift catalogs [like the CfA Redshift Catalogue (Medina Tanco, 1998a; Medina-Tanco, 1999) or the PSCz (Blanton et al., 2000)], or large scale structure formation simulations (Medina Tanco and Enßlin , 2001). The latter is a convenient way to cope with, or at least to assess the importance of, the several biases involved in the use of galaxy redshift surveys to sample the true spatial distribution of matter in 3D space.

The relevant energy losses for UHECR during propagation are: pair production via γ–γ with CMB for photons, redshift, pair production and photopion production in interactions with the CMB for nuclei and, for heavy nuclei, also photo-disintegration in interactions with the infrared background. All of these can be appropriately included (Berezinsky and Grigor'eva, 1988b; Yoshida and Teshima, 1993b; Stecker and H., 1999; Bhattacharjee and Sigl, 2000).

The spatial distribution of the sources of UHECR is tightly linked to the nature of the main particle acceleration/production mechanism involved. However, in most models, particles will either be accelerated at astrophysical sites that are related to baryonic matter, or produced via decay of dark matter particles. In both cases the distribution of galaxies (luminous matter) should be an acceptable, if certainly not optimal, tracer of the sources.

Once the previously described scenario is built, test particles can be injected at the sources and propagated through the intergalactic medium and intervening IGMF to the detector at Earth.

In contrast to the laminar IGMF case, in this scenario information regarding the large scale distribution of the sources inside the GZK-sphere can be easily recoverable ??. The supergalactic plane and the Virgo cluster, in particular, should be clearly visible at galactic longitudes $l \simeq 0\text{--}100$. There is also a considerable increase in resolution as the energy reaches the 100 EeV range and the gyroradii of UHECR protons become comparable to the size of the GZK-sphere. It is in the cellular model that the deflection angle of the incoming particle with respect to the true angular position of the source is small enough for an UHECR astronomy to develop at the largest energies.

5 Available data: present constraints on theoretical models

Cosmic rays above $\sim 10^{14}$ eV are too infrequent to be detected directly from balloons or satellites. Their detection is made indirectly through the particle cascades they produce in the atmosphere.

At the highest energies, an air shower can comprise up to 10^{11} relativistic particles at ground level, scattered over a considerable area of hundreds of meters in diameter. Correspondingly two different techniques have been used to detect these events: (a) the sampling of the shower at ground level by an array of counters covering a large area and (b) the tracking of the shower evolution through the atmosphere by observing the fluorescence light emitted isotropically in interaction with air nuclei. Both methods are able to give information on the energy of the primary, its arrival direction and, at least in a statistical way, some hint on the nature/mass of the primary.

The particle array technique was used in 5 experiments aimed at the highest energies: Volcano Ranch (USA), Haverah Park (UK), Narribri (Australia), Yakutsk (Russia) and AGASA (Japan). The latter is the largest (100 km^2) and the only experiment still in operation.

The fluorescence technique was used successfully by the Fly's Eye array, and is now being used by its high resolution successor HiReS (USA).

All the data available at present on UHECR comes from these experiments.

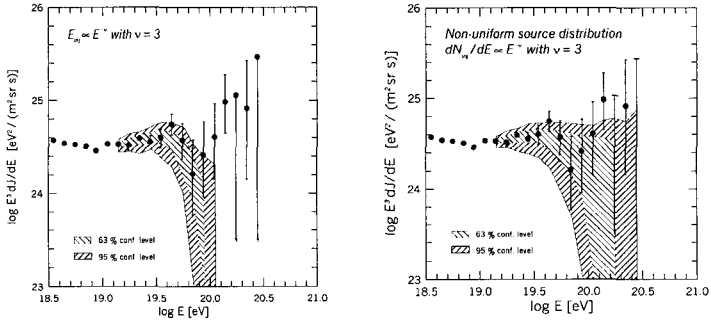

Figure 2: Statistical significance of the observed UHECR energy spectrum and the distribution of the particle sources: (a) homogeneous, (b) CfA2 catalog (Medina-Tanco, 1999).

A new very large area detector, the Auger Observatory of 3000 km^2, is currently under construction in Malargüe, Argentina, by an international consortium and will combine both techniques in a single experiment. A significant advance in our understanding of the phenomenon is expected during the next few years due to Auger. Another milestone (in a time scale of a decade?) will be the design and construction of the EUSO experiment, that will observe atmospheric fluorescence from space in order to extend the exposure area to $\sim 10^5$–10^6 km^2.

From the astrophysical point of view, there are at present two elementary observations that can be used to constraint the production and propagation models of UHECR: arrival energy and arrival direction of the individual particles, which are statistically encoded as spectral energy distribution and angular distribution respectively.

The limited size of the world data set, however, is an important obstacle (as of August 1998): 1281 events above 10^{19} eV (Haverah Park: 106, Yakutsk: 230, Fly's Eye(mono): 297, Fly's Eye(stereo): 67, AGASA: 581); 116 events above 4×10^{19} eV (Volcano Ranch: 6, HP: 27, YK: 12, FE(mono): 22, FE(stereo): 2, AGASA: 47); 14 events above 10^{20} eV (VR: 1, HP: 4, YK: 1, FE(mono): 1, FE(stereo): 0, AGASA: 7).

The extension of the UHECR spectrum beyond the GZK cut-off has long been hinted by the extreme high energy events of Volcano Ranch (Linsley, 1963; Linsley, 1978), Haverah Park (Watson, 1991; Lawrence et al., 1991), Fly's Eye (Bird, 1995) and AGASA (Hayashida, 1994), and recently confirmed by the latter experiment (Takeda, 1998; Nagano, 1998).

It is not clear, however, whether the available data is sufficient to support any conjecture about the actual shape of the spectrum above 10^{20} eV. Furthermore, it is the nearby sources that are expected to be responsible for this region of the spectrum and their distribution is far from isotropic or homogeneous. Therefore, it is not clear either what is the influence that the differential exposure in declination, peculiar to the AGASA experiment, has on the deduced spectral shape at the highest energies.

Figure 2 (Medina-Tanco, 1999) try to assess both, the statistical significance of the AGASA result (Takeda, 1998) at the very end of the energy spectrum, and the degree to which it is compatible with a non-homogeneous distribution of sources that follows closely the spatial distribution of luminous matter in the nearby Universe (as given by the CfA2 galaxy redshift catalog - see, however, Blanton, Blasi and Olinto, 2000).

In figure 2a (left), the observed spectrum is compared with the energy spectrum resulting from a homogeneous distribution of sources from $z = 0$ to $z = 0.1$ in a Friedmann-Robertson-Walker metric. The fiducial cellular IGMF model is used (see above). Individual sources were treated as standard candles supplying the same luminosity in UHECR protons above 10^{19} eV. The injected spectrum was a power law, $dN/dE \propto E^{-\nu}$, with $\nu = 3$ above the latter

threshold. The shown confidence levels take into account the dependence in declination of the quoted exposure of AGASA, an energy-independent Gaussian distribution of the errors in the determination of the arrival energy of (assumed) protons and the bin and sample size above 10^{19} used in Takeda et al, 1998. It can be seen from the figure that this model is able to fit the observed AGASA spectrum quite well up to $\sim 10^{20}$ eV. At higher energies, however, AGASA observations seem unaccountable by the homogeneous approximation, even when the quoted errors are considered. This result is statistically significant despite the low number of UHECR events available.

Figure 2b (right), compares the observed spectrum with the energy spectrum resulting from a inhomogeneous distribution, that of the galaxies in the CfA2 catalog. Everything else is as in the simulation in figure 2a. It can be seen that, in this case, it is not so clear that the GZK cut-off is not present in the data. Therefore, caution must be exercised in the interpretation of the UHECR energy spectrum until more data is available.

There have been many attempts to look for anisotropies in the arrival directions of cosmic rays in the expectation that the source of the particles might be revealed directly.

The results of the various experiments above 10^{17}eV are mainly upper limits, which increase with energy in a way that reflects the decrease in the number of events with energy (Linsley and Watson, 1977; Lloyd-Evans and Watson, 1983; Watson, 1992).

The AGASA group (Hayashida, 1999b) reported the analysis of a total of 216,000 showers above 10^{17} eV observed over 15 years. For their first report (Hayashida, 1999c) they searched a data base of 114,000 events and discovered a first harmonic in right ascension of about 4% amplitude around 1 EeV (chance probability of occurrence of $\sim 0.2\%$). Analysis in right ascension and declination showed that there were significant excesses of events from directions close to the galactic center and the Cygnus region. The most significant excess in the near-galactic centre region was found when a beam size of 20^o was assumed. Unfortunately, the AGASA array is located too far north to cover the galactic centre itself. However, what is most important about the claim, the sample in the range 1.0–2.0 EeV has recently been increased from 18274 events (Hayashida, 1999c) to 29207 events (Hayashida, 1999b). For the additional 10933 events the overall amplitude in right ascension is 4.4% with a chance probability of 5.2×10^{-3}. This is the first time, at these energies, that a claimed anisotropy has been confirmed with an independent data set at a reasonable level of significance. The signal near the galactic center is a 4.5σ excess with 506 events in a region where a background of 413.6 events was expected.

In an effort to confirm the AGASA result, the Adelaide group (Bellido et al., 2000) have used data recorded many years ago by the Sydney University shower array (Winn, 1986). The Sydney array (operated between 1968 and 1979) was located at latitude 30.5 S, and so had a full view of the galactic center. For the 54% events that triggered more than three stations in the range $10^{17.9}$ to $10^{18.5}$ eV, two regions of excess were found, one of which at $(\alpha, \delta) = (274, -22)$ is close to the AGASA galactic center signal, $\sim 7.5^o$ from the galactic centre. Within a circle of radius 5.5^o, centered on the Sydney excess, there are 21.8 events in the probability density map as compared with a background expectation of 11.8 events. However the point-like nature of the Adelaide/Sydney signal is different from the extended enhancement found by AGASA.

It is not clear at present whether these two, apparently significant signals from similar regions of the sky, are consistent with each other and could therefore originate in the same astrophysical object.If so, unless the particle source is located in the vicinity of the Sun, probably neutral particles are involved. Neutrons at 10^{18}eV, for example, have a decay length of $\sim$ 10 kpc and are able to travel without magnetic deflection from the central regions of the Galaxy.

At the highest energies, above 10^{19} eV, the situation is further complicated by the paucity of the data.

No correlation is seen with the galactic plane. Furthermore, earlier claims of a correlation between arrival directions at $E > 4 \times 10^{19}$eV and the supergalactic plane (Stanev et al., 1995) from the analysis of Haverah Park data have not been subsequently confirmed by the AGASA team.

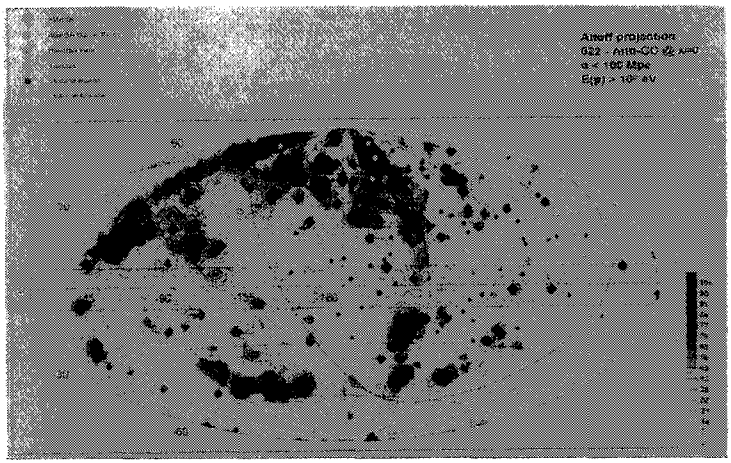

Figure 3: Expected arrival probability distribution (contour lines in the background) for the same UHECR source and IGMF cellular model as above compared with the actual published data above 4×10^{19} eV from AGASA, Haverah Park, Yakutsk and Volcano Ranch.

Figure 3 shows an Aitoff (equal area) projection, in galactic coordinates, of the expected arrival probability distribution (contour lines in the background) for the same UHECR source and IGMF cellular model as above compared with the actual published data above 4×10^{19} eV from AGASA (47 events (Takeda, 1999c)), Haverah Park (27 (Reid and Watson, 1980)), Yakutsk (24 (Afanasiev, 1995)) and Volcano Ranch (Linsley, 1980)). The mask covers the plane of the galaxy, where the actual distribution of galaxies is not well known due to obscuration by dust. The curved, thick line is the celestial equator.

The arrival probability contours trace quite well the local large scale structures. The supergalactic plane (SGP), in particular, can be easily distinguished running from North to South approximately along the $l = 135$ galactic meridian. It is apparent from the figure that, despite some conspicuous clusters in the vicinity of the SGP, the actual observed distribution of UHECR is much more isotropic than what one would expect if their sources aggregate like the luminous matter. Unfortunately, given the non-uniform exposure in declination of the various experiments and the low number statistics involved, it is not trivial to quantify this statement.

The view of the AGASA group (Takeda, 1999c) is that supra-GZK events arrive isotropically at Earth. However, this picture is further complicated by the detection of four doublets and one triplet within a separation angle of 2.5^o out of 47 events (Hayashida, 1996; Takeda, 1999c). Moreover, one of the pairs and the triplet were within 2^o of the supergalactic plane, which might hint to at least a partial correlation with this density structure (Medina Tanco, 1997b; Medina Tanco, 1998a).

Further insight can be gained, as in the case of the energy spectrum, by comparing the data with what should be expected from a homogeneous and from an inhomogeneous distribution of sources that follows closely the local luminous matter spatial distribution (LLMD).

The most elemental analysis that can be made regarding isotropy is one-dimensional in right ascension (RA), where other complicating factors like non-uniform exposure in declination and low number statistics are more easily dealt with. The expected distribution of events in RA, for a sample of size 47 protons originated in the LLMD scenario, is dominated by a large signal from the Virgo-Coma line of sight towards the North galactic pole. Deep depressions should surround the Virgo peak, corresponding to the Orion and Local voids,

the most prominent structures in our immediate neighborhood, combined with the spurious effect of obscuration of the galaxy distribution due to the galactic plane.

On the other hand, the distribution in RA when the incident UHECR flux is isotropic should be very flat. It can be demonstrated that, even with so few events as those contained in the AGASA sample, both limits should be distinguishable (Medina Tanco, 2000b).

Actually, the AGASA data is consistent with an isotropic distribution and shows no signature of either the Virgo peak or the Local void.

A more quantitative treatment to characterize the anisotropy in RA is the first harmonic analysis (Linsley, 1975). Thus, given a data sample, the amplitude $r_{1h} = \sqrt{a_{1h}^2 + b_{1h}^2}$ and phase $\Psi_{1h} = \tan^{-1}(b_{1h}/a_{1h})$ are calculated, where $a_{1h} = \frac{2}{N}\sum_{i=1}^{N}\cos\alpha_i$, $b_{1h} = \frac{2}{N}\sum_{i=1}^{N}\sin\alpha_i$ and α_i is the right ascension of an individual event.

Large number of trials with samples (same size and selection criterion as AGASA's) drawn from isotropic and anisotropic (LLMD)distributions, show that these two scenarios should be very well discriminated in the r_{1h}-Ψ_{1h} plane. In fact, the error box for the first harmonic of AGASA data (Medina Tanco and Watson, 1999) is completely consistent with an isotropic UHECR flux. Moreover, the AGASA result by itself, seems completely inconsistent with the LLMD scenario. However, when the phase and amplitudes obtained from other major experiments are considered, the picture looks suggestively different, since all the phase observations are clustered inside the same quadrant in RA, covering the right wing of the Virgo peak. That is, despite the fact that every isolated measurement is consistent with isotropy, the observed phases seem to show a systematic enhancement in the direction of the interface between the SGP and the large adjacent Local void. Three out of four first harmonic phases (Haverah Park, Yakutsk and Volcano Ranch) include the North galactic pole within one S.D. level, while the forth (AGASA) include it within two S.D.. The exclusion of the observed UHECR events inside the obscuration band, $b < 10^o$, changes the phase of the AGASA result by only 6^o (from 258^o to 252^o) and, therefore, previous conclusions are unchanged by this effect.

Clearly, a two-dimensional analysis of the data would be highly desirable in order to answer questions as simple as whether the data is isotropic or unimodal. One way of doing this (Medina Tanco, 2000b), given the small number of events involved and the non-uniformity of the distribution of events in declination due to experimental limitations, is to analyze the normalized eigenvalues τ_1, τ_2 and τ_3 of the orientation matrix $\mathbf{T}$ of the data. Defining $\mathbf{T_{i,j}} = \mathbf{\Sigma_{k=1}^{N} v_i^k v_j^k}$, where $\mathbf{v^k}$ are the N unit vectors representing the data over the celestial sphere and assuming $0 \leq \tau_1 \leq \tau_2 \leq \tau_3 \leq 1$, the shape, $\gamma = log_{10}(\tau_3/\tau_2)/log_{10}(\tau_2/\tau_1)$, and the strength parameter, $\zeta = log_{10}(\tau_3/\tau_1)$, can be built (Fisher et al., 1993). The shape criterion γ is useful in discriminating girdle-type distributions from clustered distributions. The larger the value of γ more clustered is the distribution. Uniform, nearly isotropic, distributions have $\zeta \sim 0$. Because of the nature of the experimental setup, the observed distribution of UHECR is girdle in nature, regardless of the isotropicity of the UHECR flux.

Again, trials with samples drawn from isotropic and anisotropic (LLMD) show that the isotropic and LLMD scenarios should be very well separated with the available data in the γ-ζ plane. AGASA data , on the other hand, does not fit either of these scenarios, being an intermediate case.

Therefore, while a first order interpretation of the AGASA data certainly points to an isotropic flux of UHECR, consideration of the first harmonic analysis of other data sets and of two-dimensional tests over the AGASA data itself, as well as expected numbers of doublets for isotropic and anisotropic samples (Medina Tanco, 2000a), point to a more complicated picture with a certain degree of mixture of both limiting cases.

There are at least three scenarios in which such a result could be obtained:

1. The sources involve bottom-up mechanisms associated with luminous matter but some of the events are scattered in the intergalactic medium such that we observe the composition of a diffuse and a direct component. Under plausible conditions (Medina Tanco and Enßlin , 2001), suitable scattering centers could be radio ghosts (Enßlin, 1999), plasma fossils of galactic nuclear activity (see, figure 4).
2. The sources involve bottom-up mechanisms associated with luminous matter but there

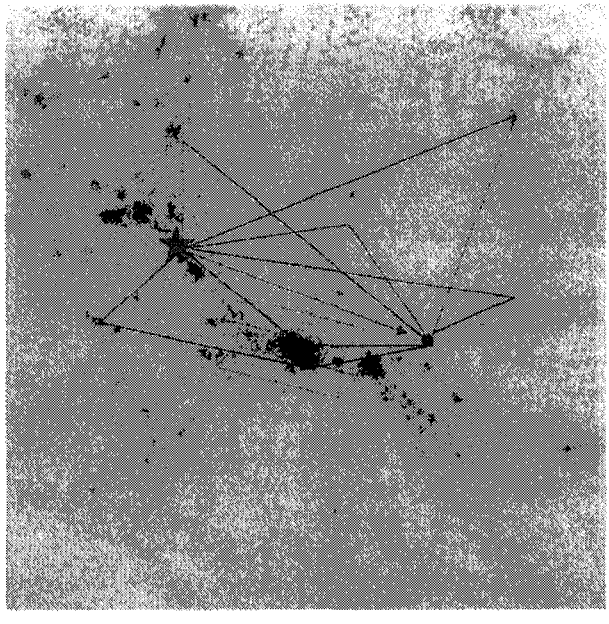

Figure 4: Radio ghosts could act as scattering centers of UHECR in the intergalactic medium, giving rise to a diffuse particle flux besides the direct, anisotropic, flux component. Thus, the observer (dot) would see the source (star) immersed in a CR background. For details see Medina Tanco and Enßlin, 2000.

is a large local magnetic structure, like a magnetized galactic wind, which isotropize the UHECR flux upon traversing the galactic halo (Ahn et al., 2000; Biermann et al., 2000). As the energy of the particles increases, and as long as they all have the same mass, the degree of isotropization should decrease making the galactic pole visible. Figure 5 shows schematically how such a focusing effect could take place inside an hypothetical Galactic wind, in the context of our nearby universe. Ahn et al. (2000), backtracked the real data above 10^{20} eV to the border of the Galaxy halo and showed that all events can be focused onto a narrow spot near the north galactic pole, some 20^{o} from the powerful radio galaxy M87, at the heart of the Virgo cluster in the supergalactic plane. Furthermore, this scenario should produce a strong asymmetry between the observable UHECR flux at the Northern and Southern Earth hemispheres. Consequently, this represents an ideal theoretical ground to be tested by the next generation Auger observatory in Malargüe, Argentina.

3. The sources involve top-down mechanisms associated with dark matter whose distribution roughly associates with the LLMD. In this case, the observed flux is the composition of an extragalactic component, whose signature is not very different from that of the LLMD, and a component originated in the halo of our own galaxy (Medina Tanco and Watson, 1999; Benson et al., 1999a; Benson et al., 1999b). It has been claimed (Dubovsky and Tinyakov, 1998) that, under general conditions, the halo component should dominate the extragalactic flux by at least two orders of magnitude. This is only true, however, in the unrealistic case of dark matter uniformly distributed in intergalactic space. Nevertheless, dark matter aggregates strongly and tends to be overabundant, by factors of $\sim 10^2$, in the center of galaxy clusters when compared to its abundance in the halos of isolated galaxies. It can therefore be shown

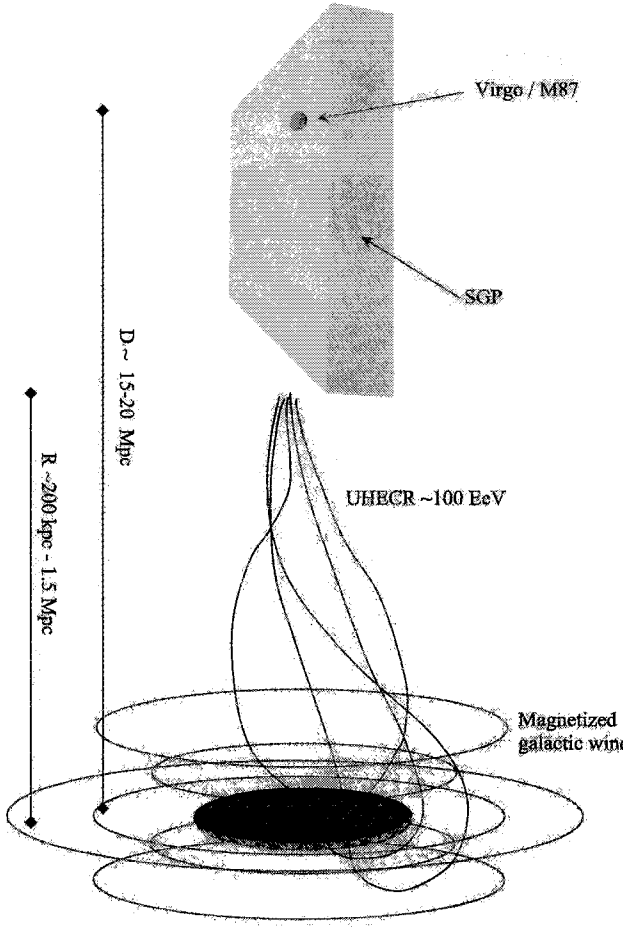

Figure 5: Schematic view of UHECR focusing by a magnetized Galactic wind in the local universe.

that, in a sample of 50 events, and assuming Virgo as the only source of extragalactic events, 3–7 events should originate in Virgo and arrive inside a solid angle of approximately the size of the cluster. This could give rise to a slight anisotropy that correlates with the SGP when combined with the almost isotropic flux originated in a large galactic halo. Note, however, that the solid angle does not need to point exactly in the direction of Virgo, depending on the large-scale structure of the intervening magnetic field. Furthermore, the present data is not even enough to constraint theoretical halo models, being able to rule out only the most unlikely (very flattened or very small) halos(Medina Tanco and Watson, 1999).

6 Conclusions

The main hindrance to our present advance in knowledge in the UHECR field is probably the lack of data. This situation should get considerably better, however, in the next few years as data from the Auger observatory accumulates. Nevertheless, UHECR are most likely charged particles; therefore, there is probably not such a thing as an easily identifiable optical counterpart to these extremely high energy events. Intervening galactic and intergalactic magnetic fields can affect propagation at energies of hundreds of EeV in a very significant way depending on the intensity and topology of the fields. This means that both, cosmic magnetic fields and UHECR are probably strongly coupled and will have to be tackled simultaneously as different aspects of the same problem. We will have to increase our knowledge on cosmic fields to better understand UHECR and, conversely, as soon as we go through a some threshold in our understanding of UHECR astrophysics, an invaluable and badly needed new diagnostic tool for probing magnetic fields inside the GZK-sphere will be available. The lower end of the UHECR regime, at $E \sim 10^{18}$ eV, looks extremely promising since a possible anisotropy in the general direction of the galactic center has been has been confirmed on independent data sets of the same experiment (AGASA) and, possibly, in a second experiment too (SUGAR). Unfortunately, Auger will not be sensitive at those "low" energies, and no other experiment will observe the EeV region of the spectrum from the Southern hemisphere in the near future.

Acknowledgements: I would like to thank the organizing committee for the invitation to deliver this talk and several colleagues for useful discussions and suggestions: Alan Watson, Peter Biermann, Michel Hillas, Todor Stanev, Torsten Enßlin, Johannes Knapp, Carlos Escobar, John Linsley, Angela Olinto, Pasquale Blasi, Elihu Boldt, Arnold Wolfendale and Eli Waxman among others. This work is partially supported by the Brazilian agencies FAPESP and CNPq.

References

Afanasiev, B. e. a., 1995, Proceedings of 24th International Cosmic Ray Conference (Roma) 2, 796

Ahn, E.-J., Medina Tanco, G. A., Biermann, P. L., and Stanev, T., 2000, astro-ph/9911123

Al-Dargazelli, S. S., Lipiski, M., Smialkowski, A., and Wdowdczyk, J, W. A., 1997, 25th ICRC (Durban) 4, 465

Arp, H., 1988, Phys. Lett. A 129, 135

Auger Design Report, 1996

Baltrusaitis, R. M., Cassiday, G. L., Elbert, J. W., Gerhardy, P. R., Loh, E. C., Mizumoto, Y., Sokolsky, P., and Steck, D., 1985, Phys. Rev. D 31, 2192

Beck, R., Brandenburg, A., Moss, D., Shukurov, A., and Sokoloff, D., 1996, Ann. Rev. Astron. Astrophys. 34, 155

Bellido, J. A., Dawson, B. R., and Johnston-Hollitt, M., 2000, Astroparticle Phys. (accepted)

Benson, A., Smialkowski, A., and W., W. A., 1999a, Astroparticle Physics 10, 313

Benson, A., Smialkowski, A., and W., W. A., 1999b, Phys. Lett. B 449, 237

Berezinsky, V., 1998, hep-ph/9802351

Berezinsky, V., Kachelrie, M., and Vilenkin, A., 1997, astro-ph/9708217
Berezinsky, V. S. and Grigor'eva, S. I., 1988a, Astron. Astrophys. 199, 1
Berezinsky, V. S. and Grigor'eva, S. I., 1988b, A & A 199, 1
Bhattacharge, P., Hill, C. T., and Schramm, D. N., 1992, Phys. Rev. Lett. 69, 567
Bhattacharjee, P. and Sigl, G., 2000, Phys. Rep. 327, 110
Biermann, P. L., 1988, Astron. Astrophy., astro-ph/9301008
Biermann, P. L., 1998, Workshop on Observing Giant Cosmic Ray Air Showers, J. F. Krizmanic, J. F. Ormes and R. E. Streitmatter (eds.), AIP Conf. Proc. 433, 22
Biermann, P. L., Ahn, E.-J., Medina Tanco, G. A., , and Stanev, T., 2000, Nucl. Phys. B 87, 417
Biermann, P. L. and Strittmatter, P. A., 1987, Astrophys. J. 322, 643
Bird, D. J., 1995, Astrophys. J. 441, 114
Birkel, M. and Sarkar, S., 1998, hep-ph/9804285
Blanton, M., P., B., and V., O. A., 2000, astro-ph/0009466
Cesarsky, C. and Ptuskin, V., 1993, 23rd ICRC (Calgary) 2, 341
Drury, L. O., 1983, Rep. Prog. Phys. 46, 973
Dubovsky, S. and Tinyakov, P., 1998, astro-ph/9802382
Enßlin, T., 1999, Ringberg Workshop on Diffuse Thermal and Relativistic Plasma in Galaxy Clusters, Eds: H. Böhringer, L. Feretti, P. Schuecker, MPE Report No. 271
Epele, L. N. and Roulet, E., 1998, Phys. Rev. Lett. 81, 3295
Fisher, N. I., Lewis, T., and Embleton, B. J. J., 1993, Cambridge Univ. Press., Cambridge
G., S., Lemoine, M., and V., O. A., 1997, Phys. Rev. D 56, 4470
Greisen, K., 1966, Phys.Rev.Letters 16, 748
Halzen, F., Vázques, R. A. abd Stanev, T., and Vankov, H. P., 1995, Astroparticle Phys. 3, 151
Han, J. L., 2000, Astrophys. and Sp. Sci. in press, astro-ph/0010537
Han, J. L. and Qiao, G. J., 1994, Astron. Astrophys. 288, 759
Hayashida, N. e. a., 1994, Phys. Rev. Lett. 63, 3491
Hayashida, N. e. a., 1996, Phys. Rev. Lett. 77, 1000
Hayashida, N. e. a., 1999a, Astropart. Phys. 10, 303
Hayashida, N. e. a., 1999b, 26th ICRC, Salt Lake City 3, 256
Hayashida, N. e. a., 1999c, Astroparticle Phys. 10, 303
Hillas, A. M., 1984, Ann. Rev. Astron. Astrophys. 22, 425
Hillas, M., 1998, Nature 395, 15
Hinton, J. A., 1999, private communication
Inoue, N. e. a., 1999, Proc. 26th ICRC, Salt Lake City 1, 361
Jokipii, J. R. and Morfill, G., 1987, Astrophys. J. 312, 170
Kang, H., Ryu, D., and T.W., J., 1996, Astrophys. J. 456, 422
Kim, K.-T., Kronberg, P. P., G., G., and T., V., 1989, Nature 341, 720
Kronberg, P. P., 1994a, Rep. Prog. Phys. 57, 325
Kronberg, P. P., 1994b, Rep. Prog. Phys. 57, 325
Lawrence, M. A., Reid, R., and Watson, A. A., 1991, J. Phys. G: Nucl. Part. Phys. 17, 733
Lemoine, M., G., S., V., O. A., and N., S. D., 1997a, Astrophys. J. Lett. 486, L115
Lemoine, M., Sigl, G., Olinto, A. V., and Schramm, D. N., 1997b, Astrophys. J. Lett. 486, L115
Linsley, J., 1963, Phys. Rev. Lett. 10, 146
Linsley, J., 1975, Phys. Rev. Lett. 34, 1530
Linsley, J., 1978, Scientific American 239, 60
Linsley, J., 1980, Catalogue of Highest Energy Cosmic Rays(ed. M Wada) WDC C2 for CR, IPCR, Tokyo 1, 61
Linsley, J. and Watson, A. A., 1977, Proc 15th ICRC, Plovdiv 12, 203
Lloyd-Evans, J. and Watson, A. A., 1983, Invited talks, 8th European CR Symp., N. Iucci et al. (eds.), Tecnoprint, Bologna
Malkan, M. A. and Stecker, F. W., 1998, Ap. J. 496, 13
Markiewicz, W. J., Drury, L. O., and Völk, H. J., 1990, Astronomy and Astrophys. 236, 487

Medina Tanco, G. A., 1997a, in 25th ICRC, Vol. 4, p. 485
Medina Tanco, G. A., 1997b, in 25th ICRC, Vol. 4, p. 481
Medina Tanco, G. A., 1997c, in 25th ICRC, Vol. 4, p. 477
Medina Tanco, G. A., 1998a, Astrophys. J. Lett. 495, L71
Medina Tanco, G. A., 1998b, Astrophys. J. Lett. 505, L79
Medina Tanco, G. A., 1999, in Proc. 16th ECRC, Alcalá de Henares, Espanha (J. Medina ed.), pp 295–298
Medina-Tanco, G. A., 1999, Astrophys. J. Lett. 510, L91
Medina Tanco, G. A., 2000a, Ap. J., Accepted
Medina Tanco, G. A., 2000b, Ap. J. (accepted)
Medina Tanco, G. A., 2000c, astro-ph/9809219,in Topics in Cosmic Ray Astrophysics, M. Duvernois (ed.),Nova Science Pub. Inc.,New York. p. 299
Medina Tanco, G. A., 2001, in preparation
Medina Tanco, G. A., de Gouveia dal Pino, E. M., and Horvath, J. E., 1997, Astroparticle Physics 6, 337
Medina Tanco, G. A., de Gouveia dal Pino, E. M., and Horvath, J. E., 1998, Astrophys. J. 492, 200
Medina Tanco, G. A. and Enßlin , T. A., 2001, Astroparticle Physics (accepted), astro-ph/0011454
Medina Tanco, G. A. and Opher, R., 1993, Astrophys. J. 411, 690
Medina Tanco, G. A. and Watson, A. A., 1999, Astroparticle Physics 12, 25
Medina-Tanco, G. A. and Watson, A. A., 1999, Astroparticle Physics 10, 157
Moraal, H. and Axford, W. I., 1983, Astronomy and Astrophys. 125, 204
Nagano, M., 1998, Workshop on Observing Giant Cosmic Ray Air Showers, J. F. Krizmanic, J. F. Ormes and R. E. Streitmatter (eds.), AIP Conf. Proc. 433, 76
Nagano, M. and Watson, A. A., 2000, Rev. Modern Phys. 72, 689
Norman, C. A., Melrose, D. B., and Achterberg, A., 1995, Astrophys. J. 454, 60
Ohno, H. and Shibata, S., 1993, MNRAS 262, 953
Protheroe, R. J. and Johnson, P., 1996, Astroparticle Phys. 4, 253
Puget, J. L., Stecker, F. W., and Bredekamp, J. H., 1976, Ap. J. 205, 638
Rand, R. J. and Kulkarni, S. R., 1989, Astrophys. J. 343, 760
Rand, R. J. and Lyne, A. G., 1994, MNRAS 268, 497
Rawlings, S. and Saunders, R., 1991, Nature 349, 138
Reid, R. J. O. and Watson, A. A., 1980, Catalogue of Highest Energy Cosmic Rays (ed. M Wada) WDC C2 for CR, IPCR, Tokyo 1, 61
Ryu, D., Kang, H., and Biermann, P. L., 1998, Astronomy and Astrophys. 335, 19
Shemi, A., 1995, MNRAS 275, 115
Shukurov, A., 2000, astro-ph/0012444
Sigl, G., Lemoine, M., and Olinto, A. V., 1997, Phys. Rev. D 56, 4470
Sigl, G., Schramm, D. N., and Bhattacharge, P., 1994, 2, 401
Sofue, Y. and Fujimoto, M., 1983, Astrophys. J. 265, 722
Stanev, T., Biermann, P. L., Lloyd-Evans, J., Rachen, J. P., and Watson, A. A., 1995, Phys. Rev. Lett. 75, 3056
Stanev, T., Schaefer, R., and Watson, A. A., 1996, Astroparticle Phys. 5, 75
Stanev, T. and Vankov, H. P., 1997, Phys. Rev. D 55, 1365
Stecker, F. W., 1998, Workshop on observing GAS from Space, J. F. Krizmanic et al. (eds.) pp 212–215
Stecker, F. W. and H., S. M., 1999, Astrophys. J. 512, 521
Takeda, M. e. a., 1998, Phys. Rev. Lett. 81, 1163
Takeda, M. e. a., 1999a, Astrophys. J. 522, 225
Takeda, M. e. a., 1999b, Proc. 26th ICRC, Salt Lake City 3, 252
Takeda, M. e. a., 1999c, Astrophys. J. 522, 225
Uchihori, Y. e. a., 1996, Proc. Int. Symp on EHECR: Astrophys. and Future Observatories, M. Nagano (ed.), ICRR, Univ. Tokyo p. 50
Vallee, J. P., 1991, Astrophys. J. 366, 450

Vallee, J. P., 1997, Fundamentals of Cosmic Physics 19, 1
Vietry, M., 1995, Astrophys. J. 453, 883
Vietry, M., 1998, Workshop on Observing Giant Cosmic Ray Air Showers, J. F. Krizmanic, J. F. Ormes and R. E. Streitmatter (eds.), AIP Conf. Proc. 433, 50
Völk, H. J. and Biermann, P. L., 1988, Ap. J. Lett. 333, L65
Watson, A. A., 1991, Proc. of the 12th European Cosmic Ray Symp.,(Nottingham) Nucl. Phys. B Suppl. 22B, 116
Watson, A. A., 1992, Nucl. Phys. B (Proc. Suppl.) 28, 3
Waxman, E., 1995, Astrophys. J. Lett. 452, L1
Waxman, E., 1998, astro-ph/9804023
Waxman, E. and J., M., 1996, Astrophys. J. Lett. 472, L98
Waxman, E. and Miralda-Escudé, J., 1996, Astrophys. J. Lett. 472, L89
Winn, M. M. e. a., 1986, J. Phys. G.: Nucl. Phys. 12, 653
Yoshida, S. and Teshima, M., 1993a, Prog. Theor. Phys. 89, 833
Yoshida, S. and Teshima, M., 1993b, Prog. Theor. Phys. 89, 833
Zatsepin, G. T. and Kuzmin, V. A., 1966, Sov. Phys. JETP Lett. 4, 78

Grzegorz Wilk

IMPRINTS OF NONEXTENSIVITY IN MULTIPARTICLE PRODUCTION

G.WILK

The Andrzej Sołtan Institute for Nuclear Studies; Hoża 69; 00-689 Warsaw, Poland
E-mail: utyuzh@fuw.edu.pl and wilk@fuw.edu.pl

Z.WŁODARCZYK

Institute of Physics, Pedagogical University; Konopnickiej 15; 25-405 Kielce, Poland
E-mail: wlod@pu.kielce.pl

The statistical methods based on the classical Boltzmann-Gibbs (BG) approach are at heart of essentially all descriptions of multiparticle production processes. In many cases, however, one observes some deviations from the expected behaviour. It is also known that conditions necessary for the BG statistics to apply are usually satisfied only approximately. Two attitudes are possible in such situations: either to abandon statistical approach trying some other model or to generalise it to the so called nonextensive statistics (widely used in the similar circumstances in many other branches of physics). We shall provide here an overview of possible imprints of non-extensitivity existing both in high energy cosmic ray physics and in multiparticle production processes in hadronic collisions, in particular in heavy ion collisions.

1 Introduction

The high energy collisions are usually connected with production of large number of secondaries (mostly π and K mesons). The strong interactions involved here make their detail descriprion *from first principles* impossible and one is forced to turn to phenomenological models of various kinds. The statistical models were the first successful approaches to the multiparticle production processes since the beginning of the subject almost half century ago [1] and they remain still very much alive today, especially in all analysis of multiparticle data performed from the point of view of the possible formation of the new state of matter - the Quark Gluon Plasma (QGP) [2]. They are all based on the Boltzmann-Gibbs form of entropy, which is identical to the so called Shannon entropy used in the information theory approach.

We would like to stress at this point that information theory can be also applied to hadronic processes [3]. Its importance there is best visualized by the following example. Suppose that some experiment provides us with data on a limited set of n observables: $R_1, R_2, \ldots, R_n$. This triggers the theory,

which follows with a variety of models, usually completely different (if not contradictory) but each claiming good agreement with these data. The models provide therefore apparently different views of the same physical reality (data) leading to confusion on what is actually going on. It happens this way because experimental data contain only *limited amount of information* to which theoretical models add their own specific assumptions born not in data but in our minds. To quantify this situation one must find the way to answer (in a model independent way) the following question: given physical assumptions of a model (plus phase space and conservation laws), what are their *most trivial* consequences? This can be done only be by resorting to information theory which defines *triviality* as the *lack of information* (the less information the more trivial). The measure of information provided by Shannon entropy (or some other kind of entropy, in our talk this will be Tsallis entropy [4]) allows us then to quantify the whole problem.

Let us elaborate this point a bit further. Experiment gives us usually set of points to which one tries to fit some distribution function $\rho(x)$, which can be thought to be some probability distribution. In this case Shannon entropy corresponding to it is

$$S = -\int \rho(x) \ln[\rho(x)]. \tag{1}$$

We are looking for the most trivial $\rho(x)$, i.e., for one containing the least information, and it means for such, which informational entropy is maximal under given circumstances (constraints)[a]. What are those constraints? At first, being a probability distribution $\rho(x)$ must be non-negative and normalized, i.e.,

$$\int \rho(x)\, dx = 1. \tag{2}$$

Further, $\rho(x)$ has to reproduce the experimental results given in the form of expectation values $\langle R^{(k)(x)} \rangle = R_k$ of measured set of observables $R^{(k)}$, i.e.,

$$\int dx\, R^{(k)}(x)\, \rho(x) = R_k;\ k = 1, \ldots, m. \tag{3}$$

[a] One should remember that formula (1) assumes that $\rho(x)$ is measured against some other distribution $\rho_0(x)$ corresponding to equal *a priori* probability being assigned to equal volumes of phase space. This is sometimes called "the first principle of statistical mechanics" [3]. The Boltzmann constant, which normally appears in (1) has been henceforth assumed unity, $k_B = 1$.

Using eqs.(2) and (3) as constraints one then maximalizes information entropy (1) and as results one gets the seek for distribution $\rho(x)$,

$$\rho(x) = \frac{1}{Z} \cdot \exp\left[-\sum_{k=1}^{m} \beta_k R^{(k)}(x)\right], \tag{4}$$

where Z is calculated from the normalization condition. This distribution reproduces known information (i.e., it tells us *the truth, the whole truth* about experiment) and contains the least information (i.e., it tells us *nothing but the truth*). In this sense it is the unique, most plausible (least biased), model independent probability distribution describing the outcomes of our experiment. The Lagrange multipliers β_k are given as solutions of the constraint equations and $R_k = \partial \ln Z(\beta_1, \ldots, \beta_m)/\partial\beta_k$.

Now we can understand why apparently completely disparate models can describe sucessfully the same experiment. It is because they share (usually in an implicite than explicite way) the same set of basic common assumptions (i.e., constraints R_k) and, at the same time, they differ completely in the rest of them, i.e., in those R_k, which contain assumptions particular for a given model (and which are completely not relevant to its agreement with experiment)[b].

This example tells us that statistical approach is not necessarily connected with any thermodynamical model but has, in fact, much broader range of applications. In our example above the formula (4) is identical with formulas used in thermal models [2] but parameters β_k can take any values depending on the energy and multiplicity of the event under considerations [3]. It is worth to remind at this point the very old observation [6] that exponential form (4) of so many distributions observed experimentally can have its origin in the fact that the actual measurements extend only to subsystems of a total system. The summation over the unmeasured (i.e., essentially overaged over) degrees of freedom introduces the randomnization, which can be most economically described as a kind of thermal bath leading to thermal-like exponential distributions with some effective "temperature "T.

[b] A completely forgotten example of such situation is discovery [5] that to explain all experimental data on the multiparticle reactions of that time it is only necessary to assume that the phase space is effectively one-dimensional (i.e., the p_T cut-off) and that not the whole initial energy $\sqrt{s}$ of reaction is used for the particle production (i.e., the existence of the inelasticity K or of the leading particle effect).

In this approach dynamics lies in our ability to reproduce the known information (i.e., is hidden in β_k). However, the big advantage of this method is that it prevents us from smuggling in anything additional, not being present in data. The outcome depends on the funtional form of the entropy. The Shannon form (1) is the most popular one because it coincides in thermodynamical limit with the Boltzmann-Gibbs (BG) form allowing for contact with standard thermodynamics. However, as newtonian mechanics is not eternal and universal (in the sense that in the limit of large velocities it must be replaced by special relativity, in the limit of vanishingly small masses quantum mechanical effects must be accounted for and in the limit of extremaly large masses (stars, galaxies,...) it must be replaced by general relativity) the same can be said about the classical BG statistical mechanics. It is fully satisfactory only if

- effective microscopic interactions are short-ranged (i.e., we have close spacial connections);
- effective microscopic memory is short-ranged (i.e, we have close time connections);
- boundary conditions are non (multi)fractal (i.e., the relevant space-time and/or phase space is non (multi)fractal).

As a matter of fact despite the popularity of BG it seems that in majority of situations we are dealing with, at least one of these conditions is not satisfied. Therefore it is justified to look for the possible generalization of BG which would provide a compactifications of all possible deviations from the ideal BG statistics into a minimal - possible only one - additional parameters. In this way we arrive at the notion of Tsallis statistics based on Tsallis entropy [4]:

$$S_q = -\frac{1-\int dx\rho(x)^q}{1-q}. \tag{5}$$

We shall not dwell too much on it here as this is the subject of separate lecture by Prof. Tsallis himself [7]. The only points we would like to stress here for our purposes are:

- for $q \to 1$ one recovers the usual Shannon entropy form of (1);
- with the normalization condition imposed on $\rho(x)$ as before and with the new definition of the mean values, $\langle R\rangle_q = \int dx R(x)\rho(x)^q$, one replaces formula (4) with

$$\rho(x) = \frac{1}{Z}\cdot\left[1-(1-q)\sum_{k=1}^{m}\beta_k R^{(k)}(x)\right]^{\frac{1}{1-q}}; \tag{6}$$

(notice that, again, for $q \to 1$ (6) goes to (4). As before, this distribution reproduces known information and conveys least information but this time information is measured in a different way, which is paramatrized by the parameter q)[c];

- the resultant staistics is non-extensive in the sense that for two subsets A and B such that probabilities $p_{ij}(A+B) = p_i(A)p_k(B)$ the entropy is not additive but instead

$$S_q(A+B) = S_q(A) + S_q(B) + (1-q)S_q(A)S_q(B) \qquad (7)$$

and additivity is recovered only in the limit $q \to 1$;

- the whole Legendre structure of thermodynamics is preserved for $q \neq 1$ [4,7].

Although the nonextensive statistics were used for a long time in many branches of physics [4], their possible imprints in multiparticle production are very fresh. In this talk we shall concentrate on some cosmic ray experiments and accelerator experiments, which provided us with examples of a nonextensive behaviour. Both will demonstrate traces of nonextensivity seen as nonexponentiality of some distributions, i.e., where $\exp(x) \Rightarrow \exp_q(q) = [1-(1-q)x]^{1/(1-q)}$. At the end we shall, however, list all other works in which one can find similar conclusions [9].

2 Cosmic Ray Example

Part of the cosmic ray detector system consists of extrathick lead emulsion chambers. Such chamber is build with a number of sandwiches of X-ray sensitive film, plate of lead and layer of emulsion (first allows to localize the point at which external particle of cosmic rays enters, second forces it to interact and to start the electromagnetic cascade process, and third allows to calculate deposited energy). In some experiments one observes that distribution of the points of first interaction (cascade starting points) does not follow the

[c]There is a formalism, which expresses both the Tsallis entropy and the expectation value using the escort probability distribution, $P_i = p_i^q / \sum p_i^{q4}$. However, it is known [8] that such an approach is different from the present nonextensive formalism since the Tsallis entropy expressed in terms of the escort probability distribution has a difficulty with the property of concavity.

expected simple exponential rule[d10]:

$$\frac{dN}{dT} = \text{const} \cdot \exp\left(-\frac{T}{\lambda}\right) \tag{8}$$

but deviates from it noticeably for larger T. This phenomenon acquired even its own name: *long flying component* (because original hadrons tend to fly longer without interaction than naively expected).

In [10] we have argued that the observed effect can be just another manifestation of the fluctuation of the corresponding hadronic cross section $\sigma = Am_N\frac{1}{\lambda}$ (where A denotes the mass number of the target and m_N is the mass of the nucleon, such a possibility is widely discussed in the literature and observed in diffraction dissociation experiments on accelerators, cf. [10] for details and references). As was shown in [10] such fluctuations of cross section (i.e., in effect $1/\lambda$) with relative variance

$$\omega = \frac{\langle\sigma^2\rangle - \langle\sigma\rangle^2}{\langle\sigma\rangle^2} \geq 0.2 \tag{9}$$

allow to describe the observed effect. However, it turns out [11] that the same data can be fitted by the nonextensive formula

$$\frac{dN}{dT} = \text{const} \cdot \left[1 - (1-q)\frac{T}{\lambda}\right]^{\frac{1}{1-q}} \tag{10}$$

with parameter $q = 1.3$ (in both cases $\lambda = 18.85 \pm 0.66$ in *c.u.* defined above), cf. Fig. 1 (reproduced from Fig. 1 of [11] with data points from [10]).

This example provides us hint on the possible physical meaning of the nonextensvity parameter q. Comparing both explanations one can suspect that perhaps, at least in this case, it has something to do with the fluctuations of the seemingly constant parameter $1/\lambda$ in the exponential formula (8). We shall argue later that this is indeed the case but before let us demonstrate another example of this kind, now from the high energy multiparticle production processes domain.

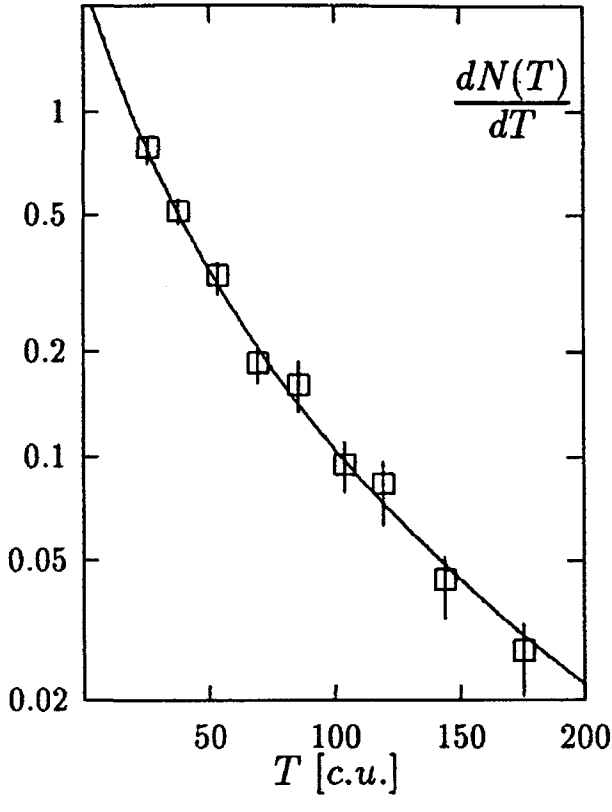

Figure 1. Depth distribution of the starting points, $dN(T)/dT$, of cascades in Pamir lead chamber. Notice the non-exponential behaviour of data points which can be fitted by Tsallis distribution (10) with $q = 1.3$.

3 Heavy ion collision example

Heavy ion collisions are of particular interest at present because they are the only place were one expects the possible formation of the QGP - a new state

[d]Here N is the number of cascades originating at depth T expressed in the so called cascade units where 1 c.u. $= 6.4$ g/cm^2 $= 0.56$cm of Pb and λ is the mean free path for the p-Pb interacions.

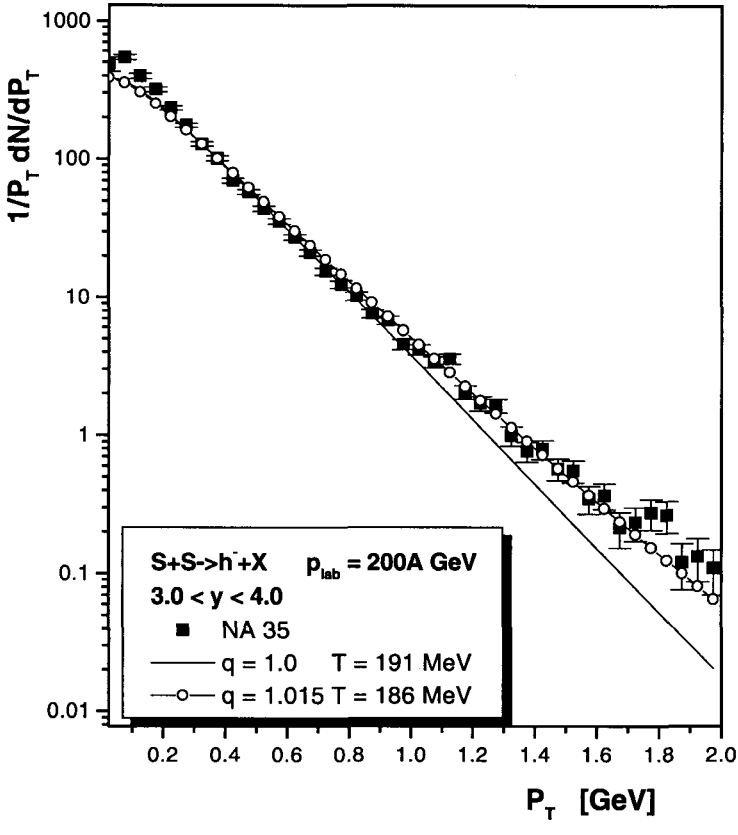

Figure 2. The results for p_T distribution $dN(p_T)/dp_T$: notice that $q = 1.015$ results describes also the tail of distribution not fitted by the conventional exponent (i.e., $q = 1$).

of matter [2]. The termal and/or all kind of statistical models are playing very important role here because one of the crucial parameter is the temperature T of reaction deduced usualy from the transverse momentum distributions, dN/dp_T. This is, however, valid procedure only when dN/dp_T is of exponential form. Therefore any deviation from such behaviour are always under detailed scrutiny in which one is searching for the possible causes. In [12] it

was suggested that the extreme conditions of high density and temperature occuring in ultrarelativistic heavy ion collisions can lead to memory effects and long-range colour interactions and to the presence of non-Markovian processes in the corresponding kinetic equations [13]. Actually, as has been shown in [12,14], $dN(p_T)/dp_T$ are best described, cf., Fig. 2 (reproduced from Fig. 3 of [14]), by a slightly nonexponential function of the type

$$\frac{dN(p_T)}{dp_T} = \text{const} \cdot \left[1 - (1-q)\frac{\sqrt{m^2+p_T^2}}{kT}\right]^{\frac{1}{1-q}} \stackrel{q\to 1}{\Longrightarrow} \text{const} \cdot \exp\left(-\frac{\sqrt{m^2+p_T^2}}{kT}\right). \tag{11}$$

Here m is the mass of produced particle, k is the Boltzmann constant (which we shall, in what follows, put equal unity) and T is, for the $q = 1$ case, the *temperature* of the reaction considered (or, rather, the temperature of the hadronic system produced). The deviation from the exponential form one finds is very small, on the level $q = 1.015$. However, as we shall demonstrate later it can lead to a quite dramatic effects. It was also shown in [12] that to first order in $|q-1|$ the generalized slope becomes the quantity

$$T_q = T + (q-1)m_T. \tag{12}$$

with T being temperature of *a purely thermal source.* This should be contrasted with the empirical relation for the slope parameter T, from which the freeze-out temperature (at which hadrons are created from the QGP) T_f is then deduced,

$$T = T_f + m\langle v_\perp\rangle^2. \tag{13}$$

The $\langle v_\perp\rangle$ is a fit parameter usually identified with the average collective (transverse) flow velocity of the hadrons being produced. In (12) one has, instead, *a purely thermal source* experiencing a kind of blue shift at high m_T (actually increasing with m_T). The nonextensivity parameter q accounts here for all possibilities one can find in [13] and could therefore be regarded as a new way of presenting experimental results with $q \neq 1$, signaling that there is something going on in the collision that prevents it from being exactly thermal-like in the ordinary sense mentioned above.

To the same cathegory belongs also analysis of the equilibrium distribution of heavy quarks in Fokker-Planck dynamics expected in heavy ion collisions [15]. Not going into details in this case, we shall only mention that it was found that thermalization of charmed quarks in a QGP surroundings

proceeding via collisions with light quarks and gluons results in a spectral shape, which can be described only in q statistics with q=1.114 (for $m_C = 1.5$ GeV and temperature of thermal gluons $T_g = 500$ GeV).

4 Fluctuations as a cause of nonextensivity?

Guided by the cosmic ray example we would like to discuss now the hypothesis that the examples of nonextensivity in which exponential distribution becomes a power-like (Lévy type) distributions is caused by the fluctuations in the system which were not accounted for and which make $q \neq 1$ [16,9]. In other words, q summarizes the action of averaging over $1/\lambda$:

$$\left\langle \exp\left[-\left(\frac{1}{\lambda}\right)\varepsilon\right]\right\rangle \Longrightarrow \left[1 - (1-q)\frac{1}{\lambda_0}\varepsilon\right]^{\frac{1}{1-q}}, \tag{14}$$

where $1/\lambda_0 = \langle 1/\lambda \rangle$. This connection, which is clear in the cosmic ray example, should also be true for the heavy ion collision. Actually, this later case is even more important and interesting because of the long and still vivid discussion on the possible dynamics of temperature fluctuations [17] and because of its connection with the problem of QGP production in heavy ion collisions [18].

Actually the conjecture (14) is known in the literature as Hilhorst integral formula [19] but was never used in the present context. It says that (for $q > 1$ case, where $\varepsilon \in (0, \infty)$)

$$\left(1 + \frac{\varepsilon}{\lambda_0}\frac{1}{\alpha}\right)^{-\alpha} = \frac{1}{\Gamma(\alpha)}\int_0^\infty d\eta\, \eta^{\alpha-1} \exp\left[-\eta\left(1 + \frac{\varepsilon}{\lambda_0}\frac{1}{\alpha}\right)\right]. \tag{15}$$

where $\alpha = \frac{1}{q-1}$. Changing variables under the integral to $\eta = \alpha\frac{\lambda_0}{\lambda}$, one obtains

$$L_{q>1}(\varepsilon;\lambda_0) = C_q\left(1 + \frac{\varepsilon}{\lambda_0}\frac{1}{\alpha}\right)^{-\alpha} = C_q\int_0^\infty \exp\left(-\frac{\varepsilon}{\lambda}\right) f\left(\frac{1}{\lambda}\right) d\left(\frac{1}{\lambda}\right) \tag{16}$$

where $f(1/\lambda)$ is given by the following gamma distribution:

$$f_{q>1}\left(\frac{1}{\lambda}\right) = f_\alpha\left(\frac{1}{\lambda}, \frac{1}{\lambda_0}\right) = \frac{\mu}{\Gamma(\alpha)}\left(\frac{\mu}{\lambda}\right)^{\alpha-1}\exp\left(-\frac{\mu}{\lambda}\right) \tag{17}$$

with $\mu = \alpha\lambda_0$ and with mean value and variation in the form:

$$\left\langle\frac{1}{\lambda}\right\rangle = \frac{1}{\lambda_0} \quad \text{and} \quad \left\langle\left(\frac{1}{\lambda}\right)^2\right\rangle - \left\langle\frac{1}{\lambda}\right\rangle^2 = \frac{1}{\alpha\lambda_0^2}. \tag{18}$$

Notice that, with increasing α the variance (18) decreases and asymptotically (for $\alpha \to \infty$, i.e, for $q \to 1$) the gamma distribution (17) becomes a delta function, $f_{q>1}(1/\lambda) = \delta(\lambda - \lambda_0)$. The relative variance for this distribution is given by

$$\omega = \frac{\left\langle \left(\frac{1}{\lambda}\right)^2 \right\rangle - \left\langle \frac{1}{\lambda} \right\rangle^2}{\left\langle \frac{1}{\lambda} \right\rangle^2} = \frac{1}{\alpha} = q - 1. \tag{19}$$

For the $q < 1$ case ε is limited to $\varepsilon \in [0, \lambda_0/(1-q)]$. Proceeding in the same way as before, i.e., making use of the following representation of the Euler gamma function (where $\alpha' = -\alpha = \frac{1}{1-q}$)

$$\begin{aligned} \left[1 - \frac{\varepsilon}{\alpha'\lambda_0}\right]^{\alpha'} &= \left(\frac{\alpha'\lambda_0}{\alpha'\lambda_0 - \varepsilon}\right)^{-\alpha'} \\ &= \frac{1}{\Gamma(\alpha')} \int_0^\infty d\eta\, \eta^{\alpha'-1} \exp\left[-\eta\left(1 + \frac{\varepsilon}{\alpha'\lambda_0 - \varepsilon}\right)\right], \end{aligned} \tag{20}$$

and changing variables under the integral to $\eta = \frac{\alpha'\lambda_0 - \varepsilon}{\lambda}$, we obtain $L_{q<1}(\varepsilon; \lambda_0)$ in the form of eq. (16) but with $\alpha \to -\alpha'$ and with the respective $f(1/\lambda) = f_{q<1}(1/\lambda)$ given now by the same gamma distribution as in (17) but this time with $\alpha \to \alpha'$ and $\mu = \mu(\varepsilon) = \alpha'\lambda_0 - \varepsilon$. Contrary to the $q > 1$ case, this time the fluctuations depend on the value of the variable in question, i.e., the mean value and variance are now both ε-dependent:

$$\left\langle \frac{1}{\lambda} \right\rangle = \frac{1}{\lambda_0 - \frac{\varepsilon}{\alpha'}} \quad \text{and} \quad \left\langle \left(\frac{1}{\lambda}\right)^2 \right\rangle - \left\langle \frac{1}{\lambda} \right\rangle^2 = \frac{1}{\alpha'} \cdot \frac{1}{\left(\lambda_0 - \frac{\varepsilon}{\alpha'}\right)^2}. \tag{21}$$

However, the relative variance

$$\omega = \frac{\left\langle \left(\frac{1}{\lambda}\right)^2 \right\rangle - \left\langle \frac{1}{\lambda} \right\rangle^2}{\left\langle \frac{1}{\lambda} \right\rangle^2} = \frac{1}{\alpha'} = 1 - q, \tag{22}$$

remains ε-independent and depends only on the parameter q. As above the resulting gamma distribution becomes a delta function, $f_{q<1}(1/\lambda) = \delta(\lambda - \lambda_0)$, for $\alpha' \to \infty$, i.e., for $q \to 1$.

Summarizing: one can indeed say that the nonextensivity parameter q in the $L_q(\varepsilon)$ distributions can be expressed by the relative variance ω of fluctuations of the parameter $1/\lambda$ in the distribution $L_{q=1}(\varepsilon)$:

$$q = 1 \pm \omega \qquad \text{for} \quad q > 1\ (+) \quad \text{and} \quad q < 1\ (-). \tag{23}$$

Actually the above result (23) is derived for the particular (Gamma-like) shape of the fluctuation distribution function. How can it be realized? To answer this question let us notice [16,9] that in the case when stochastic variable λ is decribed by the usual Langevin equation

$$\frac{d\lambda}{dt} + \left[\frac{1}{\tau} + \xi(t)\right] \lambda = \phi = \text{const} > 0, \tag{24}$$

(with damping constant τ and source term $\phi_{q<1} = \frac{1}{\tau}\left(\lambda_0 - \frac{\varepsilon}{\alpha'}\right)$ or $\phi = \phi_{q>1} = \frac{\lambda_0}{\tau}$), then for the stochastic processes defined by the *white gaussian noise* form of $\xi(t)$[e] one obtains the following Fokker-Plank equation [20] for the distribution function of the variable λ:

$$\frac{df(\lambda)}{dt} = -\frac{\partial}{\partial\lambda} K_1 f(\lambda) + \frac{1}{2}\frac{\partial^2}{\partial\lambda^2} K_2 f(\lambda), \tag{25}$$

with intensity coefficients $K_{1,2}$ defined by eq.(24) and equal to (cf., [21]):

$$K_1(\lambda) = \phi - \frac{\lambda}{\tau} + D\lambda \qquad \text{and} \qquad K_2(\lambda) = 2D\lambda^2. \tag{26}$$

Its stationary solution has precisely the Gamma-like form we are looking for:

$$f(\lambda) = \frac{c}{K_2(\lambda)} \exp\left[2\int_0^\lambda d\lambda' \frac{K_1(\lambda')}{K_2(\lambda')}\right] = \frac{1}{\Gamma(\alpha)}\mu\left(\frac{\mu}{\lambda}\right)^{\alpha-1} \exp\left(-\frac{\mu}{\lambda}\right), \tag{27}$$

with the constant c defined by the normalization condition, $\int_0^\infty d(1/\lambda) f(1/\lambda) = 1$. It depends on two parameters:

$$\mu(\varepsilon) = \frac{\phi_q(\varepsilon)}{D} \qquad \text{and} \qquad \alpha_q = \frac{1}{\tau D}, \tag{28}$$

with $\phi_q = \phi_{q>1,q<1}$ and $\alpha_q = (\alpha, \alpha')$ for, respectively, $q > 1$ and $q < 1$. Therefore eq. (23) with $\omega = \frac{1}{\tau D}$ is, indeed, a sound possibility with (in the case discussed above) parameter of nonextensivity q given by the parameter D and by the damping constant τ describing the *white noise*.

---

[e] It means that ensemble mean $\langle\xi(t)\rangle = 0$ and correlator (for sufficiently fast changes) $\langle\xi(t)\,\xi(t+\Delta t)\rangle = 2D\,\delta(\Delta t)$. Constants τ and D define, respectively, the mean time for changes and their variance by means of the following conditions: $\langle\lambda(t)\rangle = \lambda_0 \exp\left(-\frac{t}{\tau}\right)$ and $\langle\lambda^2(t=\infty)\rangle = \frac{1}{2}D\tau$. Thermodynamical equilibrium is assumed here (i.e., $t >> \tau$, in which case the influence of the initial condition λ_0 vanishes and the mean squared of λ has value corresponding to the state of equilibrium).

5 Back to heavy ion collisions

With the possibility of such interpretation of parameter q in mind we can now came back to the example of heavy ion collisions and see what are its consequences in this case. It is interesting to notice that the relatively small departure of q from unity, $q-1 \simeq 0.015$ [12,14], if interpreted in terms of the previous section, indicates that rather large relative fluctuations of temperature, of the order of $\Delta T/T \simeq 0.12$, exist in nuclear collisions. It could mean therefore that we are dealing here with some fluctuations existing in small parts of the system in respect to the whole system (according to interpretation of [22]) rather than with fluctuations of the event-by-event type in which, for large multiplicity N, fluctuations $\Delta T/T = 0.06/\sqrt{N}$ should be negligibly small [18]. This controversy could be, in principle, settled by detailed analyses of the event-by-event type. Already at present energies and nuclear targets (and the more so at the new accelerators for heavy ions like RHIC at Brookhaven, now commisioned, and LHC at CERN scheduled to be operational in the year 2006) one should be able to check whether the power-like p_T distribution $dN(p_T)/dp_T$ occurs already at every event or only after averaging over all events. In the former case we would have a clear signal of thermal fluctuations of the type mentioned above. In the latter case one would have for each event a fixed T value which would fluctuate from one event to another (most probably because different initial conditions are encountered in a given event).

One point must be clarified, however. The above conjecture rests on the stochastic equation (24). Can one expect such equation to govern the T fluctuations? To ansewer this question let us turn once more to the fluctuations of temperature [17,18,22] discussed before, i.e., to $\lambda = T$. Suppose that we have a thermodynamic system, in a small (mentally separated) part of which the temperature fluctuates with $\Delta T \sim T$. Let $\lambda(t)$ describe stochastic changes of the temperature in time. If the mean temperature of the system is $\langle T \rangle = T_0$ then, as result of fluctuations in some small selected region, the actual temperature equals $T' = T_0 - \tau\xi(t)T$. The inevitable exchange of heat between this selected region and the rest of the system leads to the equilibration of the temperature and this process is described by the following equation [23]:

$$\frac{\partial T}{\partial t} - \frac{1}{\tau}(T' - T) + \Omega_q = 0, \tag{29}$$

which is, indeed, of the type of eq. (24) (here $\Omega_{q<1} = \frac{\varepsilon}{\tau\alpha'}$ and $\Omega_{q>1} = 0$). This proves the plausability of what was said above and makes the event-by-even measurements of such phenomenon very interesting one.

6 Other imprints of nonextensivity

The above discussed examples do not exhaust the list of the possible imprints of nonextensivity in multiparticle production know (or thought of) at present. As it is impossible to review all of them here, we shall therefore only mention them.

In [12,14] the possible effects of nonextensivity on the mean occupation numbers n_q and on the event-by-event fluctuation phenomena have been discussed. It turns out, for example, that some charateristics of fluctuations are extremaly sensitive to even small departures of q from unity. Such departure can easily mimick the existing correlations or the influence of resonances.

In [24] an interesting attempt was presented to fit the energy spectra in both the longitudinal and transverse momenta of particles produced in the e^+e^- annihilation processes at high energies using q-statistical model. In this way one can have energy independent temperature T and nonextensivity parameter q rising quickly with energy from $q = 1$ to $q = 1.2$ and reflecting long range correlations in the phase space arising in the hadronization process in which quarks and gluons combine together forming hadrons (actually, this observation has general validity and applies to all production processes discussed here as well). In similar spirit is the work [25] which attemts to generalized the so called Hagedorn model of multiparticle production to q-statistics.

To the extend to which self-organized criticality (SOC) is connected with nonextensivity [4] one should also mention here a very innovative (from the point of view of high energy collision) application of the concept of SOC to such processes [26].

The other two examples do not refer to Tsallis thermostatistics directly, nevertheless they are connected to it. First is the attempt to study, by using the formalism of quantum groups, the Bose-Einstein correlations between identical particles observed in multiparticle reactions [27], second are works on intermittency and multiparticle distributions using the so called Lévy stable distributions [28]. They belong, in some sense, to the domain of nonextensivity because, as was shown in [29], there is close correspondence between the deformation parameter of quantum groups used in [27] and the nonextensivity parameter q of Tsallis statistics and there is also connection between Tsallis statistics and Lévy stable distributions [28]. Some traces of the

possible nonextensive evolution of cascade type hadronization processes were also searched for in [30]. The quantum group approach [27,29] could probably be a useful tool when studying delicate problem of interplay between QGP and hadrons produced from it. It is plausible that description in terms of q-deformed bosons (or the use of some kind of interpolating statistics) would lead to more general results than the simple use of nonextensive mean occupation numbers $< n >_q$ discussed above (for which the only known practical description is limited to small deviations from nonextensivity only).

One should mention also attempts to use Lévy-type distributions to fit the development of the cosmic ray cascades to learn of how many descendat they contain [31] or the explanation of the Feynman scaling violation observed in multiparticle distributions in terms of the q parameter [32].

7 Summary

To summarize, evidence is growing in favour of the view that the standart statistical model can be enlarged towards the nonstandart statistics and that by including one new parameter q it allows to repoduce much broader set of data than it was done so far. It was demonstrated that q is probably connected with the intrinsic fluctuations existing in the system under consideration which were previously not considered at all[f]. Let us close with the remarks that, as was shown in [34], one can also try to use power-like distributions discussed here to the new formulation of the quantum field theory (for example, in terms of lorenzian rather than gaussian path integrals, accounting in this manner for some intrinsic long range correlations impossible to dispose of and extremaly difficult to account for by other methods).

Acknowledgements: One of us (G.W.) would like to thank the organizers of the RANP2000 for support making his participation in this workshop possible. Authors are grateful to Prof. S.Abe for his valuable comments.

[f] Actually it is likely that the importance of fluctuations is more general than their applications to q-statistics only. A good example is work [33] showing how fluctuations of the vacuum can change the theoretically expected gaussian spectra in string models into the observed exponential one with a kind of effective "temperature".

References

1. L.D. Landau and S.Z. Bilenkij, *Nuovo Cim. Suppl.* **3** (1956) 15 and *Collected Papers of L.D. Landau*, ed. D. Ter Haar, Pergamon Press (1965), p. 569. This model is still in use even today for quick and straightforward estimations of some quantities of interest, cf., M.Gaździcki, *Z. Phys.* **C66** (1995) 659.
2. Cf., for example, proceedings of *Quark Matter'99*, *Nucl. Phys.* **A525** (1999) and references therein.
3. G.Wilk and Z.Włodarczyk, *Phys. Rev.* **D43** (1991) 794. The early references to all previous applications of this approach to multiparticle production can be found here as well.
4. C.Tsallis, *J. Stat. Phys.* **52** (1988) 479; cf. also C.Tsallis, cond-mat/0010150 (to appear in *Chaos, Solitons and Fractals* (2001). For updated bibliography on this subject see http://tsallis.cat.cbpf.br/biblio.htm. Its recent summary is provided in the special issue of *Braz. J. Phys.* **29** (No 1) (1999) (available also at http://sbf.if.usp.br/WWW_pages/Journals/BJP/Vol29/Num1/index.htm).
5. Y.-A. Chao, *Nucl. Phys.* **B40** (1972) 475.
6. E.T. Jaynes, *Phys. Rev.* **106** (1957) 620; **108** (1957) 171; L.Van Hove, *Z. Phys.* **C21** (1985) 93; **C27** (1985) 135.
7. Cf. lecture by C.Tsallis, this volume.
8. S.Abe, *Phys. Lett.* **A275** (2000) 250.
9. Cf., for example, G.Wilk and Z.Włodarczyk, *The imprints of nonextensive statistical mechanics in high energy collisions*; hep-ph/0004250; to be published in *Chaos, Solitons and Fractals* (2001).
10. G.Wilk and Z.Włodarczyk, *Phys. Rev.* **D50** (1994) 2318.
11. G.Wilk and Z.Włodarczyk, *Nucl. Phys.* **B** (*Proc. Suppl.*) **A75** (1999) 191.
12. W.M.Alberico, A.Lavagno and P.Quarati, *Eur. Phys. J.* **C12** (2000) 499.
13. S.Gavin, *Nucl. Phys.* **B351** (1991) 561; J.Rau, *Phys. Rev.* **D50** (1994) 6911; S.Schmidt et al., *Phys. Rev.* **D59** (1999) 094005; H.Heiselberg and X.-N.Wang, *Phys. Rev.* **D53** (1996) 1892; V.K.Magas et al., *Phys. Lett.* **B459** (1999) 33; Cs.Anderlik et al., *Phys. Rev.* **C59** (1999) 388, 3309; F.Grassi et al., *Phys. Rev.* **C62** (2000) 044904; J.Hormuzdiar et al., *Particle Multiplicities and Thermalization in High Energy Collisions*, arXiv:nucl-th/0001044.
14. O.V.Utyuzh, G.Wilk and Z.Włodarczyk, *J. Phys.* **G26** (2000) L39.
15. D.B.Walton and J.Rafelski, *Phys. Rev. Lett.* **84** (2000) 31.
16. G.Wilk and Z.Włodarczyk, *Phys. Rev. Lett.* **84** (2000) 2770.

17. T.C.P.Chui, D.R.Swanson, M.J.Adriaans, J.A.Nissen and J.A.Lipa, *Phys. Rev. Lett.* **69** (1992) 3005; C.Kittel, *Physics Today* **5** (1988) 93; B.B.Mandelbrot, *Physics Today* **1** (1989) 71; H.B.Prosper, *Am. J. Phys.* **61** (1993) 54; G.D.J.Phillires, *Am. J. Phys.* **52** (1984) 629.
18. L.Stodolsky, *Phys. Rev. Lett.* **75** (1995) 1044; E.V.Shuryak, *Phys. Lett.* **B423** (1998) 9; S.Mrówczyński, *Phys. Lett.* **B430** (1998) 9.
19. C.f., for example, S.Curilef, *Z.Phys.* **B100** (1996) 433 and references therein.
20. N.G. van Kampen, *Stochastic Processes in Physics and Chemistry*, Elsevier Science Pub. B.V., North-Holland, Amsterdam 1987 (Chapter VIII).
21. C.A.Ahmatov, Y.E.Diakov and A.Tchirkin, *Introduction to Statistical Radiophysics and Optics*, Nauka, Moscow, 1981 (in Russian).
22. L.D.Landau, I.M.Lifschitz, *Course of Theoretical Physics: Statistical Physics*, Pergmon Press, New York 1958.
23. L.D.Landau and I.M.Lifschitz, *Course of Theoretical Physics: Hydrodynamics*, Pergamon Press, New York 1958 or *Course of Theoretical Physics: Mechanics of Continuos Media*, Pergamon Press, Oxford 1981.
24. I.Bediaga, E.M.F.Curado and J.M.de Miranda, *Physica* **A286** (2000) 156.
25. C.Beck, *Physica* **A286** (2000) 164.
26. Meng Ta-chung, R.Rittel and Z.Yang, *Phys. Rev. Lett.* **82** (1999) 2044 and C.Boros et al., *Phys. Rev.* **D61** (2000) 094010 (cf. also: hep-ph/0009034).
27. D.V.Anchishkin, A.M.Gavrilik and N.Z.Iogorov, *Eur. J. Phys.* **A7** (2000) 229 and *Mod. Phys. Lett.* **15** (2000) 1637.
28. Cf., for example, R.Peschanski, *Nucl. Phys.* **B253** (1991) 225 or S.Hegyi, *Phys. Lett.* **B387** (1996) 642 (and references therein).
29. C.Tsallis, *Phys. Lett.* **A195** (1994) 329. See also A.Lavagno and P.Narayana Swamy, *Mod. Phys. Lett.* **13** (1999) 961 and *Phys. Rev.* **E61** (2000) 1218.
30. O.V.Utyuzh, G.Wilk and Z.Włodarczyk, *Czech J. Phys.* **50/S2** (2000) 132.
31. M.Rybczyński, Z.Włodarczyk and G.Wilk, *Self-organized criticality in atmospheric cascades*, presented at the *XI ISVHECRI*, Unicamp-Campinas-Brazil, July 17-21, 2000; hep-ph/0005216; to be published in *Nucl. Phys.* **B** *(Proc. Suppl.)*.
32. F.S.Navarra, O.V.Utyuzh, G.Wilk and Z.Włodarczyk, *Violation of the Feynman scaling law as a manifestation of nonextensivity*, presented at Chacaltaya Meeting on Cosmic Ray Physics, July 23-27, 2000, La Paz, Bolivia, to be published in *Nuovo Cim.* **C**; hep-ph/0009165.

33. A.Białas, *Phys. Lett.* **B466** (1999) 301.
34. R.A.Treuman, *Phys. Rev.* **E57** (1998) 5150; *Europh. Lett.* **48** (1999) 8 and *Phys. Scripta* **59** (1999) 19, 204. See also R.S.Mendes in review volume quoted in [4], p. 66.

Discussion

Question by K.Werner: *Concerning your example dN/dp_T: this seems to be quite under control,large p_T is perturbative QCD (power-like), small p_t is soft, so you have a superposition of these two processes. There seems to be no need of these additional fluctuations.*
Answer: Your proposition is just one of many around us. You are right that adding two known (in their domain of applicability) mechanisms will also fit data. But what we are saying here is that, perhaps, there is mechanism which would show itself in the intermediate region and which can be described by the nonextensive parameter q. And it can be experimentally checked in event-by-event type of analysis, as was presented above. This would answer the question is there a need for something or not. Besides, it should be stressed that using only one new parameter q one can fit quite large (in [24] the whole) region of p_T.

Question by F.Grassi: *Did you try to fit p_T distributions for other type of particles than charged?*
Answer: No, at least not yet.

Question by T.Kodama: *If q represents the measure of fluctuations of ensemble, then it would also reflect in multiplicity distributions. However, value of q is different for the p_T distribution and multiplicity distribution. How do you interpret this?*
Answer: It is difficult for me to comment because so far I have not seen such analysis of the multiplicity data. But if things are really as you say then, assuming that everything was done correctly, I would argue that multiplicity is global characteristic whereas p_T is a local one. Therefore they are sensitive to different aspects of the underlying dynamics and resulting parameters q could *a priori* be different. One can also say that for p_T distribution the situation is more clear as we are simple replacing here exp(...) by $\exp_q(...)$. Multiplicity distributions depend on q in indirect way only.

Bikash Sinha

Relics of the Cosmological Quark-Hadron Phase Transition

Bikash Sinha
Variable Energy Cyclotron Centre, 1/AF Bidhan Nagar Calcutta - 700 064
and
Saha Institute of Nuclear Physics, 1/AF Bidhan Nagar Calcutta - 700 064

1. Introduction

Quantum Chromodynamics (QCD), the theory of strong interaction, indicates that the relevant degrees of freedom of a system of hadrons at sufficiently high temperature and/or density are quarks and gluons rather than colour-neutral hadrons. In the context of the hot big-bang model of the early universe, this implies that in the early universe when the temperature of the universe was much higher than the fundamental QCD parameter $\Lambda \sim 100$ MeV, which corresponds to times earlier than ~ 10 μsec,hadrons (neutrons, protons, etc.) did not exist. Instead, this hadronic matter is thought to have existed in the form of what is called "Quark-Gluon Plasma" (QGP) consisting of deconfined quarks and gluons. As the universe expanded and cooled through a critical temperature $T_c \sim 100$ MeV, a transition from QGP to hadrons must have occurred. Is there any cosmological relic from this microsecond epoch of the early universe surviving in the universe today, whose detection would be an evidence that QGP existed in the early universe?

The QGP $\longrightarrow$ Hadron (Q $\longrightarrow$ H) transition is an event when quarks carrying colour quantum number combined to form colour-neutral hadrons. We certainly have direct evidence of a 'similar' important event that happened at a much later epoch in the history of the early universe, namely, the event of "photon decoupling" when the universe cooled to a temperature $\sim$0.3 MeV At around that temperature, almost all the free electrons and protons in the universe combined to form neutral hydrogen atoms. The photons subsequently suffered no significant scattering because of lack of sufficient abundance of free electrons. These decoupled relic photons constitute the well-known cosmic microwave background radiation. Is there any such 'decoupled' species surviving in the present universe as relics from the epoch of Q $\longrightarrow$ H transition? Due to the confinement property of QCD at low energies, there cannot be relic background of freely propagating gluons. So one must look for other kinds of possible relics.

It turns out that the question of existence of relics from Q $\longrightarrow$ H transition depends on the nature of this transition which, unfortunately, is not known with certainty. At present our understanding of the nature of this transition comes primarily from the numerical simulation of QCD on a lattice. The results of these lattice QCD simulations are, however, beset with uncertainties due to, among other things, finite lattice sizes and lattice spacings. There are, in addition, conceptual problems associated with inclusion of real dynamical quarks in the simulations in a consistent way. The opinions on the nature of the transition vary widely : Strong first-order phase transition, weak first order phase transition, second-order phase transition, and so on. In fact, it is not clear whether it is a phase transition at all in the thermodynamic sense; it could, e.g., simply be a continuous cross-over as in the case of the 'photon decoupling' transition.

In this talk I will not dwell further on the nature of the Q $\longrightarrow$ H transition. Instead, I will simply assume that it is a *phase transition*, and further, a *first-order* phase transition, in which case, there is a possibility[1] that a particular kind of relics called "quark nuggets" (QNs) containing a large fraction of the net baryon number of the universe may have been formed at the end of such a phase transition. The QNs would have tremendous

implications for cosmology and astrophysics.[2,3] In particular, they can be a good candidate for the baryonic dark matter in the universe provided they can survive up to the present epoch. The QNs which survived and floating around the universe, is there any connection with the recently discovered MACHOs between the earth and the Large Magellanic clouds?.[4]

The QNs are hypothesized to be made of "strange matter" (SM) which is composed of a roughly equal mixture of u, d, and s quarks at a density $\geq$ nuclear density. It has been hypothesized[1] that at zero temperature and zero pressure the true ground state of hadronic matter could be SM rather than ^{56}Fe ,i.e.,the energy per baryon in SM could be lower that that in ordinary nuclear matter. The latter would, however, still be effectively stable against decaying into SM because such a decay would require an extremely high order simultaneous weak interaction process with a life-time much greater than the age of the universe. For certain ranges of values of parameters involved, namely, the QCD fine structure constant (α_c) , mass of the strange quark (m_s), the vacuum bag energy (B), etc., the hypothesis of SM being the absolutely stable state of hadronic matter has been found to be quite plausible.[5,6]

A possible physical mechanism by which QNs made of SM could form during a first-order QGP $\longrightarrow$ Hadron phase transition has been described in a very lucid manner by Witten in his original paper.[1] The main requirement in Witten's scenario is that the phase transition be of first-order in which case there is a latent heat of transition associated with the discontinuous jump in the energy density of the system, this being the characteristic of all first -order phase transitions (FOPT). The FOPT from QGP to hadrons would proceed through the process of nucleation and growth of bubbles of hadronic phase in the QGP phase. As the universe expanded and cooled through a certain critical temperature $T_c \sim 100$ MeV, bubbles of hadronic matter would nucleate spontaneously in the background of QGP matter. The bubbles of sizes greater than a certain critical size would grow in size and coalesce, thereby converting larger fraction of the volume of the universe into the hadronic phase. During this process the latent heat released compensates for the cooling due to expansion of the universe. There is thus a brief epoch during which hadronic matter and QGP coexist and the universe remains at a constant temperature, even though it expands. In the end, when the fraction of volume of the universe converted to hadronic phase increases to near unity the cooling of the universe due to expansion resumes.

During the coexistence epoch, exchange of entropy (primarily by neutrinos and photons) across the phase boundary between the two phases is expected to maintain the thermal equilibrium between the two phases. However, it is a different matter whether chemical equilibrium associated with the conserved baryon number is maintained between the two phases. The baryon chemical equilibrium between the two phases requires efficient exchange of baryon number across the phases boundary. Note that baryon number in the QGP phase is carried by essentially massless quarks while in the hadronic phase it is carried by massive nucleons. The exchange of baryon number from the QGP side to the hadronic side would have to occur through a two-state process : First, three quarks of appropriate colours would have to come together to form a colourless baryon near the phase boundary, and, second, it must then 'diffuse' across the phase boundary. If this baryon transport process is inefficient, which seems very likely to be the case, as Witten argued, then it is likely that the baryon number of the universe would be largely trapped in the shrinking regions still occupied by the QGP phase. Eventually, if the baryon number density in these shrinking blobs of QGP reaches a sufficiently high value, the associated Fermi pressure would stop further shrinkage resulting in the formation of nuggets of QGP or 'strange matter' containing a large fraction of the net baryon number density of the universe.

Whether this simple mechanism of formation of QNs would actually be realized during the QCD phase transition in the early universe is not however a settled issue.[7] Moreover, as already mentioned, it is not clear whether the transition from QGP to hadrons is a process of first-order phase transition (which is crucial for the formation of QNs). While these uncertainties remain, the implications of the existence of relic QNs are important enough that several authors[8,9] have studied the question of survivability of QNs *assuming* that they are formed in the early universe. It is perhaps fair to say that even this issue of survivability of the QNs is also not a fully settled issue.

A QN formed with a given initial baryon number will be stable (and will presumably survive till the present

epoch) if it loses heat and cools without losing any significant fraction of its initial baryon number through the process of baryon evaporation.[8] In this talk I discuss this issue of baryon evaporation from and survivability of QNs highlighting , in particular, the results of a new calculation[10] done within the context of a *dynamical* model of baryon formation and evaporation from QNs. This model incorporates the phenomenologically successful chromoelectric flux-tube (CEFT) fission model[11–13] of hadron production in high energy collision experiments. In this model the rate of baryon evaporation from QNs is substantially lower than that in earlier studies[8,14] of this problem which used only thermodynamic and binding energy arguments and assumed 100% baryon transparency of the nugget surface to calculate the baryon evaporation rate. Consequently, the CEFT fission model yields substantially lower values (compared to those in Ref.,[8] for example) of the initial baryon number above which QNs survive the evaporation process. This enhances the possibility that QNs , if formed in the early universe, would survive into the present epoch.

2. Baryon Evaporation from QNs

2.1 *Binding Energy Arguments*

The first study of the question of baryon evaporation from QNs is due to Alcock and Farhi (AF)[8] who argued that nucleons could be liberated and emitted from QNs at temperatures $T \geq I_N$, where $I_N \sim$ (20-80) MeV is the nucleon "binding energy" , i.e., the difference between energy per baryon in SM at zero temperature and the mass of a free nucleon. AF calculated the rate of baryon evaporation from QNs by using the appropriate Saha equation that relates the neutron absorption rate to emission rate through detailed balance in a system consisting of QNs of all possible baryon numbers and neutrons. AF assumed geometric cross section for absorption of neutrons by QNs and complete baryon transparency of the nugget surface. This gave the result that QNs with even the largest allowed initial baryon number (i.e., the total baryon number $N_{B,hor} \approx 10^{49}$ (100 MeV/T)^3 contained in a horizon-size volume of the universe at the time of formation of the nugget, T being the temperature of the universe at that time) are unstable with respect to baryon evaporation. This result would essentially eliminate the possibility of any QN surviving till the present epoch.

Madsen et al.[14] then pointed out that since evaporation is a surface process, emission of neutrons (note that proton emission is slightly suppressed compared to neutron emission because of a coulomb barrier) makes the surface layer deficient in u and d quarks and relatively enriched with s quarks. The rate of conversion of s quarks back to u and d quarks as well as convection of u and d quarks from the core of the nugget to its surface layer are both insufficient[14–17] for establishing flavor chemical equilibrium between u, d, and s quarks on the surface layer. As a result of this deficiency of u and d quarks in the surface layer, further nucleon evaporation is suppressed (heavier baryon emission is suppressed due to their higher masses). Madsen et al.[14] find that QNs with initial baryon number $N_{B,in} \geq 10^{46}$ can be stable against baryon evaporation.

QNs at temperatures above a few MeV are also subject to the process of "boiling"[18] (i.e., spontaneous nucleation of hadronic bubbles in the bulk of the nugget and consequent conversion of the nugget into nucleons). Madsen and Olesen[9] have, however, shown that although boiling is thermodynamically allowed, the time scale for bubble nucleation inside QNs is too long compared to that for the surface evaporation process for reasonable values of the parameters involved in the problem. In this talk we will not discuss this boiling process further.

The above arguments for baryon emission involve only energetics and neglect the dynamics that determine the *probability* of baryon emission. Clearly for a realistic description of the process a *dynamical* model of baryon emission from QNs is needed.

2.2 A Dynamical Model : The CEFT Fission Model of Baryon Emission from QNs

We consider here a dynamical model of baryon evaporation from QNs formulated in terms of the so-called chromoelectric flux tube (CEFT) model of confinement in QCD. In this model, a color electric flux-tube develops behind any quark that, due to its momentum, happens to cross the nugget boundary from inside. The flux-tube connects this "leading" quark to the nugget surface by the shortest path. The constant string tension in the flux-tube gives rise to the linear attractive potential thought to be responsible for confinement. The energy stored in the flux-tube increases at the expense of the kinetic energy of the leading quark which ultimately stops and is pulled back into the nugget due to tension in the flux-tube *unless the tube fissions.* If the leading quark originally has enough momentum, the total energy stored in the tube may exceed the mass of a meson or a baryon. The flux-tube can then break ("fission") through quantum tunneling of a virtual $q-\bar{q}$ pair or a $\overline{qq}-qq$ pair, created in the uniform color electric field of the flux-tube, into a real state. The leading quark can then combine with the $\bar{q}$ (qq) of the pair, forming a meson (baryon), which escapes from the system. The remaining part of the created pair is drawn back into the nugget due to tension in the flux-tube. The energy and momentum of the escaping meson or baryon is determined by the energy and momentum of the leading quark and the space-time position (in the flux tube) where the appropriate pair creation occurs. Clearly, the baryon emission is suppressed relative to meson emission because of smaller probability of $\overline{qq}-qq$ creation relative to the $q-\bar{q}$ pair creation.

The above model has earlier been applied to study meson[19] as well as baryon[20] evaporation from the QGP phase before or during the phase transition to hadrons to study possible signatures of QGP. The model has also been used[21] in the study of baryon penetrability at the QGP-hadron phase boundary during the phase transition and to study the development of baryon inhomogeneity at the end of the transition. In applying[10] this model to QNs (which presumably are formed near the *end* of the phase transition), one has to take account of the fact that QNs are highly degenerate fermion systems described by Fermi-Dirac distribution function (as opposed to thermal distribution function in the case of QGP). In other words, the momentum scale of the quarks inside the nugget, which determines the baryon evaporation rate, is set by the temperature *and* the chemical potential (μ_q) of the quarks in the nugget, *not* by the temperature alone. In the case of QGP, on the other hand, the momentum scale of the quarks is determined by the temperature alone because $\mu_q \approx 0$ in the QGP phase.

The details of calculation of the rate of baryon evaporation from QNs in the CEFT fission model is given in Ref..[10] Here we only note a few salient points.

The dynamics of the CEFT fission model is primarily determined by the characteristic confinement momentum scale, $k^q_{c,B}$ defined as

$$k^q_{c,B} = \sqrt{\frac{3\sigma^3}{2\pi\alpha_c p^q_B}}$$

Which depends on the string tension σ, on the QCD coupling constant $\alpha_c = g^2/4\pi$ (g being the color charge), and on p^q_B, the probability per unit four volume of creation of a $qq-\overline{qq}$ pair of appropriate flavor combination required for formation of the particular baryon B by the particular leading quark flavor q. (Thus, if the leading quark is a d quark, say then for the case of emission of a $us-\bar{u}\bar{s}$ pair; see Table 1).

Typically, $k^q_{c,B}$ is the characteristic momentum that the leading quark q loses (so that the corresponding energy is stored in the flux-tube) before it can emit the baryon B with any appreciable probability, thus the leading quark must have an initial momentum $k_0 \geq k^q_{c,B}$, in order for the baryon B to be emitted; the most probable value of the momentum of the emitted baryon, is therefore, $k^B \simeq k_0 - k^q_{c,B}$.

The probability per unit four-volume (of the CEFT) of creation of a $q-\bar{q}$ pair,[13] $p(q-\bar{q})$, and $qq-\overline{qq}$ pair,[20] $p(qq-\overline{qq})$ are determined by the string tension σ and the masses of the quarks (it is sufficient to consider only u, d, and s quarks - charm quarks are too massive to be of importance in our problem). Following Refs.[19,20] we take σ=0.177 GeV^2 (deduced from the Regge trajectories of hadrons). The quark masses are, however, unknown.

Baryon(B)	y_B^u	p_B^u	y_B^d	p_B^d	y_B^s	p_B^s
$n(udd)$	1	0.065	1	0.065	0	0
$p(uud)$	1	0.065	1	0.065	0	0
$\Lambda^0(uds)$	1	3.77×10^{-3}	1	3.77×10^{-3}	1	0.065
$\Sigma^+(uus)$	1	3.77×10^{-3}	0	0	1	0.065
$\Sigma^0(uds)$	1	3.77×10^{-3}	1	3.77×10^{-3}	1	0.065
$\Sigma^-(dds)$	0	0	1	3.77×10^{-3}	1	0.065
$\Xi^0(uss)$	1	4.55×10^{-5}	0	0	1	3.77×10^{-3}
$\Xi^-(dss)$	0	0	1	4.55×10^{-5}	1	3.77×10^{-3}
$\Omega^-(sss)$	0	0	0	0	1	4.55×10^{-5}

Table 1: The values of p_B^q , the probability per unit four-volume for a leading quark of flavor $q(= u, d, s)$ to produce the various different baryons B. The values of p_B^q are given in the unit of $p(u-\bar{u}) = \sigma^2/24\pi$ (see text). The quantity y_B^q is 1 if the baryon B can be produced by the leading quark flavor q and zero otherwise. The quark compositions of the various baryons are also given for convenience.

One cannot assume arbitrary values of the quark masses here because of the constraint that the resulting values of $p(q-\bar{q})$and $p(qq-\overline{qq})$ must reproduce the observed multiplicities of mesons as well as baryons produced in collision experiments. By studying the jet phenomenology of e^+-e^- and $p-p$ collision experiments in the Lund model (which is a particular realization of the CEFT model), Andersson et al.[12] found that the observed meson and baryon multiplicities fix the *ratios* of the various relevant quark pair-creation probabilities; which in turn constrain the possible quark masses. For σ =0.177 GeV^2 and considering current quark masses, these values of the probability ratios are consistent[20] with the choice $m_u = m_d = 0$, $m_s = 200$ MeV, while for constituent quark masses the choice $m_u = m_d$ =300 MeV, $m_s = 380$ MeV is also allowed. Higher quark masses lead to a decrease in the pair creation probability and hence in the baryon evaporation rate. Because of uncertainties in the values of several parameters, we shall try in general to overestimate the evaporation rate so as to have a conservative estimate of the lowest initial baryon number of the stable QNs. We, therefore, consider only the current quark mass choice mentioned above. We shall also ignore any possible temperature and/or density dependence of the quark masses.

From the phenomenologically fixed values of the ratios of the relevant pair-creation probabilities mentioned above, one can calculate the values of p_B^q (in the unit of $p(u-\bar{u}) = \frac{\sigma^2}{24\pi}$)[13] for various baryons B and leading quark flavour q. These values are given in Table 1. The quantity y_B^q in Table 1 is the "yes-no" factor, i.e. y_B^q = 1 if the baryon B can be produced by the leading quark q and 0 otherwise.

The characteristic confinement momentum scale k_c depends on the value of α_c. The CEFT can be characterized by two independent parameters, namely, the color charge g (or $\alpha_c = \frac{g^2}{4\pi}$) and the cross-sectional area A of the flux-tube (A is assumed to be constant along the flux-tube). The color electric field strength ε is then obtained from the Gauss Law, $\varepsilon A = g/2$, and the string tension σ (i.e., the energy per unit length of the flux-tube) is then given by $\sigma = \frac{1}{2}\varepsilon^2 A$. If we take a flux-tube diameter $\sim$ 1 fm then σ = 0.177 GeV^2 corresponds to a value of $\alpha_c \approx$ 2.0. Clearly, the actual value of α_c is unknown, especially in the confinement regime of QCD relevant for our problem. We shall discuss the dependence of our results on the value of α_c.

Note that, if we consider the emission of nucleons for example, Table 1 gives $p_B^q = 0.065\left(\frac{\sigma^2}{24\pi}\right)$ so that for α_c =2.0 and σ = 0.177 GeV^2 we have $k_{c,B}^q \simeq 7$ GeV. For a *smaller* value of α_c (for a fixed value of σ), the value of $k_{c,B}^q$ is even larger. The typical chemical potential (and hence the momentum scale) of the quarks in the QN at zero temperature is $\sim$ 200-300 MeV. Since at exactly zero temperature the Fermi-Dirac (FD) distribution function has a sharp cut-off at the Fermi momentum (= chemical potential which is $\sim$ 200-300 MeV), the number

density of quarks having momenta above 7 GeV is nil and so essentially no baryon evaporation is possible. At a finite temperature, however, although the value of the chemical potential decreases, the FD distribution has a tail so that there is always a small (but finite) probability of finding some quarks with momenta beyond the value of $k^q_{c,B}$ under consideration. It is these quarks populating the tail of the FD distribution function at momenta beyond $k^q_{c,B}$ which will be responsible for emission of the baryon B. Clearly, higher the temperature, longer is the FD tail and greater is the emission probability and consequently so is the baryon evaporation rate.

To calculate the evolution of the baryon number in a nugget two simplifying assumptions can be made. Both these assumptions lead to overestimation of the evaporation rate. The assumptions are: (i) Temperature of the nugget T_{QN}, is same as the ambient temperature of the universe, T_U. In reality $T_{QN} < T_U$ because of evaporation. Since the evaporation rate is in general higher at higher temperatures we overestimate the evaporation rate by this assumption. (ii) Flavor chemical equilibrium between u, d and s quarks holds throughout the nugget volume. Any possible flavor chemical non-equilibrium suppresses[14] the evaporation rate. So here we again overestimate the evaporation rate.

Flavor chemical equilibrium implies $\mu_d = \mu_s = \mu_q$ (say), and $\mu_d = \mu_u + \mu_e$, where μ_e is the electron chemical potential. One can solve for μ_q and μ_e at any given temperature T by solving the pressure balance equation at the nugget surface and the charge neutrality condition, simultaneously. In the pressure balance equation the value of the bag constant B responsible for overall confinement of the quarks in the nugget needs to be specified. It is not clear[9] what should be a realistic value of B at the high temperatures. Results are presented below for two different values of B, namely $B^{1/4} = 140$ and 150 MeV to check the dependence of stability on the value of B. These are representative values of B derived from low-energy hadron spectroscopy. In the numerical calculations, the electron chemical potential μ_e is found to be negligibly small compared to μ_q.

The nuggets also absorb neutrons from the surrounding medium. For a homogeneous cosmological density of nucleons the absorption plays a relatively minor role (compared to emission) in the overall evolution of the baryon number of the nugget. However, if there is a significant enhancement of nucleon density around each nugget then the effect of (re)-absorption of the baryons can significantly enhance the stability of the nuggets. Our results will refer to the case of cosmological nucleon density around the nuggets, so that we again overestimate the evaporation rate.

2.3 Survivability of Quark Nuggets

Fig. 1 shows the behavior of $\tau^{-1}_{ev}(N_B) \equiv \frac{1}{N_B}\frac{dN_B}{dt}$ as a function of temperature, for $B^{1/4} = 140$ MeV, where τ_{ev} is the evaporation time scale due to baryon emission. The inverse of cosmic Hubble expansion (cooling) *time scale* of the universe (i.e., the Hubble constant $H(t) = 0.5t^{-1}$) is also shown for comparison (we consider a spatially flat universe with a present-epoch Hubble constant H_0=75 km s^{-1}Mpc^{-1}.

The evaporation time scale τ_{ev}, for QNs with initial baryon number $N_{B,in} \sim 10^{43.25}$ or less continually decreases (i.e., τ^{-1}_{ev} increases) as the temperature decreases and is always less than the expansion time scale of the universe ($\tau^{-1}_{ev} > H(t)$). These nuggets are, therefore, all unstable (see Fig. 2).

In contrast, QNs with $N_{B,in} \geq 10^{43.5}$ are stable because then τ^{-1}_{ev} decreases with decreasing temperature and eventually becomes less than $H(t)$. The curves for the case $B^{1/4} = 150$ MeV (not shown) have the same qualitative behavior except that the stability limit on $N_{B,in}$ increases. This is shown more clearly in Fig. 2 where N_B is plotted as a function of temperature. Crudely speaking, Fig. 2 is just the "upside down" version of Fig. 1. From Fig. 2 we see that a QN with $N_{B,in} = 10^{44}$ is stable for $B^{1/4} = 140$ MeV but unstable for $B^{1/4} = 150$ MeV. This general behavior is explained by the fact that the chemical potential and hence the mean momentum of the quarks in the QN is higher for a higher value of the bag constant which leads to a higher evaporation rate making the nugget less stable.

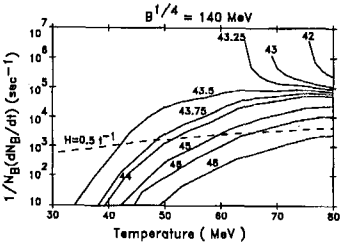

Figure 1: The inverse of the baryon evaporation time scale as a function of temperature for nuggets with different values of initial baryon number (Log$N_{B,in}$=42,43,43.25 and so on as indicated). The bag constant is $B^{1/4}$ = 140 MeV and α_c=2.0. The dashed curve is the Hubble constant whose present-epoch value is taken to be 75 km s^{-1}Mpc^{-1}.

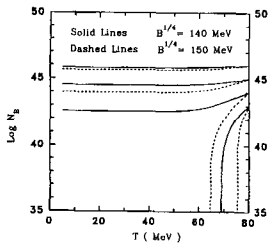

Figure 2: Evolution of baryon number of quark nuggets with temperature for two different values of the bag constant B as indicated, and with α_c=2.0 .

In Figs. 1 and 2 the initial (maximum) temperature, T_{in}, of the nuggets is taken to be 80 MeV. Previous studies[8,14] have considered T_{in}=50 MeV from considerations of efficiency of heating of the nugget due to neutrino absorption. In general, $N^{crit}_{B,in}$, the lowest value of $N_{B,in}$ below which a QN is unstable, increases if T_{in} is increased, other things being kept same. Thus our result, namely $N^{crit}_{B,in} \sim 10^{44}$ (see Fig. 2) may be regarded as conservative, i.e., the actual value may be even smaller if T_{in} is really smaller than 80 MeV.

The above results are for α_c=2.0. It is found[10] that effect of changing the value of α_c is similar to that of changing the value of B (see Fig. 2), i.e., nuggets are less stable for larger values of α_c. This is understood in terms of the fact that for a fixed value of the string constant σ, a larger value of α_c implies a smaller value of the confining momentum scale $k^q_{c,B}$, which has the effect of increasing the evaporation rate making the nugget less stable. Thus smaller values of α_c increase the stability of the nugget. In fact, it turns out[10] that for $B^{1/4} = 140$ MeV and $T_{in} = 80$ MeV, even a nugget having $N_{B,in} = 10^{42}$ can survive if $\alpha_c = 0.55$.

It should be mentioned here that throughout the above discussions we have neglected the QCD effects in determining the chemical potentials. Perturbative QCD may be expected to be valid inside the nuggets because of high density. In general, QCD corrections tend to *increase* the chemical potential of the quarks which may lead to higher evaporation rate and hence less stability of the nuggets. So on this count, we may have slightly *underestimated* the evaporation rates.

In any case, it is clear that when a dynamical model of baryon evaporation is considered, QNs formed with an initial baryon number as low as 10^{42} can in principle survive the evaporation process.

3. QNs and Baryonic Dark Matter

Is is believed that over 90% of all the matter contained in the universe is dark. Thus the next question we wish to address in this talk is whether this proverbial cosmological dark matter can be made up entirely of such quark matter; if not, then what fraction of the dark matter could be accounted for by the QN's.

The evolution of the universe in the mixed phase at the critical temperature T_c of the phase transition is governed by the Einstein equation in the Robertson-Walker spacetime, as described below :

$$\left(\frac{\dot{R}}{R}\right)^2 = \frac{8\pi\epsilon}{3m_{pl}^2}$$

$$\frac{d(\epsilon R^3)}{dt} + P\frac{dR^3}{dt} = 0$$

where ϵ is the energy density, P the pressure and G the gravitational constant. Combining the above two equations with the equation of state, we determine the scale factor $R(t)$ and the volume fraction of the quark matter $f(t)$ in the mixed phase as

$$R(t)/R(t_i) = \left[\cos\left(\arctan\sqrt{3r} - \sqrt{\frac{3}{r-1}}(t-t_i)/t_c\right)\right]^{2/3} / \left[\cos\left(\arctan\sqrt{3r}\right)\right]^{2/3}$$

and

$$f(t) = \frac{1}{3(r-1)}\left[\tan\{\arctan\sqrt{3r} - \sqrt{\frac{3}{r-1}}\frac{t-t_i}{t_c}\}\right]^2 - \frac{1}{r-1}$$

where $r \equiv g_q/g_h$, $t_c = \sqrt{3m_{pl}^2/8\pi B}$ is the characteristic time scale for the QCD phase transition in the early universe and t_i is the time when phase transition starts. The bag constant is $B = (245)^4$ MeV^4 in our calculations.

In the mixed phase, the temperature of the universe remains constant at T_c, the cooling due to expansion being compensated by the liberation of the latent heat. In the usual picture of bubble nucleation in first order phase transitions, hadronic matter starts appearing in the quark matter as individual bubbles. With the progress of time, more and more hadronic bubbles form, coalesce and eventually percolate to form a network of hadronic matter which traps the quark phase into finite domains.[22] The time when the percolation takes place is called the percolation time t_p, determined by a critical volume fraction f_c, ($f_c \equiv f(t_p)$) of the quark phase.

Detailed numerical studies on percolating systems yield the result that for bubbles with the same radial size, f_c is ~ 0.3.[23] We would also use the same value of f_c here. For the sake of simplicity, we would also assume that the trapped quark domains are all of the same size. We now get $t_p - t_i = 0.08t_c$. The values of various time scales in the present case are $t_c = 46$ μsec and $t_p = 27$ μsec.

In an ideal first order phase transition, the fraction of the high temperature phase decreases from the critical value f_c, as these domains shrink. For the QCD phase transition, however, these domains should become QN's

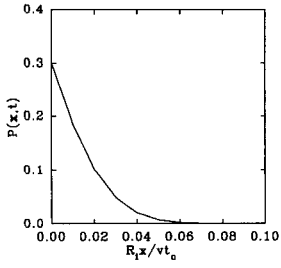

Figure 3: Probability of finding a domain of co-ordinate size X in the quark phase at time t as a function of $R_i X/vt_c$ with the nucleation rate given above.

and as such, we may assume that the lifetime of the mixed phase t_f (*i.e.*, the time when the cooling due to expansion starts to dominate again and the temperature of the universe starts falling), is $\sim t_p$. Let us, for the time being, assume that all these high-temperature domains become QNs, i.e., with 100% efficiency; we shall discuss the implication of such an idealized approximation later on.

The probability of finding a domain of trapped quark matter of co-ordinate radius X at time t_p is given by,[22]

$$P(z,x_p) \;=\; \exp\left[-\frac{4\pi}{3}v^3t_c^4\int_{x_i}^{x_p}dxI(x)\left(zr(x)+y(x_p,x)\right)^3\right]$$

where $z = XR(t_i)/vt_c$, $x = t/t_c$, $r(x) = R(x)/R(x_i)$ and $I(x)$ is the rate of nucleation per unit volume. v is the radial growth velocity of the nucleating bubbles, which we left as a parameter. $y(x_p,x)$ is given by the following equation

$$y(x,x\prime) \;=\; \int_{x\prime}^{x} r(x\prime)/r(x\prime\prime)dx\prime\prime$$

Various authors[22,24,25] have proposed different nucleation rates for the cosmic QCD phase transition. Let us start with the prescription of ref.,[22] where the nucleation rate is given by the following expression

$$I(t) \;=\; r_T\delta(t-t_i)$$

with the prefactor determined from the requirement $P(0,t_p) = f_c = 0.3$, yielding

$$r_T \;=\; \frac{3r_c}{4\pi v^3t_c^4}\frac{1}{y(x_p,x_i)}$$

with $r_c \sim 1.2$. The nucleation rate can be realized by phase transition caused by impurities, such as primordial black holes, magnetic monopoles, relic abundances of the electroweak phase transition, or cosmic strings.[26]

In Figure 3, we plot the probability $P(z,x_p)$ as a function of z. The radius of the trapped quark domain is determined by the length scale where the probability falls to f_c/e. This implies

$$\frac{r_{QN}}{vt_c} \;\approx\; 0.019$$

The number density of the QN's (n_{QN}) can be obtained by using the relation $n_{QN}V_{QN} = f_c$ as

$$n_{QN} \approx \frac{1968}{(vt_p)^3}$$

In an idealized situation where the universe is closed by the baryonic dark matter trapped in the QN's, we should have,

$$N_B^H(t_p) \;=\; N_B^{QN} n_{QN} V^H(t_p)$$

where $N_B^H(t_p)$ is the total number of baryon required to close the universe ($\Omega_B = 1$) at t_p, N_B^{QN} is the total number of baryons contained in a single quark nugget and $V_H(t_p) = 4\pi(ct_p)^3/3$ is the horizon volume.

Demanding that $v/c \leq 1/\sqrt{3}$, we get

$$N_B^{QN} \;\leq\; 10^{-4.7} N_B^H(t_p)$$

At this point it is important to reexamine the issue of total baryon number contained within the horizon limit at any epoch during the cosmological evolution. It is well known that the remarkable isotropy of the cosmological background radiation (CMBBR) allows us to estimate the number of photons (entropy) within the horizon at any given epoch. Baryon number, in contrast, cannot be estimated directly; one has to have recourse to so-called η parameter, the ratio of baryon to entropy densities, which plays a crucial role in standard (big bang) primordial nucleosynthesis (SBBN). SBBN constrains the value of η quite effectively, to 10^{-9} to 10^{-10}. Then, assuming that all the baryogenesis takes place either at the Grand Unification (GUT) scale or certainly no later than the electroweak scale, which is far above the QCD scale of a few hundred MeV, it is believed that this value of η remains fixed from the electroweak epoch onward. Accordingly, the baryon number within the horizon limit at any instant of the cosmological time is estimated from the corresponding photon number. It has to be noted that the baryon number thus estimated is what would participate in the primordial nucleosynthesis process. By this prescription, the baryon number within the horizon at the QCD epoch is $\approx 10^{49}$, as mentioned earlier.

Since the usual baryons constitute only $\sim 10\%$ of the closure density ($\Omega \sim 0.1$, from SBBN), a total baryon number of 10^{50} within the horizon at a temperature of ~ 100 MeV would close the universe baryonically, provided these baryons do not take part in SBBN, a criterion ideally fulfilled by the QNs. This would require N_B^{QN} to be $\leq 10^{45.3}$, which is clearly above the survivability limit of QN's mentioned earlier.

4. QNs as candidates for MACHOs

In recent years, there has been experimental evidence[27,28] for at least one form of dark matter - the massive compact halo objects detected through gravitational microlensing effects proposed by Paczynski some years ago.[29] To date, no clear consensus as to what these objects, referred to in the literature as well as in the following by the acronym MACHO, are made of. In this talk, I wish to demonstrate that they find a natural explanation as leftover relics from the *putative* first order cosmic quark - hadron phase transition that is predicted by the standard model of particle interactions to have occurred during the microsecond epoch of the early universe.

Since the first discovery of MACHO only a few years ago, a lot of effort has been spent in studying them observationally, as well as theoretically. In a recent update of the status report of the MACHO project[4] the mass estimate of the microlensing objects has been revised to lie within the range $0.15M_\odot$ and $0.9M_\odot$. Assuming that MACHOs are subject to the limit on total baryon number imposed by the Big Bang Nucleosynthesis (BBN), there have been suggestions that they could be white dwarfs.[30] It is difficult to reconcile this with the absence of sufficient active progenitors of appropriate masses in the galactic halo. Moreover recent studies have shown that these objects cannot be white dwarfs, as this will violate some of the very well known results of BBN.[31] On the other hand, there have been suggestions[32,33] that they could be primordial black holes (PBHs) ($\sim 1M_\odot$), arising from horizon scale fluctuations triggered by pre-existing density fluctuations during the cosmic quark - hadron phase transition.

We have already seen that primordial QN-s with baryon numbers above $\sim 10^{40-42}$ would indeed be cosmologi-

cally stable. These nuggets have tremendous appetite for neutrons. It is thus most relevant to investigate the fate of these QNs and their implications on the later evolution of the universe. Recalling that the number distribution of the QNs is sharply peaked around baryon number 10^{44},[34] we shall assume, for our present purpose, that all the QNs have a baryon number of 10^{44}. Since Ω_B is only about 0.1 from BBN, there would be about 10^7 such nuggets within the horizon limit at the microsecond epoch.

To study the evolution of the QNs in time, it has to be realized that there are two regions of interest, one for 1 MeV $< T \leq 100$ MeV and the other for $T \leq 1$ MeV, 1 MeV being the scale of the neutrino decoupling temperature.

The QNs having been formed, would interact with only the neutrinos impinging upon them. If the flux of neutrinos is sizable enough and their mean free path within the QNs is such that a substantial amount of energy is imparted to them, then the QNs would be kept in thermal equilibrium with the rest of the universe. Such a scenario would prevail only until the neutrino decouples at a temperature of 1 MeV or less. From then on, they are subject only to the gravitational interaction. It follows that below this temperature, the QNs would be free to collapse together under gravitational attraction, having become free of radiation pressure. A crucial ingredient in this context would be number of QNs that can coalesce together (*i. e.*, the number of QNs within the appropriate Jeans length), as also the time required fro such a collapse in comparison to the lifetime of the universe at that temperature.

For $T < 1$ MeV, we can have two possible scenarios. If the number of coalesced QNs is found to be sufficiently large, then we must consider (sequential) further clumping of these objects. On the other hand, if their density turns out to be very small, there can be no further clumping, and the QNs would have reached a final configuration, their total number increasing due only to the increase of the horizon radius.

We now discuss in some detail the scenarios mentioned above. The ratio of the interaction rate of the QNs with neutrinos to the Hubble rate ($T_{\nu N}/H$) can be computed for all temperatures in the usual manner. It is found that $T_{\nu N}/H >> 1$ for all temperatures down to the neutrino decoupling and as such, the QNs gets substantial amount of energy from the neutrinos. This is to be contrasted with the case of other very massive particles which freeze out much earlier and is due to the fact that the QNs have a large spatial extent (radius ~ 1) and consequently, a very large effective cross section. They would thus be in thermal equilibrium till neutrino decoupling and stable against collapse. Below this temperature, however, they would indeed tend to clump together, as already mentioned.

The study of gravitational collapse, especially in the context of galaxy formation, is a very involved numerical problem. For our present purpose, however, we can rely on the classical Jeans theory, where one can show that in a Newtonian fluid, only those fluctuations which have wave numbers larger than a critical value k_J, (the Jeans wave number) can grow. This corresponds to a *Jeans length* ($R_J \sim \pi/k$, where k_J is suitably transformed to a physical wave number through division by the scale factor R), over which the gravitational energy exceeds the thermal pressure energy. Suffice it to say that if the Jeans length is larger that the horizon scale at any time, a Newtonian analysis fails and general relativistic effects must be included.

To derive a measure of the Jeans length in our case we invoke the simple criterion that the gravitational total energy within the Jeans volume should be greater than or equal to the pressure energy:

$$G(\frac{4}{3}\pi R_J^3 \rho_r)^2/R_J \;=\; v_s^2 \rho_r \frac{4}{3}\pi R_J^3$$

where the subscript r to ρ indicates that the universe is still radiation dominated and v_s stands for the velocity of sound ($=\frac{1}{\sqrt{3}}$). We then have :

$$R_J \;=\; \frac{m_{pl}}{\sqrt{4\pi\rho_r}} \sim 1.633t$$

which is just less than the distance to the horizon ($\sim 2t$) in the radiation era. Thus a general relativistic treatment is not strictly necessary, at least for the clustering of QNs.

The number of QNs within the horizon (N_N) and their density as a function of temperature are given by the two equations

$$N_N = 10^7 \left(\frac{100MeV}{T}\right)^3$$

$$n_N = N_N/V_H = N_N/\left(\frac{4}{3}\pi(2t)^3\right).$$

Thus one can readily see that the total number of QNs in R_J at $T = 1$ MeV turns out to be ~ 0.58 X 10^{12-13}. If all these QNs clump into one, it would then have a mass of $\sim 0.5 M_\odot$, making them ideal MACHO candidates. The ratio Γ_c/H, where Γ_c is a measure of the rate of collapse of all the QNs within R_J, has been computed for all temperatures up to 1 MeV and is seen to approach the value ~ 1 from above at this temperature. Thus we argue that the individual QNs within the Jeans length can collapse to a single object at temperatures just below 1 MeV.

5. Outlook

The cosmological implications of quark hadron phase transition despite the rather premature announcement of its demise, is thriving and a whole new horizon has opened up, covering baryonic dark matter and MACHOs. To seek out the ultimate destiny of QNs floating around the universe is the immediate outlook. The culinary habits of strangelets is under emotional stress, no doubt, but to discover strangelets in "reasonable" numbers will certainly be a remarkable experience. We look forward to such adventures.

Acknowledgements:

It is a pleasure to thank J. Alam , S. Raha and P. Bhattacharya, for their collaboration in the work on the survivability of quark nuggets discussed above. I would also like to thank Prof. D.N. Shramm who died recently in a tragic air crash, a very close friend who initiated us in the 'universe'- al insight and Takeshi Kodama for inviting me to this symposium and for his warm hospitality in glorious Brazil.

REFERENCES

[1] E. Witten; Phys. Rev. **D30** (1984) 272.

[2] For a review, see J. Madsen in *Physics and Astrophysics of Quark Gluon Plasma*, Eds. B. Sinha, S. Raha and Y.P. Viyogi (World Scientific, Singapore, 1994).

[3] J. Madsen, Nucl.Phys. **24B** (1991) 84

[4] C. Alcock et.al. (MACHO collaboration), *The MACHO Project: Micro lensing results from 5.7 years of LMC observations, 2000*, astro-ph/0001272

[5] E. Farhi and R.L. Jaffe, Phys.Rev. **D30** (1984) 2379.

[6] See for a review, C. Alcock and A. Olinto, Ann. Rev.Nucl. Part. Sci.**38** (1988) 161

[7] J.H. Applegate and C.J. Hogan, Phys.Rev. **D31** (1985) 3037

[8] C. Alcock and E. Farhi, Phys.Rev. **D 32** (1985) 1273

[9] J. Madsen and M.L. Olesen, Phys. Rev. **D44** (1991) 1069; ibid**D44** (1991)566(Erratum).

[10] P. Bhattacharjee, J. Alam, B. Sinha and S. Raha , Phys. Rev. **D48** (1993) 4630

[11] A. Casher, H. Neuberger and S. Nussinov, Phys. Rev. **D20** (1979) 179

[12] B. Andersson, G. Gustafson and T. Sjostrand, Nucl. Phys. **B197** (1082)45

[13] N.K. Glendenning and T. Matsui, Phys. Rev. **D28** (1983) 2890

[14] J. Madsen, H. Heiselberg and K. Riisager, Phys. Rev. **D34** (1986)2947

[15] H. Heiselberg, J. Madsen and K. Riisager, Phys.Scr.**34** (1986)556

[16] H. Heiselberg, Phys. Scr.**46** (1992) 485

[17] J. Madsen, Phys. Rev. **D47** (1993) 325

[18] C. Alcock and A. Olinto, Phys. Rev. **D39** (1989) 1233

[19] B. Banerjee, N.K. Glendenning and T. Matsui, Phys. Lett. **B127** (1983) 453

[20] K. Sumiyoshi, K. Kusaka, T.. Kamio and T. Kajino, Phys. Lett. **B225** (1989)10

[21] K. Sumiyoshi, T. Kajino, C. Alcock and G.J. Mathews, Phys. Rev. **D42** (1990) 3963

[22] H. Kodama, M. Sasaki, K. Sato, Prog. Theo. Phys. **68**, (1982) 1979.

[23] K. Iso, H. Kodama and K. Sato, Phys. Lett. **B169**, (1986) 337.

[24] W. N. Cottingham, D. Kalafatis and R. Vinh Mau, Phys. Rev. Lett. **73**, (1994) 1328.

[25] L. D. Landau and E. M. Lifshitz, *Statistical Physics* (Pergamon Press, New York, 1969); K. Kajantie, Phys. Lett. **285B**, (1992) 331.

[26] M. B. Christiansen and J. Madsen, Phys. Rev. **D53**, (1996) 5446.

[27] C. Alcock *et al.* (MACHO Collaboration) Nature **365** (1993) 621.

[28] E. Aubourg, *et al.* (EROS Collaboration), Nature **365** (1993) 623

[29] B. Paczynski, ApJ. **304** (1986) 1

[30] B. D. Fields, K. Freese, and D. S. Graff, New Astron. **3** (1998) 347

[31] K. Freese, B. D. Fields, and D. S. Graff, astro-ph/0002058.

[32] D. N. Schramm, in *Physics and Astrophysics of Quark - Gluon Plasma (ICPA-QGP'97)* (Eds. Sinha, B., Viyogi, Y. P. and Srivastava, D. K.), 29, Narosa Publishing, New Delhi.

[33] K. Jedamzik, *Phys. Rep.* **307** (1998) 155.

[34] A.Bhattacharyya, J. Alam, S. Sarkar, P. Roy, B. Sinha, S. Raha, and P. Bhattacharjee, Phys. Rev. **D61** (2000) 083509.

Questions and Answers

E. Shuryak:

Q1) Do I Understand it right that MACHOs are much larger than $N_B \sim 10^{42} - 10^{49}$ which was your critical size?
Q2) What is the colour of QNs? (Related to the question if MACHOs are white dwarfs or not?)

BS:

A1) Yes, Edward, I tried to explain that QNs can clump together (Jeans length argument) to grow in size upto $0.5 M_{\odot}$; the idea fits in with other astro models.
A2) QNs should be dark; however they can be very very dim - if strange quark is considered of higher mass than up and down quark which is the case. However such dim objects is the cosmic scale can be dark.

J. Horvath:

I have a comment and a question. The comment is related to the absence of short duration amplification events in the EROS data which seems to rule out objects as light as $10^{-7} M_{\cdot}$. I would argue that as long as the clustering is effective, this number should be taken as the upper limit of their mass. My question is: Have you wondered how the so-called "boiling" of QNs (a bulk effect) can be treated within your model?

BS:

No, "boiling" cannot be taken into account within our framework In fact, the time scale for "boiling" (the spontaneous nucleation of hadronic bubbles in the bulk of the QN and consequent conversion of the QN into nucleons) is much larger than the time scale of surface evaporation and therefore can be neglected.

Pacheco:

Analyses of the Hubble "deep" field obtained at 3 yrs. interval indicate the presence of few blue objects with high proper motion. These are probably white dwarfs and their numbers are consistent with the expectations of MACHO experiment.

BS:

No, I am sorry I do not agree - white dwarfs just do not fit the observed properties of MACHOs.

Marcelo Chiapparini

Hadronic Chiral Mean-Field Models at Extreme Temperatures and Densities.

M. Chiapparini[1], M. E. Bracco[1] and A. Delfino[2]
[1]Instituto de Física, Universidade do Estado do Rio de Janeiro - IF/UERJ
[2]Instituto de Física, Universidade Federal Fluminense - IF/UFF

ABSTRACT

We study recent developed chiral mean field models under extreme conditions of temperature (T) and density (ρ). The thermal vacuum phase transition (ρ and high T), present in the Walecka model, also appears in some of the proposed models. A hadronic phase transition to a quark-gluon plasma phase (QGP) at $\rho \neq 0$ is also shown in the T - ρ phase diagram. From this diagram we see that, at $\rho = 0$ the critical temperature T_c is unsensitive to the employed hadronic model whereas when ρincreases and T decreases the hadronic-QGP two-phase transition becomes strongly model dependent.

1 Introduction

The understanding of nuclear matter under extreme conditions is a crucial aim of nuclear and stellar physics, especially with much more experimental information to come with RHIC and Alice/LHC accelerators. Usually, one extrapolates nuclear matter models without asking too much about the reliability and confidence of them in the extreme conditions. As first step in this direction we will push the best existing models for moderate densities and temperatures towards more extreme values of these variables and look for deviations from the behaviour expected from other sources.

The aim of our work is two-fold,

1. a sistematic comparative study of a set of hadronic models at extreme regimes and
2. its connection to the hadronic-QGP phase transition.

As a result, we obtain several new insights into the high-density and temperature behavior of these models, putting useful constraints on their parameters space, and ruling out some of them entirely. From our study, we found that only the knowledment of the incompressibility at the saturated nuclear matter itself does not guarantee the stiffness (softness) behavior of the hadronic model at higher densities, as could be naively expected. This finding helps a better undertanding of the role played by the meson-nucleon coupling constants. At finite temperature and zero density our calculations show that the thermal vacuum phase transition ($\rho = 0$ and high T), present in the Walecka model, also appears in some of the studied models.

We also analyze the behaviour of these models regarding the QGP phase transition. A natural question which arises is whether the mentioned hadronic phase transition at $\rho = 0$ and high T affects the hadronic-QGP phase

transition. We have shown that this is not the case. Practically all the analyzed models signalize approximately the same critical QGP temperature. This finding suggest strongly a QHD model independence for the QGP phase transition in this regime. To the best of our knowledment, this is a remarkable and unknown feature of the hadronic models. As the density increases a model QHD dependence starts to occur strongly. This result can be easily seen by the T - ρ phase diagram we present in this work for all the studied models. This model dependence becomes so strong that even some of the models do not present hadronic-QGP phase transition.

2 The Hadronic Models

To study the properties of hadronic matter, Walecka[1] has proposed a simple renormalizable model which is often referred as Quantum Hadrodynamics (QHD-I). In this model, nucleons interact through the exchange of σ and ω mesons. The Walecka model has achieved important goals in the description of hadronic matter as, for example, some bulk properties of nuclear matter as well as some properties of finite nuclei[2] However:

1. the incompressibility (K) indicates an equation of state stiffer than expected and
2. at moderately high density and/or temperature m^* becomes very small.

Many attempts have been made to improve this model:

1. addition of nonlinear cubic and quartic scalar meson interaction,[3]
2. addition of vector meson self coupling,[4]
3. inclusion of one-nucleon-loop vacuum effects[5] ,
4. inclusion of two-nucleon-loop effects.[6]

Recently a new family of effective Lagrangians, which incorporates the fundamental symmetries of QCD, was suggested.[7] These symmetries constrain the Lagrangian restricting the form of the possible interaction terms. The resulting effective lagrangian is expanded in powers of the fields and their derivatives, with the terms organized using Georgi's "naive dimensional analysis" (NDA). The NDA is used to identify the dimensional factors of any term. After these dimensional factors are extracted, the remaining *dimensionless* coefficients are all assumed to be of order unity (naturalness assumption). If naturalness is valid, the effective lagrangian can be truncated at a given order with a reasonable bound on the truncation error.

These models were successfully employed to calculate nuclear matter bulk properties as well as the spectra of finite nuclei. A same type of model has also been studied in the context of cold neutron matter at high density.[8]

Here we present these models, in the Hartree approximation extended to finite temperature. The energy density reads

$$\begin{aligned}\mathcal{E}(M^*,\rho_B) &= \frac{m_s^2}{g_s^2}\Phi^2\left(\frac{1}{2}+\frac{\kappa_3}{3!}\frac{\Phi}{M}+\frac{\kappa_4}{4!}\frac{\Phi^2}{M^2}\right)\\ &-\frac{1}{2g_v^2}\left(1+\eta_1\frac{\Phi}{M}+\frac{\eta_2}{2}\frac{\Phi^2}{M^2}+\frac{\eta_3}{3!}\frac{\Phi^3}{M^3}\right)m_v^2W^2\\ &-\frac{1}{4!g_v^2}\left(\zeta_\circ+\zeta_1\frac{\Phi}{M}\right)W^4+W\rho_B\\ &+\frac{\gamma}{(2\pi)^3}\int d^3k\; E^*(\mathbf{k})\;\left(f_+(\mathbf{k},T)+f_-(\mathbf{k},T)\right)\;,\end{aligned} \tag{1}$$

where

$$
\begin{aligned}
E^*(\mathbf{k}) &= \sqrt{\mathbf{k}^2 + M^{*2}}\,, \\
M^* &= M - \Phi\,, \\
f_\pm(\mathbf{k},T) &= \frac{1}{1+e^{(E^*\pm\nu)/T}}\,, \\
\nu &= \mu - g_v\omega_0\,, \\
W &= g_v\omega_0\,, \\
\Phi &= g_s\sigma\,, \\
\rho_B &= \frac{\gamma}{(2\pi)^3}\int d^3k\,[f_+(\mathbf{k},T) - f_-(\mathbf{k},T)]\,, \\
\gamma &= 4,2\,.
\end{aligned}
$$

The pressure is

$$
\begin{aligned}
p(M^*,\rho_B) &= -\frac{m_s^2}{g_s^2}\Phi^2\left(\frac{1}{2}+\frac{\kappa_3}{3!}\frac{\Phi}{M}+\frac{\kappa_4}{4!}\frac{\Phi^2}{M^2}\right) \\
&\quad -\frac{1}{2g_v^2}\left(1+\eta_1\frac{\Phi}{M}+\frac{\eta_2}{2}\frac{\Phi^2}{M^2}+\frac{\eta_3}{3!}\frac{\Phi^3}{M^3}\right)m_v^2W^2 \\
&\quad -\frac{1}{4!g_v^2}\left(\zeta_\circ+\zeta_1\frac{\Phi}{M}\right)W^4 + W\rho_B \\
&\quad +\frac{1}{3}\frac{\gamma}{(2\pi)^3}\int d^3k\frac{k^2}{E^*(\mathbf{k})}\,(f_+(\mathbf{k},T)+f_-(\mathbf{k},T))\,.
\end{aligned}
\tag{2}
$$

The effective mass M^* is obtained by minimizing $\mathcal{E}$ with respect to the mesonic fields. The condition

$$
\partial\mathcal{E}/\partial W = 0 \tag{3}
$$

will give a cubic equation for W in terms of M^*. This constraint is then implemented into the equation for $\mathcal{E}$ and, together with the condition

$$
\partial\mathcal{E}/\partial\Phi = 0\,, \tag{4}
$$

gives a self consistent equation to obtain M^* (*gap equation.*)

The constants are already adjusted to reproduce some of the bulk properties of the nuclear matter ground state (see Table 1).

Model	$W1$	$C1$	$Q1$	$Q2$	$G1$	$G2$
m_s/M	0.60305	0.53874	0.53735	0.54268	0.53963	0.55410
$g_s/4\pi$	0.93797	0.77756	0.81024	0.78661	0.78532	0.83522
$g_v/4\pi$	1.13652	0.98486	1.02125	0.97202	0.96512	1.01560
η_1		0.29577			0.07060	0.64992
η_2					-0.96161	0.10975
κ_3		1.6698	1.6582	1.7424	2.2067	3.2467
κ_4			-6.6045	-8.4836	-10.090	0.63152
ζ_0				-1.7750	3.5249	2.6416

Table 1: Model parameters, taken from Ref [7].

2.1 The hadronic phase transition

Many hadronic models exhibit a nucleon-antinucleon phase transitions at finite temperature.[9,10,1,4] For example the one at $T \approx 200$ MeV for $\rho = 0$, characterized by an abrupt decrease in the effective nucleon mass.

In reference,[4] hot nuclear matter was extensively studied using the Walecka model regarding the finite temperature behavior for zero density (nucleon-antinucleon plasma). The authors explored this model for different scalar-vector coupling constants to conclude that, depending on the values taken by those constants, the Walecka model may or may not generate a phase transition into a nucleon-antinucleon plasma. The order (first or second) of this phase transition depends crucially on the scalar coupling constant of the model.

We investigate whether the hadronic models discussed in this section may or not present this hot nucleon-antinucleon phase transition in the hadronic sector. In this case, we will investigate especially whether the representative hadronic models follow the Walecka model exhibiting this kind of phase transition for high temperatures.

2.2 The QGP phase transition

It is widely believed that hot hadronic matter undergoes a phase transition to the quark-gluon plasma (QGP) at $T \approx 200$ MeV.[11] At low temperatures and baryon densities quarks and gluons are confined inside hadrons, which are the appropriate degrees of freedom of the nuclear matter in this regime. In this region, QHD based on effective Lagrangians works quite well.

The phase transition is supposed to occur at sufficiently high temperatures and densities, where in this case the QCD running coupling constant becomes smaller than one, suggesting deconfinement of quarks and gluons. If one assumes the validity of QHD far beyond the normal nuclear matter ground state, the transition can be characterized by the process of hadrons loosing their identities, and quarks and gluons becoming the elementary degrees of freedom. The plasma composed of quark and gluons in this deconfinement scenario, should not be confused with the hadron nucleon-antinucleon phase transition for hot nuclear matter mentioned earlier in the preceding subsection.

In order to see the hadronic-quark-gluon phase transition we need distinct models for the two different phases of the baryonic matter. We describe the hadronic (meson-baryon) phase (H) by the models presented in Eq. (1). For the quark-gluon plasma phase, the pressure, energy density and baryon number density are given by[12]

$$p_{QGP}(\mu_q, T_q) = \frac{8\pi^2 T_q^4}{45}\left(1-\frac{15\alpha_s}{4\pi}\right) + N_f\left[\frac{7\pi^2 T_q^4}{60}\left(1-\frac{50\alpha_s}{21\pi}\right) + \left(\frac{\mu_q^2 T_q^2}{2}+\frac{\mu_q^4}{4\pi^2}\right)\left(1-\frac{2\alpha_s}{\pi}\right)\right] - B\,, \quad (5)$$

$$\mathcal{E}_{QGP}(\mu_q, T_q) = \frac{8\pi^2 T_q^4}{15}\left(1-\frac{15\alpha_s}{4\pi}\right) + N_f\left[\frac{7\pi^2 T_q^4}{20}\left(1-\frac{50\alpha_s}{21\pi}\right) + 3\left(\frac{\mu_q^2 T_q^2}{2}+\frac{\mu_q^4}{4\pi^2}\right)\left(1-\frac{2\alpha_s}{\pi}\right)\right] + B\,, \quad (6)$$

$$\rho_{QGP} = \frac{1}{3}N_f\left(\mu_q T_q^2 + \frac{\mu_q^3}{\pi^2}\right)\left(1-\frac{2\alpha_s}{\pi}\right)\,, \quad (7)$$

where B is the bag constant, N_f is the number of flavors and α_s is the QCD running coupling constant, depending on the quark-gluon plasma temperature T_q and the quark chemical potential μ_q through the first order perturbative expression

$$\alpha_s = 4\pi\left\{\left(11-\frac{2N_f}{3}\right)\ln\left[\left(0.8\mu_q^2+15.622T_q^2\right)/\Lambda^2\right]\right\}^{-1}\,. \quad (8)$$

The Gibbs criteria used in the analysis of this phase transition are

$$\mu_H(T_c, \rho_H^c) = \mu_{QGP}(T_c, \rho_{QGP}^c)\,, \quad (9)$$

$$p_H(T_c, \rho_H^c) = p_{QGP}(T_c, \rho_{QGP}^c)\,. \quad (10)$$

3 Results

The model for the QGP phase which we use in this paper has some parameters such as Λ, B and N_f as presented in the last section. As a first approximation, we examine the simplest case with $N_f = 2$ (quarks u and d only). The QCD scale parameter Λ is fixed at 200 MeV, consistent with the current data set.[13] We will use two different bag constants in our analysis: $B^{1/4} = 174$ MeV and $B^{1/4} = 238$ MeV, corresponding to $B = 119$ MeV fm^{-3} and $B = 418$ MeV fm^{-3} respectively. These are the limiting values of the broad range of values used in the literature.

3.1 $T = 0$ and $\rho \neq 0$

In Fig. 1 we display, for zero temperature, the nuclear matter binding energy per particle as a function of the density ratio ρ/ρ_o, ρ_o being the saturation nuclear matter density.

Model	$W1$	$C1$	$Q1$	$Q2$	$G1$	$G2$
$m^* = M^*/M$	0.530	0.657	0.597	0.614	0.634	0.664
K_o (MeV)	569	304	242	279	215	215
T_c (MeV)	186.1	-	191.1	191.1	193.7	-

Table 2: Nucleon effective mass m^*, incompressibility K and critical temperature T_c for the hadronic phase transition for each model.

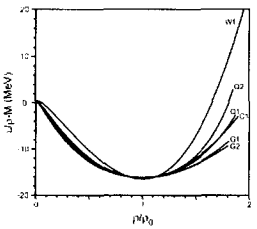

Fig. 1 The binding energy for each model.

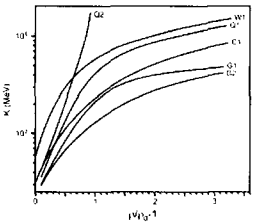

Fig. 2. The incompressibility for each model

The precise of the bulk properties produced by these models are given in the first two rows of Table II: the values for the dimensionless nucleon effective mass $m^* = M^*/M$ and the incompressibility K_o in MeV at ρ_o.

At first sight the incompressibilities might suggest that the Walecka model generates the stiffest EOS. However, since some of the models depend on the baryonic density ρ in a different way (see Eq. (1)) than the Walecka model (which has a ρ^2 dependence) it is important to investigate the evolution of the incompressibility far beyond the case $\rho = \rho_o$. We present in Fig. 2 the incompressibility $K(\rho)$ *vs.* $\rho/\rho_o - 1$. As we can see, the nonlinearity of mesonic-field couplings changes the relative increasing of the incompressibility by a fairly large amount. Note that model $Q1$ approaches the Walecka model at high density, and also how model $Q2$ diverges from the others.

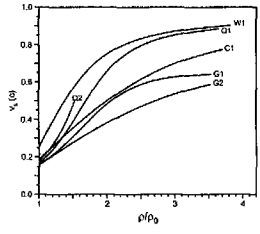

Fig. 3. The sound velocity for each model.

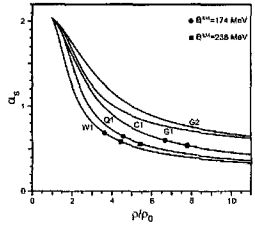

Fig. 4. The QCD running coupling constant in the onset to the QGP phase transition as a function of ρ at T=0.

The analysis of the sound velocity $v_s^2 = \partial p/\partial \mathcal{E}$ is another way to check how soft or stiff the EOS of each model is. We present v_s as a function of ρ/ρ_o in Fig. 3, just confirming the features of Fig. 2.

The fact that the $Q2$ model becomes too stiff, together with the impossibility of getting solutions for the gap equation for $\rho/\rho_0 > 2$, forced us to rule out this model.

For the hadronic-QGP phase transition, in this special case of $T = 0$, we start discussing how the running coupling constant α_s depends on the models. This dependence comes about because Eq. (8) carries a μ_q^2 dependence and the constraint Eqs. (9)-(10) we have used to connect the two different phases relates the chemical potentials in the following way $\mu_H = 3\mu_q = g_v V_o + (\mathbf{k}^2 + M^{*2})^{1/2}$. Since M^* and $g_v V_o$ assume different values for the different models, α_s becomes dependent on the hadronic model. In Fig. 4 we show α_s as a function of ρ/ρ_o for the different models. Circles and squares on the curves indicate the assumed α_s values where the hadronic-QGP phase transition begins for $B^{1/4} = 174$ MeV and $B^{1/4} = 238$ MeV respectively.

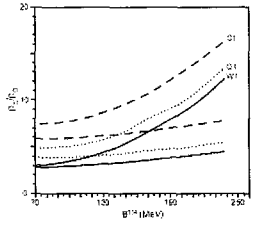

Fig. 5 The coexistence region as a function of B for three models at T=0

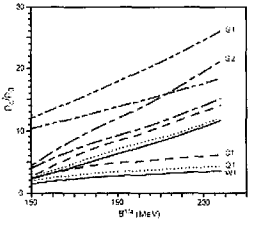

Fig. 6. The coexistence region as a function of B for all models at T=0

The critical densities ρ_H^c and ρ_{QGP}^c for the hadronic-QGP phase transition are presented in Fig. 5 as a function

of $B^{1/4}$, for the $W1$, $C1$ and $Q1$ models. The $G1$ and $G2$ models (not represented in this figure) do not generate any phase transition for $\rho_H^c/\rho_\circ < 30$ (the maximum values for which we obtained solutions). This is why they are absent also in Fig. 4. Thus the models we are dealing with fall into two different families : $W1$, $C1$ and $Q1$ on the one hand and $G1$ and $G2$ on the other. The higher order interactions of the vector mesons included in the $G1$ and $G2$ models seem to manifest themselves in an undesirable way (although they have small coupling constants as predicted by "Naturalness"), since it is generally believed that $\rho_H^c/\rho_\circ$ should lie between 5-10. To explore the impact of the quark interactions on these critical densities compared to the simplest case, the ideal (free) quark gas, we show in Fig. 6 the same graphs as in Fig. 5 but now for $\alpha_s = 0$.

It is clear that the first order phase transition is sensitive to both hadronic and QGP model parameters. Both critical densities ρ_H^c and ρ_{QGP}^c decrease as the hadronic model incompressibility increases (corresponding to a stiffer EOS, see Fig. 1b) and/or the running coupling constant α_s decreases (see Figs. 5-6, for a fixed value of B). On the other hand, the same figures show that both ρ_H^c and ρ_{QGP}^c increase as the bag constant B increases.

3.2 $T \neq 0$ and $\rho = 0$

In the following two subsections we intend to investigate how these models behave in the hot nuclear matter regime, analyzing a possible hadron nucleon-antinucleon phase transition as well as studying the QGP phase transition. In this subsection we will restrict ourselves to the nucleon-antinucleon plasma at the hadronic level. This means that we will perform the calculations at zero baryonic density following the Walecka model study of Theis *et. al.*.[4] It is easy to see that in this case the energy density functional (Eq. (1)) for all models becomes that of a nonlinear σ model with different coupling constants.

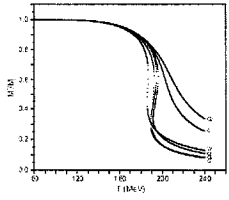

Fig. 7. The effective mass as a function of T at ρ=0

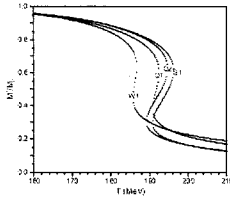

Fig. 8. The hadronic liquid-gas phase transition at ρ=0

In Fig. 7 we show m^* *vs.* T for all models. In Fig. 8 we amplify the temperature scale to demonstrate that $W1$, $Q1$, $Q2$ and $G1$ generate a first order nucleon-antinucleon phase transition in the hadronic sector. By using the Gibbs criteria of phase equilibrium $p_1 = p_2$, $\mu_1 = \mu_2$ and $T_1 = T_2$ we have obtained the critical temperatures for $W1$, $Q1$, $Q2$ and $G1$ models which are given in the third row of Table II. The critical temperatures are remarkably close. Models $C1$ and $G2$ do not present any phase transition in the zero baryonic density regime.

Now, a question which arises quite naturally is whether a pure hadronic phase transition at ρ=0 and at high temperature may or not have consequences in the hadronic-QGP phase transition. Our results show that the hadronic phase transition itself does not interfere in the hadronic-QGP phase transition. This phenomenon is not clear from the hadronic models themselves, hence when a hadronic phase transition occurs it is accomplished

to an abrupt decrease in the effective nucleon mass (around a factor 4). This fact sometimes is associated as a signal that chiral symmetry would be restored at high temperatures, substantiating construction of simple models where the hadronic phase would be quite well described as a gas of massless pions. The hadronic model itself here is not of importance at all, since the hadronic-QGP phase transition is essentially given by the QGP phase and lies very close to the temperature where p_{QGP} acrosses zero.

The hadronic-QGP phase transition is obtained by connecting the two different phases with the Gibbs criteria $p_H = p_{QGP}$, and $T_H = T_q = T_c$, and keeping in the present section $\mu_H = 3\mu_q = 0$. The critical temperature T_c for all models lies very close to 151 MeV and 198 MeV for $B^{1/4} = 174$ MeV and $B^{1/4} = 238$ MeV, respectively.

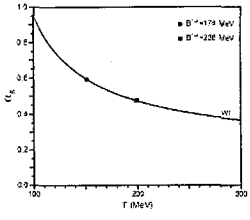

Fig. 9 The QCD running coupling constant in the onset to the QGP phase transition as a function of T at ρ=0.

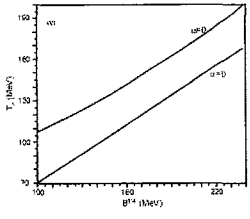

Fig. 10 The critical temperature for the QGP phase transition as a function of B at ρ=0

It is worth noting that for ρ=0, α_s (contrary to the case $T = 0$ and $\rho \neq 0$) becomes practically model independent. We present in Fig. 9 its behaviour as a function of the temperature for the $W1$ model. The circle and square on the curve indicates the value at which the phase transition takes place (for two values of $B^{1/4}$). To better see the dependence of the critical temperature T_c on B and α_s we give in Fig. 10 T_c *vs.* $B^{1/4}$ for α_s given by Eq. (8) and for the particular case $\alpha_s = 0$ (free quarks).

The critical temperature is at ρ=0 common to both phases, $T_H = T_q = T_c$, and increases as the bag constant B increases and decreases as the running coupling constant α_s decreases (see Fig. 10).

3.3 Hadronic-QGP Phase Transition

Finally, we consider the general case with finite density and temperature. To look for the phase transition we use again the Gibbs criteria given by Eqs. (9)-(10) .When the two systems satisfy these condition they can coexist in equilibrium. At higher p and T one expects that it is the quark-gluon phase which is stable. In the T *vs.* ρ/ρ_o phase coexistence diagram $(\rho/\rho_o, T)$ we have already discussed the special cases $(0, T)$ and $(\rho/\rho_o, 0)$. Now we present in Fig. 11 the complete hadronic-QGP coexistence phase diagram for the $Q1$ model in the $(\rho/\rho_o, T)$ plane. For the sake of simplicity, we present in Figs. 12-15, for all models, only the hadronic branch corresponding to the start of the coexistence curve in the $(\rho/\rho_o, T)$ plane. In these figures we omit, due the softness of the $G1$ and $G2$ models, the QGP branch.

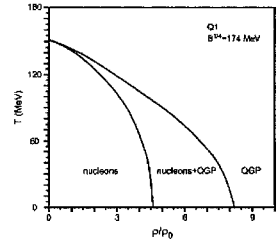

Fig. 11. The coexistence diagram for the Q1 model.

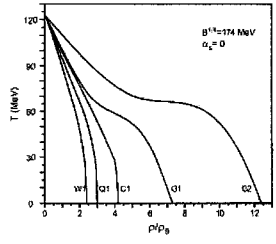

Fig 12. The onset to the coexistence region.

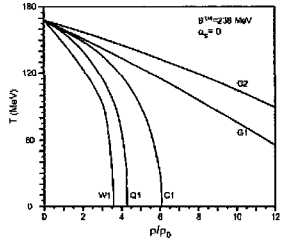

Fig. 13. The onset to the coexistence region.

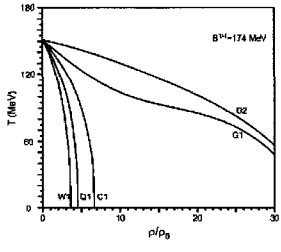

Fig 14. The onset to the coexistence region.

It turns out from these figures that the models $G1$ and $G2$ only reach the hadronic-QGP phase transition at very high critical densities ρ_H^c and ρ_{QGP}^c. This happens even when a phase transition is favored, as for instance in the particular case $\alpha_s = 0$ (free quarks),

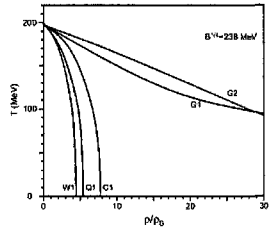

Fig. 15. The onset to the coexistence region.

given by Figs. 12 and 13. Note how the value of $B^{1/4}$ changes the character of the phase transition for the models $G1$ and $G2$. Figures 14 and 15 present T as a function of $\rho/\rho_\circ$ for the case $B^{1/4} = 174$ MeV and $B^{1/4} = 238$ MeV respectively and for α_s given by Eq. (8). We see that in both cases the $G1$ and $G2$ models do not exhibit phase transition signatures for low temperatures. Here we also remark that the $B^{1/4}$ values also change the slope of their coexistence curves.

Quite generally, we find that the first order phase transitions are very sensitive to the parameters of both hadronic and QGP models. The systematic we have found is the following. The increase of the incompressibility leads to a decrease of both critical densities ρ_H^c and ρ_{QGP}^c once with the stiffing of the EOS higher pressures are reached at low densities, making contact with the quark phase earlier in density, whereas the increase of the bag constant B leads to the increase of the critical densities and critical temperatures. The decrease of the running coupling constant α_s decreases the critical densities and the critical temperatures.

4 Conclusions

In this work we have found and studied many new features of recently introduced chiral hadronic models, in the realms of hadronic and quark-gluon plasma phase transitions, neutron star masses and quark-condensate behavior. This study acquires importance due to the fact that the understanding of nuclear matter in extreme regimes of temperature and density is an increasing challenge to new heavy ion experiments. The family composed of the $Q2$, $G1$, and $G2$ models is already very well tested and reproduces the nuclear physical observables very close.[7] The other family of models, containing $W1$, $C1$, and $Q1$, does not fit nuclear observables so well, regarding in particular the finite nuclei spectra.[7] It is important to recall here that the all studied models were developed to be reliable at low density.[7] We have repeatedly emphasized that the extrapolation of hadronic models to extreme regimes of temperature and density explores new and uncharted terrain. The results have to be seen with caution. Since the very mean-field approach application as well as other possibly important features neglected in our analysis like transition to Δ and strange matter, meson condensates and so on, take place when one probes the hadronic matter to such extreme limits. Nevertheless our findings may be important to extend information of scalar-meson, vector-meson self couplings and scalar-vector coupling as well at extreme regimes. Having this in mind let us summarize the main findings of our work.

• Only the knowledment of the incompressibility at the saturated nuclear matter itself does not guarantee the stiffness(softness) behavior of the hadronic model at extreme density regime. Here soft(stiff) refers to the behavior of some comparative physical quantities. An example is the behavior of K *vs.* ρ presented in Fig.2. It is indeed the case of the $Q2$ model which is softer than the $W1$ model at the nuclear matter saturation point but as the density increases the model becomes too stiff. In opposite, the $G1$ and $G2$ models become too soft. One might ask where such extreme stiff(soft) high density behavior for $Q2$, $G1$ and $G2$ comes from. It arises from the different signals for $\zeta_\circ$ which multiplies the vector-meson self coupling W^4 (see Table I). The W^4 interaction corresponds to a ρ^4 dependence in the energy functional in a mean-field approach. In spite of the small values for $\zeta_\circ$, such contributions tend to become dominant for high values of ρ since the other terms are of lower order in ρ. We learn from our study that the vector-meson self coupling drives the hadronic model behavior at high densities. Regarding $Q1$ and $C1$ models which carries scalar-meson self coupling and scalar-vector-meson coupling respectively we did not find any extreme behaviour for stiffness(softness).

• In the zero-density limit all the models considered in the hadronic sector merge into the nonlinear $\sigma-$model,[3] but their different parameters imply that only the $W1$, $Q1$, $Q2$ and $G1$ models exhibit a first order nucleon-antinucleon phase transition while the models $C1$ and $G2$ do not. Another interesting point is that in spite of displaying very similar behaviour in Figs. 1-4, the models $G1$ and $G2$ differ too much regarding the hadronic phase transition itself (see, for instance, Figs. 5-6 and Table II). Still at $\rho = 0$ regime, contrary to naive intuition, the existence or not of a hadronic first order nucleon-antinucleon phase transition is not manifest in the results of the hadronic-QGP phase transition. As we have discussed, the $T_c's$ are remarkably close for each chosen $B^{1/4}$.

In the case $B^{1/4} = 174$ MeV one obtains T_c's around 151 MeV, in agreement with the currently accepted value. This point addresses us to an important conclusion of our work that, the hadronic model itself here is not of importance at all, since the hadronic-QGP phase transition is essentially given by the QGP phase and very close to the temperature where p_{QGP} acrosses zero. This finding, at least from our knowledment, has never been so systematically studied or stated.

• Additional insights into the behaviour of the considered model under extreme conditions were obtained from the more general hadronic-QGP phase transition diagram. Throughout this paper we have repeatedly compared our results to the case $\alpha_s = 0$ (free quarks). The motivation was that different authors use different values for α_s as suggested by various lattice QCD simulations, usually a bit smaller than those obtained from Eq. (8). Our results show that any value for α_s between 0 (free quarks) and that given by Eq. (8) would yield a coexistence curve lying between those above limiting cases and, of course, reducing the extend of the mixed phase region. Figures 4 and 9 show the correlation between α_s and our different choices for $B^{1/4}$. This can be used to infer some qualitative information about the coexistence diagram for different values of $B^{1/4}$.

• Finally, one of the most important conclusion of our work is that the stiffness(softness) of the hadronic models, controls quite completely the boundaries of the hadronic-QGP coexistence phase. For example, Figs. 12-15 show how strongly the softness of the models $G1$ and $G2$ manifests itself in the coexistence phase diagrams. *However, for very low density the coexistence curve becomes hadronic model independent.*

5 REFERENCES

[1] J.D. Walecka, Ann. Phys. **83**, (1974) 491.

[2] B.D. Serot and J.D. Walecka, Advances in Nuclear Physics Vol. 16.

[3] J. Boguta and A.R. Bodmer, Nucl. Phys. **A292**, (1977) 414.

[4] J. Theis *et.al.* Phys. Rev. **D28**, (1983) 2286.

[5] R.J. Furnstahl and B.D. Serot, Phys. Rev.**C43**, (1991) 105.

[6] R.J. Furnstahl and B.D. Serot, Phys. Rev. **C44**, (1991) 2141.

[7] R.J. Furnstahl, B.D. Serot and Hua-Bin Tang, Nucl. Phys.**A615**, (1997) 441.

[8] H. Müeller and B.D. Serot, Nucl. Phys. **A606**, (1996) 508.

[9] R.J. Furnstahl and B.D. Serot, Phys. Rev. **C41**, (1990) 262.

[10] M. Malheiro, A. Delfino and C.T. Coelho, Phys. Rev.**C58**, (1998) 426.

[11] J.C. Collins, and M.J. Perry, Phys. Rev. Lett. **34**, (1975) 1353; H. Stöcker and W. Greiner, Phys. Rep.**137**, (1986) 277.

[12] U. Heinz, P.R. Subramanian, H. Stöker and W. Greiner, J. Phys. **G12**, (1986) 1237; Bo-Qiang Ma, Qi-Ren Zhang, D.H. Rischke and W. Greiner, Phys. Lett. **B315**, (1993) 29.

[13] see for example Particle Data Group H. Hikasa et al, Review of particle properties, Phys. Rev. **D45**, (1992) 54.

[14] H. Stöcker and W. Greiner, Phys. Rep. **137**, (1986) 277.

[15] H.Müller , Nucl.Phys. **A618**, (1997) 349.

Edward V. Shuryak

Are High Energy Heavy Ion Collisions similar to a Little Bang, or just a very nice Firework?

E.V. Shuryak
State University of New York, Stony Brook, NY 11794, USA

Abstract

The talk is a brief overview of recent progress in heavy ion physics, with emphasis on applications of macroscopic approaches. The central issues are whether the systems exhibit macroscopic behavior we need in order to interpret it as excited hadronic matter, and, if so, what is its effective Equation of State (EoS). This, in turn, depends on the collision rate in matter: we think we understand in hadronic matter near freeze-out, but certainly not at earlier stages of the collisions. Still (and this is about the most important statement we make) there is no indication that it is *not* high enough, so that a hydro description of excited matter be possible.

More specifically, we concentrate on such properties of the produced excited system as *collective flow, particle composition and fluctuations.* Note that both a generation of a pressure and the rate of fluctuation relaxation are ultimately a measure of a collision rate we would like to know. We also try to explain what exactly are the expected differences between collisions at AGS/SPS and RHIC energies.

1 Flows

1.1 QCD phase transition and flows

We start with general questions, such as: Do we produce excited matter with sufficiently large scattering rate able to ensure local equilibration? If so, what

is its EoS and whether it is close to results obtained in lattice simulations? How one can tell the Bang from a Fizzle, experimentally? There are 3 effects one can discuss: (i) longitudinal work; (ii) radial transverse flow; and (iii) elliptic flow. We address two last ones below.

Before we go to specific description of concepts and data on flow, let us discuss in general why we think that rather different phenomena at AGS/SPS and RHIC energy domain can nevertheless be described in a unified way by hydro+cascade model. Those types of models are the only ones known, which can incorporate correctly the fact that hadrons and partons live in different vacua, separated by significant "bag term" in EoS. This phenomenon generates soft "mixed phase", in which energy density ϵ grows but temperature T and pressure p do not. Purely cascade models with partons/hadrons miss this central point, and therefore have very unrealistic EoS.

The Hydro-to-Hadrons Model [1] include hydro plus transfer to hadronic cascade (RQMD), in order not to worry about freeze-out of different species, resonance decays etc. The transfer is smooth enough because the effective EoS of RQMD and our hadronic matter is about the same.

At SPS the evolution starts close to rather soft "mixed phase" (as lattice thermodynamics tells us), then proceeding to stiffer pion gas: therefore most of the radial expansion is pion-driven and happens very late. There are many proves of that: one [2] is that Ω^- which participate little in hadronic rescattering practically do not have it.

Let us first characterize flows in general. At RHIC we start well above the QCD phase transition, and so expect the so called "QGP push", then softer mixed phase, and finally a stiff hadronic phase again. (Now Ω^- is expected to flow more!)

In non-central collisions at SPS the initial almond for $b \sim R$ collisions retains basically the same almond shape: matter does not move till the final velocity $v_t \approx 0.5$ is only obtained close to the end of the expansion. At RHIC the initial almond is transformed into a completely different object called the *"nutcracker"* [8], which consists of two separated shells of matter and a small "nut" in the center. It happens by the time 8-10 fm/c, and then shells continue to move out in hadronic phase, slowly dissolving.

Radial flow is usually characterized by the slope parameter T: $dN/dp_t^2 dy \sim exp(-m_t/T), m_t^2 = p_t^2 + m^2$. T is *not* temperature: it incorporates random thermal motion and collective transverse velocity. Its prediction for various EoS (marked by latent heat, say LH8 means latent heat 800 MeV/fm^3, see

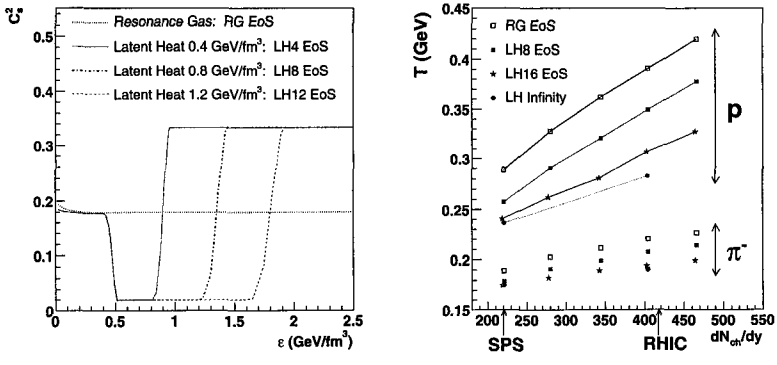

Figure 1: The speed of sound for a set of EoS used (a) and resulting transverse mass slope T (b) versus mid-rapidity (y=0) charged particle multiplicity, for AuAu collisions with b=6.

fig.1a) is shown in the following figure , for protons and pions versus basically collision energy expressed in terms of multiplicity, see fig.1b. One can see that different EoS show different growth, although picture is rather simple: the softer the EoS the less flow.

1.2 Elliptic flow

If there is no correlation between space and momentum, there is no elliptic flow. For example, *any* model like [4] in which transverse momentum increase in AA is due to initial state interaction, like in pA collision, cannot have elliptic flow. Indeed HIJING parton model [5] without rescatterng (an example of the model which produce a "firework" type final state) has nearly zero (actually slightly negative) v_2. String models like UrQMD [6] and RQMD itself also do not produce pressure at early time, and predicted respectively *smaller* v_2 at RHIC than at SPS Those are eliminated, as soon as the first STAR data [3] have shown that at RHIC v_2 is in fact twice larger than at SPS!

But hydro knows about geometry of the excited system: the pressure

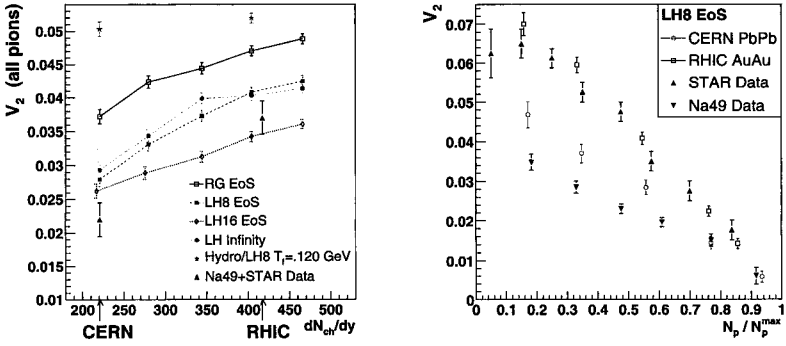

Figure 2: (a) The elliptic flow parameter V_2 versus multiplicity at b=6 fm, for different EoS. (b) V_2 is now plotted versus impact parameter b, described experimentally by the number of participant nucleons, for RHIC STAR and SPS NA49 experiments. Both are compared to our results for EoS LH8.

gradient is mostly along the narrow part of the almond. The elliptic flow is quantified experimentally by the elliptic flow parameter $V_2 = \langle cos(2\phi) \rangle$

The *energy dependence* of V_2 does not appear to be simple (in contrast to radial flow). Furthermore, we have found that if one is making EoS softer the v_2 decreases non-monotonously, first decreasing and then increasing again. It means for a given experimental value of V_2 there are two possible scenarios, we called the "QGP push" and "burning almond". In the first case the initial almond transfers to nutcracker, in which spatial anisotropy decreases and even change sign. In the second, the almond dries out, and spatial anisotropy actually grows. So, in order to answer the question whether the "QGP push" scenario we are waiting for is or is not the case, some further studies are needed. In particular, the scan in RHIC energies downward would be very useful.

Fig.2b shows data as a function of impact parameter. One can see that the agreement becomes much better at RHIC. Furthermore, one may notice that deviation from linear dependence we predict becomes visible at SPS for more peripheral collisions with $N_p/N_p^{max} < 0.6$ or so, while at RHIC only

the most peripheral point, with $N_p/N_p^{max} = 0.05$ show such deviation. This clearly shows that hydrodynamical regime in general works much better at RHIC. On the other hand, a models of single re-scattering (e.g. [7]) which approximately describes peripheral SPS data is completely inconsistent with this linear rise, seen both at SPS and RHIC.

2 Matter composition

2.1 Strangeness

The discussion of the role of s,c quarks in excited hadronic matter has a peculiar history. In the first paper addressing the subject [9] it was argued that QGP with $T \sim 500\,MeV$ should quickly equilibrate even charm, because of high rate of gluon-induced processes, and suggested to use it as a QGP signature. As for strangeness, the m_s was considered to be too small to be useful for that purposes. However later, Rafelski et al [10] had nevertheless suggested that the strangeness enhancement for exactly that role. The experiments at AGS/SPS indeed found lager strangeness per participant baryon (or per pion) in AA collisions than in pp, which is more pronounced for hyperons and especially for Ω^-. However, the following two features has been also found. First, strangeness enhancement started at very low energies, at AGS. Second, its magnitude basically described by the statistical model (see e.g.[11]), by an equilibrium at $T \approx 170\,MeV$ and μ_b depending on the collision energy. From this point of view people rather called a phenomenon a "disappearance of strangeness suppression", which has been present in pp.

But even this interpretation has been recently challenged in [12]. Already 25 years ago the issue of correct account for strangeness in small statistical systems has been addressed in [14]. The main point is, the usual statistical expressions say for K/π ratio, being the ratio of integrated Bose distribution, is only valid if the average particle number $< N_K > \gg 1$. If it is not so, exact strangeness conservation should be enforced while considering all possible states of the system, say containing KK pairs, etc. As a result, $< N_K >$ depends on volume (or $< N_\pi >$) quadratically, till $< N_K > \sim 1$. In $\bar{p}p, pp$ collisions at few GeV range the data were in perfect agreement with this prediction already in 1975 [14]. We are however still lacking a demonstration of where that happens for say Ξ, Ω: even most peripheral data at SPS do not

show a predicted transition to small-volume regime, their ratio to multiplicity remains flat. Probably lighter ions are needed to see it.

In summary: whatever strange it may appear to us, composition of hadrons, including strange ones, seem to be thermal *both* in AA (at AGS/SPS energies) and pp collisions. In the latter case it is believed to come from string fragmentation: so AA can either be also string-based, or come from QGP, which (by coincidence?) have a T_c value which mimic string decays.

2.2 Solving the anti baryon puzzle

Anti-baryon ratios, like many others, can be rather accurately characterized by the so-called *chemical* freeze-out stage with a common temperature T_{ch} $\mu_{B,ch}$ (values depend on collision energy). However, the kinetics of other particles and anti-baryons cannot be the same. The number of pions, kaons, etc. are not subject to significant changes when the system evolves from T_{ch} to T_{th}: thus *'over-saturation'* appears, the effective pion fugacity

$$z_\pi = exp(\mu_\pi / T_{th}) \approx 1.6 - 1.9$$

The situation for antibaryons is different because the pertinent annihilation cross section is *not small*, $\sigma_{p\bar{p}\to n\pi} \simeq 50$ mb. The time in which a give antinucleon is eaten is only

$$\tau_{ch} = \frac{1}{\sigma_{ann}\ \rho_B\ v_{th}} \simeq 3 \text{ fm/c}$$

and so naively one might expect most of the antiprotons to be annihilated, and various transport calculations (ARC, UrQMD) have indeed been unable to account for the measured number, falling short by significant factors. Speculations have been put forward: either a reduction of the annihilation rate or an enhanced production.

Inverse reactions, ignored in event generators, are however *not small* [15]

$$\mathcal{R}_{th} = |\mathcal{M}_n|^2 \exp[-(E_p + E_{\bar{p}})/T]\ [z_p\ z_{\bar{p}}\ - z_\pi^n]$$

The condition that this reaction goes on implies [15]

$$z_{\bar{p}} = (z_p)^{-1} \langle z_\pi^n \rangle$$

which leads to predictions consistent with the experimental value of $N_{\bar{p}}/N_p = (5.5 \pm 1)\%$ (na44). Note that it is very multi-pion reaction, with n=6-7.

After the paper by Rapp and myself, C.Greiner and S.Leupold [16] generalized it further, to $\bar{Y} + N \leftrightarrow n\pi + K$ where $Y = \Sigma\Xi, \Omega$. Similar multi-meson annihilation can also explain the long-standing puzzle about multiple production *anti-hyperons.*

2.3 Charm and J/ψ suppression

Charm production at SPS is due to hard gg collisions, which are obviously able to produce somewhat larger amount of it, compared to its equilibrium value at $T = 170\, MeV$. Direct measurements are still in the future, but we should hardly expect any surprises here. (The NA50 medium mass dilepton excess fits nicely to thermal dilepton rate [13], so I do not think it is a charm enhancement.)

Do $J/\psi, \psi'$ we observe in AA collisions know about hadronic matter which surrounds it, or their cross section is too small and too absorptive (leading to $\bar{D}D$ pairs) that all of them we see just jump intact directly from the primary production point? The latter remains the prevailing view in the field, although it has been challenged lately.

Although $\psi'/J/\psi$ ratio starts decreasing at rather peripheral collisions/ small A, as larger radius of ψ' suggests larger cross section, it then stabilizes at $\psi'/J/\psi \approx 0.05$. Furthermore, as noticed in [17], this number is consistent with *the same* $T \approx 170\, MeV$ which fits all other ratios. This leads to an idea that the observed ψ' is excited from J/ψ.

Much more radical idea has been put forward in [18]: the number of J/ψ itself is in agreement with the statistical model, provided the total charm fugacity is fixed to the parton model production. If it is not a coincidence, it then implies that J/ψ may in fact be created from the same heat bath as all other hadrons. If so, the individual string scenario is of course out of the window, and the QGP scenario (with some extra charm added to it) is in.

Much more charm is expected at RHIC: it makes recombination of floating charm pairs into charmonium states even more likely. The issue has been studied in recent paper [20]: the conclusion is that we should in fact expect a *charmonium enhancement* at RHIC.

3 Event-by-event Fluctuations

3.1 Current SPS data versus theory

Unlike pp collisions, the AA ones demonstrate small fluctuations of Gaussian shape, as measured e.g. by NA49. It is basically a consequence of a basic theorem of probability theory, roughly stating that any distribution with a maximum in high power becomes Gaussian. Still, it is quite striking how far this Gaussian goes: no deviations from it is seen for few decades, as far as data go. No trace of any large fluctuations, DCC or other bubbles, and all events with the same impact parameter are basically alike.

The question then is whether the *widths* of those Gaussians is understood. The short answer is yes. Somewhat longer answer is that one should separate [21] fluctuations of two types, of intensive or extensive variables. The latter is e.g. total charge multiplicity: it obtains about equal contributions from the initial (due to fluctuations in spectators) and final stage (resonances). The former (e.g. particle ratios like π^+/π^-) are well described by resonances at freezeout.

To give some example, consider fluctuations in charged multiplicity measured by NA49 at 5% centrality: $\frac{<\Delta N_{ch}^2>}{<N_{ch}>} \approx 2.0$, while Poisson statistics (independent production) gives 1 in the rhs.

Statistical fluctuations in a resonance gas increase the rhs. Example: if all pions would originate from $\rho^0 \to \pi^+\pi^-$, and rho would be random, then the rhs would be 2. Account for equilibrium composition lead however to the Gaussian width of only about 1.5 [21]. Correlations coming from fluctuation in the number of participants further increase it [22]: see the comparison in the figure 3: Good examples of intensive variable fluctuations are those in the mean p_t (in an event) or in electric charge Q (same as of the π^+/π^- ratio). Resonances again: e.g. $\rho^0 \to \pi^+\pi^-$ does not lead to Q but contribute to multiplicity $Q^2/ < N_c h > \approx .7 - .8$, not 1 as for Poisson. It is what is actually observed for central collisions by NA49.

3.2 Can "primordial" fluctuations be seen?

In order to do so, we need a telescope looking back into the past, through the clouds of hadronic matter. How to make it has been recently suggested in refs [23]. The idea is to use *long-wavelength fluctuations of conserved quantities*,

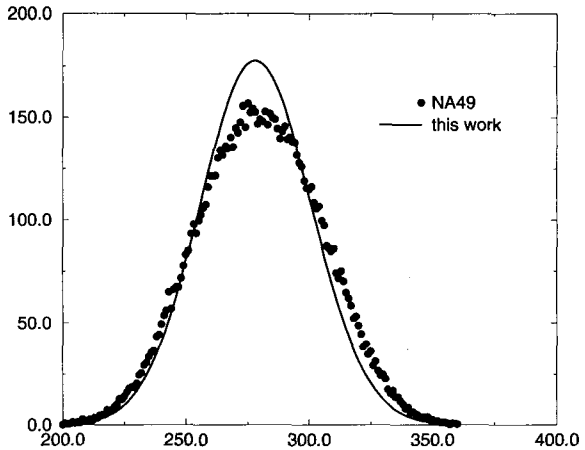

Figure 3: The calculated multiplicity distribution from our model (solid line) is compared to the observed one (points).

which have slow relaxation. Example: primordial fluctuations in microwave background give us "frozen plasma oscillations" at Big Bang. Can we find similar signal in the "Little Bang"? Yes: if relax.time is longer than lifetime of hadronic stage the fluctuations we would see are "primordial ones", from the QGP which are factor ~ 3 smaller.

Quantitative studies have been recently done by Stephanov and myself [24]. Fluctuations are governed by Langevin eqn

$$\partial_\tau f = \gamma(\tau)\, \partial_y^2 f + \xi(y,\tau)$$

and we calculated $\gamma(\tau)$ for pions in collisions. Basically we found that at RHIC/SPS pion diffuse during hadronic stage by about 2 units of rapidity. NA49 data we had are in acceptance $\Delta y = 2$ and show perfect agreement with equilibrium resonance gas. STAR detector may have $\Delta y = 4$ and additional deviation from 1 by about 20% - quite observable.

Baryon number fluctuations idea cannot work because we do not see neutrons.

4 Summary

- – If hydro description plus lattice-like EoS makes sense, we found that the QCD phase transition plays different role at AGS/SPS and RHIC: it makes the EoS effectively soft in the former case but stiff at high energy, providing early "QGP push".

- – Collective flow, especially its elliptic component, is very robust measure of the pressure in the system. STAR data at RHIC, which demonstrate increase of elliptic flow by factor 2, contradicts to string-based models and also mini-jet models without rescattering. Hydro-based model, especially H2H model with hadronic cascades, can describe these data very accurately. Still two solutions seem to be possible, one with strong QGP push (predicted by lattice-based EoS) and another with longer-time burning.

- – Strangeness seem to be well equilibrated in any collisions, and thus is not a QGP signature. Whether J/ψ can obtain significant contribution from equilibrated charm at SPS is strongly debated: it should however be the case at RHIC.

- – Event-by-event fluctuations are mostly due to final state interaction between secondaries, and available data are in agreement with equilibrium resonance gas calculations.

- – Potential observations of "primordial charge fluctuations" are limited by their relaxation time, mostly due to pion diffusion in rapidity. The outlook depends on experimental acceptance: available calculations suggest that wide STAR acceptance can be sufficient to see 10-15 percent modification of charge fluctuations.

References

[1] D.Teaney, J. Lauret and E.Shuryak, Collective Flows at RHIC as a Quark-Gluon Plasma Signal, in progress.

[2] H. van Hecke, H. Sorge, N. Xu Nucl.Phys.A661:493-496,1999

[3] K. H. Ackermann *et al.* [STAR Collaboration], "Elliptic flow in Au + Au collisions at s(N N)**(1/2) = 130-GeV," nucl-ex/0009011.

[4] A. Leonidov, M. Nardi, H. Satz, Z.Phys.C74:535-540,1997

[5] Xin-Nian Wang, Miklos Gyulassy, Phys.Rev.D44:3501-3516,1991

[6] M. Bleicher and H. Stocker, hep-ph/0006147.

[7] H. Heiselberg and A. Levy, Phys. Rev. **C59**, 2716 (1999) [nucl-th/9812034].

[8] D.Teaney and E.Shuryak,Phys. Rev. Lett. **83**, 4951 (1999); nucl-th/9904006

[9] E. Shuryak, Phys. Lett. **78B**, 150(1978); Sov. J. Nucl. Phys. 28, 408(1978). Phys. Rep. 61, 71(1980);

[10] P. Koch, B. Muller, J. Rafelski, Phys.Rept.142:167,1986

[11] P. Braun-Munzinger, I. Heppe, J. Stachel, Phys.Lett.B465:15-20,1999.

[12] K.Redlich et al, Phys.Lett.B486:61-66,2000: hep-ph/0006024

[13] R. Rapp and E.V.Shuryak, Phys.Lett.B473:13-19,2000; hep-ph/9909348

[14] E.V.Shuryak, PL 42B (1972) 357, Sov.J.Nucl.Phys.20,1975,295

[15] R. Rapp and E.V.Shuryak,Resolving the Antibaryon Puzzle, hep-ph/0008326.

[16] Carsten Greiner, Stefan Leupold, nucl-th/0009036

[17] H.Sorge, E.Shuryak, I.Zahed Phys.Rev.Lett.79:2775-2778,1997, hep-ph/9705329.

[18] P. Braun-Munzinger, J. Stachel,Phys.Lett.B490:196-202,2000; nucl-th/0007059.

[19] M.I.Gorenstein et al, hep-ph/0010148.

[20] R.L. Thews, M. Schroedter, J. Rafelski, hep-ph/0009090

[21] M. Stephanov, K. Rajagopal, E. Shuryak,Phys.Rev. D60: 114028 ,1999; hep-ph/9903292.

[22] G.V. Danilov, E.V. Shuryak, nucl-th/9908027.

[23] M.Asakawa, U.Heinz and B.Muller, hep-ph/0003169, S.Jeon and V.Koch, hep-ph/0003168.

[24] E.V.Shuryak and M.A.Stephanov, When can Long-Range Fluctuations be used as QGP signal? hep-ph/0010100.

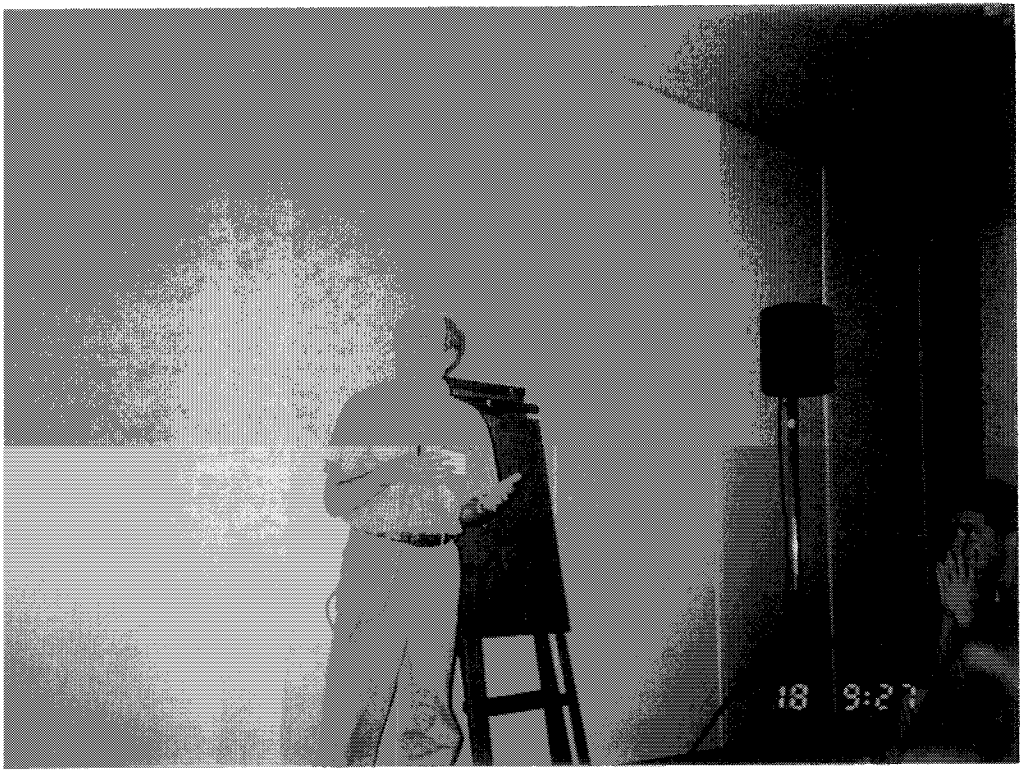

Jean-Paul Blaizot

Hard Thermal Loops and QCD Thermodynamics

J-P. Blaizot*
Service de Physique Théorique† CE-Saclay 91191 Gif-sur-Yvette, France

ABSTRACT

The entropy of the quark-gluon plasma is calculated form "first principle", using (approximately) self-consistent approximations. Lattice results on pure gauge theories at high temperature are accurately reproduced down to temperatures as low as twice the critical temperature.

1 Introduction

The best information that we have on the thermodynamical properties of the quark-gluon plasma is at present coming from lattice gauge calculations. However a lot of efforts have been devoted during the last few years to understand the results of such calculations using analytical weak coupling techniques. The motivation behind such studies is that at sufficiently high temperature the gauge coupling is small, allowing for weak coupling expansions (which howevers differ from straightforward perturbative expansions). In this talk, I shall report on recent progress along these lines, concentrating, for reasons that I shall explain, on the calculation of the entropy. I shall show that lattice results can be reproduced accurately down to temperatures of the order of $2.5T_c$. The work that I shall present was done in collaboration with E. Iancu and A. Rebhan.[1] The text below is an edited version of the oral presentation; details can be found in the publications.[1]

2 Difficulties with perturbation theory

- In a quark-gluon plasma at high temperature T, the effective coupling constant is small because of asymptotic freedom:
$$g^2(T) \propto \frac{1}{\ln(2\pi T/\Lambda_{QCD})} \qquad \Lambda_{QCD} \sim 200 MeV$$
However the dependence of g on T is logarithmic, so g is truly small only for very large T.
- Explicit calculations show that perturbation theory is badly behaved.[2]
$$P = P_0 \left[1 - 0.095g^2 + 0.12g^3 + \left(0.09 \ln g - 0.07 - 0.013 \ln\left(\frac{\mu}{2\pi T}\right)\right) g^4\right] + \cdots$$
Furthermore, infrared divergences occur,[3] starting at order g^6.
- Thus, although the coupling may be small, strict perturbation theory cannot be used, and resumations are needed. To proceed it is useful to analyze the relevant scales and degrees of freedom.

*Affiliated to CNRS
†Laboratoire de la Direction des Sciences de la Matière du Commissariat à l'Energie Atomique

3 Scales, degrees of freedom and fluctuations

In the absence of interactions, the plasma particles are distributed in momentum space according to the Bose-Einstein or Fermi-Dirac distributions:

$$N_k = \frac{1}{e^{\beta k} - 1}, \qquad n_k = \frac{1}{e^{\beta k} + 1}, \tag{1}$$

where $\beta \equiv 1/T$ and we assume vanishing chemical potentials. In such a system, the particle density n is not an independent parameter, but is determined by the temperature: $n \propto T^3$. Accordingly, the mean interparticle distance $n^{-1/3} \sim 1/T$ is of the same order as the thermal wavelength $\lambda_T = 1/k$ of a typical particle in the thermal bath for which $k \sim T$.

In the weak coupling regime, the interactions do not alter significantly the picture. The hard degrees of freedom, i.e. the plasma particles, remain the dominant degrees of freedom and since the coupling to gauge fields occurs typically through covariant derivatives, the effect of interactions on particle motion is a small perturbation unless the fields are very large, i.e., unless $A \sim T/g$, where g is the gauge coupling: only then do we have $\partial_X \sim T \sim gA$.

Considering now more generally the effects of the interactions, we note that these depend both on the strength of the gauge fields and on the wavelength of the modes under study. A measure of the strength of the gauge fields in typical situations is obtained from the magnitude of their thermal fluctuations. Let us set $\bar{A} \equiv \sqrt{\langle A^2(t,\mathbf{x})\rangle}$. In equilibrium $\langle A^2(t,\mathbf{x})\rangle$ is independent of t and $\mathbf{x}$ and given by $\langle A^2\rangle = G(t=0,\mathbf{x}=\mathbf{0})$ where $G(t,\mathbf{x})$ is the gauge field propagator. In the non interacting case we have (with $\varepsilon_k = k$):

$$\langle A^2\rangle = \int \frac{\mathrm{d}^3k}{(2\pi)^3}\frac{1}{2\varepsilon_k}(1+2N_k). \tag{2}$$

We shall use here this formula also in the interacting case, assuming that the effects of the interactions can be accounted for simply by a change of ω_k (a more complete calculation is presented in[4]). We shall also ignore the (divergent) contribution of the vacuum fluctuations (the term independent of the temperature in Eq. (2)). We then obtain the following results:

- **Hard** degrees of freedom: the plasma **particles**

$$k \sim T \qquad \langle A^2\rangle_T \sim T^2 \qquad g\bar{A}_T \sim gT \ll k$$

- **Soft** degrees of freedom: **collective modes**

$$k \sim gT \qquad \langle A^2\rangle_{gT} \sim gT^2 \qquad g\bar{A}_{gT} \sim g^{3/2}T \ll gT$$

- **Ultrasoft** degrees of freedom: **unscreened** magnetic fluctuations.

$$k \sim g^2T \qquad \langle A^2\rangle_{g^2T} \sim g^2T^2 \qquad g\bar{A}_{g^2T} \sim g^2T$$

The latter are the fluctuations responsible for the breakdown of perturbation theory at order g^6

4 Hard Thermal Loops

While the effect of thermal fluctuations at the scale $\sim T$ is a small perturbation on the motion of a hard particle (because $g\bar{A}_T \ll T$), this is not so for a soft mode with $k \sim gT$ (since then $g\bar{A}_T \sim k$). In fact at the scale

gT a rich pattern of collective phenomena develop. The dynamics of the soft modes is coded in a set of effective amplitudes, called "hard thermal loops".[5] As an example, consider the polarization tensor:

$$\Pi(\omega, p) = g^2 T^2 f(\frac{\omega}{p}, \frac{p}{T})$$

where f is a dimensionless function of its arguments. When $p \sim gT$

$$\Pi(\omega, p) \approx g^2 T^2 f(\omega/p, 0)$$

and Π is of the same order of magnitude as the bare inverse propagator ($\sim p^2$). Resummations are needed. Such resummations generate for instance the odd powers of g in the perturbative expansion.

We shall be concerned in the rest of this talk with the contributions of these collective modes to the thermodynamical functions of the quark-gluon plasma. The properties of these collective modes are determined by the hard thermal loops.[6]

5 Collective modes, quasiparticles and thermodynamics

- The thermodynamics is dominated by hard degrees of freedom. Soft collective modes should provide only corrections....when properly calculated.
- Hard thermal loops correctly account for the effects of hard degrees of freedom on soft modes. One needs also to treat accurately the effect of soft modes on hard degrees of freedom.
- We shall later formulate approximations which allow us to keep the full information on spectral weights coded in the hard thermal loops

$$D(\omega, k) = \int_{-\infty}^{+\infty} \frac{\mathrm{d}k_0}{2\pi} \frac{\rho(k_0, k)}{k_0 - \omega}$$

- This is to be contrasted with "dimensional reduction" where one keeps only one moment of the spectral density

$$D(\omega_n = 0, k) = \int_{-\infty}^{+\infty} \frac{\mathrm{d}k_0}{2\pi} \frac{\rho(k_0, k)}{k_0}$$

- The effective 3-d theory

$$\mathcal{L}_{eff} = \frac{1}{4}(F_{ij}^a)^2 + \frac{1}{2}(D_i A_0^a)^2 + \frac{1}{2} m_D^2 (A_0^a)^2 + \delta\mathcal{L}$$

$$D_i = \partial_i - ig\sqrt{T} A_i$$

is appropriate for calculating soft or ultrasoft correlation functions. But the thermodynamical functions are dominated by hard degrees of freedom and dimensional reduction may not be the best strategy to estimate them. See however ref.[7]

6 A direct approach: "screened perturbation theory"

As we have seen, hard thermal loops represent important corrections which need to be taken into account non perturbatively in any soft propagator (or vertex with soft external lines). A simple way to do that is to include the hard thermal loops at the tree level and subtract them from the interacting Lagrangian.

- **Scalar field**

The only hard thermal loop is a mass term. We then write:

$$\mathcal{L} = \mathcal{L}_0 - \frac{1}{2}m^2\phi^2 + \frac{1}{2}m^2\phi^2 + \mathcal{L}_{int}$$
$$= \mathcal{L}'_0 + \mathcal{L}'_{int}$$

where $\mathcal{L}'_0 = \mathcal{L}_0 - \frac{1}{2}m^2\phi^2$. Convergence is improved. But the method suffers from artificial UV problems and a rather strong scheme dependence.[8]

- **QCD: HTL perturbation theory**[9]

$$\mathcal{L} = \mathcal{L}_0 + \mathcal{L}_{HTL} - \mathcal{L}_{HTL} + \mathcal{L}_{int}$$
$$= \mathcal{L}'_0 + \mathcal{L}'_{int}$$

This suffers from the same problem as the scalar case. Furthermore $\mathcal{L}_{HTL}$ is not accurate for $\omega, p \gtrsim T$. However the method can potentially include vertex corrections at the same level as propagator renormalization.[9]

7 Self-consistent approximations

We turn now to more systematic methods for performaing propagator renormalization. Consider first the thermodynamic potential $\Omega = -PV$. This can be written as the following functional of the full propagator D (for simplicity, the formulae below are written for a scalar field theory):

$$\Omega = \frac{1}{2}\mathrm{Tr}\ln D^{-1} - \frac{1}{2}\mathrm{Tr}\Pi D + \Phi[D],$$

where Π is the self-energy related to the propagator by Dyson's equation

$$D^{-1} = D_0^{-1} + \Pi.$$

The quantity $\Phi[D]$ is the sum of all skeleton diagrams (2-particle irreducible):

An important property of $\Omega[D]$ is that it is stationary with respect to variations of D when Π satisfies

$$\Pi[D] = 2\frac{\delta\Phi}{\delta D}.$$

Dyson's equation becomes then a self-consistent equation. Approximations obtained by selecting some particular skeletons in Φ and solving this self-consistent Dyson equation are referred to as self-consistent approximations.[10]

8 THE ENTROPY

- The stationarity of Ω with respect to D leads to important cancellations in the calculation of the entropy leaving us with a "simple" formula:

$$\mathcal{S} = \frac{\mathrm{d}P}{\mathrm{d}T} = \left.\frac{\partial P}{\partial T}\right|_D$$

Consider then the example of the scalar field.

- The 2-loop approximation for $\Phi[D]$ involves:

- The resulting 2-loop approximation for $\mathcal{S}$ is:

$$S = -\int \frac{\mathrm{d}^4p}{(2\pi)^4} \frac{\partial N}{\partial T} \left\{ \mathrm{Im} \ln D^{-1} - \mathrm{Im}\Pi \, \mathrm{Re} D \right\}$$

where $N(\omega) \equiv 1/(\mathrm{e}^{\omega/T} - 1$. This expression of the entropy

- is effectively a one-loop expression.

- is a well behaved function of g, perturbatively correct up to order g^3.

- is manifestly ultraviolet-finite.

- makes a full use of the quasiparticle spectral information coded in the hard thermal loops.

9 A simple model with a scalar field

- Use the simple two-loop diagram for Φ.
- Ansatz for the spectral function:

$$\rho(k_0, k) = 2\pi\epsilon(k_0)\delta(k_0^2 - k^2 - m^2)$$

- Net results for the pressure (after renormalization)[1]:

$$P = -T \int \frac{\mathrm{d}^3k}{(2\pi)^3} \ln\left(1 - \mathrm{e}^{-\beta\varepsilon_k}\right) + \frac{m^2}{2} I_T(m) + \frac{m^4}{128\pi^2},$$

where $\epsilon_k = (k^2 + m^2)^{1/2}$ and

$$I_T(m) = \int \frac{\mathrm{d}^3k}{(2\pi)^3} \frac{n_k}{\varepsilon_k}.$$

- The entropy is simpler. Formally it is that of non interacting massive particles:

$$S = \int \frac{\mathrm{d}^3k}{(2\pi)^3} \left\{ (1 + n_k) \ln(1 + n_k) - n_k \ln n_k \right\},$$

with $n_k = 1/(\mathrm{e}^{\varepsilon_k/T} - 1)$.

10 APPROXIMATE SELF-CONSISTENCY

- In gauge theories complete self-consistency cannot be achieved (e.g. we do not know how to renormalize the self-consistent Dyson equation).
- But this is not desirable (propagator renormalisation should in general be done along with vertex renormalization in order to maintain gauge invariance)

- **STRATEGY**: replace fully self-consistent solutions by gauge invariant approximations for Π and evaluate S with this approximate Π. Insure that at small coupling perturbation theory is reproduced up to and including order g^3. The final results are non perturbative and gauge invariant.
- Hard thermal loops are essential building blocks in constructing approximate propagators.
- We use the 2-loop skeletons

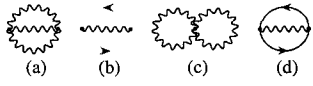

where the wavy lines denote gluons, the dotted lines ghosts and the continuous line quarks.

- In "leading order" the self-energies are the hard thermal loops: $\Pi \sim \Pi_{HTL}$ and $\Sigma \sim \Sigma_{HTL}$

At soft momenta ω, $p \sim gT$ the approximation is justified (by definition of the hard thermal loops).

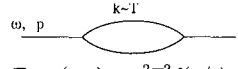

$$\equiv \quad \Pi_{HTL}(\omega, p) = g^2 T^2 f(\omega/p)$$

At hard momenta, it turns out that the HTL are also accurate since they are required only on the light-cone where they reduce to a simple mass term:

$$\Pi_{HTL}(\omega = p) \;=\; m_{th}^2 \;\equiv\; \frac{g^2 T^2 N}{6}$$

The entropy calculated within this approximation for Π is perturbatively correct to order g^2, but contains only 1/4 of the order g^3.

- The next-to-leading approximation: include corrections on hard particles due to their coupling with soft modes. Then: $\Pi_{soft} = \Pi_{HTL}$, $\Pi_{hard} = \Pi_{HTL} + \delta\Pi$

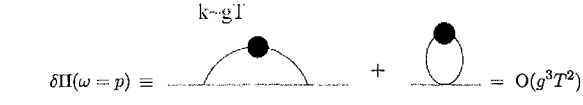

The resulting entropy is perturbatively correct up to order g^3.

11 Some results

As an illustration of the quality of the results that are obtained within that scheme, we show in fig.1 the entropy of pure SU(3) gauge theory. The bands delimiting the various lines in this figure correspond to varying the $\overline{\rm MS}$ renormalisation scale $\bar{\mu}$, which defines the renormalized coupling constant $g(\bar{\mu})$, from $\bar{\mu} = \pi T$ to $4\pi T$. One sees that in contrast to ordinary perturbation theory, going from one level of approximation to the next one is indeed a small correction. The comparison with the lattice data is quite good down to $T \gtrsim 2.5 T_c$.

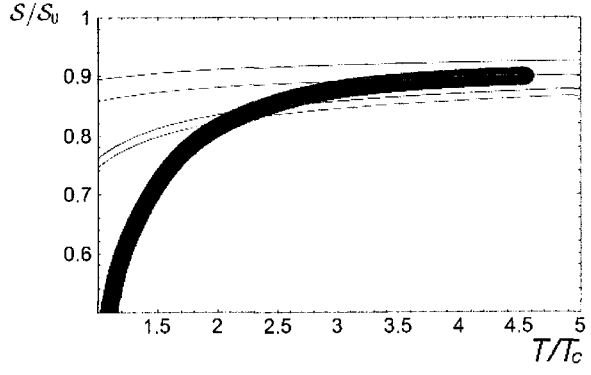

Figure 1: The entropy of pure SU(3) gauge theory normalized to the ideal gas value $\mathcal{S}_0$. The full line is the HTL entropy, the dashed-dotted line is the NLA estimate, for the $\overline{\text{MS}}$ renormalisation scale in the range $\bar{\mu} = \pi T \cdots 4\pi T$. The dark grey band represent the lattice result of ref.[11].

12 Conclusions

- Good agreement with lattice data when available down to $T \sim 2.5T_c$.
- Supports the quasiparticle picture of the quark-gluon plasma.
- The method makes full use of the spectral information on the quasiparticles.
- The approach is easily extended to finite chemical potential.
- From $N(\mu, T)$ and $S(\mu, T)$ one can reconstruct $P(\mu, T)$. Use lattice data to fix the integration constant (e.g. $P(\mu = 0, T)$).

13 REFERENCES

[1] J.-P. Blaizot, E. Iancu and A. Rebhan, Phys. Rev. Lett. **83**, 2906 (1999); Phys. Lett. B **470**; hep-ph/0005003, to be published in Phys. Rev. D.

[2] P. Arnold and C. Zhai, Phys. Rev. D **50**, 7603 (1994), *ibid.* **51**, 1906 (1995); C. Zhai and B. Kastening, *ibid.* **52**, 7232 (1995).

[3] A. Linde, Phys. Lett. **B 96**, 289 (1980).

[4] J.-P. Blaizot and E. Iancu, *The weakly coupled quark-gluon plasma: collective dynamics and hard thermal loops*, to be published in Phys. Rept.

[5] E. Braaten and R. D. Pisarski, Nucl. Phys. **B337**, 569 (1990); J. Frenkel and J. C. Taylor, Nucl. Phys. **B334**, 199 (1990).

[6] J.P. Blaizot and E. Iancu, Nucl. Phys. **B390**, 589 (1993); **417**, 608 (1994); Phys. Rev. Lett. **70**, 3376 (1993).

[7] K. Kajantie, M. Laine, K. Rummukainen, Y. Schröder, hep-ph/0007109.

[8] F. Karsch, A. Patkós, and P. Petreczky, Phys. Lett. B **401**, 69 (1997); hep-ph/9708244; J. O. Andersen, E. Braaten, and M. Strickland, hep-ph/0007159.

[9] J. O. Andersen, E. Braaten, and M. Strickland, Phys. Rev. Lett. **83**, 2139 (1999), Phys. Rev. D **61**, 014017, 074016 (2000).

[10] J. M. Luttinger and J. C. Ward, Phys. Rev. **118**, 1417 (1960); C. De Dominicis and P.C. Martin, J. Math. Phys. **5**, 14, 31 (1964); G. Baym, Phys. Rev. **127**, 1391 (1962).

[11] G. Boyd *et al.*, Nucl. Phys. **B469**, 419 (1996).

Questions and comments

F. Braghin: Is the coupling constant $\alpha_s(T)$ an effective coupling constant for the "whole system"?

J.-P. Blaizot I am not sure what the question is. In the calculation of a thermodynamical quantity which is dominated by hard degrees of freedom, the natural scale for the effective coupling is indeed $2\pi T$. Now, if one looks at processes involving only soft degrees of freedom, the appropriate scale may be that soft scale.

F. Braghin: Which Interaction yields the collective modes you showed?

J.-P. Blaizot The QCD interactions between quarks and gluons, or among gluons themselves.

M. Malheiro: Coming back to the quasiparticle picture of the quark-gluon plasma: Do you have any idea of what is the value of the self-energy close to T_c, or how it goes with increasing of T in your hard thermal loop approximation?

J.-P. Blaizot Calculating the self energies near T_c is hard. At high T, the self-energies are accurately given by hard thermal loops which are typically proportional to T^2.

E. Shuryak: *"Non perturbative" has two meanings which are very different. One is resummation of diagrams,* e.g. as in BCS, or what has been doen in the talk. Others, like instantons, which are e^{-const/g^2} are invisible in perturbation theory.

E. Shuryak: Consider B (the bag constant) I discussed. In ε it is $+B$, in P it is $-B$. In S it cancels (also in partcle density if $\mu \neq 0$). So J.-P. *is right: the entropy is* simpler, also with respect to B. But B comes back as the integration constant that was mentioned at the end, in $P = \int_{T_1}^{T_2} S(T)\,\mathrm{d}T + const.$

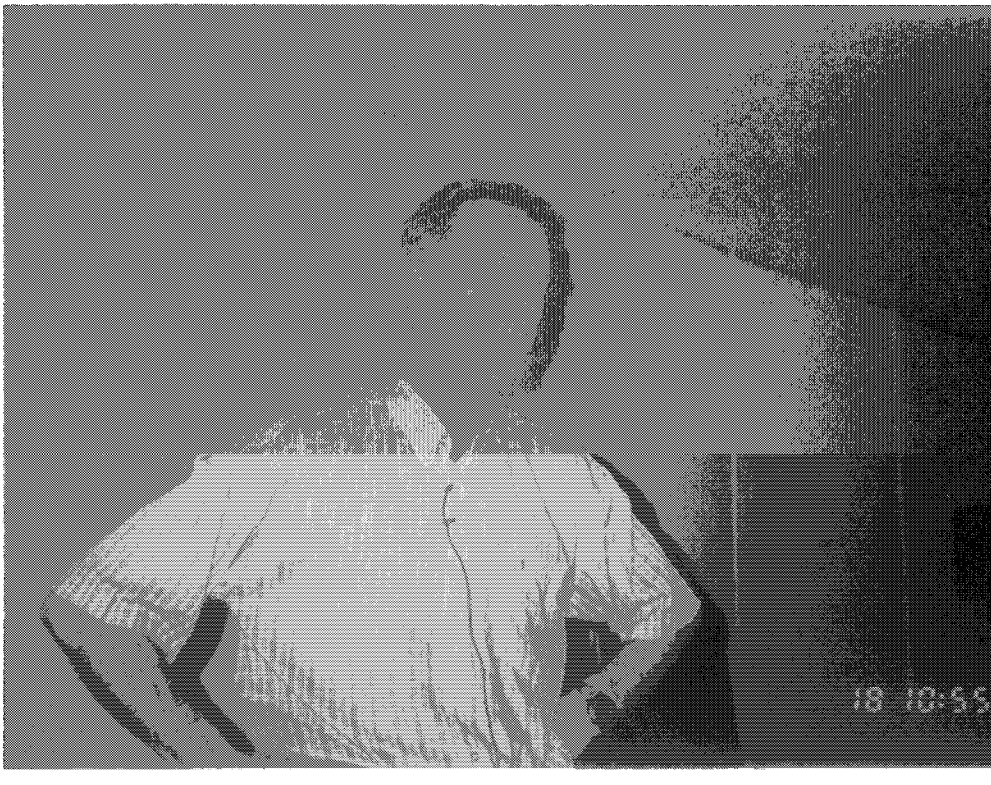

Marcus B. Pinto

Optimized Perturbation Theory: Finite Temperature Applications

Marcus Benghi Pinto*
Departamento de Física, Universidade Federal de Santa Catarina
88040-900 Florianópolis, SC, Brazil

ABSTRACT

We review the optimized perturbation theory (or linear δ-expansion) illustrating with an application to the anharmonic oscillator. We then apply the method to multi-field $O(N_1) \times O(N_2)$ scalar theories at high temperatures to investigate the possibility of inverse symmetry breaking (or symmetry non restoration). Our results support inverse symmetry breaking and reveal the possibility of other high temperature symmetry breaking patterns for which the last term in the breaking sequence is $O(N_1 - 1) \times O(N_2 - 1)$.

1 Introduction

The possibility that symmetries may be broken (or remain broken) at high temperatures is not new.[1] This phenomenon is usually called inverse symmetry breaking (ISB) (or symmetry nonrestoration (SNR)). The idea of ISB (or SNR) is *per se* a very interesting one due to its possible implementation in realistic particle physics models and its consequences in the context of high temperature phase transitions in the early Universe, with applications ranging from problems involving CP violation and baryogenesis, topological defect formation, inflation, etc. Bajc[2] points out three cases where this counter intuitive phenomenon can take place: i) a prototype case like the the two scalar model studied by Weinberg,[1] ii) flat directions in supersymmetric theories and iii) large charge density (or chemical potential). Here we shall concentrate on the first case. A recent investigation of the third case was carried out by Hong and Kogut[3] who considered the Gross-Neveu model.

The study of finite temperature related phenomena calls for the use of nonperturbative approximation since perturbation theory may break down at high temperatures. In this work, we use the linear δ expansion (or optimized perturbation theory)[4] to investigate ISB in the $O(N_1) \times O(N_2)$ model. This method, which is presented in the next section, combines the advantages of perturbation theory (as far as the evaluation and renormalization of Feynman diagrams is concerned) generating nonperturbative results thanks to a variational optimization procedure.

2 The linear δ expansion

The optimized linear δ expansion (LDE) is an alternative nonperturbative approximation which has been successfully used in a plethora of different problems in particle theory,[4–8] quantum mechanics[9,10] , nuclear matter[11]

*fsc1mep@fsc.ufsc.br

and condensed matter.[12] One advantage of this method is that the selection and evaluation (including renormalization) of Feynman diagrams are done exactly as in perturbation theory using a very simple modified propagator which depends on an arbitrary mass parameter. The results are optimized with respect to this parameter at the end of the calculation. The standard application of the LDE to a theory described by some Lagrangian density $\mathcal{L}$ starts with an interpolation defined by

$$\mathcal{L}_\delta = (1-\delta)\mathcal{L}_0(\eta) + \delta\mathcal{L} = \mathcal{L}_0(\eta) + \delta[\mathcal{L} - \mathcal{L}_0(\eta)], \tag{1}$$

where $\mathcal{L}_0(\eta)$ is the Lagrangian density of a solvable theory which can contain arbitrary mass parameters η. The Lagrangian density $\mathcal{L}_\delta$ interpolates between the solvable $\mathcal{L}_0(\eta)$ (when $\delta = 0$) and the original $\mathcal{L}$ (when $\delta = 1$). To illustrate how the method works let us consider the anharmonic oscillator described by

$$\mathcal{L} = \frac{1}{2}(\partial_0\phi)^2 - \frac{1}{2}m^2\phi^2 - \frac{\lambda}{4}\phi^4 \,. \tag{2}$$

Following the interpolation prescription given by Eq. (1) one may choose

$$\mathcal{L}_0(\eta) = \frac{1}{2}(\partial_0\phi)^2 - \frac{1}{2}m^2\phi^2 - \frac{1}{2}\eta^2\phi^2 \,, \tag{3}$$

obtaining

$$\mathcal{L}_\delta = \frac{1}{2}(\partial_0\phi)^2 - \frac{1}{2}\Omega^2\phi^2 - \delta\frac{\lambda}{4}\phi^4 + \frac{\delta}{2}\eta^2\phi^2 \,, \tag{4}$$

where $\Omega^2 = m^2 + \eta^2$. The general way the method works becomes clear by looking at the Feynman rules generated by $\mathcal{L}_\delta$. First, the original ϕ^4 vertex has its original Feynman rule $-i6\lambda$ modified to $-i6\delta\lambda$. This minor modification is just a reminder that one is really expanding in orders of the artificial parameter δ. Most importantly, let us look at the modifications implied by the addition of the arbitrary quadratic part. The original bare propagator,

$$S(k) = i(k^2 - m^2 + i\epsilon)^{-1} \,, \tag{5}$$

becomes

$$S(k) = i(k^2 - \Omega^2 + i\epsilon)^{-1} = \frac{i}{k^2 - m^2 + i\epsilon}\left[1 - \frac{i}{k^2 - m^2 + i\epsilon}(-i\eta^2)\right]^{-1} \,, \tag{6}$$

indicating that the term proportional to $\eta^2\phi^2$ contained in $\mathcal{L}_0$ is entering the theory in a nonperturbative way. On the other hand, the piece proportional to $\delta\eta^2\phi^2$ is only being treated perturbatively as a quadratic vertex (of weight $i\delta\eta^2$). Since only an infinite order calculation would be able to compensate for the infinite number of $(-i\eta^2)$ insertions contained in Eq. (6), one always ends up with a η dependence in any quantity calculated to finite order in δ. Then, at the end of the calculation one sets the dummy parameter δ to unity (the value at which the original theory is retrieved) and fixes η with the variational procedure known as the Principle of Minimal Sensitivity (PMS)[13] which requires that a physical quantity P calculated *perturbatively* in powers of δ be evaluated at the point where it is less sensitive to variations of the arbitrary η. That is, one optimizes the perturbative calculation by requiring

$$\frac{\partial P(\eta)}{\partial\eta}\Big|_{\bar{\eta}} = 0 \,. \tag{7}$$

This procedure gives $\bar{\eta}$ as a function of the original parameters, including the couplings, and generates nonperturbative results as shown in the inumerous applications cited above.

As a warm-up for our application we follow Bellet, Garcia and Neveu[9] evaluating the ground state energy density $\mathcal{E}$ and the vacuum expectation value $\langle\phi^2\rangle$ for the anharmonic oscillator. By taking $m = 0$ in Eq. (13) one

obtains the Lagrangian density for the pure anharmonic oscillator (PAO) which cannot be treated by ordinary perturbation theory. The exact result

$$\mathcal{E}^{\text{exact}} = \lambda^{1/3}\, 0.420804974478... \tag{8}$$

has been obtained by Bender, Olaussen and Wang,[14] while Banerjee et al.[15] have obtained the exact result for $\langle\phi^2\rangle$

$$\langle\phi^2\rangle^{\text{exact}} = \lambda^{-1/3}\, 0.456119955748... \tag{9}$$

In quantum field theory, the ground state energy density is represented by vacuum to vacuum diagrams. The relevant contributions to $\mathcal{O}(\delta^2)$ are[9]

$$\begin{aligned}
\mathcal{E}^{(2)}(\eta) &= -\frac{i}{2}\int_{-\infty}^{+\infty}\frac{dp}{2\pi}\ln\left[p^2-\Omega^2\right] - \delta\frac{i}{2}\int_{-\infty}^{+\infty}\frac{dp}{2\pi}\frac{\eta^2}{p^2-\Omega^2} \\
&- \delta\lambda\frac{3}{4}\left(\int_{-\infty}^{+\infty}\frac{dp}{2\pi}\frac{1}{p^2-\Omega^2}\right)^2 + \delta^2\frac{i}{4}\int_{-\infty}^{+\infty}\frac{dp}{2\pi}\left[\frac{\eta^2}{p^2-\Omega^2}\right]^2 \\
&+ \delta^2\lambda\frac{3}{2}\int_{-\infty}^{+\infty}\frac{dp}{2\pi}\frac{1}{p^2-\Omega^2}\int_{-\infty}^{+\infty}\frac{dp}{2\pi}\frac{\eta^2}{(p^2-\Omega^2)^2} \\
&- \delta^2\lambda^2\frac{9}{4}\left(\int_{-\infty}^{+\infty}\frac{dp}{2\pi}\frac{1}{p^2-\Omega^2}\right)^2\int_{-\infty}^{+\infty}\frac{dp}{2\pi}\frac{1}{(p^2-\Omega^2)^2} \\
&- \delta^2\lambda^2\frac{3}{4}\int_{-\infty}^{+\infty}\frac{dp}{2\pi}\int_{-\infty}^{+\infty}\frac{dq}{2\pi}\int_{-\infty}^{+\infty}\frac{dl}{2\pi}\left[\frac{1}{(p^2-\Omega^2)(q^2-\Omega^2)(l^2-\Omega^2)}\right. \\
&\times \left.\frac{1}{(p+q+l)^2-\Omega^2}\right] + O(\delta^3)\ .
\end{aligned} \tag{10}$$

Note that the second, fourth and fifth contributions are due to the extra quadratic vertex, while all the others would also appear in an ordinary perturbative expansion to $\mathcal{O}(\lambda^2)$. Setting $m = 0$ (PAO), evaluating the integrals and eliminating the divergent $\mathcal{O}(\delta^0)$ term one obtains

$$\mathcal{E}^{(2)}(\eta) = \mathcal{E}^{(1)}(\eta) + \delta^2\frac{3\lambda}{16\eta^2} - \delta^2\frac{21\lambda^2}{128\eta^5}\ , \tag{11}$$

where

$$\mathcal{E}^{(1)}(\eta) = \delta\frac{1}{4}\eta + \delta\frac{3\lambda}{16\eta^2}\ . \tag{12}$$

Good numerical results appear already at first order where the application of the PMS to $\mathcal{E}^{(1)}(\eta)$ yields $\mathcal{E}^{(1)}(\bar{\eta}) = \lambda^{1/3}\ 0.4290$ at $\bar{\eta} = (\lambda\ 1.5)^{1/3}$. To second order the authors in Ref.[9] obtain $\mathcal{E}^{(2)}(\bar{\eta}) = \lambda^{1/3}\ 0.4210$ and then carry on improving this result to show convergence. The interested reader is referred to Ref.[9] for details concerning the optimization procedure (selection of roots, etc).

3 The Linear δ-Expansion Applied to the $O(N_1) \times O(N_2)$ Model

3.1 The original model and one-loop results

In this work we consider the scalar $O(N_1) \times O(N_2)$ model described by

$$\mathcal{L} = \sum_{i=1}^{2}\left[\frac{1}{2}(\partial_\mu\phi_i)^2 - \frac{1}{2}m_i^2\phi_i^2 - \frac{\lambda_i}{4!}\phi_i^4\right] - \frac{\lambda}{4}\phi_1^2\phi_2^2 + \mathcal{L}_{\text{ct}}\ , \tag{13}$$

where

$$\mathcal{L}_{\rm ct} = \sum_{i=1}^{2} \left[A_i \frac{1}{2} (\partial_\mu \phi_i)^2 - \frac{1}{2} B_i \phi_i^2 - \frac{1}{4!} C_i \phi_i^4 \right] - \frac{1}{4} C \phi_1^2 \phi_2^2 \tag{14}$$

represents the counterterms needed to render the model finite. Note that $\mathcal{L}_{\rm ct}$ requires an extra piece if one attempts to evaluate the thermal effective potential,[8] which is not the case here. The boundness condition for the model described by (13) requires that the coupling constants satisfy the inequalities

$$\lambda_1 > 0, \quad \lambda_2 > 0 \quad \text{and} \quad \lambda_1 \lambda_2 > 9\lambda^2 \, . \tag{15}$$

As noticed by Weinberg[1] this boundness condition allows for negative values of the cross coupling λ which may lead to the nonrestoration of symmetries at high temperatures. Another possibility is that theories which are symmetric at $T = 0$ may be broken at large T due to this negative value of λ. The thermal masses for this model have been first calculated using the one-loop approximation which, at high T, gives

$$M_1^2 \simeq m_1^2 + \frac{T^2}{24} \left[\lambda_1 \left(\frac{N_1 + 2}{3} \right) + \lambda N_2 \right] \, , \tag{16}$$

and

$$M_2^2 \simeq m_2^2 + \frac{T^2}{24} \left[\lambda_2 \left(\frac{N_2 + 2}{3} \right) + \lambda N_1 \right] \, . \tag{17}$$

Let us consider the interesting case where $\lambda < 0$ and setting m_1^2 and m_2^2 positive to have a symmetric theory at $T = 0$. Inverse symmetry breaking takes place if one chooses, for example

$$\lambda > \frac{\lambda_1}{N_2} \left(\frac{N_1 + 2}{3} \right) \, , \tag{18}$$

which makes the T^2 coefficient of M_1^2 negative while the same coefficient for M_2^2 is kept positive, due to the boundness condition. In this case, high temperatures will induce the breaking $O(N_1) \times O(N_2) \rightarrow O(N_1 - 1) \times O(N_2)$ at the critical temperature

$$\frac{T_c^2}{m_1^2} = 24 \left[\lambda N_2 - \lambda_1 \left(\frac{N_1 + 2}{3} \right) \right]^{-1} \, . \tag{19}$$

At his point one be suspicious that this counter intituitive phenomenon is just an artifact of perturbation theory. To settle this point we will carry out our calculation to the tow loop level.

3.2 The interpolated model

For the present model one may choose

$$\mathcal{L}_0(\eta_i) = \sum_{i=1}^{2} \left[\frac{1}{2} (\partial_\mu \phi_i)^2 - \frac{1}{2} m_i^2 \phi_i^2 - \frac{1}{2} \eta_i^2 \phi_i^2 \right] \, , \tag{20}$$

and following the general prescription one can write

$$\mathcal{L}^{\delta} = \sum_{i=1}^{2}\left[\frac{1}{2}(\partial_{\mu}\phi_{i})^{2} - \frac{1}{2}\Omega_{i}^{2}\phi_{i}^{2} - \delta\frac{\lambda_{i}}{4!}\phi_{i}^{4} + \frac{\delta}{2}\eta_{i}^{2}\phi_{i}^{2}\right] - \delta\frac{\lambda}{4}\phi_{1}^{2}\phi_{2}^{2} + \mathcal{L}_{\rm ct}^{\delta}\ , \tag{21}$$

where $\Omega_i^2 = m_i^2 + \eta_i^2$. The term $\mathcal{L}_{\rm ct}^{\delta}$, which contains the counterterms needed to render the model finite, is given by

$$\mathcal{L}_{\rm ct}^{\delta} = \sum_{i=1}^{2}\left[A_{i}^{\delta}\frac{1}{2}(\partial_{\mu}\phi_{i})^{2} - \frac{1}{2}B_{i}^{\delta}(\Omega_{1},\Omega_{2})\phi_{i}^{2} - \frac{1}{4!}\delta C_{i}^{\delta}\phi_{i}^{4} + \frac{1}{2}\delta B_{i}^{\delta}(\eta_{1},\eta_{2})\phi_{i}^{2}\right] - \frac{1}{4}\delta C^{\delta}\phi_{1}^{2}\phi_{2}^{2}\ , \tag{22}$$

where A_i^{δ}, B_i^{δ}, C_i^{δ} and C^{δ} are the counterterms coefficients. One should note that the δ-expansion interpolation introduces only "new" quadratic terms not altering the renormalizability of the original theory. That is, the counterterms contained in $\mathcal{L}_{\rm ct}^{\delta}$, as well as in the original $\mathcal{L}_{\rm ct}$, have the same polynomial structure.

4 The Thermal Masses up to order-δ^2

We can now start our evaluation of the thermal masses, defined by

$$M_{i}^{2} = \Omega_{i}^{2} + \Sigma_{i}^{\delta}(p)\ , \tag{23}$$

where $\Sigma_i^{\delta}(p)$ is the thermal self-energy. Here, only the lowest order (first order in δ) contributions are presented in detail. The order-δ^2 contributions which invlove one and two loop diagrams are discussed in Ref..[6] To order-δ, the relevant contributions, which are momentum independent, are given by ($i,j = 1,2$ and $i \neq j$)

$$\Sigma_{i,1}^{\delta^1}(p) = -\delta\eta_{i}^{2} + \delta\frac{\lambda_{i}}{2}\left(\frac{N_{i}+2}{3}\right)\int_{T}\frac{d^{d}k}{(2\pi)^{d}}\frac{i}{k^{2}-\Omega_{i}^{2}+i\epsilon} + \delta\frac{\lambda}{2}N_{j}\int_{T}\frac{d^{d}k}{(2\pi)^{d}}\frac{i}{k^{2}-\Omega_{j}^{2}+i\epsilon}\ . \tag{24}$$

The temperature dependence can be readily obtained by using the standard imaginary time formalism prescription

$$p_{0} \to i\omega_{n}\ , \qquad \int_{T}\frac{d^{d}k}{(2\pi)^{d}} \to iT\sum_{n}\int\frac{d^{d-1}\mathbf{k}}{(2\pi)^{d-1}}\ . \tag{25}$$

Then, the self-energy becomes

$$\Sigma_{i}^{\delta^1}(p) = -\delta\eta_{i}^{2} + \delta T\frac{\lambda_{i}}{2}\left(\frac{N_{i}+2}{3}\right)\sum_{n}\int\frac{d^{d-1}\mathbf{k}}{(2\pi)^{d-1}}\frac{1}{\omega_{n}^{2}+E_{i}^{2}} + \delta T\frac{\lambda}{2}N_{j}\sum_{n}\int\frac{d^{d-1}\mathbf{k}}{(2\pi)^{d-1}}\frac{1}{\omega_{n}^{2}+E_{j}^{2}}\ , \tag{26}$$

where $E^2 = \mathbf{k}^2 + \Omega^2$. Summing over Matsubara's frequencies one gets

$$\begin{aligned}\Sigma_{i}^{\delta^1}(p) &= -\delta\eta_{i}^{2} + \delta\frac{\lambda_{i}}{2}\left(\frac{N_{i}+2}{3}\right)\int\frac{d^{d-1}\mathbf{k}}{(2\pi)^{d-1}}\left\{\frac{1}{2E_{i}} - \frac{1}{E_{i}[1-\exp(E_{i}/T)]}\right\} \\ &+ \delta\frac{\lambda}{2}N_{j}\int\frac{d^{d-1}\mathbf{k}}{(2\pi)^{d-1}}\left\{\frac{1}{2E_{j}} - \frac{1}{E_{j}[1-\exp(E_{j}/T)]}\right\}\ .\end{aligned} \tag{27}$$

Then, using dimensional regularization ($d = 4 - 2\epsilon$) one obtains the thermal mass

$$\begin{aligned} M_i^2 &= \Omega_i^2 - \delta\eta_i^2 + \delta\frac{\lambda_i}{32\pi^2}\left(\frac{N_i+2}{3}\right)\left\{\Omega_i^2\left[-\frac{1}{\epsilon} + \ln\left(\frac{\Omega_i^2}{4\pi\mu^2}\right) + \gamma_E - 1\right]\right] + 32\pi^2T^2h\left(\frac{\Omega_i}{T}\right)\Big\} \\ &+ \delta\frac{\lambda}{32\pi^2}N_j\left\{\Omega_j^2\left[-\frac{1}{\epsilon} + \ln\left(\frac{\Omega_j^2}{4\pi\mu^2}\right) + \gamma_E - 1\right]\right] + 32\pi^2T^2h\left(\frac{\Omega_j}{T}\right)\Big\} , \end{aligned} \tag{28}$$

where μ is a mass scale introduced by dimensional regularization and

$$h(y_i) = \frac{1}{4\pi^2}\int_0^\infty dx \frac{x^2}{[x^2+y_i^2]^{\frac{1}{2}}[\exp(x^2+y_i^2)^{\frac{1}{2}} - 1]} . \tag{29}$$

Note that the temperature independent term diverges and must be renormalized. In this paper we chose the Minimal Subtraction (MS) scheme where the counterterms eliminate the poles only. At this order the only divergence in (28) is

$$\Sigma^{\delta^1}_{\mathrm{div},i} = -\frac{\delta}{32\pi^2\epsilon}\left(\lambda_i\frac{N_i+2}{3}\Omega_i^2 + \lambda N_j\Omega_j^2\right) , \tag{30}$$

which is easily eliminated by the $O(\delta)$ mass counterterm

$$\Sigma^{\delta^1}_{\mathrm{ct},i} = B_i^{\delta^1}(\Omega_1,\Omega_2) = \frac{\delta}{32\pi^2\epsilon}\left(\lambda_i\frac{N_i+2}{3}\Omega_i^2 + \lambda N_j\Omega_j^2\right) . \tag{31}$$

By looking at Eq. (28) one can see that the terms proportional to δ represent exactly those that appear at first order in the coupling constants in ordinary perturbation theory excepted that we now have Ω_i^2 instead of m_i^2, $\delta\lambda_i$ instead of λ_i and $\delta\lambda$ instead of λ. Therefore, it is not surprising that to this order the renormalization procedure implied by the interpolated theory is identical to the procedure implied by the original theory at first order in the coupling constants.

Let us now analyze the temperature dependent integral which is expressed, in the high temperature limit ($y_i = \Omega_i/T \ll 1$), as[16]

$$h(y_i) = \frac{1}{24} - \frac{1}{8\pi}y_i - \frac{1}{16\pi^2}y_i^2\left[\ln\left(\frac{y_i}{4\pi}\right) + \gamma_E - \frac{1}{2}\right] + \mathcal{O}(y_i^3) . \tag{32}$$

In principle, since η_i is arbitrary, one could be reluctant in taking the limit $\Omega_i/T \ll 1$. However, as discussed in our previous work,[5] the use of both forms for the integral $h(y_i)$ does not lead to any significant numerical changes in the optimization procedure. This is also true in the present work. Then, by taking $h(y_i)$ in the high temperature limit, one obtains the $\mathcal{O}(\delta)$ thermal mass:

$$M_i^2 = \Omega_i^2 - \delta\eta_i^2 + \delta\lambda_i\left(\frac{N_i+2}{3}\right)X_i(T) + \delta\lambda N_jX_j(T) + \mathcal{O}(\delta^2) , \tag{33}$$

where we have defined the quantity $X_i(T)$

$$X_i(T) = \frac{T^2}{24} - \frac{T\Omega_i}{8\pi} + \frac{\Omega_i^2}{32\pi^2}L(T) , \tag{34}$$

with $L(T)$ given by

$$L(T) = \ln\left(\frac{4\pi T^2}{\mu^2}\right) - \gamma_E . \tag{35}$$

For notational convenience when expressing the remaining contributions to the self-energies, we also define the additional quantities $Y_i(T)$, $Z_i(0)$, $W_i(0)$ and $R_i(T)$ given by

$$Y_i(T) = -\frac{T\Omega_i}{16\pi} + \frac{\Omega_i^2}{32\pi^2} L(T) \,, \tag{36}$$

$$Z_i(0) = \frac{1}{2}\left[\ln\left(\frac{\Omega_i^2}{4\pi\mu^2}\right) + \gamma_E\right]^2 + \frac{\pi^2}{12} \,, \tag{37}$$

$$W_i(0) = \frac{1}{2}\left[\ln\left(\frac{\Omega_i^2}{4\pi\mu^2}\right) + \gamma_E - 1\right]^2 + \frac{1}{2} + \frac{\pi^2}{12} \,, \tag{38}$$

and

$$R_i(T) = -\frac{T\Omega_i^2}{16\pi\Omega_j} + \frac{\Omega_i^2}{32\pi^2} L(T) \,. \tag{39}$$

At $O(\delta^2)$ the self-energy receives contributions from momentum independent as well as momentum dependent diagrams whose evaluation, although more cumbersome, follow the pattern discussed for the order-δ case. We do not present this calculation here and the interested reader is referred to Ref.[6] for details. The sum of the remaining finite terms of each contribution to the self-energy makes the total contribution to the thermal mass up to order δ^2, $M_i^2 = \Omega_i^2 - \delta\eta_i^2 + \Sigma_{i,1} + \ldots + \Sigma_{i,13}$.

5 Numerical Results

We are now in position to set $\delta = 1$ and apply the PMS to the thermal masses. We work in units of the arbitrary scale μ introduced by dimensional regularization, by extremizing the dimensionless quantity M_i^2/μ^2. To search for inverse symmetry breaking at high temperatures one must ensure that the symmetries are restored at $T = 0$. This is achieved by setting $m_i^2 > 0$ and by observing the boundness condition while setting $\lambda \to -\lambda$ in all our equations. In order to access the reliability of the method, he limiting $N_1 = N_2 = 1$ case (which is equivalent to $Z_2 \times Z_2$) is also discussed in Ref..[6] Here, we only present the the more realistic $O(N_1) \times O(N_2)$ case. We follow Bimonte and Lozano, in the first reference in,[17] by choosing $N_1 = 90$ and $N_2 = 24$ so that the model can be thought of as representing the Kibble-Higgs sector of a $SU(5)$ grand unified model. Let us start by estimating some critical temperatures and comparing our results with the lowest order one-loop results given by Eqs. (16) and (17). Our results, shown in table I, suggest that the parameter region for ISB predicted by the δ-expansion is smaller than the one predicted by the lowest order 1LA prediction.

TABLE I : Results for the criticaltemperature in the $O(90) \times O(24)$ scalar model.

λ_1	λ_2	λ	T_c^{1-loop}/m_1	$T_c^{\delta^2}/m_1$
0.06	1.8	−0.1	6.5	15.3
0.0167	0.6	−0.025	16.5	65.4
0.9	1.0	−0.141	2.2	5.0
0.8	0.7	−0.091	3.4	10.0

Figure 1 shows our $\mathcal{O}(\delta^2)$ result (dot-dashed line) compared with the results produced by the 1LA at lowest order (thin continuous line) for fixed $\lambda_1 = 0.8$ and $T = 5.0\ \mu$. The upper parabola represents the limiting region for boundness. The dashed line is the Bimonte and Lozano's next to leading order one-loop (BLA) result for an arbitrarily large T.

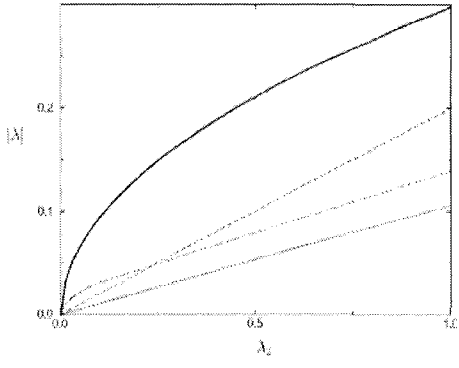

Figure.1: Region of ISB at fixed $\lambda_1 = 0.8$ for $N_1 = 90$ and $N_2 = 24$.

Note that the next to leading order correction considered in[17] for the one-loop approximation reduces significantly the region of ISB given at lowest order. However, the next to leading order calculation of the BLA approach considers up to the second term, which is mass dependent, in the expansion of the temperature dependent integral given by Eq. (29). This means that their procedure does not take into account logarithmic terms in the expansion of $h(y_i)$ since they would give corrections of order $\lambda_i^2 \ln \lambda_i$ which also arise from two-loop diagrams. Our calculations, on the other hand, avoid these bookkeeping problems and all contributions are consistently and explicitly considered in a given order.

Finally, let us investigate the possible patterns for ISB. According to the one-loop approach (to lowest and next to leading order) as well as to the RGA, there are only two possible phases at high T: either the theory is completely symmetric or one of the two symmetries is broken. However, including two-loop contributions and going beyond the simple perturbative expansion could alter this picture introducing a third possibility where the two symmetries are broken at high T. To analyze this possibility one must increase the temperature beyond the critical values shown in Tables I which display only the T_c connected with the phase transition from the symmetric phase to one of the nonsymmetric phases. Surprisingly we find, that for some parameter values, the mass associated with the symmetry which survives the first transition has a tendency to decrease as the temperature increases beyond the first critical value. As an example of this, we show in Fig. 2 the results for the case analyzed in the first row of Table I for both M_1^2 and M_2^2. M_2^2 is positive right above the critical temperature shown (now labeled T_{c1}) which is associated with the breaking in the ϕ_1 direction. We see that, very quickly, M_2^2 becomes monotonically decreasing with the temperature and becomes negative, through a second order phase transition, at $T_{c2}/m_2 \simeq 18.9$. The same behavior is observed for the parameters shown in the second row of Table I, where we observe symmetry breaking in ϕ_2 direction at $T_{c2}/m_2 \simeq 139$. However, analyzing the other two cases shown in the third and fourth rows of Table I, we find that the would be mass associated with the second symmetry breaking increases monotonically with the temperature, signalling that this symmetry possibly remains unbroken at high temperatures. Note that just by interchanging the values of λ_1 and λ_2 one trivially

observes yet another pattern this time with $T_{c2} < T_{c1}$. Which pattern will be actually followed depends on our initial choice for the values of the couplings.

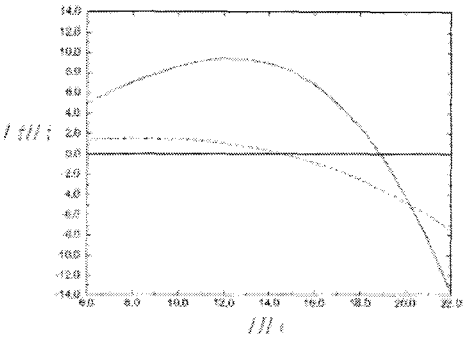

Figure 2: The behavior of M_1^2 (dashed line) and M_2^2 (upper full line) as a function of the temperature for $\lambda_1 = 0.06$ $\lambda_2 = 1.8$ and $\lambda = -0.1$ ($N_1 = 90$ and $N_2 = 24$).

Therefore, our results suggest that a possible symmetry breaking along the second field direction takes place, for large values of N, in a narrow region of parameters. It is possible that this alternative symmetry breaking pattern will show up only in nonperturbative calculations which consider up to two loop terms. It would be interesting to investigate this possibility using other nonperturbative approaches.

6 Conclusions

We have used the optimized linear δ expansion to investigate inverse symmetry breaking at high temperatures using multi-field theories. Our order-δ^2 calculations take full consideration of two-loop contributions, including the momentum dependent "setting sun" type of diagrams. To our knowledge, a complete calculation associated with the phenomenon of ISB/SNR which includes these contributions in the $O(N_1) \times O(N_2)$ model has not been fully considered before. In order to asure the reliability of the method we have started with the scalar $Z_2 \times Z_2$ model which has been extensively investigated in connection with inverse symmetry breaking problem. We have shown that our optimized results agree well with those obtained with the Renormalization Group approach, especially as far as the critical temperatures are concerned. This has allowed us to establish the δ-expansion as a reliable nonperturbative technique to investigate ISB. We have then investigated the more realistic scalar $O(N_1) \times O(N_2)$ model which may be related to the Kibble-Higgs sector of a $SU(5)$ grand unified model. All our results strongly support the possibility of inverse symmetry breaking (or symmetry nonrestoration) at high temperatures. Surprisingly, we have also found evidence for a second phase transition taking place for some values of the couplings and large values of N. According to our results two other possible high temperature inverse symmetry breaking patterns are

$$O(N_1) \times O(N_2) \xrightarrow{T_{c1}} O(N_1 - 1) \times O(N_2) \xrightarrow{T_{c2}} O(N_1 - 1) \times O(N_2 - 1) \, ,$$

where $T_{c1} < T_{c2}$, or

$$O(N_1) \times O(N_2) \xrightarrow{T_{c2}} O(N_1) \times O(N_2 - 1) \xrightarrow{T_{c1}} O(N_1 - 1) \times O(N_2 - 1) \, ,$$

where $T_{c1} > T_{c2}$.

I would like to thank the organizers, especially Takeshi Kodama and Yogiro Hama, for their invitation.

7 REFERENCES

[1] S. Weinberg, Phys. Rev. **D9**, 3357 (1974).

[2] B. Bajc, *COSMO 98*, ed. D. Caldwell (AIP, New York, 1999); hep-ph/0002187.

[3] S.I Hong and J.B. Kogut hep-th/0007216

[4] A. Okopińska, Phys. Rev. **D35** 1835 (1987); A. Duncan and M. Moshe, Phys. Lett. **B215** 352 (1988).

[5] M. B. Pinto and R. O. Ramos, Phys. Rev. **D60**, 105005 (1999).

[6] M. B. Pinto and R. O. Ramos, Phys. Rev. **D61**, 125016 (2000).

[7] M. B. Pinto, Phys. Rev **D50**, 7673 (1994).

[8] S. Chiku and T. Hatsuda, Phys. Rev. **D58**, 076001 (1998).

[9] B. Bellet, P. Garcia and A. Neveu, Int. J. of Mod. Phys **A11**, 5587 (1997); *ibid.* **A11**, 5607 (1997).

[10] I. R. C. Buckley, A. Duncan and H. F. Jones, Phys. Rev. **D47**, 2554 (1993); A. Duncan and H. F. Jones, *ibid.* **D47**, 2560 (1993); C. M. Bender, A. Duncan and H. F. Jones, *ibid.* **D49**, 4219 (1994); C. Arvanitis, H. F. Jones and C. S. Parker, Phys. Rev. **D52**, 3704 (1995).

[11] G. Krein, D. P. Menezes and M. B. Pinto, Phys. Lett. **B370**, 5 (1996); G. Krein, R. S. M. Carvalho, D. P. Menezes, M. Nielsen, M. B. Pinto, Eur. Phys. **J. A1**, 45 (1998).

[12] F.F. de Souza Cruz, M.B. Pinto and R.O. Ramos; "Transition temperature for weakly interacting homogeneous Bose gases", cond-matt/0007151 ; see also contribution to these proceedings.

[13] P. M. Stevenson, Phys. Rev. **D23** 2916 (1981).

[14] C.M. Bender, K. Olausen and P.S. Wang, Phys. Rev. **D16** 1780 (1977).

[15] K. Banerjee, S.P. Bhatnager, V. Choudry and S.S. Kanwal, Proc. R. Soc. London **A360** 575 (1978).

[16] J. Kapusta, *Finite Temperature Field Theory* (Cambridge University Press, Cambridge, England, 1985).

[17] G. Bimonte and G. Lozano, Phys. Lett. **B366**, 248 (1996); Nucl. Phys. **B460**, 155 (1996).

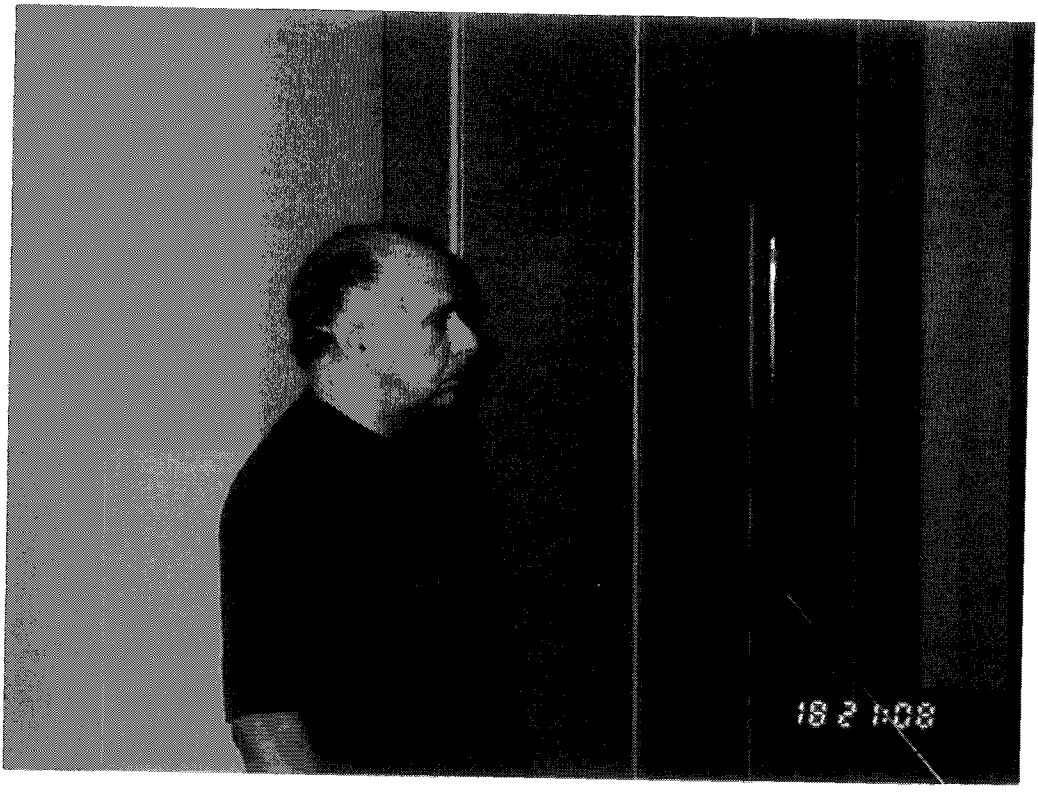

José A. F. Pacheco

Potential Gravitational Wave Sources and Laser Beam Interferometers

J.A.F. Pacheco
Observatoire de la Côte d'Azur,
B.P. 229, F-06304 Nice Cedex 4, France
e-mail: pacheco@obs-nice.fr

ABSTRACT

The properties of potential gravitational wave sources like neutron stars, black holes and binary systems are reviewed, as well as the different contributions (stochastic and continuous) to the gravitational wave background. The detectability of these sources by the present generation of laser beam interferometers, which will be fully operational around 2002, is also considered.

1 Introduction

Gravitational waves (GW) are predicted by the General Relativity Theory (GRT) and the slow inspiral observed in the binary pulsar PSR 1913+16 (Hulse & Taylor 1975) is an indirect proof of their existence. GW are fundamentally different from electromagnetic waves. While the latter propagate in the framework of space and time, the former are waves of the spacetime itself, created by asymmetric mass motions. A direct detection of GW has not been achieved up to date.

A resonant-mass antenna is, in principle, the simplest detector of GW (Weber 1960). A suspended cylindric detector, during the passage of a gravitational wave, has its normal modes excited and monitored by transducers. Present day resonant bars (or "spheres") are fairly narrowband detectors, with bandwidths of only a few Hz around frequencies in the kHz range and sensitivities around $\mathbf{h} \approx 10^{-19}$. Future detectors should have bandwidths of the order of 100 Hz or better and sensitivities of about 10^{-21}.

In the early seventies emerged the idea that laser interferometers might have a better chance of detecting GW (Weiss 1971; Moss, Miller & Forward 1971). These detectors are essentially constituted by a two-arm Michelson interferometer, which measures the phase difference between a splitted laser beam having propagated along two perpendicular directions. This is the quantity that would be changed by a passing and properly oriented gravitational wave. Laser beam interferometers are wideband detectors, being sensitive to GW in the frequency range 10-10^4 Hz. Plans for kilometer-size interferometers have been developed in the past decades. The US project **LIGO** is under development at two widely separated sites (Hanford and Livingston), both localities hosting a 4 km interferometer. The 3 km French-Italian antenna **VIRGO** is being built in Cascina, near Pisa, and a sophisticated seismic isolation system will allow this detector to measure frequencies down to 5 Hz. **GEO 600** is a 0.6 km arm interferometer in construction by a British-German collaboration, in a site near Hannover. Presently, the only operational laser interferometer is **TAMA** (0.3 km arms), located in Mitaka (Japan). Besides these ground based antennas, there is also a project supported by NASA and ESA to launch a large spatial interferometer (5

million km arms), constituted by three platforms. The **LISA** antenna will search for low-frequency (mHz) GW sources, which cannot be observed from the ground because of tectonic activity.

The best signal-to-noise (S/N) ratio that can be achieved from these detectors implies the use of "matched-filter" techniques, that require a priori knowledge of the waveform. Thus, in this context, the study of the most probable GW sources is of fundamental importance. In this work, the properties of some GW sources that have been discussed in the literature in the past years will be reviewed, as well as the expected detectability by the major interferometers under development in the world.

2 Neutron Stars

2.1 Rotating neutron stars - pulsars

Rotating neutron stars may have a time-varying quadrupole moment and hence radiate GW, by either having a triaxial shape or a misalignment between the symmetry and the spin axes, which produces a wobble in the stellar motion (Ferrari & Ruffini 1969; Zimmerman & Szednits 1979). In the former case the GW frequency is equal to twice the rotation frequency, whereas in the latter two modes are possible: one in which the GW have the same frequency as the rotation, and another in which the GW have twice the rotation frequency. The first mode dominates by far at small wobble angles while the importance of the second increases for large values of the misalignment.

In the case of a rotating triaxial neutron star, the gravitational strain amplitude of both polarization modes are:

$$h_+(t) = 2A(1+\cos^2 i)\cos(2\Omega t) \tag{1}$$

and

$$h_X(t) = 4A\cos i \sin(2\Omega t) \tag{2}$$

where i is the angle between the spin axis and the wave propagation vector, assumed to coincide with the line of sight, Ω is the angular rotation velocity of the neutron star,

$$A = \frac{G}{rc^4}\varepsilon I_{zz}\Omega^2 \tag{3}$$

G is the gravitation constant, c is the velocity of light, r is the distance to the source and the ellipticity ε is defined as

$$\varepsilon = \frac{I_{xx} - I_{yy}}{I_{zz}} \tag{4}$$

with I_{ij} being the principal inertia moments of the star.

The detected signal by an interferometric antenna is

$$h(t) = h_+(t)F_+(\theta,\phi,\psi) + h_X(t)F_X(\theta,\phi,\psi) \tag{5}$$

where F_+ and F_X are the beam factors of the interferometer, which are functions of the zenith distance θ, the azimuth ϕ as well as of the wave polarization plane orientation ψ (see, for instance, Jaranowski et al. 1998, for details).

Detection of both gravitational polarization modes of a radio pulsar leads immediately to the value of the spin projection angle i and to an estimate of the ellipticity, if the distance is known by measuring the dispersion of radio signals through the interstellar plasma. Upper limits of ε have been obtained by assuming that the observed spin-down of pulsars is essentially due to the emission of GW. In this case, for "normal" pulsars one

obtains $\varepsilon \leq 10^{-3}$ whereas "recycled" millisecond pulsars seem to have equatorial deformations less than 10^{-8}. Monte Carlo simulations of the galactic pulsar population by Regimbau & de Freitas Pacheco (2000a) indicate that with the planned VIRGO sensitivity (better than LIGO at lower frequencies) and integration times of the order of 10^7 s, a few detections should be possible if $\varepsilon = 10^{-6}$.

What are the physical mechanisms able to deform the star ? Different scenarios leading to a distorted star have been discussed in the literature, as anisotropic stresses from strong magnetic fields, and tilting of the symmetry axis during the initial cooling phase when the crust solidifies. Bildsten (1998) pointed out that a neutron star in a state of accretion may develop non-axisymmetric temperature variations in the surface, which produce horizontal density patterns able to create a mass quadrupole moment of the order of 10^{38} g.cm^{-2}, if the elastic response of the crust is neglected. More detailed calculations by Ushomirsky et al. (2000) indicate that the inclusion of the crustal elasticity decreases by a factor 20-50 the expected mass quadrupole moment. Nevertheless, the deformation induced by the accretion process is able to balance the angular momentum gained by mass transfer to that lost by GW emission, imposing limits to the maximum rotation frequency attained by the "recycled" neutron star. Strong magnetic fields are also able to distort the star (Gunn & Ostriker 1970; Bonazzola & Gourgoulhon 1996). Recent calculations by Konno et al. (2000) including general relativity corrections permit to estimate the ellipticity by the relation

$$\varepsilon_B \approx 4 \times 10^{-8} g B_{14}^2 \tag{6}$$

where g is a parameter depending on the structure of the neutron star, in particular on the adopted equation of state, and B_{14} is the magnetic field strength in units of 10^{14} Gauss. According to those authors, a typical value of the structure factor is g $\approx$ 14. In this case, if an ellipticity of 10^{-6} is required, then from the above equation a field of 1.3×10^{14} G is derived. The number of pulsars in the Galaxy with magnetic fields higher than 10^{14} may be considerable, about 23% of the total population, if the magnetic field decay timescale is much longer than the pulsar lifetime (Regimbau & de Freitas Pacheco 2000b). However these objects can be discarded as potential GW sources since they are rapidly decelerated by magnetic dipole emission and, consequently, most of them have presently periods higher than 20 s.

2.2 Bar-mode instabilities

Rotating and self-gravitating incompressible fluids are subjected to non-axisymmetric instabilities when the ratio $\beta = \mathrm{T}/|\,W\,|$ of the rotational energy T to the gravitational energy W is sufficiently large (Chandrasekhar 1969). These instabilities correspond to global nonradial toroidal modes with eigenfunctions $\propto e^{\pm im\phi}$, where m = 2 is the so-called "bar" mode, the fastest growing mode when rotation is very rapid. Incompressible Newtonian stars in the presence of some dissipative mechanism (viscosity or gravitational radiation reaction) become *secularly* unstable against bar formation when $\beta \geq 0.14$. In this case, the instability growth is essentially determined by the shortest dissipative timescale. On the other hand, when $\beta \geq 0.27$, the star becomes *dynamically* unstable to bar formation, and the growth of the instability is determined by the hydrodynamical timescale of the system. These instability limits have rigorously been derived for homogeneous and uniformly rotating Newtonian stars, but further relativistic numerical studies using polytropic equations of state and assuming ad-hoc rotation velocity profiles concluded that the onset of the instabilities occurs approximately at the same limits (see, for instance, Shibata et al. 2000).

Numerical simulations indicate that bar formation in dynamically unstable stars is accompanied by mass and angular momentum losses (Houser et al. 1994; Lai & Shapiro 1995), with the ejected matter forming spiral arms in the equatorial plane. The subsequent evolution is rather uncertain. Some simulations suggest that the bar shape is short lived, while other simulations predict a lifetime of many bar-rotation periods (see, for instance, New et al. 1999). The angular momentum carried out by the ejected mass and by gravitational waves reduces β to values below the dynamical instability limit, but still above the secular stability limit. The resulting axisymmetric system may evolve into a nonaxisymmetric configuration on a secular dissipation timescale (Lai & Shapiro 1995), as we shall see later.

Estimates of the characteristic gravitational strain amplitude for the dynamical instability phase ($\beta \geq 0.27$) performed by different authors (Houser et al. 1994; Houser & Centrela 1996; Brown 2000; Shibata et al. 2000) seem to be in rough agreement, namely, they predict a characteristic strain amplitude $h_c \approx 3{\times}10^{-22}$ at a distance of 20 Mpc. However the characteristic frequency of the waves differs considerably from author to author, ranging from 0.49 kHz (Brown 2000) up to 4.0 kHz (Houser et al. 1994). Adopting the low frequency estimate a signal-to-noise ratio S/N $\approx$ 2.0 is obtained if the planned VIRGO sensitivity curve is used (a similar result is obtained for LIGO), whereas a S/N ratio one order of magnitude smaller is expected if the characteristic frequency is higher than 2-3 kHz.

Most of the numerical studies suggest that after the dynamical instability phase (if the system was initially set beyond the limit $\beta_{crit} \approx 0.27$), it recovers almost an axisymmetric shape, but with β still above the secular instability threshold. In this case, the system may evolve away from the axisymmetric configuration, in a timescale determined by the gravitational radiation reaction, which is of the order of few seconds for β in the range 0.20-0.25, as simulations suggest. This evolutionary path is possible if gravitation radiation reaction overcomes viscosity. Then during the evolution the fluid circulation is conserved (but not angular momentum) and the system evolves toward a Dedekind ellipsoid, whose configuration is a fixed triaxial figure with an internal fluid circulation of constant vorticity. In the opposite situation, when viscosity drives the instability, angular momentum is conserved (but not the fluid circulation) and the system evolves toward a Jacobi ellipsoid.

The transition to a Dedekind configuration manifests in the form of strong hydrodynamic waves in the outer layers and mantle, propagating in the opposite direction of the star's rotation. According to Lai & Shapiro (1995), the frequency of the GW is an increasing function of the angular velocity of the star. The frequency of the waves is maximum at the beginning of the transition ($\nu_{max} \sim$ 800 Hz) and then it decreases monotonically. Since GW carry away the star angular momentum, the final configuration is a nonrotating triaxial ellipsoid, which no more emits GW. Thus, the wave amplitude first increases, reaches a maximum (when $\nu \sim$ 500 Hz) and then decreases to zero again. Lai & Shapiro (1995) estimated that the total gravitational wave energy radiated during the transition could be as large as $4 \times 10^{-3}\mathrm{Mc}^2$. This is much larger than the expected energy ($\sim 10^{-8}Mc^2$) radiated in the axisymmetric collapse and bounce preceding the neutron star formation (Zwerger & Muller 1997). Using the wave amplitude estimated by Lai & Shapiro (1995), the expected S/N ratios for sources at a distance of 20 Mpc are 4.0 and 3.0 for VIRGO and LIGO respectively.

2.3 R-modes in rotating neutron stars

The r-mode (r for rotation) is a member of the class of gravitational radiation driven instabilities (including the secular bar-mode instability) excited by the so-called CFS (Chandrasekhar-Friedman-Schutz) mechanism (see a recent review by Andersson & Kokkotas 2000). The criterion for triggering the instability is quite simple: if the pattern speed of the mode is forward-going as seen from a distant observer, but backward-going with respect to the rotation of the star, then when the disturbance radiates away the star angular momentum, the system can find a state of lower energy and angular momentum. These large scale toroidal fluid oscillations are similar to the well known geophysical Rossby waves and, in both cases, the restoring force is the Coriolis force.

In the first tens of seconds after the formation of the neutron star, the temperature is very high (T$\approx 10^{10}$ K) and the instabilities discussed in the preceding section (bar-modes) are thought to be at work. If the temperature is still higher, the bulk viscosity is expected to suppress the CFS instability, whereas the shear viscosity plays a stabilizing role for temperatures T$\leq 10^7$ K. Thus, there is a well defined window in which the "newly-born" neutron star is unstable. In the plane $\Omega{\times}$T, the instability limit region can roughly be estimated by imposing that the total energy rate of the mode is zero, or equivalently

$$\frac{1}{\tau_{gr}} + \frac{1}{\tau_b} + \frac{1}{\tau_s} = 0 \tag{7}$$

where τ_{gr}, τ_b and τ_s are respectively the gravitation radiation, bulk and shear viscosity damping timescales. For

the m=2 mode, these timescales are approximately given by

$$\frac{1}{\tau_{gr}} = -0.303(\frac{\Omega^2}{\pi G\rho})^3 \ s^{-1} \tag{8}$$

$$\frac{1}{\tau_b} = 5 \times 10^{-12} T_9^6 (\frac{\Omega^2}{\pi G\rho}) \ s^{-1} \tag{9}$$

and

$$\frac{1}{\tau_s} = 3.3 \times 10^{-9} T_9^{-2} \ s^{-1} \tag{10}$$

where T_9 is the temperature in units of 10^9 K, Ω is the angular velocity of the star and ρ its mean density. As the star cools by neutrino emission and decelerates by GW emission, it stabilizes around periods of 15-25 ms. According to this scenario, no "newly-born" pulsar faster than this limit should be observed. However, these estimates depend not only on damping effects due to different physical mechanisms, most of which are still badly understood, but also on the role played by the crust and magnetic field.

For purposes of detection, the most important properties of the GW signal from r-modes are: a) the frequencies, which at the lowest order in the angular velocity of the star are given by

$$\omega_r = \frac{(m-1)(m+2)}{(m+1)}\Omega \tag{11}$$

Thus, when m = 2, the GW frequency is $\nu_{gr} = \frac{4}{3}\nu_{rot}$; b) the emission is connected with current multipoles instead of mass multipoles.

The amplitude of the mode is small at the beginning, but it increases in a timescale of about 100 s, until a non-linear regime is reached and when saturation effects occur. This saturation phase is the most likely to be detected and lasts about 10^4-10^5 s for a crusted star and about 10^6-10^7 s for a fluid star. The expected strain amplitude in the saturation phase, calculated for a polytropic equation of state with n=1 and for a canonical neutron star of 1.4 $M_\odot$ is (Andersson & Kokkotas 2000)

$$h(t) \approx 9.25 \times 10^{-25} \alpha (\frac{20Mpc}{r}) \tag{12}$$

where α is the dimensionless radial amplitude of the mode and r is the distance to the source. In order to estimate the expected S/N ratio the usual matched-filtering approach is adopted, although it must be recognized that such a tecnique is unlikely to be possible for this kind of signal. In this case, the S/N ratio is given by

$$(\frac{S}{N})^2 = 4 \int_0^\infty (\frac{h_c}{h_n})^2 dln\nu \tag{13}$$

where $h_n = [\nu S_n(\nu)]^{1/2}$, $S_n(\nu)$ is the noise spectral density and h_c is the characteristic amplitude defined by

$$h_c = h(t)[\nu^2 \mid \frac{dt}{d\nu} \mid]^{1/2} \tag{14}$$

This last relation is a consequence of the stationary phase approximation, meaning that the detectability of a quasi-periodic signal is improved as the square root of the number of cycles at a given frequency ν. Using the planned VIRGO sensitivity curve one obtains for a source at a distance of 20 Mpc, S/N $\approx 2.2\alpha$ if no crust is present and S/N $\approx 1.5\alpha$ if a crust is already present in the star. These S/N ratios are smaller by a factor 2-3 for LIGO and almost one order of magnitude higher for the planned advanced LIGO. These estimates indicate that if the mode amplitude at saturation is nearly unity, then fast rotating newly born neutron stars could be good source candidates for the present generation of laser beam interferometers.

2.4 Oscillating neutron stars

Neutron stars have a large number of families of distinct pulsating modes (see Kokkotas 1997 for a review). Nonradial oscillating modes as an emission mechanism of GW were already discussed in the late sixties (Thorne & Campolattaro 1967; Thorne 1969). These early calculations were concentrated mainly in the so-called f (fundamental) mode, since this is the mode through which most of the mechanical energy of the star is radiated away. All the other possible fluid modes as g (gravity), p (pressure), s (shear), t (toroidal) and i (interface) can be calculated with sufficient accuracy using Newtonian dynamics, since they don't emit significant amounts of gravitational radiation.

The eigenfunctions of the f-modes have no nodes inside the star, reaching a maximum at the surface of the star. Lindblom & Detweiler (1983) calculated quadrupole f-modes for a series of neutron stars characterized by different equations of state (see also Kokkotas & Schutz 1992). Frequencies are in the range 1.5-4.0 kHz and the damping timescales are of the order of few tenths of second. In a first approximation, f-mode frequencies and damping timescales can be estimated from the formulae

$$\nu_{kHz} = 46.13 M^{0.255} R^{-1.32} \tag{15}$$

and

$$\tau_{sec} = 5.164 \times 10^{-3} R^{1.60} M^{-0.813} \tag{16}$$

where M and R are in solar units and km respectively.

As mentioned above, other oscillation modes are present in a real star. Pressure is the restoring force for p-modes and frequencies associated to these modes depend on the travel time for acoustic waves to cross the star. These frequencies are higher than 5 kHz and the oscillations are damped in timescales longer than those of f-modes. The g-modes, restored by gravity, depend critically on the internal composition and temperature profile, having frequencies tipically of the order of few hundred Hz. The interplay of all these modes in a neutron star is quite complex, since these objects have a solid crust and a central fluid interior. The modes f, p and g belong to the class of polar modes, but if the shear modulus in the crust is non-zero, axial modes should exist as well as families (i-modes) associated with the interface between distinct phases of the matter inside neutron stars (McDermott et al. 1988). Besides these "Newtonian-modes", there is a class of modes uniquely associated with perturbations of the spacetime itself, the so-called w-mode (Kojima 1988; Kokkotas & Schultz 1992). These gravitational wave modes arise because of the trapping of GW by the spacetime curvature generated by the background density. The w-modes exist for both polar and axial perturbations since they do not depend on perturbations of a fluid. These modes have high frequencies (above 7 kHz) and are damped in timescales shorter than one millisecond. They are probably the natural way to recover any initial deformation of the spacetime, as those expected to occur during the gravitational collapse, leading to black hole formation.

One of the problems concerning the gravitational wave emission from oscillating neutron stars is the absence of a convincing mechanism able to excite those modes. Once the solid crust is formed, stresses will exist by the presence of a strong magnetic field or/and rotation. These stresses induce tectonic activity and the stored elastic energy may be released as a consequence of quakes. The elastic energy is converted into shear waves that excite nonradial oscillation modes damped by GW. However, the maximum elastic energy that can be channeled into oscillating modes is likely to be about 10^{45} erg, restricting considerably the detection of gravitational wave sources excited by tectonic activity.

The maximum distance that a given source can be detected by a gravitational wave antenna can be estimated by the following considerations. After filtering the signal, the expected S/N ratio is given by the equation

$$(S/N)^2 = 4 \int_0^\infty \frac{\mid \bar{h}(\nu) \mid^2}{S_n(v)} d\nu \tag{17}$$

where $\bar{h}(\nu)$ is the Fourier transform of the signal, here a sinusoidal damped oscillation of amplitude h_0, and $S_n(\nu)$ is the noise power spectrum of the detector. Performing the required calculations, the S/N ratio can be written

as

$$(S/N)^2 = \frac{4}{5} h_0^2 (\frac{\tau_f}{S_n(\nu_0)}) \frac{Q^2}{1+4Q^2} \tag{18}$$

where τ_f is the damping time, $Q = \pi\nu_0\tau_f$ is the quality factor of the oscillation and ν_0 is the frequency of the considered mode. In the above equation, the angle averaged beam factors of the detector were already included. The amplitude of the signal is related with the total released energy E by the equation

$$h_0 = \frac{2}{\pi\nu_0 r} [\frac{GE}{\tau_f c^3}]^{1/2} \tag{19}$$

where r is again the distance to the source. From these equations, once the energy and the S/N ratio are fixed, the maximum distance to a given source that a gravitational antenna can probe can be estimated. Using the planned sensitivities of VIRGO and LIGO as well as the oscillation properties of neutron star models calculated by Lindblom & Detweiler (1983), it is clear that sources excited by starquakes cannot be detected beyond distances of about 2.5 kpc (de Freitas Pacheco 1998).

Another possible excitation mechanism of nonradial oscillations is the micro-collapse suffered by a neutron star when a phase transition occurs in the core, caused by a softening of the equation of state. There are presently several arguments in favor of a stiff equation of state for the nuclear matter:

Firstly, high frequency quasi-periodic oscillations (QPOs) have been found in the X-ray emission originated from the accretion disk around neutron stars associated to low-mass binaries (see van der Klis 2000, for a review). These oscillations are observed in the range 300-1300 Hz, and are often splitted into pairs with a nearly constant separation of 250-350 Hz. A possible interpretation of such a modulation in the X-ray emission is the presence of instabilities ("hot spots") near the "last stable" orbit ($r = \frac{6GM}{c^2}$) and modulated by the local orbital frequency. In this case, the mass of the neutron star is directly related with the orbital frequency by

$$M = \frac{1}{(216)^{1/2}} \frac{c^3}{G\Omega_{orb}} \approx 2.2\nu_{kHz}^{-1} \; M_\odot \tag{20}$$

If this interpretation is correct, neutron stars with masses up to 2.0 $M_\odot$ are present in those low-mass X-ray binaries as a consequence of the accretion process. Moreover, the analysis of the orbital motion of some massive X-ray binaries seems also to suggest the presence of massive neutron stars (for instance, 1.8 $M_\odot$ for 4U1700-37 and 1.75 $M_\odot$ for Vela X-1). These high mass values favor stiff equations of state (Akmal et al. 1998). Secondly, post-glitch recovery analyzes of isolated pulsars are not consistent with soft equations of state (Link et al. 1992; Alpar et al. 1993)

Masses of neutron stars derived from NS-NS binaries cluster around 1.4 $M_\odot$. Neutron star models of 1.4 $M_\odot$ built with stiff and moderately stiff equations of state suggest central densities of about (4-5)n_0 (de Freitas Pacheco et al. 1993; Akmal et al. 1998), where $n_0 = 0.16$ fm^{-3} is the nuclear saturation density. These densities are lower than the critical density for kaon condensation, if kaon-nucleon and nucleon-nucleon correlations are taken into account (Pandharipande et al. 1995). In this case, according to those calculations, the kaon condensation should only occur for densities around (6-7)n_0. The appearance of a kaon condensate will soften the equation of state reducing the maximum stable mass, yielding the star unstable (however, there are no evidences in favor of the presence of black holes in those low-mass X-ray binary systems!). It is worth mentioning that the deconfinement of cold matter is expected to occur around (7-9)n_0 (de Freitas Pacheco et al. 1993). If the neutron star accretes mass, the central density increases and may eventually to overcome the critical density necessary to occur a phase transition. Further increase of the neutron star mass leads the star into a metastable situation, until the occurrence of a structural transition of the whole star into a new configuration of minimum energy. Consider, for instance, the appearance of quark matter in the core. Since the energy density of the quark matter is higher than that of the hadron matter, the star must to contract (in a dynamical timescale) in order to extract gravitational energy, which will provide the "latent" heat of the phase transition. In the "metastable" hadron state, a 1.81 $M_\odot$ neutron star has a central density $n_c = 7.6n_0$ and a radius R = 9.9127 km, while after the micro-collapse the radius is reduced by **5.2 m** and a quark core matter of 0.44 km radius is formed. The event releases a total

gravitational energy of about 4.7× 10^{50} erg, from which 85% go to the phase transition and, about 7× 10^{49} erg are converted into heat and/or into mechanical energy (de Freitas Pacheco 1999). In the ideal case, if the latter amount of energy is channeled into the quadrupole f-mode (the coupling with rotation favors the excitation of nonradial modes) , the emitted GW from the considered neutron star model will have a frequency of 2.6 kHz and the corresponding damping timescale will be $\tau_f = 0.124$ s. Using equations (18) and (19), the maximum distance that these signals can be detected by the present generation of interferometers is about 85 kpc, which includes all sources in the Milky Way and in the Magellanic Clouds.

3 Gravitational Waves from Black Holes

Black holes are expected to exist in our universe with masses ranging from a few solar masses up to 10^{10} $M_\odot$. Stellar mass black holes may be formed in the core collapse of massive stars, by accretion either of a massive neutron star or a small hole, by merging of two neutron stars at the end-point of their inspiral in a binary system, whereas very massive holes, probably present in a considerable number of galactic nuclei, can be formed by different routes.

Recent 2D-hydrodynamic simulations of core collapse (Fryer 1999) for a large range of progenitor masses, indicate that partial fallback of the envelope drives the compact core to collapse into a black hole. This occurs for progenitors with masses M> 20 $M_\odot$ while progenitors more massive than 40 $M_\odot$ form black holes directly. In spite all the uncertainties present in those simulations, they permit nevertheless an estimate of the mass distribution and of the formation rate of these objects.

Newly formed black holes are likely to be quite "deformed". They need to radiate away energy in order to settle down into a quiescent and axisymmetric state characterized only by their mass M and angular momentum J (a Kerr black hole). Detailed calculations suggest that black hole oscillations are easy to trigger and that quadrupole modes dominate the emission (Stark & Piran 1985a, 1985b). The waveform of the initial burst depends on the details of the collapse, but the late-time behavior (the "ring-down" phase) has a well established damped oscillatory form, which is essentially a function of M and J (see, for instance, Echeverria 1989; Finn 1992). For the mode l = m = 2, using the results of Echeverria (1989), the frequency and the damping timescale are respectively estimated from

$$\nu_{gw} \approx 12(\frac{M_\odot}{M_{bh}})F(a)\ \ kHz \tag{21}$$

and

$$\tau_{gw} \approx 5.55 \times 10^{-5}(\frac{M_{bh}}{M_\odot})K(a)\ \ s \tag{22}$$

where a = $\frac{Jc}{GM^2}$ and useful fitting formulae for the functions F(a), K(a) are

$$F(a) \approx \frac{100}{37} - \frac{63}{37}(1-a)^{0.3}\ \ and\ \ K(a) \approx (1-a)^{-0.45} \tag{23}$$

The amplitude of the signal can be written as

$$h_0 = \frac{2.3 \times 10^{-21}}{D_{Mpc}\sqrt{(F(a)Q)}}(\frac{\varepsilon}{10^{-4}})^{1/2}(\frac{M_{bh}}{M_\odot}) \tag{24}$$

where Q is again the quality factor of the oscillation, D_{Mpc} is the distance to the source in megaparsec and the radiation efficiency was defined such as E = $\varepsilon M_{bh}c^2$ be the total gravitational wave energy emitted by the source. Equations (24) and (18) permit an estimate of the maximum distance that a given event could be detected, once the S/N ratio, the radiation efficiency, the mass and the angular momentum of the hole are fixed. Here, estimates were performed for a typical black hole mass of 9.0 $M_\odot$, a radiation efficiency $\varepsilon = 10^{-4}$ and a S/N ratio equal to two. The results are given in table 1 for two values of the angular momentum parameter a.

a	Q	ν_{gw} (kHz)	VIRGO	LIGO	LIGO-ad
0.2	2.57	1.48	1.25	0.43	83
0.9	10.9	2.46	0.44	0.16	9

Table 1: Maximum Probed Distances (Mpc)

Inspection of table 1 shows that the detection of slow rotating holes are more favorable, in spite of fast rotating holes have a higher oscillation quality factor. The reason is that the fundamental quadrupole frequency increases for higher angular momentum values and the sensitivity of most interferometers decreases for $\nu > 1$ kHz. A serious handicap to detect these events is that the signal is completely damped out after only a few cycles and could easily be confounded with transient disturbances produced, for instance, by the suspension of the mirrors. Moreover, the expected maximum distances for the present planned sensitivity of VIRGO and LIGO imply quite small detection rates and, only for the advanced LIGO a high event rate should be expected, namely, about one event/month under the assumption that all stars with M$\geq$ 40 $M_\odot$ produce black holes.

4 Binary Systems

The gravitational wave emission resulting from the merger of two compact stars (NS-NS, NS-BH, BH-BH) is a very attractive possibility due to the huge energy power implied in the process. This mechanism was already discussed in the late seventies by Clark et al. (1979), who suggested that gravitational antennas could be able to probe the universe up to distances of about 200 Mpc. Here, the case of a binary system constituted by two neutron stars (NS-NS system) will be discussed in more detail.

In the late inspiral phase, which precedes the final coalescence, relativistic effects or post-Newtonian (PN) corrections are necessary in order to describe the wave form and the amplitude of the signal (Damour & Deruelle 1981; Blanchet & Sathyaprakash 1994, 1995). The main features of the GW emission during the inspiral motion are an increasing radiated power and a wave frequency equal to twice the orbital frequency. The "last" stable orbit imposes a limit to the maximum wave frequency (see eq. (20), with M now being the total mass of the system). For a binary system constituted by two "canonical" neutron stars (1.4 $M_\odot$) such a limit frequency is about 1.6 kHz. As a consequence, during the epoch when the GW emission is in the bandwidth where the sensitivity of VIRGO or LIGO is the greatest, the motion is still well described by the Newtonian picture, whereas PN corrections become important at frequencies where the sensitivity of those detectors is already considerably reduced.

After averaging both polarization components with respect to the inclination angle of the orbital plane, the Fourier transform of the signal is

$$\mid \bar{h}(\nu) \mid^2 = < \mid \bar{h}_+(\nu) \mid^2 + \mid \bar{h}_X(\nu) \mid^2 > = \frac{1}{12}\left(\frac{G^5 M^2}{\pi^4 c^9}\right)^{1/3} \frac{\mu}{r^2 \nu^{7/3}} \tag{25}$$

where M is the total mass of the system and μ is the reduced mass. Combining eqs.(17) and (25), the maximum distance probed by the detector can be estimated by assuming M = 2.8 $M_\odot$ and S/N = 2. For VIRGO, r_{max} = 46 Mpc and for LIGO, r_{max} = 36 Mpc, if the planned sensitivity of these detectors is used.

The maximum distance permits to evaluate the expected event rate if the coalescence rate is known. Regimbau (private communication) has recently reviewed the formation rate of NS-NS systems. She assumed an initial binary system constituted by progenitors with masses greater than 9 $M_\odot$. The more massive evolves faster, explodes and produces a neutron star. Then, as the less massive star evolves it loses mass, affecting the rotation period of the first formed pulsar. The evolving star becomes a "He-star" and explodes probably as a type Ib supernovae.

The system is supposed to remain bounded after both explosions. If evolution of the newly formed pulsar is not affected by external torques other than the canonical magnetic dipole, then its rotation period will have a secular increase similar to that observed for "isolated" pulsars. Table 2 summarizes the present census of NS-NS systems. The first column identifies the pulsar and the others give respectively the rotation period in ms, the logarithm of the period derivative, the orbital period in days, the orbital eccentricity and the total mass of the system. Notice that for B1820-11 only a lower limit for the total mass is known since the rate of the relativistic advance of the longitude of the periastron is poorly determined. All the systems, excepting PSR B1820-11, seem to contain recycled pulsars, indicating that the first formed neutron star is the one being observed. On the other hand, in the case of B1820-11, the period derivative, the magnetic field and the indicative age favor the interpretation of a young and non-recycled pulsar. However, the nature of the companion is not yet well established. Lyne & McKenna (1989) suggested that the system is indeed constituted by two neutron stars, but alternative possibilities like a main-sequence star (Phinney & Verbunt 1991) or a white dwarf (Portegies Zwart & Yungelson 1999) have also been discussed in the literature. According to the simulations by Regimbau, in order to observe one system like B1820-11, the present formation rate $R_b(T)$ of NS-NS binaries must be equal to 1.2×10^{-5} yr^{-1}, consistent with other recent estimates (Kalogera & Lorimer 2000).

PSR	P (ms)	$\log(\dot{P})$	P_{orb} (days)	e	$M/M_\odot$
B1913+16	59.03	-17.10	0.323	0.617	2.83
J1518+49	40.94	-19.40	8.634	0.248	2.62
B1534+12	37.90	-17.60	0.420	0.274	2.68
B2127+11C	30.53	-17.30	0.335	0.681	2.71
J1811-17	104.18	-17.74	18.779	0.828	2.60
B1820-11	279.83	-14.86	357.76	0.795	>0.54

Table 2: NS-NS Binary Systems

The coalescence rate can now be calculated following the procedure by de Freitas Pacheco (1997). The first step is to compute the fraction γ_b of formed stars giving rise to NS-NS systems. The formation rate of NS-NS systems can be written as

$$R_b(t) = \gamma_b k M_g(t) \int_{m_1}^{m_2} \xi(m) dm \tag{26}$$

where $kM_g(t)$ is the star formation rate (k in yr^{-1} is the star formation efficiency and $M_g(t)$ is the gas mass in solar masses in the Galaxy), $\xi(m)$ is the initial mass function and $m_1 = 0.1M_\odot$, $m_2 = 80M_\odot$ are respectively the minimum and the maximum stellar masses. Adopting a galactic age T=15 Gyr and using the NS-NS formation rate estimated above, from eq.(26) one obtains for the fraction of formed NS-NS binaries $\gamma_b = 2.6\times10^{-6}$. Then, assuming γ_b constant in time, the second step consists to compute the coalescence rate ϖ from the equation (de Freitas Pacheco 1997)

$$\varpi(t) = \int_{t_0}^{t} R_b(t-t')\phi(t')dt' \tag{27}$$

where $\phi(\tau) = \frac{B}{\tau}$ is the probability for a NS-NS system to merge in a timescale τ and t_0 is the minimum time required for a given pair to coalesce. Solving the above integral, the resulting coalescence rate in the Galaxy at present is $\varpi(T) = 3.0\times10^{-5}\ yr^{-1}$. This procedure can now be applied to an elliptical galaxy, assuming the same value of γ_b, but a higher efficiency for the star formation rate. Then, a "cosmic" mean coalescence rate can be estimated by using a weighted contribution of 20% of ellipticals and 80% of spiral galaxies. These calculations give $\bar{\varpi} = 7.0\times10^{-7}$ $Mpc^{-3}yr^{-1}$, from which an event rate of one merging every 3.5 yr is expected for VIRGO and one every 7.3 yr for LIGO. Clearly, reasonable event rates will only be obtained with the "enhanced" versions of these detectors. However, it is worth mentioning that already a gain of a factor of two in the sensitivity implies an increase of one order of magnitude in the probed volume and the consequences of such an achievement may drastically change the situation. It seems to be rather well established now that at a distance of about

60 Mpc, in the direction of Centaurus, there is a huge concentration of galaxies dubbed the Great Attractor (Burstein 1990). The estimated mass of this supercluster is about 5×10^{16} $M_\odot$ (but see Staveley-Smith et al. 2000), implying a coalescence rate of 11 events/yr from the Great Attractor alone. However, we should have in mind the uncertainties still present in all these estimates, once they are based on rather poor statistics of NS-NS pairs.

5 The Stochastic and the Cosmological Background

The stochastic background is the GW emission arising from a very large number of unresolved and uncorrelated sources. A quantity which is often used to measure whether the collective effect of bursts generates a continuous background or not, is the so-called duty cycle defined by

$$D(z) = \int_0^z \tau_*(1+z')dR_*(z') \tag{28}$$

where τ_* is the average duration of a single burst at emission, $R_*(z)$ is event rate at redshift z and the factor (1+z) takes into account the time dilation. If D<<1, the background cannot be considered as a continuous one, but should rather be seen as a shot noise process. Supernovae (Blair et al.1997) and distorted stellar black-holes (Ferrari et al. 1999a; de Araújo et al. 2000) are examples of sources which may produce a shot noise like background. On the opposite situation, when D>>1 a truly continuous background will be produced, as that due to the r-mode emission from neutron stars (Owen et al. 1998; Ferrari et al. 1999b) or from processes that took place very shortly after the big-bang.

In order to compare the importance of the GW background with other forms of energy which dominate the expansion of the universe, it is usual to define an equivalent energy density parameter Ω_{gw} associated to GW by the relation

$$\Omega_{gw}(\nu) = \frac{1}{\rho_c}\left(\frac{d\rho_{gw}}{dln\nu}\right) \tag{29}$$

where $\rho_c = \frac{3c^3H_0^2}{8\pi G}$ is the critical density and ρ_{gw} is the energy density under the form of gravitational waves.

Primordial nucleosynthesis and millisecond pulsars impose relevant constraints on the closure density due to GW. The outcome from primordial nucleosynthesis depends on the balance between the nuclear reaction rates and the expansion of the universe. Thus, in order not to spoil the predict abundances of ^{2}H, ^{3}He, ^{4}He and ^{7}Li, which are in agreement with present data, the energy density under the form of GW cannot exceed a certain limit. This bound is usually established in terms of an effective number of neutrino species N_ν and is given by (Kolb & Turner 1990)

$$\int \Omega_{gw}(\nu)dln\nu \leq 1.3\times10^{-5}(N_\nu - 3) \tag{30}$$

if the Hubble expansion parameter H_0 is taken to be equal to 65 km/s/Mpc. Primordial nucleosynthesis constrains the number of massless neutrinos to be $N_\nu \leq 3.2$, restricting the background spectrum of GW over a wide range of frequencies to have an equivalent amplitude $\Omega_{gw} < 10^{-6}$. Notice that this is not a very restrictive constraint.

Millisecond pulsars are very precise and stable clocks. The regularity of the pulses can be described in terms of timing residuals, which represent the errors in predicting the arrival time of these pulses. GW passing between the pulsar and the observer cause a fluctuation in the arrival time proportional to the amplitude of the perturbing waves. Eight years of monitoring of PSR B1855+09 give an upper limit at $\nu \sim 10^{-8}$ Hz of $\Omega_{gw} < 10^{-8}$.

It is interesting to compare these upper bounds with the expected sensitivity of laser beam interferometers. At lower frequencies, $\nu \sim 1$ mHz, LISA will be able to detect after one year integration, a GW background corresponding to a closure density $\Omega_{gw} \sim 10^{-12}$. The present generation of ground based interferometers like

VIRGO and LIGO, after one year integration and using signal correlation techniques, may detect a GW background equivalent to $\Omega_{gw} \sim 10^{-5}$, while the next generation will be able to detect at frequencies in the range 0.1 - 1.0 kHz, amplitudes several orders of magnitude smaller, namely, $\Omega_{gw} \sim 10^{-10}$ (Maggiore 2000).

The GW emission from core collapse (see section 2.2) is likely to be of the order of 10^{-8} Mc^2. Thus, the expected contribution to the stochastic background will be about $\Omega_{gw} \leq 10^{-15}$, a extremely small value in comparison with the expected amplitude from other sources. The GW stochastic background due to black hole formation after the core collapse of a massive star was estimated by Ferrari et al. (1999a) and de Araújo et al. (2000). Both studies conclude that the spectral energy distribution attains a maximum around 1 kHz with an amplitude corresponding to a closure density of about $\Omega_{gw} \approx 10^{-10}$. This result indicates that such an emission will not be detected by the present generation of laser beam interferometers but it is within the capabilities of the advanced versions. The GW background resulting from the r-mode instability in young and rapidly rotating neutron stars may be a more promising possibility. According to the computations by Ferrari et al. (1999b), the closure density has a maximum amplitude plateau of $\Omega_{gw} \sim 7 \times 10^{-8}$ in the frequency range 0.5 - 1.7 Hz, which is about two orders of magnitude above the expected detection threshold for the advanced interferometers.

Different physical processes which could have taken place in the early universe and which produce a continuous GW background, have been discussed in the literature. The first mechanism consists on GW generated by quantum perturbations in a inflationary scenario. As the universe cools, it pass through a phase dominated by the vacuum energy, where the scale factor increases exponentially, followed by a rapid transition to a radiation dominated phase. GW quanta are produced by quantum fluctuations during such a transition and the resulting closure density is (Allen 1997)

$$\Omega_{gw} = \frac{16\hbar G^2}{9c^7}\rho_v \tag{31}$$

where ρ_v is the energy density of the vacuum in the inflationary phase. The spectrum is flat at frequencies seen by LISA or ground based interferometers like VIRGO and LIGO, and the expected amplitude is of the order of $\Omega_{gw} \sim 10^{-13}$. This value is well below the expected detection limit of LISA and ground based advanced interferometers. Another scenario was developed by Vilenkin (1985) (see also Vilenkin & Shelard 1994), who considered the GW background produced by a network of cosmic strings formed during a symmetry breaking phase transition. This scenario offers a situation more favorable for a future detection. The spectrum is almost flat in the frequency range 10^{-9}-10^{9} Hz with an amplitude $\Omega_{gw} \sim 10^{-8}$. The existence of this possible background component can be confirmed or not by a continuous monitoring of the timing residuals of millisecond pulsars, by future space observations as well as by the next generation of laser interferometers. More recent studies in this domain (Damour & Vilenkin 2000) seem to indicate that the stochastic background produced by strings is non-Gaussian, including occasional bursts emanating from cusps, that stands above the mean amplitude. According to those authors, the GW bursts might be accompanied by gamma-ray bursts, what could be a decisive signature of such a mechanism.

A more fascinating possibility is related with theories which describe our world as a (mem)brane embedded in a higher dimensional space, having the purpose of solving the huge energy gap that separates the electroweak scale from the Planck scale, the so-called hierarchy problem (Randall & Sundrum 1999). In this scenario, GW are produced by coherently excited radions (geometrical degree of freedom controlling the size or curvature of the extra dimensions) and Nambu-Goldstone modes (Hogan 2000). According to estimates by Hogan (2000), the typical GW frequency is $\nu \sim 10^{-4}$ Hz and the amplitude corresponds to a closure density of about $\Omega_{gw} \sim 8 \times 10^{-5}$. Notice that this amplitude is higher than the bound imposed by primordial nucleosynthesis.

6 Concluding Remarks

The direct detection of GW will constitute an extraordinary scientific accomplishment, giving further support to the General Relativity Theory, opening a new window to explore the Universe.

GW from oscillating neutron stars excited by core phase transitions, from unstable newly born proto-neutron stars (r-modes) or from the last phases of the coalescence of a NS-NS binary, will give an important insight on the properties of the nuclear matter in these objects. Moreover, the eventual detection of GW from the "ringdown" phase of a newly formed black hole will permit to probe directly their properties like mass and angular momentum. The detection rate of these events, if estimated by the future advanced interferometers, will impose severe constraints on the last evolutionary phases of massive stars.

The Universe is highly transparent to GW and the detection of a background will probe the very early phases of the big-bang, when radiation and matter are still strongly coupled. Modern unified theories can also be tested as well as the spacetime structure of our world.

7 REFERENCES

[98] Akmal A., Pandharipande V.R., Ravenhall D.G., 1998, PRC 58, 1804

[97] Allen B. 1997, in Relativistic Gravitation and Gravitational Radiation, eds. J.-A. Marck, J.-P. Lasota, Cambridge University Press, p. 373

[93] Alpar M.A., Chau H.F., Cheng K.S., Pines D., 1993, ApJ 409, 345

[00] Andersson N., Kokkotas K.D., 2000, gr-qc/0010102

[98] Bildsten L., 1998, ApJ 501, L89

[97] Blair D.G., Burman R., Woodings L.J.S., Mulder M., Zadnik, M.G., 1997, in Omnidirectional Gravitational Radiation Observatory, eds. W.F.Velloso, O.D. Aguiar, N.S.Magalhães, World Scientific, p.251

[94] Blanchet L., Sathyaprakash B.S., 1994, Class.Q.Grav. 11, 2807

[95] Blanchet L., Sathyaprakash B.S., 1995, PRL 74, 1067

[96] Bonazzola S., Gourgoulhon E., 1996, A&A 312, 675

[00] Brown J.D., 2000, gr-qc/0004002

[90] Burstein D., 1990, Rep.Pro.Phys. 53, 421

[69] Chandrasekhar S., 1969, Ellipsoidal Figures of Equilibrium, Yale University Press

[79] Clark J.P.A., van den Heuvel E.P.J., Sutantyo W., 1979, A&A 72, 120

[81] Damour T., Deruelle N., 1981, Phys.Lett. 87A, 81

[00] Damour T., Vilenkin A., 2000, gr-qc/0004075

[00] de Araújo J.C.N., Miranda O.D., Aguiar O.D., 2000, astro-ph/0004395

[97] de Freitas Pacheco J.A., 1997, Ast.Phys. 8, 21

[98] de Freitas Pacheco J.A., 1998, A&A 336, 397

[99] de Freitas Pacheco J.A., 1999, in Structure and Stability of Nucleon and Nuclear Systems, eds. A.A. Raduta, S. Stoica and I.I. Ursu, World Scientific, p. 547

[93] de Freitas Pacheco J.A., Horvath J.E., Araújo J.C.N., Cattani M., 1993, MNRAS 260, 499

[89] Echeverria F., 1989, PRD 40, 3194

[69] Ferrari A., Ruffini R., 1969, ApJ 158, L71

[99] Ferrari V., Matarrese S., Schneider R., 1999a, MNRAS 303, 247

[99b] Ferrari V., Matarrese S., Schneider R., 1999b, MNRAS 303, 258

[92] Finn L.S., 1992, PRD 46, 5236

[99] Fryer C.L., 1999; astro-ph/9902315

[70] Gunn J.E., Ostriker J.P., 1970, ApJ 160, 979

[00] Hogan C.J., 2000, PRL 85, 2044

[94] Houser J.L., Centrella J.M., Smith S.C., 1994, PRL 72, 1314

[96] Houser J.L., Centrella J.M., 1996, PRD 54, 7278

[75] Hulse R.A., Taylor J.H., 1975, ApJ 195, L51

[98] Jaranowski P., Królak A., Schutz B.F., 1998, gr-qc/9804014

[00] Kalogera V., Lorimer D.R., 2000, ApJ 530, 890

[88] Kojima Y., 1988, Prog.Theor.Phys. 79, 665

[97] Kokkotas K.D., 1997 in Relativistic Gravitation and Gravitational Radiation, eds. J.A. Marck and J.P. Lasota, Cambridge University Press, p.89

[92] Kokkotas K.D., Schutz B.F., 1992, MNRAS 255, 119

[90] Kolb E.W., Turner M., 1990 in The Early Universe, Frontiers in Physics, Addison Wesley

[00] Konno K., Obata T., Kojima Y., 2000, astro-ph/0001397

[95] Lai D., Shapiro S.L., 1995, ApJ 442, 259

[83] Lindblom L., Detweiler S.L., 1983, ApJS 553, 73

[92] Link B., Epstein R.I., van Riper K.A., 1992, Nat 359, 616

[89] Lyne A.G., McKenna J.M., 1989, Nat 340, 367

[00] Maggiore M., 2000, gr-qc/0008027

[88] McDermott P.N., van Horn H.M., Hansen C.J., 1988, ApJ 325, 725

[71] Moss G.E., Miller L.R., Forward R.L., 1971, Appl.Opt. 10, 2495

[99] New K.C.B., Centrella J.M., Tohline J.E., 1999, astro-ph/9911525

[98] Owen B.J., Lindblom L., Cutler C., Schutz B.F., Vecchio A., Andersson N., 1998, PRD 58, 084020

[95] Pandharipande V.R., Pethick C.J., Thorsson V., 1995, PRL 75, 4567

[91] Phinney E.S., Verbunt F., 1991, MNRAS 248, 21

[99] Portegies Zwart S.F., Yungelson L.R., 1999, astro-ph/9904305

[99] Randall L., Sundrum R., 1999, PRL 83, 3370

[00a] Regimbau T., de Freitas Pacheco J.A., 2000a, A&A 359, 242

[00b] Regimbau T., de Freitas Pacheco J.A., 2000b, submitted

[00] Shibata M., Baumgarte T.W., Shapiro S.L., 2000, astro-ph/0005378

[85] Stark R.F., Piran T., 1985a, PRL 55, 891

[85] Stark R.F., Piran T., 1985b, PRL 56, 97

[00] Staveley-Smith L., Juraszek S., Henning P.A., Koribalski B.S., Kraan-Korteweg R.C., 2000, astro-ph/0009223

[69] Thorne K.S., 1969, ApJ 158, 1

[67] Thorne K.S., Campolattaro A., 1967, ApJ 149, 591

[00] Ushomirsky G., Cutler C., Bildsten L., 2000, astro-ph/0001136

[00] van der Klis M., 2000, astro-ph/0001167

[85] Vilenkin A., 1985, Phys.Rep. 121, 263

[94] Vilenkin A. & Shelard S., 1994, Cosmic Strings and other Topological Defects, Cambridge University Press

[60] Weber J., 1960, Phys. Rev. 117, 306

[71] Weiss R., 1971, Quaterly Progress Report of RLE, MIT 105, 54

[79] Zimmerman M., Szednits E., 1979, PRD 20, 351

[97] Zwerger T., Muller E., 1997, A&A 320, 209

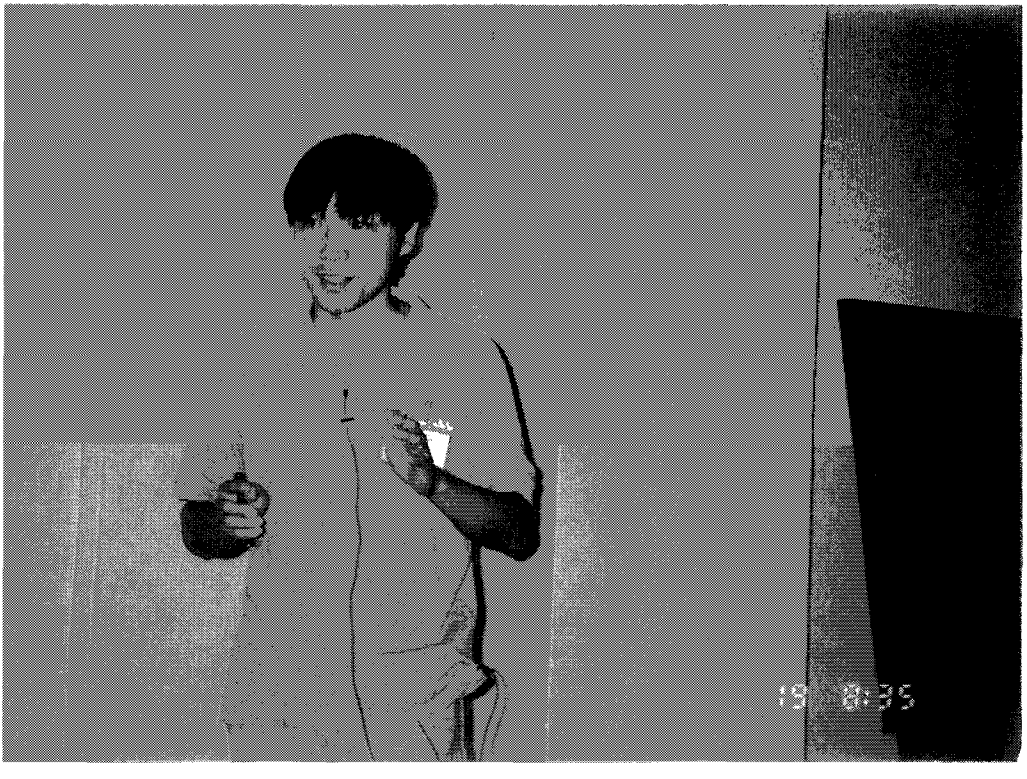

Takeshi Osada

Event-by-event analysis of ultra-relativistic heavy-ion collisions in smoothed particle hydrodynamics

T. Osada[1], C.E. Aguiar[2], Y. Hama[1] and T. Kodama[2]
[1] *Instituto de Física, Universidade de São Paulo,*
[2] *Instituto de Física, Universidade Federal do Rio de Janeiro*

Abstract

The method of smoothed particle hydrodynamics (SPH) is applied for ultra-relativistic heavy-ion collisions. The SPH method has several advantages in studying event-by-event fluctuations, which attract much attention as the signal of quark gluon plasma (QGP) formation, because it gives a rather simple scheme for solving hydrodynamical equations. Using initial conditions for Au+Au collisions at RHIC energy produced by NeXus event generator, we solve the hydrodynamical equation in event-by-event basis and study the fluctuations of hadronic observables such as dN/dy due to the initial conditions. In particular, fluctuations of elliptic flow coefficient v_2 is investigated for both the cases, with and without QGP formation.

1 Introduction

One of the central issues of the high-energy heavy-ion physics is to investigate the phases of the hadronic and quark matter. Hydrodynamical descriptions[1], which have a rather long history, may be a powerful tool for studying such phase diagrams because we can handle the equation of state directly in the model. However, to extract precisely information about the equation of state, we must be careful in comparing the model predictions with experimental data because procedures of event averaging may make signal of QGP ambiguous.

Event-by-event analysis[2] is one of promising ways to extract clear information from the experimental data, in particular at RHIC and LHC energy regions. The fluctuations at the initial stage (for example, the initial energy density fluctuation) must affect the formation of QGP and the later space-time evolution of the whole system. Fig.1 shows the energy density (counter plot, at $z = 0\ fm$ plane) for a Au+Au collision at $\sqrt{s} = 200A\ GeV$, $b = 0\ fm$, produced by NeXus code[3]. As shown in Fig.1, the fluctuations at the initial stage of relativistic heavy-ion collisions are not negligible. To achieve an event-by-event analysis using relativistic hydrodynamical model, the numerical code

must deal with arbitrary initial conditions and equation of state with suitable calculational speed and precision. The method of smoothed particle hydrodynamics (SPH)[4], which was first introduced for astrophysical applications[5], satisfy such requirements. The main characteristic of SPH is the introduction of "particles" attached to some conserved quantity which are described in terms of discrete Lagrangian coordinates. This feature of the model enables to easily carry out calculations of the ultra-relativistic heavy-ion collisions, which is accompanied by prominent longitudinal expansion. Another advantage of using SPH method is that we can choose a suitable precision in solving hydrodynamical equations because of the smoothing kernel, which allows to smooth out often unnecessary very precise local aspects and then achieve a reduction of computational time. This is a very profitable point in the event-by-event analysis.

In the following section, we briefly formulate the entropy-based SPH, using the variational approach[6]. In Sec.3, to check the performance of SPH, we apply it for solving problems of relativistic hydrodynamics whose solutions are known analytically or numerically. Then, in Sec.4, we demonstrate hydrodynamical evolutions of both resonance gas and quark gluon plasma starting from the same simple initial conditions. In Sec.5, after giving a brief explanation how to take the initial conditions of NeXus into our code, we present typical hydrodynamical evolution of an event at RHIC energy. To introduce freeze-out process into our code, we formulate Cooper-Frye formula in terms of SPH and show several results on single-particle spectrum in Sec.6. Then, we study the event-by-event fluctuation of elliptic flow coefficient v_2[7] at RHIC energy[8] in Sec.7. Finally we close our discussions with some concluding remarks.

2 Relativistic SPH equations

2.1 SPH representation

To specify the hydrodynamical state of a fluid, we need to locally know the thermodynamical quantities such as the energy density ε and the collective velocity field, besides equation of state of the fluid. If local thermal equilibrium is well established, the thermodynamical variables may be expressed by a smooth functions of the coordinates. Let us choose N space points to specify the state of the whole system. To know the physical quantities in other space points, we may use an interpolation using the known N points. (Hereafter we use the word 'particles' instead of 'points'.)

In SPH, for an arbitrary extensive thermodynamical quantity of A, the density (in the space-fixed frame) a^* is parametrized in the following way:

$$a^*(\boldsymbol{x},t) = \sum_i^N \nu_i \, W(\boldsymbol{x} - \boldsymbol{x}_i(t); h) \ , \tag{1}$$

where $W(\boldsymbol{x} - \boldsymbol{x}_i(t); h)$ is a positive definite kernel function with the properties

$$\int d\boldsymbol{x}' \, W(\boldsymbol{x}' - \boldsymbol{x}) \equiv 1 \qquad \text{and} \qquad W(\boldsymbol{x}' - \boldsymbol{x}, h) = \delta(\boldsymbol{x}' - \boldsymbol{x}) \quad \text{when } h \to 0 \ ,$$

where h is a parameter of smoothing scale. Using the normalization of above, we have

$$A_{total} = \int d^3\boldsymbol{x}\ a^*(\boldsymbol{x},t) = \sum_i^N \nu_i\ . \tag{2}$$

From eq.(2) the quantity ν_i can be interpreted as a portion of A which is carried by the i th particle. The velocities of particles, identified as the velocities of the fluid, satisfy

$$\boldsymbol{v}_i(t) = \frac{d\boldsymbol{x}_i(t)}{dt}\ . \tag{3}$$

If A is a conserved quantity, ν_i must be constant in time. In this case, from eqs.(1) and (3), we obtain

$$\frac{\partial}{\partial t}\ a^*(\boldsymbol{x},t) = -\boldsymbol{\nabla}\cdot\boldsymbol{j}(\boldsymbol{x},t)\ , \tag{4}$$

where

$$\boldsymbol{j}(\boldsymbol{x},t) = \sum_i\ \nu_i\boldsymbol{v}_i(t)\ W(\boldsymbol{x}-\boldsymbol{x}_i(t);h) \tag{5}$$

is interpreted as the current density of the thermodynamical quantity A and eq.(4) is then the corresponding continuity equation.

2.2 Equations of motion for SPH particles

To know the time evolution of the fluid, we have to find the equation of motion for each SPH particle. It can be obtained by the variational method[6] with the following Lagrangian[4]

$$L_{\rm SPH}(\{\boldsymbol{x}_i,\boldsymbol{v}_i\}) = -\sum_i \nu_i\ \frac{\varepsilon_i}{a_i^*} \tag{6}$$

It should be noted here that the factor ν_i/a_i^* can be regarded as the volume V_i (in the space-fixed frame) occupied by the i th 'particle'. Then each term in eq.(6) is equal to E_i/γ_i, where E_i and γ_i are the energy (in the rest frame) and the gamma factor of the i th particle, respectively. Then we also write

$$L_{\rm SPH}(\{\boldsymbol{x}_i,\boldsymbol{v}_i\}) = -\sum_i \frac{E_i(\boldsymbol{x}_i,\boldsymbol{v}_i)}{\gamma_i(\boldsymbol{v}_i)}\ . \tag{7}$$

The equations of motion of SPH particles are obtained minimizing the action $I_{\rm SPH}$ with respect to $\{\boldsymbol{x}_i\}$ with the constraint of eq.(3) taken into account

$$\delta I_{\rm SPH}(\{\boldsymbol{x}_i,\boldsymbol{v}_i\}) = -\delta\int dt\ \frac{E_i}{\gamma_i} = 0\ . \tag{8}$$

Using the adiabatic condition

$$\delta E_i = P\delta V_i \quad = P_i\ \delta\Big(\frac{\nu_i\gamma_i}{a_i^*}\Big)\ , \tag{9}$$

we obtain

$$\frac{d}{dt}(\nu_i\frac{P_i+\varepsilon_i}{a_i}\gamma_i\boldsymbol{v}_i) + \sum_j \nu_j\Big[\frac{P_i}{a_i^{*2}} + \frac{P_j}{a_j^{*2}}\Big]\ \boldsymbol{\nabla}W(\boldsymbol{x}_i - \boldsymbol{x}_j; h) = 0\ , \tag{10}$$

where P_i is the pressure. Because of the adiabatic condition, eqs.(10) are the equations of motion for the ideal fluid. For the extension to the non-adiabatic case, see ref.[4].

2.3 Entropy based SPH in general coordinate system

As a possible candidate for the thermodynamical extensive quantity a^*, we may consider baryon number density, entropy density, energy density and so on. In the case of energy density, we have (cf. eq.(6) and (7))

$$\nu_i = E_i(\boldsymbol{x}_i, \boldsymbol{v}_i)\ . \tag{11}$$

However, this is only the internal energy, so ν_i is not constant with respect to the variation of $\boldsymbol{x}_i$ in eq.(8), introducing an additional complication without any practical merit. On the other hand, for entropy or baryon number density, for example, ν_i can be kept constant. Since we will apply SPH to ultra-relativistic heavy-ion collisions, baryon number density is not so suitable choice because it is expected to be very small in the central rapidity region. Let us choose the entropy density for a^* in eq.(1).

In relativistic heavy-ion collisions, initial conditions of fluid are often given at constant $\tau \equiv \sqrt{t^2 - z^2}$. Then, it is convenient to formulate SPH in the coordinates

$$x^0 \equiv \tau = \sqrt{t^2 - z^2},\quad x^1 \equiv x,\quad x^2 \equiv y,\quad x^3 \equiv \eta = \frac{1}{2}\ln\frac{t+z}{t-z}\ . \tag{12}$$

The SPH equations in generalized coordinate system are easily derived in a similar way[4]. In the case of the coordinate above, the SPH equations of motion should be written as

$$s(\tau, \boldsymbol{x}) = \frac{1}{\tau u^0}\sum_i \nu_i W(\boldsymbol{x} - \boldsymbol{x}_i : h)\ , \tag{13}$$

$$\frac{d}{d\tau}(\nu_i\frac{P_i+\varepsilon_i}{s_i}\gamma_i\boldsymbol{v}_i) + \sum_j \frac{\nu_j}{\tau}\Big[\frac{P_i}{{s_i}^2{u_i^0}^2} + \frac{P_j}{{s_j}^2{u_j^0}^2}\Big]\ \boldsymbol{\nabla}W[\boldsymbol{x}_i - \boldsymbol{x}_j; h] = 0\ . \tag{14}$$

3 Numerical check of SPH

To check the performance of SPH formulated in Sec.2, we applied it to a problem of relativistic hydrodynamics whose solution is known analytically. When the longitudinal rapidity α and the transverse one β are given as

$$\alpha \equiv \eta,\quad \beta \equiv \frac{1}{2}\ln\frac{\tau + \sqrt{x^2+y^2}}{\tau - \sqrt{x^2+y^2}}\ , \tag{15}$$

it is known that the entropy density is given by

$$s = \frac{s_0}{[\tau^2 - x^2 - y^2]^{3/2}} \ , \tag{16}$$

where s_0 is a constant which is determined by the initial conditions. A comparison of the numerical results by SPH with the analytical solution eq.(16) is shown in Fig.2, where the equation of state used is $c_s^2 = 1/3$. It is verified that SPH solves this problem correctly. For a further check, we applied it also to another problem, namely, relativistic hydrodynamics with the longitudinal scaling and the Landau-type initial condition in the transverse directions,

$$\alpha \equiv \eta, \quad \beta \equiv 0 \ . \tag{17}$$

Figure 3 shows a comparison of the SPH results with those obtained by Hama and Pottag[9]. The initial conditions and the equation of state used are exactly the same as in ref.[9]. We found that SPH works well also in this problem.

4 Equations of state and hydrodynamical evolutions

To complete the theory of relativistic hydrodynamics, the equation of state (EoS) for the fluid is required. We use two possible EoS in the present study, namely, a resonance gas EoS[10] and an EoS containing both resonance gas and QGP via a first order phase transition[11]. The EoS are parametrized as follows (See also Fig.4.);

$$P/\varepsilon = 0.20 \quad (\text{ constant for whole } \varepsilon \text{ region }) \tag{18}$$

for the resonance gas (RG) and

$$P/\varepsilon = \begin{cases} 0.20 & 0.00\ GeV/fm^3 < \varepsilon < 0.28\ GeV/fm^3 \\ 0.056/\varepsilon & 0.28\ GeV/fm^3 < \varepsilon < 1.45\ GeV/fm^3 \\ 1/3 - 4B/3\varepsilon & 1.45\ GeV/fm^3 < \varepsilon \end{cases} \tag{19}$$

for the quark gluon plasma (QGP). The bag constant $B = 0.32 GeV/fm^3$ is determined to give the critical temperature $T_c = 160\ MeV$. We show some results of the hydrodynamical evolution using such RG and QGP Eos in Figs. 5 and 6. Fot the both cases, the initial ($\tau = 1.0\ fm$) entropy density s, longitudinal and transverse rapidity α, β are set as

$$s = 40[1/fm^3], \quad \alpha = \eta \ , \quad \beta = 0 \ . \quad \text{for } \sqrt{x^2 + y^2} < 7.0\ fm,\ |\eta| < 7.0 \ . \tag{20}$$

As seen in Figs.5 and 6, the space-time evolution of the fluid strongly depends on the EoS. In comparison with the RG case, the temperature of the fluid in QGP EoS drops much slowly due to the existence of the mixed phase, where the pressure is constant.

5 Initial conditions produced by NeXus

The most fundamental assumption of hydrodynamical models is the thermalization of partonic or hadronic system produced after a high-energy heavy-ion collision. In our stusdy, we set the initial conditions using information from Nexus event generator[3], in the following 2 steps.

1. Align all primary hadrons on the $\tau = \tau_0$ hypersurface. Here we assume that the primary hadrons move freely with the momentum p^μ. In the present study, we use $\tau_0 = 1.0\ fm$.

2. Initial energy density and momentum density are estimated using the interpolation kernel W.

$$\varepsilon(\tau_0; \boldsymbol{x}) = \sum_i p_i^0 W(\tau_0, \boldsymbol{x} - \boldsymbol{x}_i; h) \ ,$$

$$\boldsymbol{p}(\tau_0; \boldsymbol{x}) = \sum_i \boldsymbol{p}_i W(\tau_0, \boldsymbol{x} - \boldsymbol{x}_i; h) \ ,$$

where $\boldsymbol{x}_i = (x_i, y_i, \eta_i)$ are the coordinates of the i-th primary hadron after the alignment on $\tau = \tau_0$. The smoothing scale parameter $h = 1\ fm$ is used, which is the rough size of the hadrons. The collective velocity field is then given by $\boldsymbol{v}(\tau_0, \boldsymbol{x}) = \boldsymbol{p}(\tau_0, \boldsymbol{x})/\varepsilon(\tau_0, \boldsymbol{x})$.

In Fig.7, we show the hydrodynamical evolution of a typical event of $Au + Au$ collision at energy $\sqrt{s} = 130A\ GeV$ for the impact parameter $b = 7.0fm$ given by our hydro code, SPheRIO[1], connected to the NeXus event generator.

6 Cooper-Frye formula in SPheRIO

The Cooper-Frye formula[12] is widely used in calculations of single particle spectra using hydrodynamical models because of its simplicity. So, as the first trial to evaluating single particle densities, we shall follow it.

In SPH, using eq.(13), the usual Cooper-Frye formula can be rewritten as

$$E\frac{d^3N}{d\boldsymbol{p}^3} = \frac{g}{(2\pi)^3}\sum_j \nu_j \int_{F.O.} \tau dx dy d\eta \ \frac{\sigma_\mu p^\mu}{\tau\ su^0}\ W(\boldsymbol{x} - \boldsymbol{x}_j(\tau); h)\ \frac{1}{e^{u_\mu p^\mu/T_f} \mp 1} \ , \qquad (21)$$

where σ_μ is defined by

$$\sigma_\mu \equiv \left(1, \frac{n_x}{n_\tau}, \frac{n_y}{n_\tau}, \frac{n_\eta}{n_\tau} \right) \qquad (22)$$

[1]**S**moothed **P**article **h**ydrodynamical **e**volution of **R**elativistic heavy **IO**n collisions

and $n_\mu = (n_\tau, n_x, n_y, n_\eta)$ is the normal vector of the isothermals:

$$n_\mu \equiv \Big(-\frac{\partial T}{\partial \tau}, -\frac{\partial T}{\partial x}, -\frac{\partial T}{\partial y}, -\frac{\partial T}{\partial \eta} \Big) \ . \tag{23}$$

The integration is usualy done over a constant temperature hypersurface, $T = T_f$. When the spline-type kernel function[4, 5] is used, $W(\boldsymbol{x} - \boldsymbol{x}';\ h) = 0$ for $|\boldsymbol{x} - \boldsymbol{x}'| > 2h$. Then, within the approximation of small h,

$$\begin{aligned} E\frac{d^3N}{d\boldsymbol{p}^3} &\approx \frac{g}{(2\pi)^3} \sum_j \nu_j \Big[\frac{p^\mu}{e^{u_\mu p^\mu / T_f} \mp 1} \Big]_j \int \tau dx dy d\eta \ \frac{\sigma_\mu}{\tau\ su^0}\ W(\boldsymbol{x} - \boldsymbol{x}_j(\tau_{\rm F}(\boldsymbol{x}))\ ; h) \\ &= \frac{g}{(2\pi)^3} \sum_j \Big[\frac{p^\mu}{e^{u_\mu p^\mu / T_f} \mp 1} \Big]_j \int dx dy d\eta \ \frac{\nu_j}{su^0}\ \frac{\sigma_\mu W(\boldsymbol{x} - \boldsymbol{x}_j\ ; h)}{|1 + v_j^x \frac{n_x}{n_\tau} + v_j^y \frac{n_y}{n_\tau} + v_j^\eta \frac{n_\eta}{n_\tau}|} \ , \end{aligned} \tag{24}$$

where $\boldsymbol{x}_j$ gives the point where j-th SPH-particle crosses the freeze-out hypersurface. The result of the single-particle spectra, $1/m_{\rm T} dN/dm_{\rm T}$, dN/dy and $dN/d\varphi$ for Au+Au collisions at $\sqrt{s} = 130A\ GeV$, $b = 7.0\ fm$ are shown in Figs. 8, 9 and 10, respectively. The freeze-out temperature used is $T_f = 140\ MeV$.

7 Event-by-event analysis of hadronic observables

7.1 Elliptic flow coefficient v_2

The flow phenomena[13] can be important candidates of QGP signals because they may carry much information about EoS during the expansion of quark or hadronic matter. In particular, the elliptic flow coefficients[7] is one of interesting observables since it is sensitive to the early stage of high-energy heavy-ion collisions. Because it is expected that different EoS responds to the initial fluctuations in different way, the measure of fluctuation, for example, $\delta v_2 \equiv \sqrt{\langle v_2^2 \rangle - \langle v_2 \rangle^2}$ is also very important. For this purpose, we investigate v_2 distribution using different EoS. In Figs.11, 12 and Table 1, we show results of the v_2 distribution for $Au + Au$ collisions at energy $\sqrt{s} = 130A\ GeV$ in RG and QGP EoS cases.

As seen in Table 1, the fluctuations of flow coefficients v_1 and v_2 in QGP is about 20 $\sim$ 30% smaller than those in RG (cf. the difference of $\langle v_2 \rangle$ in RG and QGP is about a few %.). The b dependence of δv_1 and δv_2 are also found. Hence, it is expected that δv_1 and δv_2 also bring us useful information to infer the phase passed in the early stage of high-energy nuclear collisions.

7.2 Fluctuation of the slope parameter

It is also interesting to study the fluctuation of the so-called slope parameter in the transverse momentum spectra. The slope parameter $\tilde{T}$ can be obtained by fitting $1/m_{\rm T} dN/dm_{\rm T}$ with a function $\mathcal{N} \exp[-m_{\rm T}/\tilde{T}]$. In the present study, $0 < m_{\rm T} - m_\pi < 1.0\ GeV$ interval

is used for the fitting. The results are shown in Table 2. We found $\tilde{T}$ and $\delta\tilde{T}$ of QGP is systematically smaller than that of RG.

7.3 Multiplicity fluctuation in the central region

Other interesting measurement may be multiplicity fluctuation. Let us define the fluctuation measure as

$$\delta n_{y_c} \equiv \sqrt{\langle n_{y_c}^2 \rangle - \langle n_{y_c} \rangle^2} \tag{25}$$

where

$$n_{y_c} = \frac{1}{2y_c} \int_{-y_c}^{+y_c} dy \, \frac{dN}{dy} \, . \tag{26}$$

We investigate the rapidity window y_c, impact parameter b and EoS dependence of the multiplicity fluctuation and summarize results in Table 3. As seen in Table 3, the multiplicity fluctuations δn_{y_c} has clear EoS dependence, namely, δn_{y_c} in RG decrease much slower those in QGP. When energy density is not extremely high comparing with the critical energy density, the multiplicity fluctuation of QGP is expected to be larger than those of RG without first order phase transition. See Appendix. Therefore, it is considered that the b dependence of the δn_{y_c} in QGP is directly related to the ratio of mixed and QGP phase. Hence, δn_{y_c} can be good measure to detect the first order phase transition. The values of ratio $\delta n_{y_c}/\langle n_{y_c} \rangle$ of QGP is slightly larger than those of RG. This point discussed generally in Appendix.

8 Concluding remarks and discussions

We developed a new hydrodynamical code, SPheRIO, based on the smoothed particle hydrodynamics (SPH), for studying high-energy heavy-ion collisions in event-by-event basis. In this study, we set the initial conditions based on the results of NeXus event generator and used two types of possible equation of states (EoS), *ie.*, the resonance gas (RG) and quark gluon plasma (QGP)EoS. In the freeze-out processes, single particle spectra are calculated by the Cooper-Frye formula for each initial condition and EoS. Analysing those single particle spectra obtained, the fluctuations in flow coefficients, slope parameter $\tilde{T}$ and multiplicities in the central region are investigated at RICH energy.

As seen in the results of Table 1, we found prominent differences of δv_1 and δv_2 between RG and QGP EoS. This means that the measure of the fluctuations is also helpful to infer the phase passed in the high-energy heavy-ion collisions. In the QGP EoS case, the fluctuations are smaller than that in RG case about $20 \sim 30$ %.

To take effects of resonance decay into account in the analysis of flow, we introduce ρ meson production and decay into our model. The results are shown in Table 4. The effects of ρ decays enhance expectation values of $\langle v_1 \rangle$ and $\langle v_2 \rangle$ in QGP case. Although the magnitude of difference between QGP and RG are weaken, our conclusions above are

hold fundamentally. The fluctuation of slop parameter $\tilde{T}$ is small, which is a few % of $\tilde{T}$. We found the fluctuation of multiplicity has clear EoS dependence. The energy or impact parameter dependence of n_{y_c} can be a good measure to detect of the first order phase transition.

Acknowledgments: The authors acknowledge stimulating discussions with K. Werner, O. Socolwski Jr and H.J. Drescher. This work was partially supported by FAPESP(contract no.s 98/02249-4 and 98/00317-2), PRONEX(contract no. 41.96.9886.00), FAPERJ(contract no. E-26/150.942/99) and CNPq, Brasil.

A Entropy fluctuations in first order phase transition

When each sound velocity of phase is given by constant, the total entropy S for a system produced is given as

$$
\begin{aligned}
S &= \int_{x\in RG} d^3x\; s_1 \Big[\, \frac{\bar{\varepsilon}(x)+\delta\varepsilon(x)}{\varepsilon_1} \,\Big]^{1/[1+c_{s;r}^2]} \\
&\quad + \int_{x\in Mix} d^3x\; s_1 \Big[\, \frac{\bar{\varepsilon}(x)+\delta\varepsilon(x)}{\varepsilon_1} \,\Big]^{1/[1+c_{s;m}^2]} + \int_{x\in QGP} d^3x\; s_1\Big(\frac{\varepsilon_2}{\varepsilon_1}\Big)\Big[\, \frac{\bar{\varepsilon}(x)+\delta\varepsilon(x)}{\varepsilon_2} \,\Big]^{1/[1+c_{s;q}^2]} \\
&\approx \int_{x\in RG} d^3x\; s_1\Big(\frac{\bar{\varepsilon}(x)}{\varepsilon_1}\Big)^{1/[1+c_{s;r}^2]} \Big[\, 1+\frac{1}{1+c_{s;r}^2}\Big(\frac{\delta\varepsilon(x)}{\varepsilon_1}\Big) - \frac{c_{s;r}^2}{2[1+c_{s;r}^2]^2}\Big(\frac{\delta\varepsilon(x)}{\varepsilon_1}\Big)^2 + \cdots \,\Big] \\
&\quad + \int_{x\in Mix} d^3x\; s_1\Big(\frac{\bar{\varepsilon}(x)}{\varepsilon_1}\Big)^{1/[1+c_{s;m}^2]} \Big[\, 1+\frac{1}{1+c_{s;m}^2}\Big(\frac{\delta\varepsilon(x)}{\varepsilon_1}\Big) - \frac{c_{s;m}^2}{2[1+c_{s;m}^2]^2}\Big(\frac{\delta\varepsilon(x)}{\varepsilon_1}\Big)^2 + \cdots \,\Big] \\
&\quad + \int_{x\in QGP} d^3x\; s_1\Big(\frac{\varepsilon_2}{\varepsilon_1}\Big)\Big(\frac{\bar{\varepsilon}(x)}{\varepsilon_2}\Big)^{1/[1+c_{s;q}^2]} \Big[\, 1+\frac{1}{1+c_{s;q}^2}\Big(\frac{\delta\varepsilon(x)}{\varepsilon_2}\Big) - \frac{c_{s;q}^2}{2[1+c_{s;q}^2]^2}\Big(\frac{\delta\varepsilon(x)}{\varepsilon_2}\Big)^2 + \cdots \,\Big],
\end{aligned}
\tag{A1}
$$

where $c_{s;r}=1/\sqrt{5}$,$c_{s;m}=0$,$c_{s;q}=1/\sqrt{3}$ are sound velocities in resonance gas(RG), mixed phase(Mix), quark gluon plasma phase(QGP), ε_1 and ε_2 are critical energy densities of RG and QGP phase. The entropy density s_1 is the critical entropy density corresponding to the ε_1. $\bar{\varepsilon}(x)$ and $\delta\varepsilon(x)$ denote (event averaged) mean and fluctuations of energy density, respectively. Then, dispersion of entropy S distribution is

$$
\begin{aligned}
D_{QGP}^2 &= \langle S^2\rangle - \langle S\rangle^2 \\
&\approx \int_{x\in RG} d^3x\;\; s_1^2\,\Big(\frac{\bar{\varepsilon}(x)}{\varepsilon_1}\Big)^{2/[1+c_{s;r}^2]} \frac{1}{[1+c_{s;r}^2]^2}\Big\langle\Big(\frac{\delta\varepsilon(x)}{\varepsilon_1}\Big)^2\Big\rangle \\
&\quad + \int_{x\in Mix} d^3x\;\; s_1^2\,\Big(\frac{\bar{\varepsilon}(x)}{\varepsilon_1}\Big)^{2/[1+c_{s;m}^2]} \frac{1}{[1+c_{s;m}^2]^2}\Big\langle\Big(\frac{\delta\varepsilon(x)}{\varepsilon_1}\Big)^2\Big\rangle
\end{aligned}
$$

$$+\int_{x\in QGP} d^3x\ s_1^2\,(\frac{\varepsilon_2}{\varepsilon_1})\Big(\frac{\bar{\varepsilon}(x)}{\varepsilon_2}\Big)^{2/[1+c_{s;q}^2]}\frac{1}{[1+c_{s;q}^2]^2}\Big\langle\Big(\frac{\delta\varepsilon(x)}{\varepsilon_2}\Big)^2\Big\rangle\ . \tag{A2}$$

Let us define D for the RG without phase transition as the following.

$$D_{RG}^2=\int_{all\ x} d^3x\ \ s_1^2\ \Big(\frac{\bar{\varepsilon}(x)}{\varepsilon_1}\Big)^{2/[1+c_{s;r}^2]}\frac{1}{[1+c_{s;r}^2]^2}\Big\langle\Big(\frac{\delta\varepsilon(x)}{\varepsilon_1}\Big)^2\Big\rangle\ . \tag{A3}$$

Hence, when $\bar{\varepsilon}(x)<\varepsilon_2$ is satisfied for whole x, we have

$$D_{QGP}^2>D_{RG}^2, \qquad \bar{\varepsilon}(x)\ <\ \varepsilon_2\ \text{ for whole } x \tag{A4}$$

because of $c_{s;r}>c_{s;m}$. On the other hand, since $c_{s;r}>c_{s;q}$, in high-energy energy density limit, $\bar{\varepsilon}(x)\gg\varepsilon_2$ for whole x, we have

$$D_{QGP}^2<D_{RG}^2, \qquad \bar{\varepsilon}(x)\ \gg\ \varepsilon_2\ \text{ for whole } x. \tag{A5}$$

For the $\bar{\varepsilon}(x)<\varepsilon_2$ case, the difference of dispersion and entropy between QGP and RG are given by

$$\Delta D^2\ \equiv\ D_{QGP}^2-D_{RG}^2=\int d^3x\ s_1^2\Big\{\ \Big(\frac{\bar{\varepsilon}(x)}{\varepsilon_1}\Big)^2-\frac{25}{36}\Big(\frac{\bar{\varepsilon}(x)}{\varepsilon_1}\Big)^{5/3}\ \Big\}\Big\langle\Big(\frac{\delta\varepsilon(x)}{\varepsilon_1}\Big)^2\Big\rangle\ , \tag{A6}$$

$$\Delta S\ \equiv\ \langle S_{QGP}\rangle-\langle S_{RG}\rangle=\int d^3x\ s_1\Big\{\ \Big(\frac{\bar{\varepsilon}(x)}{\varepsilon_1}\Big)-\Big(\frac{\bar{\varepsilon}(x)}{\varepsilon_1}\Big)^{5/6}\ \Big\}\ . \tag{A7}$$

Then, a relation of $D^2/\langle S\rangle^2$ between QGP and RG is

$$\frac{D_{QGP}^2}{\langle S_{QGP}\rangle^2}\approx\frac{D_{RG}^2}{\langle S_{RG}\rangle^2}\Big\{\ 1+\frac{\Delta D^2}{D_{RG}^2}-2\frac{\Delta S}{\langle S_{RG}\rangle}\ \Big\}\ . \tag{A8}$$

References

[1] See for examples, L.D. Landau, *Izv. Akd. Nauk SSSR* **17** (1953), 51; L.D. Landau and S. Z. Belenkij, *Usp. Phys. Nauk* **56** (1956), 309; *Nuovo Cimento Suppl.* **3** (1956), 15; *Collected Papers of L. D. Landau*, ed. Ter Haar (Gordon and Breach, New York, 1965); J.D. Bjorken, *Phys. Rev. D* **27** (1983), 140.

[2] For recent review, see for example, H. Heiselberg, nucl-th/0003046.

[3] H.J. Drescher, M. Hladik, S. Ostapchenko T. Pierog and K. Werner, hep-ph/0007198, See also, H.J. Drescher, S. Ostapchenko, T. Pierog and K. Werner, hep-ph/0011219.

[4] C.E. Aguiar, T. Kodama, T. Osada and Y. Hama, hep-ph/0006239, to be published in *J. Phys. G.*

[5] See for a review, J.J. Monaghan, *Annu. Rev. Astrophys.* **30** (1992), 543; *Comput. Phys. Comm.* **48** (1998), 89.

[6] H-T. Elze, Y. Hama, T. Kodama, M. Makler and J. Rafelski, *J. Phys. G* **25** (1999) 1935.

[7] S.A. Voloshin and Y. Zhang, *Z. Phys. C* **70** (1996), 665; A.M. Poskanzer and S.A. Voloshin, *Phys. Rev. C* **58** (1998), 1671.

[8] STAR Collaboration (K.H. Ackermann*et al.*), nucl-ex/0009011.

[9] Y. Hama and F.W. Pottag, IFUSP/p-481 (1984).

[10] E.V. Shuryak, *Yad. Fiz.* **16** (1972), 395.

[11] C.M. Hung and E.V. Shuryak, *Phys. Rev. Lett.* **75** (1995), 4003.

[12] F. Cooper and G. Frye, *Phys. Rev. D* **10** (1974), 186.

[13] For recent review, P. Danielewicz, nucl-th/0009091.

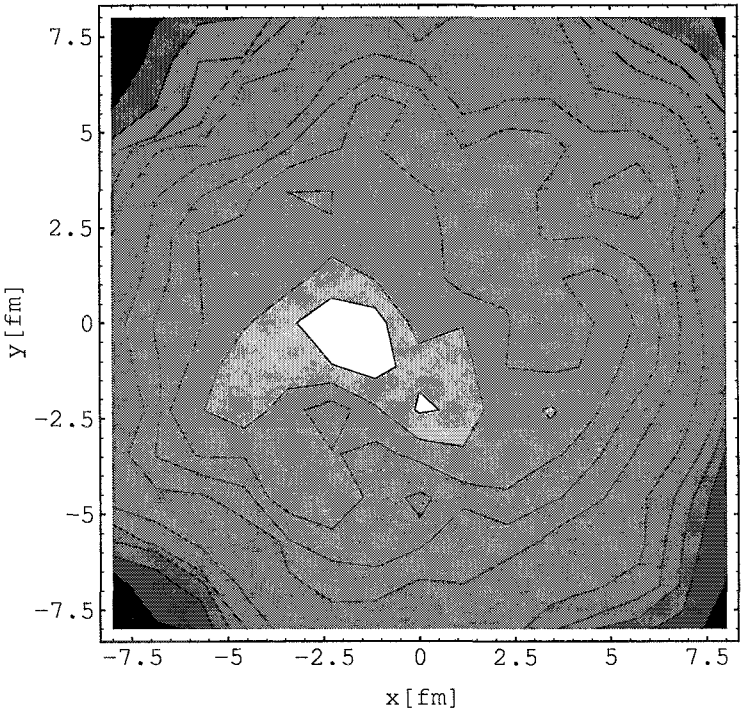

Figure 1: Initial energy density (counter plot $z = 0\ fm$ plane) of a typical event of Au+Au collision at energy $\sqrt{s} = 200A\ GeV$, impact parameter $b = 0fm$, produced by NeXus event generator[3].

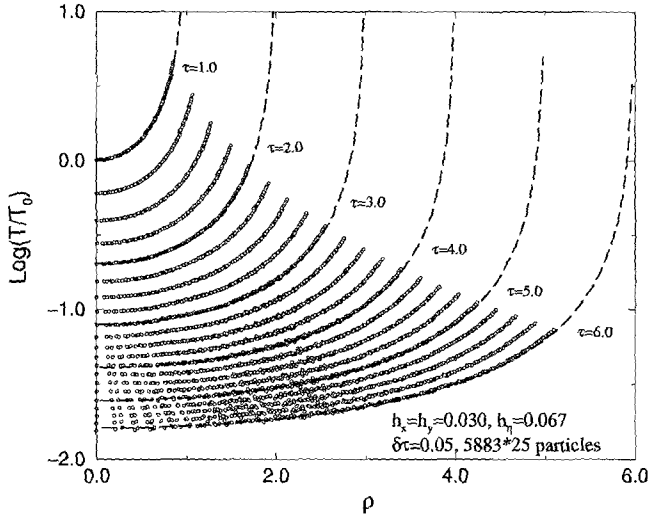

Figure 2: Comparison of results by SPH (open circles) with the analytical solution, eq.(16). The sizes of the parameters $h_x(=h_y)$, h_η and $d\tau$ used were 0.030, 0.067 and 0.05, respectively.

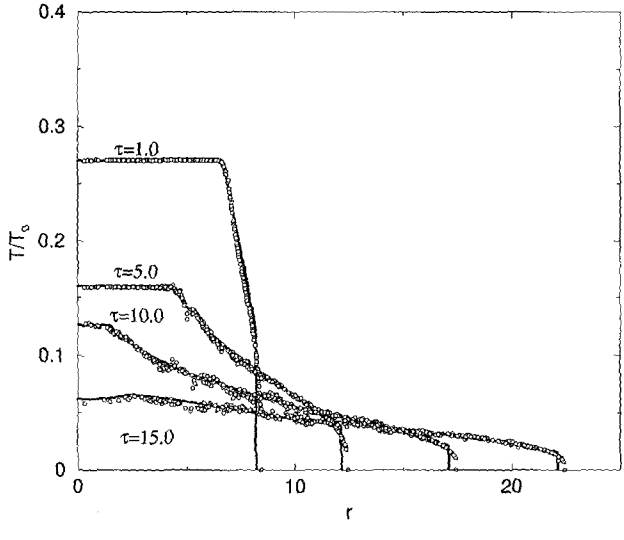

Figure 3: Numerical results by SPH (open circles) for the problem of longitudinaly scaling hydrodynamics using the Landau-type initial conditions in the transverse directions. The solid line has been obtained numerically by Hama and Pottag [9].

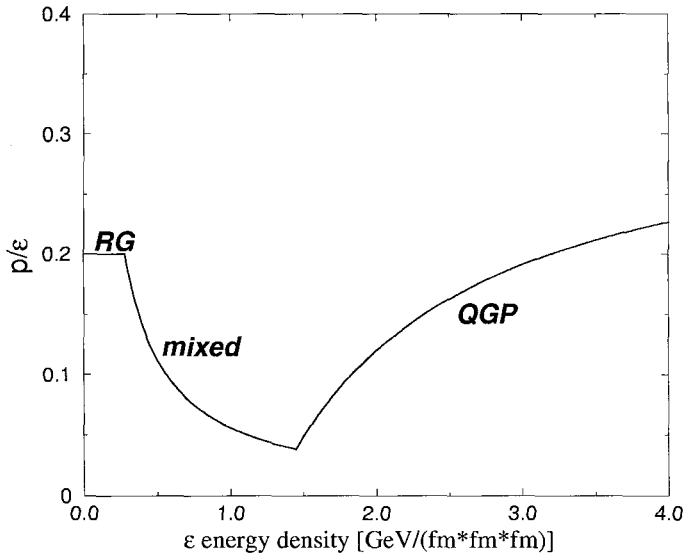

Figure 4: Equation of state which contains the QGP phase transition[11]. For resonance gas case, c_s^2=0.2(constant) is used.

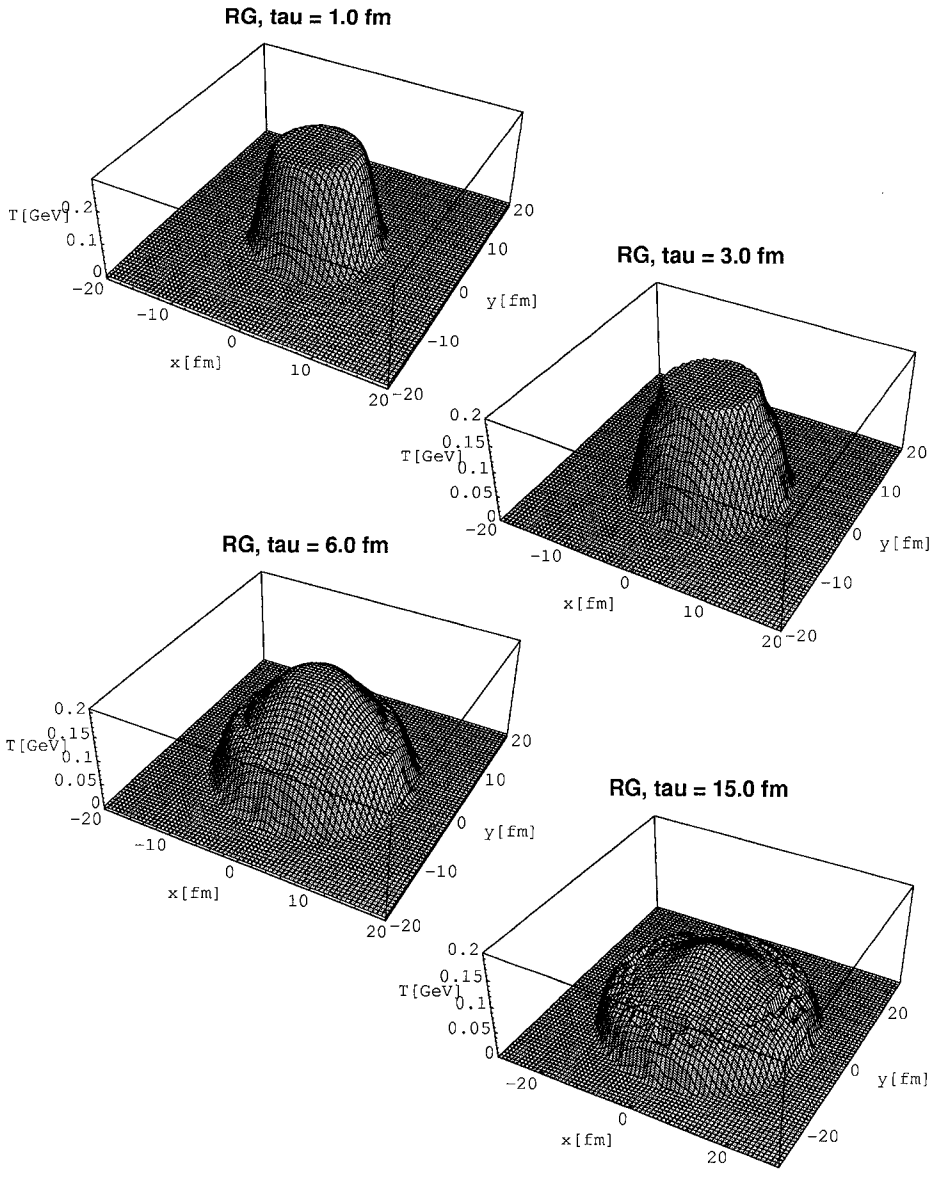

Figure 5: Hydrodynamical evolution (temperature T $[GeV]$ at $z = 0fm$ plane) using RG Eos. The smoothing scale parameter h used in x-y space is 1.0 fm and in η space 1.0, respectively.

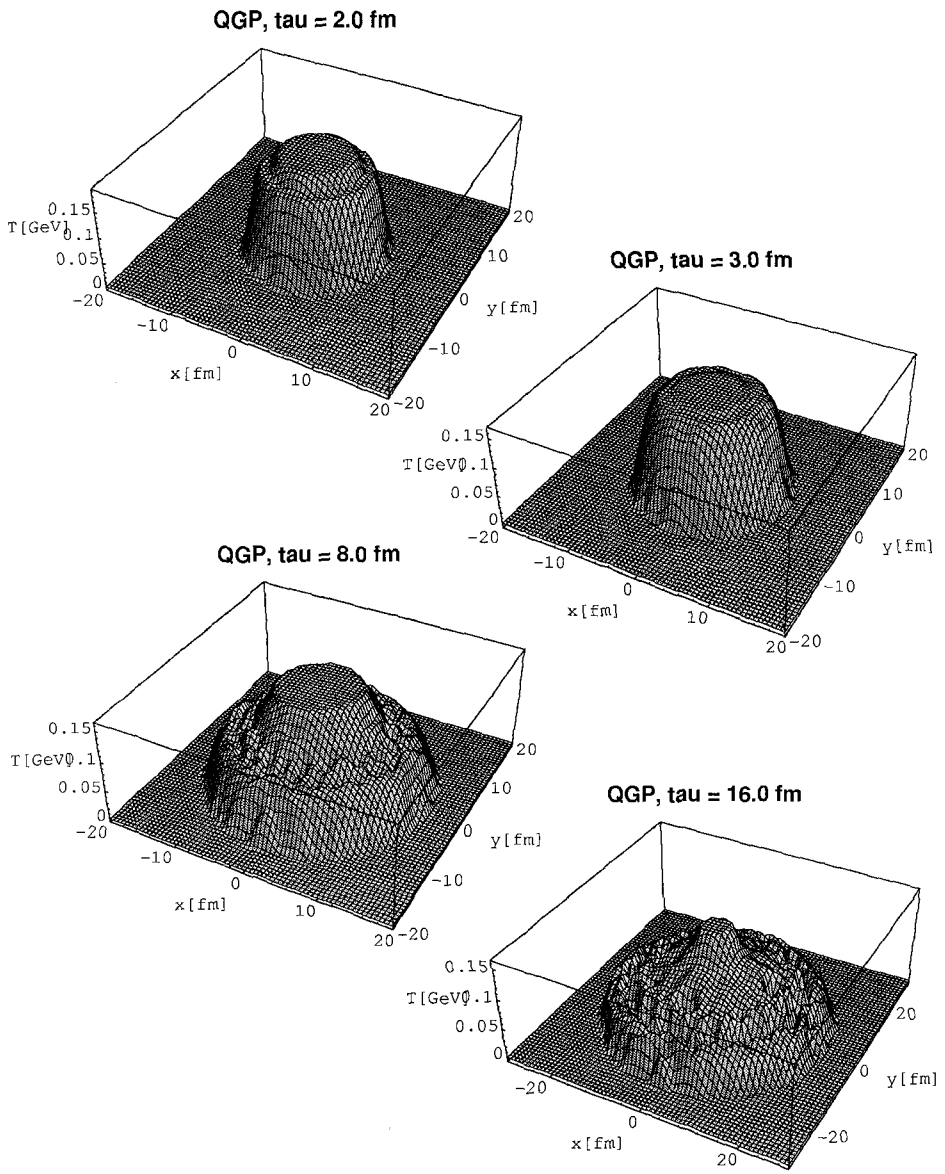

Figure 6: Hydrodynamical evolution (temperature T $[GeV]$ at $z = 0fm$ plane) using QGP Eos. At $\tau = 2.0$ fm, we can observe QGP phase (above $T > T_c = 0.16$ GeV) and mixed phase($T = T_c$) clearly. At around $\tau \sim 3$ fm, QGP phase almost disappear. Mixed phase survives up to about 25 fm.

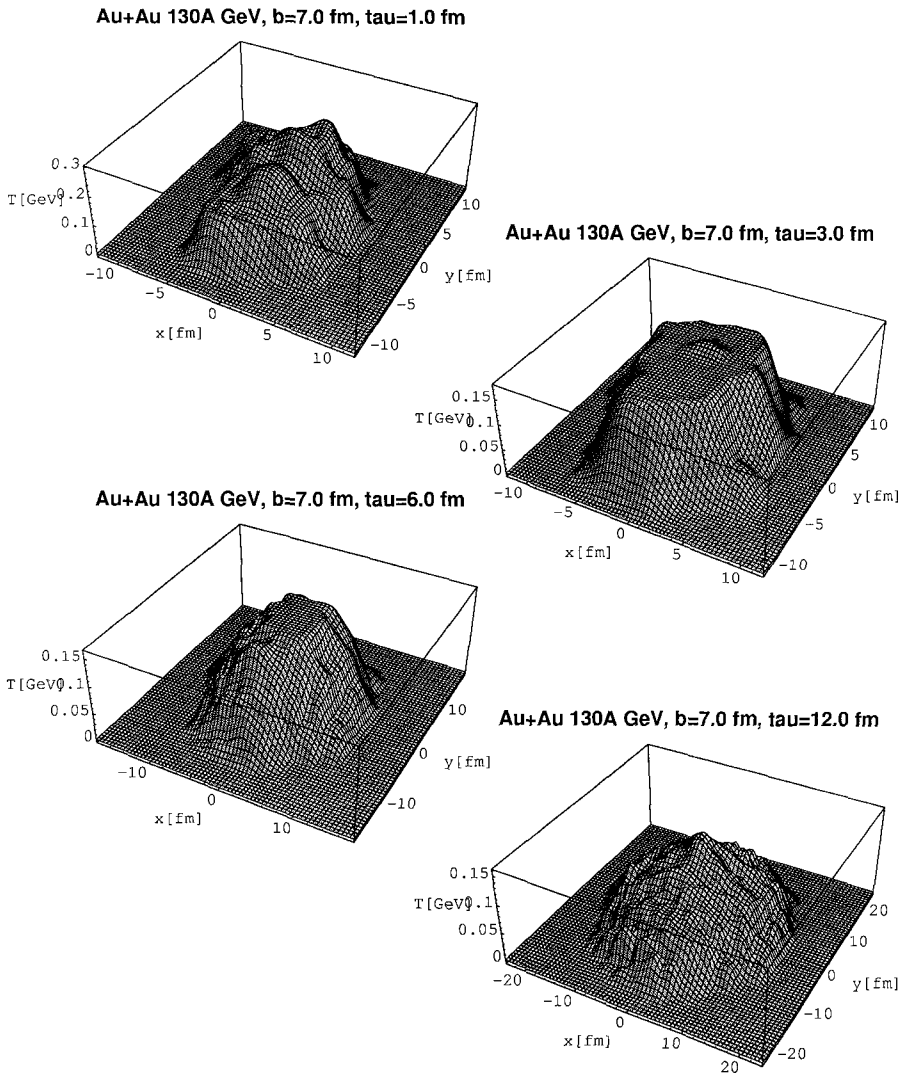

Figure 7: Hydrodynamical evolution (temperature T $[GeV]$) of a typical event in $Au+Au$ collision at energy $\sqrt{s} = 130A$ GeV for the impact parameter $b = 7.0$ fm (at $z = 0$ fm, impact parameter direction is parallel to x direction.). The initial conditions are produced by NeXus[3]. The EoS used is QGP one.

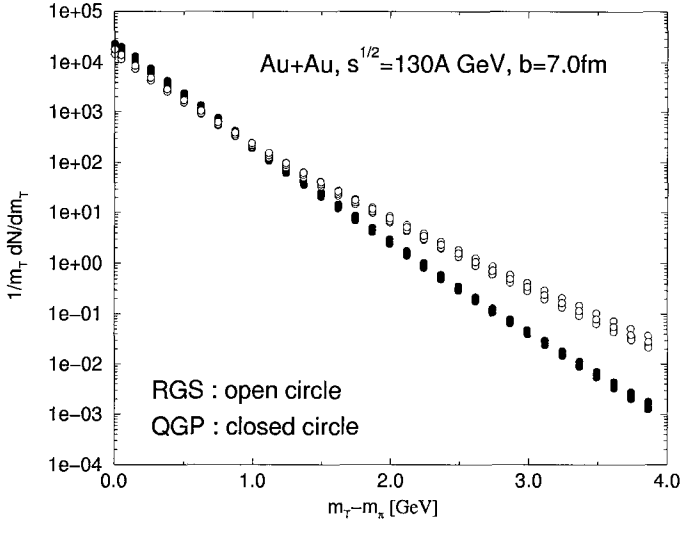

Figure 8: m_{T}-spectra in $Au + Au$ collisions at $\sqrt{s} = 130A\ GeV$, $b = 7.0\ fm$, for 5 events (open circles for RG and closed circles for QGP).

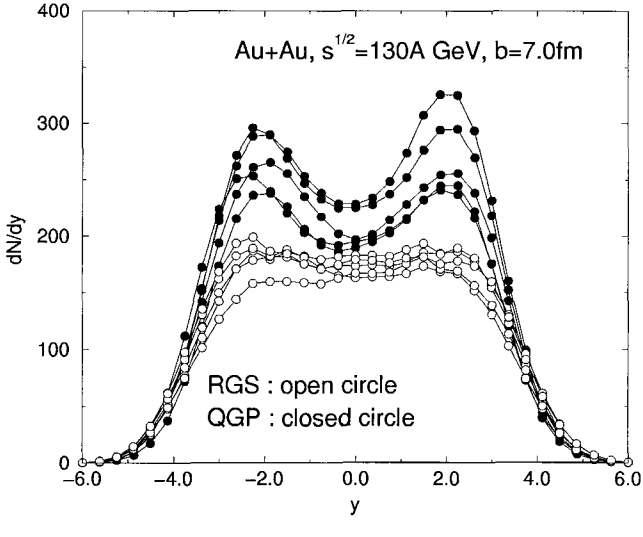

Figure 9: dN/dy in $Au+Au$ collisions at $\sqrt{s} = 130A\ GeV$, $b = 7.0\ fm$, for 5 events (open circles for RG and closed circles for QGP).

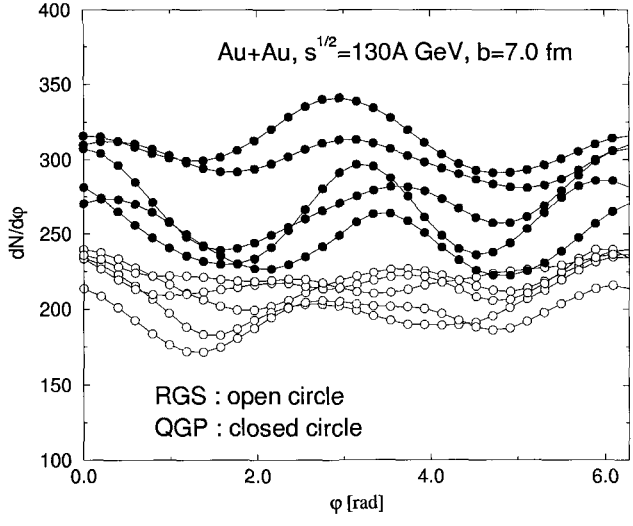

Figure 10: $dN/d\varphi$ in $Au + Au$ collisions at $\sqrt{s} = 130A\ GeV$, $b = 7.0\ fm$, for 5 events (open circles for RG and closed circles for QGP).

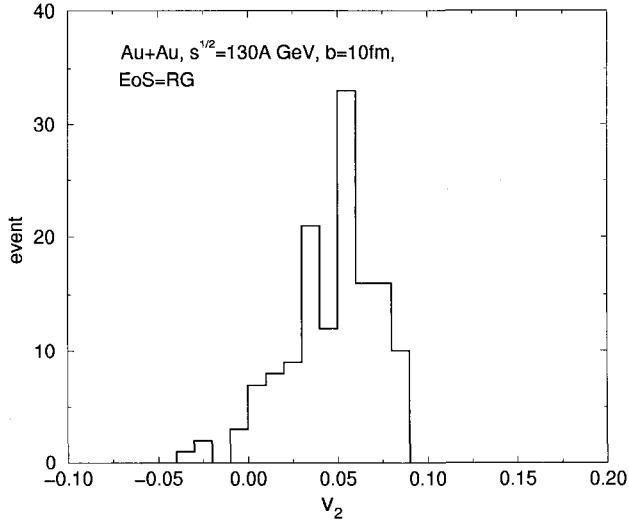

Figure 11: The distribution of elliptic-flow coefficients v_2 for $Au + Au$ collisions at energy $\sqrt{s} = 130A\ GeV (b = 10\ fm)$. RG EoS is used.

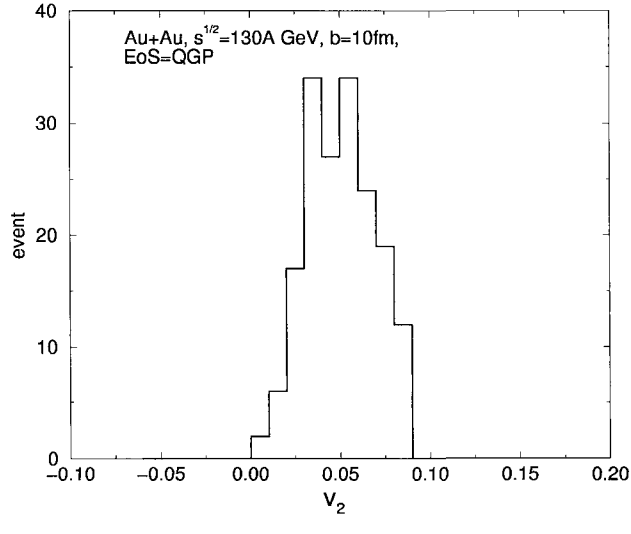

Figure 12: The distribution of elliptic-flow coefficients v_2 for $Au + Au$ collisions at energy $\sqrt{s} = 130A\ GeV (b = 10\ fm)$. QGP EoS is used.

$b\ [fm]$	EoS	event	$\langle v_1 \rangle$	δv_1	$\langle v_2 \rangle$	δv_2
7.0	RG	68	0.0151	0.0267	0.0406	0.0165
	QGP	72	0.0116	0.0210	0.0412	0.0140
10.0	RG	160	0.0144	0.0417	0.0497	0.0280
	QGP	180	0.0098	0.0240	0.0515	0.0199
12.0	RG	95	0.0076	0.0410	0.0535	0.0323
	QGP	119	0.0077	0.0262	0.0514	0.0237

Table 1: The average value and dispersions of the directed(v_1) and elliptic(v_2) flow coefficients for $Au + Au$ collisions at energy $\sqrt{s} = 130A\ GeV$.

$b\ [fm]$	EoS	event	$\tilde{T}$	$\delta\tilde{T}$
7.0	RG	55	0.231	0.0032
	QGP	58	0.215	0.0021
10.0	RG	90	0.233	0.0041
	QGP	119	0.214	0.0026
12.0	RG	79	0.234	0.0047
	QGP	100	0.213	0.0033

Table 2: The slope parameter $\tilde{T}$ and its dispersion $\delta\tilde{T}$.

$b\ [fm]$	EoS	event	y_c=1.875			y_c=3.00		
			$\langle n_{yc} \rangle$	δn_{yc}	$\delta n_{yc}/\langle n_{yc} \rangle$	$\langle n_{yc} \rangle$	δn_{yc}	$\delta n_{yc}/\langle n_{yc} \rangle$
7.0	RG	55	613.3	49.5	0.081	977.4	71.6	0.073
	QGP	58	926.1	81.1	0.087	1530.5	123.7	0.081
10.0	RG	160	312.8	43.0	0.137	506.1	65.8	0.130
	QGP	180	437.5	66.5	0.151	740.7	103.9	0.140
12.0	RG	79	162.8	35.6	0.219	268.9	56.2	0.209
	QGP	100	220.1	52.8	0.240	379.8	85.2	0.224

Table 3: Rapidity window y_c, impact parameter b and EoS dependence of the multiplicity fluctuation.

type	EoS	event	$\langle v_1 \rangle$	δv_1	$\langle v_2 \rangle$	δv_2
π	RG	160	0.0144	0.0417	0.0497	0.0280
	QGP	180	0.0098	0.0240	0.0515	0.0199
$\pi + \rho$ decay	RG	31	0.0135	0.0311	0.0530	0.0277
	QGP	43	0.0148	0.0180	0.0548	0.0246

Table 4: The average value and dispersions of the directed(v_1) and elliptic(v_2) flow coefficients for π and $\pi + \rho$ decay cases in $Au + Au$ collisions at energy $\sqrt{s} = 130A\ GeV$, impact parameter $b = 10.0\ fm$.

Marina Nielsen

Hadronic form factors from QCD Sum Rules

M. Nielsen [a] , F.S. Navarra [a] , F.O. Durães [a] , M.E. Bracco [b] , M. Chiapparini [b] and C. L. Schat [b]

[a]Instituto de Física, Universidade de São Paulo,
C.P. 66318, 05389-970 São Paulo, SP, Brazil

[b]Instituto de Física, Universidade do Estado do Rio de Janeiro,
Rua São Francisco Xavier 524 - 20559-900, Rio de Janeiro, RJ, Brazil

The $ND(D^*)\Lambda_c$ and $DD^*\pi$ form factors are evaluated in a full QCD sum rule calculation. We study the double Borel sum rule for the three point function of the hadron currents up to order six in the operator product expansion. The double Borel transform is performed with respect to the nucleon and Λ_c momenta, in the case of the $ND(D^*)\Lambda_c$ vertex and with respect of the D and D^* momenta, in the case of the $DD^*\pi$ vertex, and the form factor is evaluated as a function of the momentum Q^2 of the heavy meson or pion respectively. These form factors are relevant to evaluate the charmonium absorption cross section by hadrons. Our results are compatible with constant form factors in the $ND(D^*)\Lambda_c$ vertex and a gaussian form factor in the $DD^*\pi$ vertex.

1. Introduction

Of all experimental observables that are sensitive to the presence of the quark-gluon plasma (QGP), charmonium suppression [1] is among the most promising ones. Experimental investigation of charmonium production in nuclear reactions have been carried out for over a decade at CERN-SPS (p+A, O+U, S+U, Pb+Pb) and at Fermilab Tevatron (p+A) [1–5]. These studies have shown that the J/ψ and ψ' production on nuclear target is indeed suppressed relative to expectations from nucleon-nucleon reactions.

For p+A collisions the observed suppression of J/ψ and ψ' can be explained as absorption of a common precursor, probably a non-resonant, color-octet ($c\bar{c}$) state, on nucleons [6]. This systematics extends to O+U and S+U reactions for J/ψ, but for ψ' additional suppression is observed [4]. This additional suppression can be quantitatively described as absorption of the ψ' on co-moving hadrons [7–9]. Only recent data from Pb+Pb collision [5] have revealed the presence of an additional "anomalous" suppression mechanism for J/ψ. As a matter of fact, in ref. [5] it was claimed that the anomalous suppression of J/ψ observed in $Pb+Pb$ collisions at CERN-SPS indicated already the formation of QGP, since these experimental data ruled out conventional hadronic models for the J/ψ suppression.

However, there are calculations that reproduce the new NA50 data reasonably well up to the highest transverse energies [10–12], based on hadronic J/ψ dissociation alone. Therefore, while there are suggestions that the anomalous suppression may be due to the formation of the QGP, other more conventional mechanisms based on J/ψ absorption by comovers and nucleons have to be still considered.

The main ingredient in the calculations based on hadronic J/ψ dissociation is the magnitude of the J/ψ absorption cross section by hadrons, which is not known experimentally. In refs. [10–12] this cross section was introduced as a free parameter. Therefore, in order to use the J/ψ suppression as a signature for the formation of the QGP in heavy ion collisions it is important to have a better knowledge on the interactions between charmonium states and co-moving hadrons.

Various approaches have been used in evaluating the charmonium absorption cross section by hadrons. Some of them use meson exchange models based on hadronic effective lagrangians [13–18]. The couplings and form factors needed in these effective lagrangians are not phenomenologically known, and sometimes SU(4) relations are used to estimate them. However, we don't have

any evidence that SU(4) relations should be taken seriously into account. Also, in general, it is assumed a monopole form factor at the hadronic vertex [15,16], with another unknown parameter (the cut-off). The results obtained for the cross section are very sensitive to the couplings and to the form factors [15–17]. As an example, in ref. [15] it was shown that the $\pi J/\psi \to DD^*$ cross section may vary by almost one order of magnitude depending on the value of the cut-off. Therefore, it is very important to estimate these couplings and form factors with a more theoretical approach.

In this talk we report the use the QCD sum rule (QCDSR) method [19] based on the three-point function to evaluate the $ND(D^*)\Lambda_c$ and $DD^*\pi$ form factors and coupling constants.

2. The QCDSR Calculation

The fundamental assumption of the QCDSR approach is the principle of duality. Specifically one assumes that there exist a momentum interval over which a correlation function may be equivalentely described at both, the quark level and at the hadron level. Therefore, the underlying procedure of the QCDSR technique is the following: on one hand we calculate the correlation function at the quark level in terms of quark and gluon fields. On the other hand, the correlation function is calculated at the hadron level introducing hadron characteristics as masses, decay constants, form factors, etc. At the quark level the complex structure of the QCD vacuum leads us to employ the Wilson's operator product expansion (OPE). The calculation of the correlation function at the hadron level (or phenomenological side) proceeds by writing a dispersion relation for each one of the invariant structures of the correlator.

As usual, our goal is to make a match between the two representations of the correlation function. To improve the matching a Borel transform [19] is performed in both sides of the sum rule. The Borel transform is defined by

$$\tilde{f}(M^2) = \lim_{Q^2,n\to\infty} \frac{(Q^2)^{n+1}}{n!} \left(-\frac{d}{dQ^2}\right)^n f(Q^2) \,, \quad (1)$$

where $M^2 \equiv Q^2/n$ is the Borel mass. The Borel transform suppresses higher dimension operators in the OPE side by a factorial factor, and changes a power-law suppression to an exponential suppression of the higher mass states in the phenomenological side.

The basic idea, supported by ample successful applications, is that taking into account only the first few terms in the OPE, complemented by rather simple assumptions for the higher mass contributions to the dispersion relation, will already provide a good estimate to the amplitudes of interest.

Let us start with the $ND(D^*)\Lambda_c$ vertex. In a previous work [20] we have evaluated the $ND\Lambda_c$ coupling using the QCDSR. We have obtained $g_{ND\Lambda_c} = 6.7 \pm 2.1$ while SU(4) relations used in ref. [16] give $g_{ND\Lambda_c} = 14.8$. Of course the relevance of this difference can not be underestimated since the cross section is proportional to the square of the coupling constant. To calculate nucleon-meson-Λ_c form factor using the QCD sum rule approach [19] we consider the three-point function:

$$\Gamma_M(p,p',q) = \int d^4x d^4y e^{ip'x} e^{-iqy} \times \langle 0|T\{\eta_{\Lambda_c}(x) j_M(y) \overline{\eta}_N(0)\}|0\rangle \,, \quad (2)$$

where the $D(D^*)$ current, $j_5(j_\mu)$, is generically called j_M, and the currents are given by [21,22]

$$\eta_{\Lambda_c} = \varepsilon_{abc}(u_a^T C\gamma_5 d_b) Q_c \,, \quad (3)$$

$$\eta_N = \varepsilon_{abc}(u_a^T C\gamma^\mu u_b)\gamma_5\gamma_\mu d_c \,, \quad (4)$$

$$j_5 = \overline{Q} i\gamma_5 u \,, \quad (5)$$

$$j_\mu = \overline{Q}\gamma_\mu u \,. \quad (6)$$

Q, u and d are the charm, up and down quark fields respectively, C is the charge conjugation matrix and $q = p' - p$.

The above expression can be easily generalized to the $DD^*\pi$ vertex with an off-shell pion, by changing $\eta_{\Lambda_c} \to j = i\bar{Q}\gamma_5 u$, $\overline{\eta}_N \to j_\mu^\dagger = \bar{d}\gamma_\mu Q$ and $j_M \to j_\pi = i\bar{u}\gamma_5 d$, which are the interpolating fields for D, D^* and π respectively.

The phenomenological side of the vertex function is obtained by the consideration of the Λ_c and

N intermediate states contribution to the matrix element in Eq.(2):

$$\Gamma_M^{(phen)}(p,p',q) = \lambda_{\Lambda_c}\lambda_N \frac{(\not{p}' + M_{\Lambda_c})}{p'^2 - M_{\Lambda_c}^2} g_M(q^2)$$

$$\times \frac{(\not{p} + M_N)}{p^2 - M_N^2} + \text{higher resonances}\,, \qquad (7)$$

where λ_{Λ_c} and λ_N are the couplings of the currents with the respective baryonic states obtained from the respective mass sum rules for Λ_c [22] and for the nucleon [21]:

$$|\lambda_{\Lambda_c}|^2 = e^{M_{\Lambda_c}^2/M_M'^2}\left\{\frac{m_c^4}{512\pi^4}\int_{m_c^2}^{u_o} du\, e^{-u/M_M'^2}\right.$$

$$\times \left[\left(1-\frac{m_c^4}{u^2}\right)\left(1-\frac{8u}{m_c^2}+\frac{u^2}{m_c^4}\right)\right.$$

$$\left. - 12\ln\left(\frac{m_c^2}{u}\right)\right]\frac{\langle\bar{q}q\rangle^2}{6}e^{-m_c^2/M_M'^2}\Bigg\}\,, \qquad (8)$$

$$|\lambda_N|^2 = e^{M_N^2/M_M^2}\left(\frac{M_M^8}{32\pi^4}E_2 + \frac{2}{3}\langle\bar{q}q\rangle^2\right)\,, \qquad (9)$$

where $E_2 = 1-e^{-s_0/M_M^2}(1+s_0/M_M^2+s_0^2/(2M_M^4))$ accounts for the continuum contribution with u_0 and s_0 being the continuum thresholds for Λ_c and the nucleon respectively. We have neglected the contribution of the gluon condensate in the mass sum rules, since it is of little influence. In Eqs. (8) and (9) M_M^2 and $M_M'^2$ represent the Borel masses in the two-point function of the nucleon and Λ_c respectively.

The current-meson-baryon couplings appearing in Eq. (7) are given in terms of the form factors $g_{ND\Lambda_c}(q^2)$ and $g_{ND^*\Lambda_c}(q^2)$ by

$$g_5(q^2) = i\gamma_5 \frac{m_D^2 f_D}{m_c}\frac{g_{ND\Lambda_c}(q^2)}{q^2-m_D^2}\,, \qquad (10)$$

$$g_\mu(q^2) = m_{D^*} f_{D^*}\frac{g_{ND^*\Lambda_c}(q^2)}{q^2-m_{D^*}^2}\left(-\gamma_\mu + \frac{\not{q}q_\mu}{m_{D^*}^2}\right)\,, \qquad (11)$$

where m_D, m_D^*, f_D and f_{D^*} are the masses and decay constants of the mesons D and D^* respectively, and m_c is the c quark mass.

The general expression for the vertex function in Eq.(2) has four independent structures in the case of Γ_5 [20] and twelve in the case of Γ_μ [23]. In principle any of the four (twelve) invariant structures appearing in the Γ_M expression can be used to calculate the form factor and the sum rules should yield the same result. However, each sum rule could have uncertainties due to the truncation in the OPE side, at the quark level, and different contributions from the continuum, at the hadron level. Therefore, depending on the Dirac structure we can obtain different results due to the uncertainties mentioned above. The tradicional way to control these uncertainties, and therefore to check the reliability of the sum rule, is to evaluate the stability of the result as a function of the Borel mass.

Recently, in ref.[24] it was pointed out that a better determination of $g_{\pi NN}$ can be done with the help of the $\gamma_5\sigma_{\mu\nu}$ structure, since this structure is independent of the effective models employed in the phenomenological side and it gets a smaller contribution from the single pole term coming from $N \to N^*$ transition. This was confirmed also in the case of the g_{NKY} coupling constant [25]. Therefore, we will also employ the $\sigma^{\mu\nu}\gamma_5 p'_\mu p_\nu$ structure to evaluate the $ND\Lambda_c$ form factor and coupling constant, and compare our results with the previous evaluation [20] carried out in the $i\not{q}\gamma_5$ structure. In the case of $ND^*\Lambda_c$ vertex, we will study the sum rule based on the $\not{p}'\gamma_\mu\not{p}$ structure since, in general, the structures with a large number of γ matrices are more likely to be stable. We call F the invariant amplitude associated with these structures. The contribution of higher resonances and continuum in Eq. (7) will be taken into account as usual in the standard form of ref. [26].

As mentioned before, the QCD side, or theoretical side, of the vertex function is evaluated by performing the OPE of the operator in Eq. (2). Since the dimension of Eq.(2) is four and $p'p$ takes away two dimensions, only even dimension operators contribute to structures $\sigma^{\mu\nu}\gamma_5 p'_\mu p_\nu$ and $\not{p}'\gamma_\mu\not{p}$. The diagrams that contribute, after a double Borel transformation, up to dimension six are the perturbative, quark condensate times the charm quark mass and the four-quark conden-

sate. The gluon condensate also contributes, but it always appears with a large suppression factor which arises from the two-loop internal momentum integration. Therefore, its contribution is of little influence and will be neglected. The perturbative contribution is evaluated by writing a double dispersion relation to the invariant amplitude, F, and using the Cutkosky's rules [27] to evaluate the double discontinuity (see ref.[26]). After doing a double Borel transformation [26] in both variables $P^2 = -p^2 \to M^2$ and $P'^2 = -p'^2 \to M'^2$, and subtracting the continuum contribution, we get

$$\left[\tilde{F}(M^2, M'^2, Q^2)\right]_{per} = -\frac{1}{4\pi^2}\int_{m_c^2}^{u_0} du \int_0^{s_0} ds \,(\rho(u,s,Q^2)\, e^{-u/M'^2} e^{-s/M^2}) \,, \tag{12}$$

with

$$\rho(u,s,Q^2) = \pm\frac{3}{8\pi^2}\frac{1}{\sqrt{\lambda(s,u,Q^2)}}\int_0^s dm^2 \,\{m^2 \left(-1 + \frac{m_c^2(s-u-Q^2)+(s-u)^2+Q^2(s+u)}{\lambda(s,u,Q^2)}\right) + \frac{2m^4Q^2}{\lambda(s,u,Q^2)}\Big\}\Theta(1-(\overline{\cos\theta_K})^2)\Theta(u-Q^2- m_c^2+\frac{Q^2u}{m_c^2}-s)\,, \tag{13}$$

where

$$\overline{\cos\theta_K} = 2s\frac{u+m^2-m_c^2-p_0'(s+m^2)/\sqrt{s}}{(s-m^2)\sqrt{\lambda(s,u,Q^2)}}\,, \tag{14}$$

with $p_0' = (s+u+Q^2)/(2\sqrt{s})$ and $\lambda(s,u,Q^2) = s^2+u^2+Q^4-2su+2Q^2s+2Q^2u$.

In Eq.(12) $\tilde{F}$ stands for the double Borel transformation of the amplitude F, and the subscript "*per*" refers to the perturbative contribution. u_0 and s_0 are the continuum thresholds for the baryons Λ_c and nucleon respectively.

The next lowest dimension operator is the quark mass times the quark condensate with dimension four. Since we are neglecting the light quark masses, only terms proportional to $m_c\langle\bar{q}q\rangle$ will appear. These terms give, after the double Borel transformation

$$\left[\tilde{F}(M^2,M'^2,Q^2)\right]_{<\bar{q}q>} = -\frac{m_c\langle\bar{q}q\rangle}{4\pi^2}\int_{m_c^2}^{u_0} du \times \int_0^{s_0} ds\,\alpha(s,u,Q^2)e^{-u/M'^2}e^{-s/M^2}\,, \tag{15}$$

where

$$\alpha(s,u,Q^2) = \pm\frac{s(2m_c^2+s-u+Q^2)}{(\lambda(s,u,Q^2))^{3/2}}\Theta(u - Q^2-m_c^2+\frac{Q^2u}{m_c^2}-s)\,. \tag{16}$$

The contribution from the diagram involving the four-quark condensate $\langle\bar{q}q\bar{q}q\rangle$ ($\simeq\langle\bar{q}q\rangle^2$) is:

$$\left[\tilde{F}(M^2,M'^2,Q^2)\right]_{<\bar{q}q>^2} = \pm\frac{\langle\bar{q}q\rangle^2}{3}e^{-m_c^2/M'^2}\,. \tag{17}$$

In Eqs. (13) (16) and (17) the + and − sign refers to the $ND\Lambda_c$ and $ND^*\Lambda_c$ vertices repectively.

The Borel transformation of the phenomenological side is given by

$$\left[\tilde{F}(M^2,M'^2,Q^2)\right]_{phen} = \lambda_{\Lambda_c}\lambda_N G_{NM\Lambda_c}(Q^2) \times e^{-M_N^2/M^2}e^{-M_{\Lambda_c}^2/M'^2}\,, \tag{18}$$

where the continuum contribution has already been incorporated in the OPE side, through the continuum thresholds s_0 and u_0. In Eq. (18) we have defined

$$G_{NM\Lambda_c}(Q^2) = \frac{m_D^2 f_D}{m_c}\frac{g_{ND\Lambda_c}(Q^2)}{Q^2+m_D^2} = m_{D^*}f_{D^*}\frac{g_{ND^*\Lambda_c}(Q^2)}{Q^2+m_{D^*}^2}\,, \tag{19}$$

for $M = D$ and for $M = D^*$ respectively.

The form factors $g_{ND\Lambda_c}(Q^2)$ and $g_{ND^*\Lambda_c}(Q^2)$ are obtained by matching Eq. (18) with the sum of Eqs. (12), (15) and (17). We obtain:

$$g_{ND\Lambda_c}(Q^2) = \frac{e^{M_N^2/M^2}e^{M_{\Lambda_c}^2/M'^2}}{\lambda_{\Lambda_c}\lambda_N}\frac{m_c(Q^2+m_D^2)}{m_D^2 f_D}$$

$$\times \quad \left[-\frac{1}{4\pi^2} \int_{m_c^2}^{u_0} du \int_0^{s_0} ds\, e^{-u/M'^2} e^{-s/M^2} \right.$$
$$\times \quad \left(\rho(u,s,Q^2) + m_c \langle \bar{q}q \rangle \alpha(s,u,Q^2) \right)$$
$$+ \quad \left. \frac{\langle \bar{q}q \rangle^2}{3} e^{-m_c^2/M'^2} \right] , \qquad (20)$$

and

$$g_{ND^*\Lambda_c}(Q^2) = -\frac{e^{M_N^2/M^2} e^{M_{\Lambda_c}^2/M'^2}}{\lambda_{\Lambda_c} \lambda_N} \frac{Q^2 + m_{D^*}^2}{m_{D^*} f_{D^*}}$$

$$\times \quad \left[-\frac{1}{4\pi^2} \int_{m_c^2}^{u_0} du \int_0^{s_0} ds\, e^{-u/M'^2} e^{-s/M^2} \right.$$
$$\times \quad \left(\rho(u,s,Q^2) + m_c \langle \bar{q}q \rangle \alpha(s,u,Q^2) \right)$$
$$+ \quad \left. \frac{\langle \bar{q}q \rangle^2}{3} e^{-m_c^2/M'^2} \right] , \qquad (21)$$

Comparing Eqs. (20), (21), (8) and (9) we can see that the exponentials multiplying Eqs. (20) and (21) disappear if we choose

$$2M_M^2 = M^2 \quad \text{and} \quad 2{M'_M}^2 = M'^2 . \qquad (22)$$

Indeed, this way of relating the Borel parameters in the two- and three-point functions is a crucial ingredient for the incorporation of heavy quark symmetries, and leads to a considerable reduction of the sensitivity to input parameters, such as continuum thresholds s_0 and u_0, and to radiative corrections [23,28].

In the case of the $DD^*\pi$ vertex, the phenomenological side of the correlation function, $\Gamma_\mu(p,p',q)$, is obtained by the consideration of D and D^* state contribution to the matrix element in Eq. (2) [29]:

$$\Gamma_\mu^{(phen)}(p,p',q) = C_{DD^*} \frac{g_{D^*D\pi}(q^2)}{q^2 - m_\pi^2} \frac{1}{p^2 - m_{D^*}^2} \times$$
$$\frac{1}{p'^2 - m_D^2} \left(-p'_\mu + \frac{m_{D^*}^2 + m_D^2 - q^2}{2m_{D^*}^2} p_\mu \right) +$$
$$\text{higher resonances} , \qquad (23)$$

where

$$C_{DD^*} = \frac{m_D^2 m_{D^*} m_\pi^2 f_D f_{D^*} f_\pi}{(m_u + m_d) m_c} . \qquad (24)$$

After a double Borel transform, the sum rule on the structure p_μ, which we found to be the more stable one, is given by

$$-C_{DD^*} \frac{m_{D^*}^2 + m_D^2 + Q^2}{2m_{D^*}^2} \frac{g_{D^*D\pi}(q^2)}{Q^2 + m_\pi^2} \times$$
$$e^{-m_{D^*}^2/M^2} e^{-m_D^2/M'^2} = -\frac{1}{4\pi^2} \int_{m_c^2}^{s1_0} ds \int_{m_c^2}^{u1_0} du \left[\right.$$
$$\left. \rho_1(s,u,Q^2) e^{-s/M^2} e^{-u/M'^2} \right] , \qquad (25)$$

where $s1_0$ and $u1_0$ are the continuum thresholds for the D^* and D mesons respectively.

We consider diagrams up to dimension four which include the perturbative diagram and the gluon condensate. The quark condensate term does not contribute since it depends only on one external momentum and, therefore, it is eliminated by the double Borel transformation. Higher dimension condensates are strongly suppressed in the case of heavy quarks [30–33]. The double discontinuity of the perturbative contribution reads:

$$\rho_1^{(pert)}(s,u,Q^2) = -\frac{3Q^2 u(2m_c^2 - s - u - Q^2)}{[(s+u+Q^2)^2 - 4su]^{3/2}} , \qquad (26)$$

and the integration limit condition is

$$(s - m_c^2)(u - m_c^2) \geq Q^2 m_c^2 . \qquad (27)$$

For consistency we use in our analysis the QCDSR expressions for the decay constants up to dimension four in lowest order of α_s [31].

3. Results and Discussion

The parameter values used in all calculations are: $m_u + m_d = 14$ MeV, $m_c = 1.5$ GeV, $m_D = 1.87$ GeV, $m_{D^*} = 2.01$ GeV,$M_N = 938$ MeV, $M_{\Lambda_c} = 2.285$ GeV, $f_D = 170$ MeV $f_{D^*} = 240$ MeV [31], $f_\pi = 131.5$ MeV, $\langle \bar{q}q \rangle = -(0.23)^3$ GeV^3, $\langle g^2 G^2 \rangle = 0.5$ GeV^4.

In the case of the $ND(D^*)\Lambda_c$ form factors we parametrize the continuum thresholds as

$$s_0 = (M_N + \Delta_s)^2 , \qquad (28)$$

and

$$u_0 = (M_{\Lambda_c} + \Delta_u)^2 . \qquad (29)$$

The values of u_0 and s_0 are extracted from the two-point function sum rules for M_{Λ_c} and M_N in

Eqs. (8) and (9) and the respective sum rules in the **1** structure given in refs. [21,22]. We found a good stability for M_{Λ_c} and M_N, being able to reproduce the experimental values for the masses in the Borel mass $M_M^2 \sim 1\,\mathrm{GeV}^2$ and $M_M'^2 \sim 6\,\mathrm{GeV}^2$, with $\Delta_s = 0.7\,\mathrm{GeV}$ and $\Delta_u = 0.6\,\mathrm{GeV}$, which are the values that we are going to use in the calculations.

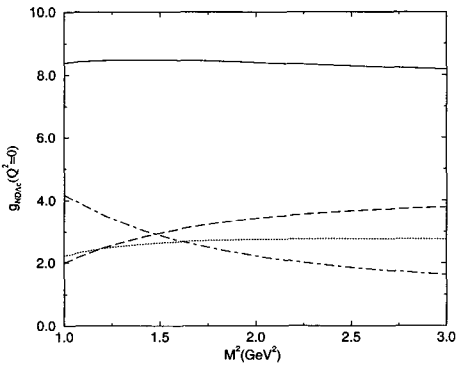

Figure 1. Borel dependence of the perturbative (dashed line), quark condensate (dotted line) and four quark condensate (dot-dashed line) contributions to the $ND\Lambda_c$ form factor (solid line) at $Q^2 = 0$.

To allow for different values of M^2 and M'^2 we take them proportional to the respective baryon masses. In this way we study the sum rule as a function of M^2 at a fixed ratio

$$\frac{M^2}{M'^2} = \frac{M_N^2}{M_{\Lambda_c}^2} \,. \tag{30}$$

In Fig. 1 we show the behavior of the perturbative, quark condensate and four quark condensate contributions to the form factor $g_{ND\Lambda_c}(Q^2)$ at $Q^2 = 0\ \mathrm{GeV}^2$ as a function of the Borel mass M^2. We observe that the different contributions add to give a very stable result as a function of the Borel mass. Since the Borel masses in the two- and three-point functions are related by Eq. (22) and since $M_M^2 \sim 1\,\mathrm{GeV}^2$, to study the Q^2 dependence of the form factor we fix $M^2 = 2.5\,\mathrm{GeV}^2$ where the perturbative contribution is the dominant one. The behaviour of the curve for other Q^2 values is similar, however, for $Q^2 > 1.5\,\mathrm{GeV}^2$ the perturbative contribution is no longer the dominant one. In Fig. 2 we show the Q^2 dependence of

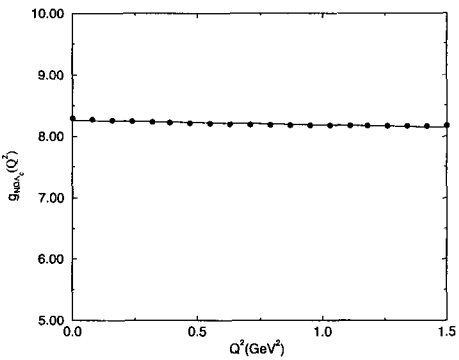

Figure 2. Momentum dependence of the $ND\Lambda_c$ form factor (dots). The solid line give the parametrization of the QCDSR results with a monopole form.

the form factor in the region $0 \leq Q^2 \leq 1.5\,\mathrm{GeV}^2$ (dots) where we believe we can trust the QCDSR results. We see that the form factor is practically constant in this region, showing a tiny decrease. We can fit the QCDSR results with a monopole form, as can be seen by the solid line in Fig. 2, and we get $g_{ND\Lambda_c}(Q^2) = 843/(102 + Q^2)$ which corresponds to a cut-off of order of 10 GeV, much bigger than the values used in ref. [16]. If we vary the value of the Borel mass used to extract the Q^2 dependence of the form factor we can even get a result that shows a tiny increase in the considered region. Therefore, in view of the uncertainties involved in the approach, we can say that the QCDSR give a constant value for the form factor. Considering 20% variation in the continuum thresholds and f_D varying in the interval

$f_D = 170 \pm 10$ MeV [31] we get:

$$g_{ND\Lambda_c}(Q^2) = 7.9 \pm 0.9\,, \qquad (31)$$

in agreement with our previous estimate of the coupling constant [20].

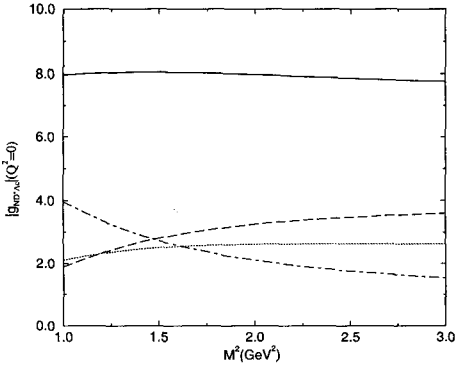

Figure 3. Borel dependence of the perturbative (dashed line), quark condensate (dotted line) and four quark condensate (dot-dashed line) contributions to the $ND^*\Lambda_c$ form factor (solid line) at $Q^2 = 0$.

The same analysis can be done for $g_{ND^*\Lambda_c}(Q^2)$ and in Fig. 3 we show the perturbative, quark condensate and four quark condensate contributions to the form factor $g_{ND^*\Lambda_c}(Q^2)$ at $Q^2 = 0$ GeV^2 as a function of the Borel mass M^2. Since the OPE sides of both form factors differ only by a sign the aspect of Fig. 2 is very similar to Fig. 3. In Fig. 4 we show the Q^2 dependence of the form factor $g_{ND^*\Lambda_c}(Q^2)$, extracted at $M^2 = 2.5$ GeV, in the region $0 \leq Q^2 \leq 1.5$ GeV^2 (dots). Again we observe that the form factor is practically constant in this region, showing a tiny decrease. Fitting the QCDSR results with a monopole form (solid line in Fig. 4) we get $g_{ND^*\Lambda_c}(Q^2) = -204/(26.2 + Q^2)$ which corresponds to a cut-off of order of 5 GeV, still much bigger than the values used in ref. [16]. Despite the fact that for this particular choice of M^2, s_0

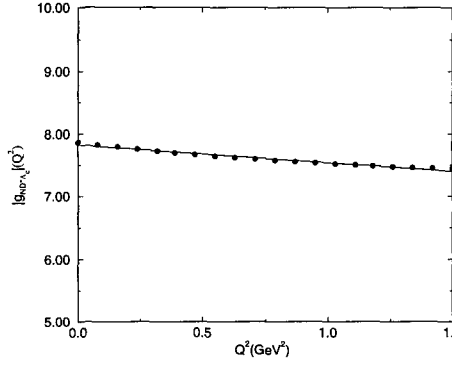

Figure 4. Momentum dependence of the $ND^*\Lambda_c$ form factor (dots). The solid line give the parametrization of the QCDSR results with a monopole form.

and u_0 we get a form factor with a smaller cut-off than obtained for $g_{ND\Lambda_c}(Q^2)$, varying M^2 and the continuun thresholds we still can get results that show a tiny increase in the considered region. Therefore, also in this case, due to the uncertainties involved in the approach, we conclude that the QCDSR give a constant value for the form factor. Considering 20% variation in the continuum thresholds and f_{D^*} varying in the interval $f_{D^*} = 240 \pm 20$ MeV [31] we get:

$$g_{ND^*\Lambda_c}(Q^2) = -7.5 \pm 1.1\,, \qquad (32)$$

It is important to mention that constant form factors in hadronic vertices have already been found in the context of QCDSR. This is the case of the $g_{DD^*\pi}$ form factor. This form factor has been studied in the QCDSR approach for an off-shell D^* [31,34–36], and for an off-shell pion [29]. As a matter of fact, in refs. [31,34–36] the authors analyze the semileptonic $f_+(t)$ form factor defined by

$$\begin{aligned}\langle \pi(p_\pi)|\bar{u}\gamma_\mu c|D(p_D)\rangle &= (p_\pi + p_D)_\mu f_+(t) \\ &+ (p_D - p_\pi)_\mu f_-(t)\,, \qquad (33)\end{aligned}$$

where $t = q^2 = (p_D - p_\pi)^2$. Since the vector current $V_\mu = \bar{u}\gamma_\mu c$ has the same quantum numbers as the vector meson D^*, the same sum rules

studied in refs. [31,34–36] can be used to study the hadronic form factor $g_{DD^*\pi}(t)$, for an off-shell D^* meson. It is only the phenomenological side of the sum rule that has to be modified to allow for a coupling between the vector current and the vector meson:

$$\langle\pi(p_\pi)|V_\mu|D(p_D)\rangle = \langle 0|V_\mu|\pi(-p_\pi)D(p_D)\rangle$$

$$= \langle 0|V_\mu|D^*(q)\rangle\frac{1}{t-m_{D^*}^2}\langle D^*(q)\pi(p_\pi)|D(p_D)\rangle \ . (34)$$

The $g_{DD^*\pi}(t)$ form factor is defined by the strong amplitude

$$\langle D^*(q,\epsilon)\pi(p_\pi)|D(p_D)\rangle = g_{DD^*\pi}(p_D+p_\pi)^\alpha\epsilon_\alpha \ . (35)$$

Therefore, using the the vacuum to vector meson transition amplitude defined in terms of the vector meson decay constant f_{D^*}:

$$\langle D^*(q,\epsilon)|V_\mu|0\rangle = m_{D^*}f_{D^*}\epsilon_\mu^* \ ; \qquad (36)$$

we can rewrite Eq. (34) as

$$\langle\pi(p_\pi)|V_\mu|D(p_D)\rangle = -\frac{m_{D^*}f_{D^*}g_{DD^*\pi}(t)}{t-m_{D^*}^2}\Big((p_\pi$$

$$+p_D)_\mu - \frac{q_\mu(p_D^2-p_\pi^2)}{m_{D^*}^2}\Big) \ . \qquad (37)$$

Comparing Eqs. (33) and (37) we imediately see that $g_{DD^*\pi}(t)$ and $f_+(t)$ are related by

$$f_+(t) = \frac{m_{D^*}f_{D^*}g_{DD^*\pi}(t)}{m_{D^*}^2-t} \ . \qquad (38)$$

The authors of refs. [31,35] claim that the QCDSR results for $f_+(t)$ can be well fitted by a monopole form with a pole mass $m_{pol} = m_{D^*}$. According with Eq. (38) this implies a constant $g_{DD^*\pi}(t)$. More recently the authors of [36], tried to fit their QCDSR results with a double pole parametrization of the type

$$f_+(t) = \frac{f_+(0)}{(1-t/m_{D^*}^2)(1-\alpha t/m_{D^*}^2)} \ . \qquad (39)$$

They have obtained $\alpha = 0.01\ ^{+0.11}_{-0.07}$ and, therefore, they have concluded that α is consistent with zero, which means the complete dominance of the vector meson pole to f_+ with a consequent prediction of a constant hadronic form factor in the $DD^*\pi$ vertex.

It is interesting to notice that, due to the uncertainties in the value of α given above, one can not even rule out a $DD^*\pi$ form factor that slightly growns in the Euclidian region, as mentioned above in the case of $ND(D^*)\Lambda_c$.

A very different result for the form factor in the $DD^*\pi$ vertex is obtained in the case of an off-shell pion [29]. This form factor is important in the processes described in ref. [37], which could contribute to explain the enhacement in the production of dileptons of intermediate masses, also observed in the NA50 experiment.

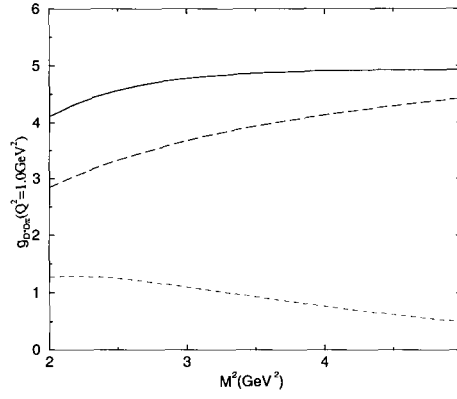

Figure 5. M^2 dependence of the perturbative (long-dashed line) and gluon condensate (dashed line) contributions to the $D^*D\pi$ form factor at $Q^2 = 1$ GeV^2 (solid line) for $\Delta_s = \Delta_u = 0.5$ GeV.

The continuum thresholds for the sum rule Eq. (25) are of order $s1_0 = (m_{D^*} + \Delta_{s1})^2$ and $u1_0 = (m_D + \Delta_{u1})^2$ with $\Delta_{s1} = \Delta_{u1} = 0.5\,\text{GeV}$. In our study we allow for a small variation in Δ_{s1} and Δ_{u1} to test the sensitivity of our results to the continuum contribution. In this case the

Borel masses are related by:

$$\frac{M^2}{M'^2} = \frac{m_{D^*}^2}{m_D^2} \,. \tag{40}$$

In Fig. 5 we show the behavior of the perturbative and gluon condensate contributions to the form factor $g_{D^*D\pi}(Q^2)$ at $Q^2 = 1$ GeV as a function of the Borel mass M^2 using $\Delta_{s1} = \Delta_{u1} = 0.5$ GeV. We can see that, in the case of this form factor, the gluon condensate is not negligible and it helps the stability of the curve, as a function of M^2, providing a rather stable plateau for $M^2 \geq 3$ GeV^2. Fixing $M^2 = 3.5$ GeV^2 we show, in Fig. 6, the momentum dependence of the form factor (dots). Since the present approach cannot be used at $Q^2 = 0$, to extract the $g_{D^*D\pi}$ coupling from the form factor we need to extrapolate the curve to $Q^2 = 0$ (in the approximation $m_\pi^2 = 0$). In order to do this extrapolation we fit the QCD sum rule results with an analytical expression. We tried to fit our results with a monopole form, but the fit is very poor. We obtained good fits using both the gaussian form

$$g_{D^*D\pi}(Q^2) = g_{D^*D\pi}\, e^{-(Q^2+m_\pi^2)^2/\Gamma^4} \tag{41}$$

and a curve of the form

$$g_{D^*D\pi}(Q^2) = g_{D^*D\pi} \frac{1+(a/\Lambda)^4}{1+(a/\Lambda)^4 e^{(Q^2+m_\pi^2)^2/\Lambda^4}} \,. \tag{42}$$

The Q^2 dependence of the form factor can be well reproduced by the parametrization in Eqs. (41) and (42) [29]. The value of the parameters in Eqs. (41) and (42) are given in Table I for two different values of the continuum threshold.

$\Delta_{s1} = \Delta_{u1}$ (GeV)	$g_{D^*D\pi}$	Λ (GeV)	a (GeV)
0.5	5.3	1.66	1.90
0.6	6.0	1.89	3.05
$\Delta_{s1} = \Delta_{u1}$ (GeV)	$g_{D^*D\pi}$	Γ (GeV)	
0.5	5.7	1.74	
0.6	6.1	1.92	

TABLE I: Values of the parameters in Eqs. (41) and (42) which reproduce the QCDSR results for $g_{D^*D\pi}(Q^2)$, for two different values of the continuum thresholds.

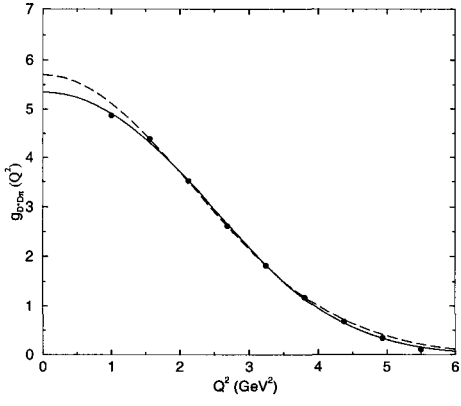

Figure 6. Momentum dependence of the $D^*D\pi$ form factor for $\Delta_{s1} = \Delta_{u1} = 0.5$ GeV (dots). The solid and dashed lines give the parametrization of the QCDSR results through Eqs. (42) and (41) respectively.

In view of the uncertainties involved, the results obtained with the two parametrizations are consistent with each other, the systematic error being of the order of 10%.

To test if our fit gives a good extrapolation to $Q^2 = 0$ we can write a sum rule, based on the three-point function Eq. (2), but valid only at $Q^2 = 0$, as suggested in [38] for the pion-nucleon coupling constant. This method was also applied to the nucleon-hyperon-kaon coupling constant [25] and to the nucleon$-\Lambda_c - \bar{D}$ coupling constant [20]. It consists in neglecting the pion mass in the denominator of Eq. (23) and working at $Q^2 = 0$, making a single Borel transformation to both $P^2 = P'^2 \to M^2$.

The problem of doing a single Borel transformation is the fact that the single pole contribution, associated with the $N \to N^*$ transition, is not suppressed [31,30]. However, the single pole contribution can be taken into account through the introduction of a parameter A, in the phenomenological side of the sum rule [31,25]. Therefore, neglecting m_π^2 in the denominator of Eq. (23) and doing a single Borel transform in $P^2 = P'^2$,

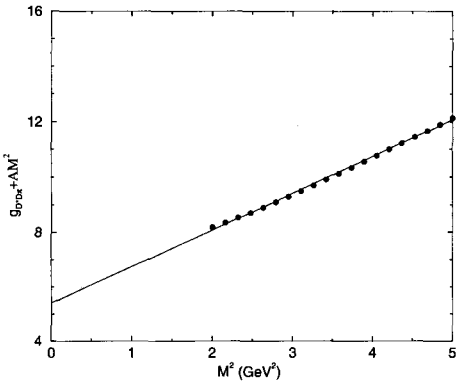

Figure 7. $D^*D\pi$ coupling constant as a function of the squared Borel mass M^2 from the QCDSR valid at $Q^2 = 0$ (dots). The straight line gives the extrapolation to $M^2 = 0$.

we get for the structure p_μ

$$\tilde{\Gamma}_1^{(phen)}(M^2, Q^2) = -\frac{C_{DD^*}}{2m_D^2 Q^2} \frac{m_D^2 + m_{D^*}^2 + Q^2}{m_{D^*}^2 - m_D^2} \left(e^{-m_D^2/M^2} - e^{-m_{D^*}^2/M^2}\right) (g_{D^*D\pi} + AM^2) , \quad (43)$$

where C_{DD^*} in given in Eq. (24).

On the OPE side only terms proportional to $1/Q^2$ will contribute to the sum rule. Therefore, up to dimension four the only diagram that contributes is the quark condensate given by

$$\tilde{\Gamma}_1^{<\bar{q}q>}(M^2, Q^2) = \frac{2m_c\langle\bar{q}q\rangle}{Q^2} e^{-m_c^2/M^2} . \quad (44)$$

Equating Eqs. (43) and (44) and taking $Q^2 = 0$ we obtain the sum rule for $g_{D^*D\pi}+AM^2$, where A denotes the contribution from the unknown single poles terms. In Fig. 7 we show, for $\Delta_{s1} = \Delta_{u1} = 0.5$ GeV, the QCDSR results for $g_{D^*D\pi} + AM^2$ as a function of M^2 (dots) from where we see that, in the Borel region $2 \leq M^2 \leq 5$ GeV^2, they follow a straight line. The value of the coupling constant is obtained by the extrapolation of the line to $M^2 = 0$. Fitting the QCDSR results to a straight line we get

$$g_{D^*D\pi} \simeq 5.4 , \quad (45)$$

in excellent agreement with the values obtained with the extrapolation of the form factor to $Q^2 = 0$, given in Table I. It is reassuring that both methods, with completely different OPE sides and Borel transformation approaches, give the same value for the coupling constant. Considering the variation in the continuum thresholds and different approaches our results for the coupling constant is:

$$g_{D^*D\pi} = 5.7 \pm 0.4 , \quad (46)$$

The $D^*D\pi$ coupling is directly related with the $D^* \to D\pi$ decay width through

$$\Gamma(D^{*-} \to \overline{D}^0\pi^-) = \frac{g_{D^*D\pi}^2 |\vec{q}_\pi|^3}{24\pi m_{D^*}^2} . \quad (47)$$

Using Eq. (46) we get

$$\Gamma(D^{*-} \to \overline{D}^0\pi^-) = 6.3 \pm 0.9 \text{ keV} , \quad (48)$$

which is much smaller then the current upper limit [39] $\Gamma(D^{*-} \to \overline{D}^0\pi^-) < 89$ keV.

4. Conclusions

In conclusion, in this work we have calculated the form factors for the hadronic vertices $ND\Lambda_c$, $ND^*\Lambda_c$ and $D^*D\pi$ using QCD sum rules. These form factors are important to evaluate the charmonium dissociation cross section by hadrons, in the framework of meson exchange models based on effective lagrangians. In the construction of the sum rules for $ND\Lambda_c$ and $ND^*\Lambda_c$ we have performed a double Borel transformation with respect to the nucleon and Λ_c momenta, and we have evaluated the form factors as a function of the heavy meson momentum Q^2. We have studied the sum rules in the structures $\sigma^{\mu\nu}\gamma_5 p'_\mu p_\nu$ for $g_{ND\Lambda_c}(Q^2)$ and $\not{p}'\gamma_\mu\not{p}$ for $g_{ND^*\Lambda_c}(Q^2)$. In the studied Q^2 region, our results are compatible with constant form factors in these vertices. Considering 20% of variation in the continuum thresholds, and around 10% of variation in the meson decay constants we got:

$$\begin{aligned} g_{ND\Lambda_c}(Q^2) &= 7.9 \pm 0.9 \\ g_{ND^*\Lambda_c}(Q^2) &= -7.5 \pm 1.1 . \end{aligned} \quad (49)$$

It is important to stress that constant form factors where also found, in the framework of

QCDSR, in the vertex $D^*D\pi$ with an off shell D^*. Off course for very large values of Q^2 the form factors should go to zero, but, according to our results, this means that the values of the cut-offs in these form factors should be much larger than 2 GeV, which is the typical value used in refs. [15–17].

In the case of the $D^*D\pi$ vertex, we have performed a double Borel transformation with respect to the D and D^* momenta, and we have evaluated the form factors as a function of pion momentum Q^2. In contrast with the form factors at the $ND(D^*)\Lambda_c$ vertices, we found that the $D^*D\pi$ form factor shows a very pronounced Q^2 dependence, with Q^2 being the squared momentum of the off-shell pion in the Euclidian region. This result might be suggesting that the size of a hadronic vertex depends on which particle is off-shell. If the off-shell particle is light, then the vertex is not point like. However, if the off-shell particle is heavy, then the vertex is point like with a consequent constant form factor.

Acknowledgements: This work has been supported by FAPESP and CNPq.

REFERENCES

1. T. Matsui and H. Satz, *Phys. Lett.* **B178**, 416 (1986).
2. E772 Collaboration (D.M. Alde et al.), *Phys. Rev. Lett.* 66, 133 (1991).
3. NA38 Collaboration (C. Baglin et al.), *Phys. Lett.* B255, 459 (1991).
4. NA38 Collaboration (B. Ronceux et al.), *Phys. Lett.* B345, 617 (1995).
5. NA50 Collaboration (M.C. Abreu et al.), *Phys. Lett.* **B477**, 28 (2000).
6. D. Kharzeev and H. Satz, *Phys. Lett.* **B366**, 316 (1996).
7. D. Kharzeev, C. Lourenço, M. Nardi and H. Satz , *Z. Phys.* **C74**, 307 (1997).
8. C.Y. Wong, *Phys. Rev. Lett.* **76**, 196 (1996).
9. A. Capelle et al., *Phys. Lett.* **B393**, 431 (1997).
10. W. Cassing, E.L. Bratkovskaya and S. Juchem, nucl-th/0001024, *Nucl. Phys.* **A674**, 249 (2000).
11. A. Capella, E.G. Ferreiro and A.B. Kaidalov, hep-ph/0002300, *Phys. Rev. Lett.* **85**, 2080 (2000).
12. A. Sibirtsev, K. Tsushima, K. Saito and A.W. Thomas, nucl-th/9904015, *Phys. Lett.* **B484**, 23 (2000).
13. S.C. Matinyan and B. Müller, *Phys. Rev.* **C58**, 2994 (1998).
14. K.L. Haglin, nucl-th/9907034, *Phys. Rev.* **C61**, 031902 (2000).
15. Z. Lin and C.M. Ko, nucl-th/9912046, *Phys. Rev.* **C62**, 034903 (2000).
16. A. Sibirtsev, K. Tsushima and A.W. Thomas, nucl-th/0005041.
17. K.L. Haglin and C. Gale, nucl-th/0010017.
18. Y. Oh, T. Song and S.H. Lee, nucl-th/0010064.
19. M.A. Shifman, A.I. Vainshtein and V.I. Zakharov, *Nucl. Phys.* **B120**, 316 (1977).
20. F.S. Navarra and M. Nielsen, *Phys. Lett.* **B443**, 285 (1998).
21. B.L. Ioffe, *Nucl. Phys.* **B188**, 317 (1981).
22. E. Bagan, M. Chabab, H.G. Dosch and S. Narison, *Phys. Lett.* **B278**, 367 (1992); **B287**, 176 (1992); **B301**, 243 (1993).
23. R.S. Marques de Carvalho et al., *Phys. Rev.* **D60**, 034009 (1999).
24. H. Kim, S.H. Lee and M. Oka, *Phys. Lett.* **B453**, 199 (1999); *Phys. Rev.* **D60**, 034007 (1999); H. Kim, T. Doi, M. Oka and S.H. Lee, nucl-th/0002011.
25. M.E. Bracco, F.S. Navarra and M. Nielsen, *Phys. Lett.* **B454**, 346 (1999).
26. B.L. Ioffe and A.V. Smilga, *Nucl. Phys.* **B216** 373 (1983); *Phys. Lett.* **B114**, 353 (1982).
27. R.E. Cutkosky, *J. Math Phys.* **1**, 429 (1960).
28. E. Bagan, P. Ball and P. Gosdzinsky, *Phys. Lett.* **B301**, 249 (1993).
29. F.S. Navarra, M. Nielsen, M.E. Bracco, M. Chiapparini and C.L. Schat, hep-ph/0005026, *Phys. Lett.* **B489**, 319 (2000).
30. P. Colangelo et al., *Phys. Lett.* **B339**, 151 (1994); V.L. Eletsky and Ya.I. Kogan, *Z. Phys.* **C28**, 155 (1985); A.A. Ovchinnikov, *Sov. J. Nucl. Phys.* **50**, 519 (1989).
31. V.M. Belyaev, V.M. Braun, A. Khodjamirian and R. Rückl, *Phys. Rev.* **D51**, 6177 (1995).
32. A.G. Grozin and O.I. Yakovlev, *Eur. Phys. J.*

C2, 721 (1998).
33. H.G. Dosch and S. Narison, *Phys. Lett.* **B368**, 163 (1996).
34. A. Khodjamirian et al., *Phys. Lett.* **B457**, 25 (1999).
35. P. Ball, V.M. Braun and H.G. Dosch, *Phys. Lett.* **B273**, 316 (1991).
36. A. Khodjamirian et al., hep-ph/0001297, to appear in *Phys. Rev. D.*
37. Z. Lin, C.M. Ko and B. Zhang, *Phys. Rev.* **C61**, 024904 (2000).
38. L.J. Reinders, H. Rubinstein and S. Yazaki, *Phys. Rep.* **127**, 1 (1985).
39. Particle Data Group (C. Caso et al.), *Eur. Phys. J.* **C3**, 1 (1998).

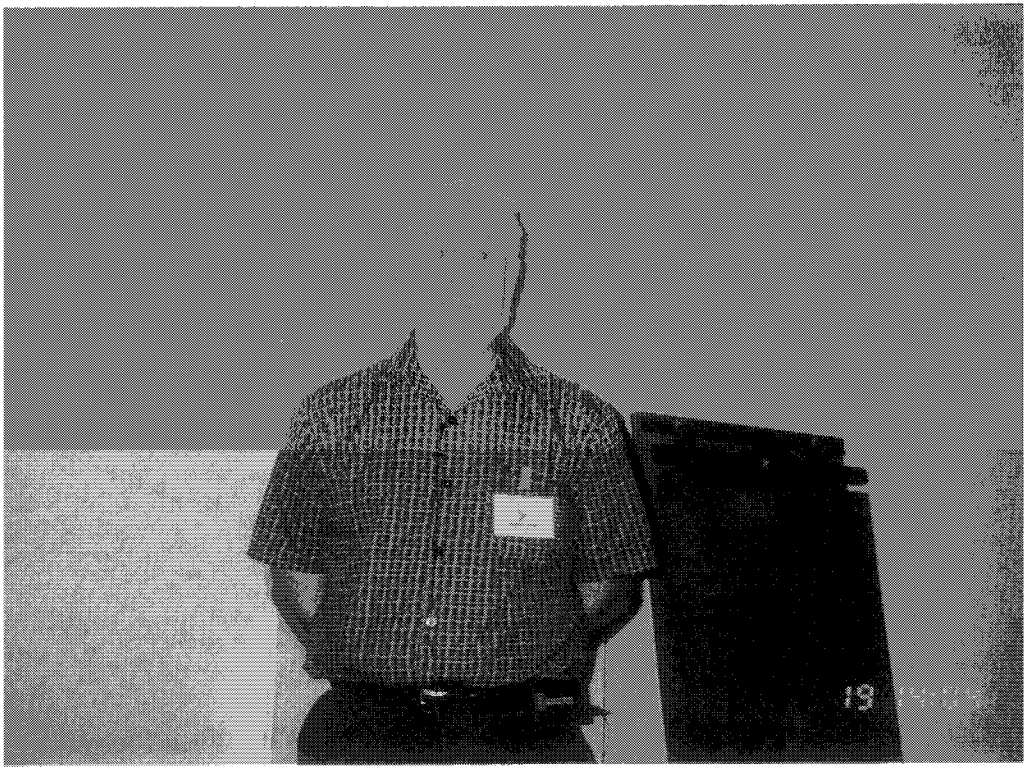

Robert L. Thews

Quarkonium Production in High Energy Heavy Ion Collisions

Robert L. Thews and Johann Rafelski
Department of Physics, University of Arizona
Tucson, AZ 85721, USA

Abstract

We have estimated in a kinetic model the effects of a new production mechanism for quarkonium states in high energy heavy ion collisions. In this mechanism, bound states are formed from a quark and an antiquark which were originally produced in separate incoherent interactions. This requires the mobility of heavy quarks in an extended space-time region, and so will impact predictions of quarkonium production as a signal of deconfinement. Our calculations predict that at RHIC energies the deconfinement signal will change from suppression to enhancement of J/ψ production. The dependence on centrality and total heavy quark population will serve as indicators for the presence of this new mechanism.

The formation of quarkonium states in high energy hadronic interactions is generally visualized as the production of a quark-antiquark pair via some pointlike interaction calculable in perturbative QCD followed by some nontperturbative hadronization process. The extension of this picture to heavy ion collisions has received much attention, since color screening in a quark-gluon plasma would be expected to suppress the final yields[1].

One invokes the argument that in a plasma of free quarks and gluons the color forces will experience a Debye-type screening. Thus the quark and antiquark in a quarkonium bound state will no longer be subject to a confining force and diffuse away from each other during the lifetime of the quark-gluon plasma. As the system cools and the deconfined phase disappears, these heavy quarks will most likely form a final hadronic state with one of the much more numerous light quarks. The result will be a decreased population of heavy quarkonium relative to those formed initially in the heavy ion collision.

There is now extensive data on J/ψ production using nuclear targets and beams[2]. The results in p-A collisions and also from Oxygen and Sulfur beams on Uranium show a systematic nuclear dependence of the cross section, which has been interpreted as a break-up of an initial quarkonium state by interactions with nucleons[3]. The recent NA50 results from Pb-Pb interactions reveal an "anamalous" additional suppression of about 25%, prompting claims that this effect could be the expected signature of deconfinement[4]. There is also interesting structure as a function of the centrality of the collision, as measured by the energy directed transverse to the beam. This can be interpreted as threshold behavior due to dissociation of charmonium states in a plasma[5]. However, several alternate scenarios have been proposed which do not involve deconfinement effects[6]. These models are difficult to rule out at present, since there is significant uncertainty in many of the parameters.

At and above RHIC energy, the deconfinement scenario would anticipate that J/ψ suppression would be complete at all centralities. Aside from those which come from B decay, only a few percent would be formed outside the deconfined regions and survive to be detected after hadronization[7]. However, at these energies there will be a very important quantitative difference in the initial production rates for heavy quarks. Based on perturbative QCD calculations for the cross section, one expects about 10 charm quarks pairs in each central collision at RHIC, rising to several hundred pairs at LHC[8]. Then *if and only if a space-time region of deconfined quarks and gluons is present*, it will be possible for quarkonium states to be formed from combinations of heavy quarks and antiquarks which were initially produced in unrelated primary nucleon-nucleon interactions. Since the formation rate is expected to be

proportional to the square of the number of unbound quark pairs, this new mechanism has the possibility to be the dominant factor in determining the final heavy quarkonium population.

For the purposes of this study, we consider a physical picture of deconfinement in which quarkonium is suppressed via collisions with free gluons[9]. Then the dominant formation process is simply the inverse of the breakup reaction, in which a quark and an antiquark in a relative color octet state are captured into a color singlet bound quarkonium state and emit a color octet gluon. It is then an inevitable consequence of this picture of suppression that there also exists the corresponding formation process. However, it is not until one reaches energies for which many quark pairs coexist in the deconfined region of each central collision that this formation process becomes numerically significant. It is clear that this new formation mechanism can only be significant for deeply-bound states, since only these states can still exist in a deconfined region[10]. Equivalently, the gluon breakup mechanism will dominate over recombination for weakly-bound states, and we can neglect them in our explicit calculations.

As an example, we consider the dynamical evolution of the $c\bar{c}$ pairs which have been produced in a central Au-Au collision at $\sqrt{s} = 200$A GeV[11]. For simplicity, we assume the deconfined phase is a spatially homogeneous ideal gas of free gluons and light quarks, with equilibrium momentum distributions given by a spatially-independent but time-varying temperature T. The momentum distribution of the charm quarks is allowed to vary over a wide range of possibilities. At one extreme we use a thermal equilibrium distribution at the QGP temperature. We also consider a distribution unchanged from that introduced in the initial perturbative QCD processes, plus several intermediate distributions with decreasing rapidity widths.

Any J/ψ in this medium will be subject to dissociation via collisions with gluons, and the unbound charm quarks in the medium will be able to form J/ψ via the inverse process. The competition between the rates of these reactions integrated over the lifetime of the QGP then determines the final J/ψ population. We can omit consideration of other reactions involving charm quarks in the QGP, since the rates are much smaller than those above. For example, formation of the ψ' and also D and D_s mesons is not possible at the high initial temperatures expected at RHIC since their lower binding energies prevents them from existing in a hot QGP, or equivalently these bound systems are ionized (or light quarks stripped) on very short time scales. They will be formed predominantly at hadronization, but this process is too late to affect the final J/ψ population. We also neglect the effects of light quarks, since their population is expected to be very much suppressed relative to gluons during the early times when the dissociation reaction rate has its most significant effect[12].

The time evolution if the J/ψ population is then given by

$$\frac{dN_{J/\psi}}{d\tau} = \lambda_F N_c \rho_{\bar{c}} - \lambda_D N_{J/\psi} \rho_g \,, \tag{1}$$

where τ is the proper time and ρ_i denotes the number density of species i. The reactivity λ is the reaction rate $\langle \sigma v_{\rm rel} \rangle$ averaged over the momentum distribution of the initial participants, i.e. c and $\bar{c}$ for λ_F and J/ψ and g for λ_D. The gluon density is determined by the equilibrium value in the QGP at each temperature. To get a lower bound on the J/ψ production rate, we neglect additional production of charm pairs in the deconfined region, and use only the initial number $N_c(\text{initial}) = N_{\bar{c}}(\text{initial}) \equiv N_0$ produced in the collision. Exact charm conservation is enforced throughout the calculation. The initial volume at $\tau = \tau_0$ is allowed to undergo longitudinal expansion $V(\tau) = V_0 \tau/\tau_0$. The expansion is taken to be isentropic, $VT^3 =$ constant, which then provides

a generic temperature-time profile.

For our quantitative estimates, we utilize a cross section for the dissociation of J/ψ due to collisions with gluons which is based on the operator product expansion [13]:

$$\sigma_D(k) = \frac{2\pi}{3}\left(\frac{32}{3}\right)^2\left(\frac{2\mu}{\epsilon_o}\right)^{1/2}\frac{1}{4\mu^2}\frac{(k/\epsilon_o - 1)^{3/2}}{(k/\epsilon_o)^5}, \tag{2}$$

where k is the gluon momentum, ϵ_o the binding energy, and μ the reduced mass of the quarkonium system. This form assumes the quarkonium system has a spatial size small compared with the inverse of Λ_{QCD}, and its bound state spectrum is close to that in a nonrelativistic Coulomb potential. The magnitude of the cross section is controlled just by the geometric factor $4\mu^2$, and its rate of increase in the region just above threshold is due to phase space and the p-wave color dipole interaction. This same cross section is utilized with detailed balance factors to calculate the primary formation rate for the capture of a charm and anticharm quark into the J/ψ.

If the net number of J/ψ remains a small fraction of the total charm quark number N_0, we can write an analytic expression for the the solution of Eq. 1 which exhibits the anticipated quadratic dependence.

$$N_{J/\psi}(\tau_f) = \epsilon(\tau_f) \times [N_{J/\psi}(\tau_0) + N_0^2 \int_{\tau_0}^{\tau_f} \lambda_F \, [V(\tau)\, \epsilon(\tau)]^{-1} \, d\tau], \tag{3}$$

where τ_f is the hadronization time determined by the initial temperature (T_0 is a variable parameter) and final temperature (T_f = 150 MeV ends the deconfining phase), and

$$\epsilon(\tau_f) = e^{-\int_{\tau_0}^{\tau_f} \lambda_D \, \rho_g \, d\tau}, \tag{4}$$

would be the equilvalent suppression factor in this scenario if the formation mechanism were neglected.

Results of numerical solutions to Eq. 1 for the J/ψ final population are shown in Fig. 1. We use parameter values for thermalization time τ_0 = 0.5 fm, initial volume $V_0 = \pi R^2 \tau_0$ with R = 6 fm, and a wide range of initial temperatures 200 MeV $< T_0 <$ 600 MeV, using thermal charm momentum distributions. This calculation maintained exact charm conservation, so that the solutions followed evolution of both bound and free charm quarks.

The quadratic nature of these solutions is evident, verifying our expectations that the decrease in initial unbound charm is a small effect. To calculate the average J/ψ population per central event, we first average over $N_{initial}$ at fixed N_0. Since the initial formation is expected to be of the order of 1 % of total charm [14], the $N_{initial} = 0$ solutions will give the dominant contribution. We show in Fig. 2 these results for various charm quark momentum distributions, parameterized in terms of the width in rapidity. For comparison, a linear curve is shown for the number of J/ψ expected to be initially produced, and the same curve reduced by typical screening predicted at RHIC. One sees that for total charm number of 10 pairs per central event, this new formation mechanism predicts a J/ψ **enhancement** ranging up to factors of 5 over the expected initial production. The contrast with an otherwise almost complete suppression in the screening scenario could be manifestly evident in the experimental results at RHIC.

Finally, we consider the effects of variations in our parameters and assumptions, i.e. we evaluate the "systematic theoretical error".

1. The initial charm production at RHIC could be decreased due to nuclear shadowing of the gluon structure functions. Model estimates indicate this effect

could result in about a 20% reduction in initial charm [15]. This factor would directly reduce the new production to charm ratio by the same amount.

2. The validity of the cross section used assumes strictly nonrelativistic bound states, which is somewhat marginal for the J/ψ. All of the existing alternative models predict larger values for this cross section. If we arbitrarily increase the cross section by a factor of two, or alternatively set the cross section to its maximum value (1.5 mb) at all energies, we find an increase in the final J/ψ population of about 15%. This occurs because the kinetics always favors formation over dissociation, and a larger cross section just allows the reactions to approach completion more easily within the lifetime of the QGP. This behavior is shown in Fig. 3.

3. A nonzero transverse expansion will be expected at some level, which will reduce the lifetime of the QGP and reduce the efficiency of the new formation mechanism. We have calculated results for central collisions with variable transverse velocity, and find a decrease in the parameter β of about 15% for each increase of 0.2 in the transverse velocity. This behavior is shown in Fig. 4.

4. In our model of a deconfined region, we have used the vacuum values for masses and binding energy of J/ψ, and assumed that the effects of deconfinement are completely included by the dissociation via gluon collisions. For a complementary viewpoint, we have also employed a deconfinement model in which the J/ψ is completely dissociated when temperatures exceed some critical screening value T_s. Below that temperature, the new formation mechanism will still be able to operate, and we use the same cross sections and kinematics. We find that for $T_s = 280$ MeV, the final J/ψ population is approximately unchanged, while decreasing T_s to 180 MeV could reduce the J/ψ production by factors of 2 or 3. For details of these results see [16].

5. Model calculations of the approach to chemical equilibrium for light quarks and gluons indicate that the initial density of gluons in a QGP fall substantially below that for full phase space occupancy. We have checked our model predictions in this scenario, using a factor of two decrease in the gluon density at τ_0. As one would expect, this decreases the effectiveness of the dissociation process, such that the final J/ψ production is increased by about 35%. This behavior is shown in Fig. 5.

6. A hadronic analog of our new production mechanism can also occur for interactions in a hot hadronic gas. This has been investigated for J/ψ production by collisions of D mesons [17]. It was found that the magnitude of these hadronic processes will be entirely negligible at RHIC energies. Even at the LHC, only a small effect may be possible to observe for ψ' production. If there is a period of mixed phase in a first-order transition, additional J/ψ formation may take place also in the deconfined portion. We have not included such a possibility here, but the net effect would always increase the total J/ψ yield in a deconfined region.

All of these variations in our standard scenario for the new production mechanism predict either increases or decreases in the final J/ψ population at RHIC by amounts typically in the tens of percents, with a few factors ranging up to 2 or 3. It is highly unlikely that our enhancement factor for central collisions could be changed into a suppression factor by the cumulative effect of these variations.

In summary, we predict that at high energies the J/ψ production rate will provide an even better signal for deconfinement than originally proposed. Consideration of multiple heavy quark production made possible by higher collision energy effectively adds another dimension to the parameter space within which one searches for patterns of quarkonium behavior in a deconfined medium. The increase predicted at RHIC by our new production mechanism provides a signal which will be difficult to imitate with conventional hadronic

processes. The extension of this scenario to LHC energies, where we encounter hundreds of initially-produced charm quark pairs, will be striking.

Acknowledgment: This work was supported by a grant from the U.S. Department of Energy, DE-FG03-95ER40937.

1. T. Matsui and H. Satz, *Phys. Lett.* **B178**, 416 (1986).
2. E866/NuSea Collaboration (M.J. Leitch et al.), *Phys. Rev. Lett.* **84**, 3256 (2000); D. M. Alde et al., *Phys. Rev. Lett.* **66**, 133 (1991); M.C. Abreu et al., *Phys. Lett.* **B444**, 516 (1998).
3. C. Gerschel and J. Hüfner, *Z. Phys.* **C47**, 171 (1992).
4. NA50 Collaboration, M.C. Abreu et al., *Phys. Lett.* **B477**, 28 (2000).
5. M. Nardi and H. Satz, *Phys. Lett.* **B442**, 14 (1998).
6. A. Capella, E.G. Ferreiro, and A.B. Kaidalov, preprint LPTHE-ORSAY-00-21, Feb 2000, hep-ph/0002300; J. Qiu, J. Vary, and X. Zhang, preprint BNL-HET-98-33, Sep 1998, hep-ph/9809442; Y. He, J. Hüfner, and B. Kopeliovich, *Phys. Lett.* **B477**, 93 (2000); P. Hoyer, and S. Peigné, *Phys. Rev.* **D59**, 034011 (1999).
7. R. Vogt, *Nucl. Phys.* **A661**, 250c (1999).
8. P. L. McGaughey, E. Quack, P. V. Ruuskanen, R. Vogt, and X.-N. Wang, in "Hard Processes in Hadronic Interactions", *Int. J. Mod. Phys.* **A10**, 2999 (1995).
9. D. Kharzeev and H. Satz, *Phys. Lett.* **B334**, 155 (1994); D. Kharzeev, "Quarkonium Interactions in QCD", presented at the Enrico Fermi School of Physics, Varenna, Italy, June 1995, nucl-th/9601029.
10. F. Karsch and H. Satz, *Z. Phys.* **C51**, 209 (1991).
11. This model is adapted from our previous calculation of the formation of B_c mesons. For details, see M. Schroedter, R.L. Thews, and J. Rafelski, *Phys. Rev.* **C62**, 024905 (2000).
12. See for example S. M. H. Wong, *Phys. Rev.* C54, 2588 (1996) and *Phys. Rev.* C56, 1075 (1997).
13. M. E. Peskin, *Nucl. Phys.* **B156**, 365 (1979); G. Bhanot and M. E. Peskin, *Nucl. Phys.* **B156**, 391 (1979).
14. R. Gavai, D. Kharzeev, H. Satz, G. Schuler, K. Sridhar, and R. Vogt, in "Hard Processes in Hadronic Interactions", *Int. J. Mod. Phys.* **A10**, 3043 (1995).
15. K.J. Eskola, V.J. Kolhinen and C.A. Salgado, *Eur. Phys. J.* C9, 61 (1999), hep-ph/9807297; J. Jalilian-Marian and X.-N. Wang, hep-ph/0005071.
16. R. L. Thews, M. Schroedter and J. Rafelski, hep-ph/0009090, To be published in the proceedings of 5th International Conference on Strangeness in Quark Matter (Quark matter 2000), Berkeley, California, 20-25 Jul 2000.
17. P. Braun-Munzinger and K. Redlich, hep-ph/0001008.

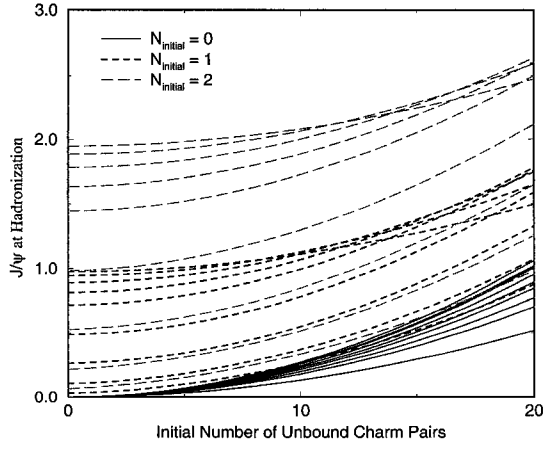

Figure 1: Calculated J/ψ formation in deconfined matter at several initial temperatures, for central collisions at RHIC as a function of initial charm pair and J/ψ production.

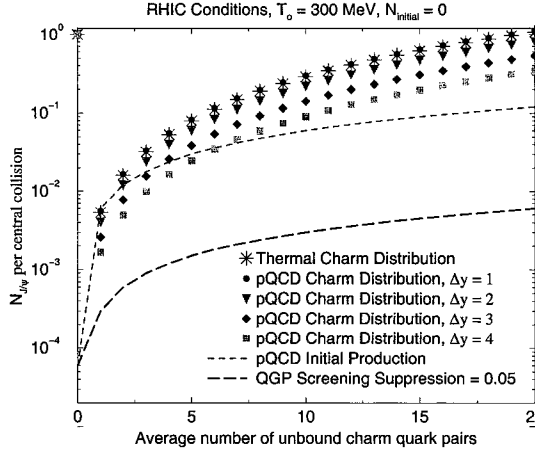

Figure 2: Calculated J/ψ formation in deconfined matter using several charm momentum distributions, compared with initial and suppressed expectations without the new formation mechanism.

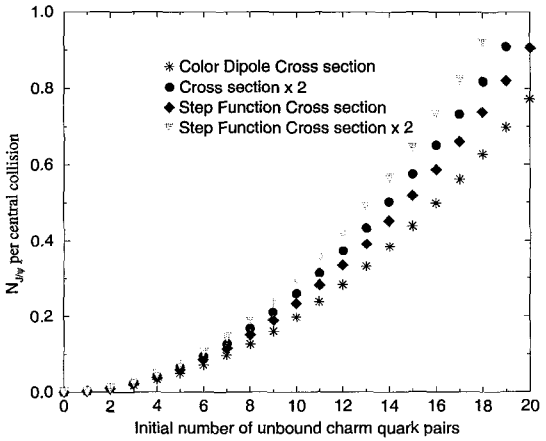

Figure 3: Dependence of J/ψ formation in deconfined matter on the magnitude and shape of the fundamental cross section.

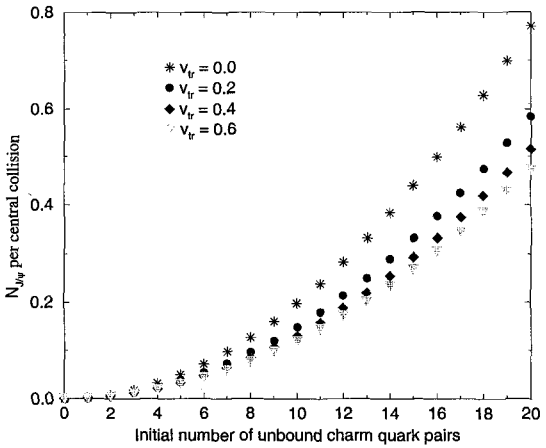

Figure 4: Dependence of J/ψ formation in deconfined matter on the transverse expansion rate of the QGP.

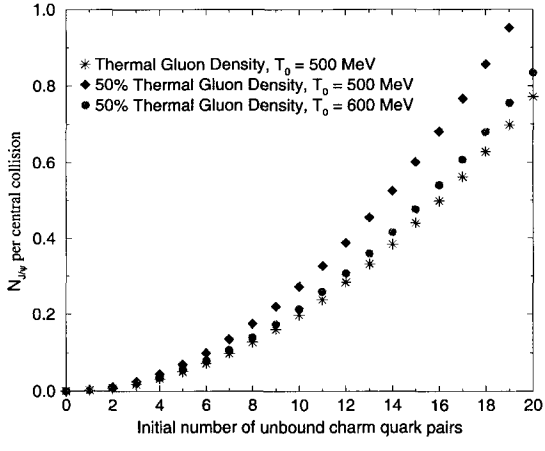

Figure 5: Dependence of J/ψ formation in deconfined matter on the degree of saturation of the gluon population.

Fernando S. Navarra

CHARMONIUM-HADRON CROSS SECTION IN NONPERTURBATIVE QCD MODELS

R.S. de Azevedo[1]*, R.Z. Denke[1]†, F.S. Navarra[1]‡, M. Nielsen[1]§ and M.S.K. Souza[1]¶

[1] *Instituto de Física, Universidade de São Paulo*
C.P. 66318, 05315-970 São Paulo, SP, Brazil

Abstract

We review the attempts to compute the charmonium - hadron cross sections and present two calculations, one based on the dipole - condenser model and another with the model of the stochastic vacuum. We also give a quantitative discussion of pre-resonance formation and medium effects.

1 Introduction

The search for Quark Gluon Plasma (QGP) has started in the early eighties and since then it has been subject of intense debate [1, 2]. The last CERN results on Pb-Pb collisions have attracted a great attention and increased the hope that a new phase of nuclear matter is "just around the corner".

*e-mail: regina@if.usp.br
†e-mail: soliton@if.usp.br
‡e-mail: navarra@if.usp.br
§e-mail: mnielsen@if.usp.br
¶e-mail: simone@if.usp.br

The signature of QGP formation has been and still remains a theoretical and experimental challenge. Indeed there is so far no "crucial test" able to disentangle the possible new phase from the dense hadronic background. Among the proposed signatures the most interesting is the suppression of J/Ψ [3]. This suppression was observed experimentally by the NA38 collaboration in 1987 in collisions with light ions and also and more dramatically by the NA50 collaboration in 1995-1996 in Pb-Pb collisions [4, 5].

Whereas the old data could be reasonably well explained by a "conventional" approach the new Pb-Pb results of the NA50 collaboration created a big controversy [6]. The entire set of the J/Ψ data from pA and AB collisions available before the advent of the Pb beam at CERN SPS has been found to be consistent with the nuclear absorption model. However, in the case of the new Pb-Pb data, the density of secondaries, which (together with primary nucleons flying around) are presumably responsible for the charmonium absorption, is so high that the hadronic system in question is hardly in a hadronic phase. Nevertheless, a conventional treatment of the problem is not yet discarded [7].

Reliable values for the charmonium nucleon cross sections are of crucial importance in the present context. One needs to know the cross section $\sigma_{J/\psi}$ in order to predict a nuclear suppression of J/Ψ without assuming a so called "deconfining regime". Estimates using perturbative QCD give values which are too small to explain the observed absorption conventionally, but they are certainly not reliable for that genuine nonperturbative problem. A nonperturbative estimate may be tried by applying vector dominance to J/Ψ and Ψ' photoproduction. In this way a cross section of $\sigma_{J/\psi} \simeq 1.3$ mb for $\sqrt{s} \simeq 10$ GeV and $\sigma_{\psi'}/\sigma_{J/\psi} \simeq 0.8$ has been obtained [8, 9]. In ref. [10] strong arguments against the vector dominance with only few intermediate vector mesons were put forward even in the case of the production of light vector mesons and which apply a fortiori to the production of heavy vector mesons. The instability of the vector dominance model can be seen from a more refined multichannel analysis [8] where a value $\sigma_{J/\psi} \simeq 3 - 4$ mb has been obtained. Even this value is too small in order to explain the absorption in p-A collisions which is of the order $\sigma_{\psi}^{abs} \simeq 7.3$ mb [11, 12]

These hadron-hadron cross sections involve nonperturbative aspects of QCD dynamics and therefore require a nonperturbative model to be calculated. In a recent letter [13] the nonperturbative QCD contribution to the charmonium-nucleon cross section was evaluated by using an interpolation formula for the dependence of the cross section on the transverse size of a quark-gluon configuration.

Very recently many works appeared trying to calculate J/Ψ - nucleon and J/Ψ - pion cross sections with the help of effective lagrangians [14]. This method not only contains nonperturbative physics but also should be most applicable exactly in the low (collision) energy range where most of the interactions within the hadronic fireball take place. However since the exchanged mesons (D and D^*) are so heavy, the physics involved starts to contain short distance (perturbative) processes.

In this work we calculate the J/Ψ and Ψ' - nucleon cross sections in two nonperturbative models of QCD: the dipole - condenser model and the model of the stochastic vacuum (MSV). We also investigate the influence of the nuclear matter and arrive at rather stringent limits for the cross sections in an environment different from the vacuum and where the properties of the medium are reflected in a shift of the J/Ψ mass [15].

2 The Dipole - Condenser Model

Given that the charmonium dissociation seems to be very often a nonperturbative process, we shall use the dipole condenser model (DCM), which has been advanced some time ago [16]. In its original formulation this model did not include any information about the spatial structure of the colliding particles and we expect it to be relevant in nonperturbative physics. Another feature of the DCM was that no precise statement about the potential generated by the condenser was made, all the emphasys was given to the color exchange aspect. In the present reformulation of the model, all these aspects are included.

The interaction between a color dipole and an external (condenser) color field is given by the following interaction hamiltonian:

$$H_{int} = -g \sum_{k=1}^{2} \frac{\lambda^a_{(k)}}{2} \vec{x}_k \,.\, \vec{E}^a \;=\; -g \sum_{k=1}^{2} \frac{\lambda^a_{(k)}}{2} \vec{r} \,.\, \vec{E}^a \;=\; -\sum_{k=1}^{2} V_{ij}(\vec{x}_k, t) \quad (1)$$

where $\vec{r}$ and $\vec{E}^a$ are, respectively the dipole radius and the condenser chromoelectric field; $\vec{x}_1$ and $\vec{x}_2$ are the coordinates of the quark and antiquark and i and j are the initial and final color indices of the k quark (or antiquark).

The typical interquark separation will be approximated by a constant value

$$\vec{r} \;=\; \vec{x}_1 - \vec{x}_2 \simeq \vec{a} \quad (2)$$

Describing the collision in the rest frame of the quark pair, the condenser of typical size d moves with velocity $\vec{v}$ along the z axis and hits the charmonium at zero impact paramter (just for the sake of simplicity). Initially the pair is in a localized region and is represented by the following wave function:

$$\Psi_i = N_i \, exp\left[-\frac{(\vec{x}_1 - \vec{x}_2)^2}{\vec{a}^2}\right] exp(-iE_i t) \tag{3}$$

where N_i is a normalization constant and E_i the charmonium intial energy. Under the action of the potential the initial wave function Ψ_i evolves to a final state Ψ_f, which describes two free quarks:

$$\Psi_f = N_f \; exp\,(i\vec{p}_1.\vec{x}_1) \; exp\,(i\vec{p}_2.\vec{x}_2) \; exp\,(-iE_f t) \tag{4}$$

Of course, this is not an asymptotic state because quarks can not escape freely but the fragmentation process with the subsequent formation of D mesons is not relevant here. It may change the momentum distributions of the outgoing mesons but it does not change the total cross section. The interaction potential has the strength given in (1) and has also some space time distribution. Therefore we have to modify (1) in order to include its localization in space and time. We assume that it has a gaussian shape and moves with constant velocity v along the z direction even after the collision:

$$V_{ij}(\vec{x}_k, t) = \gamma \, \lambda^a_{ij} \, \vec{a}\,.(g\,\vec{E}^a) \; exp\left(-\frac{x_k^2}{d^2} - \frac{y_k^2}{d^2}\right) \; exp\left(-\gamma^2 \, \frac{[vt - z_k]^2}{d^2}\right) \tag{5}$$

where $k = 1, 2$ and γ is the Lorentz factor. The transition amplitude is given by:

$$T_{fi} = < \Psi_f | V(\vec{x}_1, t) \; + \; V(\vec{x}_2, t) | \Psi_i > \tag{6}$$

The cross section is obtained from the transition probability per unit time as:

$$d\sigma = \frac{1}{F} \, C_F \, \frac{|T_{fi}|^2}{T} d(PS) \tag{7}$$

where the flux factor F is given by

$$F = \frac{v}{V} \tag{8}$$

and phase space element is given by:

$$d(PS) = \frac{V d^3 p_1}{(2\pi)^3} \; \frac{V d^3 p_2}{(2\pi)^3} \tag{9}$$

With these definitions the calculation of the cross section is straigthforward. There is only one approximation, concerning the energy transfer from the condenser to the dipole $\omega = E_f - E_i$. In principle, to compute the total cross section we must integrate over all values of p_1 and p_2. Arbitrary large values of these momenta lead to a very large E_f and consequently a very large energy transfer ω. This is not acceptable first because we design the model exactly to study low energy (and small ω) interactions, where perturbative QCD is not applicable and where most of the charmonium - comover interactions take place. The second reason for avoiding this kinematic region is that, since our potential is external and time dependent we do not have energy conservation. This is not a bad approximation as long as ω is small. On the other hand, since the binding energy of the J/ψ is around 600 MeV, we arrive at the following allowed range for ω

$$1\,\mathrm{GeV} < \omega < 3\,\mathrm{GeV} \tag{10}$$

We shall take $\omega = 2$ GeV. This implies that the final state is non relativistic. The averaging over all possible condenser orientations ($\vec{a}\,.\,\vec{E} = |\vec{a}||\vec{E}|cos\theta$) gives us a factor 1/2. The color factor is given by:

$$C_F = \frac{1}{3}\sum_{i=1}^{3}\frac{1}{8}\sum_{a=1}^{8}\sum_{j=1}^{3}(\lambda_{ij}^{a}\ \lambda_{ij}^{a*}) \tag{11}$$

In this factor we are averaging over the initial quark colors (i), averaging over the condenser field configurations (a) and summing over the final quark colors (j). The c and $\overline{c}$ form intially a color singlet object. After the interaction they may be in a color octet configuration. Our color factor has this unusual structure because the quarks are individually changed in color space by uncorrelated gluon fields.

The final integrated cross section is then:

$$\sigma = \frac{\pi^3}{4}\ <gE>^2\ a^2\ d^4\ exp\left(-\frac{\omega^2 d^2}{2\gamma^2 v^2}\right) \tag{12}$$

A first interesting feature of this expression is the energy dependence. The cross section first grows and then saturates at high energies (γ's). Many nonperturbative calculation exhibit this behaviour. Some of them, as the next one in this work and the DCM calculations of Ref. [16] do not have any energy dependence. If, on one hand a very strong energy dependence should not be expected (since we believe that most of the rise in cross sections is

due to perturbative QCD), no dependence at all is also unacceptable. We are in between these extremes.

The expectation value of the average strength of electric field inside the proton, $< g\,E >$, can be taken from recent calculations with the field correlator method [17]:

$$< g\,E > \simeq 1 \text{ GeV / fm} \tag{13}$$

The typical sizes are $a = 0.2$ fm and $d = 0.8$ fm. Using these numbers in (12) we obtain cross sections growing up to

$$\sigma = 30\,\text{mb} \tag{14}$$

This is a somewhat large value compared to perturbative QCD estimates or photoproduction data anlysis (in the charmonium - proton case), but it is in line with the estimates obtained with meson exchange models. In computing $< g\,E >$ we need an average value, in the sense that, the electric field is much stronger in the center of the condenser and much weaker in the extremities. There is an uncertainty in this averaging procedure. In fact, $< g\,E >$ can also be related to the moments of the gluon distribution in the nucleon, as pointed out in [18]. In this way of estimating $< g\,E >$ one obtains much smaller values. It also becomes more clear how to distinguish a proton from a pion, since one can use information from deep inelastic scattering data. In view of this, the above value has to be regarded as an upper limit.

3 The Model of the Stochastic Vacuum

In what follows we present another nonperturbative estimate of the charmonium - nucleon cross section, based on the MSV. We give here only part of the results and for the complete calculation we refer the reader to Ref. [19].

The basis of the MSV is the calculation of the scattering amplitude of two colourless dipoles [10, 23] based on a semiclassical treatment developped by Nachtmann [24]. For details we refer to the literature and show here only some intermediate steps necessary for the understanding of the text. The dipole-dipole scattering amplitude is expressed as the expectation value of two Wegner-Wilson loops with lightlike sides and transversal extensions $\vec{r}_{t1}$ and $\vec{r}_{t2}$ respectively. This leads to a profile function $J(\vec{b}, \vec{r}_{t1}, \vec{r}_{t2})$ from which hadron-hadron scattering amplitudes are obtained by integrating over different dipole sizes with the transversal densities of the hadrons as weight

functions according to

$$\sigma^{tot}_{J/\Psi} = \int d^2b\, d^2r_{t1}\, d^2r_{t2}\, \rho_{J/\Psi}(\vec{r}_{t1})\, \rho_N(\vec{r}_{t2})\, J(\vec{b}, \vec{r}_{t1}, \vec{r}_{t2}) \,. \tag{15}$$

Here $\rho_{J/\Psi}(\vec{r}_{t1})$ and $\rho_N(\vec{r}_{t2})$ are the transverse densities of the J/Ψ and nucleon respectively.

The basic ingredient of the model is the gauge invariant correlator of two gluon field strength tensors. The latter is characterized by two constants: the value at zero distance, the gluon condensate $< g^2FF >$, and the correlation length a. We take these values from previous applications of the model [10] (and literature quoted there):

$$< g^2FF >= 2.49\mathrm{GeV}^4 \qquad \mathrm{a} = 0.346\mathrm{fm} \,. \tag{16}$$

The wave functions of the proton have been determined from proton-proton and proton-antiproton scattering respectively. It turns out that the best description for the nucleon transverse density is given by that of a quark diquark system with transversal distance $\vec{r}_t$ and density:

$$\rho_N(\vec{r}_t) = |\Psi_p(\vec{r}_t)|^2 = \frac{1}{2\pi}\frac{1}{S_p^2}\, e^{-\frac{|\vec{r}_t|^2}{2S_p^2}} \,. \tag{17}$$

The value of the extension parameter, $S_p = 0.739$ fm, obtained from proton-proton scattering agrees very well with that obtained from the electromagnetic form factor in a similar treatment.

For the wave function of the J/Ψ we used two approaches:
1) A numerical solution of the Schroedinger equation with the standard Cornell potential [25]:

$$V = -\frac{4}{3}\frac{\alpha_s}{r} + \sigma r \,. \tag{18}$$

2) A Gaussian wave function determined by the electromagnetic decay width of the J/Ψ which has been used in a previous investigation of J/Ψ photoproduction [10].

For the Ψ' no analysis of photoproduction in the model has been made so we use only the solution of the Schroedinger equation.

The linear potential can be calculated in the model of the stochastic vacuum which yields the string tension:

$$\sigma = \frac{8\kappa}{81\pi} < g^2FF > a^2 \; = 0.179\,\mathrm{GeV}^2 \,, \tag{19}$$

where the parameter κ has been detemined in lattice calculations to be $\kappa = 0.8$ [26].

The other parameters, the charmed (constituent) mass and the (frozen) strong coupling can be adjusted in order to give the correct J/Ψ and Ψ' mass difference and the J/ψ decay width

$$m_c = 1.7\text{GeV} \qquad \alpha_s = 0.39 \; . \tag{20}$$

We also use the standard Cornell model parameters [25]:

$$\alpha_s = 0.39, \sigma = 0.183 \text{ GeV}^2 \text{ and } m_c = 1.84 \text{ GeV}. \tag{21}$$

From the numerical solution $\psi(|\vec{r}|)$ of the Schroedinger equation the transversal density is projected:

$$\rho_{J/\Psi}(\vec{r}_t) = \int \left|\psi(\sqrt{\vec{r}_t^{\,2} + r_3^2})\right|^2 dr_3 \; , \tag{22}$$

where $\vec{r}_t$ is the J/Ψ transversal radius.

Given the values of α_s, σ and m_c we solve the non-relativistic Schroedinger equation numerically, obtain the wave function, compute the transverse wave function and plugg it into the MSV calculation [23]. The results are shown in Table I. In this table $\sqrt{< r^2 >}$ is the root of the mean square distance of quark and antiquark and $\sqrt{< r_t^2 >}$ is the root of the mean square transversal distance of quark and antiquark. Wave function A) is the one obtained with the parameters given by Eqs. (19) and (20). Wave function B) corresponds to the standard Cornell model parameters [25] Eq. (21).

Wave function	$\sqrt{< r^2 >}$ fm	$\sqrt{< r_t^2 >}$ fm	σ_{tot} [mb]
$J/\Psi(1S)$			
A	0.393	0.321	4.48
B	0.375	0.306	4.06
C			4.69
$\Psi(2S)$			
A:	0.788	0.640	17.9

TABLE I $J/\Psi - N$ and $\Psi' - N$ cross section. A and B: numerical solution of the Schroedinger equation with parameters in Eqs. (20) and (21) respectively. C: Cross section obtained by the weighted average of the longitudinally and transversely polarized J/Ψ wave functions of ref. [10].

In ref. [10] a gaussian ansatz was made to construct vector meson wave functions that describe well the electromagnetic decay of the vector meson and photo and electroproduction cross sections. In Table I, wave function C) gives the result for the $J/\Psi - N$ cross section obtained with the weighted average of the longitudinally and transversely polarized J/Ψ wave functions from [10] with transversal sizes $\sqrt{< r_t^2 >} = 0.327$ fm and 0.466 fm.

Averaging over our results for different wave functions, our final result for the $J/\Psi - N$ cross section is

$$\sigma_{J/\psi} = 4.4 \pm 0.6\,\text{mb}\,. \tag{23}$$

The error is an estimate of uncertainties coming from the wave function and the model. The only other nonperturbative calculation of the $J/\Psi - N$ cross section that we are aware of was done in ref.[13] and the obtained cross section was $\sigma_{J/\psi} = 3.6$ mb, in a fair agreement with our result and with recent analysis of J/Ψ photoproduction data [8]. For Ψ' our cross section is also of the same order as the value obtained in [13]: $\sigma_{\psi'} = 20.0$ mb.

Since one of the possible explanations of the observed J/Ψ suppression is based on the pre-resonance absorption model [11] we present numerical calculations of the nucleon - pre-resonant charmonium state cross section, σ_{ψ}. In the pre-resonance absorption model, the pre-resonant charmonium state is either interpreted as a color-octet, $(c\bar{c})_8$, and a gluon in the hybrid $(c\bar{c})_8 - g$ state, or as a coherent $J/\Psi - \Psi'$ mixture. We use a gaussian transverse wave function, as in Eq. (17), to represent a state with transversal

radius $\sqrt{< r_t^2 >} \simeq 0.82\sqrt{< r^2 >} = \sqrt{2}S_\psi$ (S_ψ is the pre-resonance extension parameter analogous to S_p). With the knowledge of the wave functions and transformation properties of the constituents we can compute the total cross section given by the MSV. The resulting nucleon - pre-resonant charmonium state cross section will be different if the pre-resonant charmonium state consists of entities in the adjoint representation (as $(c\bar{c})_8 - g$) or in the fundamental representation (as a $J/\Psi - \Psi'$ mixture), the relation being $\sigma_{\text{adjoint}} = \frac{2N_C^2}{N_C^2-1}\sigma_{\text{fundamental}}$, with $N_C = 3$. In Table II we show the results for these two possibilities and different values of the transverse radius.

$\sqrt{< r_T^2 >}$ (fm)	$\sigma_{c\bar{c}}$ (mb)	$\sigma_{(c\bar{c})_8-g}$ (mb)
0.20	1.79	4.02
0.25	2.76	6.21
0.30	3.96	8.91
0.35	5.30	11.92
0.40	6.81	15.32
0.45	8.50	19.12
0.50	10.28	23.13

TABLE II The cross section charmonium-nucleon for gaussian wave-functions and different values of the transverse radius ($\sqrt{< r_t^2 >}$) of the $c\bar{c}$ in a singlet state (first row) or in a hybrid $(c\bar{c})_8 - g$ state (second row).

From our results we can see that a cross-section $\sigma_\psi^{abs} \simeq 6 - 7$ mb, needed to explain the J/Ψ and Ψ' suppression in p-A collisions in the pre-resonance absorption model [11, 7], is consistent with a pre-resonant charmonium state of size $\simeq 0.50 - 0.55$ fm if it is a $J/\Psi - \Psi'$ mixture or $\simeq 0.30 - 0.35$ fm for a $(c\bar{c})_8 - g$ state.

So far the calculations were done with the vacuum values of the correlation length and gluon condensate generally used in the MSV [23]. However, since the interaction between the charmonium and the nucleon occurs in a hadronic medium, these values may change. Indeed, lattice calculations [26, 27] show that both the correlation length and the gluon condensate tend to decrease in a dense (or hot) medium. The reduction of the string tension, σ, leads to two competing effects, which can be quantitatively compared in

the MSV. On one hand the cross section tends to decrease strongly when the gluon condensate or the correlation length decrease. On the other hand, when the string tension is reduced the $c-\bar{c}$ state becomes less confined and will have a larger radius, which, in turn, would lead to a larger cross section for interactions with the nucleons in the medium. It is of major interest to determine which of these effects is dominant.

The dependence of the total cross section, Eq. (15), on the extension parameters S_p and S_ψ is quite well parametrized as:

$$\sigma_{J/\psi} \propto < g^2FF >^2 a^{10} \left(\frac{S_p}{a}\right)^{1.5} \left(\frac{S_\psi}{a}\right)^2 \tag{24}$$

In the MSV the string tension, σ, is related to the gluon condensate and to the correlation length through Eq. (19). Therefore, the dependence of the cross section on the string tension and correlation length is approximately given by:

$$\sigma_\psi \propto \sigma^2 a^6 \left(\frac{S_p}{a}\right)^{1.5} \left(\frac{S_\psi}{a}\right)^2 . \tag{25}$$

In a rough approximation the hadron radii can be estimated, using the Ritz variational principle, to be:

$$S \propto \left(\frac{1}{\sigma}\right)^{1/3} , \tag{26}$$

and thus we finally obtain the following three possibilities to express the cross section as a function of the string tension, σ, the correlation length, a, and the gluon condensate, $< g^2FF >$:

$$\sigma_{\psi N} \propto \begin{cases} \sigma^{5/6} a^{5/2} \\ \sigma^{25/12} < g^2FF >^{-5/4} \\ < g^2FF >^{5/6} a^{25/6} \end{cases} \tag{27}$$

From the equation above we see that the final effect of the medium is a reduction in the cross section. We can also see that a 10% variation in the parameters lead to large variations on the cross sections.

Using the values of the correlation length and the gluon condensate reduced by 10%: $a = 0.31$ fm , $\langle g^2FF \rangle = 2.25$ GeV^4, we obtain a 40% reduction in the cross sections. Taking this reduction into account the cross sections obtained in this work are smaller than the ones needed (both in Refs. [11] and [7]) to explain experimental data. However, since in our

model the nucleon - pre-resonant charmonium state cross section is much bigger than the $J/\Psi - N$ cross section if the pre-resonance charmonium state is a hybrid $(c\bar{c})_8 - g$ state, the reduction in the cross sections due to medium effects favors the pre-resonant model for the hadronic explanation of the observed J/Ψ suppression.

In order to get more precise results we have varied only one the parameters a and $< g_s^2 FF >$ and kept the other fixed. This was done in such a way as to decrease the string tension according to equation (5) to the values given in Table III, first row. The numerically evaluated values for the mass of the J/Ψ (serving as a physical measure of the change) and the cross sections are given in rows 2 to 4, using Gaussian wave functions determined by the variational principle.

string tension [GeV^2] (GeV^2)	ΔE [MeV] MeV	σ_{tot} [mb] (mb) a const.	σ_{tot} [mb] (mb) $< g^2 FF >$ const.
σ_0	0	4.48	4.48
$0.9\sigma_0$	-33	3.86	3.38
$0.75\sigma_0$	- 83	3.27	2.2
$0.50\sigma_0$	-174	2.0	0.83
$0.25\sigma_0$	-275	0.91	0.13

TABLE III J/Ψ-Nucleon total cross sections as function of the string tension with either the correlation length or the gluon condensate kept constant. ΔE is the mass decrease of the J/Ψ due to the change of string tension.

4 Conclusions

We have calculated the nonperturbative $J/\Psi - \pi$, $J/\Psi - N$ and $\Psi' - N$ cross sections in two different nonperturbative approaches. In both of them, the basic ingredients are the wave functions of projectile and target and the low momentum modes of the gluon field inside the hadrons and in the vacuum. In the DCM, the main ingredient is the chromoelectric field in the hadrons. In the MSV, the basic ingredient is the gauge invariant correlator of two gluon field strength tensors which is characterized by two constants: the gluon condensate and the gluon field correlation length. Using for these quantities values fixed in previous applications and using well accepted charmonium wave functions we obtain $\sigma_{J/\psi N} \sim 4$ mb and $\sigma_{\psi' N} \sim 18$ mb. An

interesting prediction of the MSV is the strong depedence on the parameters of the QCD vacuum which will most likely lead to a drastic reduction of them at higher temperatures and perhaps also at higher densities.

Acknowledgements: This work has been supported by FAPESP and CNPq.

References

[1] *Proceedings of the Quark Matter '97 Conference*, *Nucl. Phys.* **A638** (1998).

[2] B. Müller, "Quark Matter '99 - Theoretical Summary. What Next?", nucl-th/9906029.

[3] T. Matsui and H. Satz, *Phys. Lett.* **B178** (1986) 416.

[4] C. Baglin et al. (NA38 Collab.), *Phys. Lett.* **B251** (1990) 472; **B270** (1991) 105; **B345** (1995) 617.

[5] M.C. Abreu et al. (NA50 Collab.), *Phys. Lett.* **B410** (1997) 327; M. Gonin et al. (NA50 Collab.), *Nucl. Phys.* **A610** (1996) 404c.

[6] D. Kharzeev, *Nucl. Phys.* **A638** (1998) 279c.

[7] C. Spieles *et al.*, "Modelling J/Ψ production and absorption in a microscopic nonequilibrium approach", hep-ph/9902337 and references therein.

[8] J.Hüfner and B.Z.Kopeliovich, *Phys. Lett.* **B426** (1998) 154 and references therein.

[9] L. Frankfurt and M. Strikman, *Nucl. Phys.* **B250** (1985) 147.

[10] H.G. Dosch, T. Gousset, G. Kulzinger and H.J. Pirner, *Phys. Rev.* **D55** (1997) 2602.

[11] D. Kharzeev, C. Lorenço, M. Nardi and H. Satz, *Z. Phys.* **C74** (1997) 318.

[12] D. Kharzeev and H. Satz, *Phys. Lett.* **B366** (1996) 316; **B356** (1995) 365; **B334** (1994) 155.

[13] L. Gerland *et al.*, *Phys. Rev. Lett.* **81** (1998) 762.

[14] Z. Lin, T.G. Di and C.M. Ko, nucl-th/0006086; Z. Lin and C.M. Ko, nucl-th/9912046; K. Haglin, *Phys. Rev.* **C61** (2000) 031912; K. Haglin and C. Gale, nucl-th/0010017; A.Sibirtsev, K. Tsushima and A.W. Thomas, nucl-th/0005041.

[15] F.S. Navarra and C.A.A. Nunes, *Phys. Lett.* **B356** (1995) 439.

[16] J. Hüfner, C. Lewenkopf and M.C. Nemes, *Nucl. Phys.* **A518** (1990) 297.

[17] V. Kuzmenko and Y.A. Simonov, hep-ph/0006192

[18] D. Kharzeev, H. Satz, A. Syamtomov and G. Zinovjev, hep-ph/9901375, and references therein.

[19] H.G. Dosch, F.S. Navarra, M. Nielsen and M. Rueter, *Phys. Lett.* **B466** (1999) 363.

[20] H.G. Dosch, *Phys. Lett.* **B190** (1987) 177.

[21] H.G. Dosch and Y.A. Simonov, *Phys. Lett.* **B205** (1988) 339.

[22] Y.A. Simonov, *Nucl. Phys.* **B307** (1988) 512.

[23] H.G. Dosch, E. Ferreira, A. Krämer, *Phys. Rev.* **D50** (1994) 1992 and references therein.

[24] O. Nachtmann, *Lectures, Schladming (Austria)*, hep-ph-9609365 (1996); *Annals Phys.* **209** (1991) 436.

[25] E. Eichten, K. Gottfried, T. Kinoshita, K.D. Lane and T.-M. Yan, *Phys. Rev.* **D17** (1978) 3090; *Phys. Rev.* **D21** (1980) 203.

[26] A. Di Giacomo, E. Meggiolaro and H. Panagopolos, *Nucl. Phys. Proc. Suppl.* **A54** (1997) 343.

[27] D.E. Miller, *Acta Phys. Polon.* **B28** (1997) 2937.

Constantino Tsallis

Remark on the Second Principle of Thermodynamics

Constantino Tsallis

Centro Brasileiro de Pesquisas Fisicas, Rua Xavier Sigaud 150, 22290-180 Rio de Janeiro-RJ, Brazil (tsallis@cbpf.br)

Abstract

All presently available results lead to the conclusion that nonextensivity, in the sense of nonextensive statistical mechanics (i.e., $q \neq 1$), does *not* modify anything to the second principle of thermodynamics, which therefore holds in the usual way. Moreover, some claims in the literature that this principle can be violated for specific anomalous systems (e.g., granular materials) can be shown to be fallacious. One recent such example is analyzed, and it is suggested how $q \neq 1$ distributions could in fact restore the validity of macroscopic time irreversibility, a cornerstone of our present understanding of nature.

The Second Principle of Thermodynamics, i.e., time irreversibility of the macroscopic world, appears to be one of the most solid laws of theoretical physics. Usual statistical mechanics, i.e., Boltzmann-Gibbs statistical mechanics, is consistent with this principle through the celebrated H-theorem. We address here what happens with this principle within the nonextensive statistical mechanics proposed in 1988 [1] and characterized by an entropic index q (the particular case $q = 1$ recovers standard Boltzmann-Gibbs statistical mechanics). The answer seems to be very simple: no hope for *moto perpetuo* within this formalism! Indeed, the H-theorem appears to be q-invariant, more precisely, excepting for very quick microscopic fluctuations, S_q cannot decrease (increase) with time if $q > 0$ ($q < 0$), a fact which is consistent with the concavity (convexity) of S_q, with regard to the set of probabilities, for $q > 0$ ($q < 0$) (hence, S_q is respectively maximal and minimal for $q > 0$ and

$q < 0$). This q-invariance was first pointed by Mariz [2] assuming detailed balance, and since then by many other authors (see [3] and references therein) in a variety of generic situations. In addition to this, the present nonextensive thermostatistics provides a possible path for solving amazing "violations" of the second principle of thermodynamics. The rest of this paper is dedicated to the re-analysis of one such example that appeared recently in the literature of granular materials.

Through molecular dynamics simulations using the inelastic hard sphere model to mimic fluidized granular media, Soto, Mareschal and Risso addressed [4] a very interesting question, namely the validity (or not) of Fourier's law and of the second principle of thermodynamics for dissipative macroscopic systems. They simulated a simple $d = 2$ system in the presence of a "vertical" (y axis) gravitational field, the top and bottom edges of a square box providing, to the arriving particles, a Maxwellian distribution of velocities at a fixed (dimensionless) temperature $T = 1$. The average density n_0 and the dissipation coefficient q_{SMR} (we use here the notation q_{SMR} instead of the original notation q [4] in order to avoid confusion with the nonextensive entropic index q) were held fixed during a given simulation ($q_{SMR} = 0$ corresponds to the conservative limit, i.e., elastic collisions). They measured, as functions of the height y, the density n, the temperature T and the heat flux $\mathbf{J}$. After long runs the system achieved a stationary state, like the one illustrated in their Fig. 1. The authors verified that $T(y)$ exhibits a minimum at $y = y^*$, whereas $\mathbf{J}$ vanishes at a value of y *larger* than y^*. Consequently, the authors conclude that Fourier's law, which reads $\mathbf{J} = -k\nabla T$, k being the thermal conductivity, is violated. Moreover, for all values of y not exceedingly above y^*, the heat appears to flow from the cold regions to the hot regions, therefore the authors consistently conclude that the second law of thermodynamics is violated as well. The way out from this paradoxal situation that Soto et al advocate is that an extra, n-dependent, term must be included in the expression of $\mathbf{J}$.

The purpose of the present remark is to argue that the proof provided by Soto et al would be very neat were it not a subtle weakness that we now address. The quantities n and $\mathbf{J}$ observed in the simulations are calculated essentially through their definitions. This is *not*

the case of T, which the authors set *equal to the average kinetic energy per particle.* This equality holds for the well known Maxwellian distribution, *an assumption which is certainly false inside the box* (see, for instance, [5,6]). In order to illustrate the subtleties, let us use nonextensive statistical mechanics. Indeed, the use of such generalized statistics for the present system is quite natural since the stationary distribution observed by Taguchi and Takayasu in a vibrating-bed fluidized state *precisely* corresponds, as we shall see, to $q = 3$ (similarly to what occurs in Lévy and correlated anomalous diffusions [7]), whereas they observe a Maxwellian distribution (i.e., $q = 1$) in the so-called solid state. The possibility of applicability of this formalism to such materials has also been recently mentioned by Herrmann [8].

For the Hamiltonian $\mathcal{H} = \frac{1}{2}\sum_{i=1}^{N} \mathbf{v}_i^2$, the nonextensive formalism yields, for the velocity distribution probability,

$$p_q(\{\mathbf{v}_i\}) = \frac{\left[1-(1-q)(\mathcal{H}-U_q)/T_q\right]^{\frac{1}{1-q}}}{Z_q} \tag{1}$$

where $Z_q \equiv \int\left[\Pi_{j=1}^{N} d\mathbf{v}_j\right]\left[1-(1-q)(\mathcal{H}-U_q)/T_q\right]^{\frac{1}{1-q}}$, $U_q \equiv \int\left[\Pi_{j=1}^{N} d\mathbf{v}_j\right] p_q^q\ \mathcal{H} / \int\left[\Pi_{j=1}^{N} d\mathbf{v}_j\right] p_q^q$ and $T_q \equiv T Z_q^{1-q}$. This equilibrium distribution has been obtained by optimizing $S_q = \left(1-\int\left[\Pi_{j=1}^{N} d\mathbf{v}_j\right] p^q\right)/(q-1)$ with appropriate constraints (Boltzmann constant k_B has been taken equal to unity). It recovers the usual Maxwellian distribution for $q = 1$ and a power-law for $q \neq 1$. Also, we verify that $1/T = \partial S_q / \partial U_q$. Finally, we can rewrite Eq. (1) as follows:

$$p_q = \frac{\left[1-(1-q)\mathcal{H}/T'\right]^{\frac{1}{1-q}}}{Z'_q} \tag{2}$$

where $Z'_q \equiv \int\left[\Pi_{j=1}^{N} d\mathbf{v}_j\right]\left[1-(1-q)\mathcal{H}/T'\right]^{\frac{1}{1-q}}$ and $T' \equiv T_q + (1-q)U_q$.

We verify that, for $q = 1$, $T_q = T' = T$, but such simplification disappears if $q \neq 1$, which might be the case for the system considered by Soto et al. In particular, if we identify p_q^q (p_q being the $N = 1$ distribution (2)) with the distribution numerically obtained in [5] for the vibrating-bed fluidized state, we obtain $q/(q-1) = 3/2$, hence $q = 3$. In other words, some

further considerations are necessary before drawing any conclusion about the validity (or not) of Fourier's law and of the second principle of thermodynamics. A remarkable simplification does exist due to the fact that Yamano and others (see [10] and references therein) have recently shown [9] that each quadratic velocity term contributes to U_q with $T_q/2$. But, for the rest, the entire Fourier law would have to be rededuced, possibly in the $q \neq 1$ scenario. A variety of mathematical tools [11] (e.g., the q-generalization of Kubo's linear response theory) are already available in the literature for performing such generalization. It is clear nevertheless that this is not a trivial task. Only *after* such an analysis, the interesting computer simulations of Soto et al could led us to further conclusions. It could even happen that, in the present granular matter fluidized state, the generalized $\mathbf{J}$ vanishes precisely when T_q attains its minimum!

REFERENCES

[1] C. Tsallis, J. Stat. Phys. **52**, 479 (1988); E.M.F. Curado and C. Tsallis, J. Phys. A **24**, L69 (1991) [Corrigenda: **24**, 3187 (1991) and **25**, 1019 (1992); C. Tsallis, R.S. Mendes and A.R. Plastino, Physica A **261**, 534 (1998); the bibliography of the subject is regularly updated at http://tsallis.cat.cbpf.br/biblio.htm; for recent reviews see C. Tsallis, in *Nonextensive Statistical Mechanics and Thermodynamics*, eds. S.R.A. Salinas and C. Tsallis, Braz. J. Phys. **29**, 1 (1999) [accessible at http://sbf.if.usp.br/WWW_pages/Journals/BJP/Vol29/ Num1/index.htm], and C. Tsallis, in *Nonextensive Statistical Mechanics and its Applications*, eds. S. Abe and Y. Okamoto, Series *Lecture Notes in Physics* (Springer-Verlag, Berlin, 2000), in press.

[2] A.M. Mariz, Phys. Lett. A **165**, 409 (1992).

[3] J.D. Ramshaw, Phys. Lett. A **175**, 169 and 171(1993); M. Shiino, J. Phys. Soc. Japan **67**, 3658 (1998); L. Borland, A.R. Plastino and C. Tsallis, J. Math. Phys. **39**, 6490 (1998) [Errata: J. Math. Phys. **40**, 2196 (1999)]; T.D. Frank, Phys. Lett. A **267**, 298 (2000).

[4] R. Soto, M. Mareschal and D. Risso, Phys. Rev. Lett. **83**, 5003 (1999).

[5] Y.-H. Taguchi and H. Takayasu, Europhys. Lett. **30**, 499 (1995); see also A. Kudrolli and J. Henry, Phys. Rev. E **62**, R1489 (2000).

[6] L.P. Kadanoff, Rev. Mod. Phys. **71**, No 1 (1999) and references therein.

[7] C. Tsallis, S.V.F. Levy, A.M.C. Souza and R. Maynard, Phys. Rev. Lett. **75**, 3589 (1995) [Erratum: Phys. Rev. Lett. **27**, 5442 (1996)]; D. Prato and C. Tsallis, Phys. Rev. E Phys. Rev. E **60**, 2398 (1999); A.R.Plastino and A.Plastino, Physica A **222**, 347 (1995); C. Tsallis and D.J. Bukman, Phys. Rev. E **54**, R2197 (1996).

[8] H.J. Herrmann, *Dynamics of granular systems*, Physica A (2001), in press.

[9] T. Yamano, Phys. Lett. A **264**, 276 (1999).

[10] R.S. Mendes and C. Tsallis, *Renormalization group approach to nonextensive statistical mechanics*, preprint (2000) [cond-mat/0003365].

[11] A.K. Rajagopal, Phys. Rev. Lett. **76**, 3469 (1996); E.K. Lenzi, L.C. Malacarne and R.S. Mendes, Phys. Rev. Lett. **80**, 218 (1998); A.K. Rajagopal, R.S. Mendes and E.K. Lenzi, Phys. Rev. Lett. **80**, 3907 (1998); S. Abe, Eur. Phys. J. B **9**, 679 (1999); E.K. Lenzi, R.S. Mendes and A.K. Rajagopal, Phys. Rev. E **59**, 1398 (1999).

Gerald A. Miller

Light Front Nuclear Theory and the HERMES Effect

Gerald A. Miller
Department of Physics
University of Washington
Seattle, Washington 98195-1560

Abstract

I discuss applications of relativistic light front dynamics (the use of light cone variables) to computing the nucleonic and mesonic components of nuclear wave functions. Our method is to use a Lagrangian and its associated energy-momentum tensor $T^{+\mu}$ to define the total momentum operators P^{μ}, with P^{+} as the plus-momentum and P^{-} the light cone time development operator. The aim of this unusual approach to nuclear physics is the desire to use wave functions, expressed in terms of plus-momentum variables, which are used to analyze high energy experiments such as deep inelastic scattering, Drell-Yan production, (e,e') and (p,p') reactions. We discuss or mention the topics: infinite nuclear matter within the mean field approximation; finite nuclei using the mean field approximation; nucleon-nucleon scattering, within the one boson exchange approximation; and, infinite nuclear matter including the effects of two-nucleon correlations. Standard good results for nuclear saturation properties are obtained, with a possible improvement in the lowered value, 180 MeV, of the computed nuclear compressibility. In our approach, manifest rotational invariance can't be used to simplify calculations. But for each of the examples reviewed here, manifest rotational invariance emerges at the end of the calculation. Thus nuclear physics can be done in a manner in which modern nuclear dynamics is respected, boost invariance in the z-direction is preserved, and in which rotational invariance is maintained. A salient feature is that ω, σ and π mesons are obtained from the nuclear structure theory as important constituents of nuclei. I then argue that these constituents can contribute coherently to enhance the electroproduction cross section on nuclei for longitudinal virtual photons at low Q^2 while depleting the cross section for transverse photons. Thus the recent HERMES inelastic lepton-nucleus scattering data at low Q^2 and small x can be described using photon-meson and meson-nucleus couplings which are consistent with (but not determined by) constraints obtained from meson decay widths, nuclear structure, deep inelastic scattering, and lepton pair production data. Our model makes a variety of predictions testable in future experiments.

I. INTRODUCTION

This talk consists of two parts. The first is concerned with the subject of light front nuclear theory [1]- [4], and the second with the application [5] of that theory to an effect discovered in high energy lepton-nucleus scattering by the HERMES collaboration [6].

In this work, we will consider the regime in which the nucleus treated as being made of nucleons and mesons. Our goal is to get the ground state wave function at zero temperature in terms of light front coordinates. Using these coordinates to evaluate the consequences of a given Lagrangian is also called light front dynamics. We shall begin by giving a few more details concerned with answering the following questions. What is light front nuclear theory? Why do it?

We shall present examples and results of three studies: infinite nuclear matter treated using the mean field approximation; finite nuclei also treated with that approximation; and, infinite nuclear matter including correlations between two nucleons (light front Brueckner Theory). In each application we find that vector and scalar mesons are prominent components of nuclear wave functions.

The second part is concerned with searching for experimental consequences of these components. Thus we discuss the HERMES effect [6] as a signature of these nuclear mesons. This effect is observed in the interaction of 27.5 GeV positrons with nuclei, and arises because virtual photons have longitudinal L polarization as well as the usual transverse T polarization. The HERMES collaboration measures a ratio of cross sections for the scattering of photons with different polarizations. They find [6]:

$$\left(\frac{\sigma_L(A)}{\sigma_L(D)}\right) / \left(\frac{\sigma_T(A)}{\sigma_T(D)}\right) \approx 5, \tag{1.1}$$

for $x = 0.01$, and $Q^2 = 0.5$ GeV^2. This is truly a remarkable result. It has long been known that for deep inelastic scattering from a free nucleon one measures $\left(\frac{\sigma_L}{\sigma_T}\right) \ll 1$. The vanishing of this ratio is known (in other notation) as the Callan-Gross relation [7], and its verification provided the evidence for the finding that the partons observed in deep inelastic scattering are fermions (quarks). Now we have an experiment that seems to indicate that in nuclei the partons are bosons.

II. WHAT IS LIGHT FRONT DYNAMICS?

I try to mention only the most essential features. This dynamics is a relativistic many-body dynamics in which the fields are quantized at a "time", $t + z = x^0 + x^3 \equiv x^+$ and the canonically conjugate "energy" is given by $p^0 - p^3 \equiv p^-$. Indeed, p^- is the x^+ evolution operator, just as the Hamiltonian, p^0 is the x^0 time evolution operator. If x^+ is "time", then for "space" we must have $x^- \equiv t - z$, with the canonically conjugate "momentum" as $p^+ = p^0 + p^3 \equiv p^+$. The other coordinates are treated as usual $\vec{x}_\perp, \vec{p}_\perp$. The use of the p^+ as the momentum variable is, for me, the reason behind the use of light front dynamics. This is because for a particle moving with large speed such that $\vec{v} \approx c\hat{e}_3$, p^+ is BIG, and for this reason is the experimentalists variable. Many observables are best expressed using

this notation. In deep inelastic scattering the famous Bjorken variable $x_{Bj} = Q^2/2M\nu$ is actually a ratio of plus momenta of the struck quark to that of the entire struck nucleon. With our choice of variables: $A^{\pm} \equiv A^0 \pm A^3$, and the dot product of two four vectors is given by

$$A \cdot B = A^{\mu}B_{\mu} = \frac{1}{2}\left(A^{+}B^{-} + A^{-}B^{+}\right) - \vec{A}_{\perp} \cdot \vec{B}_{\perp}. \tag{2.1}$$

The most important application of Eq. (2.1) is the energy-momentum relation for a free particle:

$$p^{\mu}p_{\mu} = m^2 \quad = p^{+}p^{-} - {p_{\perp}}^2, \tag{2.2}$$

so that

$$p^{-} = \frac{1}{p^{+}}(p_{\perp}^2 + m^2). \tag{2.3}$$

One has a relativistic expression for the energy without a square root operator. This is an enormous simplification when one wants to separate the coordinates of the center-of-mass from the rest of the wave function. We may provide an approximate summary of light front dynamics: Do ordinary quantum mechanics with energy denominators expressed in terms of p^{-}.

Another feature is that, when one uses the Lagrangians of nuclear physics the usual lore about light front dynamics should be true. That is the vacuum really is empty. This is because nucleons are heavy enough so that nucleon pairs do not form vacuum condensates. Thus we should not ask what the light front dynamics can do for nuclear physics. Instead we should ask what nuclear physics can do for light front dynamics. This is to provide solutions of realistic, four-dimensional problems with relevance to observables.

III. MOTIVATION FOR LIGHT FRONT NUCLEAR PHYSICS

Since much of this work is motivated by the desire to understand nuclear deep inelastic scattering and related experiments, it is worthwhile to review some of the features of the EMC effect [8–10]. One key experimental result is the suppression of the structure function for $x \sim 0.5$. This means that the valence quarks of bound nucleons carry less plus-momentum than those of free nucleons. Some other degrees of freedom must carry the plus-momentum, and some authors therefore postulate that mesons carry a larger fraction of the plus-momentum in the nucleus than in free space [11,12]. While such a model explains the shift in the valence distribution, one consequently obtains a meson (i.e. anti-quark) distribution in the nucleus, which is enhanced compared to free nucleons, and which should be observable in Drell-Yan experiments [13]. However, no such enhancement has been observed experimentally [14], and this has been termed as a severe crisis for nuclear theory in Ref. [15].

The EMC effect is rather small, so that one may begin by regarding the nucleus as being made of nucleons. In this case, we say that deep inelastic scattering proceeds when

a virtual photon is absorbed by a quark carrying plus-momentum p^+, which came from a nucleon carrying a plus-momentum k^+. In the parton model, the kinematic variable $x_{Bj} = Q^2/2M_N\nu$ is given by

$$x_{Bj} = \frac{p^+}{k^+}. \tag{3.1}$$

Thus one needs to know the probability $f_N(k^+)$ that a nucleon has k^+. One also wants to know the related probability for a meson, for example: $f_\pi(k^+)$.

Light front dynamics applies to nucleons within the nucleus as well as to partons of the nucleons, and this is a useful approach whenever the momentum of initial or final state nucleons is large compared to their mass [16]. For example, this technique can be used for $(e, e'p)$ and $(p, 2p)$ reactions at sufficiently high energies.

The essential technical advantage of using light cone variables is that the light cone energy P^- of a given final state does not appear in the delta function which expresses the conservation of energy and momentum. Thus one may use closure to perform the sum over final states which appears in the calculation of an exclusive nuclear cross section. The result is that the cross sections may be expressed in terms of the probabilities:

$$\sigma \propto f_N(k^+) \sim \int d^2k_\perp \cdots \mid \Psi_{A,i}(k^+, k^\perp, \cdots) \mid^2, \tag{3.2}$$

where Ψ represents the ground state wave function.

For all these reasons we are concerned with calculating $f_N(k^+)$. One standard approach to the calculation, based on using the shell model equal time formulation is that: $E_\alpha + k^3 \to k^+$. But this can not be correct because k^+ is a continuous kinematic variable which is not related to any discrete eigenvalues. Thus we need realistic calculations, with real dynamics and symmetries. This brings me to the conclusion that it is necessary to redo nuclear physics on the light front.

IV. LIGHT FRONT QUANTIZATION LITE

Our attitude towards this topic is that we need $\mathcal{L}$ no matter how bad! This is because, in contrast with approaches based on symmetries, we try to obtain all of the necessary operators from a given Lagrangian $\mathcal{L}$. The basic idea is to use the standard procedure to go from $\mathcal{L}$ to $T^{\mu\nu}$, with the essential difference from the usual procedure being that

$$P^\mu = \frac{1}{2}\int d^2x_\perp dx^- T^{+\mu}. \tag{4.1}$$

A technical challenge arises because we need to express $T^{+\mu}$ in terms of independent variables. For example, the spin 1/2 nucleon is always represented by 4 component spinor. Thus it has only 2 independent degrees of freedom. One needs to express the two dependent variables in terms of the two independent variables. This procedure is discussed in the references.

We use two Lagrangians. The first is that of the Walecka model [17]: $\mathcal{L}(\phi, V^\mu, N)$ which contains the fields: nucleon N, neutral vector meson V^μ, neutral scalar meson ϕ. This is the

simplest model which provides a reasonable caricature of the nucleus. The binding is caused by the attractive effects occurring at relatively long range when nucleons exchange scalar mesons. The nucleus is prevented from collapsing by the short distance repulsion arising from the exchange of vector mesons.

We also shall show results obtained using a more complicated chiral Lagrangian: in which the fields are $N, \pi, \sigma, \omega, \rho, \eta, \delta$. Our plan is to first use the Walecka model in the mean field approximation, and then to include NN correlations using the chiral Lagrangian.

V. INFINITE NUCLEAR MATTER IN MEAN FIELD APPROXIMATION– WALECKA MODEL

The basic idea behind the solution is very well known. One assumes that the sources are strong, and produce sufficiently many mesons to justify a classical treatment. In infinite nuclear matter, one works in a limit in which the nuclear volume Ω is considered to be infinite, so that all positions, and directions equivalent in the nuclear rest frame. In this limit the fields ϕ and $V^{\pm}$ become constant, with $V_{\perp} = 0$. These features simplify the solution of the field equations. One easily obtains the operators $T^{\pm}$, and the light front "momentum" and "energy" are given by

$$\frac{P^{\pm}}{\Omega} = \langle T^{\pm} \rangle, \tag{5.1}$$

in which the expectation value is over the nuclear ground state.

The nuclear momentum content is the essential feature we wish to understand here. The results are that

$$\frac{P^{-}}{\Omega} = m_s^2 \phi^2 + \frac{4}{(2\pi)^3} \int_F d^2k_{\perp} dk^{+} \, \frac{k_{\perp}^2 + (M + g_s\phi)^2}{k^{+}} \tag{5.2}$$

$$\frac{P^{+}}{\Omega} = m_v^2 (V^{-})^2 + \frac{4}{(2\pi)^3} \int_F d^2k_{\perp} dk^{+} \, k^{+}. \tag{5.3}$$

The first term of P^{+} is the plus momentum carried by vector mesons, and the second term is the plus momenta carried by the nucleons. Here g_s is the scalar-meson-nucleon coupling constant, and the vector meson-nucleon coupling constant g_v enters in the expression for V^{-}. The interpretation of these results is aided by a change of variables:

$$k^{+} \equiv \sqrt{(M + g_s\phi)^2 + \vec{k}^2} + k^3, \tag{5.4}$$

which defines defines the variable k^3. Using this variable one can show that rotational invariance is respected and obtain a spherical Fermi surface. Furthermore, one may show that $E \equiv \frac{1}{2}(P^{-} + P^{+})$ is the same as the usual expression obtained in the Walecka model.

For nuclear matter in its rest frame we need to obtain $P^{+} = P^{-} = M_A$. This is the light front expression of the statement that the pressure on the system must vanish [3]. Indeed the minimization

$$\left(\frac{\partial (E/A)}{\partial k_F} \right)_{\Omega} = 0, \tag{5.5}$$

determines the value of the Fermi momentum and is an expression that gives $P^+ = P^- = M_A$.

We can quickly obtain the relevant numerical results using the 1974 parameters of Chin & Walecka. These are

$$g_v^2 M_N^2/m_v^2 = 195.9 \qquad g_s^2 M_N^2/m_s^2 = 267.1. \tag{5.6}$$

With these parameters $M_N + g_s\phi = 0.56 M_N$ and $g_v V^- = 270$ MeV. These are the HUGE scalar and vector potentials which are characteristic of the Walecka model. The interesting variables are those associated with the total nuclear plus momentum $\frac{P^+}{\Omega}$. With the above parameters, the vector meson contribution to this quantity: $m_v^2(V^-)^2$ is a monumental 0.35 $\frac{P^+}{\Omega}$, while the nucleon contribution $\frac{4}{(2\pi)^3}\int_F d^2k_\perp dk^+\, k^+$ is only $0.65\frac{P^+}{\Omega}$. Only 65 % of P^+ carried by nucleons, but 90% is needed to understand the EMC effect in infinite nuclear matter [18]. This difference is huge. One can't plot the results of the theory in comparison with the experimental results using pages of ordinary size.

So the large plus momentum carried by the vector mesons is a feature of the Walecka model, which seems very odd. One needs to find means to reduce this percentage from 35%, but one also expects that within any model the vector mesons would carry some plus-momentum and it therefore becomes desirable to search for an experimental verification of this feature.

VI. BEYOND INFINITE NUCLEAR MATTER– MEAN FIELD THEORY

One possibility is that the large plus momentum carried by vector mesons arises as an artifact of using infinite nuclear matter. We (Blunden, Burkardt and I, [2]) therefore investigated the subject of light front Hartree Fock theory by performing nucleus mean field theory calculations.

The motivation is the need to find a way to reduce the plus-momentum carried by vector mesons, but one encounters a significant difficulty in the theory because the use of the variables $(x^-, \vec{x}_\perp)$ entails the loss of manifest rotational invariance. We found that the procedure of minimizing $\langle P^- \rangle$ subject to the constraint $\langle P^+ \rangle = \langle P^- \rangle$, led to the recovery of rotational invariance. This was seen by counting the number of degenerate levels $(2j+1)$ that emerges from a numerical calculation in which only rotational invariance about the z-axis could be used to simplify the calculation. This is important for understanding the existence of magic numbers in nuclei. The result of doing the lengthy calculations was that nucleons were found (using the Walecka model) to carry about 70% of total P^+. This was only a modest improvement over the nuclear matter result of 65%, and does not resolve the problem.

VII. BEYOND MEAN FIELD THEORY

The interactions between nucleons are strong, and the mean field approximation is unlikely to provide a description of nuclear properties which involve high momentum observables. We developed [1,3] a version of light front theory in which the correlations between two nucleons are included. The theory was applied to infinite nuclear matter.

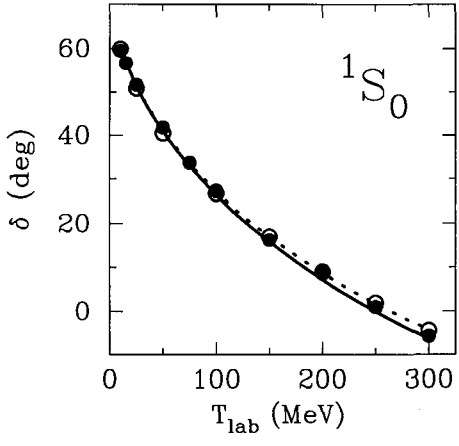

FIG. 7.1. Phase shift as a function of energy. Solid: our theory, dashed: an earlier relativistic theory.

The calculation required three principal steps. (1) Light front quantization of chiral $\mathcal{L}$. (2) Derive Light Front version of the NN one boson exchange potential. This could be done exploiting the relationship between the Weinberg equation and the Blankenbecler-Sugar equation. A sample of results for the phase shift is shown in Fig. 7.1. The third step is to develop the many body theory. This turns out to be a long story [3]. The net result is that the light front theory looks like the usual relativistic Brueckner theory theory except that the Blankenbecler-Sugar equation is used, and the effects of retardation are kept. The resulting nuclear matter saturation curve is shown in Fig. 7.2. Standard good results for nuclear saturation properties are obtained, with a possible improvement in the lowered value, 180 MeV, of the computed nuclear compressibility.

The results for deep inelastic scattering and the related Drell-Yan process seem very promising. The nucleons carry at least 84% of the nuclear plus momentum. This is calculated using only the Fermi gas part of the wave function. The percentage might increase to about 90% (the target value for deep inelastic scattering) if the effects of the two-particle two-hole states are included. In these calculations the nucleus does have a pionic component, which arises as a result of going beyond teh mean field approximation. The number of excess pions per nucleon is about 5%, and although the distribution function of nuclear pions has not yet been computed, this seems small enough to avoid a contradiction with the Drell-Yan data

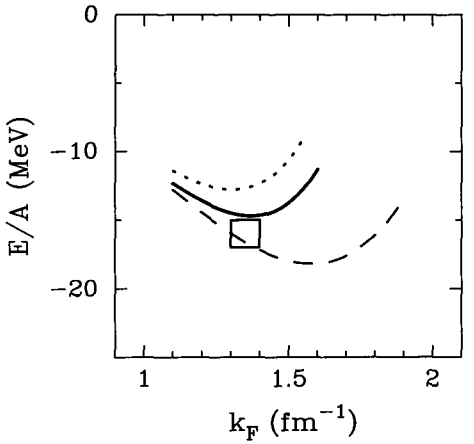

FIG. 7.2. Nuclear matter binding energy per particle. Solid: our theory, dashed: non-relativistic theory, dotted ignoring the effects of retardation.

[19].

It seems that nuclear physics can be done in a manner in which modern nuclear dynamics is respected, boost invariance in the z-direction is preserved, and in which the rotational invariance so necessary to understanding the basic features of nuclei is maintained. A salient feature is that ω, σ and π mesons are important constituents of nuclei. Another point, not much dicussed here, is that it seems possible to find Lagrangians that yield reasonable descriptions of nuclear deep inelastic scattering and Drell-Yan reactions.

In the remainder of this talk I pursue the idea that the HERMES effect provides a signature for the presence of nuclear ω and σ mesons.

VIII. COHERENT CONTRIBUTIONS OF NUCLEAR MESONS TO ELECTROPRODUCTION– HERMES EFFECT

Let us discuss the nature of the HERMES effect [6]. Everyone is very familiar with the idea that lepton-nucleon or lepton nucleus scattering proceeds by the exchange of a virtual photon of four momentum $q = (\nu, \vec{q})$. The important structure functions depend mainly on x_{Bj}, with dependence on the logarithm of $Q^2 = -q^2$. However, the cross sections depend on a third variable: $y = \frac{\nu}{E}$, where E is the energy of the incident lepton. The energy at which HERMES runs, 27.5 GeV, is small enough so that the experiment covers a wide range of values of y. This feature is what allows a new effect to be observed. In particular, the cross section depends on the scattering of transversely T and longitudinally L polarized photons [20]:

$$\sigma \propto \sigma_T + \epsilon \sigma_L \tag{8.1}$$

$$\epsilon \approx \frac{4(1-y)}{4(1-y)+2y^2}. \tag{8.2}$$

It is conventional to make the definition

$$R \equiv \frac{\sigma_L}{\sigma_T}. \tag{8.3}$$

In that case, one may manipulate the standard relations between the cross section and structure function to find

$$\frac{\sigma_A}{\sigma_D} = \frac{F_2^A}{F_2^D} \quad \frac{1+\epsilon R_A}{1+R_A} \quad \frac{1+R_D}{1+\epsilon R_D}. \tag{8.4}$$

A linear dependence of the ratio on ϵ provides a signature of a large value of R_A. Indeed, the HERMES collaboration extracted $\frac{F_2^A}{F_2^D}$,and R_A from x, Q^2, and ϵ dependence of $\frac{\sigma_A}{\sigma_D}$. The results are that

$$\frac{\sigma_L(A)}{\sigma_L(D)} > 1, \qquad \frac{\sigma_T(A)}{\sigma_T(D)} < 1, \tag{8.5}$$

with the largest effects

$$\frac{R_A}{R_D} \approx 5 \tag{8.6}$$

obtained for $x \approx 0.01$, $Q^2 = 0.5$ GeV^2. As noted in the Introduction, this represents a huge violation of the Callan-Gross relation [7], a violation large enough to indicate that, in nuclei, bosons are the partons of deep inelastic scattering! In the following, I describe the work of Ref. [5].

IX. NUCLEAR ENHANCEMENT OF σ_L

We wish to describe the nuclear enhancement of σ_L and the nuclear suppression of σ_T using a single input theory. We start with σ_L. We found that a process in which a virtual photon of four momentum q is converted in its interaction with a nuclear ω meson into a scalar meson of four momentum p, with $p^0 \approx \nu$, produces the desired enhancement.

To evaluate the effects of this process, we need to determine the $\gamma\omega\sigma$ interaction. We postulate a gauge-invariant form

$$\mathcal{L}_I = \frac{g\, e}{2m_\omega} F^{\mu\nu}(\omega_\nu \partial_\mu \sigma - \omega_\mu \partial_\nu \sigma) \tag{9.1}$$

where $F^{\mu\nu}$ is the photon field strength tensor. In momentum space one can use

$$\mathcal{M} = \frac{g}{m_\omega}\,(p\cdot q\;\epsilon^\gamma\cdot\epsilon^\omega - p\cdot\epsilon^\gamma\; q\cdot\epsilon^\omega)\, F_V(Q^2) \tag{9.2}$$

in which we include a form factor F_V. We seek a constraint on the value of g from the decay: $\omega \to \sigma\gamma$. The branching ratio for $\omega \to \pi^+\pi^-\gamma < 3.6 \times 10^{-3}$ [21], which we assume to come from the process $\omega \to \gamma\sigma$ followed by the two pion decay of the σ meson. We may determine an upper limit for g: $g_{UL}^2\alpha = .013 \approx 2\alpha$.

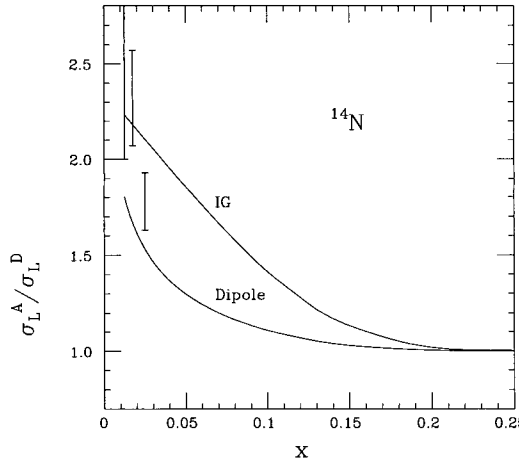

FIG. 9.1. $\frac{\sigma_L(A)}{\sigma_L(D)}$, A=14, HERMES data. The labels IG, dipole refer to form factors, see text.

Using this coupling constant, we obtained [5]

$$\delta W^{00} \sim (V^-)^2 A^{1/3}\, \nu^3\, F_V^2(Q^2), \tag{9.3}$$

in which V^- is the value of the vector meson field at the center of the nucleus. We use values which are consistent with nuclear saturation, and DIS, DY reactions. Notice the presence of the ν^3 term which arises from the factors of momentum appearing in Eq. (9.2). This dependence is essential because standard kinematics gives the result

$$\frac{\sigma_L(A)}{\sigma_L(D)} = 1 + \frac{Q^4}{\nu(\nu^2+Q^2)} \frac{\delta W^{00}}{F_2^D R_D}(1+R_D). \tag{9.4}$$

The form factor $F_V(Q^2)$ is obtained from Ref. [22], we also use a dipole form factor. The results are shown in Fig. (9.1). One is able to account for the large enhancement.

X. NUCLEAR SUPPRESSION OF $\sigma_T(A)$

Our explanation of the nuclear transverse cross section σ_T data requires a significant destructive interference effect at low $Q^2 \approx 0.5 - 2$ GeV^2. For small values of x, in the target rest frame, the interaction proceeds by γ^* decaying into a $q\bar{q}$ pair, which then interacts with a target nucleon and emerges as a vector meson V_f. For a nuclear target, we suppose that the virtual photon interacts with a nuclear σ meson and is converted to an intermediate vector boson V, which is converted into the final vector meson V_f by a final state interaction.

We need to find the necessary $\gamma^*\sigma \to V$ interaction. For consistency with data taken at larger value of Q^2, we need an interaction which decreases rapidly as Q^2 increases. Furthermore, the shadowing of the real photon ($Q^2 = 0$) is not very strong, and it is well explained

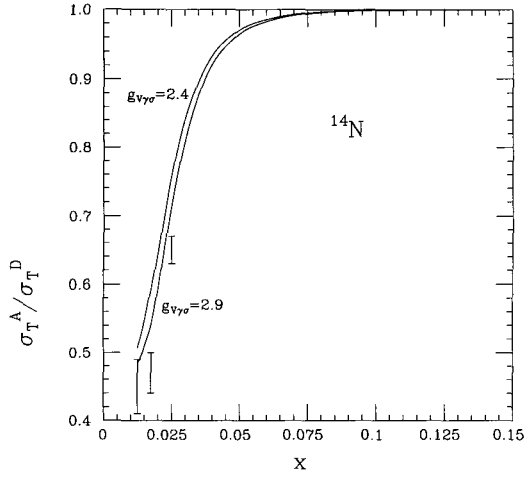

FIG. 10.1. $\sigma_T(A)/\sigma_T(D)$, A=14, HERMES data

by conventional vector meson dominance models [23]. Thus consistency with all available data demands an amplitude for $\gamma^*\sigma \to V$ which vanishes, or is small, as the Q^2 of the virtual photon γ^* approaches 0. This means that measuring the real photon decays of the vector mesons provides no constraints on the coupling constant.

We postulate the gauge-invariant interaction

$$\delta\mathcal{L}_I = \sum_V \frac{g_{\gamma V\sigma}}{2m_\sigma} e\, F_{\mu\nu}\left[V^{\mu\nu}\sigma + V^\mu\partial^\nu\sigma - V^\nu\partial_\mu\sigma\right] F_1^V, \tag{10.1}$$

which in momentum space is $\propto Q^2$. The details of the application are given in the published work. The results are shown in Fig.(10.1).

The nuclear enhancement of R is obtained from computing the ratio of the previous results. This is shown in Fig.(10.2), where it is seen one has a reasonably good description of the data.

We may summarize the results of our studies of the HERMES effect. We find that $\sigma_L(A)$ is enhanced by the presence of nuclear vector mesons, and that $\sigma_T(A)$ is depleted by the presence of nuclear scalar mesons. Both types of mesons are needed to obtain nuclei with correct binding energies and densities. The values of the strong coupling constants used are also roughly consistent with data on nuclear deep inelastic scattering data taken at larger values of Q^2.

Much verification of the present model is needed. Further tests of our model are possible. An immediate consequence would be the observation of exclusive mesonic states in the current fragmentation region. In particular, our description of $\sigma_L(A)$ implies significant nuclear-coherent production of σ mesons along the virtual photon direction. Our model for the strong shadowing of coherent meson effects in $\sigma_T(A)$ can be tested by measurements performed at the same value of x but different values of Q^2 than HERMES used.

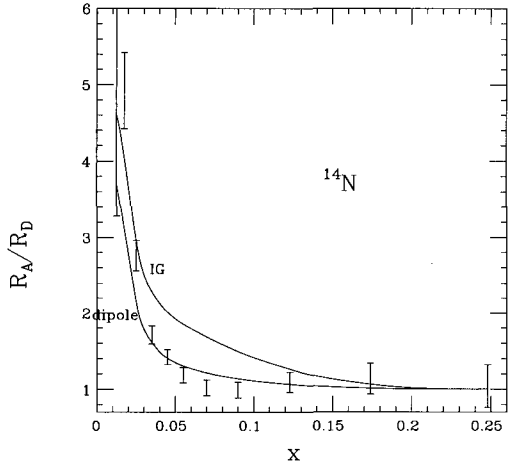

FIG. 10.2. $R(A)/R(D)$, A=14

The prospect that the mesonic fields which are responsible for nuclear binding can be directly confirmed as effective fundamental constituents of nuclei at small x and $Q^2 \sim 1$ GeV^2 is an exciting development at the interface of traditional nuclear physics and QCD. The empirical confirmation of nuclear-coherent meson contributions in the final state would allow the identification of a specific dynamical mechanism for higher-twist processes in electroproduction. Clearly, these concepts should be explored further, both experimentally and theoretically.

ACKNOWLEDGMENTS

This work was supported in part by the United States Department of Energy under contract and DE-FG03-97ER4104. I thank all of the collaborators whose work I discuss here: P. Blunden, S.Brodsky, M. Burkardt, M.Karliner, and R. Machleidt.

REFERENCES

[1] G.A. Miller, Phys. Rev. C **56** (1997) R8; **56** (1997) 2789.

[2] P.G. Blunden, M. Burkardt, and G.A. Miller, Phys. Rev. **C59** (1999) R2998; Phys. Rev. C 60 (1999) 55211.

[3] G.A. Miller and R. Machleidt, Phys. Lett. **B455** (1999) 19; Phys. Rev. **C60** (1999) 035202-1.

[4] G. A. Miller, Prog. Part. Nucl. Phys. **45**, 83 (2000).

[5] G. A. Miller, S. J. Brodsky and M. Karliner, Phys. Lett. **B481**, 245 (2000).

[6] K. Ackerstaff *et al.* [HERMES Collaboration], hep-ex/9910071.

[7] C.G. Callan and D.J. Gross, Phys. Rev. Lett. **22** (1969) 156.

[8] J. Aubert *et al.*, Phys. Lett. **123B** (1982) 275; R.G. Arnold *et al.*, Phys. Rev. Lett. **52** (1984) 727; A. Bodek *et al.*, Phys. Rev. Lett. **51** (1983) 534.

[9] Piller and Weise L.L. Frankfurt and M.I. Strikman, Phys. Rep. **160**(1988) 235; M. Arneodo, Phys. Rep. **240** (1994) 301; D.F. Geesaman, K. Saito, A.W. Thomas, Ann. Rev. Nucl. Part. Sci. **45** (1995) 337.

[10] L.L. Frankfurt and M.I. Strikman, Phys. Rep. **160** (1988) 235.

[11] C.H. Llewellyn Smith **B128** (1983) 107.

[12] M. Ericson and A.W. Thomas, Phys. Lett. **B128** (1983) 112.

[13] R.P. Bickerstaff, M.C. Birse, and G.A. Miller, Phys. Rev. Lett. **53**, (1984) 2532; M. Ericson and A.W. Thomas, Phys. Lett. **148B** (1984) 191.

[14] D.M. Alde *et al.*, Phys. Rev. Lett. **64** (1990) 2479.

[15] G.F. Bertsch, L. Frankfurt, and M. Strikman, Science **259** (1993) 773.

[16] L.L. Frankfurt and M.I. Strikman, Phys. Rep. **76**, (1981) 215.

[17] B.D. Serot and J.D. Walecka, Adv. Nucl. Phys. **16** (1986)1; R. J. Furnstahl and B. D. Serot, nucl-th/9912048.

[18] I. Sick and D. Day, Phys. Lett. **B274** (1992) 16.

[19] H. Jung and G.A. Miller, Phys. Rev. **C41**(1990) 659.

[20] R. G. Roberts, *Cambridge, UK: Univ. Pr. (1990) 182 p. (Cambridge monographs on mathematical physics).*

[21] C. Caso *et al.*, Eur. Phys. J. **C3**, 1 (1998).

[22] H. Ito and F. Gross, Phys. Rev. Phys. Rev. Lett. **71**, 2555 (1993).

[23] T. H. Bauer, R. D. Spital, D. R. Yennie and F. M. Pipkin, Rev. Mod. Phys. **50** (1978) 261.

Klaus Werner

Nuclear Scattering at Very High Energies

K. Werner[1,*], H.J. Drescher[1,4], S. Ostapchenko[1,2,3], T. Pierog[1]

[1] *SUBATECH, Université de Nantes - IN2P3/CNRS - Ecole des Mines, Nantes, France*
[2] *Skobeltsyn Institute of Nuclear Physics, Moscow State University, Moscow, Russia*
[3] *Institute f. Kernphysik, Forschungszentrum Karlsruhe, Karlsruhe, Germany*
[4] *Physics Department, New York University, New York, USA*

Abstract

We discuss the current understanding of nuclear scattering at very high energies. We point out several serious inconsistencies in nowadays models, which provide big problems for any interpretation of data at high energy nuclear collisions.

We outline how to develop a fully self-consistent formalism, which in addition uses all the knowledge available from studying electron-positron annihilation and deep inelastic scattering, providing a solid basis for further developments concerning secondary interactions.

1 Introduction

We will report on efforts to construct realistic and reliable models for nuclear collisions at very high energies, say above 100 GeV cms energy per nucleon. There are several reasons why such models are needed, related to large scale experimental programs presently and in the future.

In astrophysics, one of the open problems is the origin of cosmic rays at very high energies. Whereas at low energies direct measurements are possible using balloons or satellites, at high energies – due to the small flux – only indirect measurements are possible, counting the secondary particles created in a so-called extended air-shower. Here, theoretical models for hadron-nucleus and nucleus-nucleus collisions play a decisive role in order to provide some information on the origin of the primary particle.

In nuclear physics, there are ongoing efforts to produce and to investigate the so-called quark-gluon plasma, a new state of matter of quarks and gluons. The SPS program at CERN has revealed many interesting results, but a final conclusion will never be made without a profound theoretical understanding, based on realistic microscopic models.

The outline of this paper is as follows: we will first discuss the present status concerning models for the initial stage of a nucleus-nucleus collision. We find that even the most advanced approaches show severe theoretical inconsistencies, which make any interpretation of experimental data questionable. It is in fact a well known problem which has been brought up a decade ago, but

no solution has been proposed so far. We will discuss how to solve the above-mentioned problem, introducing a self-consistent formalism for nuclear scattering at very high energies.

2 Present Status

Many popular models [1, 2, 3] are based on the so-called Gribov-Regge theory (GRT) [4, 5]. This is an effective field theory, which allows multiple interactions to happen "in parallel", with the phenomenological object called "Pomeron" representing an elementary interaction. Using the general rules of field theory, one may express cross sections in terms of a couple of parameters characterizing the Pomeron. Interference terms are crucial, they assure the unitarity of the theory. Here one observes an inconsistency: the fact that energy needs to be shared between many Pomerons in case of multiple scattering is well taken into account when calculating particle production (in particular in Monte Carlo applications), but energy conservation is not taken care of in cross section calculations. This is a serious problem and makes the whole approach inconsistent.

Provided factorization works for nuclear collisions, one may employ the parton model [6, 7], which allows to calculate inclusive cross sections as a convolution of an elementary cross section with parton distribution functions, with these distribution functions taken from deep inelastic scattering. In order to get exclusive parton level cross sections, some additional assumptions are needed, which follow quite closely the Gribov-Regge approach, encountering the same difficulties.

Before presenting new theoretical ideas, we want to discuss the open problems in the parton model approach and in Gribov-Regge theory somewhat more in detail.

Gribov-Regge Theory

Gribov-Regge theory is by construction a multiple scattering theory. The elementary interactions are realized by complex objects called "Pomerons", who's precise nature is not known, and which are therefore simply parameterized: the elastic amplitude T corresponding to a single Pomeron exchange is given as

$$T(s,t) \sim i\, s^{\alpha_0+\alpha' t}$$

with a couple of parameters to be determined by experiment. Even in hadron-hadron scattering, several of these Pomerons are exchanged in parallel. Using general rules of field theory (cutting rules), one obtains an expression for the inelastic cross section,

$$\sigma_{\text{inel}}^{h_1h_2}(s) = \int d^2b\, \{1 - \exp(-G(s,b))\} = \sum \sigma_m^{h_1h_2}(s), \tag{1}$$

with

$$\sigma_m^{h_1h_2}(s) = \int d^2b\, \frac{(G(s,b))^m}{m!} \exp(-G(s,b)), \tag{2}$$

where the so-called eikonal $G(s,b)$ (proportional to the Fourier transform of $T(s,t)$) represents one elementary interaction. The cross sections $\sigma_m^{h_1h_2}(s)$ for m inelastic collisions are referred to as topological cross sections. One can generalize to nucleus-nucleus collisions, where corresponding formulas for cross sections may be derived.

In order to calculate exclusive particle production, one needs to know how to share the energy between the individual elementary interactions in case of multiple scattering. We do not want to discuss the different recipes used to do the energy sharing (in particular in Monte Carlo applications). The point is, whatever procedure is used, this is not taken into account in the calculation of cross sections discussed above. So, actually, one is using two different models for cross section calculations and for treating particle production. Taking energy conservation into account in exactly the same way will modify the cross section results considerably.

This problem has first been discussed in [8],[9]. The authors claim that following from the non-planar structure of the corresponding diagrams, conserving energy and momentum in a consistent

way is crucial, and therefore the incident energy has to be shared between the different elementary interactions, both real and virtual ones.

Another very unpleasant and unsatisfactory feature of most "recipes" for particle production is the fact, that the second Pomeron and the subsequent ones are treated differently than the first one, although in the above-mentioned formula for the cross sections all Pomerons are considered to be identical.

The Parton Model

The standard parton model approach to hadron-hadron or also nucleus-nucleus scattering amounts to presenting the partons of projectile and target by momentum distribution functions, f_{h_1} and f_{h_2}, and calculating inclusive cross sections for the production of parton jets with the squared transverse momentum $p_\perp^2$ larger than some cutoff Q_0^2 as

$$\sigma_{\rm incl}^{h_1h_2} = \sum_{ij} \int dp_\perp^2 \int dx^+ \int dx^- f_{h_1}^i(x^+, p_\perp^2) f_{h_2}^j(x^-, p_\perp^2) \frac{d\hat{\sigma}_{ij}}{dp_\perp^2}(x^+x^-s)\theta(p_\perp^2 - Q_0^2)\,,$$

where $d\hat{\sigma}_{ij}/dp_\perp^2$ is the elementary parton-parton cross section and i, j represent parton flavors.

This simple factorization formula is the result of cancelations of complicated diagrams (AGK cancelations) and hides therefore the complicated multiple scattering structure of the reaction. The most obvious manifestation of such a structure is the fact that at high energies ($\sqrt{s} \gg 10$ GeV) the inclusive cross section in proton-(anti-)proton scattering exceeds the total one, so the average number $\bar{N}_{\rm int}^{pp}$ of elementary interactions must be greater than one:

$$\bar{N}_{\rm int}^{h_1h_2} = \sigma_{\rm incl}^{h_1h_2}/\sigma_{\rm tot}^{h_1h_2} > 1\,.$$

The usual solution is the so-called eikonalization, which amounts to re-introducing multiple scattering, based on the above formula for the inclusive cross section:

$$\sigma_{\rm inel}^{h_1h_2}(s) = \int d^2b \left\{1 - \exp\left(-A(b)\,\sigma_{\rm incl}^{h_1h_2}(s)\right)\right\} = \sum \sigma_m^{h_1h_2}(s), \tag{3}$$

with

$$\sigma_m^{h_1h_2}(s) = \int d^2b \frac{\left(A(b)\,\sigma_{\rm incl}^{h_1h_2}(s)\right)^m}{m!} \exp\left(-A(b)\,\sigma_{\rm incl}^{h_1h_2}(s)\right) \tag{4}$$

representing the cross section for n scatterings; $A(b)$ being the proton-proton overlap function (the convolution of two proton profiles). In this way the multiple scattering is "recovered". This makes the approach formally equivalent to Gribov-Regge theory, encountering therefore the same problems: energy conservation is not at all taken care of in the above formulas for cross section calculations.

3 A Solution: Parton-based Gribov-Regge Theory

In this paper, we present a new approach for hadronic interactions and for the initial stage of nuclear collisions, which is able to solve the above-mentioned problems. We provide a rigorous treatment of the multiple scattering aspect, such that questions as energy conservation are clearly determined by the rules of field theory, both for cross section and particle production calculations. In both (!) cases, energy is properly shared between the different interactions happening in parallel, see fig. 1 for proton-proton and fig. 2 for proton-nucleus collisions (generalization to nucleus-nucleus is obvious). This is the most important and new aspect of our approach, which we consider to be a first necessary step to construct a consistent model for high energy nuclear scattering.

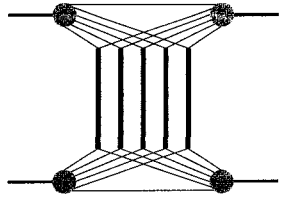

Figure 1: Graphical representation of a contribution to the elastic amplitude of proton-proton scattering. Here, energy conservation is taken into account: the energy of the incoming protons is shared among several "constituents" (shown by splitting the nucleon lines into several constituent lines), and so each Pomeron disposes of only a fraction of the total energy, such that the total energy is conserved.

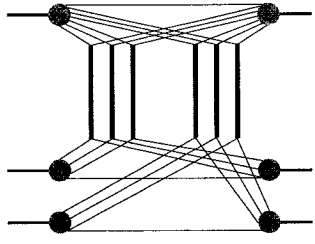

Figure 2: Graphical representation of a contribution to the elastic amplitude of proton-nucleus scattering, or more precisely a proton interacting with (for simplicity) two target nucleons, taking into account energy conservation. Here, the energy of the incoming proton is shared between all the constituents, which now provide the energy for interacting with two target nucleons.

The elementary interactions, shown as the thick lines in the above figures, are in fact a sum of a soft, a hard, and a semi-hard contribution, providing a consistent treatment of soft and hard scattering. To some extend, our approach provides a link between the Gribov-Regge approach and the parton model, we call it "Parton-based Gribov-Regge Theory".

4 Parton-Parton Scattering

Let us first investigate parton-parton scattering, before constructing a multiple scattering theory for hadronic and nuclear scattering.

We distinguish three types of elementary parton-parton scatterings, referred to as "soft", "hard" and "semi-hard", which we are going to discuss briefly in the following. The detailed derivations can be found in [10].

The Soft Contribution

Let us first consider the pure non-perturbative contribution, where all virtual partons appearing in the internal structure of the diagram have restricted virtualities $Q^2 < Q_0^2$, where $Q_0^2 \simeq 1$ GeV^2 is a reasonable cutoff for perturbative QCD being applicable. Such soft non-perturbative dynamics is known to dominate hadron-hadron interactions at not too high energies. Lacking methods to calculate this contribution from first principles, it is simply parameterized and graphically represented as a 'blob', see fig. 3. It is traditionally assumed to correspond to multi-peripheral production of partons (and final hadrons) [11] and is described by the phenomenological soft Pomeron exchange amplitude $T_{\rm soft}(\hat{s}, t)$ [4]. The corresponding profile function is twice the imaginary part of the

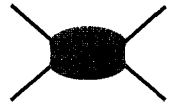

Figure 3: The soft contribution.

Fourier transform $\tilde{T}_{\rm soft}$ of $T_{\rm soft}$, divided by the initial parton flux $2\hat{s}$,

$$\begin{aligned} D_{\rm soft}(\hat{s},b) &= \frac{1}{2\hat{s}} 2{\rm Im} \frac{1}{4\pi^2} \int d^2q_\perp \, \exp\left(-i\vec{q}_\perp \vec{b}\right) \, T_{\rm soft}\left(\hat{s}, -q_\perp^2\right) \\ &= \frac{2\gamma_{\rm part}^2}{\lambda_{\rm soft}^{(2)}(\hat{s}/s_0)} \left(\frac{\hat{s}}{s_0}\right)^{\alpha_{\rm soft}(0)-1} \exp\left(-\frac{b^2}{4\lambda_{\rm soft}^{(2)}(\hat{s}/s_0)}\right), \end{aligned} \tag{5}$$

with

$$\lambda_{\rm soft}^{(n)}(z) = nR_{\rm part}^2 + \alpha'_{\rm soft} \ln z,$$

where $\hat{s}$ is the usual Mandelstam variable for parton-parton scattering. The parameters $\alpha_{\rm soft}(0)$, $\alpha'_{\rm soft}$ are the intercept and the slope of the Pomeron trajectory, $\gamma_{\rm part}$ and $R^2_{\rm part}$ are the vertex value and the slope for the Pomeron-parton coupling, and $s_0 \simeq 1$ GeV^2 is the characteristic hadronic mass scale. The external legs of the diagram of fig. 3 are "partonic constituents", which are assumed to be quark-anti-quark pairs.

The Hard Contribution

Let us now consider the other extreme, when all the processes are perturbative, i.e. all internal intermediate partons are characterized by large virtualities $Q^2 > Q_0^2$. In that case, the corresponding hard parton-parton scattering amplitude can be calculated using the perturbative QCD techniques [12, 13], and the intermediate states contributing to the absorptive part of the amplitude can be defined in the parton basis. In the leading logarithmic approximation of QCD, summing up terms where each (small) running QCD coupling constant $\alpha_s(Q^2)$ appears together with a large logarithm $\ln(Q^2/\lambda^2_{\rm QCD})$ (with λ_{QCD} being the infrared QCD scale), and making use of the factorization hypothesis, one obtains the contribution of the corresponding cut diagram for $t = q^2 = 0$ as the cut parton ladder cross section $\sigma^{jk}_{\rm hard}(\hat{s}, Q_0^2)$ [1], as shown in fig. 4, where all horizontal rungs

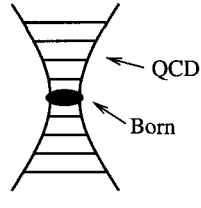

Figure 4: The hard (or val-val) contribution.

are the final (on-shell) partons and the virtualities of the virtual t-channel partons increase from

[1] Strictly speaking, one obtains the ladder representation for the process only using axial gauge.

the ends of the ladder towards the largest momentum transfer parton-parton process (indicated symbolically by the 'blob' in the middle of the ladder):

$$\begin{aligned}\sigma^{jk}_{\rm hard}(\hat{s},Q_0^2) &= \frac{1}{2\hat{s}}2{\rm Im}\,T^{jk}_{\rm hard}(\hat{s},t=0,Q_0^2)\\ &= K\sum_{ml}\int dx_B^+dx_B^-dp_\perp^2\frac{d\sigma^{ml}_{\rm Born}}{dp_\perp^2}(x_B^+x_B^-\hat{s},p_\perp^2)\\ &\times\ E^{jm}_{\rm QCD}(Q_0^2,M_F^2,x_B^+)\,E^{kl}_{\rm QCD}(Q_0^2,M_F^2,x_B^-)\theta(M_F^2-Q_0^2)\,,\end{aligned}$$

Here $d\sigma^{ml}_{\rm Born}/dp_\perp^2$ is the differential $2\to 2$ parton scattering cross section, $p_\perp^2$ is the parton transverse momentum in the hard process, m,l and $x_B^\pm$ are correspondingly the types and the shares of the light cone momenta of the partons participating in the hard process, and M_F^2 is the factorization scale for the process (we use $M_F^2=p_\perp^2/4$). The 'evolution function' $E^{jm}_{\rm QCD}(Q_0^2,M_F^2,z)$ represents the evolution of a parton cascade from the scale Q_0^2 to M_F^2, i.e. it gives the number density of partons of type m with the momentum share z at the virtuality scale M_F^2, resulted from the evolution of the initial parton j, taken at the virtuality scale Q_0^2. The evolution function satisfies the usual DGLAP equation [14] with the initial condition $E^{jm}_{\rm QCD}(Q_0^2,Q_0^2,z)=\delta^j_m\,\delta(1-z)$. The factor $K\simeq 1.5$ takes effectively into account higher order QCD corrections.

In the following, we shall need to know the contribution of the uncut parton ladder $T^{jk}_{\rm hard}(\hat{s},t,Q_0^2)$ with some momentum transfer q along the ladder (with $t=q^2$). The behavior of the corresponding amplitudes was studied in [15] in the leading logarithmic$(1/x\,)$ approximation of QCD. The precise form of the corresponding amplitude is not important for our application; we just use some of the results of [15], namely that one can neglect the real part of this amplitude and that it is nearly independent on t, i.e. that the slope of the hard interaction $R^2_{\rm hard}$ is negligible small, i.e. compared to the soft Pomeron slope one has $R^2_{\rm hard}\simeq 0$. So we parameterize $T^{jk}_{\rm hard}(\hat{s},t,Q_0^2)$ in the region of small t as [16]

$$T^{jk}_{\rm hard}(\hat{s},t,Q_0^2)=i\hat{s}\,\sigma^{jk}_{\rm hard}(\hat{s},Q_0^2)\,\exp\left(R^2_{\rm hard}\,t\right) \tag{6}$$

The corresponding profile function is twice the imaginary part of the Fourier transform $\tilde{T}_{\rm hard}$ of $T_{\rm hard}$, divided by the initial parton flux $2\hat{s}$,

$$D^{jk}_{\rm hard}(\hat{s},b)=\frac{1}{2\hat{s}}2{\rm Im}\tilde{T}^{jk}_{\rm hard}(\hat{s},b),$$

which gives

$$\begin{aligned}D^{jk}_{\rm hard}\,(\hat{s},b) &= \frac{1}{8\pi^2\hat{s}}\int d^2q_\perp\,\exp\left(-i\vec{q}_\perp\vec{b}\right)\,2{\rm Im}\,T^{jk}_{\rm hard}(\hat{s},-q_\perp^2,Q_0^2)\\ &= \sigma^{jk}_{\rm hard}\,(\hat{s},Q_0^2)\,\frac{1}{4\pi R^2_{\rm hard}}\exp\left(-\frac{b^2}{4R^2_{\rm hard}}\right),\end{aligned} \tag{7}$$

In fact, the above considerations are only correct for valence quarks, as discussed in detail in the next section. Therefore, we also talk about "valence-valence" contribution and we use $D_{\rm val-val}$ instead of $D_{\rm hard}$:

$$D^{jk}_{\rm val-val}\,(\hat{s},b)\equiv D^{jk}_{\rm hard}\,(\hat{s},b)\,,$$

so these are two names for one and the same object.

The Semi-hard Contribution

The discussion of the preceding section is not valid in case of sea quarks and gluons, since here the momentum share x_1 of the "first" parton is typically very small, leading to an object with a large mass of the order Q_0^2/x_1 between the parton and the proton [17]. Microscopically, such

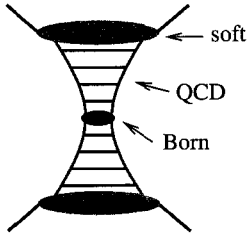

Figure 5: The semi-hard "sea-sea" contribution: parton ladder plus "soft ends".

'slow' partons with $x_1 \ll 1$ appear as a result of a long non-perturbative parton cascade, where each individual parton branching is characterized by a small momentum transfer squared $Q^2 < Q_0^2$ [4, 18]. When calculating proton structure functions or high-p_t jet production cross sections this non-perturbative contribution is usually included in parameterized initial parton momentum distributions at $Q^2 = Q_0^2$. However, the description of inelastic hadronic interactions requires to treat it explicitly in order to account for secondary particles produced during such non-perturbative parton pre-evolution, and to describe correctly energy-momentum sharing between multiple elementary scatterings. As the underlying dynamics appears to be identical to the one of soft parton-parton scattering considered above, we treat this soft pre-evolution as the usual soft Pomeron emission, as discussed in detail in [10].

So for sea quarks and gluons, we consider so-called semi-hard interactions between parton constituents of initial hadrons, represented by a parton ladder with "soft ends", see fig. 5. As in the case of soft scattering, the external legs are quark-anti-quark pairs, connected to soft Pomerons. The outer partons of the ladder are on both sides sea quarks or gluons (therefore the index "sea-sea"). The central part is exactly the hard scattering considered in the preceding section. As discussed in length in [10], the mathematical expression for the corresponding amplitude is given as

$$iT_{\text{sea-sea}}(\hat{s},t) = \sum_{jk}\int_0^1 \frac{dz^+}{z^+}\frac{dz^-}{z^-}\,\text{Im}\,T^j_{\text{soft}}\Big(\frac{s_0}{z^+},t\Big)\,\text{Im}\,T^k_{\text{soft}}\Big(\frac{s_0}{z^-},t\Big)\,iT^{jk}_{\text{hard}}(z^+z^-\hat{s},t,Q_0^2),$$

with $z^\pm$ being the momentum fraction of the external leg-partons of the parton ladder relative to the momenta of the initial (constituent) partons. The indices j and k refer to the flavor of these external ladder partons. The amplitudes T^j_{soft} are the soft Pomeron amplitudes discussed earlier, but with modified couplings, since the Pomerons are now connected to a parton ladder on one side. The arguments $s_0/z^\pm$ are the squared masses of the two soft Pomerons, $z^+z^-\hat{s}$ is the squared mass of the hard piece.

Performing as usual the Fourier transform to the impact parameter representation and dividing by $2\hat{s}$, we obtain the profile function

$$D_{\text{sea-sea}}(\hat{s},b) = \frac{1}{2\hat{s}}\,2\text{Im}\,\tilde{T}_{\text{sea-sea}}(\hat{s},b)\,,$$

which may be written as

$$D_{\text{sea-sea}}(\hat{s},b) = \sum_{jk}\int_0^1 dz^+dz^-E^j_{\text{soft}}(z^+)\,E^k_{\text{soft}}(z^-)\,\sigma^{jk}_{\text{hard}}(z^+z^-\hat{s},Q_0^2) \times \frac{1}{4\pi\,\lambda^{(2)}_{\text{soft}}(1/(z^+z^-))}\exp\left(-\frac{b^2}{4\lambda^{(2)}_{\text{soft}}(1/(z^+z^-))}\right) \tag{8}$$

with the soft Pomeron slope $\lambda^{(2)}_{\rm soft}$ and the cross section $\sigma^{jk}_{\rm hard}$ being defined earlier. The functions $E^j_{\rm soft}(z^\pm)$ representing the "soft ends" are defined as

$$\mathrm{E}^j_{\rm soft}(z^\pm) = \mathrm{Im}\, T^j_{\rm soft}\Big(\frac{s_0}{z^\pm}, t=0\Big)\,.$$

We neglected the small hard scattering slope $R^2_{\rm hard}$ compared to the Pomeron slope $\lambda^{(2)}_{\rm soft}$. We call $E_{\rm soft}$ also the " soft evolution", to indicate that we consider this as simply a continuation of the QCD evolution, however, in a region where perturbative techniques do not apply any more. As discussed in [10], $E^j_{\rm soft}(z)$ has the meaning of the momentum distribution of parton j in the soft Pomeron.

Consistency requires to also consider the mixed semi-hard contributions with a valence quark on one side and a non-valence participant (quark-anti-quark pair) on the other one, see fig. 6. We

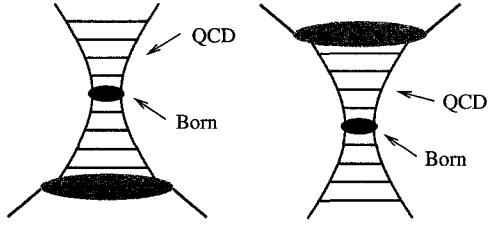

Figure 6: Two "mixed" contributions.

have

$$iT^j_{\rm val-sea}(\hat{s}) = \int_0^1 \frac{dz^-}{z^-} \sum_k \mathrm{Im}\, T^k_{\rm soft}\Big(\frac{s_0}{z^-}, q^2\Big)\, iT^{jk}_{\rm hard}\left(z^-\hat{s}, q^2, Q_0^2\right)$$

and

$$D^j_{\rm val-sea}(\hat{s}, b) = \sum_k \int_0^1 dz^-\, E^k_{\rm soft}\left(z^-\right)\, \sigma^{jk}_{\rm hard}\left(z^-\hat{s}, Q_0^2\right) \times \frac{1}{4\pi\, \lambda^{(1)}_{\rm soft}(1/z^-)} \exp\left(-\frac{b^2}{4\lambda^{(1)}_{\rm soft}(1/z^-)}\right) \tag{9}$$

where j is the flavor of the valence quark at the upper end of the ladder and k is the type of the parton on the lower ladder end. Again, we neglected the hard scattering slope $R^2_{\rm hard}$ compared to the soft Pomeron slope. A contribution $D^j_{\rm sea-val}(\hat{s}, b)$, corresponding to a valence quark participant from the target hadron, is given by the same expression,

$$D^j_{\rm sea-val}(\hat{s}, b) = D^j_{\rm val-sea}(\hat{s}, b)\,,$$

since eq. (9) stays unchanged under replacement $z^- \to z^+$ and only depends on the total c.m. energy squared $\hat{s}$ for the parton-parton system.

5 Hadron-Hadron Scattering

To treat hadron-hadron scattering we use parton momentum Fock state expansion of hadron eigenstates [8]

$$|h\rangle = \sum_{k=1}^{\infty} \frac{1}{k!} \int_0^1 \prod_{l=1}^{k} dx_l\, f^h_k(x_1, \ldots x_k)\, \delta\left(1 - \sum_{j=1}^{k} x_j\right)\, a^+(x_1)\cdots a^+(x_k)\,|0\rangle\,,$$

where $f_k(x_1,\dots x_k)$ is the probability amplitude for the hadron h to consist of k constituent partons with the light cone momentum fractions $x_1,\dots,x_k$ and $a^+(x)$ is the creation operator for a parton with the fraction x. A general scattering process is described as a superposition of a number of pair-like scatterings between parton constituents of the projectile and target hadrons. Then hadron-hadron scattering amplitude is obtained as a convolution of individual parton-parton scattering amplitudes considered in the previous section and "inclusive" momentum distributions $\frac{1}{n!}\tilde{F}_h^{(n)}(x_1,\dots x_n)$ of n "participating" parton constituents involved in the scattering process($n \geq 1$), with

$$\frac{1}{n!}\tilde{F}_h^{(n)}(x_1,\dots x_n) = \sum_{k=n}^{\infty}\frac{1}{k!}\frac{k!}{n!\,(k-n)!}\int_0^1\prod_{l=n+1}^{k}dx_l\ |f_k(x_1,\dots x_k)|^2\ \delta\left(1-\sum_{j=1}^{k}x_j\right)$$

We assume that $\tilde{F}^{(n)}_{h_1(h_2)}(x_1,\dots x_n)$ can be represented in a factorized form as a product of the contributions $F^h_{\rm part}(x_l)$, depending on the momentum shares x_l of the "participating" or "active" parton constituents, and on the function $F^h_{\rm remn}\left(1-\sum_{j=1}^{n}x_j\right)$, representing the contribution of all

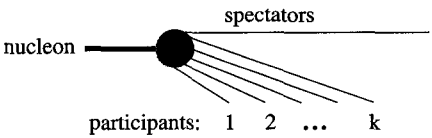

Figure 7: Nucleon Fock state.

"spectator" partons, sharing the remaining share $1-\sum_j x_j$ of the initial light cone momentum (see fig. 7):

$$\tilde{F}_h^{(n)}(x_1,\dots x_n) = \prod_{l=1}^{n}F^h_{\rm part}(x_l)\ F^h_{\rm remn}\left(1-\sum_{j=1}^{n}x_j\right) \tag{10}$$

The participating parton constituents are assumed to be quark-anti-quark pairs (not necessarily of identical flavors), such that the baryon numbers of the projectile and of the target are conserved. Then, as discussed in detail in [10], the hadron-hadron amplitude may be written as

$$iT_{h_1h_2}(s,t) = 8\pi^2 s\sum_{n=1}^{\infty}\frac{1}{n!}\int_0^1\prod_{l=1}^{n}dx_l^+dx_l^-\ \prod_{l=1}^{n}\left[\frac{1}{8\pi^2\hat{s}_l}\int d^2q_\perp\ iT^{h_1h_2}_{1\!\!\rm P}(x_l^+,x_l^-,s,-q_{l\perp}^2)\right]$$
$$F^{h_1}_{\rm remn}\left(1-\sum_{j=1}^{n}x_j^+\right)\ F^{h_2}_{\rm remn}\left(1-\sum_{j=1}^{n}x_j^-\right)\ \delta^{(2)}\left(\sum_{k=1}^{n}\vec{q}_{k\perp}-\vec{q}_\perp\right), \tag{11}$$

where the partonic amplitudes are defined as

$$T^{h_1h_2}_{1\!\!\rm P} = T^{h_1h_2}_{\rm soft} + T^{h_1h_2}_{\rm sea-sea} + T^{h_1h_2}_{\rm val-val} + T^{h_1h_2}_{\rm val-sea} + T^{h_1h_2}_{\rm sea-val},$$

with the individual contributions representing the "elementary partonic interactions plus external legs". The soft or semi-hard sea-sea contributions are given as

$$T^{h_1h_2}_{\rm soft/sea-sea}(x^+,x^-,s,-q_\perp^2) = T_{\rm soft/sea-sea}(s,-q_\perp^2)\ F^{h_1}_{\rm part}(x^+)\,F^{h_2}_{\rm part}(x^-)$$
$$\times\ \exp\left(-\left[R_{h_1}^2+R_{h_2}^2\right]q_\perp^2\right), \tag{12}$$

the hard contribution is

$$T^{h_1h_2}_{\text{val}-\text{val}}(x^+,x^-,s,q^2) = \int_0^{x^+} dx_v^+ \frac{x^+}{x_v^+}\int_0^{x^-} dx_v^- \frac{x^-}{x_v^-}\sum_{j,k} T^{jk}_{\text{hard}}\left(x_v^+x_v^-s,q^2,Q_0^2\right) \times \bar{F}^{h_1,j}_{\text{part}}(x_v^+,x^+-x_v^+)\,\bar{F}^{h_2,k}_{\text{part}}(x_v^-,x^--x_v^-)\,\exp\!\left(-\left[R^2_{h_1}+R^2_{h_2}\right]q^2_{l_\perp}\right),$$

the mixed semi-hard "val-sea" contribution is given as

$$T^{h_1h_2}_{\text{val}-\text{sea}}(x^+,x^-,s,q^2) = \int_0^{x^+} dx_v^+ \frac{x^+}{x_v^+}\sum_j T^{j}_{\text{val}-\text{sea}}\left(x_v^+x^-s,q^2,Q_0^2\right) \times \bar{F}^{h_1,j}_{\text{part}}(x_v^+,x^+-x_v^+)\,F^{h_2}_{\text{part}}(x^-)\,\exp\!\left(-\left[R^2_{h_1}+R^2_{h_2}\right]q^2_{l_\perp}\right),$$

and the contribution "sea-val" is finally obtained from "val-sea" by exchanging variables,

$$T^{h_1h_2}_{\text{sea}-\text{val}}(x^+,x^-,s,q^2) = T^{h_2h_1}_{\text{val}-\text{sea}}(x^-,x^+,s,q^2).$$

Here, we allow formally any number of valence type interactions (based on the fact that multiple valence type processes give negligible contribution). In the valence contributions, we have convolutions of hard parton scattering amplitudes T^{jk}_{hard} and valence quark distributions $\bar{F}^{j}_{\text{part}}$ over the valence quark momentum share $x_v^\pm$ rather than a simple product, since only the valence quarks are involved in the interactions, with the anti-quarks staying idle (the external legs carrying momenta x^+ and x^- are always quark-anti-quark pairs).

The profile function γ is as usual defined as

$$\gamma_{h_1h_2}(s,b) = \frac{1}{2s}2\text{Im}\tilde{\text{T}}_{h_1h_2}(s,b),$$

which may be evaluated using the AGK cutting rules with the result (assuming imaginary amplitudes)

$$\begin{aligned}\gamma_{h_1h_2}(s,b) &= \sum_{m=1}^{\infty}\frac{1}{m!}\int_0^1\prod_{\mu=1}^{m}dx_\mu^+dx_\mu^-\prod_{\mu=1}^{m}G^{h_1h_2}_{1\!\!\text{P}}(x_\mu^+,x_\mu^-,s,b)\\ &\sum_{l=0}^{\infty}\frac{1}{l!}\int_0^1\prod_{\lambda=1}^{l}d\tilde{x}_\lambda^+d\tilde{x}_\lambda^-\prod_{\lambda=1}^{l}-G^{h_1h_2}_{1\!\!\text{P}}(\tilde{x}_\lambda^+,\tilde{x}_\lambda^-,s,b)\\ &F_{\text{remn}}\left(x^{\text{proj}}-\sum_\lambda\tilde{x}_\lambda^+\right)F_{\text{remn}}\left(x^{\text{targ}}-\sum_\lambda\tilde{x}_\lambda^-\right),\end{aligned}\tag{13}$$

with $x^{\text{proj/targ}} = 1-\sum x_\mu^\pm$ being the momentum fraction of the projectile/target remnant, and with a partonic profile function G given as

$$G^{h_1h_2}_{1\!\!\text{P}}(x_\lambda^+,x_\lambda^-,s,b) = \frac{1}{2s}2\text{Im}\,\tilde{T}^{h_1h_2}_{1\!\!\text{P}}(x_\lambda^+,x_\lambda^-,s,b),\tag{14}$$

see fig. 8. This is a very important result, allowing to express the total profile function $\gamma_{h_1h_2}$ via the elementary profile functions $G^{hg_1h_2}_{1\!\!\text{P}}$.

6 Nucleus-Nucleus Scattering

We generalize the discussion of the last section in order to treat nucleus-nucleus scattering. In the Glauber-Gribov approach [19, 5], the nucleus-nucleus scattering amplitude is defined by the

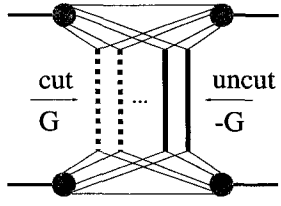

Figure 8: The hadronic profile function γ expressed in terms of partonic profile functions $G \equiv G_{1\mathbb{P}}^{h_1 h_2}$.

sum of contributions of diagrams, corresponding to multiple scattering processes between parton constituents of projectile and target nucleons. Nuclear form factors are supposed to be defined by the nuclear ground state wave functions. Assuming the nucleons to be uncorrelated, one can make the Fourier transform to obtain the amplitude in the impact parameter representation. Then, for given impact parameter $\vec{b}_0$ between the nuclei, the only formal difference from the hadron-hadron case will be the averaging over nuclear ground states, which amounts to an integration over transverse nucleon coordinates $\vec{b}_i^A$ and $\vec{b}_j^B$ in the projectile and in the target respectively. We write this integration symbolically as

$$\int dT_{AB} := \int \prod_{i=1}^{A} d^2 b_i^A \, T_A(b_i^A) \prod_{j=1}^{B} d^2 b_j^B \, T_B(b_j^B), \tag{15}$$

with A, B being the nuclear mass numbers and with the so-called nuclear thickness function $T_A(b)$ being defined as the integral over the nuclear density $\rho_{A(B)}$:

$$T_A(b) := \int dz \, \rho_A(b_x, b_y, z). \tag{16}$$

It is convenient to use the transverse distance b_k between the two nucleons from the k-th nucleon-nucleon pair, i.e.

$$b_k = \left| \vec{b}_0 + \vec{b}_{\pi(k)}^A - \vec{b}_{\tau(k)}^B \right|,$$

where the functions $\pi(k)$ and $\tau(k)$ refer to the projectile and the target nucleons participating in the k^{th} interaction (pair k). In order to simplify the notation, we define a vector b whose components are the overall impact parameter b_0 as well as the transverse distances $b_1, ..., b_{AB}$ of the nucleon pairs,

$$b = \{b_0, b_1, ..., b_{AB}\}.$$

Then the nucleus-nucleus interaction cross section can be obtained applying the cutting procedure to elastic scattering diagram and written in the form

$$\sigma_{\text{inel}}^{AB}(s) = \int d^2 b_0 \int dT_{AB} \, \gamma_{AB}(s, b), \tag{17}$$

where the so-called nuclear profile function γ_{AB} represents an interaction for given transverse coordinates of the nucleons.

The calculation of the profile function γ_{AB} as the sum over all cut diagrams of the type shown in fig. 9 does not differ from the hadron-hadron case and follows the rules formulated in the preceding section:

- For a remnant carrying the light cone momentum fraction x (x^+ in case of projectile, or x^- in case of target), one has a factor $F_{\text{remn}}(x)$.

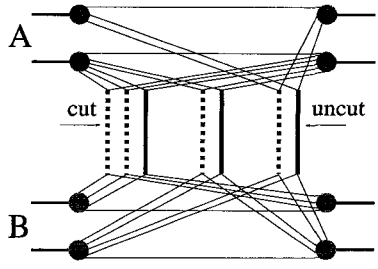

Figure 9: Example for a cut multiple scattering diagram, with cut (dashed lines) and uncut (full lines) elementary diagrams. This diagram can be translated directly into a formula for the inelastic cross section (see text).

- For each cut elementary diagram (real elementary interaction = dashed vertical line) attached to two participants with light cone momentum fractions x^+ and x^-, one has a factor $G(x^+, x^-, s, b)$. Apart from x^+ and x^-, G is also a function of the total squared energy s and of the relative transverse distance b between the two corresponding nucleons (we use G as an abbreviation for $G_{1\mathbb{P}}^{NN}$ for nucleon-nucleon scattering).
- For each uncut elementary diagram (virtual emissions = full vertical line) attached to two participants with light cone momentum fractions x^+ and x^-, one has a factor $-G(x^+, x^-, s, b)$, with the same G as used for the cut diagrams.
- Finally one sums over all possible numbers of cut and uncut Pomerons and integrates over the light cone momentum fractions.

So we find

$$\begin{aligned}
\gamma_{AB}(s,b) &= \sum_{m_1 l_1} \cdots \sum_{m_{AB} l_{AB}} (1-\delta_{0\Sigma m_k}) \int \prod_{k=1}^{AB} \left\{ \prod_{\mu=1}^{m_k} dx_{k,\mu}^+ dx_{k,\mu}^- \prod_{\lambda=1}^{l_k} d\tilde{x}_{k,\lambda}^+ d\tilde{x}_{k,\lambda}^- \right\} \\
&\times \prod_{k=1}^{AB} \left\{ \frac{1}{m_k!} \frac{1}{l_k!} \prod_{\mu=1}^{m_k} G(x_{k,\mu}^+, x_{k,\mu}^-, s, b_k) \prod_{\lambda=1}^{l_k} -G(\tilde{x}_{k,\lambda}^+, \tilde{x}_{k,\lambda}^-, s, b_k) \right\} \\
&\times \prod_{i=1}^{A} F_{\text{remn}} \left(x_i^+ - \sum_{\pi(k)=i} \tilde{x}_{k,\lambda}^+ \right) \prod_{j=1}^{B} F_{\text{remn}} \left(x_j^- - \sum_{\tau(k)=j} \tilde{x}_{k,\lambda}^- \right) \qquad (18)
\end{aligned}$$

with

$$\begin{aligned}
x_i^{\text{proj}} &= 1 - \sum_{\pi(k)=i} x_{k,\mu}^+ , \\
x_j^{\text{targ}} &= 1 - \sum_{\tau(k)=j} x_{k,\mu}^- .
\end{aligned}$$

The summation indices m_k refer to the number of cut elementary diagrams and l_k to number of uncut elementary diagrams, related to nucleon pair k. For each possible pair k (we have altogether AB pairs), we allow any number of cut and uncut diagrams. The integration variables $x_{k,\mu}^{\pm}$ refer to the μ^{th} elementary interaction of the k^{th} pair for the cut elementary diagrams, the variables $\tilde{x}_{k,\lambda}^{\pm}$ refer to the corresponding uncut elementary diagrams. The arguments of the remnant functions F_{remn} are the remnant light cone momentum fractions, i.e. unity minus the momentum fractions

of all the corresponding elementary contributions (cut and uncut ones). We also introduce the variables $x_i^{\rm proj}$and $x_j^{\rm targ}$, defined as unity minus the momentum fractions of all the corresponding cut contributions, in order to integrate over the uncut ones (see below).

The expression for γ_{AB} sums up all possible numbers of cut Pomerons m_k with one exception due to the factor $(1-\delta_{0\Sigma m_k})$: one does not consider the case of all m_k's being zero, which corresponds to "no interaction" and therefore does not contribute to the inelastic cross section. We may therefore define a quantity $\bar{\gamma}_{AB}$, representing "no interaction", by taking the expression for γ_{AB} with $(1-\delta_{0\Sigma m_k})$ replaced by $(\delta_{0\Sigma m_k})$:

$$\begin{aligned}\bar{\gamma}_{AB}(s,b) &= \sum_{l_1}\cdots\sum_{l_{AB}}\int\prod_{k=1}^{AB}\left\{\prod_{\lambda=1}^{l_k}d\tilde{x}_{k,\lambda}^{+}d\tilde{x}_{k,\lambda}^{-}\right\}\prod_{k=1}^{AB}\left\{\frac{1}{l_k!}\prod_{\lambda=1}^{l_k}-G(\tilde{x}_{k,\lambda}^{+},\tilde{x}_{k,\lambda}^{-},s,b_k)\right\}\\ &\times\prod_{i=1}^{A}F^{+}\left(1-\sum_{\pi(k)=i}\tilde{x}_{k,\lambda}^{+}\right)\prod_{j=1}^{B}F^{-}\left(1-\sum_{\tau(k)=j}\tilde{x}_{k,\lambda}^{-}\right).\end{aligned}\tag{19}$$

One now may consider the sum of "interaction" and "no interaction", and one obtains easily

$$\gamma_{AB}(s,b)+\bar{\gamma}_{AB}(s,b)=1.\tag{20}$$

Based on this important result, we consider γ_{AB} to be the probability to have an interaction and correspondingly $\bar{\gamma}_{AB}$ to be the probability of no interaction, for fixed energy, impact parameter and nuclear configuration, specified by the transverse distances b_k between nucleons, and we refer to eq. (20) as "unitarity relation". But we want to go even further and use an expansion of γ_{AB} in order to obtain probability distributions for individual processes, which then serves as a basis for the calculations of exclusive quantities.

The expansion of γ_{AB} in terms of cut and uncut Pomerons as given above represents a sum of a large number of positive and negative terms, including all kinds of interferences, which excludes any probabilistic interpretation. We have therefore to perform summations of interference contributions – sum over any number of virtual elementary scatterings (uncut Pomerons) – for given non-interfering classes of diagrams with given numbers of real scatterings (cut Pomerons)[20]. Let us write the formulas explicitly. We have

$$\begin{aligned}\gamma_{AB}(s,b) &= \sum_{m_1}\cdots\sum_{m_{AB}}(1-\delta_{0\sum m_k})\int\prod_{k=1}^{AB}\left\{\prod_{\mu=1}^{m_k}dx_{k,\mu}^{+}dx_{k,\mu}^{-}\right\}\\ &\times\prod_{k=1}^{AB}\left\{\frac{1}{m_k!}\prod_{\mu=1}^{m_k}G(x_{k,\mu}^{+},x_{k,\mu}^{-},s,b_k)\right\}\Phi_{AB}\left(x^{\rm proj},x^{\rm targ},s,b\right),\end{aligned}\tag{21}$$

where the function Φ representing the sum over virtual emissions (uncut Pomerons) is given by the following expression

$$\begin{aligned}\Phi_{AB}\left(x^{\rm proj},x^{\rm targ},s,b\right) &= \sum_{l_1}\cdots\sum_{l_{AB}}\int\prod_{k=1}^{AB}\left\{\prod_{\lambda=1}^{l_k}d\tilde{x}_{k,\lambda}^{+}d\tilde{x}_{k,\lambda}^{-}\right\}\prod_{k=1}^{AB}\left\{\frac{1}{l_k!}\prod_{\lambda=1}^{l_k}-G(\tilde{x}_{k,\lambda}^{+},\tilde{x}_{k,\lambda}^{-},s,b_k)\right\}\\ &\times\prod_{i=1}^{A}F_{\rm remn}\left(x_i^{\rm proj}-\sum_{\pi(k)=i}\tilde{x}_{k,\lambda}^{+}\right)\prod_{j=1}^{B}F_{\rm remn}\left(x_j^{\rm targ}-\sum_{\tau(k)=j}\tilde{x}_{k,\lambda}^{-}\right).\end{aligned}\tag{22}$$

This summation has to be carried out, before we may use the expansion of γ_{AB} to obtain probability distributions. This is far from trivial, the necessary methods are described in [10]. To make the

notation more compact, we define matrices X^+ and X^-, as well as a vector m, via

$$\begin{aligned} X^+ &= \left\{x^+_{k,\mu}\right\}, \\ X^- &= \left\{x^-_{k,\mu}\right\}, \\ m &= \{m_k\}, \end{aligned}$$

which leads to

$$\begin{aligned} \gamma_{AB}(s,b) &= \sum_m (1-\delta_{0m}) \int dX^+ dX^- \Omega^{(s,b)}_{AB}(m,X^+,X^-), \\ \bar{\gamma}_{AB}(s,b) &= \Omega^{(s,b)}_{AB}(0,0,0), \end{aligned}$$

with

$$\Omega^{(s,b)}_{AB}(m,X^+,X^-) = \prod_{k=1}^{AB} \left\{ \frac{1}{m_k!} \prod_{\mu=1}^{m_k} G(x^+_{k,\mu}, x^-_{k,\mu}, s, b_k) \right\} \Phi_{AB}\left(x^{\rm proj}, x^{\rm targ}, s, b\right).$$

This allows to rewrite the unitarity relation eq. (20) in the following form,

$$\sum_m \int dX^+ dX^- \Omega^{(s,b)}_{AB}(m,X^+,X^-) = 1.$$

This equation is of fundamental importance, because it allows us to interpret $\Omega^{(s,b)}(m,X^+,X^-)$ as probability density of having an interaction configuration characterized by m, with the light cone momentum fractions of the Pomerons being given by X^+ and X^-.

7 Virtual Emissions and Markov Chain Techniques

What did we achieve so far? We have formulated a well defined model, introduced by using the language of field theory, solving in this way the severe consistency problems of the most popular current approaches. To proceed further, one needs to solve two fundamental problems:

- the sum Φ_{AB} over virtual emissions has to be performed,
- tools have to be developed to deal with the multidimensional probability distribution $\Omega^{(s,b)}_{AB}$,

both being very difficult tasks. Introducing new numerical techniques, we were able to solve both problems, as discussed in very detail in [10].

Calculating the sum over virtual emissions (Φ_{AB}) is done by parameterizing the functions G as analytical functions and performing analytical calculations. By studying the properties of Φ_{AB}, we find that at very high energies the theory is no longer unitary without taking into account screening corrections due to triple Pomeron interactions. In this sense, we consider our work as a first step to construct a consistent model for high energy nuclear scattering, but there is still work to be done.

Concerning the multidimensional probability distribution $\Omega^{(s,b)}_{AB}(m,X^+,X^-)$, we employ methods well known in statistical physics (Markov chain techniques). So finally, we are able to calculate the probability distribution $\Omega^{(s,b)}_{AB}(m,X^+,X^-)$, and are able to generate (in a Monte Carlo fashion) configurations (m,X^+,X^-) according to this probability distribution.

8 Summary

What are finally the principal features of our basic results, summarized in eqs. (17, 21, 22)? Contrary to the traditional treatment (Gribov-Regge approach or parton model), all individual elementary contributions G depend explicitly on the light-cone momenta of the elementary interactions, with the total energy-momentum being precisely conserved. Another very important feature is the explicit dependence of the screening contribution Φ_{AB} (the contribution of virtual emissions) on the remnant momenta. The direct consequence of properly taking into account energy-momentum conservation in the multiple scattering process is the validity of the so-called AGK-cancelations in hadron-hadron and nucleus-nucleus collisions in the entire kinematical region.

The formulas (17, 21, 22) allow to develop a consistent scheme to simulate high energy nucleus-nucleus interactions. The corresponding Monte Carlo procedure is exactly based on the cross section formulas so that the entire model is fully self-consistent.

References

[1] A. B. Kaidalov and K. A. Ter-Martirosyan, Nucl. Phys. **B75**, 471 (1974).

[2] K. Werner, Phys. Rep. **232**, 87 (1993).

[3] A. Capella, U. Sukhatme, C.-I. Tan, and J. Tran Thanh Van, Phys. Rept. **236**, 225 (1994).

[4] V. N. Gribov, Sov. Phys. JETP **26**, 414 (1968).

[5] V. N. Gribov, Sov. Phys. JETP **29**, 483 (1969).

[6] T. Sjostrand and M. van Zijl, Phys. Rev. **D36**, 2019 (1987).

[7] X.-N. Wang, Phys. Rept. **280**, 287 (1997), hep-ph/9605214.

[8] V. A. Abramovskii and G. G. Leptoukh, Sov.J.Nucl.Phys. **55**, 903 (1992).

[9] M. Braun, Yad. Fiz. (Rus) **52**, 257 (1990).

[10] H. J. Drescher, M. Hladik, S. Ostapchenko, T. Pierog, and K. Werner, (2000), hep-ph/0007198, to be published in Physics Reports.

[11] D. Amati, A. Stanghellini, and S. Fubini, Nuovo Cim. **26**, 896 (1962).

[12] G. Altarelli, Phys. Rep. **81**, 1 (1982).

[13] E. Reya, Phys. Rep. **69**, 195 (1981).

[14] G. Altarelli and G. Parisi, Nucl. Phys. **B126**, 298 (1977).

[15] L. N. Lipatov, Sov. Phys. JETP **63**, 904 (1986).

[16] M. G. Ryskin and Y. M. Shabelski, Yad. Fiz. (Rus.) **55**, 2149 (1992).

[17] A. Donnachie and P. Landshoff, Phys. Lett. B **332**, 433 (1994).

[18] M. Baker and K. A. Ter-Martirosyan, Phys. Rep. **28**, 1 (1976).

[19] R. J. Glauber, *in Lectures on theoretical physics* (N.Y.: Inter-science Publishers, 1959).

[20] V. A. Abramovskii, V. N. Gribov, and O. V. Kancheli, Sov.J.Nucl.Phys. **18**, 308 (1974).

Horst and Oda Stöcker

CURRENT STATUS OF QUARK GLUON PLASMA SIGNALS

S. SCHERER, D. ZSCHIESCHE, M. BLEICHER, J. BRACHMANN,
L. GERLAND, K. PAECH, C. SPIELES, H. WEBER, H. STÖCKER,
W. GREINER
Institut für Theoretische Physik, J.W. Goethe Universität
60054 Frankfurt a.M., Germany
E-mail: ziesche@th.physik.uni-frankfurt.de

S. BASS
Department of Physics, Duke University
27708-0305 Durham, NC, USA
and
RIKEN BNL Research Center, Brookhaven National Laboratory
Upton, NY 11973, USA

S. SOFF
Physics Department, Brookhaven National Laboratory
Upton, NY 11973, USA

Compelling evidence for a new form of matter has been claimed to be formed in Pb+Pb collisions at SPS. We discuss the uniqueness of often proposed experimental signatures for quark matter formation in relativistic heavy ion collisions. It is demonstrated that so far none of the proposed signals like J/Ψ meson production/suppression, strangeness enhancement, dileptons, and directed flow unambigiously show that a phase of deconfined matter has been formed in SPS Pb+Pb collisions. We emphasize the need for systematic future measurements to search for simultaneous irregularities in the excitation functions of several observables in order to come close to pinning the properties of hot, dense QCD matter from data.

1 Introduction

In the last few years researchers at Brookhaven and CERN have succeeded to measure a wide spectrum of observables with heavy ion beams, $Au + Au$ and $Pb + Pb$. While these programs continue to measure with greater precision the beam energy-, nuclear size-, and centrality dependence of those observables, it is important to recognize the major milestones passed thusfar in that work. The experiments have conclusively demonstrated the existence of strong nuclear A dependence of, among others, J/ψ and ψ' meson production and suppression, strangeness enhancement, hadronic resonance production, stopping and directed collective transverse and longitudinal flow of baryons and mesons – in and out of the impact plane, both at AGS and SPS energies –, and dilepton-enhancement below and above the ρ meson mass. These obser-

vations support that a novel form of "resonance matter" at high energy- and baryon density has been created in nuclear collisions. The global multiplicity and transverse energy measurements prove that substantially more entropy is produced in $A + A$ collisions at the SPS than simple superposition of $A \times pp$ would imply. Multiple initial and final state interactions play a critical role in all observables. The high midrapidity baryon density (stopping) and the observed collective transverse and directed flow patterns constitute one of the strongest evidence for the existence of an extended period ($\Delta\tau \approx 10$ fm/c) of high pressure and strong final state interactions. The enhanced ψ' suppression in $S + U$ relative to $p + A$ also attests to this fact. The anomalous low mass dilepton enhancement shows that substantial in-medium modifications of multiple collision dynamics exist, probably related to in-medium collisional broadening of vector mesons. The non-saturation of the strangeness (and anti-strangeness) production shows that novel non-equilibrium production processes arise in these reactions. Finally, the centrality dependence of J/ψ absorption in $Pb + Pb$ collisions presents further hints towards the nonequilibrium nature of such reactions. Is there evidence for the long sought-after quark-gluon plasma that thusfar has only existed as a binary array of predictions inside teraflop computers?

As we will discuss, it is too early to tell. Theoretically there are still too many "scenarios" and idealizations to provide a satisfactory answer. Recent results from microscopic transport models as well as macroscopic hydrodynamical calculations differ significantly from predictions of simple thermal models, e. g. in the flow pattern. Still, these nonequilibrium models provide reasonable predictions for the experimental data. We may therefore be forced to rethink our concept of what constitutes the deconfined phase in ultrarelativistic heavy-ion collisions. Most probably it is not a blob of thermalized quarks and gluons. Hence, a quark-gluon plasma can only be the source of *differences* to the predictions of these models for hadron ratios, the J/Ψ meson production, dilepton yields, or the excitation function of transverse flow. And there are experimental gaps such as the lack of intermediate mass $A \approx 100$ data and the limited number of beam energies studied thusfar, in particular between the AGS and SPS. Now the field is at the doorstep of the next milestone: $A + A$ at $\sqrt{s} = 30 - 200$ AGeV which have started a few months ago.

2 J/Ψ production

The QCD factorization theorem is used to evaluate the PQCD cross sections of heavy quarkonium interactions with ordinary hadrons. However, the charmonium states (here denoted X) are not sufficiently small to ignore nonperturba-

tive QCD physics. Thus, we evaluate the nonperturbative QCD contribution to the cross sections of charmonium-nucleon interaction by using an interpolation between known cross sections [3]. The J/Ψ-N cross section evaluated in this paper is in reasonable agreement with SLAC data [4].

Indeed, the A-dependence of the J/Ψ production studied at SLAC at $E_{inc} \sim 20$ GeV exhibits a significant absorption effect [4] leading to $\sigma_{abs}(J/\Psi$-$N) = 3.5 \pm 0.8$ mb. It was demonstrated [5] that, in the kinematic region at SLAC, the color coherence effects are still small on the internucleon scale for the formation of J/Ψ's. So, in contrast to the findings at higher energies, at intermediate energies this process measures the *genuine* J/Ψ-N interaction cross section at energies of $\sim$ 15-20 GeV [5].

To evaluate the nonperturbative QCD contribution we use an interpolation formula [3] for the dependence of the cross section on the transverse size b of a quark-gluon configuration Three reference points are used to fix our parametrization of the cross sections (cf. Tab. 1). The X-N cross sections is calculated via: $\sigma = \int \sigma(b) \cdot |\Psi(x,y,z)|^2 \mathrm{d}x\,\mathrm{d}y\,\mathrm{d}z$, where $\Psi(x,y,z)$ is the charmonium wave function. In our calculations we use the wave functions from a non-relativistic charmonium model (see [6]).

We follow the analysis of [7] to evaluate the fraction of J/Ψ's (in pp collisions) that come from the decays of the χ and Ψ'. The suppression factor S of J/Ψ's produced in the nuclear medium is calculated as: $S = 0.6 \cdot (0.92 \cdot S^{J/\Psi} + 0.08 \cdot S^{\Psi'}) + 0.4 \cdot S^{\chi}$. Here S^X are the respective suppression factors of the different pure charmonium states X in nuclear matter. The S^X are for minimum bias pA collisions within the semiclassical approximation (cf. [8]).

The charmonium states are produced as small configurations, then they evolve to their full size. Therefore, if the formation length of the charmonium states, l_f, becomes larger than the average internucleon distance, one has to take into account the evolution of the cross sections with the distance from the production point [5].

The formation length of the J/Ψ is given by $l_f \approx 2p/(m^2_{\Psi'} - m^2_{J/\Psi})$, where p is the momentum of the J/Ψ in the rest frame of the target. For a J/Ψ produced at midrapidity at SPS energies, this yields $l_f \approx 3$ fm. Due to the lack of better knowledge, we use the same $l_f \approx 3$ fm for the χ. For the Ψ' we use $l_f \approx 6$ fm, because it is not a small object, but has the size of a normal hadron, i.e. the pion. For $E_{lab} = 800$ AGeV we get a factor of two for the formation lengths due to the larger Lorentz factor.

However, this has a large impact on the Ψ' to J/Ψ-ratio depicted in Fig. 1, which shows the ratio $0.019 \cdot S_{\Psi'}/S_{J/\Psi}$ calculated with (squares (200 GeV) and triangles (800 GeV)) and without (crosses) expansion. The factor 0.019 is the measured value in pp collisions, because the experiments do not measure

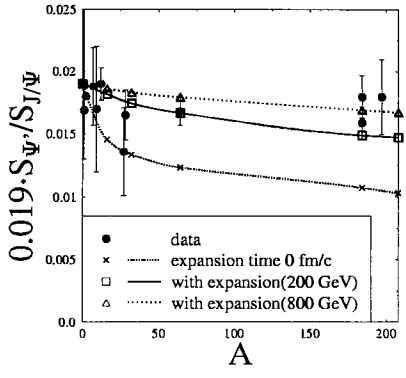

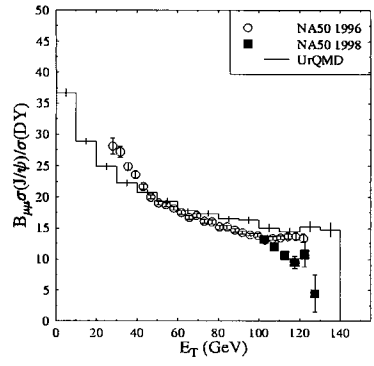

Figure 1: Left: The ratio $0.019 \cdot S_{\Psi'}/S_{J/\Psi}$ is shown in pA (crosses) in comparison to the data (circles). The squares and the triangles shows the ratio calculated with the expansion of small wave packages. Right: The ratio of J/ψ to Drell-Yan production as a function of E_T for Pb+Pb at 160 GeV.

the calculated value $S_{\Psi'}/S_{J/\Psi}$ but $(B_{\mu\mu}\sigma(\Psi'))/(B_{\mu\mu}\sigma(J/\Psi))$. $B_{\mu\mu}$ are the branching ratios for J/Ψ, $\Psi' \to \mu\mu$.

The calculations which take into account the expansion of small wave packages show better agreement with the data (circles) (taken from [9]) than the calculation without expansion time, i.e. with immediate J/Ψ formation, $l_f = 0$. We calculated this effect both at $E_{lab} = 200$AGeV and 800 AGeV. The data have been measured at different energies ($E_{lab} = 200$, 300, 400, 450, 800 GeV and $\sqrt{s} = 63$GeV). One can see that this ratio is nearly constant in the kinematical region of the data, but it decreases at smaller momentum (e.g. $E_{lab} = 200$AGeV and $y < 0$) due to the larger cross section of the Ψ'.

However, the P-states yield two vastly different cross sections (see Tab. 1) for χ_{10} and χ_{11}, respectively. This leads to a higher absorption rate of the χ_{11} as compared to the χ_{10}. This new form of color filtering is predicted also for the corresponding states of other hadrons; e.g. for the bottomium states which are proposed as contrast signals to the J/Ψ's at RHIC and LHC!

$c\bar{c}$-state	J/Ψ	Ψ'	χ_{c10}	χ_{c11}
σ (mb)	3.62	20.0	6.82	15.9

Table 1: The total quarkonium-nucleon cross sections σ. For the χ two values arise, due to the spin dependent wave functions ($lm = 10, 11$).

Furthermore it is important to also take into account comoving mesons. Therefore we use the UrQMD model[10,11]. Particles produced by string fragmentation are not allowed to interact with other hadrons – in particular with a charmonium state – within their formation time (on average, $\tau_F \approx 1$ fm/c). However, leading hadrons are allowed to interact with a reduced cross section even within their formation time . The reduction factor is 1/2 for mesons which contain a leading constituent quark from an incident nucleon and 2/3 for baryons which contain a leading diquark.

Figure 1 shows the J/ψ to Drell-Yan ratio as a function of E_T for Pb+Pb interactions at 160 GeV compared to the NA50 data[12,13]. The normalization of $B_{\mu\mu}\sigma(J/\psi)/\sigma(\mathrm{DY}) = 46$ in pp interactions at 200 GeV has been fit to S+U data within a geometrical model[7]. The application of this value to our analysis is not arbitrary: the model of Ref. [7] renders the identical E_T-integrated J/ψ survival probability, $S = 0.49$, as the UrQMD calculation for this system. An additional factor of 1.25[14] has been applied to the Pb+Pb calculation in order to account for the lower energy, 160 GeV, since the J/ψ and Drell-Yan cross sections have different energy and isospin dependencies.

The gross features of the E_T dependence of the J/ψ to Drell-Yan ratio are reasonably well described by the model calculation. No discontinuities in the shape of the ratio as a function of E_T are predicted by the simulation. The new high E_T data[13] decreases stronger than the calculation. This could be caused by underestimated fluctuations of the multiplicity of secondaries in the UrQMD model. This occurs, since high E_T-values are a trigger for very central events with a secondary multiplicity larger than in average[15].

3 Dilepton production

Beside results from hadronic probes, electromagnetic radiation – and in particular dileptons – offer an unique probe from the hot and dense reaction zone: here, hadronic matter is almost transparent. The observed enhancement of the dilepton yield at intermediate invariant masses ($M_{e^+e^-} > 0.3$ GeV) received great interest: it was prematurely thought that the lowering of vector meson masses is required by chiral symmetry restoration (see e.g.[16] for a review).

Fig. 2 shows a microscopic UrQMD calculation of the dilepton production in the kinematic acceptance region of the CERES detector for Pb+Au collisions at 158 GeV. This is compared with the '95 CERES data[18]. Aside from the difference at $M \approx 0.4$ GeV there is a strong enhancement at higher invariant masses. It is expected that this discrepancy at $m > 1$ GeV could be filled up by direct dilepton production in meson-meson collisions[19] as well as by the mechanism of secondary Drell-Yan pair production proposed in[20].

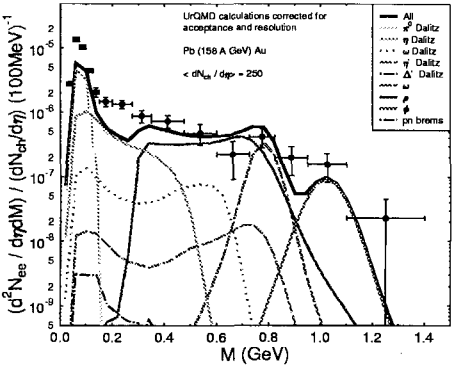

Figure 2: Microscopic calculation of the dilepton production in the kinematic acceptance region of the CERES detector for $Pb + Au$ collisions at 158 GeV. No in-medium effects are taken into account. Plotted data points are taken at CERES in '95.

4 Strangeness production

Strange particle yields are most interesting and useful probes to examine excited nuclear matter[21,22,23,24,25,26,27] and to detect the transition of (confined) hadronic matter to quark-gluon-matter. The relative enhancement of strange and especially multistrange particles in central heavy ion collisions with respect to peripheral or proton induced interactions have been suggested as a signature for the transient existence of a QGP-phase[21]. Here the main idea is that the strange (and antistrange) quarks are thought to be produced more easily and hence also more abundantly in such a deconfined state as compared to the production via highly threshold suppressed inelastic hadronic collisions. The relative enhanement of (anti)hyperons has clearly been measured by the WA97 an the NA49 collaboration in Pb-Pb collisions as compared to p-Pb collisions[25,26] . This data has been investigated within microscopic transport models (e.g. UrQMD[10]). In[22,28] it was shown that within such an appraoch strangeness enhancement is predicted for Pb-Pb due to rescattering. However, for central Pb-Pb collisions the experimentally observed hyperon yields are underestimated by the calculation in[22,28]. This result seems to confirm the conclusion that a deconfined QGP is formed in Pb-Pb collisions at SPS. But in[27,29] it was shown, that the antihyperon production by multi-mesonic reactions like $n_1\pi + n_2 K \rightarrow \bar{Y} + p$ could drive these rare particles towards local chemical quilibrium with pions, nucleons and kaons on a timescale of 1-3 fm/c. Accordingly this mechanism, which is a consequence of detailed balance could provide a convenient explanation for the antihyperon yields at CERN-SPS energies without any need of a deconfined quark-gluon-plasma phase. At the moment such back-reactions cannot be handled within the present transport codes. Therefore the aim for the future will be to find a way to include these processes in microscopic transport models.

5 Particle ratios

Ideal gas model calculations have been used for a long time to calculate particle production in relativistic heavy ion collisions, e.g. [30,31,32,33,34,35]. Fitting the particle ratios as obtained from those ideal gas calculations to the experimental measured ratios at SIS, AGS and SPS for different energies and different colliding systems yields a curve of chemical freeze-out in the $T-\mu$ plane. Now the question arises, how much the deduced temperature and chemical potentials depend on the model employed. Especially the influence of changing hadron masses and effective potentials should be investigated, as has been done for example in [36,37,38,39]. This is of special importance for the quest of a signal of the formation of a deconfined phase, i.e. the quark-gluon plasma. As deduced from lattice data [40], the critical temperature for the onset of a deconfined phase coincides with that of a chirally restored phase. Chiral effective models of QCD therefore can be utilized to give important insights on signals from a quark-gluon plasma formed in heavy-ion collisions.

Therefore we compare experimental measurements for Pb+Pb collisions at SPS with the ideal gas calculations and results obtained from a chiral SU(3) model [39,41]. This effective hadronic model predicts a chiral phase transition at $T \approx 150$MeV. Furthermore the model predicts changing hadronic masses and effective chemical potentials, due to strong scalar and vector fields in hot and dense hadronic matter, which are constrained by chiral symmetry from the QCD Lagrangean.

In [32] the ideal gas model was fitted to particle ratios measured in Pb+Pb collisions at SPS. The lowest χ^2 is obtained for $T = 168$MeV and $\mu_q = 88.67$MeV. Using these values as input for the chiral model leads to dramatic changes due to the changing hadronic masses in hot and dense matter [42] and therefore the freeze-out temperature and chemical potential have to be readjusted to account for the in-medium effects of the hadrons in the chiral model. We call the best fit the parameter set that gives a minimum in the value of χ^2, with $\chi^2 = \sum_i \frac{\left(r_i^{exp} - r_i^{model}\right)^2}{\sigma_i^2}$. Here r_i^{exp} is the experimental ratio, r_i^{model} is the ratio calculated in the model and σ_i represents the error in the experimental data points as quoted in [32]. The resulting values of χ^2 for different $T-\mu$ pairs are shown in figure 3.

In all calculations μ_s was chosen such that the overall net strangeness f_s is zero. The best values for the parameters are $T = 144$MeV and $\mu_q \approx 95$MeV. While the value of the chemical potential does not change much compared to the ideal gas calculation, the value of the temperature is lowered by more than 20 MeV. Furthermore Figure 3 shows, that the dropping effective masses and the reduction of the effective chemical potential make the reproduction

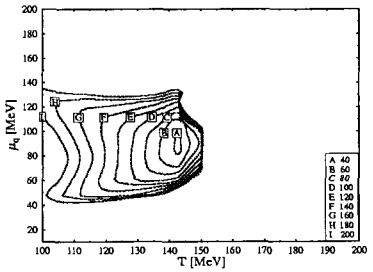

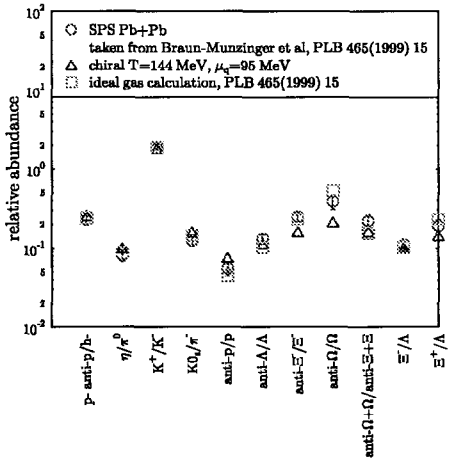

Figure 3: χ^2 (left) and resulting particle ratios compared to ideal gas calculation and data (right) for chiral model, data taken from [32]. The best fit parameters are $T = 144$MeV and $\mu_q \approx 95$MeV.

of experimentally measured particle ratios as seen at CERN's SPS within this model impossible for $T > T_c$. Using the best fit parameters a reasonable description of the particle ratios used in the fit procedure can be obtained (see fig.3, data from [32]).

We want to emphasize, that in spite of the strong assumption of thermal and chemical equilibrium the obtained values for T and μ differ significantly depending on the underlying model, i.e. whether and how effective masses and effective chemical potentials are accounted for. Note that we assume implicitly, that the particle ratios are determined by the medium effects and freeze out during the late stage expansion - no flavor changing collisions occur anymore, but the hadrons can take the necessary energy to get onto their mass shall by drawing energy from the fields. Rescattering effects will alter our conclusion but are presumably small when the chemical potentials are frozen.

6 Collective flow and the EOS

The in-plane flow has been proposed as a measure of the "softening" of the EoS [43], therefore we investigate the excitation function of directed in-plane flow. A three-fluid model with dynamical unification of kinetically equilibrated fluid elements is applied [44]. This model assumes that a projectile- and a target fluid interpenetrate upon impact of the two nuclei, creating a third fluid via new source terms in the continuity equations for energy- and momentum flux. Those source terms are taken from energy- and rapidity loss measurements in high energy pp-collisions. The equation of state (EoS) of this model assumes

equilibrium only in each fluid separately and allows for a first order phase transition to a quark gluon plasma in fluid 1, 2 or 3, if the energy density in the fluid under consideration exceeds the critical value for two phase coexistence. Pure QGP can also be formed in every fluid separately, if the energy density in that fluid exceeds the maximum energy density for the mixed phase. Integrating up the collective momentum in x-direction at given rapidity, and dividing by the net baryon number in that rapidity bin, we obtain the so-called directed in-plane flow per nucleon.

Its excitation function (Fig. 4) shows a local minimum at 8 AGeV and rises until a maximum around 40 AGeV is reached. Fig. 4 shows the excitation function of directed flow calculated in the three-fluid model in comparison to that obtained in a one-fluid calculation. Due to non-equilibrium effects in the early stage of the reaction, which delay the build-up of transverse pressure[45], the flow shifts to higher bombarding energies. While measurements of flow at AGS[46] have found a decrease of directed flow with increasing bombarding energy, a minimum has so far not been observed.

In a recent investigation of the directed flow excitation functions[47] it has been shown, that the directed flow excitation functions are sensitive to the underlying EoS and that a different EoS can predict a slowly and smoothly decrease of the averaged directed flow as a function of bombarding energies. This different behaviour is due to the different phase transitions in the underlying equations of state. While in the two phase EoS based on a $\sigma - \omega$ model for the hadronic phase and a bag model for the deconfined phase a first-order phase transition occurs, the EoS in[47] provides a continues phase transition of the cross-over type.

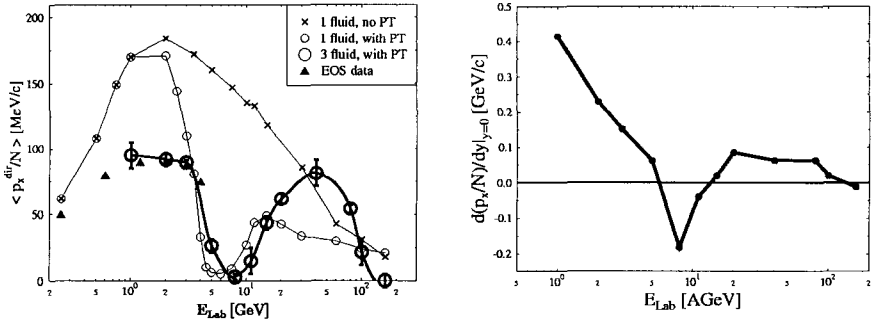

Figure 4: Excitation function of transverse flow as obtained from three fluid hydrodynamics with a first order phase transition and (Right) the slope of the directed in-plane momentum per nucleon at midrapidity.

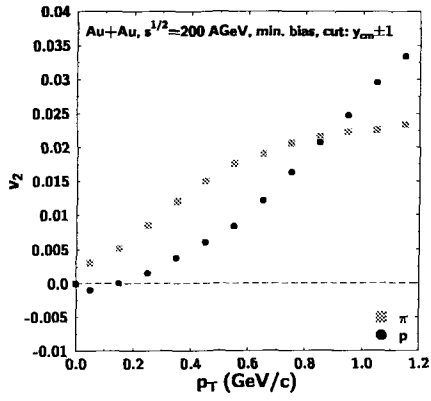

Figure 5: Elliptic flow parameter v_2 at midrapidity as a function of transverse momentum in minimum biased Au+Au reactions at $\sqrt{s} = 200$AGeV

The slope of the directed in-plane momentum per nucleon at midrapidity, $d(p_x/N)/dy$, is shown in Fig. 4 as a function of beam energy. We find a steady decrease of $d(p_x/N)/dy$ up to about top BNL-AGS energy, where the flow around midrapidity even becomes negative due to preferred expansion towards $p_x \cdot p_{long} < 0$. At higher energy, $E_{Lab} \simeq 40A$ GeV, the isentropic speed of sound becomes small and we encounter the following expansion pattern : flow towards $p_x \cdot p_{long} < 0$ can not build up ! Consequently, $d(p_x/N)/dy$ increases rapidly towards $E_{Lab} = 20 - 40A$ GeV, decreasing again at even higher energy because of the more forward-backward peaked kinematics which is unfavorable for directed flow.

Thus, the $Pb + Pb$ collisions (40 GeV) runs performed recently at the CERN-SPS may provide a crucial test of the picture of a quasi-adiabatic first-order hadronization phase transition at small isentropic velocity of sound.

7 Collective Flow at RHIC

Let us now compare the first results on elliptic flow (v_2) at $\sqrt{s_{NN}} = 130$GeV as reported by the STAR-Collaboration [48] with a string hadronic model simulation: The experimental data indicates a strongly rising v_2 as a function of p_t with an average v_2 value of 6% at midrapidity and p_t approximately 600MeV. While the strong increase of v_2 with p_t has been predicted by the UrQMD model [49] the absolute magnitude of v_2 at $p_t = 600$MeV is underpredicted by a factor 3 (cf. fig. 5).

When the formation time of hadrons in the initial strings is strongly reduced (to mimic short mean free paths in the early interaction region) the calculated flow values approach the hydrodynamic limit [50,49] and get in line

with the measured elliptic flow values. This shows, that the pressure in the reaction zone is much higher than expected from simple stringlike models and supports the breakdown of pure string hadronic dynamics in the initial stage of Au-Au-collisions at RHIC energies. However, to get a consistent picture and to finally rule out the string hadronic approach the v_1 values and transverse momentum spectra[51] as given by the model calculation need to be exceeded by the experimental data.

8 Insights from quark molecular dynamics

Further insights about the possible formation of deconfined matter can be obtained from the Quark Molecular Dynamics Model (qMD)[52] which explicitly includes quark degrees of freedom. The qMD can provide us with detailed information about the dynamics of the quark system and the parton-hadron conversion. Correlations between the quarks clustering to build new hadrons can be studied[53].

Figure 6 shows (for S+Au collisions at SPS energies of 200 GeV/N) the number distribution for the mean path travelled by quarks forming a hadron (a) from the same initial hadron (solid line) and (b) from different initial hadrons (dotted line).

A measure of the relative mixing within the quark system and thus for thermalization is the relative number of hadrons formed by quarks from the same initial hadron correlation versus hadrons formed by quarks from different initial hadron correlations. This ratio is $r = 0.574 \pm 0.008$ for the S+Au collision. Since a value of $r = 1$ would indicate complete rearrangement of quarks and thus complete loss of correlations in the quark system, one would expect a much larger value of r, considering the presumed transition to the quark-gluon plasma in Pb+Pb collisions at 160 GeV/N,

Outlook

The latest data of CERN/SPS on flow, electro-magnetic probes, strange particle yields (most importantly multistrange (anti-)hyperons) and heavy quarkonia will be interesting to follow closely. Simple energy densities estimated from rapidity distributions and temperatures extracted from particle spectra indicate that initial conditions could be near or just above the domain of deconfinement and chiral symmetry restoration. Still the quest for an *unambiguous* signature remains open.

Directed flow has been discovered – now a flow excitation function, filling the gap between 10 AGeV (AGS) and 160 AGeV (SPS), will be extremely

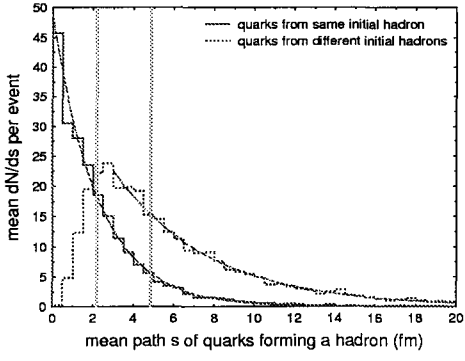

Figure 6: Hadronization in S+Au collisions at SPS (200 GeV/N): Number density distribution of mean diffusion path of quarks forming a hadron from the same initial hadron (solid line) and from different initial hadrons (dashed line) within qMD. Fitting the decay profiles yields diffusion lengths of 2.2 fm and 4.8 fm, respectively.

interesting: look for the softening of the QCD equation of state in the coexistence region. The investigation of the physics of high baryon density (e.g. partial restoration of chiral symmetry via properties of vector mesons) has been pushed forward by the 40 GeV run at SPS. Also the excitation function of particle yield ratios (π/p, d/p, K/π...) and, in particular, multistrange (anti-)hyperon yields, can be a sensitive probe of physics changes in the EoS. The search for novel, unexpected forms of matter, e.g. *hypermatter*, *strangelets* or even *charmlets* is intriguing. Such exotic QCD multi-meson and multi-baryon configurations would extend the present periodic table of elements into hitherto unexplored dimensions. A strong experimental effort should continue in that direction.

Now we have entered the exciting RHIC era, where the predicted deconfined and chirally restored phase should be formed and live long enough to produce clear and unambigious signals of it's existence. The LHC-program will top this scientific endeavour in 4 years.

Acknowledgments

This work was supported by DFG, GSI, BMBF, Graduiertenkolleg Theoretische und Experimentelle Schwerionenphysik, the A. v. Humboldt Foundation, and the J. Buchmann Foundation.

1. T. Matsui and H. Satz, Phys. Lett. **B178**, 416 (1986).
2. D. Kharzeev, Nucl. Phys. **A610**, 418c (1996).
3. L. Gerland, L. Frankfurt, M. Strikman, H. Stöcker, and W. Greiner, Phys. Rev. Lett. **81**, 762 (1998).
4. R. L. Anderson *et al.*, Phys. Rev. Lett. **38**, 263 (1977).

5. G. R. Farrar, L. L. Frankfurt, M. I. Strikman, and H. Liu, Phys. Rev. Lett. **64**, 2996 (1990).
6. L. Frankfurt, W. Koepf, and M. Strikman, Phys. Rev. **D54**, 3194 (1996).
7. D. Kharzeev, C. Lourenco, M. Nardi, and H. Satz, Z. Phys. **C74**, 307 (1997).
8. C. Gerschel and J. Hufner, Phys. Lett. **B207**, 253 (1988).
9. C. Lourenco, Nucl. Phys. **A610**, 552c (1996).
10. S. A. Bass *et al.*, Prog. Part. Nucl. Phys. **41**, 225 (1998).
11. C. Spieles, R. Vogt, L. Gerland, S. A. Bass, M. Bleicher, H. Stocker and W. Greiner, Phys. Rev. **C60** (1999) 054901 [hep-ph/9902337].
12. A.Romana *et al.*, in Proceedings of the XXXIIIrd Rencontres de Moriond, March 1998, Les Arcs, France.
13. M. C. Abreu *et al.*, Phys. Lett. **B477**, 28 (2000).
14. R. Vogt, Phys. Rept. **310**, 197 (1999).
15. A. Capella, E. G. Ferreiro, and A. B. Kaidalov, hep-ph/0002300 (2000).
16. V. Koch, Int. Jour. Mod. Phys. **E6** (1997) 203.
17. W. Cassing, E. L. Bratkovskaya, R. Rapp, and J. Wambach, Phys. Rev. C**57** (1998) 916
18. G. Agakishiev et al., Phys. Lett. **B402** (1998) 405.
19. G. Q. Li and C. Gale, Phys. Rev. **C58** (1998) 2914.
20. C. Spieles et al., Eur. Phys. J. **C5** (1998) 349
21. J. Rafelski, B. Müller Phys. Rev. Lett.**48**, (1982) 1066; (E) **56** (1986) 2334; P. Koch, B. Müller, J. Rafelski *Phys. Rep.* **142**, (1986) 167; P. Koch, B. Müller, H. Stöcker, W. Greiner *Mod. Phys. Lett.* **A3**, (1988) 737
22. S. Soff, S. A. Bass, M. Bleicher, L. Bravina, M. Gorenstein, E. Zabrodin, H. Stöcker, W. Greiner Phys. Lett. **B471**, (1999) 89 and refs. therein
23. P. Senger, H. Ströbele J. Phys. G**25**, (1999) R59
24. R. Stock Phys. Lett.**B456**, (1999) 277
25. E. Andersen et al.(WA97 collaboration) Phys. Lett. **B433**, (1998) 209; S. Margetis et al.(NA49 collaboration) J. Phys. G **25**, (1999) 189
26. F. Sikler et al.(NA49 collaboration) Nucl. Phys. **A661**, (1999)
27. C. Greiner, S. Leupold nucl-th/0009036
28. S. Soff *et al.*, J. Phys. G in print, nucl-th/0010103.
29. C. Greiner, nucl-th/0011026.
30. D. Hahn and H. Stöcker, Nucl. Phys. **A452**, 723 (1986).
31. D. Hahn and H. Stöcker, Nucl. Phys. **A476**, 718 (1988).
32. P. Braun-Munzinger, J. Heppe, and J. Stachel, Phys. Lett. B **465**, 15 (1999).
33. J. Rafelski and J. Letessier, nucl-th/9903018 (1999).

34. F. Becattini, J. Cleymans, A. Keranen, E. Suhonen, and K. Redlich, hep-ph/0002267 (2000).
35. G. D. Yen and M. I. Gorenstein, Phys. Rev. **C59**, 2788 (1999).
36. H. Stöcker and W. Greiner, Z. Phys. A **286**, 121 (1978).
37. J. Theis, G. Graebner, G. Buchwald, J. A. Maruhn, W. Greiner, H. Stöcker and J. Polonyi, Phys. Rev. **D28** (1983) 2286.
38. J. Schaffner, I. N. Mishustin, L. M. Satarov, H. Stöcker, and W. Greiner, Z. Phys. **A341**, 47 (1991).
39. D. Zschiesche, P. Papazoglou, S. Schramm, C. Beckmann, J. Schaffner-Bielich, H. Stöcker, and W. Greiner, Springer Tracts in Modern Physics **163**, 129 (2000).
40. F. Karsch, hep-lat/9903031 (1998).
41. P. Papazoglou, D. Zschiesche, S. Schramm, J. Schaffner-Bielich, H. Stöcker, and W. Greiner, Phys. Rev. C **59**, 411 (1999).
42. D. Zschiesche, L. Gerland, S. Schramm, J. Schaffner-Bielich, H. Stöcker and W. Greiner, nucl-th/0007033.
43. D. H. Rischke, Y. Pürsün, J.A. Maruhn, H. Stöcker, W. Greiner, Heavy Ion Physics **1** (1995) 309.
44. J. Brachmann, A. Dumitru, J.A. Maruhn, H. Stöcker, W. Greiner, D.H. Rischke, Nucl. Phys. **A619** (1997) 391.
45. H. Sorge, Phys. Rev. Lett. **78**, 2309 (1997)
46. H. Liu et al. (E895 Collaboration), Nucl. Phys. **A638**, 451c (1998)
47. Y. B. Ivanov, E. G. Nikonov, W. Noerenberg, A. A. Shanenko and V. D. Toneev, nucl-th/0011004.
48. K. H. Ackermann *et al.* [STAR Collaboration], nucl-ex/0009011.
49. M. Bleicher and H. Stöcker, hep-ph/0006147.
50. P. Huovinen, priv. comm.;
    P. F. Kolb, J. Sollfrank and U. Heinz, Phys. Lett. **B459** (1999) 667 [nucl-th/9906003].
51. M. Bleicher *et al.*, Phys. Rev. **C62** (2000) 024904 [hep-ph/9911420].
52. M. Hofmann, S. Scherer, M. Bleicher, L. Neise, H. Stöcker, and W. Greiner, Phys. Lett. **B478** (200) 161
53. S. Scherer, M. Hofmann, M. Bleicher, L. Neise, H. Stöcker, and W. Greiner, N. Journ.Phys. *to be publ.*

Jan Rafelski

THE STRANGE QUARK-GLUON PLASMA

JOHANN RAFELSKI AND GIORGIO TORRIERI
Department of Physics, University of Arizona, Tucson, AZ, 85721

JEAN LETESSIER
Laboratoire de Physique Théorique et Hautes Energies
Université Paris 7, 2 place Jussieu, F–75251 Cedex 05

Strangeness flavor has turned out to be a very effective diagnostic tool of relativistic heavy ion physics. The absolute yield provides information about conditions arising in first instants of the interaction. Strange hadrons are abundant allowing a precise study of the chemical freeze-out conditions in the dense matter fireball. The thermal and chemical freeze-out universality seen in strange hadrons confirms sudden hadronization as the breakup mechanism. A plausible cause of sudden fireball breakup is the mechanical instability arising when a quark-gluon plasma phase supercools deeply in its adiabatic expansion. Applying these ideas, we interpret CERN-SPS and the first results on hadronic particle ratios obtained at RHIC.

1 Introduction

It is believed today that a new state of matter has been formed in relativistic nuclear collisions at CERN. The question is if this is the hot quark matter (quark-gluon plasma) state of matter, which has been for 30 years a predicted new form of elementary matter: as early as 1970, the development of the quark model lead to a first consideration of quark matter stellar structure. [1]

These ideas were deepened by the development of the quantum many body theory of quark matter, [2,3] which lead on to the formal recognition within the framework of asymptotically free quantum-chromodynamics (QCD) that a very high temperature perturbative quark matter state must exist. [4] Other reasoning based on a study of the 'boiling state' of dense hadron gas within the scheme of Hagedorn's statistical bootstrap of hadronic matter has independently lead from a different direction to the consideration of the transition to a hadron substructure phase. [5] Considering the present day lattice-QCD numerical simulations, [6] we understand today quite well the properties of the baryon number free quark-gluon plasma (QGP), as we today call hot quark matter

However, it is still common to study ad-hoc ideas about new phases of fundamental matter. This is a natural approach considering the history of nuclear physics which developed without fundamental knowledge about the quark/QCD nature of nuclear interactions. Nuclear physics advanced by the

development of models, and this tradition remains strong. In fact there was little initial interest in quarks, gluons, and QCD among nuclear physisists. The first of the series of formative workshops in the field of relativistic heavy ion collisions, the "Bear Mountain" meeting in November 1974 had not a single mention of quarks, let alone of quark matter. At the time ultra dense nuclei, multi-hyperon nuclear states, and "pion condensates", were all considered as the discovery potential of these new and coming tools of nuclear physics research.

As the ideas about QGP formation in high energy nuclear collision matured, an unexpected challenge emerged 20 years ago: how can the locally deconfined state which exists a mere 10^{-22}s be distinguished from the gas of confined hadrons? This is also a question of principle, considering that both quark and hadron pictures of the reaction could be equivalent, for it has been argued that a quark-gluon based description is merely a change of Hilbert space expansion basis, if the rules of quantum mechanics with pure states are considered. This view contradicts the intuition, and about everybody in our field has come to believe that QGP phase is observable, since the quantum solution decoheres, even if the argument is being made with a lot of hand waving.

In the Galilean tradition, such a difficult question about existence and observability of a new phase of elementary matter, the QGP, must be settled by an experiment. This requires that a probe of QGP operational on the collision time scale of $5{\cdot}10^{-23}$ s is developed, which is sensitive to the local color charge deconfinement, and that it depends on the gluon degree of freedom, which is the characteristic new ingredient of the quark matter phase.

One of us (JR) proposed strangeness as the signature of QGP noticing more than 20 years ago that when color bonds are broken, the chemically equilibrated deconfined state has an unusually high number of strange quark pairs. [7] A study of the dynamics of strangeness (chemical) equilibration process has shown that only the gluon component in the QGP is capable to produce strangeness rapidly [8], allowing the formation of (nearly) chemically equilibrated dense phase of deconfined, hot, strangeness-rich quark matter in relativistic nuclear collisions. Therefore, strangeness enhancement is related directly to the presence of gluons in QGP.

The high density of strangeness available in the fireball favors during hadronization the formation of multi-strange hadrons, [9,10] which are produced quite rarely if only individual hadrons collide. [11,12] A large enhancement of multi strange (anti)baryons has been continuously advanced and defended by one of us (JR) as a characteristic signature of the QGP over the past 20 years. A systematic enhancement has been now reported, rising with strangeness

content. [13] Here the enhancement of strange antibaryons is reported with a base being the expectation derived from the scaled nucleon-nucleon and nucleon-nucleus reactions.

These experimental results are consistent with particle production occurring from a strangeness dense source in which the strange quarks are already made, are freely moving around and are readily available. This is by definition, the deconfined state we refer to as the quark-gluon plasma. We are not aware of a consistent interpretation of the rich and diverse experimental results not using QGP formation. It is important here to remember that since there are many results on strange hadron production, any alternative description has to be tested on all data available.

We think that strangeness enhancement has turned out to be a very practical signature of quark-gluon plasma physics. This report summarizes our work of past 18 months in this area – for further details the reader may consult our recent articles. [14,15,16,17] In the following section 2 we will describe our most recent advances in the study of properties of QGP at time of its formation and its sudden breakup. [15] The initial conditions are determining the overall strangeness yield. We use the properties of QGP at sudden breakup in the following section 3, testing the consistency of the chemical freeze-out condition with the properties of the QGP. [14] Recently, [16] we have been able to understand the mechanism of sudden QGP hadronization in terms of a mechanical instability arising within a supercooled and rapidly expanding fireball, as we will discuss in section 4.

An important experimental observation pointing to sudden QGP breakup is that strange baryons and antibaryons have very similar $m_\perp$-spectra [18] and are thus produced by the same mechanism. [19] Moreover, as we will show in section 5, these spectra imply that the thermal freeze-out of these rarely produced particles occurs together with the chemical (abundance) freeze-out. [17] This occurs for all collision centralities measured by experiment WA97.

In recent months first strangeness results have been obtained at RHIC. Our analysis effort regarding these results has just begun. Some of our RHIC predictions [20,21] can already be compared with experiment, and we will show in section 6 to be in agreement with our picture of how strangeness and QGP evolves at RHIC.

2 QGP fireball

2.1 Formulation of the QGP model

Using the latest lattice-QCD results, we have been able to better model the properties of the QGP, [15] compared to our earlier considerations. [22] The key ingredients of our current approach are:

1. We relate the QCD scale to the temperature $T = 1/\beta$, we use for the scale the Matsubara frequency [23] (μ without a subscript is *not* a chemical potential, it is the QCD scale):

$$\mu = 2\pi\beta^{-1}\sqrt{1 + \frac{1}{\pi^2}\ln^2\lambda_{\rm q}} = 2\sqrt{(\pi T)^2 + \mu_{\rm q}^2}\,. \tag{1}$$

This extension to finite chemical potential $\mu_{\rm q}$, or equivalently quark fugacity $\lambda_{\rm q} = \exp\mu_{\rm q}/T$, is motivated by the form of plasma frequency entering the computation of the vacuum polarization function. [24]

2. We obtain the interacting strength $\alpha_s(\mu)$ integrating numerically the renormalization group equations

$$\mu\frac{\partial\alpha_s}{\partial\mu} = -b_0\alpha_s^2 - b_1\alpha_s^3 + \ldots \equiv \beta_2^{\rm pert}\,. \tag{2}$$

$\beta_2^{\rm pert}$ is the beta-function of the renormalization group in two loop approximation, and

$$b_0 = \frac{11 - 2n_{\rm f}/3}{2\pi}\,, \quad b_1 = \frac{51 - 19n_{\rm f}/3}{4\pi^2}\,.$$

$\beta_2^{\rm pert}$ does not depend on the renormalization scheme, and solutions of Eq. (2) differ from higher order renormalization scheme dependent results by less than the error introduced by the experimental uncertainty in the measured value of $\alpha_s(\mu = M_Z) = 0.118 + 0.001 - 0.0016$.

3. We introduce, in the domain of freely mobile quarks and gluons, a finite vacuum energy density:

$$\mathcal{B} = 0.19\,\frac{\rm GeV}{\rm fm^3}\,.$$

This also implies, by virtue of relativistic invariance, that there must be a (negative) associated pressure acting on the surface of this volume, aiming to reduce the size of the deconfined region. These two properties of the vacuum follow consistently from the vacuum partition function:

$$\ln\mathcal{Z}_{\rm vac} \equiv -\mathcal{B}V\beta\,. \tag{3}$$

4. The partition function of the quark-gluon liquid comprises interacting gluons, n_q flavors of light quarks, [25] and the vacuum $\mathcal{B}$-term. We incorporate further the strange quarks by assuming that their mass in effect reduces their effective number $n_s < 1$:

$$\frac{T}{V}\ln \mathcal{Z}_{QGP} \equiv P_{QGP} = -\mathcal{B} + \frac{8}{45\pi^2}c_1(\pi T)^4 + \frac{n_q}{15\pi^2}\left[\frac{7}{4}c_2(\pi T)^4 + \frac{15}{2}c_3\left(\mu_q^2(\pi T)^2 + \frac{1}{2}\mu_q^4\right)\right] + \frac{n_s}{15\pi^2}\left[\frac{7}{4}c_2(\pi T)^4 + \frac{15}{2}c_3\left(\mu_s^2(\pi T)^2 + \frac{1}{2}\mu_s^4\right)\right] \quad (4)$$

where:

$$c_1 = 1 - \frac{15\alpha_s}{4\pi} + \cdots, \quad c_2 = 1 - \frac{50\alpha_s}{21\pi} + \cdots, \quad c_3 = 1 - \frac{2\alpha_s}{\pi} + \cdots. \quad (5)$$

2.2 Properties of QGP-liquid

We show properties of the quark-gluon liquid defined by Eq. 3 in a wider range of parameters at fixed entropy per baryon S/B, in the range $S/B = 10$–60 in step of 5 units. In the top panel in figure 1, we show baryo-chemical potential μ_b, in middle panel baryon density n/n_0, here $n_0 = 0.16/\mathrm{fm}^3$, and bottom left the energy per baryon E/B. In top and middle panel the low entropy results are top-left in figure, in bottom panel bottom left. The highlighted curve, in figure 1, is for the value $S/B = 42.5$, applicable to the 158 AGeV Pb–Pb collisions. The dotted line, at the minimum of $E/B|_{S/B}$, is where the vacuum and quark-gluon gas pressure balance.

Little entropy is produced during the nearly adiabatic evolution of the QGP fireball. [26] Thus the lines in the lower panel of figure 1 characterize the approximate trajectory in time of the fireball. After initial drop in energy per baryon due to transfer of energy to accelerating expansion of the fireball, during the deep supercooling process, the motion is slowed and thus energy per baryon increases. The thick line is our expectation for the fireball made in Pb–Pb interactions at the projectile energy 158A GeV. The cross shows the result of chemical freeze-out analysis presented in next section 3. [14]

We also have compared the chemical freeze-out conditions with the phase transition properties. The hadron gas behavior is obtained evaluating and summing the contributions of all known hadronic resonances considered to be point particles. The thin solid line in the T, μ_b plane in figure 2 shows where the pressure of the quark-gluon liquid equals the equilibrated hadron gas pressure. When we allow for finite volume of hadrons, [27] we find that

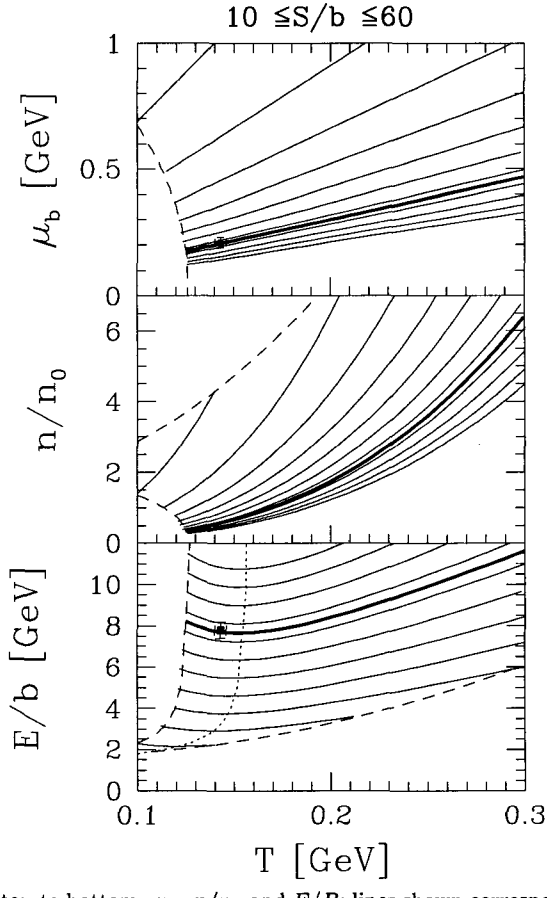

Figure 1. From top to bottom: μ_b, n/n_0 and E/B; lines shown correspond to fixed entropy per baryon $S/B = 10$ to 60 by step of 5 (left to right). Thick solid lines: result for $S/B = 42.5$. Limits: energy density $\varepsilon_{q,g} = 0.5\,\mathrm{GeV/fm^3}$ and baryo-chemical potential $\mu_b = 1\,\mathrm{GeV}$. The experimental points denote chemical freeze-out analysis result. [14]

the hadron pressure is slightly reduced, leading to some (5 MeV) reduction in the equilibrium transition temperature, as is shown by the dashed line in figure 2. For vanishing baryo-chemical potential, we note in figure 2 that the equilibrium phase transition temperature is $T_{\mathrm{pt}} \simeq 172\,\mathrm{MeV}$, and when finite hadron size is allowed, $T_{\mathrm{fp}} \simeq 166\,\mathrm{MeV}$, The scale in temperature we discuss is result of comparison with lattice gauge results. Within the lattice calculations [6], it arises from the comparison with the string tension.

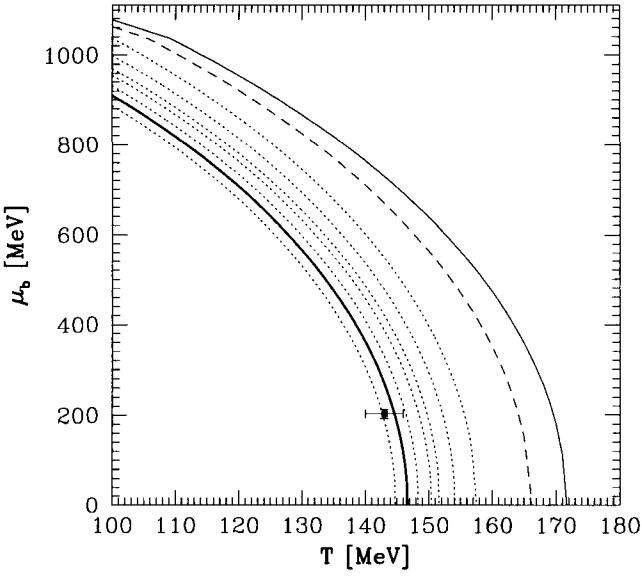

Figure 2. Thin solid and dashed lines: equilibrium phase transition from hadron gas to QGP liquid without and with excluded volume correction, respectively. Dotted: breakup condition at shape parameter $\kappa = 0.6$, for expansion velocity $v_c^2 = 0, 1/10, 1/6, 1/5, 1/4$ and $1/3$, and thick line for $v_c = 0.54$. The experimental point denotes chemical non-equilibrium freeze-out analysis result. [14]

The dotted lines, in figure 2, show where the flowing QGP liquid has a pressure which balances the vacuum pressure, and thus these lines correspond to sudden break up at a velocity for (from right to left) $v_c^2 = 0, 1/10, 1/6, 1/5, 1/4$ and $1/3$, see section 4, specifically the dotted lines in figure 2 correspond to the condition Eq. (9) using the shape parameter $\kappa = 0.6$, Eq. (12). The last dotted line corresponds thus to an expansion flow with the velocity of sound of relativistic noninteracting massless gas. The thick solid line corresponds to an expansion with $v_c = 0.54$. The hadron analysis result is also shown as presented in section 3. [14] Comparing in figure 2 thin solid/dashed with the thick line, we recognize the deep supercooling as required for the explosive fireball disintegration. The super-cooled zero pressure $P = 0$ baryonfree QGP temperature is at $T_{sc} = 157\,\mathrm{MeV}$, (see the intercept of the first dashed line to the right in figure 2) and an expanding fireball can deeply super-cool to $T_{dsc} \simeq 147\,\mathrm{MeV}$ (see the intercept of thick solid line) before the mechanical instability occurs.

2.3 Initial conditions in QGP formation

The formation of the QGP occurs well before chemical equilibration of quarks. We model this situation varying n_f. For $n_f = 1$ we show, in figure 3, lines of fixed energy per baryon E/B =3, 4, 5, 6, 8, 10, 20, 50 and 100 GeV, The horizontal solid line is where the equilibrated hadronic gas phase has the same pressure as QGP-liquid with semi-equilibrated quark abundance. The free energy of the QGP liquid must be lower (pressure higher) in order for hadrons to dissolve into the plasma phase. The dotted lines in figure 3, from bottom to top, show where the pressure of the semi-equilibrated QGP phase is equal to $\eta = 20\%, 40\%, 60\%, 80\%$ and 100%, η being the 'stopping' fraction of the dynamical collisional pressure [22]:

$$P_{\rm col} = \eta \rho_0 \frac{P_{\rm CM}^2}{E_{\rm CM}} \,. \tag{6}$$

The rationale to study, in figure 3, lines at fixed E/B is that, during the nuclear collision which lasts about $2R_N/\gamma_L 2c \simeq 13/18\,{\rm fm}/c$, where γ_L is the Lorentz factor between the lab and CM frame and R_N is the nuclear radius, parton collisions lead to a partial (assumed here to be 1/2) chemical equilibration of the hadron matter. At that time, the pressure exercised corresponds to collisional pressure $P_{\rm col}$. This stopping fraction, seen in the transverse energy produced, is about 40% for S–S collisions at 200A GeV and 60% for Pb–Pb collisions at 158A GeV. If the momentum-energy and baryon number stopping are similar, as we see in the experimental data, then the SPS collisions at 160–200A GeV are found in the highlighted area left of center of the figure. In the middle of upper boundary of this area, we would expect the beginning evolution of the thermal but not yet chemically equilibrated Pb–Pb fireball, and in the lower left corner of the S–S fireball. We note that the temperature reached in S–S case is seen to be about 25 MeV lower than in the Pb–Pb case. The lowest dotted line (20% stopping) nearly coincides with the non-equilibrium phase boundary (solid horizontal line, in figure 3) and thus we conclude that this is, for the condition $n_f = 1$, the lowest stopping that can lead to formation of a deconfined QGP phase. Such a low stopping would be encountered possibly in lighter than S–S collision systems or/and at large impact parameter interactions of larger nuclei.

The highlighted area, right of center of the figure 3, corresponds to the expected conditions in Pb–Pb collisions at 40A GeV. If we assume that the stopping here is near 80%, then the initial conditions for fireball evolution would be found towards the upper right corner of this highlighted area. We recognize that the higher stopping nearly completely compensates the effect of reduced available energy in the collision and indeed, we expect that we form

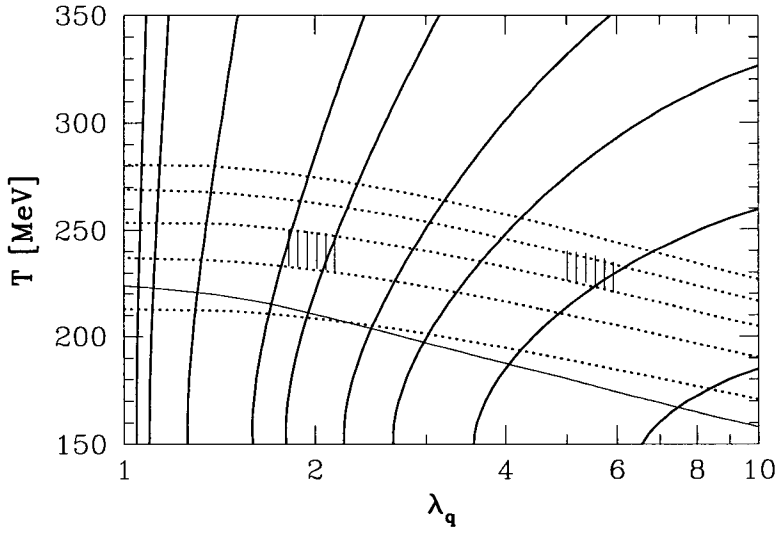

Figure 3. Contours of energy per baryon in QGP in the T–λ_q plane for $n_f = 1$: From right to left E/B=3, 4, 5, 6, 8, 10, 20, 50 and 100 GeV. Thin, nearly horizontal line: hadronic gas phase has the same pressure as the QGP-liquid with semi-equilibrated quark flavor. Dotted lines from bottom to top: pressure in QGP liquid equals 20%, 40%, 60%, 80%, and 100%, of the dynamical collisional pressure.

QGP also at these collision energies. It is important to realize that we are entering a domain of parameters, in particular λ_q, for which the extrapolation of the lattice results is not necessarily reliable, and thus our equations of state have increased systematic uncertainty.

3 Fermi-model data analysis

3.1 Properties of hadronic matter fireball

A full account of our prior analysis of the 158A GeV Pb–Pb collision system has appeared. [14] We briefly summarize the results that we require for the study of QGP properties at fireball breakup. In table 1, in upper section, we present the parameters T_f (the chemical freeze-out temperature), v_c (the

collective flow velocity at sudden breakup), λ_q (the light quark fugacity), λ_s (the strange quark fugacity), γ_q (the light quark phase space occupancy), γ_s (the strange quark phase space occupancy). These chemical properties are derived from analysis of all hadrons excluding Ω and $\overline{\Omega}$, which data points are not following the same systematic production pattern. These parameters characterize completely the physical properties of the produced hadrons, and these properties are shown in the bottom section of table 1.

In the heading of the table, the total error, χ^2 is shown, along with the number of data points N, parameters p and data point constraints r. The confidence level that is reached in our description is near or above 90%, depending on scenario considered. The scenarios we consider are seen in the columns of table 1: an unconstrained description of all data in the first column, constraint to exact strangeness conservation in the observed hadrons, second column. Since in both cases the parameter γ_q assumes value that maximizes the entropy and energy content in the pion gas, we assume this value in the so constrained third column.

We can now check the consistency between the statistical parameters (top panel of table 1) and the physical properties of the fireball (bottom panel of table 1) which are maintained in the process of hadronization. We note that the energy shown in this table, is the intrinsic energy in the flowing frame. The CM-laboratory energy includes the kinetic energy of the flow and thus is greater, to be obtained multiplying the result shown in table 1 by the Lorenz factor $\gamma = 1/\sqrt{1 - v_c^2} = 1.19$. Thus the initial value of the energy per baryon that the system had before expansion started has been $E^0/B \simeq 9.3\,\mathrm{GeV}$.

3.2 Interpretation in terms of QGP

In the bottom panel in figure 1, we saw that the Temperature $T_f = 143 \pm 3\,\mathrm{MeV}$ and intrinsic (frame at rest) energy per baryon $E/B = 7.8\,\mathrm{GeV}$ where just at $S/B = 42.5$ seen table 1. Similarly, in the top panel, the baryo-chemical potential $\mu_b = 3T_f \ln \lambda_q = 204 \pm 10\,\mathrm{MeV}$ is as required for the consistency of QGP properties. The fireball hadron freeze-out and/or breakup condition is thus found well below the QGP to HG phase transition temperature. Both the specific energy and entropy content of the fireball are consistent with the statistical parameters T_f and μ_b according to our equations of state of the quark-gluon liquid. We can also evaluate the hadronic phase space energy density. We allow the excluded volume correction. [27] Considering that the point particle phase space energy density $\varepsilon_{pt} = 1.1\,\mathrm{GeV/fm^3}$, we obtain $\varepsilon_{HG} \simeq 0.4\,\mathrm{GeV/fm^3}$ at chemical freeze-out, using the value of $\mathcal{B} = 0.19\,\mathrm{GeV/fm^3}$. This energy density is neraly the same as one finds in QGP. Thus we see that

Table 1. Results of study of Pb–Pb hadron production: [14] in the heading: the total quadratic relative error $\chi^2_{\rm T}$, number of data points N, parameters p and redundancies r; in the upper section: statistical model parameters which best describe the experimental results for Pb–Pb data. Bottom section: specific energy, entropy, anti-strangeness, net strangeness of the full hadron phase space characterized by these statistical parameters. In column one, all statistical parameters and the flow vary. In column two, we fix λ_s by requirement of strangeness conservation, and in column three, we fix γ_q at the pion condensation point $\gamma_q = \gamma_q^c$.

	$\mathrm{Pb}\vert_v$	$\mathrm{Pb}\vert_v^{\rm sb}$	$\mathrm{Pb}\vert_v^{\rm sc}$
$\chi^2_{\rm T}$; $N;p;r$	2.5; 12; 6; 2	3.2; 12; 5; 2	2.6; 12; 5; 2
T_f [MeV]	142 ± 3	144 ± 2	142 ± 2
v_c	0.54 ± 0.04	0.54 ± 0.025	0.54 ± 0.025
λ_q	1.61 ± 0.02	1.605 ± 0.025	1.615 ± 0.025
λ_s	1.09 ± 0.02	1.10^*	1.09 ± 0.02
γ_q	1.7 ± 0.5	1.8 ± 0.2	$\gamma_q^{c*} = e^{m_\pi/2T_f}$
γ_s/γ_q	0.79 ± 0.05	0.80 ± 0.05	0.79 ± 0.05
E_f/B	7.8 ± 0.5	7.7 ± 0.5	7.8 ± 0.5
S_f/B	42 ± 3	41 ± 3	43 ± 3
s_f/B	0.69 ± 0.04	0.67 ± 0.05	0.70 ± 0.05
$(\bar{s}_f - s_f)/B$	0.03 ± 0.04	0^*	0.04 ± 0.05

the chemical freeze-out is due to the direct fireball breakup.

More generally, the chemical analysis evidence for the QGP nature of the fireball is as follows: [14]

a) The value of strange quark fugacity λ_s we find in our analysis can also be obtained from the requirement that strangeness balances, $\langle N_s - N_{\bar{s}} \rangle = 0$, in QGP, which for a source in which all s an $\bar{s}$ quarks are unbound and thus have symmetric phase space, implies $\lambda_s = 1$. However, the Coulomb distortion of the strange quark phase space plays an important role in the understanding of this constraint for Pb–Pb collisions, citeRaf91 leading to the Coulomb-deformed value $\lambda_s \simeq 1.1$, which is identical to the value obtained from experimental data analysis $\lambda_s^a = 1.09 \pm 0.02$.

b) The phase space occupancy of light quarks γ_q even if it were before gluon fragmentation near or at the equilibrium value $\gamma_q = 1$, must increase above this equilibrium value. There is an upper limit: $\gamma_q < \gamma_q^c \equiv e^{m_\pi/2T_f} \simeq 1.67$, which arises to maximize the entropy density in the confined hadron phase. In our analysis we find values in this narrow interval $1 \leq \gamma_q \leq \gamma_q^c$

c) The strange quark phase space occupancy γ_s we compute within the framework of kinetic theory where strangeness pair production arises in gluon fu-

sion, [9]. The result depends on temperature reached in early stages of the collision, and following dilution effect in which the already produced strangeness can even over saturate the 'thiner' low temperature phase space. Moreover, some gluon fragmentation also enriches γ_s as measured by hadron abundance, and thus we find $gmma_s \geq 1$. We note that the ratio γ_s/γ_q has been earlier confounded with γ_s, which therefore is stated in table 1.
d) The strangeness yield, $N_s/B = N_{\bar{s}}/B \simeq 0.7$, predicted early on as the result of QGP formation [9] is also one of the results of data analysis seen in table 1. This result we obtain within the modern kinetic model of strangeness production in QGP. [14] The results are shown in figure 4 as function of the intrinsic specific energy available in the fireball E/B, for the three collision systems S-Au/W/Pb (short-dashed line), Ag–Ag (long dashed) and Pb–Pb (solid line). The solid square is the 'experimental' result obtained in our analysis of the S-Au/W/Pb system, and the open square is for Pb–Pb. The experimental value of stopping we employ (see legend to figure 4) were obtained by NA49 collaboration, [29].

Stopping enters the computation of the initial temperature from the collision energy, see Eq. (6). We extrapolate as function of E/B, assuming that the stopping fraction for the collisional pressure is known, and as here assumed, not changing with collision energy in the narrow interval shown in figure 4, leading to a steep rise of strangeness production with collision energy.

4 Supercooling and sudden breakup

4.1 Instability condition

Sudden hadronization of dense matter fireballs formed in 158A GeV Pb–Pb collisions requires that a global instability of the dense hadronic matter fireball is encountered in its evolution. Given the hadronization temperature we found, $T \simeq 143\,\mathrm{MeV}$, which is about 15 MeV below the equilibrium phase transition of QGP phase to hadron gas it is a natural step to consider the possibility of supercooling of the QGP phase. As many of us have experienced in diverse daily life experiences, once the supercooled phase is disturbed, a truly sudden break-up occurs. QGP instability was suggested by Csörgő and Csernai [28] to explain sudden hadronization. [30] Despite extensive ensuing study of potential microscopic mechanisms, [31,32,33] a convincing elementary instability mechanism has not been found.

As the fireball expands, energy is transfered from thermal motion to collective flow in adiabatic fashion. At a certain point in deep supercooling, energy flow is reversed, and the matter flow begins to slow down. However, if

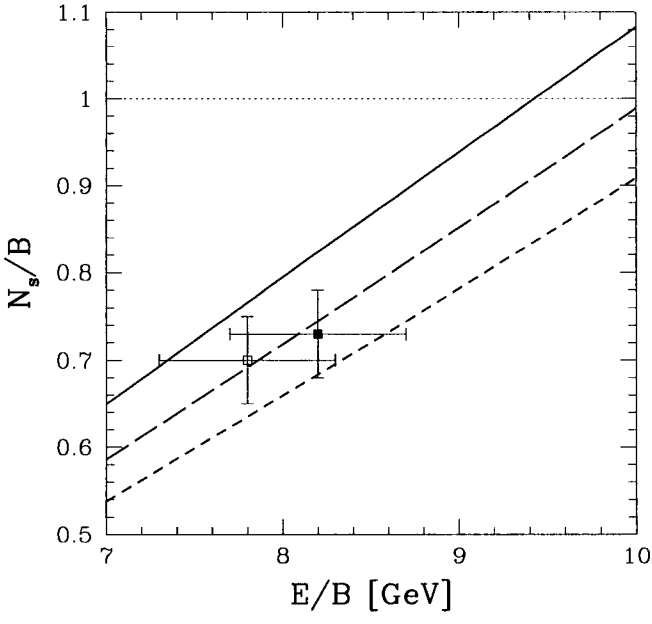

Figure 4. QGP fireball specific per baryon strangeness abundance as function of E/B energy per baryon in the fireball, for running $\alpha_s(M_Z) = 0.118$ and $m_s(1GeV) = 200\,\mathrm{MeV}$, corresponding to $m_s(M_Z) = 90\,\mathrm{MeV}$. Solid lines: for Pb–Pb, stopping 57% and 360 participants, long-dashed lines: for Ag–Ag, stopping 54% and 180 participants, short-dashed lines: for S–Au/W/Pb stopping 52% and 90 participants in QGP fireball. The solid square is the result of an analysis for S-Au/W/Pb 200A GeV reaction system, and open square for Pb–Pb at 158A GeV, as shown in the lower section of table 1.

the flow velocity remains large but the surface pressure $\mathcal{P} \to 0$, continued expansion must rip the fireball apart. This is the natural mechanical instability we proposed as the sudden hadronization condition. [16] This simple mechanism does not require a microscopic process for the onset of instability.

We consider the exploding fireball dynamics in its center of momentum frame of reference. The surface normal vector of exploding fireball is $\vec{n}$, and the local velocity of matter flow $\vec{v}_c$. The rate of momentum flow vector $\vec{\mathcal{P}}$ at the surface is obtained from the energy-stress tensor T_{kl}: [34]

$$\vec{\mathcal{P}} = P^{(i)}\vec{n} + (P^{(i)} + \varepsilon^{(i)})\frac{\vec{v}_c\,\vec{v}_c\cdot\vec{n}}{1-\vec{v}_c^{\,2}}\,. \tag{7}$$

The upper index (i) refers for the intrinsic energy density ε and pressure P of matter in the frame of reference, locally at rest, *i.e.,* observed by a co-moving observer. We omit the superscript (i) in the following. For the fireball expansion to continue, $\mathcal{P} \equiv |\vec{\mathcal{P}}| > 0$ is required. For $\mathcal{P} \to 0$ at $v_c \neq 0$, we have a conflict between the desire of the motion to stop or even reverse, and the continued inertial expansion.

When the flow velocity remains large but $\mathcal{P} \to 0$, the intrinsic pressure P must be negative. As illustration consider the fireball to be made of a quark-gluon liquid confined by an external vacuum pressure $\mathcal{B}$. The total pressure and energy comprise particle (subscript p) and the vacuum properties:

$$P = P_p - \mathcal{B}\,, \quad \varepsilon = \varepsilon_p + \mathcal{B}\,. \tag{8}$$

Eq. (7) with $\vec{\mathcal{P}} = 0$ thus reads:

$$\mathcal{B}\vec{n} = P_p\vec{n} + (P_p + \varepsilon_p)\frac{\vec{v}_c\,\vec{v}_c\cdot\vec{n}}{1 - v_c^2}\,, \tag{9}$$

and it describes the (equilibrium) condition where the pressure of the expanding quark-gluon fluid is just balanced by the external vacuum pressure.

Expansion beyond $\mathcal{P} \to 0$ is in general not possible. A surface region of the fireball that reached it but continues to flow outwards must be torn apart. This is a collective instability and thus the ensuing disintegration of the fireball matter will be very rapid, provided that much of the surface reaches this condition. We adopt the condition $\vec{\mathcal{P}} = 0$ at any surface region to be the instability condition of an expanding hadron matter fireball.

Negative internal pressure $P < 0$ is a requirement. At this stage the fireball must thus be significantly supercooled. The adiabatic transfer of internal heat into accelerating flow of matter provides the mechanism which leads on the scale of $\tau = 2\,10^{-23}$ s to the development of this 'deep' supercooling.

4.2 Consistency with QGP properties

The sudden break up due to mechanical instability of course will occur for all phases of elementary matter and thus we consider next in how far the observed freeze-out conditions and other features of hadronization process are consistent with the QGP mechanical breakup, and explore if experiments show evidence for supercooling.

It is possible to determine experimentally if the condition $P < 0$ has been reached. Namely, the Gibbs-Duham relation for a unit volume:

$$P = T\sigma + \mu_b\nu_b - \varepsilon\,, \tag{10}$$

relates the pressure, to entropy density $\sigma = S/V$, energy density $\varepsilon = E/V$, and baryon density $\nu_{\rm b} = b/V$, V is the volume, T is the temperature, and $\mu_{\rm b}$ the baryochemical potential. Dividing by ε we obtain:

$$\frac{PV}{E} = \frac{T_{\rm h}}{E/S} + \frac{\mu_{\rm b}}{E/B} - 1\,. \tag{11}$$

The microscopic processes governing the fireball breakup determine how the quantities entering the right hand side of Eq. (11) are changed as hadrons emerge. Understanding this we can determine, if the intrinsic fireball pressure prior to breakup, has been negative.

The energy E and baryon content b of the fireball are conserved. Entropy S is conserved when the gluon content of a QGP fireball is transformed into quark pairs in the entropy conserving process $G+G \to q+\bar{q}$. Similarly, when quarks and antiquarks recombine into hadrons, entropy is conserved in the range of parameters of interest here. Thus also E/B and S/B is conserved across hadronization condition. The sudden hadronization process also maintains the temperature T and baryo-chemical potential μ_b across the phase boundary. What changes in QGP breakup are the chemical occupancy parameters. As gluons convert into quark pairs and hadrons $\gamma_g \to 0$ but the number occupancy of light valance quark pairs increases $\gamma_q > \gamma_{q_0} \simeq 1$ increases significantly, along with the number occupancy of strange quark pairs $\gamma_s > \gamma_{s_0} \simeq 1$.

Evaluating Eq. (11) using the results of the data analysis presented above, we indeed obtain $P_f < 0$. The magnitude of $|P_f|$ can vary between a few percent (in terms of energy density E_f/V), up to 20% for the latest published result. [14] The precise value, which arises from several cancellations of larger numbers is sensitive to the strategy of how the currently available experimental data is described, *e.g.,* if strangeness conservation is implemented, and if so, if differentially at each rapidity, or as an overall conservation law; how many high mass resonances can be excited in hadronization process, etc ...

Understanding in detail the breakup condition $\mathcal{P} \to 0$ requires that we model the shape and direction of flow in the late stage of fireball evolution, obviously not an easy task. However, considering $\vec{n}\cdot\vec{\mathcal{P}} \to 0$, we find the constraint:

$$\frac{-PV/E}{1+PV/E} = \kappa\frac{v_{\rm c}^2}{1-v_{\rm c}^2}\,, \quad \kappa = (\vec{v}_{\rm c}\cdot\vec{n})^2/v_{\rm c}^2\,. \tag{12}$$

For an exactly symmetrical, spherical expansion the two vectors $\vec{v}_{\rm c}$ and $\vec{n}$ are everywhere parallel, thus $\kappa \to 1$. However, in 158A GeV Pb–Pb reactions the longitudinal flow is considerably greater than the transverse flow, [29] and we

note $\kappa \to 0$ for a longitudinally evolving cylindrical fireball. For the Pb–Pb collisions considered here, our analysis suggest $0.1 < \kappa < 0.6$.

We now substitute, in Eq. (12), the fireball matter properties employing the Gibbs-Duham relation, Eq. (10), and arrive at:

$$\frac{E}{S} = \left(T_{\rm h} + \frac{\mu_{\rm b}}{S/B}\right)\left\{1 + \kappa\frac{v_{\rm c}^2}{1-v_{\rm c}^2}\right\}. \tag{13}$$

Eq. (13) establishes a general constraint characterizing the fireball breakup condition.

Deep supercooling requires a first order phase transition, and this in turn implies presence of latent heat $\mathcal{B}$. Physical consistency then requires presence of external (negative) vacuum pressure $-\mathcal{B}$. We now combine the theoretical properties of the QGP equations of state with the dynamical fireball properties in order to constrain $\mathcal{B}$. Reviewing Eq. (11), we obtain:

$$-\frac{PV}{E}\varepsilon_{\rm QGP} + P_{\rm p} = \mathcal{B}\,, \tag{14}$$

To evaluate $\mathcal{B}$, we note that lattice results for $\varepsilon_{\rm QGP}$ are well represented by $\varepsilon_{\rm QGP} = aT^4$, with $a \simeq 11$, value extrapolated for the number of light quark flavors being $n_f = 2.5$ at the hadronization point. [15] We obtain, for the fireball formed in Pb–Pb reactions,

$$0.2 \cdot 11 T_{\rm h}^4 \simeq 0.17\ {\rm GeV/fm}^3 \leq \mathcal{B}\,.$$

5 Thermal freeze-out

5.1 Direct and decay $m_\perp$-spectra

We next study the shape of hadron $m_\perp$-spectra. These are strongly influenced by resonance decays, which have also contributed in an important fashion to the yield of all stable hadrons observed.

The final particle distribution is composed of directly produced particles and decay products of heavier hadronic resonances:

$$\frac{dN_X}{dm_\perp} = \left.\frac{dN_X}{dm_\perp}\right|_{\rm direct} + \sum_{\forall R\to X+2+\cdots} \left.\frac{dN_X}{dm_\perp}\right|_{R\to X+2+\cdots} \tag{15}$$

Here, $R(M, M_T, Y) \to X(m, m_T, y) + 2(m_2) + \cdots$, where we indicate by the arguments that only for the decay particle X we keep the information about the shape of the momentum spectrum.

In detail, the decay contribution to yield of X is:

$$\frac{dN_X}{dm_\perp^2 dy} = \frac{g_r b}{4\pi p^*} \int_{Y_-}^{Y_+} dY \int_{M_{T_-}}^{M_{T_+}} dM_T^2 \, J \, \frac{d^2 N_R}{dM_T^2 dY} \tag{16}$$

$$J = \frac{M}{\sqrt{P_T^2 p_T^2 - \{M E^* - M_T m_T \cosh \Delta Y\}^2}}$$

We have used $\Delta Y = Y - y$, and $\sqrt{s}$ is the combined invariant mass of the decay products other than particle X and $E^* = (M^2 - m^2 - m_2^2)/2M$, $p^* = \sqrt{E^{*2} - m^2}$ are the energy and momentum of the decay particle X in the rest frame of its parent. The limits on the integration are the maximum values accessible to the decay product X:

$$Y_\pm = y \pm \sinh^{-1}\left(\frac{p^*}{m_T}\right)$$

$$M_{T_\pm} = M \frac{E^* m_T \cosh \Delta Y \pm p_T \sqrt{p^{*2} - m_T^2 \sinh^2 \Delta Y}}{m_T^2 \sinh^2 \Delta Y + m^2}$$

The theoretical primary particle spectra (both those directly produced and parents of decay products) are derived from the Boltzmann distribution by Lorenz-transforming from a flowing intrinsic fluid element to the CM-frame, and integrating over allowed angles between particle direction and local flow.

We introduce in the current analysis two velocities: a local flow velocity v of fireball matter where from particles emerge, and hadronization surface (breakup) velocity which we refer to as $v_f^{-1} \equiv dt_f/dx_f$. Particle production is controlled by the effective volume element, which comprises this quantity. In detail:

$$dS_\mu p^\mu = d\omega \left(1 - \frac{\vec{v}_f^{-1} \cdot \vec{p}}{E}\right), \qquad d\omega \equiv \frac{d^3x d^3p}{(2\pi)^3}. \tag{17}$$

The Boltzmann distribution we adapt has thus the form

$$\frac{d^2N}{dm_T dy} \propto \left(1 - \frac{\vec{v}_f^{-1} \cdot \vec{p}}{E}\right) \gamma \, m_T \cosh y \, e^{-\gamma \frac{E}{T}\left(1 - \frac{\vec{v}\cdot\vec{p}}{E}\right)}, \tag{18}$$

where $\gamma = 1/\sqrt{1 - v^2}$.

The normalization for each hadron type $h = X, R$ is

$$N^h = V_{\mathrm{QGP}} \prod_{i \in h}^{n} \lambda_i \gamma_i .$$

We use the chemical parameters λ_i, γ_i $i = q, s$ which are as defined in [14] and commonly used to characterize relative and absolute abundances of light and strange quarks.

The best thermal and chemical parameters which minimize the total relative error $\chi^2_{\rm T}$,

$$\chi^2_{\rm T} = \sum_i \left(\frac{F_i^{\rm theory} - F_i}{\Delta F_i} \right)^2 ,$$

for all experimental measurement points F_i having measurement error ΔF_i are determined by considering simultaneously all strange baryon and antibaryon results of experiment WA97, [18] *i.e.*, Λ, $\overline{\Lambda}$, Ξ, $\overline{\Xi}$, $\Omega + \overline{\Omega}$, as well as K^0_S, except that we assign additional systematic error to these data (see below).

5.2 Λ-, $\overline{\Lambda}$-, Ξ-, $\overline{\Xi}$-$m_\perp$-*spectra*

In recent months experiment WA97 determined the absolute normalization of the published $m_\perp$ distribution, [18] and we took the opportunity to perform the shape analysis together with yield analysis in order to check if the thermal and chemical freeze-out conditions are the same. [17] Our analysis addresses the data differentiated in four different collision centralities. This allows to study the effect of the changing volume within the limits of precision set by the current data.

Since particle spectra we consider have a good relative normalization, only one parameter is required for each centrality in order to describe the absolute normalization of all six hadron spectra. This is for two reasons important:
a) we can check if the volume from which strange hadrons are emitted grows with centrality of the collision as we expect;
b) we can determine which region in $m_\perp$ produces the excess of Ω noted in the chemical fit. [14]

However, since the normalization $V_{\rm QGP}$ common for all particles at given centrality comprises additional experimental acceptance normalization which we have not yet studied, we have not normalized the value of the fireball emission volume at each centrality. Hence we will be presenting the volume parameter as function of centrality in arbitrary units.

If thermal and chemical freeze-outs are identical, our present results must be consistent with earlier chemical analysis of hadron yields. Since the experimental data we here study is dominated by the shape of $m_\perp$-spectra and not by relative particle yields, our analysis is de facto comparing thermal and chemical freeze-outs.

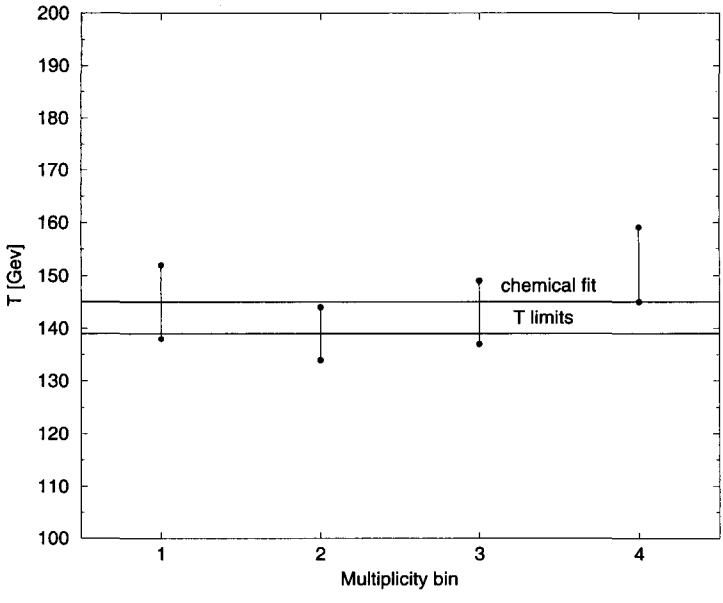

Figure 5. Thermal freeze-out temperature T for different centrality bins compared to the chemical freeze-out analysis.

We next show the parameters determining the shape of the $m_\perp$ distributions, that is T, v, v_f. As function of the centrality bin 1, 2, 3, 4 with the most central bin being 4 we show in figure 5 the freeze-out temperature T of the $m_\perp$ spectra. The horizontal lines delineate range of result of the chemical analysis. It is reassuring that we find a result consistent with the purely chemical analysis of data that included non-strange hadrons. [14] There is no indication of a significant or systematic change of T with centrality though there is a somewhat higher value in the most central 4th bin. This is consistent with the believe that the formation of the new state of matter at CERN is occurring in all centrality bins explored by the experiment WA97. Only most peripheral interactions produce a change in the pattern of strange hadron production. [35]

The (unweighted) average of all results shown in figure 5 produces a freeze-out temperature at the upper boundary of the the pure chemical freeze-out analysis result, $T \simeq 145\,\mathrm{MeV}$. It should be noted that in chemical analysis we have not distinguished between the flow v and freeze-out v_f velocity and both

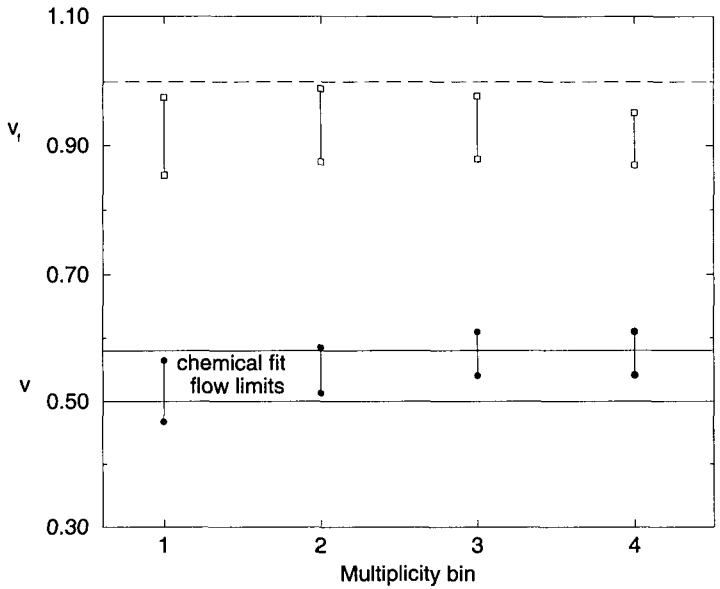

Figure 6. Thermal freeze-out flow velocity v (top) and break up (hadronization) velocity v_f for different centrality bins. Upper limit $v_f = 1$ (dashed line) and chemical freeze-out analysis limits for v (solid lines) are also shown.

are denoted as v_c, which may be the cause of this slight difference between current analysis average and the earlier purely chemical analysis result.

The magnitudes of the collective expansion velocity v and the break-up (hadronization) speed parameter v_f are presented in figure 6. For v (lower part of the figure) we again see consistency with earlier chemical freeze-out analysis results, and there is no confirmed systematic trend in the behavior of this parameter as function of centrality.

Though within the experimental error, one could argue inspecting figure 6 that there is systematic increase in transverse flow velocity v with centrality and thus size of the system. This is expected, since the more central events comprise greater volume of matter, which allows more time for development of the flow. Interestingly, it is in v and not T that we find the slight change of spectral slopes noted in the presentation of the experimental data. [18]

The value of the beak-up (hadronization) speed parameter v_f shown in

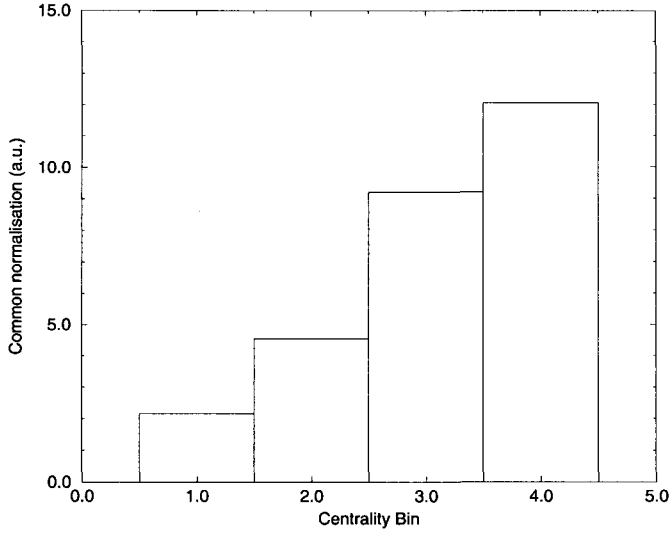

Figure 7. Hadronization volume (arbitrary units) for different centrality bins.

the top portion of figure 6 is near to velocity of light which is consistent with the picture of a sudden breakup of the fireball. This hadronization surface velocity v_f was in the earlier chemical fit set to be equal to v, as there was not enough sensitivity in purely chemical fit to determine the value of v_f.

Unlike the temperature and two velocities, the overall normalization of hadron yields, V^h is found to be strongly centrality dependent, as is seen in figure 7. This confirms in quantitative way the believe that the entire available fireball volume is available for hadron production. The strong increase in the volume by factor six is qualitatively consistent with a geometric interpretation of the collision centrality effect. Not shown is the error propagating from the experimental data which is strongly correlated to the chemical parameters discussed next. This systematic uncertainty is another reason we do not attempt an absolute unit volume normalization.

The four chemical parameters $\lambda_q, \lambda_s, \gamma_q, \gamma_s/\gamma_q$ are shown in the following figures 8, 9. These parameters determine along with V^h the final particle yield. Since we have 5 parameters determining normalization of 6 strange hadron spectra, and as discussed we reduce the statistical weight of Kaons, there is obviously a lot of correlation between these 4 quantities, and thus the

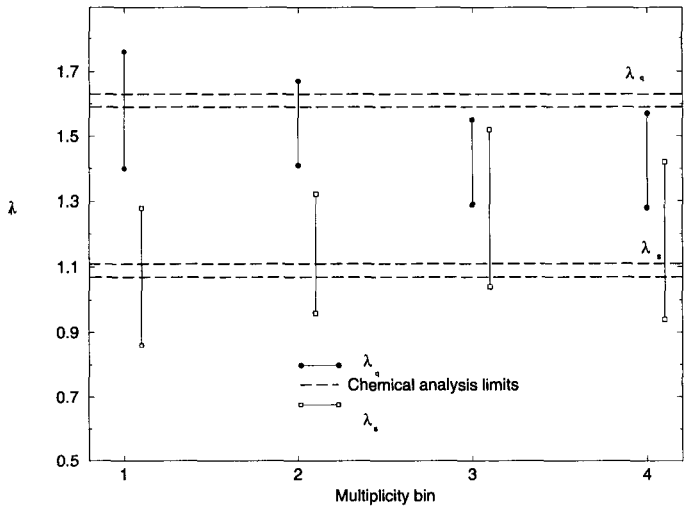

Figure 8. Thermal analysis chemical quark fugacity λ_q (top) and strange quark fugacity λ_s (bottom) for different centrality bins compared to the chemical freeze-out analysis results.

error bar which reflects this correlation, is significant.

The chemical fugacities λ_q and λ_s shown in figure 8 do not exhibit a systematic centrality dependence. This is consistent with the result we found for T in that the freeze-out properties of the fireball are seen to be for the temperature and chemical potential values independent of the size of the fireball. Comparing to the earlier chemical freeze-out result in figure 8 one may argue that there is a systematic downward deviation in λ_q. However, this could be caused by the fact that the chemical freeze-out analysis allowed for isospin-asymmetric $\Xi^-(dss)$ yield, [14] while out present analysis is not yet distinguishing light quarks.

The ratio γ_s/γ_q shown in bottom portion of figure 9 is systematically smaller than unity, consistent with many years of prior analysis: when $\gamma_q = 1$ is tacitly chosen, this ratio is the value of γ_s in analysis of strange baryons. We have not imposed a constrain on the range of γ_q (top of figure 9) and thus values greater than the pion condensation point $\gamma_q^* = e^{m_\pi/2T} \simeq 1.65$ (thick line) can be expected, but in fact do not arise.

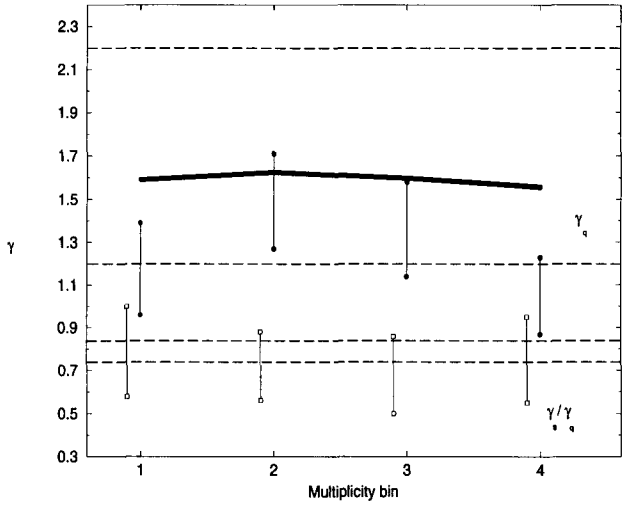

Figure 9. Thermal analysis chemical quark abundance parameter γ_q (top) and γ_s/γ_q (bottom) for different centrality bins compared to the chemical freeze-out analysis. Thick line: upper limit arising with pion condensation.

It is important to explicitly check how well the particle $m_\perp$-spectra are reproduced. We group all bins in one figure and show in figures 10, 11, 12, 13 in sequence Λ, $\overline{\Lambda}$, Ξ, $\overline{\Xi}$. Overall, the description of the shape of the spectra is very satisfactory.

5.3 Omega and Meson spectra

In figure 14 all four centrality bins for the sum $\Omega + \overline{\Omega}$ are shown. We see that we systematically under predict the two lowest $m_\perp$ data points. Some deviation at high $m_\perp$ may be attributable to acceptance uncertainties, also seen in the the Ξ result presented earlier in figure 13. We recall that there is a disagreement between theoritical expectation and the Omega yields. In the here presented thermal analysis, we see that this disagreement is arising at low momentum. We could include all experimental results in the present analysis since the omega data have a relative low statistical evidence and thus other hyperon data determine the behavior of Ω-spectrum.

The low-$m_\perp$ anomaly also explains why the inverse $m_\perp$ slopes for Ω, $\overline{\Omega}$ are smaller than the values seen in all other strange (anti)hyperons. One can presently only speculate about the processes which contribute to this anomaly.

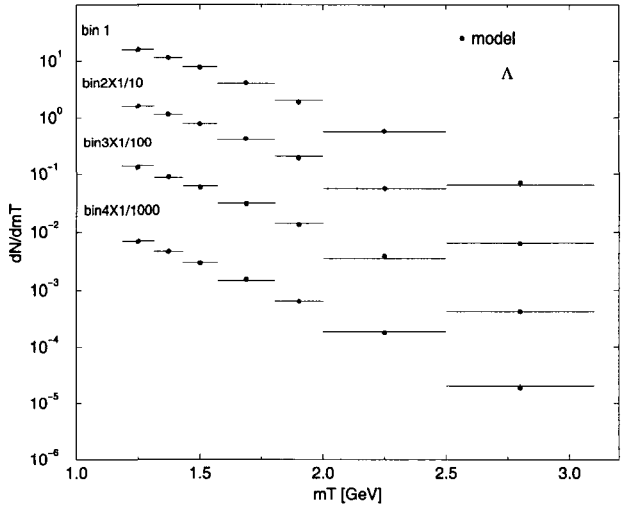

Figure 10. Thermal analysis m_T spectra: Λ

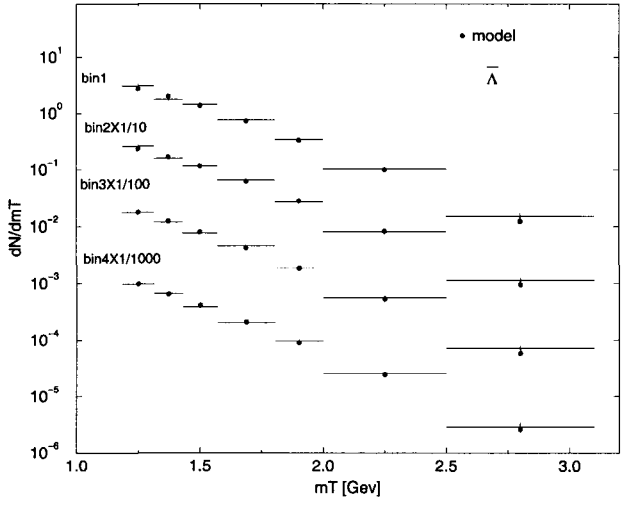

Figure 11. Thermal analysis m_T spectra: $\overline{\Lambda}$.

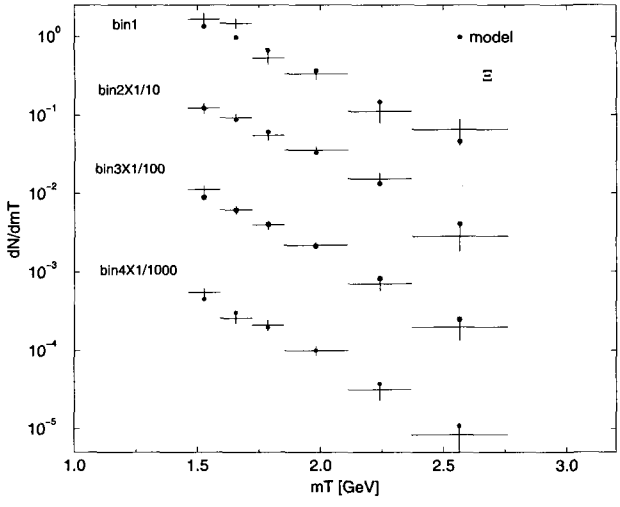

Figure 12. Thermal analysis m_T spectra: Ξ

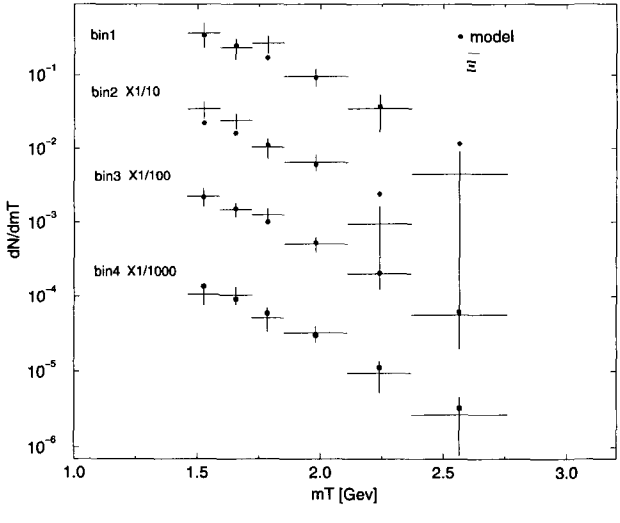

Figure 13. Thermal analysis m_T spectra: $\overline{\Xi}$

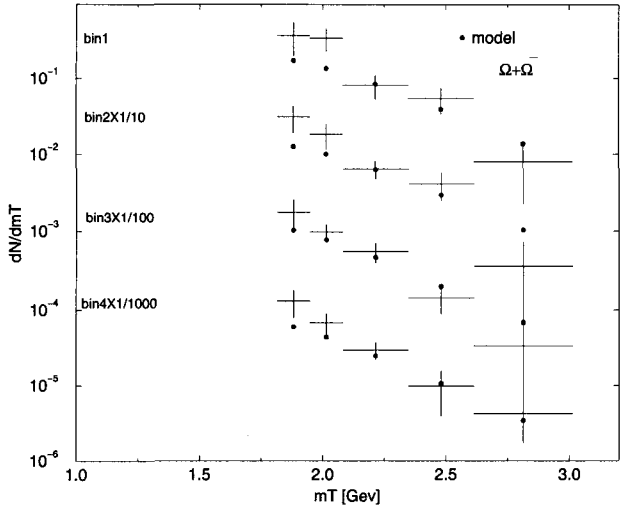

Figure 14. Thermal analysis m_T spectra: $\Omega + \overline{\Omega}$.

We note that the 1–2s.d. deviations in the low $m_\perp$-bins of the $\Omega+\overline{\Omega}$ spectrum translates into 3s.d. deviations from the prediction of the chemical analysis. This is mainly a consequence of the fact that after summing over centrality and $m_\perp$, the statistical error which dominates $\Omega+\overline{\Omega}$ spectra becomes relatively small, and as can be seen the low $m_\perp$ excess practically doubles the yield.

For kaons K^0 the statistical errors are very small, and we find in a more in depth statistical analysis that they must be smaller than the systematic errors not considered. This is done checking the influence of the deletion of individual measurement points in the spectrum on the fit result, which influences the outcome in case of kaons only. We assign in a somewhat arbitrary manner a systematic error that we arbitrarily choose to be 5 times greater than statistical error.

With this modification we included the kaon data in the analysis which included the above presented strange baryon and antibaryon results. Because of the large error we assigned, there is relatively little influence the kaon spectra have on the baryon/antibaryon analysis. In fact the kaon results show how the hyperon/antihyperon experimental results predict K^0_S-$m_\perp$ spectra. We describe the kaon data well, and especially so in the $m_\perp$ range which is the same as that for hyperons considered earlier, as is seen in figure 15.

We now turn to the pion spectra measured by the WA98 collaboration. [36]

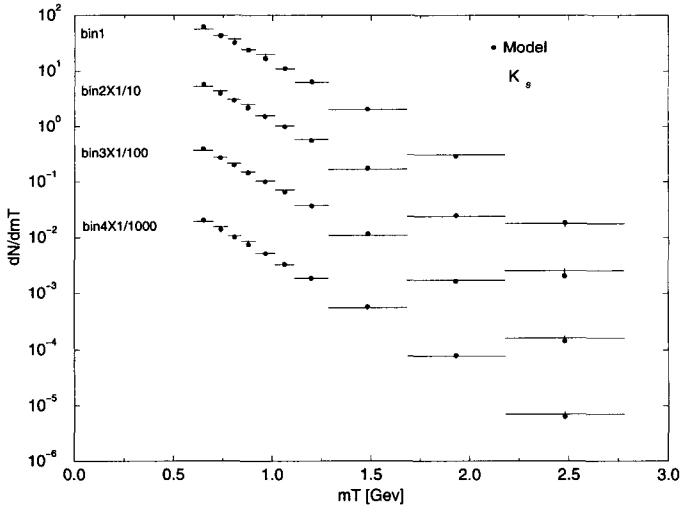

Figure 15. Thermal analysis m_T spectra: K_s.

This is a very difficult matter, since at low momenta there are many mechanisms of pion production which we have not analyzed. Moreover, we have not fully understood how the longitudinal flow influences through the secondary decays the observed pion spectra. Compared to strange hadrons we study the π^0 data in a very wide range of $m_\perp$ in which the yield changes by 6 orders of magnitude.

We use a set of parameters obtained fro the hyperon data, *i.e.*, $T_f = 143\,\mathrm{MeV}$, setting also freeze-out surface velocity $0.99c$. We include in the results shown in figure 16 aside of directly produced pions the two body decay of the ρ. We allow a direct hard parton QCD component contribution, [38] of the form

$$Ed^3N/d^3p \propto 1/p_\perp^\kappa\,.$$

Thus, we vary four parameters: two normalizations (thermal and QCD direct component), and also $\kappa = 5.6 \pm 1.2$, $v_c = 0.55 \pm 0.02$, with resulting best fits as stated. This procedure yields a good description of the data as seen in figure 16, with $\chi^2/\mathrm{dof} < 1.4$. Considering that only statistical error is being considered, and we were not evaluating contributions of 3-body decay resonances, we see this as a noteworthy confirmation that the hard pions are also created primarily in the sudden hadronization process. We note that the

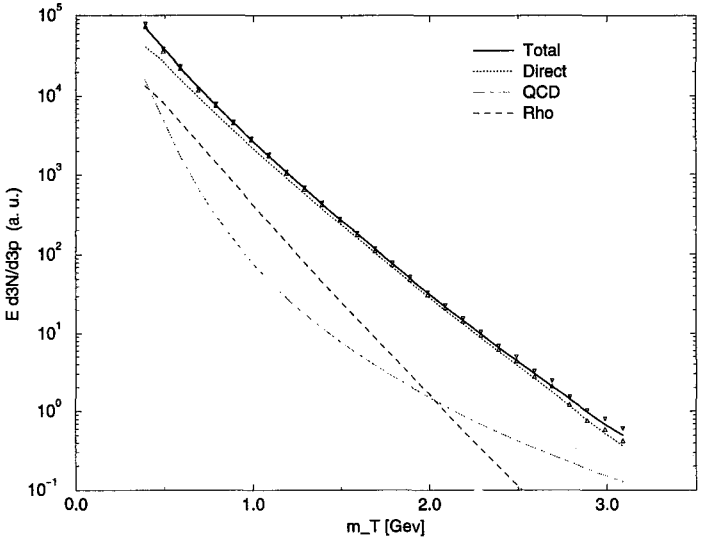

Figure 16. Central rapidity data of experiment WA98 for π^0 are compared to the spectra expected in a sudden freeze-out reaction picture. See text for details.

direct QCD component is at 1–20% level, and thus before proceeding further a more precise model of this contribution needs to be developed.

Our analysis is not contradicting results shown in [36], for these authors did not consider that the freeze-out surface velocity is different from the flow velocity, and they did not allow for direct parton-parton scattering contributions in their analysis of pion spectra.

Our results confirm the finding that the apparent temperature hierarchy for different mass particles is due to a collective expansion of the source. [37]

6 Strangeness at RHIC

6.1 Expectations

The abundances of particles produced from QGP within the sudden freeze-out model are controlled by several parameters we restate here: the light quark fugacity $1 < \lambda_q < 1.1$, value is limited by the expected small ratio between baryons and mesons (baryon-poor plasma) when the energy per baryon is above 100 GeV, strangeness fugacity $\lambda_s \simeq 1$ which value for locally neutral plasma assures that $\langle s - \bar{s} \rangle = 0$; the light quark phase space occupancy $\gamma_q \simeq$

Table 2. For $\gamma_s = 1.25$, $\lambda_s = 1$ and γ_q, λ_q as shown: Top portion: strangeness per baryon s/B, energy per baryon E/B[GeV] and entropy per baryon S/B. Bottom portion: sample of hadron ratios expected at RHIC.

γ_q	1.25	1.5	1.5	1.5	1.60
λ_q	1.03	1.025	1.03	1.035	1.03
E/B[GeV]	117	133	111	95	110
s/B	18	16	13	12	12
S/B	630	698	583	501	571
$p/\bar{p}$	1.19	1.15	1.19	1.22	1.19
Λ/p	1.74	1.47	1.47	1.45	1.35
$\bar{\Lambda}/\bar{p}$	1.85	1.54	1.55	1.55	1.44
$\bar{\Lambda}/\Lambda$	0.89	0.91	0.89	0.87	0.89
Ξ^-/Λ	0.19	0.16	0.16	0.16	0.15
$\overline{\Xi^-}/\bar{\Lambda}$	0.20	0.17	0.17	0.17	0.16
$\overline{\Xi}/\Xi$	0.94	0.95	0.94	0.93	0.94
Ω/Ξ^-	0.147	0.123	0.122	0.122	0.115
$\overline{\Omega}/\overline{\Xi^-}$	0.156	0.130	0.130	0.131	0.122
$\overline{\Omega}/\Omega$	1	1.	1.	1.	1.
$\frac{\Omega+\overline{\Omega}}{\Xi^-+\overline{\Xi^-}}$	0.15	0.13	0.13	0.13	0.12
$\frac{\Xi^-+\overline{\Xi^-}}{\Lambda+\bar{\Lambda}}$	0.19	0.16	0.16	0.16	0.15
K^+/K^-	1.05	1.04	1.05	1.06	1.05

1.5, overabundance value due to gluon fragmentation. Given these narrow ranges of chemical parameters and the sudden freeze-out temperature $T_f = 150$ MeV expected for nearly baryon free domain, we compute the particle production at break-up.

Taking $\gamma_q = 1.5^{+0.10}_{-0.25}$, we choose the value of λ_q, see the header of table 2, for which the energy per baryon (E/B) is similar to the collision condition (100 GeV), which leads to the range $\lambda_q = 1.03 \pm 0.005$. We evaluate for these examples aside of E/B, the strangeness per baryon s/B and entropy per baryon S/B as shown in the top section of the table 2. We do not enforce $\langle s - \bar{s} \rangle = 0$ at central rapidity exactly, but since baryon asymmetry is small, strangeness is balanced to better than 2% in the parameter range considered. In the bottom portion of table 2, we present the compatible particle abundance ratios, computed according to the procedure we developed, and described above. [14] We have given, aside of the baryon and antibaryon relative yields, also the relative kaon yield, which is also well determined within this approach.

The meaning of these results can be better appreciated when we assume in an example the central rapidity density of direct protons is $dp/dy|_{\text{cent.}} = 25$.

Table 3. $dN/dy|_{\rm cent.}$ assuming in this example $dp/dy|_{\rm cent.} = 25$.

γ_q	λ_q	b	p	$\bar{p}$	$\Lambda{+}\Sigma^0$	$\overline{\Lambda}{+}\overline{\Sigma}^0$	$\Sigma^{\pm}$	$\overline{\Sigma}^{\mp}$	Ξ^0	$\overline{\Xi}^0$	$\Omega{=}\overline{\Omega}$
1.25	1.03	17	25*	21	44	39	31	27	17	16	1.2
1.5	1.025	13	25*	22	36	33	26	23	13	11	0.7
1.5	1.03	16	25*	21	37	33	26	23	12	11	0.7
1.5	1.035	18	25*	21	36	32	26	22	11	10	0.7
1.60	1.03	15	25*	21	34	30	24	21	10	9.6	0.6

In table 3, we present the resulting (anti)baryon abundances. The net baryon density $db/dy \simeq 16 \pm 3$, there is baryon number transparency. We see that (anti)hyperons are indeed more abundant than non-strange (anti)baryons. Taking into account the disintegration of strange baryons, we are finding a much greater number of observed protons $dp/dy|^{\rm obs.}_{\rm cent.} \simeq 65 \pm 5$ in the central rapidity region. It is important when quoting results from table 3 to recall that:

1) we have chosen arbitrarily the overall normalization in table 3, only particle ratios were computed, and

2) the rapidity baryon density relation to rapidity proton density is a consequence of the assumed value of λ_q, which we chose to get $E/B \simeq 100\,\mathrm{GeV}$ per participant.

6.2 Comparison of theory and experiment

Our study of RHIC results has just begun and we expect that it remains an ongoing project as we enter the period of RHIC data collection and analysis. Some of our predictions can already be compared with experiment (STAR at RHIC). These results are in agreement with our model of how QGP evolves at RHIC.

In order to compare with experiment, we need to adjust from the assumed 100+100A GeV RHIC energy to the RHIC run energy in 2000 which is 65+65A GeV. We consider the $\overline{\Lambda}/\Lambda$ ratio. At 8.6+8.6A GeV (corresponding to 160A GeV the experimental result is $\overline{\Lambda}/\Lambda \simeq 0.12$ while at 100+100A GeV we predict $\overline{\Lambda}/\Lambda = 0.89 \pm 0.02$ in table 2. We also made a prediction for 35+35A GeV [21], where we found $\overline{\Lambda}/\Lambda \simeq 0.5$. The interpolated result for the 65+65A GeV RHIC run is $\overline{\Lambda}/\Lambda \simeq 0.68 \pm 0.05$, which is nearly exactly the October 2000 APS-meeting STAR ratio $\overline{\Lambda}/\Lambda = 0.7 \pm 0.05 \pm 0.2$. From our

$\overline{\Lambda}/\Lambda$ ratio one obtains

$$\frac{\bar{p}}{p} = \frac{\lambda_s^2}{\lambda_q^2}\frac{\overline{\Lambda}}{\Lambda},$$

and this implies taking note of the heading and caption in table 2 that the $\bar{p}/p$ ratio is about 7% smaller compared to $\overline{\Lambda}/\Lambda$ ratio. In fact STAR reported $\bar{p}/p = 0.65 \pm 0.05$, in agreement with our result.

Both particle ratios can thus be well described within our understanding of the hadronization and properties of QGP at RHIC. In their absolute values reflect on the expected small baryon content at the initial RHIC energy. Both should increase by 25–30% at the top RHIC energy (100+100 AGeV).

The most interesting result seen in table 3, which confirmation we anticipate and await with anxiety is the hyperon-dominance of the baryon yields at RHIC, a fact which as we believe does not depend on a detailed model hypothesis. Another interesting property of the hadronizing hot RHIC matter, as seen in table 2, is that strangeness yield per participant is expected to be 13–23 times greater than seen at present in Pb–Pb interactions at SPS energies, where we have 0.75 strange quark pairs per baryon.

7 Summary and conclusions

The enhanced strangeness yield observed at 158–200A GeV reactions corresponds according to our study to $\mathcal{O}(0.75)$ $s\bar{s}$-pairs of quarks per participant baryon, see section 3. Considering the properties of QGP-liquid explored in section 2 and the resulting initial gluon temperatures we have shown that this exceptionally high yield is achievable in a short time that the collision is known to last by in-plasma gluon-fusion reactions, $G + G \rightarrow s + \bar{s}$, as was proposed many years ago. [9]

Beyond strangeness enhancement, multi strange baryons and antibaryons have been recognized as being even a more specific source of information about the deconfined state of the matter. The analysis of experimental results from 158AGeV Pb–Pb interactions carried out in sections 3 (chemical abundance analysis) and in section 5 (spectral $m_\perp$ shape) confirms this. We find that strange baryons and antibaryons are dominantly produced in sudden hadronization of the quark-gluon fireball with chemical and thermal decoupling occurring at the same time.

From the appearance of first results we recognized that sudden hadronization is required. [30] However, initially the mechanisms leading to direct hadronization (hadron production from QGP fireball without equal rescattering), have not been theoretically understood. Here, we have presented

in section 4 a complete reaction picture consistent with QGP equations of state. [16] The sudden breakup (direct hadronization) into final state particles occurs as the QGP fireball super-cools, and in this state encounters a mechanical instability, which drives the explosive disintegration. Deep supercooling requires a first order phase transition, and this in turn implies presence of a latent heat and we have estimated its magnitude in section 4.

There are several experimental facts that lead us to consider sudden QGP hadronization. The most recent point has been the results presented in section 5 which show agreement between thermal and chemical freeze-out analysis. An important experimental input is the identity of the $m_\perp$ spectra for strange baryons and antibaryons. We have been motivated initially to pursue sudden QGP hadronization by the need to use chemical nonequilibrium to describe hadron production. At first we have proposed this for the case of strange quarks, and more recently as the experimental data became more comprehensive, we also recognized the need to consider light quark chemical nonequilibrium — we described details of these developments elsewhere. [14]

The light quark pair excess is a convenient way to understand hadron multiplicity excess, which we have related to an entropy excess. [39] But is this the only good way to understand the experimental hadron production data? It is hard to check all possibilities. However, we explored (in medium) changes of hadron masses. We have found that invariably the statistical significance of the analysis decreases as we modify individual hadron properties, as long as we have been assuming chemical equilibrium of hadron abundances, and a consistent change of both mesons and baryons properties. Our extensive trial and error searches have convinced us that the only theoretical description of hadron production data that works ($\chi^2/\mathrm{dof} < 1$) requires excess of valence light quark pair abundance, irrespective of the detailed strategy of data analysis.

So how it can be that there are many people who believe that one can describe hadron production data assuming chemical equilibrium of light quarks. In fact, if we take hadronization to somehow occur in chemical equilibrium, or/and ignore the possibility of plasma formation, we find $\chi^2/\mathrm{dof} > 2.5$, $\mathrm{dof} = 10$ in our analysis, which agrees when carried out with this assumption with results of others. [40] Even though this χ^2 is without convincing physical significance, what has caused that this result has not been forgotten is that the chemical freeze-out temperature for equilibrium condition comes out to be near to the expected equilibrium phase transition condition, $T \simeq 170\,\mathrm{MeV}$, see section 2. Thus the assumption of equilibrium seems to be consistent with the properties of QGP phase. Furthermore, the study of soft pions suggests (unlike it is with hard pions or other hadrons) that the

thermal freeze-out occurs at about 120 MeV. Naturally, soft pions can be produced by more complex collective processes not considered in the conventional thermal analysis and we thus did not introduce these particles into our study, preferring to depend on the numerous other results in section 5.

Further study of details of chemical freeze-out, involving consideration of strong resonances may lead to a direct experimental differentiation of these two alternatives. We are presently considering $\Sigma^*(1385)$, [41] which if freeze-out occurs at $T = 170\,\mathrm{MeV}$ would be the dominant source of Λ considering the decay $\Sigma^*(1385) \to \Lambda + \pi$ (88%). But we are already today quite certain about the correctness of the sudden hadronization picture since:

1. the experimental strange and non-strange, hadron abundance results statistically strongly favor chemical nonequilibrium in hadronization;
2. baryons and antibaryons have the same $m_\perp$ spectra; and
3. our recent finding from the analysis of $m_\perp$ spectra described in section 5 that the thermal freeze-out temperature is the same as the chemical non-equilibrium freeze-out condition.

Our enhanced understanding of the fireball supercooling and resulting sudden breakup, as well as our study of thermal freeze-out properties has in the past year considerably strengthened our case. Not only we can now argue that the point of instability agrees with the thermal and chemical freeze-out, but also we have considered the freeze-out surface dynamics and have shown that the break-up velocity v_f is nearly velocity of light, as would be expected in a sudden breakup of a QGP fireball.

What are the possible causes of the chemical non-equilibrium? Certainly even if the breakup of the QGP-fireball is sudden we could have abundance equilibrium. In fact, the microscopic processes governing the fireball breakup determine how the physical and statistical properties of the fireball change at the breakup point. In particular as gluons convert into quark pairs and hadrons, the gluon abundance parameter $\gamma_g \to 0$ and the quark chemical occupancy parameters have to increase significantly, as we determine in data analysis. On the other hand the energy E and baryon content b of the fireball are conserved. Entropy S is conserved when the gluon content of a QGP fireball is transformed into quark pairs in the entropy conserving process $G + G \to q + \bar{q}$. Similarly, when quarks and antiquarks recombine into hadrons, entropy is conserved in the range of parameters of interest here. Thus also E/B and S/B is conserved across hadronization condition. The sudden hadronization process also maintains the temperature T and baryo-chemical potential μ_b across the phase boundary.

We have described strange hadron $m_\perp$-spectra with astounding precision in all available centrality bins. The remarkable similarity of $m_\perp$ spectra reported by the WA97 experiment is interpreted by a set of freeze out parameters, and we see that production mechanism of Λ, $\overline{\Lambda}$, and Ξ, $\overline{\Xi}$ is the same. This symmetry, including matter–antimatter production is an important cornerstone of the claim that the strange antibaryon data can only be interpreted in terms of direct particle emission from a deconfined phase. In presence of conventional hadron collision based physics, the production mechanism of antibaryons is quite different from that of baryons and a similarity of the $m_\perp$ spectra is not expected. Moreover, even if QGP is formed, but a equal phase of confined particles is present, the annihilation of antibaryons in the baryon rich medium created at CERN-SPS energy would deplete more strongly antibaryon yields, in particular so at small momenta, with the more abundant baryons remaining less influenced. This effect is not observed. [18]

Similarity of $m_\perp$-spectra does not at all imply, and one should not expect a similarity of particle rapidity spectra. As hyperon are formed at the fireball breakup, any remaining longitudinal flow present among fireball constituents will be imposed on the product particle, thus Λ-spectra containing potentially two original valence quarks are stretched in y, which $\overline{\Lambda}$-y-spectra are not, as they are made from newly formed particles. All told, one would expect that anti-hyperons can appear with a thermal rapidity distribution, but hyperons will not. But both have the same thermal-explosive collective flow controlled shape of $m_\perp$-spectra.

The only systematic disagreement we see is that the $\Omega + \overline{\Omega}$ results have a noticeable systematic low $p_\perp$ enhancement anomaly visible in two lowest $m_\perp$ bins in all centrality bins. This result shows that it is not a different temperature of freeze-out of $\Omega + \overline{\Omega}$ that leads to more enhanced yield, but a soft momentum secondary source which contributes almost equal number of soft $\Omega + \overline{\Omega}$ compared to the yield expected in view of the behavior of other strange hadrons.

We have presented here a short overview of our recent work developing further strangeness as a signature of the formation of quark-gluon plasma, and as a diagnostic tool allowing the study of its properties. The understanding of the properties of the QGP formed in CERN-SPS experiment has greatly improved in past 18 months.

Acknowledgments

Work supported in part by a grant from the U.S. Department of Energy, DE-FG03-95ER40937.

Laboratoire de Physique Théorique et Hautes Energies, LPTHE, at University Paris 6 and 7 is supported by CNRS as Unité Mixte de Recherche, UMR7589.

References

1. N. Itoh, *Prog. Theor. Phys.* **44**, 291 (1970).
2. P. Carruthers, *Collectuve Phenomena* **1**, 147 (1973).
3. F. Iachello, W.D. Langer and W.D. Lande, *Nucl. Phys.* A **219**, 612 (1974).
4. J.C. Collins and M.J. Perry, *Phys. Rev. Lett.* **34**, 1353 (1975).
5. R. Hagedorn, in Quark Matter'84, p53, K. Kajantie, ed., Springer Lecture Notes in Physics, Vol. 221 (Springer, Berlin, 1985).
6. F. Karsch, E. Laermann and A. Peikert, *Phys. Lett.* B **478**, 447 (2000).
7. J. Rafelski, "Extreme States of Nuclear Matter", p. 282 in *Future Relativistic Heavy Ion Experiments*, R. Bock and R. Stock, Eds., GSI Report 1981-6;
   J. Rafelski, and R. Hagedorn, "From Hadron Gas to Quark Matter II", p. 253 in *Statistical Mechanics of Quarks and Hadrons*, H. Satz, ed.; (North Holland, Amsterdam, 1981);
   J. Rafelski, "Hot Hadronic Matter", p. 619 in *New Flavor and Hadron Spectroscopy*, J. Tran Thanh Van, Ed., Ed. Frontières (Paris 1981);
   J. Rafelski, "Extreme states of nuclear matter". *Nucl. Physics* A **374**, 489c (1982).
8. J. Rafelski and B. Müller, *Phys. Rev. Lett* **48**, 1066 (1982); **56**, 2334E (1986);
   P. Koch, B. Müller and J. Rafelski, *Z. Phys.* A **324**, 453 (1986).
9. J. Rafelski, *Phys. Rep.* **88**, 331 (1982).
10. J. Rafelski and M. Danos, *Perspectives in High Energy Nuclear Collisions*, NBS-IR 83-2725 Monograph, U.S. Department of Commerce, National Bureau of Standards, June 1983;
    Updated version appeared in *Nuclear Matter under Extreme Conditions*, D. Heiss, Ed., Springer Lecture Notes in Physics **231**, pp. 362-455 (1985).
11. P. Koch and J. Rafelski, *Nucl. Phys.* A **444**, 678 (1985).
12. P. Koch, B. Müller and J. Rafelski, *Phys. Rep.* **142**, 167 (1986).
13. F. Antinori *et al.*, WA97 Collaboration *Nucl. Phys.* A **663**, 717 (2000);
    E. Andersen *et al.*, WA97 collaboration, *Phys. Lett.* B **433**, 209 (1998);
    E. Andersen *et al.*, WA97 collaboration, *Phys. Lett.* B **449**, 401 (1999).
14. J. Letessier and J. Rafelski, *Int. J. Mod. Phys.* E **9**, 107, (2000), and references therein.
15. S. Hamieh, J. Letessier, and J. Rafelski, *Phys. Rev.* C **62**, 064901 (2000).

16. J. Rafelski and J. Letessier, *Phys. Rev. Lett.* **85**, 4695 (2000).
17. G. Torrieri and J. Rafelski, submitted to New J. Phys., E-print hep-ph/0012102
18. F. Antinori *et al.*, WA97 Collaboration *Eur. Phys. J.* C **14**, 633, (2000), and private communication.
19. J. Rafelski and M. Danos, *Phys. Lett.* B, **192**, 432 (1987).
20. J. Rafelski and J. Letessier, *Phys. Lett.* B **469**, 12 (1999).
21. S. Bass *et al.*, *Nucl. Phys.* A **661**, 260 (2000).
22. J. Rafelski, J. Letessier and A. Tounsi, *Acta Phys. Pol.* B **27**, 1035 (1996).
23. A. Peshier, B. Kämpfer and G. Soff, *Phys. Rev.* C **61**, 45203, (2000).
24. H. Vija and M.H. Thoma, *Phys. Lett.* B **342**, 212, (1995).
25. S.A. Chin, *Phys. Lett.* B, **78**, 552, (1978).
26. J. Letessier, A. Tounsi and J. Rafelski, *Phys. Rev.* C **50**, 406 (1994); J. Rafelski, J. Letessier and A. Tounsi, *Acta Phys. Pol.* A **85**, 699 (1994).
27. R. Hagedorn and J. Rafelski *Phys. Lett.* B **97**, 136 (1980).
28. T. Csörgő, and L.P. Csernai, *Phys. Lett.* B **333**, 494 (1994).
29. H. Appelshäuser *et al.*, NA49, *Phys. Rev. Lett.* **82**, 2471 (1999).
30. J. Rafelski, *Phys. Lett.* B **262**, 333 (1991); J. Letessier and J. Rafelski, *Acta Phys. Pol.* B **30**, 153 (1999).
31. L.P. Csernai, I.N. Mishustin, *Phys. Rev. Lett.* **74**, 5005, (1995).
32. T.S. Biró, P. Lévai, J. Zimányi, *Phys. Rev.* C **59**, 1574 (1999).
33. I.N. Mishustin, *Phys. Rev. Lett.* **82**, 4779 (1999).
34. L.D. Landau and E.M. Lifschitz, "Fluid Mechanics", (Oxford 1999); S. Weinberg, "Gravitation and Cosmology", (New York, 1972).
35. S. Kabana *et al.*, NA52 collaboration, *Nucl. Phys.* A **661**, 370c (1999); S. Kabana *et al.*, NA52 collaboration, *J. Phys.* G *Nucl. Part. Phys.* **25**, 217 (1999).
36. M. Aggarwal *et al.*, WA98 Collaboration *Phys. Rev. Lett.* **83**, 926 (1999); we thank T. Petizmann for making available the data as published.
37. I.G. Bearden *et al.*, NA44 Collaboration *Phys. Rev. Lett.* 78, 2080 (1997).
38. R.D. Fields and R.P. Feynman, *Phys. Rev.* D **15**, 2590 (1977); and R.P. Feynman, R.D. Fields and G.C. Fox, *Phys. Rev.* D **18**, 3320 (1978).
39. J. Letessier, *et al.*, *Phys. Rev. Lett.* **70**, 3530 (1993); *Phys. Rev.* D **51**, 3408 (1995).
40. P. Braun-Munzinger, I. Heppe and J. Stachel, *Phys. Lett.* B **465**, 15 (1999).
41. G. Torrieri and J. Rafelski, Σ^* *as signature of freeze-out dynamics*, E-print hep-ph/01

Screening Effects in the Q^2 Logarithmic Slope of F_2

E. Ferreira [*a] **and U. Maor**[†b]

[a] *Instituto de Fisica, Universidade Federal do Rio de Janeiro, Rio de Janeiro RJ21945-970, BRASIL*

[b] *HEP Department, School of Physics and Astronomy, Raymond and Beverly Sackler Faculty of Exact Science, Tel-Aviv University, Ramat Aviv, 69978, ISRAEL*

Abstract

Results are presented of a detailed study of $\partial F_2/\partial \ln Q^2$, which has the purpose of improving our knowledge of characteristic features of the evolution equations for the proton structure functions. In particular, the effects of screening corrections on the logarithmic derivative have been investigated. All HERA experimental measurements are analysed and compared with the predictions of several schemes, including a Regge type model. It is shown that several approaches that have very different basic construction are not discriminated by the data. Consequently signals of gluon saturation cannot be considered as conclusive.

1 Introduction

This presentation is based on a recent study [1] done in collaboration with E. Gotsman, E. Levin and E. Naftali.

The physics of small Q^2 and small x is associated with the search for the scale where gluon saturation [2], implied by s-channel unitarity [3], sets in. Gluon saturation signals the transition from the perturbative (hard) to the non perturbative (soft) QCD regime. We expect this transition to be preceded by signatures of screening corrections (SC) ewhich should be experimentally visible even though the relevant scattering amplitude has not yet reached the unitarity (black disk) limit. Although, the general theoretical framework for saturation is reasonably well understood [2][3], the specific kinematic domain where we expect to see evidence of the role it plays, is as yet not determined. Consequently, this QCD feature depends on the relevant DIS experimental data and the associated phenomenology. While the global analysis of the proton structure function F_2 (or $\sigma_{tot}^{\gamma^* p}(W, Q^2)$) data shows no significant deviations from DGLAP [4], there are dedicated HERA measurements of the Q^2 logarithmic derivative of the

*E-mail: erasmo@if.ufrj.br

†E-mail: maor@post.tau.ac.il

proton structure function F_2 [5][6][7], which add to our knowledge as they provide detailed information on the rate of change of the logarithmic Q^2 dependence of F_2, and, hence, they magnify possible deviations from the expected DGLAP behaviour at small x and small Q^2.

The interest in $\partial F_2/\partial \ln Q^2$ stems from the obsevation that in leading order DGLAP the Q^2 logarithmic slope of F_2 at low x, is directly proportional to the gluon structure function [8]

$$\frac{\partial F_2(x,Q^2)}{\partial \ln Q^2} = \frac{2\alpha_S}{9\pi} x G^{DGLAP}(x,Q^2), \tag{1}$$

where $xG^{DGLAP}(x,Q^2)$ denotes the DGLAP gluon distribution of the proton. $\partial F_2/\partial \ln Q^2$ is also related to the dipole cross section [9] by

$$\frac{\partial F_2(x,Q^2)}{\partial \ln Q^2} = \frac{Q^2}{3\pi^3}\sigma_{dipole}(r_\perp^2,x) = \frac{Q^2}{3\pi^2}\int db_t^2 Im a_{el}(r_\perp^2,x), \tag{2}$$

where $a_{el}(r_\perp^2,x)$ is the elastic scattering amplitude at fixed impact parameter b_t of a dipole of size $r_\perp^2 = 4/Q^2$ with energy x. The elastic amplitude is bounded by the unitarity constraint $a_{el}(r_\perp^2,x) \leq 1$.

In the following we present a detailed study of $\partial F_2/\partial \ln Q^2$. Our goal is to utilize this quantity, which is relatively well measured, to examine whether the system of partons within the proton target has reached the QCD regime of gluon saturation. The complexity and difficulty of this investigation is illustrated by Fig. 1 which shows two different limits of $\partial F_2/\partial \ln Q^2$: (i) the DGLAP limit at low x for different parton distribution functions (pdf) [10][11][12] satisfying the evolution equations; and (ii) The unitarity limit, implied by gluon saturation, which is attained at very long distances (low Q^2). From Fig. 1 we can see that both DGLAP and the unitarity bound have the same qualitative behaviour decreasing at low Q^2. The saturation scale ($Q_s^2(x)$) at which the DGLAP solution crosses the unitarity bound is very low. Such a low value for the saturation scale indicates that we shall have difficulty attempting to distinguish between models with gluon saturation effects, and models that include soft and hard interactions, since the matching of the components occurs at similar values of Q^2.

Our study incorporates the conclusions obtained in recent measurements of F_2 [13], extending to very low Q^2 which find that it has a monotonic behaviour extending to the photo production limit. These data suggest a smooth transition from the perturbative (DGLAP, high Q^2) to the non perturbative (Regge or classical gluon field, exceedingly small Q^2) regime. Preliminary HERA data [6][7] on $\partial F_2/\partial \ln Q^2$ at small Q^2 and small x do not show any turnover when plotted at fixed x or fixed Q^2. In general, an approach which provides a way of successfully describing $\partial F_2/\partial \ln Q^2$ should also be able to reproduce data in other channels which are sensitive to $xG(x,Q^2)$ such as F_2^c, F_L and the photo and DIS production of heavy vector mesons.

In our work we investigate the ability of conventional DGLAP, using the pdfs [10] [11] [12], to reproduce the available data on $\partial F_2/\partial \ln Q^2$. We also investigate the role of the screening corrections (SC). In this approach [14][15][16], DGLAP is modified by SC due to the $q\bar{q}$ percolation through the target, as well as by modifications due to screening in the gluon distribution $xG(x,Q^2)$.

Within the framework of pQCD no allowance is made for explicit soft contributions, both in the non-screened and screened formulations of DGLAP. The later provides a smooth interpolation between the high and low Q^2 regimes. In the present investigation we have checked the validity of our methods at low values of Q^2, i.e. just above the DGLAP Q_0^2 threshold (defined for each pdf input). For the case with SC, we have also considered an extrapolation for $Q^2 \leq Q_0^2$. Our aim is to determine the values of Q^2 that one can successfully describe without the help a soft component. To this end we compare with the Donnachie and Landshoff (DL) two Pomeron model [17], which explicitly uses the sum of a hard and a soft Pomeron.

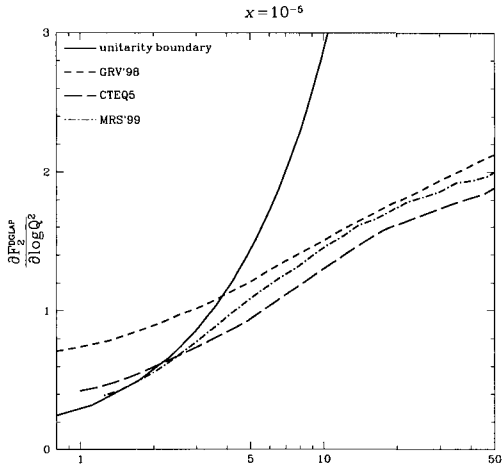

Figure 1: *The Q^2 behaviour of $\partial F_2/\partial \ln Q^2$ at $x = 10^{-5}$ (Q^2 is in* GeV^2*)* .

We conclude with a critical discussion and caution remarks regarding attempts that have been made to determine the gluon saturation scale using data with highly correlated variables such as in the Caldwell and fixed W plots [5][7][18]. We also comment on the general problems associated with gluon saturation and screening corrections relating to other models which include SC [18][19][21].

2 $\partial \mathbf{F_2}/\partial \ln \mathbf{Q^2}$ behaviour at small $\mathbf{Q^2}$ and small x

As is well known, a global DGLAP analysis of the data with the recent pdfs [10][11][12] is in good agreement with the experimental data. A study [22] comparing the screened and non screened DGLAP calculations of $F_2(x, Q^2)$ showed only a small difference due to SC even in the small Q^2 and x region attained by present HERA measurements. A significant deviation of the data from Eq. (1), where xG^{DGLAP} is obtained from the global F_2 analysis, may serve as an experimental signature indicating the growing importance of unitarity corrections. This was recently suggested by Caldwell [5], showing a rather complicated plot of $\partial F_2/\partial \ln Q^2$ in which each measured point had different correlated values of Q^2 and x. The Caldwell plot suggested a dramatic turnover of $\partial F_2/\partial \ln Q^2$ corresponding to Q^2 of about 3 GeV^2 and $x < 5 \cdot 10^{-3}$, in contrast to the behavior expected from GRV94 [23] at sufficiently small Q^2 and x. The problem with this presentation is that, as suggestive as it may seem, it does not discriminate between different dynamical interpretations [14][15][17][18][19] [21]. It is actually compatible with an overall data generator [24] as well as the latest pdfs which were adjusted to account for this observation.

Better discrimination is achieved if we carefully study the small Q^2 and x dependences of $\partial F_2/\partial \ln Q^2$ at either fixed Q^2 or fixed x values, so as to be free of the kinematic correlation between Q^2 and x that is endemic in the data displayed in the Caldwell plot. Such preliminary HERA data have recently became available [6][7]. Note that the method that has been used to

specify the logarithmic derivative of the structure function F_2 in [6][7] is by fitting the F_2 data at fixed x, to the expression

$$F_2(x,Q^2) = a(x) + b(x)\ln Q^2 + c(x)[\ln Q^2]^2 \tag{3}$$

and then make the identification

$$\frac{\partial F_2}{\partial \ln Q^2} = b(x) + 2c(x)\ln Q^2 \ . \tag{4}$$

H1 [6] compared the results using Eq. (4) with the results obtained by taking the analytic derivative of their QCD parameterization (H1 QCD fit). They find that for $x \geq 0.0002$, the L.H. and R.H. sides of Eq. (4) match very well, however, for $x < 2\times 10^{-4}$ there is a discrepancy. We note that the experimental data of [6][7] are correlated, such that the lower values of x are associated with the lower values of Q^2.

At the initial stage of our investigation we examined whether DGLAP (using the pfds [10][11][12] in the NLO approximation) reproduce the data. The results are shown in Fig. 2. We note that: (i) GRV98 overestimates the low $Q^2 \leq 5$ GeV^2 data. For higher Q^2, the reproduction of the data is good; (ii) MRS99 underestimates the data at $Q^2 = 1.9$ and 40 GeV^2. It is above the data in the $3 \leq Q^2 \leq 10$ GeV^2 range and does well for $Q^2 = 12$ and 30 GeV^2; (iii) CTEQ5 (we have used CTEQ5HQ as it reproduces the energy dependence of J/ψ photo production [25]) provides a good reproduction of the experimental data over the entire range $1.9 \leq Q^2 \leq 40$ GeV^2. A few words of explanation are called for regarding the numerical NLO calculation of F_2 from the CTEQ pdf (we discuss only CTEQ in this context since both GRV98 and MRS99 supply a code for calculating the structure function, from which the parton densities have been parameterized). When calculating F_2 in NLO one should take care when inserting the threshold for charm production, so that F_2 remains a smooth function of Q^2. The effect of the threshold is small if one looks at the structure function, but it can be rather large when examining it's Q^2 derivative. We found that by following the consistent treatment of charm in [26], we obtain a smooth behaviour of both F_2 and $\partial F_2/\partial \ln Q^2$.

In order to study the role of SC in our calculations, we follow the eikonal SC formalism presented in Ref.[15][1], where screening is calculated in DLA in both the quark sector, to account for the percolation of a $q\bar{q}$ through the target, and the gluon sector, to account for the screening of $xG(x,Q^2)$. The factorizable result that we obtain is

$$\frac{\partial F_2^{SC}(x,Q^2)}{\partial \ln Q^2} \ = \ D_q(x,Q^2)D_g(x,Q^2)\frac{\partial F_2^{DGLAP}(x,Q^2)}{\partial \ln Q^2}. \tag{5}$$

In the quark sector SC are given by

$$D_q(x,Q^2)\frac{\partial F_2^{DGLAP}(x,Q^2)}{\partial \ln Q^2} \ = \ \frac{Q^2}{3\pi^2}\int db^2 \left(1 \ - \ e^{-\kappa_q(x,Q^2;b^2)}\right), \tag{6}$$

$$\kappa_q \ = \ \frac{2\pi\alpha_S}{3Q^2}xG^{DGLAP}(x,Q^2)\Gamma(b^2). \tag{7}$$

The calculation is simplified if we assume a Gaussian parameterization for the two gluon non perturbative form factor,

$$\Gamma(b^2) \ = \ \frac{1}{R^2}e^{-b^2/R^2}. \tag{8}$$

In the gluon sector SC are given by

$$xG^{SC}(x,Q^2) \ = \ D_g(x,Q^2)xG^{DGLAP}(x,Q^2), \tag{9}$$

[1]For theoretical and phenomenological status of this approach see Ref. [16].

where

$$xG^{SC}(x,Q^2) = \frac{2}{\pi^2}\int_x^1 \frac{dx'}{x'}\int_0^{Q^2} dQ'^2 \int db^2 \left(1 - e^{-\kappa_g(x',Q'^2;b^2)}\right), \qquad (10)$$

and $\kappa_g = \frac{9}{4}\kappa_q$.

An obvious difficulty in the above calculation of xG^{SC} stems from the fact that the Q'^2 integration spans not only the short (pQCD), but also the long (npQCD) distances. To overcome this difficulty we assume that

$$xG\left(x,Q^2\right) = \frac{Q^2}{\mu^2} xG\left(x,\mu^2\right) \ , \ \ Q^2 < \mu^2 \ . \qquad (11)$$

Our choice of the above extrapolation is motivated by the gauge invariance requirement that $xG \propto Q^2$ when $Q^2 \to 0$, and is supported by recent ZEUS measurements of F_2 at exceedingly small Q^2 [13].

The SC calculation described above can be applied to any given input pdf where the only adjusted parameters are R^2 and μ^2. For the radius R^2, see Eq. (8), we use the value 8.5 GeV^{-2} which is determined directly from the forward slope of J/Ψ photo production [26]. μ^2 is conveniently fixed at Q_0^2, the lowest Q^2 value accessible for the input pdf we use. Once we have chosen our pdf, our SC calculation is essentially parameter free. We have checked that our output results are not sensitive to the fine tuning of these fixed parameters.

Before presenting our results we would like to recall two important features of SC. One is that they can only dampen (reduce) the results obtained with the unscreened input dpfs. A second feature is that SC are negligible for large enough Q^2 and/or x. This can be easily deduced from the functional dependence of κ_q and κ_g on Q^2 and x [15].

Throughout the SC calculation we have used as input the $\overline{MS}$ version of NLO GRV98. The results obtained using GRV98 DIS are very similar.

Our fixed Q^2, and fixed x results are displayed in Fig. 3 and Fig. 4, respectively. As can be seen in the limit of small Q^2 and x there is a significant difference between the screened and non screened values of $\partial F_2/\partial \ln Q^2$. As expected the SC results are smaller and softer than the non screened input. All in all, our reproduction of the experimental data for $Q^2 > 2$ GeV^2 is very good. The ZEUS fixed $Q^2 = 1.9$ GeV^2 data are somewhat softer than our predictions. This feature is conspicuous when we compare with the very small $Q^2 = 0.3$ and 0.75 GeV^2 data, where we have made use of the extrapolation given in Eq. (11). In Fig. 4 we see that, using this extrapolation, screened GRV'98 is also successful in describing the data at values of $Q^2 \leq 1$ GeV^2, where in the DL parameterization (see Fig. 6) the soft component dominates.

To further examine the role of the soft (non perturbative) component in $\partial F_2/\partial \ln Q^2$, we compare the above DGLAP results with the DL two Pomeron model [17]. The DL parameterization is based on the Regge formalism, and consists of the coherent sum of contributions from a hard and soft Pomeron, a normal Reggeon and an additional contribution from the charmed sector which is proportional to the hard Pomeron. Each of these fixed j-poles are multiplied by a fitted Q^2 form factor. The hard Pomeron with a fixed trajectory has an intercept of 1.43 at t=0, while the soft Pomeron has an intercept of 1.08 at t=0. As can be seen in Fig. 3, the DL model reproduces the data at all values of Q^2.

We conclude that one can obtain a good description of $\partial F_2/\partial \ln Q^2$ data with $Q^2 \geq 1.9$ GeV^2 using any of the following options: (i) Conventional DGLAP evolution using CTEQ5 pdfs as input; (ii) DGLAP evolution using GRV98 pdfs as input, provided SC are included; (iii) The two Pomeron (DL) model combining hard and soft components.

For smaller Q^2 ($< Q_0^2$), a soft contribution is called for, for which there are several parameterizations available, but not yet a precise theory.

Recently, Golec-Biernat and Wuesthoff [18] have suggested studying the Q^2 and x behaviour of $\partial F_2/\partial \ln Q^2$ at fixed W as a method to determine the gluon saturation scale from the anticipated turnover in these plots. The new ZEUS low Q^2 presentations [7] of these plots show,

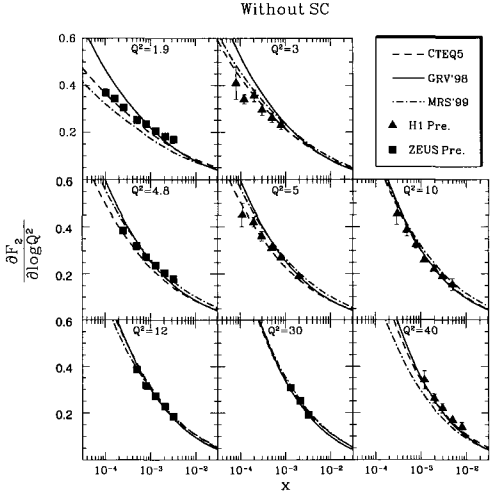

Figure 2: *x dependence of HERA data for the logarithmic slope at fixed Q^2 (in GeV^2) compared with calculations for the unscreened pdfs.*

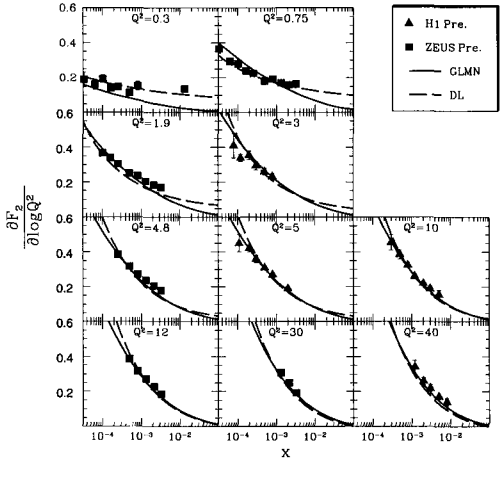

Figure 3: *x dependence of HERA data for logarithmic slope at fixed Q^2 (in GeV^2) compared with our calculations for screened GRV98 and the DL model.*

indeed, the anticipated turnover structure in these figures, suggesting that gluon saturation is attained at $Q^2 \simeq$ a few GeV^2. We advocate using the invariant variables x and Q^2 when describing F_2. Introducing other variables such as W to study the structure function gives rise to spurious effects which are predominantly kinematic. In the specific procedure suggested by Golec-Biernat and Wuesthoff, the combination of the kinematic relation between x, Q^2 and W with the very general behaviour of $xG(x, Q^2)$ is sufficient to produce a turnover. Its exact location depends on the details of the numerical input. Consequently, the suggested fixed W plots do not convey any new dynamical information on the saturation problem even if such information is contained in the analyzed data. We note that a fixed W plot is natural and informative for Regge type models. It appears that any parameterization for F_2 (or xG) which has factorizable Q^2 and x dependences, and provides a reasonable description of the data such as the Buchmueller- Haidt (BH) model [27], gives rise to the fixed W turnover effect.

To illustrate this point we consider the fixed W behaviour in three parameterizations which have completely different dynamics:

1- DGLAP with CTEQ5 pdf. As noted, the results of this parameterization are close to the experimental data for $\partial F_2/\partial \ln Q^2$ at fixed Q^2 and at fixed x values over the kinematic range of interest. This parameterization does not include a specific soft component.

2- The GLMN model [15], which is a pure pQCD dipole model with SC. As such, the model relates indirectly to gluon saturation, even though it is constructed so as to include unitarity corrections below actual saturation. This parameterization has no explicit soft component.

3- The DL two Pomeron parameterization [17].

All three models, as well as the BH parameterization, follow the experimental behaviour of $\partial F_2/\partial \ln Q^2$ at fixed W rather well, including the observed turnover. We demonstrate this in Fig. 5 by comparing the ZEUS data [7] with the results of our SC model. In Fig. 6 we plot the DL model predictions versus the data at fixed W. We also display in this figure the contribution of the hard DL Pomeron.

We conclude with three important general remarks:

(i) Gluon saturation is not unique in producing a turnover at fixed W;

(ii) The gluon saturation scale may be estimated theoretically from the contours produced at the boundary of $\kappa_g = 1$, as discussed in our papers [14][15]. This theoretical analysis suggests that gluon saturation occurs at $Q^2 \approx 1$ GeV^2. Note that κ_g depends on $xG(x, Q^2)$, which is determined from a DGLAP pdf fit to the global F_2 data;

(iii) We note that in the BH and DL parameterizations the soft contributions are concentrated at a rather large typical scale $\geq$ 2 GeV^2. This observation supports the idea that the soft Pomeron originates from rather short distances [28].

3 Discussion and Conclusions

The main experimental observations regarding $\partial F_2/\partial \ln Q^2$ are that at fixed x it is a monotonic decreasing function of Q^2, and for fixed Q^2 it increases as x becomes smaller. This is the observed pattern even for the lowest measured value of $Q^2 = 0.3$ GeV^2 [7]. The main purpose of our investigation was to check whether the preliminary H1 [6] and ZEUS [7] data contains a decisive experimental signature indicating signs of gluon saturation. This effect is associated with the transition from the relatively well understood pQCD hard domain to the more complex, and less understood soft domain. We have shown in this paper that the gluon saturation is capable of describing all HERA data on $\partial F_2/\partial \ln Q^2$ and, therefore, the data do not contradict the idea that HERA has reached a new QCD regime: high parton density QCD.

However, the final conclusion of our analysis is that the present data can be described by a number of models, which are very different in their basic construction. Specifically, we show that all available data with $Q^2 > Q_0^2$, of $\partial F_2/\partial \ln Q^2$ can be described by DGLAP using the CTEQ5 pdf as input, as well as GRV98 pdf which have been corrected for screening. The DL

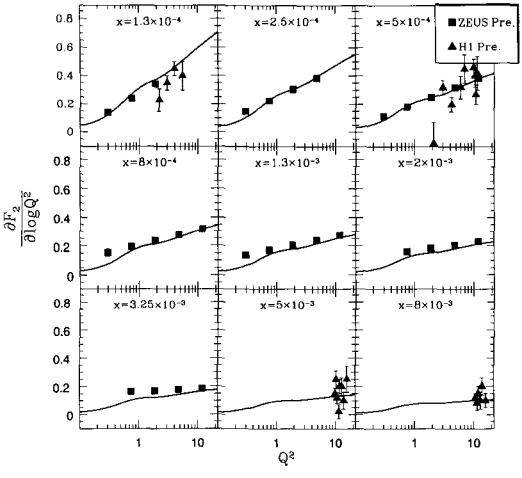

Figure 4: *Q^2 dependence of H1 and ZEUS logarithmic slope data at fixed x compared with our calculations for screened GRV98 (Q^2 is in* GeV^2*).*

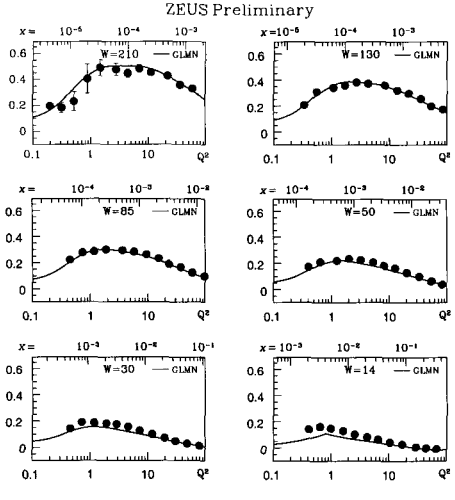

Figure 5: *ZEUS logarithmic slope data at fixed W compared with our SC calculation with GRV98 input.(Q^2 is in* GeV^2*).*

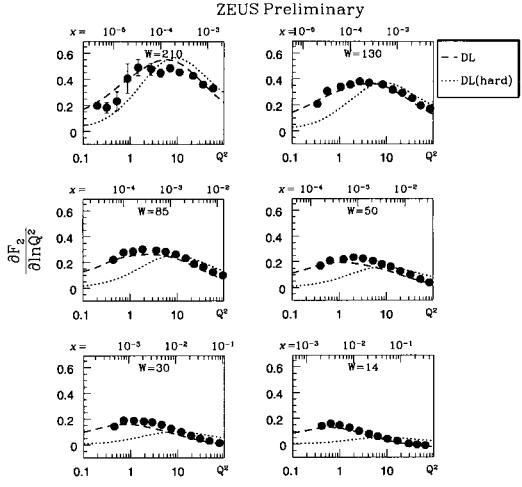

Figure 6: *ZEUS logarithmic slope data at fixed W compared with DL two Pomeron model.*Q^2 *is in* GeV^2

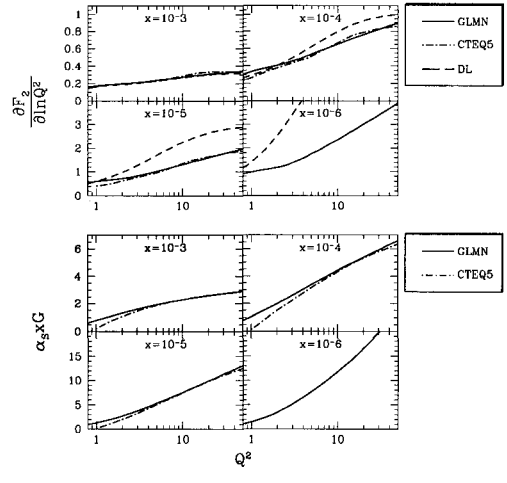

Figure 7: *Predictions for the different parameterizations at fixed low values of* x.*(*Q^2 *is in* GeV^2*).*

model which is Regge motivated and includes a significant soft component, also provides a good description of the data.

We have shown that the turnover seen in $\partial F_2/\partial \ln Q^2$ at fixed W, as a function of either fixed Q^2 or x, is not necessarily connected with saturation effects and cannot be used to discriminate between models. There has also been a successful reproduction of the Caldwell plot by Kaidalov et al. [19] within the framework of the CMKT model [20], and by Forshaw et al.[21] using a colour dipole model formalism. We are of the opinion that fitting the Caldwell as well as the fixed W plots is a necessary first step, but a comparison with all the detailed measurements is essential to test the adequacy of a given model.

In Fig. 7 we attempt to clarify the similarities and differences between the non screened CTEQ5 and the screened GRV98 DGLAP calculations whose results are very similar, (see Figs. 2 and 3). To this end we display the calculated distributions of $\partial F_2/\partial \ln Q^2$ and $\alpha_s xG(x,Q^2)$ at fixed values $x = 10^{-3}, 10^{-4}, 10^{-5}$ and 10^{-6}. As can be seen the results using CTEQ5 (non screened) and GRV98 (screened) in the limit of very small x are very similar. It is therefore suggestive, that CTEQ5 contains significant screening effects, that are absent in the boundary conditions used in GRV98. Note that CTEQ5 is not defined for $x < 10^{-5}$. Our estimates of SC for the CTEQ5 parameterization (based on Eq. (5) - Eq. (10)) is about 10%, which should be considered as the uncertainty in this parameterization. We also show the DL predictions for $\partial F_2/\partial \ln Q^2$, which differ from the hard partonic DGLAP at small enough x.

The ZEUS data at exceedingly low Q^2 [13] are of particular interest when investigating the transition from the DGLAP dominated region to the non perturbative (low Q^2) region. This transition was expected to be observed experimentally since $F_2 \approx Q^2$ as $Q^2 \to 0$ due to gauge invariance requirements, and for large Q^2, $F_2 \approx (Q^2)^\gamma$ from DGLAP evolution, where γ is the anomalous dimension. This transition has been seen by ZEUS [13] in their measurements of $F_2(x,Q^2)$ at small values of x and Q^2, where the transition appears to be at $Q^2 \approx 1$ GeV^2, and is compatible with our early theoretical estimates [14][15]. This provides an indirect indication that this is the scale for the onset of gluon saturation, but we still lack a decisive signature for this effect.

Based on our present investigation we conclude that the behaviour of $\partial F_2/\partial \ln Q^2$ as measured in the kinematic region presently accessible at HERA, does not display unambiguous signs of saturation. This is compatible with the information displayed in Fig. 1 where we see that the anticipated gluon saturation scale is close to Q_0^2, and to the scale at which the soft contribution becomes significant.

We are extending our search for possible effects of gluon saturation to the channel of photo and DIS production of J/Ψ [25], where the cross section should be very sensitive to this signal, as it is proportional to $[xG(Q^2,x)]^2$.

Acknowledgments: We wish to thank our colleagues E. Gotsman, E. Levin and E. Naftali for a very constructive and friendly collaboration. UM wishes to thank UFRJ and FAPERJ (Brazil) for their support. This research was supported in part by the Israel Academy of Science and Humanities and by BSF grant # 98000276.

References

[1] E. Gotsman, E. Ferreira, E. Levin and E. Naftali, *"Scaling violations in the Q^2 logarithmic derivative of F_2"*, hep-ph/0011257.

[2] A.H. Mueller, *" Small x physics, high parton density and parton saturation in QCD"*, CU-TP-954, Aug 1999. Lectures given at International Summer School on Particle Production Spanning MeV and TeV Energies (Nijmegen 99), hep-ph/9911289.

[3] L.V. Gribov, E.M. Levin and M.G. Ryskin, *Phys. Rep.* **100** (1983) 1; A.H. Mueller and J. Qiu, *Nucl. Phys.* **B268** (1996) 427; L. McLerran and R. Venugopalan, *Phys. Rev.* **D49** (1994) 2233 and 3352, and *Phys. Rev.* **D50** (1994) 2225; L. McLerran, R. Venugopalan, A. Ayala, and J. Jalilian-Marian, *Phys. Rev.* **D53** (1996) 458; L. McLerran and R. Venugopalan *Phys. Rev.* **D59** (1999) 094002.

[4] G. Altarelli and G. Parisi, *Nucl. Phys.* **B126** (1977) 298; Yu.L. Dohshitzer, D.I. Dyakonov and S.I. Troyan, *Phys. Lett.* **B78** (1978) 290; V.N. Gribov and L.N. Lipatov *Sov. J. Nucl. Phys.* **15** (1978) 72.

[5] A. Caldwell (ZEUS Coll.): Invited talk, DESY Theory Workshop, Hamburg, October 1997; ZEUS Collaboration, J. Breitweg et al.: *Eur. Phys. J.* **C7** (1999) 609.

[6] H1 Collaboration, *"Deep inelastic inclusive ep scattering at low x and a measurement of* α_s*"*, submitted to the 30th Int. Conf. on High Energy Physics, Osaka, July, 2000; M. Klein (H1 Collaboration), Talk given at 19-th Int. Symposium on Lepton-Photon Interaction at High Energy, `hep-ex/0001059`. These data are preliminary and the data points were read off the plots.

[7] ZEUS Collaboration, *"A Study of scaling violations in the proton structure function* F_2 *at HERA"*, submitted to the 30th Int. Conf. on High Energy Physics, Osaka, July, 2000; B. Foster (ZEUS Collaboration): Invited talk, Royal Society Meeting, London, May 2000; ZEUS Collaboration, J. Breitweg et al.: DESY 00-071. These data are preliminary and the data points were read off the plots.

[8] K. Prytz, *Phys. Lett.* **B311** (1993) 286, and *Phys. Lett.* **B332** (1994) 393; J. Bartels, K. Charchula and J. Feltesse, Proceedings of the DESY Workshop 1991 *"Physics at HERA" vol 1, page 193, edited by W. Buchmuller and G. Ingelman.*

[9] A.H. Mueller, *Nucl. Phys.* **B335** (1990) 115, and **B415** (1994) 373; A.L Ayala Filho, M. B. Gay Ducati and E. Levin, *Phys. Lett.* **B388** (1996) 188.

[10] M. Gluck, E. Reya and A. Vogt, *Eur. Phys. J.* **C5** (1998) 461.

[11] A.D. Martin, R.G. Roberts, W.J. Stirling and R.S. Thorne, *Eur. Phys. J.* **C4** (1998) 463.

[12] CTEQ Collaboration, H.L. Lai et al., *Eur. Phys. J.* **C12** (2000) 375.

[13] ZEUS Collaboration, *Phys. Lett.* **B487** (2000) 53.

[14] E. Gotsman, E.M. Levin and U. Maor, *Phys. Lett.* **B425** (1998) 369.

[15] E. Gotsman, E.M. Levin, U. Maor and E. Naftali, *Nucl. Phys.* **B539** (1999) 535.

[16] E. Gotsman et al., *"Has HERA reached a new QCD regime?"*, DESY-00-149, TAUP-2649-2000, Oct 2000, `hep-ph/0010198`.

[17] A. Donnachie and P.V. Landshoff, *Phys. Lett.* **B437** (1998) 408, *Phys. Lett.* **B470** (1999) 243.

[18] K. Golec-Biernat and M. Wuesthoff, *Phys. Rev.* **D59** (1998) 014017.

[19] A.B. Kaidalov, C. Merino and D. Pertermann, *"On the behaviour of* F_2 *and its logarithmic slopes"*, `hep-ph/0004237`.

[20] A. Capella et al., *Phys. Lett.* **B343** (1995) 403, *Phys. Rev.* **D53** (1996) 2309.

[21] J. Forshaw, G. Kerley and G. Shaw, *" Color dipoles and saturation"*, MC-TH-00-04, Apr 2000, Talk given at 8th International Workshop on Deep Inelastic Scattering and QCD (DIS 2000), Liverpool, England, 25-30 Apr 2000, hep-ph/0007257.

[22] A.L. Ayala Filho, M.B. Gay Ducati and E.M. Levin, *Nucl. Phys.* **B493** (1997) 305.

[23] M. Gluck, E. Reya and A. Vogt, *Z. Phys.* **C67** (1995) 433.

[24] H. Abramowicz, E.M. Levin, A. Levy and U. Maor, *Phys. Lett.* **B269** (1991) 465;
H. Abramowicz and A. Levy, *The ALLM parameterization of* $\sigma_{\rm tot}(\gamma * p)$ *- an update"*, DESY 97-251, hep-ph/9712415.

[25] E. Gotsman, E. Ferreira, E. Levin, U. Maor and E. Naftali, *(to be published).*

[26] A.D. Martin, R.G. Roberts, M.G. Ryskin and W.J. Stirling, *Eur. Phys. J.* **C2** (1998) 287.

[27] W. Buchmueller and D. Haidt, *"Double-logarithmic scaling of the structure function* F_2 *at small* x*"*, DESY-96-061 and hep-ph/9605428. D. Haidt, *Nuc. Phys. (Proc. Suppl.)* **B79** (1999) 186. (R.S. Thorne at Low x Workshop, Oxford, July 2000).

[28] D. Kharzeev and E. Levin, *Nucl. Phys.* **B578** (2000) 351.

Charm meson interactions in hadronic matter*

C. M. Ko and Ziwei Lin
Cyclotron Institute and Physics Department
Texas A&M University, College Station, Texas 77843-3366, USA

ABSTRACT

Both charmonium and charm mesons are relevant for finding the signatures of the quark-gluon plasma formed in ultra-relativistic heavy ion collisions. To study their interactions in hadronic matter, a hadronic Lagrangian based on the SU(4) flavor gauge invariance has been introduced. With coupling constants determined either empirically or by the SU(4) symmetry, the absorption cross section of J/Ψ and the scattering cross sections of D and $D^{\pm}$ by π and ρ mesons are found to be appreciable.

1 Introduction

Suppression of J/ψ production in high energy heavy ion collisions is one of the most studied signals for the quark-gluon plasma expected to be formed in ultra-relativistic heavy ion collisions.[1] Recent data from the Pb+Pb collision at $P_{\rm lab}$ = 158 GeV/c in the NA50 experiment at CERN[2] have shown an anomalously large J/ψ suppression in events with high transverse energies. While there are suggestions that this anomalous suppression may be due to the formation of the quark-gluon plasma,[3,4] more conventional mechanisms based on J/ψ absorption by comoving hadrons have also been proposed as possible explanations.[5,6] To understand the observed anomalous J/ψ suppression thus requires information on the J/ψ absorption cross section by hadrons.[7] For heavy ion collisions at the Relativistic Heavy Ion Collider, where the quark-gluon plasma is most likely to be formed, J/ψ absorption by hadrons may still play a non-negligible role.[8] Furthermore, one needs to know if J/ψ can also be produced from the hot hadronic matter in heavy ion collisions.[9,10]

The formation of the quark-gluon plasma in heavy ion collisions may also be inferred from the energy spectrum of charm mesons as it has been shown that charm quarks can lose appreciable energies in the quark-gluon plasma.[11,12] However, this requires that charm mesons do not interact strongly in the hadronic matter during the later stage of heavy ion collisions. Whether this is the case depends on the charm meson scattering cross sections with hadrons, which are not known empirically. Also, if the charm meson spectrum is significantly hardened by hadronic scattering, then dileptons from their decays will be important in the invariant mass region $M > 2$ GeV/c^2.[13,14] In this case, it will be more difficult to identify the thermal dileptons from the quark-gluon plasma.

Various approaches have been used in evaluating the J/ψ absorption cross section by hadrons. In the quark-interchange model, an earlier study[15] has shown that the J/ψ absorption cross section by pion has a peak value of about 7 mb at a center of mass kinetic energy of 0.8 GeV, but a recent study[16] gives a peak value of only about 1

*Supported by the National Science Foundation under Grant No. PHY-9870038, the Welch Foundation under Grant No. A-1358, and the Texas Advanced Research Program under Grant No. FY99 - 010366 - 0081.

mb at the same energy. On the other hand, the perturbative QCD approach[17] predicts that the J/ψ dissociation cross section increases monotonously with the center of mass kinetic energy and has a value of only about 0.1 mb around 0.8 GeV. The J/ψ absorption cross section by hadrons has also been studied in meson-exchange models based on hadronic Lagrangians. Including only pseudoscalar-pseudoscalar-vector-meson (PPV) couplings and without form factors at the interaction vertices, Matinyan and Müller[18] have found the J/ψ absorption cross section by pion is about 0.3 mb at center of mass energy of 0.8 GeV. In more recent studies, Haglin[19] as well as Lin and Ko[20] have also included the three-vector-meson (VVV) and four-point couplings (or contact terms), and obtained much larger values for the J/ψ absorption cross sections. The same hadronic Lagrangian has been used for studying the charm meson scattering cross sections with pion and rho meson,[21] and they are also found to be appreciable.

In this paper, results on J/ψ absorption cross section and D and D^* meson scattering cross sections by hadrons based on the hadronic Lagrangian approach are presented.

2 The hadronic Lagrangian

The free Lagrangian for pseudoscalar and vector mesons in the limit of SU(4) invariance can be written as

$$\mathcal{L}_0 = \mathrm{Tr}\left(\partial_\mu P^\dagger \partial^\mu P\right) - \frac{1}{2}\mathrm{Tr}\left(F^\dagger_{\mu\nu} F^{\mu\nu}\right), \tag{1}$$

where $F_{\mu\nu} = \partial_\mu V_\nu - \partial_\nu V_\mu$, and P and V denote, respectively, the 4×4 pseudoscalar and vector meson matrices in SU(4)[22]:

$$P = \frac{1}{\sqrt{2}} \begin{pmatrix} \frac{\pi^0}{\sqrt{2}} + \frac{\eta}{\sqrt{6}} + \frac{\eta_c}{\sqrt{12}} & \pi^+ & K^+ & \bar{D}^0 \\ \pi^- & -\frac{\pi^0}{\sqrt{2}} + \frac{\eta}{\sqrt{6}} + \frac{\eta_c}{\sqrt{12}} & K^0 & D^- \\ K^- & \bar{K}^0 & -\sqrt{\frac{2}{3}}\eta + \frac{\eta_c}{\sqrt{12}} & D_s^- \\ D^0 & D^+ & D_s^+ & -\frac{3\eta_c}{\sqrt{12}} \end{pmatrix},$$

$$V = \frac{1}{\sqrt{2}} \begin{pmatrix} \frac{\rho^0}{\sqrt{2}} + \frac{\omega'}{\sqrt{6}} + \frac{J/\psi}{\sqrt{12}} & \rho^+ & K^{*+} & \bar{D}^{*0} \\ \rho^- & -\frac{\rho^0}{\sqrt{2}} + \frac{\omega'}{\sqrt{6}} + \frac{J/\psi}{\sqrt{12}} & K^{*0} & D^{*-} \\ K^{*-} & \bar{K}^{*0} & -\sqrt{\frac{2}{3}}\omega' + \frac{J/\psi}{\sqrt{12}} & D_s^{*-} \\ D^{*0} & D^{*+} & D_s^{*+} & -\frac{3J/\psi}{\sqrt{12}} \end{pmatrix}. \tag{2}$$

Introducing the minimal substitution

$$\partial_\mu P \to \mathcal{D}_\mu P = \partial_\mu P - \frac{ig}{2}\left[V_\mu, P\right], \tag{3}$$

$$F_{\mu\nu} \to \partial_\mu V_\nu - \partial_\nu V_\mu - \frac{ig}{2}\left[V_\mu, V_\nu\right], \tag{4}$$

leads to the following Lagrangian for the interacting hadrons:

$$\begin{aligned} \mathcal{L} &= \mathcal{L}_0 + ig\mathrm{Tr}\left(\partial^\mu P\left[P, V_\mu\right]\right) - \frac{g^2}{4}\mathrm{Tr}\left(\left[P, V_\mu\right]^2\right) \\ &+ ig\mathrm{Tr}\left(\partial^\mu V^\nu\left[V_\mu, V_\nu\right]\right) + \frac{g^2}{8}\mathrm{Tr}\left(\left[V_\mu, V_\nu\right]^2\right). \end{aligned} \tag{5}$$

Since hadron masses explicitly break the SU(4) symmetry, mass terms based on the experimentally determined values are added to Eq. (5).

3 J/ψ absorption cross section

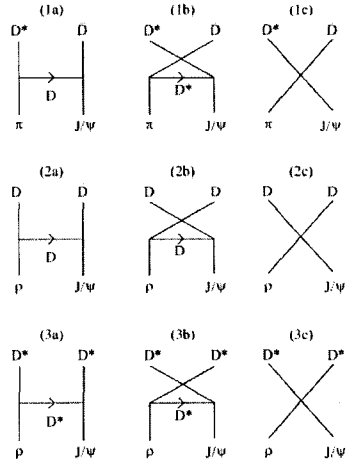

Figure 1: Diagrams for J/ψ absorption processes.

The above hadronic Lagrangian allows one to study the following processes for J/ψ absorption by π and ρ mesons:

$$\pi\psi \to D^*\bar{D},\ \pi\psi \to D\bar{D}^*,\ \rho\psi \to D\bar{D},\ \rho\psi \to D^*\bar{D}^*.$$

Corresponding diagrams for these processes, except the process $\pi\psi \to D\bar{D}^*$ that has the same cross section as the process $\pi\psi \to D^*\bar{D}$, are shown in Fig. 1.

To determine the magnitude of the cross sections for these processes requires knowledge on the coupling constants. For the coupling constant $g_{\pi DD^*}$, studies based on the the QCD sum rules[23] give $g_{\pi DD^*} = 4.4$, which is consistent with that determined from the upper bound for the D^* decay width. Using the vector meson dominance model, other three-point coupling constants can be determined as

$$g_{\rho DD} = g_{\rho D^*D^*} = 2.52\ ,\ g_{\psi DD} = g_{\psi D^*D^*} = 7.64\ .$$

For the four-point coupling constants, there is no empirical information, and one thus has to rely on the SU(4) symmetry to determine their values, i.e.,

$$g_{\pi\psi DD^*} = g_{\pi DD^*}g_{\psi DD},\ g_{\rho\psi DD} = 2\, g_{\rho DD}g_{\psi DD},\ g_{\rho\psi D^*D^*} = g_{\rho D^*D^*}g_{\psi D^*D^*}.$$

Because of the finite size of hadrons, form factors are needed at interaction vertices. Since there is no empirical information on form factors involving J/ψ and charm mesons, the usual monopole form is used in Ref.[21] for the three-point t and u channel vertices, i.e., $f_3(t \text{ or } u) = \Lambda^2/(\Lambda^2 + \mathbf{q}^2)$. In the above, Λ is a cutoff parameter, and $\mathbf{q}^2$ is the squared three momentum transfer in the center of mass frame. For simplicity, the same value for all

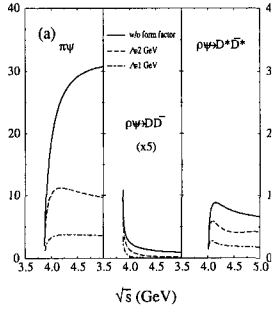

Figure 2: J/ψ absorption cross sections as functions of energy.

cutoff parameters, i.e., $\Lambda_{\pi DD^*} = \Lambda_{\rho DD} = \Lambda_{\rho D^*D^*} = \Lambda_{\psi DD} = \Lambda_{\psi D^*D^*} \equiv \Lambda$, is used in Ref..[21] Furthermore, Λ is chosen to be either 1 or 2 GeV to study the uncertainties due to form factors. These values are comparable to that determined from the QCD sum rules for the πDD^* form factor.[24] As to the form factor at four-point vertices, it is completely unknown. In Ref.,[21] it is simply taken as $f_4 = \left[\Lambda^2/(\Lambda^2 + \vec{\mathbf{q}}^2)\right]^2$, where $\vec{\mathbf{q}}^2$ is the average value of the squared three momentum transfers in the t and u channels.

The J/ψ absorption cross sections obtained by using the above coupling constants and form factors are shown in Fig. 2 as functions of the center of mass energy of initial-state mesons. Although form factors strongly suppress the cross sections, the J/ψ absorption cross sections remain appreciable. The values for $\sigma_{\pi\psi}$ and $\sigma_{\rho\psi}$ are roughly 7 and 3 mb, respectively, and are comparable to those used in phenomenological studies of J/ψ absorption by comoving hadrons in relativistic heavy ion collisions.[5,6,25]

For J/ψ absorption in a hot hadronic matter, it is of interest to evaluate the thermal average of the cross sections, and they are shown in Fig. 3. At temperature of 150 MeV, which is the typical value for the hadronic matter in relativistic heavy ion collisions, $\langle\sigma_{\pi\psi}v\rangle$ and $\langle\sigma_{\rho\psi}v\rangle$ are about 1 and 2 mb, respectively.

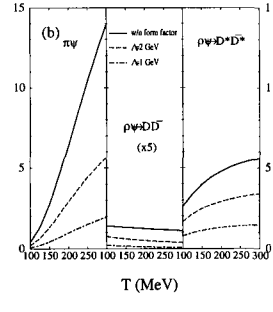

Figure 3: Thermal-averaged J/ψ absorption cross sections as functions of temperature.

4 Charm meson scattering

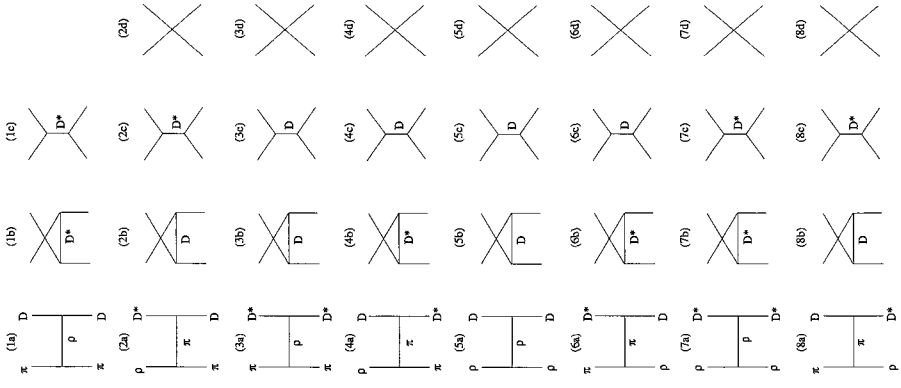

Figure 4: Diagrams for charm meson scattering by pion and rho meson.

The above hadronic Lagrangian also allows one to study the following processes for charm meson scattering by π and ρ mesons:

$$\pi D \leftrightarrow \rho D^*,\ \pi D \rightarrow \pi D,\ \pi D^* \rightarrow \pi D^*,\ \pi D^* \leftrightarrow \rho D,\ \rho D \rightarrow \rho D,\ \rho D^* \rightarrow \rho D^*.$$

There are similar processes for anticharm mesons. Fig. 4 shows the diagrams for these processes.

For the coupling constants, one obtains $g_{\rho\pi\pi} = 6.1$ from the decay width of rho meson.[26] The SU(4) symmetry then gives $g_{\rho\rho\rho} = g_{\rho\pi\pi}$ and the following relations for the four-point couplings:

$$g_{\pi\rho DD^*} = g_{\pi DD^*} g_{\rho DD},\ g_{\pi\pi D^* D^*} = 2g^2_{\pi DD^*},\ g_{\rho\rho DD} = 2g^2_{\rho DD},\ g_{\rho\rho D^* D^*} = g^2_{\rho D^* D^*}. \tag{6}$$

Form factors at the s channel vertices are taken as $f_3(s) = \Lambda^2/(\Lambda^2 + \mathbf{k}^2)$,[27] with $\mathbf{k}$ denoting the three momentum of either the incoming or outgoing particles in the center of mass frame. For form factors at four-point vertices, they are take to be $f_4' = \left[\Lambda^2/(\Lambda^2 + \bar{\mathbf{k}^2})\right]^2$ in Ref.,[27] where $\bar{\mathbf{k}^2}$ is the average value of the squared three momenta in the form factors for the s, t, and u channels.

The charm meson scattering cross sections and their thermal averages are shown in Fig. 5 and Fig. 6, respectively. As expected, the magnitude of the cross sections decreases with decreasing cutoff parameter. For cutoff parameters of 1 to 2 GeV, the cross sections for $\pi D, \pi D^*, \rho D$ and ρD^* scattering and their thermal average are all between 10 and 20 mb. Because of the small momentum transfer in the dominant elastic processes, form factors only suppress these cross sections and thermal averages by about a factor of two and less. This is in contrast to the cross section for the process $\pi\psi \rightarrow D^*\bar{D}$ for J/ψ absoprtion, which is reduced significantly (about a factor of 8) by the form factor due to its large threshold.

5 Summary

In summary, a hadronic Lagrangian based on the SU(4) flavor gauge symmetry has been used to study the interactions of J/ψ and charmed mesons in hadronic matter. With physical hadron masses and the coupling constants given either empirically or by the SU(4) symmetry, the absorption cross sections of J/ψ and scattering cross sections of charmed mesons by π and ρ mesons have been studied. Including form factors at the interaction vertices, the values for $\sigma_{\pi\psi}$ and $\sigma_{\rho\psi}$ are about 7 mb and 3 mb, respectively, and their thermal averages at temperature of 150 MeV are about 1 mb and 2 mb, respectively. These values will be even larger if one also includes the process $J/\psi + \pi \to \eta_c + \rho$, which has been shown to be also appreciable.[28] Therefore, the absorption of J/ψ by comoving hadrons is non-negligible for J/ψ suppression in relativistic heavy ion collisions. It is also found that the scattering cross sections of D and D^* by π and ρ mesons as well as their thermal averages are all about 10 mb. One thus expects these scatterings to significantly modify the charm meson spectra in heavy ion collisions, making it more difficult to verify the formation of the quark-gluon plasma in heavy ion collisions through the energy spectrum of charm mesons and the abundance of intermediate mass dileptons.

The hadronic Lagrangian discussed here has been extended in Ref.[29] to include the anomalous parity interactions involving the PVV and PPPV couplings. Effects of these interactions are, however, small. Also, the hadronic Lagrangian has been extended to SU(5) in Ref.[30] for studying the Υ absorption cross section by hadrons. It is found that although the cross section is comparable to that for J/ψ absorption, its thermal average is only a fraction of mb as a result of the large threshold effect. Therefore, Υ absorption in hadronic matter is unimportant in heavy ion collisions, and its suppression is expected to be a better signal for the quark-gluon plasma than J/ψ suppression.

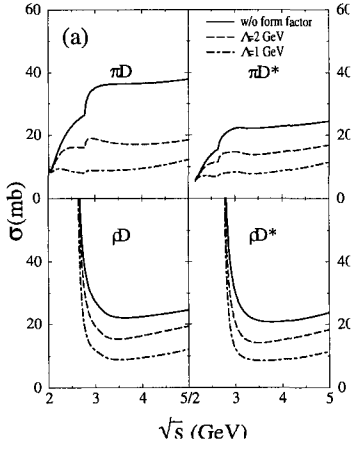

Figure 5: Scattering cross sections of D and D^* as functions of energy.

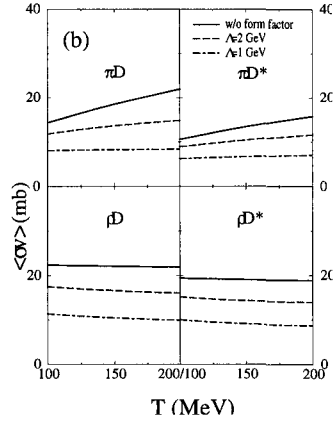

Figure 6: Thermal-averaged cross sections as functions of temperature.

6 REFERENCES

[1] T. Matsui and H. Satz, Phys. Lett. B 178, 416 (1986).

[2] M. Gonin *et al.* (NA50 Collaboration), Nucl. Phys. A 610, 404c (1996); M. C. Abreu *et al.* (NA50 Collaboration), Phys. Lett. B 450, 456 (1999).

[3] J. P. Blaizot and J. Y. Ollitrault, Phys. rev. Lett. 77, 1703 (1996).

[4] C. Y. Wong, Nucl. Phys. A 630, 487 (1998).

[5] W. Cassing and C. M. Ko, Phys. Lett. B 396, 39 (1997); W. Cassing and E. L. Bratkovskaya, Nucl. Phys. A 623, 570 (1997).

[6] N. Armesto and A. Capella, Phys. Lett. B 430, 23 (1998).

[7] For recent reviews, see, e.g., R. Vogt, Phys. Rep. 310, 197 (1999); H. Satz, Rept. Prog. Phys. 63, 1511 (2000).

[8] B. Zhang, C. M. Ko, B. A. Li, Z. Lin, and B. H. Sa, Phys. Rev. C 62, 054905 (2000).

[9] C. M. Ko, X. N. Wang, B. Zhang, and X. F. Zhang, Phys. Lett. B 444, 237 (1998).

[10] P. Braun-Munzinger and K. Redlich, Nucl. Phys. A 661, 546 (1999).

[11] E. Shuryak, Phys. Rev. C 55, 961 (1997).

[12] Z. Lin, R. Vogt, and X. N. Wang, Phys. Rev. C 57, 899 (1998).

[13] R. Vogt, B. V. Jacak, P. L. McGaughey, and P. V. Ruuskanen, Phys. Rev. D 49, 3345 (1994).

[14] Z. Lin and X. N. Wang, Phys. Lett. B 444, 245 (1998).

[15] K. Martins, D. Blaschke, and E. Quack, Phys. Rev. C 51, 2723 (1995).

[16] C. Y. Wong, E. S. Swanson, and T. Barnes, Phys. Rev. C 61, 044905 (2000).

[17] D. Kharzeev, and H. Satz, Phys. Lett. B 334, 155 (1994).

[18] S. G. Matinyan and B. Müller, Phys. Rev. C 58, 2994 (1998).

[19] K. Haglin, Phys. Rev. C 61, 031902 (2000).

[20] Z. Lin and C. M. Ko, Phys. Rev. C 62, 034903 (2000).

[21] Z. Lin Z, T. G. Di, and C. M. Ko, Nucl. Phys. A, in press, nucl-th/0006086.

[22] Z. Lin, C. M. Ko, and B. Zhang, Phys. Rev. C 61, 024904 (2000).

[23] P. Colangelo, F. De Fazio, and G. Nardulli, Phys. Lett. B 334, 175 (1994); V. M. Belyaev, V. M. Braun, A. Khodjamirian, and R. Ruckl, Phys. Rev. D 51, 6177 (1995).

[24] F. S. Navarra, M. Nielsen, M. E. Bracco, M. Chiapparini, and C. L. Schat, Phys. Lett. B 489, 319 (2000).

[25] D. E. Kahana and S. H. Kahana , Phys. Rev. C 59, 1651 (1999); B. H. Sa, A. Tai, H. Wang, and F. H. Liu, Phys. Rev. C 59, 2728 (1999); C. Spieles, R. Vogt, L. Gerland, S. A. Bass, M. Bleicher, H. Stöcker, and W. Greiner, Phys. Rev. C 60, 054901 (1999).

[26] G. E. Brown, C. M. Ko, Z. G. Wu, and L. H. Xia, Phys. Rev. C 43, 1881 (1991); C. M. Ko and D. Seibert, Phys. Rev. C 49, 2198 (1994).

[27] K. Tsushima, S. W. Huang, and A. Faessler, Phys. Lett. B 337, 245 (1994); E. L. Bratkovskaya and C. M. Ko, Phys. Lett. B 445, 265 (1999).

[28] K. Haglin and C. Gale, nucl-th/0010017.

[29] Y. Oh, T. Song, and S. H. Lee, nucl-th/0010064.

[30] Z. Lin and C. M. Ko, Phys. Lett. B, in press, nucl-th/0007027.

Contributed Papers

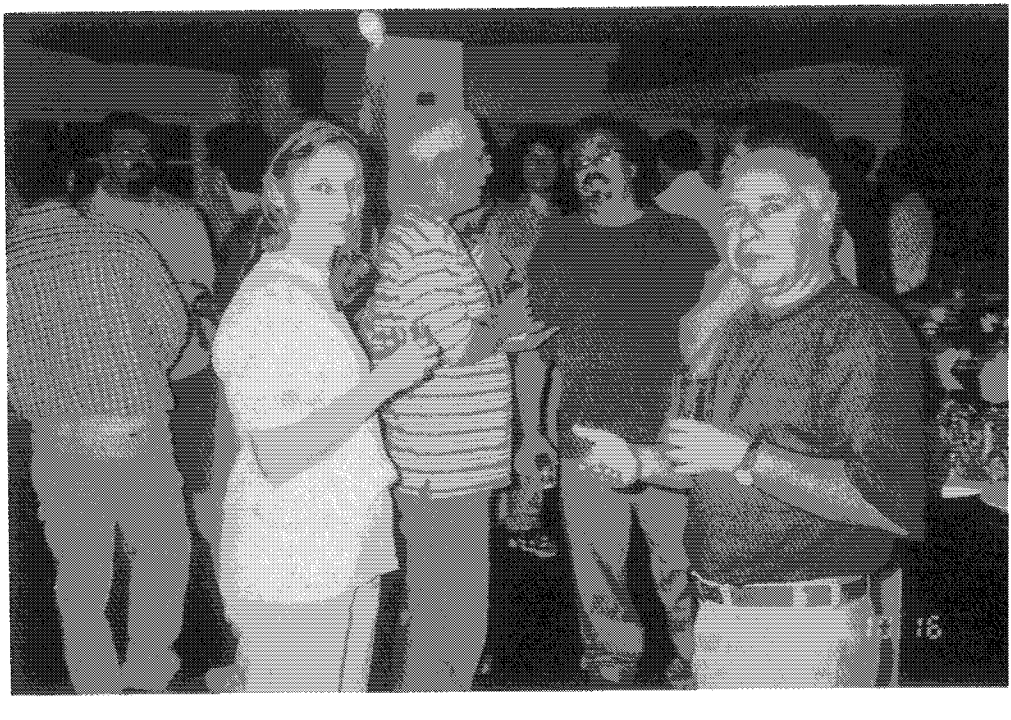

Dependence of the forward neutral energy $E_{\rm n}$ on transverse energy $E_{\rm T}$ in Relativistic Heavy Ions Collisions

J. Barrette[1], R. Bellwied[6], P. Braun-Munzinger[6], R. G. Burgugi[7], W. E. Cleland[5], M. Clemen[5], G. David[6], J. Dee[6], O. Dietzsch[5,7], E. Duek[1], M. Fatyga[1], D. Fox[2], S. V. Greene[9], J. R. Hall[4], T. K. Hemmick[9], N. Herrmann[6], B. Hong[6], K. Jayananda[5], D. Kraus[5], B. Shiva Kumar[9], R. Lacasse[3], D. Lissauer[1], W. J. Llope[6], T. Ludlam[1], S. K. Mark[3], S. McCorle[1], J. T. Mitchell[9], J. M. Muthuswamy[6], E. O'Brien[1], C. Pruneau[3], F. S. Rotondo[9], C. L. da Silva[7], N. C. da Silva[7], J. Simon-Gillo[8], U. Sonnadara[5], J. Stachel[6], E. M. Takagui[5,7], H. Takai[1], T. G. Throwe[1], L. Waters[6], C. Winter[9], K. Wolf[8], D. Wolfe[4], C. L. Woody[1], N. Xu[6], Y. Zhang[6], Z. Zhang[5], and C. Zou[6]

[1] Brookhaven National Laboratory, Upton, NY, USA
[2] Los Alamos National Laboratory, Los Alamos, New Mexico
[3] McGill University, Montreal, Canada
[4] University of New Mexico, Albuquerque, New Mexico
[5] University of Pittsburgh, Pittsburgh, Pennsylvania
[6] State University of New York, Stony Brook, New York
[7] Universidade de São Paulo, São Paulo, Brazil
[8] Texas AM University, College Station, Texas
[9] Yale University, New Haven, Connecticut

E-mail: rogerio@wslip1.if.usp.br

Abstract

We are carrying out a study of the forward neutral energy and its correlation with produced transverse energy in collisions of ^{28}Si ions of momentum 14.6A GeV/c with targets of Al, Cu, and Pb, investigated by Experiment 814 at the Brookhaven AGS. We find that the forward neutral energy $E_{\rm n}$ has a strong dependence on transverse energy $E_{\rm T}$ produced in the collision, resulting in a nearly linear dependence of mean transverse energy on forward neutral energy over a wide range of event centrality. An efficient parametrization of this data set is accomplished through the use of a statistical model which relates the number of spectators in the collision to the number of neutrons detected in the forward direction.

1. Introduction

The acceleration of heavy ions to relativistic energies, during the past years, has made possible the investigation of projectile fragmentation in a regime which was not possible before. The nucleus-nucleus collisions occur mainly through either the strong or the electromagnetic interactions. These two interactions can be classified according to the impact parameter b. The collisions with $|R_T - R_P| < b < R_T + R_P$, where R_T and R_P are the target and projectile radii, respectively, occur mainly via strong interactions, leading to nuclear fragmentation.

A study of the nuclear fragmentation was formerly investigated by Experiment 814 [1] (Section 2) at the Alternating Gradient Synchrotron (AGS) at Brookhaven National Laboratory (BNL). We have taken the opportunity to carry out a study of collisions with nuclear fragmentation measuring transverse and forward neutral energy, using only some detectors (Section 2). We find that the forward neutral energy $E_{\rm n}$ has a strong dependence on transverse energy $E_{\rm T}$ produced in the collision, resulting in a nearly linear dependence of mean transverse energy on forward neutral energy over a wide range of event centrality. Another interesting feature of the data is a small (barely significant) increase in $<E_{\rm n}>$ at high $E_{\rm T}$, also observed in ^{197}Au+^{197}Au collisions [2].

A simple model for fragmentation was used in the present study. This model divides the initial state baryons in relativistic heavy ion collisions into spectators and participants. The participants in the interaction undergo one or more strong inelastic collisions, and the spectator nucleons are presumed to be unaffected by the collisions. The mean number of forward, beam rapidity nucleons as a function of some parameter broadly proportional to the number of participants (such as transverse

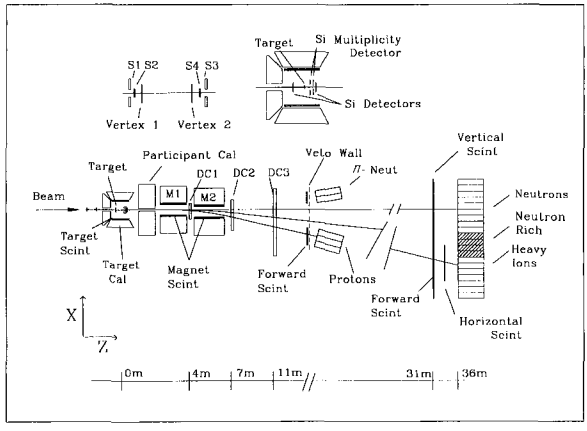

Figure 1. Schematic diagram of the E814 setup.

energy) provides an interesting test of the model. Such a measurement is also a test of the stopping power of the nucleus, and of the validity of the notion of 'unaffected' spectators. This model forms the basis for the parametrization [2] of our data discussed in Section 3.

2. The Experiment 814

The Experiment 814 (fig.1) was a fixed target Relativistic Heavy-Ion experiment operating at the Alternate Gradient Synchrotron (AGS) at Brookhaven National Laboratory (BNL). The experiment was projected for the investigation of a wide range of physics on central, semi-peripheral and peripheral collisions [3]. In the experiment ^{28}Si ions of momentum 14.6A GeV/c interact with ^{27}Al, ^{64}Cu, and ^{208}Pb targets. The experiment has a calorimetric coverage nearly complete around the target, and a high resolution forward spectrometer. The main detectors of the usptream detector group are the multiplicity detector (MULT), the target calorimeter (TCAL) and the participant calorimeter (PCAL). The main detectors of the downstream detector group (forward spectrometer) are the tracking chambers (DC1, DC2, and DC3), the forward scintillators (FSCI), the horizontal scintillators (HSCI) and the U/Cu calorimeters (UCAL). The forward scintillator counters measure the charge, time of fligth and vertical coordinate of the forward going particles. Below is a short description of the main detectors used in this work.

Multiplicity detector - The multiplicity detector [4] consists of two concentric silicon discs, each 300 μm thick, and divided into 512 elements. The first disc is placed 3.4 cm downstream of the target, and the second disc, 8.2 cm downstream of the target. They cover an angular range of 2^o-40^o. These two detectors provide the charge multiplicity for any event.

Participant Calorimeter - The participant calorimeter [5] is a lead-scintillator calorimeter read out through wave-length shifting fibers into 512 photomultiplier tubes. It is divided into 16 azimuthal and eigth radial segments in four depth layers (two electromagnetic and two hadronic). It has the same angular coverage as the multiplicity detector.

U/Cu Calorimeters - They consist of 25 U/Cu calorimeter modules [6] installed downstream of the magnets (M1, M2) at two locations, z=13 m and z=36 m, to measure the energy and the position of reaction fragments at the downstream end of the spectrometer. Each module is approximately $20\times100\times120$ cm^3 and they cover the same area as the forward scintillator hodoscopes.

3. The Statistical Model

The model assumes [2] that the forward neutrons emerge from the projectile spectator at beam rapidity. For a given value of E_T, we assume that the number of spectator nucleons N_S is fixed.

The incident projectile contains N_A nucleons, of which N_n are neutrons and N_p are protons. For a collision with N_S spectators, under the simplifying assumption that all configurations of neutrons and protons are equally likely, the distribution $Q(n)$ for the number of neutrons n among the spectators is that of sampling without replacement

(hypergeometric distribution),

$$Q(n) = \frac{\binom{N_n}{n}\binom{N_A - N_n}{N_s - n}}{\binom{N_A}{N_s}} = \frac{\binom{N_n}{n}\binom{N_p}{N_s - n}}{\binom{N_A}{N_s}}. \quad (1)$$

We introduce a parameter p, which describes the probability that a spectator neutron will proceed forward unbound with beam rapidity. We assume that the number of such neutrons follows a binomial probability distribution,

$$P(m,n,x) = \binom{n}{n-m}(1-x)^{n-m}x^m, \quad (2)$$

where x is the probability for sucess, and $P(m,n,x)$ is the probability that m out of n neutrons will succeed. The probability for detection of the neutrons is described in a similar maner. The number of forward neutrons actually sampled is also assumed to be given by a binomial probability distribution, the parameter of sucess being f ($\approx$75%) [2], the fraction of the production distribution covered by our fiducial area (neutral region UCAL). Combining all distributions, we obtain the probability that k>0 neutrons will be detected, given by:

$$R(k) = \sum_{n=k}^{N_s} Q(n) \sum_{m=k}^{n} P(m,n,p)P(k,m,f). \quad (3)$$

4. Preliminary Events Selection

To exclude peripheral events we require that the TCAL total energy be greater than 35 MeV [7]. Events with high transverse energy and low multiplicity were also discarded since they correspond to upstream interactions (figs. 2a, 2b, 2c). To determine the neutral energy E_n the charged particles were discarded by analyzing the signals from the scintillators in front of the neutral region of the U/Cu calorimeters (fig. 2d).

5. Results and Conclusion

Figure 3 shows the mean neutral region energy $<E_n>$ as a function of transverse energy E_T for the ^{28}Si beam incident on Al, Cu and Pb targets. Figure 4 shows the mean neutral region energy spectra for four E_T bins. The curves shown in the graphs are those calculated from a fit (table 1) *using the probability function R(k)* (3). The data sets correspond to ^{28}Si beam incident on the Al target. The fit program was developed in the ROOT framework [8] and Minuit Routines [9] were used. The MAPLE program [10] was also used to rewrite (3) in a convenient way, which allowed the results of the fit to be independent on the starting values given to the fit routines. Figures 5 and 6 shows the parameters (N_S and p) obtained in the fit

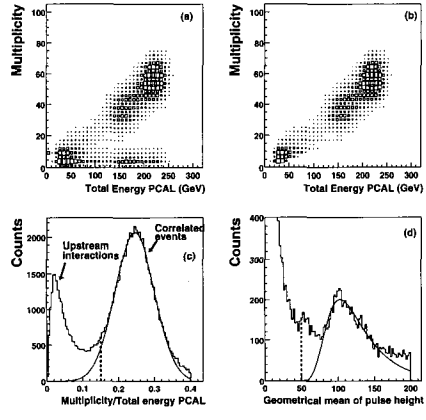

Figure 2. (a) Scatter plot of charged particle multiplicity versus total energy in PCAL. (b) Same as (a) but with veto for upstream interactions. (c) The ratio of multiplicity to total energy in PCAL, for defining the cut value for vetoing the upstream interactions. The curve shown in the graph is that calculated from a fit using a Gaussian distribution. The dashed line is the cut value. (d) Sum of forward scintillator pulse heights covering the neutral region, for minimum ionizing particles, for defining the charged particle veto. The curve shown in the graph is that calculated from a fit using a Landau distribution. The dashed line is the cut value.

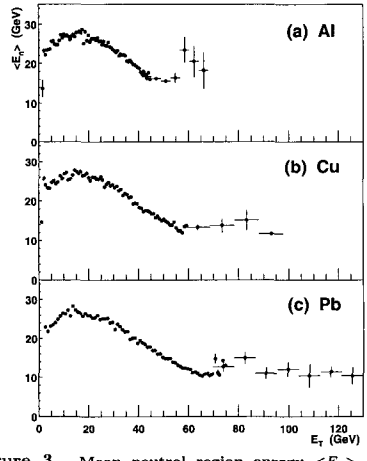

Figure 3. Mean neutral region energy $<E_n>$ as a function of transverse energy E_T for ^{28}Si beam incident on (a) Al, (b) Cu, and (c) Pb targets. The horizontal error bars correspond to the bin E_T, and computation of vertical errors bars is based on the counting statistics.

Table 1. The parameters obtained in the fit of 3 to ^{28}Si beam incident on the Al target data.

E_T (GeV)	N_S	σ_{N_S}	p	σ_p	χ^2/D.F.
29.5-32.5	17	3	0.18	0.04	0.64
35.5-38.5	7.8	0.7	0.32	0.03	4.51
41.5-44.5	6.0	0.7	0.32	0.04	1.22
44.5-47.5	2.65	0.18	0.67	0.05	0.35

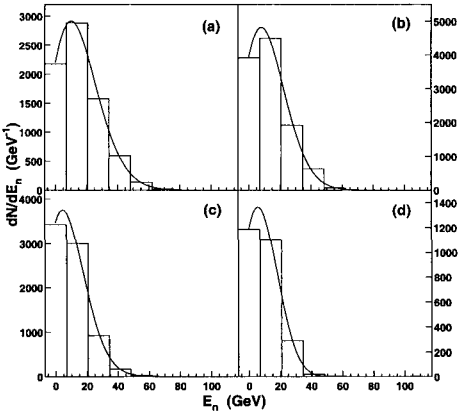

Figure 4. Mean neutral region energy spectra in bins of beam rapidity energy for four E_T bins: (a) 29.5-32.5 GeV, (b) 35.5-38.5 GeV, (c) 41.5-44.5 GeV, and (d) 44.5-47.5 GeV. The curves shown in the graphs are those calculated from a fit using the probability function $R(k)$ (3). The data sets correspond to ^{28}Si beam incident on the Al target.

to the Al, Cu, and Pb targets data. The data used in the fit program correspond to the linear range of E_T values. The small bump in the forward neutral energy at high E_T values, seen in fig. 3, has yet to be understood. This same behaviour was seen in ^{197}Au+^{197}Au collisions at 11.7A GeV/c using the same apparatus [2]. If this bump persists at collider energies, a decrease in trigger efficiency for the most central events using zero-degree energy may be expected. From figs. 5 and 6 it can be seen that, as the transverse energy increases, the number of spectator nucleons N_S decreases and the probability p that a neutron emerges forward unbound increases, as expected.

References

[1] J. Barrette et al. (E814 Collaboration), Phys. Rev. C **52**, 956 (1995).
[2] Studies of forward neutral energy as a centrality trigger at a relativistic heavy ion

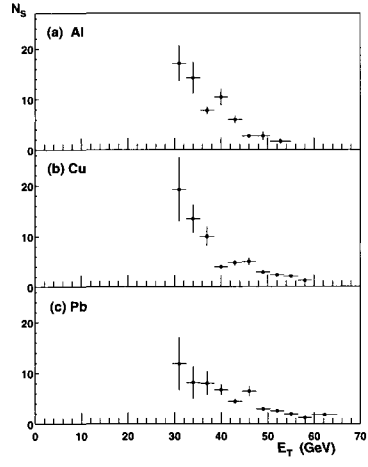

Figure 5. Parameter values from the fit of (3) to the neutron spectra obtained with (a) Al, (b) Cu, and (c) Pb targets. Here N_S is number of spectators.

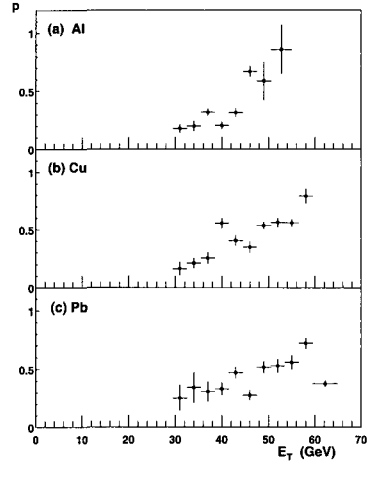

Figure 6. Parameter values from the fit of (3) to the neutron spectra obtained with (a) Al, (b) Cu, and (c) Pb targets. Here p is the probability that a spectator neutron emerges from the collision as a beam-rapidity neutron.

collider, M. Clemen et al., PITT/RHI 97-1, unpublished.
[3] Study of Extremely Peripheral Collisions and of the Transition from Peripheral to Central Collisions in Reactions Induced by Relativistic Heavy Ions, P. Braun-Munzinger et al., E814 proposal submitted to the AGS committee 56 (1985).
[4] J. Barrette et al. (E814 Collaboration), Phys. Rev. **C46**, 312, (1992).
[5] J. Simon-Gillo et al., Nucl. Instr. and Meth. **A309**, 427 (1991).
[6] M. Fatyga et al., Nucl. Instr. and Meth. **A284**, 323 (1989).
[7] J. Barrette et al. (E814 Collaboration), Phys. Rev. **C51**, 865, (1995).
[8] ROOT framework, http://root.cern.ch
[9] MINUIT - Function Minimization and Error Analysis, CERN Program Library entry D506.
[10] MAPLE V, Waterloo Maple Inc., http://www.maplesoft.com

Effective nucleon-nucleon interaction in the RPA

E.F. Batista,B.V. Carlson,C. De Conti and T. Frederico
Dep. de Física, ITA-CTA,S.J. dos Campos,S.P.

1 Introduction

The purpose of the present work is to study the properties of the effective nucleon-nucleon interaction, in a infinite system of mesons and baryons, using the relativistic Hartree-Fock-Bogoliubov approximation[1]. To derive the RHFB equations in a systematic fashion, we use Dyson's equation to sum to all orders the self-consistent tadpole and exchange contributions to the extended baryon Green's function (the Gorkov propagator). The meson propagator is computed as a sum over ring diagrams which consist in repeated insertions of the lowest-order proper polarization graph. The sum is the diagramatic equivalent of the relativistic random phase aproximation(RPA) that describes the well-known collective modes. In the nuclear medium, the σ and ω propagators are linked because of scalar-vector mixing, a density-dependent effect that generates a coupling between the Dyson's equation for the meson propagators. We use the dressed meson propagator to obtain the effective interaction and investigate its effect on the $^1S_0$ pairing in nuclear matter. The effective interaction has little effect on the self-energy mean field, since the latter is dominated by the Hartree contribution, which is determined by the free meson propagators. The pairing field, however, is obtained from an exchange term, in which the effective interaction can play an important role. As the polarization corrections to the meson propagators tend to increase the σ-meson mass and decrease the ω-meson mass, they result in an effective interaction which is more repulsive than the bare one. We would expect this to result in a decrease in the $^1S_0$ pairing, similar to that seen in nonrelativistic calculations[2].

2 The meson Propagator

To compute the meson propagators, we sum over ring diagrams, which consist of repeated insertions of the lowest-order one-loop proper polarization part. The sum yields the relativistic random phase approximation(RRPA). To include the $\sigma - \omega$ mixing it is convenient to use a meson propagator $\mathcal{D}_{ab}$ in the form of a 5 X 5 matrix where the indices a, b run from 1 to 5, with 5 refering to the σ channel and 1 to 4 to the ω channel.

Dyson's equation for the full propagator, $\mathcal{D}$, is given by

$$\mathcal{D}_{ad} = \mathcal{D}^0_{ad} + \mathcal{D}^0_{ab}\Pi_{bc}\mathcal{D}_{cd}, \tag{1}$$

where, $\mathcal{D}^0$ consists of the scalar-vector noninteracting propagators. The polarization insertion is given by,

$$\Pi_{ab}(q) = -i \int \frac{d^4k}{(2\pi)^4} Tr[\Gamma_a G(k)\Gamma_b G(k+q)]. \tag{2}$$

The collective modes can be obtained from the poles of $\mathcal{D}_{ab}$. Evaluating Eq.(1), we define the dieletric function ϵ as,

$$\epsilon = det(1 - \mathcal{D}^0\Pi). \tag{3}$$

Demanding $\epsilon = 0$, we obtain the eigencondition for determining the excitation spectra of the collective modes. The determinant can be factored into three pieces,

$$\epsilon(q) = \epsilon^2_T(q) \times \epsilon_L(q), \tag{4}$$

where,

$$\epsilon_T = 1 - D^0\Pi_T, \tag{5}$$

$$\epsilon_L = (1 - D^0\Pi_L)(1 - \Delta^0\Pi_S) - \frac{q^2_\mu}{q^2} D^0\Delta^0(\Pi^m_0)^2, \tag{6}$$

corresponding to the transverse and longitudinal dieletric function respectively. In the Eq.(6), the last term mixes the scalar and vector contributions. When this term is zero, the scalar and vector mesons decouple from each

other. The effective mass of the mesons in nuclear matter are obtained by diagonalizing the meson propagator,

$$(\mathcal{D}^{-1})^{\mu}{}_{\nu} = (q_{\rho}^2 - m_{ef}^2)\delta^{\mu}{}_{\nu} - \Pi^{\mu}{}_{\nu} \tag{7}$$

where we have,

$$\begin{aligned}
\Omega_T^2 &= q^2 - m_{\omega}^2 - \Pi^1{}_1 \\
\Omega_L^2 &= -\frac{E_{\sigma}^2 + E_{\omega}^2 + \Pi_L + \Pi_S \pm \sqrt{[E_{\sigma}^2 - E_{\omega}^2 + \Pi_S - \Pi_L]^2 - 4\Pi_m^2}}{2}
\end{aligned}$$

with, $E_{\sigma}^2 = q^2 + m_{\sigma}^2$, $E_{\omega}^2 = q^2 + m_{\omega}^2$ and Ω_T and Ω_L are the transverse and longitudinal collective modes respectively.

The meson masses in nuclear matter are modified by the collective modes. This results in a modified effective nucleon-nucleon interaction, which we intend to investigate in $^1S_0$ pairing.

Acknowledgments

E.F.B and C. De Conti acknowledge the support of FAPESP.
B.V.C. and T. Frederico acknowledge partial support from FAPESP and CNPq.

References

[1] F.B. Guimarães, B.V. Carlson and T. Frederico, Phys. Rev.**C54** (1996) 2385; F.B. Guimarães, B.V. Carlson and T. Frederico, Phys. Rev.**C56** (1997) 3097.

[2] T.L. Ainsworth, J. Wambach and D. Pines, Phys. Lett. **222B** (1989) 173; T.L. Ainsworth, J. Wambach and D. Pines, Nuc. Phys. **A555** (1993) 128; H.-J. Schultz, J. Cugnon, A. Lejeune, M. Baldo and U. Lombardo, Phys. Lett. **375B** (1996) 1.

B and D meson coupling constant and form factor calculations from QCD sum rules

M.E. Bracco [2],F.S. Navarra[1],M. Nielsen[1],M. Chiapparini[2] and C. L. Schat [2]
[1]*Instituto de Física, Universidade de São Paulo,*
C.P. 66318, 05389-970 São Paulo, SP, Brazil
[2]*Instituto de Física, Universidade do Estado do Rio de Janeiro,*
Rua São Francisco Xavier 524 - 20559-900, Rio de Janeiro, RJ, Brazil

Recent experiments at CERN SPS have shown an anomalously large suppession of J/Ψ production in central Pb+Pb collisions. The J/Ψ would be dissociated in quark-gluon plasma due to collor screening, the observed J/Ψ suppression in heavy ion collisions is one of the signatures of quark-gluon plasma (QGP)formation [1]. On the other hand, it has also been shown the J/Ψ absorption by comoving pions and ρ mesons is of fundamental importance. The reaction of $\pi + J/\psi \rightarrow D + \overline{D^*}$ and consequently the coupling $g_{D^*D\pi}$ are of special relevance [2]. Since bottomonium states in the QGP are also sensitive to the color screening effect, then the Υ suppression can be used as a signature for QGP as well. As in the case of J/Ψ , one needs to understand the effects of Υ absoption cross sections by pion mesons, in particular is needed the $g_{B^*B\pi}$ [3]. Also this coupling is particulary important since it can be helpfull in the analysis of the semileptonic decay $B \rightarrow \pi\, l\, \nu_l$. The $D^*D\pi$ and $B^*B\pi$ couplings have been studied by several authors using different approaches in Ref. [4–8]. Unfortunately, the numerical results from these calculations may differ by almost a factor two.

In this work we use the three-point function approach to evaluate the $D^*D\pi$ and $B^*B\pi$ form factors and coupling constants. The advantage of using the three-point function approach with a double Borel transformation compared with the two-point function with a single Borel transformation is the elimination of the terms associated with the pole-continuum transitions [9]. The three-point function associated with a $H^*H\pi$ vertex, where H and H^* are respectively the lowest pseudoscalar and vector heavy mesons, is given by

$$\Gamma_\mu(p,p') = \int d^4x\, d^4y\, \langle 0|T\{j(x) j_5(y) j_\mu^\dagger(0)\}|0\rangle \; e^{ip'.x}\, e^{-i(p'-p).y}\,, \tag{1}$$

where $j = i\bar{Q}\gamma_5 u$, $j_5 = i\bar{u}\gamma_5 d$ and $j_\mu^\dagger = \bar{d}\gamma_\mu Q$ are the interpolating fields for H, π^- and H^* respectively with u, d and Q being the up, down, and heavy quark fields.

The phenomenological side of the vertex function, $\Gamma_\mu(p,p')$, is obtained by the consideration of H and H^* state contribution to the matrix element in Eq. (1):

$$\Gamma_\mu^{(phen)}(p,p') = \frac{1}{p^2 - m_{H^*}^2}\frac{1}{p'^2 - m_H^2}\langle 0|j|H(p')\rangle \times \langle H(p')|j_5|H^*(p,\epsilon)\rangle\langle H^*(p,\epsilon)|j_\mu^\dagger|0\rangle + \text{higher res.}\,. \tag{2}$$

The matrix element of the pseudoscalar element, j_5, defines the vertex form factor $g_{H^*H\pi}(q^2)$:

$$\langle H(p')|j_5|H^*(p,\epsilon)\rangle = \frac{f_\pi m_\pi^2}{m_u + m_d}\frac{g_{H^*H\pi}(q^2)}{q^2 - m_\pi^2} q_\nu \epsilon^\nu\,, \tag{3}$$

where $q = p' - p$, f_π is the pion decay constant and ϵ^ν is the polarization of the vector meson. The vacuum to meson transition amplitudes appearing in Eq. (2) are given in terms of the corresponding meson decay constants f_H and f_{H^*} by $\langle 0|j|H(p')\rangle = \frac{m_H^2 f_H}{m_Q}$, and $\langle H^*(p,\epsilon)|j_\mu^\dagger|0\rangle = m_{H^*} f_{H^*} \epsilon_\mu^*$. Therefore, using Eq. (3) and the expressions for f_H and f_{H^*} in Eq. (2) we get

$$\Gamma_\mu^{(phen)}(p,p') = C_{HH^*} \frac{g_{H^*H\pi}(q^2)}{q^2 - m_\pi^2} \frac{1}{p^2 - m_{H^*}^2} \frac{1}{p'^2 - m_H^2} \left(-p'_\mu + \frac{m_{H^*}^2 + m_H^2 - q^2}{2m_{H^*}^2} p_\mu \right) + \text{higher res.} , \quad (4)$$

where $C_{HH^*} = \frac{m_H^2 m_{H^*} m_\pi^2 f_H f_{H^*} f_\pi}{(m_u + m_d) m_Q}$.

The QCD side, or theoretical side, of the vertex function is evaluated by performing Wilson's operator product expansion (OPE) of the operator in Eq. (1). Writing Γ_μ in terms of the invariant amplitudes:

$$\Gamma_\mu(p,p') = \Gamma_1(p^2,p'^2,q^2) p_\mu + \Gamma_2(p^2,p'^2,q^2) p'_\mu , \quad (5)$$

we can write a double dispersion relation for each one of the invariant amplitudes $\Gamma_i\,(i = 1,2)$, over the virtualities p^2 and p'^2 holding $Q^2 = -q^2$ fixed:

$$\Gamma_i(p^2,p'^2,Q^2) = -\frac{1}{4\pi^2} \int_{m_Q^2}^\infty ds \int_{m_Q^2}^\infty du \frac{\rho_i(s,u,Q^2)}{(s-p^2)(u-p'^2)} , \quad (6)$$

where $\rho_i(s,u,Q^2)$ equals the double discontinuity of the amplitude $\Gamma_i(p^2,p'^2,Q^2)$ on the cuts $m_Q^2 \le s \le \infty$, $m_Q^2 \le u \le \infty$, which can be evaluated using Cutkosky's rules [10].

Finally we perform a double Borel transformation in both variables $P^2 = -p^2 \to M^2$ and $P'^2 = -p'^2 \to M'^2$ and equate the two representations described above. We get one sum rule for each invariant function. In this paper we focus on the structure p_μ, which we found to be the more stable one, and study the sum rule as a function of M^2 at a fixed ratio: $M^2/M'^2 = m_{H^*}^2/m_H^2$. We will consider diagrams up to dimension four which include the perturbative diagram and the gluon condensate. The quark condensate term does not contribute since it depends only on one external momentum and, therefore, it is eliminated by the double Borel transformation.

The parameter values used in all calculations are $m_u + m_d = 14$ MeV, $m_c = 1.5$ GeV, $m_b = 4.7$ GeV, $m_\pi = 140$ MeV, $m_D = 1.87$ GeV, $m_{D^*} = 2.01$ GeV, $m_B = 5.28$ GeV, $m_{B^*} = 5.33$ GeV, $f_\pi = 131.5$ MeV, $\langle \bar{q}q \rangle = -(0.23)^3$ GeV^3, $\langle g^2 G^2 \rangle = 0.5$ GeV^4. The continuum thresholds for the sum rule are of order $s_0 = (m_{H^*} + \Delta_s)^2$ and $u_0 = (m_H + \Delta_u)^2$ with $\Delta_s \sim \Delta_u \sim 0.5$ GeV. In our study we will allow for a small variation in Δ_s and Δ_u to test the sensitivity of our results to the continuum contribution. We first discuss the $D^* D\pi$ form factor. We find that the perturbative and gluon condensate contribuit to a rigth stability of the curve, as a function of M^2, providing a rather stable plateau for $M^2 \ge 3$ GeV^2. Fixing $M^2 = 3.5$ GeV^2 we evaluate the momentum dependence of the form factor. Since the present approach cannot be used at $Q^2 = 0$, to extract the $g_{D^* D\pi}$ coupling from the form factor we need to extrapolate the curve to $Q^2 = 0$ (in the approximation $m_\pi^2 = 0$). In order to do this extrapolation we fit the QCD sum rule results with an analytical expression. We tried to fit our results with

a monopole form, since this is very often used for form factors, but the fit is very poor. We obtained good fits using both the gaussian form

$$g_{H^*H\pi}(Q^2) = g_{H^*H\pi}\, e^{-(Q^2+m_\pi^2)^2/\Gamma^4} \qquad (7)$$

and a curve of the form

$$g_{H^*H\pi}(Q^2) = g_{H^*H\pi}\frac{1+(a/\Lambda)^4}{1+(a/\Lambda)^4 e^{(Q^2+m_\pi^2)^2/\Lambda^4}} \; . \qquad (8)$$

The Q^2 dependence of the form factor can be well reproduced by the parametrization in Eqs. (7) and (8). The value of the parameters in Eqs. (7) and (8) are given in Table I for two different values of the continuum threshold.

$\Delta_s = \Delta_u$ (GeV)	$g_{D^*D\pi}$	Λ (GeV)	a (GeV)	Γ (GeV)
0.5	5.3	1.66	1.90	-
0.6	6.0	1.89	3.05	-
0.5	5.7	-	-	1.74
0.6	6.1	-	-	1.92

TABLE I: Values of the parameters in Eqs. (7) and (8)which reproduce the QCDSR results for $g_{D^*D\pi}(Q^2)$, for two different values of the continuum thresholds.

To test if our fit gives a good extrapolation to $Q^2 = 0$ we can write a sum rule, based on the three-point function Eq. (1), but valid only at $Q^2 = 0$, as suggested in [11] for the pion-nucleon coupling constant. This method was also applied to the nucleon-hyperon-kaon coupling constant [12,13] and to the nucleon$-\Lambda_c - D$ coupling constant [14]. It consists in neglecting the pion mass in the denominator of Eq. (4) and working at $Q^2 = 0$, making a single Borel transformation to both $P^2 = P'^2 \to M^2$. As discussed in the introduction, the problem of doing a single Borel transformation is the fact that the single pole contribution, associated with the $N \to N^*$ transition, is not suppressed [4]. The single pole contribution can be taken into account through the introduction of a parameter A, in the phenomenological side of the sum rule [5,8]. Thus, neglecting m_π^2 in the denominator of Eq. (4) and doing a single Borel transform in $P^2 = P'^2$, we get for the structure p_μ

$$\tilde{\Gamma}_1^{(phen)} = -\frac{C_{H^*H}}{2m_H^2 Q^2}\frac{m_H^2 + m_{H^*}^2 + Q^2}{m_{H^*}^2 - m_H^2}(e^{-m_H^2/M^2} - e^{-m_{H^*}^2/M^2})(g_{H^*H\pi} + AM^2) \; , \qquad (9)$$

where C_{H^*H} in given after Eq.(4) with f_H and f_{H^*} given by a trivial calculation. On the OPE side only terms proportional to $1/Q^2$ will contribute to the sum rule. Therefore, up to dimension four the only diagram that contributes is the quark condensate given by

$$\tilde{\Gamma}_1^{<\bar{q}q>}(M^2, Q^2) = \frac{2m_Q\langle\bar{q}q\rangle}{Q^2}\, e^{-m_Q^2/M^2} \; . \qquad (10)$$

Equating Eqs. (9) and (10) and taking $Q^2 = 0$ we obtain the sum rule for $g_{H^*H\pi} + AM^2$, where A denotes the contribution from the unknown single poles terms. Analysing the QCDSR results for $g_{D^*D\pi} + AM^2$ as a function of M^2 [15] we found that in the Borel region $2 \leq M^2 \leq 5$ GeV^2, they follow a straight line. The value of the coupling constant is obtained by the extrapolation of the line to $M^2 = 0$ [15]. Fitting the QCDSR results to a straight line we get [15] $g_{D^*D\pi} \simeq 5.4$, in excellent agreement with the values obtained with the extrapolation of the form factor to $Q^2 = 0$, given in Table I. It is reassuring that both methods, with completely different OPE sides and Borel transformation approaches, give the same value for the coupling

constant. In the case of $B^*B\pi$ vertex, the $Q^2 = 0$ sum rule results for $g_{B^*B\pi} + AM^2$ as a function of M^2. It also follows a straight line in the Borel region $10 \leq M^2 \leq 25$ GeV^2, and the extrapolation to $M^2 = 0$ gives $g_{B^*B\pi} \simeq 10.6$. Here the perturbative and gluon condensate have a small contribuition but it still goes in the right direction of providing a stable plateau for $M^2 \geq 15$ GeV^2. Fixing $M^2 = 17$ GeV^2 we evaluate the form factor. The fit with Eq. (7) is not so good [15]. In Table II we give the value of the parameters in Eqs. (7) and (8) that reproduce our results for two different choices of the continuum thresholds. In this case the agreement of the two different approaches to extract the coupling constant is not so good, but the numbers are still compatible. One possible reason for that is the fact that for heavier quarks the perturbative contribution (or hard physics) becomes more important.

$\Delta_s = \Delta_u$ (GeV)	$g_{B^*B\pi}$	Λ (GeV)	a (GeV)	Γ (GeV)
0.5	14.7	1.62	1.37	-
0.6	16.3	1.81	1.67	-
0.5	17.2	-	-	1.79
0.6	18.4	-	-	1.97

TABLE II: Values of the parameters in Eqs. (7) and (8) which reproduce the QCDSR results for $g_{B^*B\pi}(Q^2)$, for two different values of the continuum thresholds.

In conclusion, we extracted the $H^*H\pi$ coupling constant using two different approaches of the QCDSR based on the three-point function. We have obtained for the coupling constants: $g_{D^*D\pi} = 5.7 \pm 0.4$, $g_{B^*B\pi} = 14.5 \pm 3.9$, where the errors reflect variations in the continuum thresholds, different parametrizations of the form factors and the use of two different sum rules. There are still sources of errors in the values of the condensates and in the choice of the Borel mass to extract the form factor, which were not considered here. Therefore, the errors quoted are probably underestimated.

[1] T. Matsui and H. Satz, *Phys. Lett.* **B178**, 416 (1986).

[2] S.G. Matinyan and B. Müller, *Phys. Rev.* **C58**, 2994 (1998).

[3] Z. Lin and C.M. Ko, nucl-th/0007027.

[4] P. Colangelo et al., *Phys. Lett.* **B339**, 151 (1994); V.L. Eletsky and Ya.I. Kogan, *Z. Phys.* **C28**, 155 (1985); A.A. Ovchinnikov, *Sov. J. Nucl. Phys.* **50**, 519 (1989).

[5] V.M. Belyaev et al., *Phys. Rev.* **D51**, 6177 (1995).

[6] A. Khodjamirian et al., *Phys. Lett.* **B457**, 25 (1999).

[7] A.G. Grozin and O.I. Yakovlev, *Eur. Phys. J.* **C2**, 721 (1998).

[8] H.G. Dosch and S. Narison, *Phys. Lett.* **B368**, 163 (1996).

[9] B.L. Ioffe and A.V. Smilga, *Nucl. Phys.* **B216** 373 (1983); *Phys. Lett.* **B114**, 353 (1982).

[10] R.E. Cutkosky, *J. Math Phys.* **1**, 429 (1960).

[11] L.J. Reinders, H. Rubinstein and S. Yazaki, *Phys. Rep.* **127**, 1 (1985).

[12] S. Choe, M.K. Cheoun and S.H. Lee, *Phys. Rev.* **C53**, 1363 (1996); S. Choe, *Phys. Rev.* **C57**,2061 (1998).

[13] M.E. Bracco, F.S. Navarra and M. Nielsen, *Phys. Lett.* **B454**, 346 (1999).

[14] F.S. Navarra and M. Nielsen, *Phys. Lett.* **B443**, 285 (1998).

[15] F.S. Navarra, M. Nielsen, M.E. Bracco, M. Chiapparini and C.L. Schat,*Phys. Lett.***B489**, (2000),319-328.

Quantum contributions for the temporal evolution of non homogeneous configurations of the $\lambda\phi^4$ model

Fábio L. Braghin*and F.S. Navarra†
Instituto de Física da Universidade de São Paulo
C.P. 66.318, C.E.P. 05315-970, São Paulo, Brasil

ABSTRACT

Using a time dependent gaussian approach for zero temperature $\lambda\phi^4$ model the temporal evolution of non homogenous configurations is studied in a lattice of 1+1 dimensions. The scalar field is decomposed into classical and quantum parts which evolve associatedly. A dynamical phase transition (not in the thermodynamical sense) is observed due to initial non-equilibrium conditions.

PACS numbers: 11.30.Qc; 11.10.-z; 11.15.Tk; 11.90.+t

1 INTRODUCTION AND EQUATIONS OF MOVEMENT

It is well known there are many motivations for the study of time dependent and independent non perturbative methods in Quantum Field Theory (QFT). In particular, the study of phase transitions[1] from a dynamical point of view can also be contemplated with a suitable formalism for non-equilibrium initial conditions and systems. Some physical examples of localized highly energetic configurations are found in the Relativistic Heavy Ion Collisions (several experiments are currently being prepared/executed in CERN and LBL) which intend to probe hadronic matter at very high excitation energies (densities and temperatures). In these cases a very high energy density region starts expanding (and cooling) after the collision.

Due to the extreme complexity of realistic theories, as QCD, one usually is lead to study effective models which respects the major properties of the fundamental theory and reproduces the main issues of it in some range of a relevant variable (as energy or density). In the present work, however, a still more simplified version of the reality is considered just in order to check qualitative effects by means of the $\lambda\phi^4$ model. Many times it is considered as a test model, although its scalar field may be considered as the relevant degree of freedom for inflationnary models in Cosmology.[2] Several related question can be addressed in the experiments performed in large colliders as, for instance, the particle-anti-particle production which must have happened in the early stages of Universe, including the baryon-anti-baryon asymmetry observed nowadays.[2] These two effects, seemingly so different, may be related to each other and have deeper common origin which could explain the so large matter-anti- matter asymmetry in the observed Universe [1].

*braghin@if.usp.br
†navarra@if.usp.br

[1] In fact, there may exist other explanations for this. For example, Lorentz covariance is broken somewhere in the Physical micro to macro scales, this may yield different interactions and properties for the matter from the anti-matter, and either make the latter

In the last decade a quite large amout of work have been done in order to shed light in some of the above mentioned subjects. In the frame of a (out of equilibrium) time dependent Hartree Fock Bogoliubov, which is used in the present work, several works were done in continuous and discretized space-time, for example see.[1,5–7] In this last work the contribution of quantum effects to the expanding localized energetic classical configuration was studied "self consistently". Among other several different effects, here we point out the attention of the reader for the resembling a phase transition shown in,[6] where the existence of a non-equilibrium (in principle, not in the thermodynamical sense) initial condition makes the system undergo a symmetry restoration. This make the condensate to oscillate around a "symmetrical potential"- see figures 1b, 2b and 4a from this last work and in.[8,3] This was precluded, for example, in[1] and used somehow by de Vega and Boyanovsky and others.

In the present work we study non homogeneous numerical evolution of the $\lambda\phi^4$ in the frame of the gaussian approach for out of equilibrium initial conditions in a lattice of 1+1 dimensions. The Hamiltonian density is given by:

$$H = \frac{1}{2}\left(\pi^2(\mathbf{x}) + (\boldsymbol{\nabla}\phi(\mathbf{x}))^2 + m_0^2\phi^2(\mathbf{x}) + \frac{\lambda}{12}\phi^4(\mathbf{x})\right). \tag{1}$$

For the time dependent variational method in the Schrodinger picture stated in[9] an averaged action I is calculated with trial gaussian wave functionals. These trial functionals are parametrized in terms of variational parameters. In our case, we consider the two-point Green's function $G(x,y,t)$ which is a measure of the quantum fluctuations, a conjugated variable $\Sigma(x,y,t)$ associated to the imaginary part of the wave functional and, for the system in the asymmetric phase, the classical part $\bar{\phi}(x,t)$ and its conjugated momentum $\bar{\pi}(x,t)$. The equations can then be calculated by the variations[10,1]:

$$\frac{\delta I}{\delta\Sigma(\mathbf{x},\mathbf{y},t)} \quad \frac{\delta I}{\delta G(\mathbf{x},\mathbf{y},t)} \quad \frac{\delta I}{\delta\bar{\pi}(\mathbf{x},t)} \quad \frac{\delta I}{\delta\bar{\phi}(\mathbf{x},t)}. \tag{2}$$

As remarked before the quartic interaction enters into a self consistent mass ("mean field"). It still is worth to recall that this approach treats quantum fluctuations in a mean field fashion. Their average contribute as real numbers for the equations of movement and observables. This makes it to break the particle number violation among other symmetries of the system. This approach also endows the system with a consistent frame for the description of the spontaneously symmetry breaking. The condensate-classical part of the field- has a non zero value in the vacuum $\pm\bar{\phi}_0$ in a mexican hat-type potential. This picture of (effective) potential, however, is valid only for static situations. In this work, the equations of movement are evolved in a lattice of 100 points with 10 fm.

2 RESULTS

In the Figures 1a and 1b

expand too fast outer of the observed universe or decay in other ((un)known or undetected) particles.[3] As the photons may probably be viewed as the Goldstone Bosons of the Spontaneously Covariant Symmetry Breaking[4] this may indicate a preference of Nature for "matter-like" vacua states rather than for "anti-matter-like" vacua states.

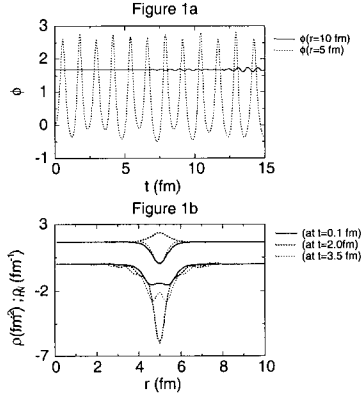

a) Evolution of the profile condensate in two different points of the lattice: at r=5fm (dotted line) and r=10fm (solid line) for a coupling constant of $b = 60fm^{-2}$ and mass $\mu = 50MeV$. b) In the lower part it is seen the potential energy density configuration for different time values ($t = 0.1fm$ solid line, $t = 2.fm$ the thick dotted line, $t = 3.5$ the thin dotted line). In the upper part the particle number density for the same time values.

the temporal evolution of the condensate without quantum fluctuations is shown for the coupling constant $\lambda = 6fm^{-2}$ and physical mass $\mu = 450MeV$. As initial condition it was considered a static profile with the following form for the classical field:

$$\bar{\phi}(r, t = 0) = \bar{\phi}_0(r) tanh^2 \left(\frac{r - r_0}{0.5} \right), \tag{3}$$

where $\bar{\phi}_0$ is the value of the condensate in the vacuum. This corresponds to a "bubble" of high energy centered in the point r_0 of the lattice. In 1a the field profiles ($\bar{\phi}$) of two points of the lattice (r=5fm and r=10fm) are shown. The condensate at the central point $\bar{\phi}(r = 5, t)$ oscillate fastly during the time with a (very slowly) diminishing amplitude. As the total energy excess in this point "expands" towards the extremes of the lattice the field profile at the extreme $\bar{\phi}(r = 10, t)$ starts ot oscillate with very small amplitude. This analysis is not yet done for large times intervals of evolution, that will be shown elsewhere.[3] In figure 1b it is shown the average particle number (ρ_N, the total particle number being not conserved in this approach) in the upper part and the potential energy at time steps $t = 0.1fm$, $t = 2.0fm$ and $t = 3.5fm$ in the lower part. The distribution of the potential energy - that not associated to $\dot{\bar{\phi}}$, centered in the point r_0 to the extremes of the lattice, seems to happen done quite slowly.

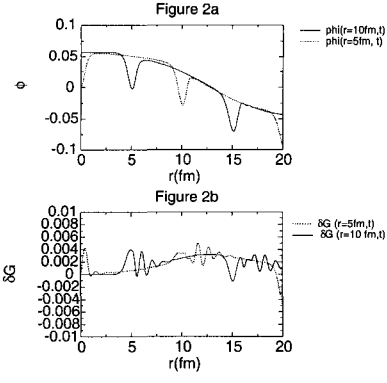

a) The same as Figure 1a) taking into account the quantum fluctuations. b) The deviation of the quantum fluctuations from the value in the vacuum $\delta G(r,t) = G(r,t) - G_0$ at $r = 5, 10$ fm.

The contribution of the quantum part within the method quoted above for the field profile can be seen in part in figures 2a and 2b for $\lambda = 60fm^{-2}$ and $\mu = 50MeV$. In spite of the differences between the parameters of the two worked examples, we have control that the main effect is caused by the switch on of the quantum fluctuations which are larger for smaller masses and higher coupling constants. Otherwise, the field and density are changed by a overall normalization. The classical part of the field in the centre of the lattice (dotted line) as well as in one extremity (solid line). Following the field profile in the extremity of the lattice it is interesting to show that at the initial time $t = 0$ it has the value of the condensate in the vacuum ϕ_0. As the time evolves, it starts to oscillate: firstly in the positive side of the potential and when $t \simeq 12 - 13fm$ the field seems to pass to the other side of the potential in this point (this also happen for the central point of the lattice in the present case-dotted line, but it is not necessarily simultaneous for the other regions). As a matter of fact instead of this "tunnelling" (which may likely have something to do with the instantons also present in the $\lambda\phi^4$ model) there is another possibility: due to the initial condition (that of expression (3)) there may be occuring a dynamical phase transition which restores the symmetry from the mexican-hat potential-type to a (more) symmetrical one- these points are under (and deserves) further attention.[3] One fact is certain: this effect can be clearly attributed to the quantum fluctuations and to the initial condition.

In figure 2b the deviation of the quantum fluctuations from value in the vacuum $\delta G = G(r,t) - G_0$ at the same points of the lattice as figure 2a are shown. Both points oscillates in different ways, showing the energy transfer from the initially "energetic classical part" of the total energy to the quantum part contribution.

3 Summary

The temporal evolution of non-homogeneous configurations of the $\lambda\phi^4$ model considering the gaussian approach for the quantum fluctuations in a one-dimensional lattice was investigated in this work. I have been able to study the influence of the quantum fluctuations on the classical field dynamics as well as the opposite effect. The energy is transfered from one degree of freedom to another in a way which depends on the parameters of the model and also on the initial conditions. The scalar field profile function has been shown and when the quantum fluctuations are introduced the oscillations in the extremity of the lattice occur much earlier than in the purely classical case.

Furthermore, quantum fluctuations introduce a new qualitative effect which may have two different explanations: there can occur a *"tunnelling" of the field* from one side of the mexican hat potential to the other **or** there can happen a *symmetry restoration* due to the non homogeneous initial conditions, being a non thermodynamical phase transition as discussed in.[7,3] In spite of being a pure states formalism it allows for out of equilibrium initial conditions. Thus it would be interesting to implement the fully consistent finite temperature formalism for the numerical evolution of the equations of mouvement.

We have been concerned mainly with short time intervals evolution, but the longstanding problem of the possible "dissipation" of the quantum degrees of freedom into classical/thermal effects. This question arises other possible effects as the influence of the discretization and finite size of space in lattices as well as the appearance of dissipation in systems without "dissipative interactions". It would also be interesting to perform a Fourier transformation of the above results in order to obtain the energy spectra of the respective systems and compare with each other.

Acknowledgements
This work was supported by FAPESP- Brazil. F.L.B. wishes to thank D. Vautherin with whom part of this work was initiated, A. Abada with whom F.L.B. had useful discussions concerning numerical methods and F.S. Navarra for discussions concerning hydrodynamical models and related questions. Most part of the numerical calculations was performed in the machines of the Laboratory for Computation of the University of São Paulo - LCCA-USP.

4 REFERENCES

[1] F.L. Braghin, *Doctoral Thesis*, DPT- IPN Orsay- France, 1995.

[2] F.L. Braghin, *under development.*

[3] F.L. Braghin, *in preparation.*

[4] I apologise I do not rememeber the reference, neither the name or place, of the famous Japanese researcher who showed this SSB. Probably in the mid 80's.

[5] F.L. Braghin, Phys. Rev.**D 57**, 3548, (1998).

[6] F.L. Braghin, in *International Workshop on Hadron Physics 2000*, São Paulo, Brazil, April 2000, ed. by F.S. Navarra, World Scientific.

[7] F.L. Braghin and F.S. Navarra, *in preparation.*

[8] F.L. Braghin, in *Encontro Nacional de Física de Partículas e Teoria de Campos*, São Paulo, Brazil, October 2000, ed. by M. Menon, SBF-Brazil.

[9] R. Jackiw and A. Kerman, Phys. Lett. **A 71** (1979) 158.

[10] F. Cooper and E. Mottola, Phys. Rev. **D36** (1987) 3114; O. Éboli, R. Jackiw and So Young Pi, Phys. Rev. **D37** 3557, (1988); J. Baacke, K. Heitmann, C. Pätzold, Phys. Rev. **D 576**406, (1989).

QCD Sum Rules for Heavy Λ Semileptonic Decays

R.S. Marques de Carvalho and M. Nielsen
Instituto de Física - Universidade de São Paulo
São Paulo - SP

1 The $\Lambda_I \to \Lambda_F l\nu$ Decay

According to the QCDSR method, a $\Lambda_I \to \Lambda_F l\nu_l$ decay is represented by a three point correlation function [1],

$$\Pi_\mu(p_F, p_I) = i^2 \int d^4x d^4y \langle 0|T\{\eta_{\Lambda_F}(x) J_\mu(0) \overline{\eta}_{\Lambda_I}(y)\}|0\rangle e^{ip_F x} e^{-ip_I x}, \quad (1)$$

where η_{Λ_I} and η_{Λ_F} are the baryon interpolating fields and $J_\mu = \overline{Q}_F \gamma_\mu (1 - \gamma_5) Q_I$ is the weak current with the quarks fields Q_F and Q_I.

1.1 The Phenomenological Side

In the phenomenological side we get to the correlator

$$\begin{aligned} \Pi_\mu^{phen}(p_F, p_I) &= \frac{f_F \not{p}_F + f'_F}{p_F^2 - M_{\Lambda_F}^2} [\gamma_\mu (F_1^V + F_1^A \gamma_5) + i\sigma_{\mu\nu} q^\nu (F_2^V + F_2^A \gamma_5) \\ &\quad + q_\mu (F_3^V + F_3^A \gamma_5)] \frac{f_I \not{p}_I + f'_I}{p_I^2 - M_{\Lambda_I}^2}, \end{aligned} \quad (2)$$

where we have defined $f'_I = f_I M_{\Lambda_I}$ and $f'_F = f_F M_{\Lambda_F}$. From this equation we see that we can build four sum rules to each one of the form factors ($F_i^{V,A}$, where $i = 1, 2, 3$).

1.2 The QCD Side

The QCD side is obtained when we make the Operator Product Expansion (OPE) of the correlator and take the expectation value with respect to the physical vacuum. In order to construct the theoretical amplitude, we choose the interpolating field of the heavy lambda, Λ_H as

$$\eta_{\Lambda_H} = \epsilon_{abc}[(u_a^t C\gamma^5 d_b)Q_c + B(u_a^t C d_b)\gamma^5 Q_c], \tag{3}$$

where Q represents the heavy quark. This is a generalization of the work done in [1] where it was considered $B = 0$, where B is a parameter of admixture of the two possible fields with the quantum numbers of Λ_H. Proceeding in this way, we can build and calculate the corresponding diagrams of the correlator.

1.3 The Sum Rule

We can write a double dispersion relation of the form:

$$f_I^{(\prime)} f_F^{(\prime)} \frac{F_i^{V,A}(t)}{(s - M^2_{\Lambda_I})(u - M_{\Lambda_F^2})} = \frac{1}{\pi^2}\int_{m_I^2}^{\infty} ds' \int_{m_F^2}^{\infty} du' \frac{\rho_{ibc}^{V,A}(s', u', t')}{(s' - s)(u' - u)} + ... \tag{4}$$

where $-4\rho_{ibc}^{V,A}(s, u, t)$ is the double discontinuity of the amplitude $\frac{F_i^{V,A}(t)}{(s-M^2_{\Lambda_I})(u-M_{\Lambda_F^2})}$ and $t = q^2$. The dots are subtraction polinomials in s and u, which will vanish under the double Borel transform [2]. Applying the double Borel transform to Eq.(4) and subtracting the continuum contribution we get

$$\begin{aligned} F_i^{V,A}(t) f_I^{(\prime)} f_F^{(\prime)} e^{-\frac{M^2_{\Lambda_I}}{M_I^2}} e^{-\frac{M^2_{\Lambda_F}}{M_F^2}} &= \frac{1}{\pi^2}\int_{m_I^2}^{\infty} ds' \int_{m_F^2}^{\infty} du'\, R_{cont}(s', u', s_0, u_0) \\ &\quad \times \rho_{ibc}^{V,A}(s', u', t) e^{-\frac{s'}{M_I^2}} e^{-\frac{u'}{M_F^2}}, \end{aligned} \tag{5}$$

where M_I^2 and M_F^2 are the Borel parameters and $R_{cont}(s', u', s_0, u_0)$ defines the continuum model with the thresholds (s_0 for Λ_I and u_0 for Λ_F) obtained from mass sum rules.

In the OPE side we can evaluate the double discontinuity of the amplitude, by using the Cutkosky's rules. With these quantities, we can obtain the form factors.

2 Results

2.1 The $\Lambda_b \to \Lambda_c l \nu_l$ Decay

We observed that the best results for the mass sum rules are obtained with $0 \leq B_{b(c)} \leq 0.1$. The results for the form factor almost don't change for $B_{b(c)}$ kept in the region $0 \leq B_{b(c)} \leq 0.1$, showing a very good stability of the results with the choice of the interpolating field. The first term in eq.(3) is the dominant one, so, all the calculations can be done using $B_{b(c)} = 0$.

Using the sum rules that contain the $f_b f_c$ structure we get the general result

$$F_1^A(t) = -F_1^V(t) \ , \quad F_2^V(t) = F_3^V(t) = F_2^A(t) = F_3^A(t) = 0. \tag{6}$$

Having the form factor we can calculate the decay width. Using $V_{cb} = 0.04$, we get

$$\Gamma(\Lambda_b \to \Lambda_c l \nu_l) = (3.3 \pm 1.1) \times 10^{-14} \text{ GeV}. \tag{7}$$

This result agrees with the experimental upper limit [3],

$$\Gamma(\Lambda_b \to \Lambda_c^+ + l + \overline{\nu}_l + \text{anything}) = (4.4 \pm 1.8) \times 10^{-14} \text{ GeV}. \tag{8}$$

2.2 The $\Lambda_c \to \Lambda l \nu_l$ Decay

In this case, we considered $B_{c(s)} = 0$. We first analyse the Λ mass sum rule. As to Λ_b, we observed a very good stability with the Borel Mass. To the form factors, we can observe that the region in the Borel mass where the perturbative and non-perturbative contributions are in equilibrium is above 4 GeV^2. The importance of the four-quark condensate is much larger in Λ_c than in Λ_b decay.

The t-dependence of the form factor F_1^V can be fitted as a pole, and in the structure $f_c f_s$, they are related as shown in eq.6. If we use the triangular region instead of the rectangular region for the continuum we obtain larger values for the form factor.

Using the form factors obtained for the determination of the continuum threshold for Λ_c and $V_{cs} = 0.975$, we get for the decay width

$$\Gamma(\Lambda_c \to \Lambda l \nu_l) = (8.7 \pm 1.2) \times 10^{-14} \text{ GeV}. \tag{9}$$

Within the errors the above result agrees with the reported experimental value [3]

$$\Gamma_{\rm exp}(\Lambda_c \to \Lambda l \nu_l) = (6.3 \pm 1.9) \times 10^{-14}\ {\rm GeV}\ . \qquad (10)$$

2.3 The $\Lambda_b \to p l \nu_l$ Decay

This decay was recently studied in the partial HQET framework [4] with result $\Gamma(\Lambda_b \to p l \nu_l) = (1.43 \pm 0.07) \times 10^{-11} |V_{ub}|^2 {\rm GeV}$.

Our results for the proton mass and form factor as functions of the Borel mass are very similar to the ones obtained for the Λ_c decay, being only a little less stable. The region in the Borel mass where the perturbative and non-perturbative contributions to the form factor are in equilibrium is above 3 GeV^2. Therefore, we evaluate the sum rules at $M_F^2 = 3$ GeV^2 which give $M_{Mp}^2 \simeq 1.5$ GeV^2 and $M_{Mb}^2 \simeq 18$ GeV^2 for the value of the Borel parameters in the mass sum rules of the proton and Λ_b respectively.

Using also either the rectangular or the triangular region for the continuum contribution we obtain

$$\Gamma(\Lambda_b \to p l \nu_l) = (1.7 \pm 0.7) \times 10^{-11} |V_{ub}|^2 {\rm GeV}\ , \qquad (11)$$

in agreement with the result of the HQET calculation [5].

This work was partially supported by CNPq.

References

[1] R.S. Marques de Carvalho, F.S. Navarra, M. Nielsen, E. Ferreira, and H.G. Dosch. *Phys. Rev.*, D60, 034009, (1999).

[2] B.L. Ioffe and A.V. Smilga. *Nucl. Phys.*, B216, 373, (1983); *Phys. Lett.*, B114, 353, (1982).

[3] Particle Data Group. *Eur. Phys. Jour.*, C3, 1, (1998).

[4] C.-S. Huang, C.-F. Qiao, and H.-G. Yan. *Phys. Lett.*, B437, 403, (1998).

[5] P. Ball and V.M. Braun. *Phys. Rev.*, D55, 5561, (1997).

Non perturbative Quantum Field Methods in Bose Einstein Condensates

Frederico F. de Souza Cruz[1], Marcus B. Pinto[1] and Rudnei O. Ramos[2,3]
[1]Universidade Federal de Santa Catarina, 88040-900 Florianópolis, SC, Brazil
[2]Department of Physics and Astronomy, Dartmouth College,Hanover, NH 03755-3528
[3]Universidade do Estado do Rio de Janeiro, 20550-013 Rio de Janeiro, RJ, Brazil

ABSTRACT

We apply the nonperturbative optimized linear δ expansion method to the $O(N)$ scalar field model in three-dimensions to determine the transition temperature of a dilute homogeneous Bose gas.

1 Introduction

The experimental realization of the Bose-Einstein condensation in dilute atomic gases has greatly stimulated an enormous number of theoretical studies in this field (for recent reviews on the theory and experiments, see for instance, Refs.[1,2]). Most of this interest comes from the fact that in these experiments a great deal of control can be achieved in almost every parameter of the system. Thus, experiments in dilute Bose gases provide a perfect ground to test inumerous models and ideas, as for example those commonly used in quantum field theory, applied to non-relativistic systems. In particular, a theoretical study which has attracted some attention very recently is the determination of the behavior of the transition temperature in the presence of a repulsive interaction. This non trivial problem has been treated by different methods with different results. Taking a dilute bose gas, with a repulsive interaction characterized by the scattering length parameter a, the dependence on a for the difference between the critical temperature with and without interaction $(\Delta T/T_c = (T_c - T_c^0)/T_c)$ is a highly controversial point, be with respect to the functional dependence on a or even regarding the sign.[3] An early Hartree Fock calculation[4] with a non delta interaction gave a negative sign for ΔT. This very same sign was also obtained by Toyoda[5] using one loop renormalization group. However we should mention that this sign is doubted by Huang[6] and a more recent renormalization group calculation going beyond one loop expansion yields a positive sign and a functional dependence as $\Delta T/T_c = \gamma\left(a^3 n\right)^{1/6}$ where n is the density . Grü ter, Ceperley and Laloe[8] and Holzmann and Krauth[9] investigated the dependence of ΔT numerically using Monte Carlo methods. They obtained ,in the low density limit, a dependence of the type $\Delta T/T_c = \gamma\left(a^3 n\right)^{1/3}$ but with different values for γ. The main reason for the multitude of results and methods stem from the fact that at transition temperature ordinary perturbation theory fails (due to infrared divergences) and we must resort to non perturbative methods. That is, we can truncate the series but sum up an infinite subset of diagrams.

The authors in Ref.[11] use a self-consistent calculation obtaining $\Delta T_c/T_c = \gamma a n^{1/3}$, with $\gamma \simeq 2.9$. The nonperturbative $1/N$ method has been also used to determine the shift. Its leading order contribution has been evaluated by Baym, Blaizot and Zinn-Justin[12] who obtain $\Delta T_c/T_c = \gamma a n^{1/3}$, with $\gamma \simeq 2.33$ for $N = 2$. Considering the next to leading order term, Arnold and Tomásik,[13] determine a correction to this large-N expansion, obtaining a value for $\Delta T_c/T_c$ which is $\sim 26\%$ smaller. The results obtained by Baym et al.[11] and

Bijlsma and Stoof[7] were compared whith temperature transition data in the Vycor-^4He system by Reppy et al.[10] Those experiments seem to give a somewhat larger value for the constant γ, as $\gamma \sim 5$.[10] This value is close to $\gamma \simeq 4.66$ which is the one obtained in Ref.,[7] with renormalization group techniques. Nevertheless some authors argue that this system would not exactly correspond to a dilute bose gas of hard spheres.[13] In this paper we apply the nonperturbative linear δ expansion (or optimized perturbation theory)[14] (for earlier references see, *e.g.*,[15]) to an effective model for dilute homogeneous Bose gases. This approximation has been shown to be a powerful nonperturbative method, and sufficiently simple to use in very different applications, including the study of nonperturbative high temperature effects, as shown very recently in the context of finite temperature quantum field theory[17] as well as finite chemical potential.[18] A more detailed explanation of this work can be seen in.[19]

2 The interpolated model for dilute homogeneous Bose gases

Let us start by considering the typical model that describes a gas of interacting boson particles, described by a complex scalar field ψ with Lagrangian density given by

$$\begin{aligned} \mathcal{L} &= \psi^*(\mathbf{x},t)\left(i\frac{d}{dt}+\frac{1}{2m}\nabla^2\right)\psi(\mathbf{x},t)+\mu\psi^*(\mathbf{x},t)\psi(\mathbf{x},t) \\ &- \frac{1}{2}\int d^3x'\psi(\mathbf{x},t)\psi^*(\mathbf{x},t)V(\mathbf{x}-\mathbf{x}')\psi(\mathbf{x}',t)\psi^*(\mathbf{x}',t)\,, \end{aligned} \tag{1}$$

where μ is the chemical potential. Let us take the interatomic interaction potential as being the one for a hard sphere gas,

$$V(\mathbf{x}-\mathbf{x}') = \frac{4\pi a}{m}\delta(\mathbf{x}-\mathbf{x}')\,, \tag{2}$$

where a is the s-wave scattering length.

We want to determine the deviation of the critical temperature T_c, of the interacting model, in relation to the critical temperature for Bose-Einstein condensation for a free gas, T_0.

As discussed in Refs.[12] and,[13] close to the critical point we can reduce (1) to an effective three-dimensional model for the zero Matsubara frequency modes (the static modes) of the fields ψ, given by the functional integration of the non-zero modes, obtaining an effective action defined by

$$S = \int d^3x\left[\frac{1}{2}|\nabla\phi|^2+\frac{1}{2}r\phi^2+\frac{u}{4!}(\phi^2)^2\right]\,, \tag{3}$$

where $\phi = (\phi_1,\phi_2)$ is related to the original real components of ψ by $\psi_1 = (mT)^{1/2}\phi_1$ and $\psi_2 = (mT)^{1/2}\phi_2$ while r and u are given by

$$r = -2m\mu\,, \quad u = 48\pi amT\,. \tag{4}$$

By considering the usual interpolation prescription given by we write

$$S \to S_\delta = \delta S + (1-\delta)S_0\,,$$

where S_0 is quadratically (exactly solvable) in the fields.

One can choose

$$S_0 = \frac{1}{2}\left[|\nabla\phi|^2 + R\phi^2\right] \ , \tag{6}$$

where $R = r + \eta^2$, obtaining

$$S_\delta = \int d^3x \left[\frac{1}{2}|\nabla\phi|^2 + \frac{1}{2}R\phi^2 - \frac{\delta}{2}\eta^2\phi^2 + \frac{\delta u}{4!}(\phi^2)^2\right] \ , \tag{7}$$

with η being an arbitrary parameter, with mass dimensions, which is fixed at a finite order in δ by the Principle of Minimal Sensitivity (PMS),[16] which requires that a physical quantity P calculated in powers of δ be evaluated at the point $\bar{\eta}$ where it is less sensitive to variations of the arbitrary parameter η. That is ,

$$\frac{\partial P}{\partial \eta}|_{\eta=\bar{\eta}} = 0 \tag{8}$$

Here we optimize the physical quantity represented by $\langle\phi^2\rangle$ which is directly related to the critical temperature shift $\Delta T_c/T_c$.

$$\frac{\Delta T_c}{T_c} \simeq -\frac{2mT_0}{3n}\Delta\langle\phi^2\rangle = -\frac{2mT_0}{3n}\left[\langle\phi^2\rangle_u - \langle\phi^2\rangle_0\right] \ , \tag{9}$$

and we get

$$\frac{\Delta T_c}{T_c} \simeq 3.059\ an^{\frac{1}{3}} \ . \tag{10}$$

Using the $1/N$ expansion Baym, Blaizot and Zinn-Justin[12] obtain $\Delta T_c/T_c \simeq 2.33an^{1/3}$ in the leading order while Arnold and Tomásik[13] obtain $\Delta T_c/T_c \sim 1.71an^{1/3}$ considering the next to leading order in the same approximation. Our numerical result is closer to $\Delta T_c/T_c \simeq 2.9an^{1/3}$ obtained in Ref.[11] with a method which sums setting sun contributions in a self consistent way. Finally let us remark that the result given by Eq. (9) is valid only for finite N. A thorough discussion and comparison with the 1/N method can be seen in.[19]

The authors thank Philippe Garcia and Franck Laloë for interesting discussions regarding Bose-Einstein condensation as well as the method employed in this work. F.F.S.C. was partially supported by CNPq-Brazil. R.O.R. was supported by CNPq-Brazil and SR2-UERJ.

3 REFERENCES

[1] F. Dalfovo, S. Giorgini and L. P. Pitaevskii, Rev. Mod. Phys. 71, 463 (1999).

[2] W. Ketterle, D. S. Durfee and D. M. Stamper-Kurn, in Bose-Einstein Condensation in Atomic Gases, Proceedings of the International School of Physics "Enrico Fermi", editors M. I. Inguscio, S. Stringari and C. E. Wieman (IOS Press, Amsterdam 1999). cond-mat/9904034.

[3] M. Holzmann, P. Grüter, F. Laloë, Eur. Phys. J. B 10,739,(1999)

[4] A.L. Fetter and J.D. Walecka, "Quantun Theory of Many-Particle Systems"(McGraw Hill,1971),section 28.

[5] T. Toyoda, Ann. Phys. (N.Y.) 141,154 (1982).

[6] K. Huang ,cond-mat/9904027.

[7] M. Bijlsma and H. T. C. Stoof, Phys. Rev. A54, 5085 (1996).

[8] P. Grüter, D. Ceperley and F. Laloë, Phys. Rev. Lett. 79, 3549 (1997).

[9] M. Holzmann and W. Krauth, Phys. Rev. Lett. 83, 2687 (1999).

[10] J. Reppy, B. Crooker, B. Hebral, A. Corwin, J. He and G. Zassanhaus, Phys. Rev. Lett. 84, 2060 (2000).

[11] G. Baym, J.-P. Blaizot M. Holzmann, F. Laloë and D. Vautherin, Phys. Rev. Lett. 83, 1703 (1999).

[12] G. Baym, J.-P. Blaizot and J. Zinn-Justin, Europhys. Lett. 49, 150 (2000).

[13] P. Arnold and B. Tomásik, cond-mat/0005197.

[14] A. Okopińska, Phys. Rev. D35, 1835 (1987); A. Duncan and M. Moshe, Phys. Lett. B215, 352 (1988).

[15] V. I. Yukalov, Mosc. Univ. Phys. Bull. 31, 10 (1976); R. Seznec and J. Zinn-Justin, J. Math. Phys. 20, 1398 (1979); J. C. LeGuillou and J. Zinn-Justin, Ann. Phys. 147, 57 (1983).

[16] P. M. Stevenson, Phys. Rev. D23 2916 (1981)

[17] M. B. Pinto and R. O. Ramos, Phys. Rev. D60, 105005 (1999); ibid. D61, 125016 (2000).

[18] H.F. Jones and P. Parkin, hep-th/0005069.

[19] "Transition Temperature for Weakly Interacting Homogeneous" - F.F. de Souza Cruz, M. B. Pinto e R.O. Ramos submitted to Physical Review B Bose Gases

[20] H. F. Jones, P. Parkin and D. Winder, hep-th/0008069.

Asymmetries in Heavy Meson Production in the Meson Cloud Model Scenario

F. Carvalho, F. O. Durães, F. S. Navarra and M. Nielsen
Instituto de Física, Universidade de São Paulo - C.P. 66318,
05315-970 São Paulo, SP, Brazil

We have applied the meson cloud model to calculate the asymmetry in D meson production in high energy Σ-nucleus and π^--nucleus collisions. We find a good agreement with recent data. Our results suggest that the asymmetry may decrease at large x_F.

Recent data taken by the WA89 collaboration[1] with a Σ^- beam have not only confirmed the asymmetry and the leading particle effect but have also observed this effect in D_s and Λ_c production. An interesting feature of the WA89 data is that they suggest, inspite of very large error bars and poor statistics, that the asymmetry decreases at very large x_F. The purpose of this letter is to show that in the meson cloud model (MCM)[2] we can reproduce data and accomodate a possible decrease of the asymmetry.

In the MCM we assume that quantum fluctuations in the projectile play an important role. Both the Σ^- and π^- may be decomposed in a series of Fock states. In order to keep the calculation simple, we shall assume $|\Sigma^-\rangle = Z\,[\,|\Sigma_0^-\rangle + |\Sigma\,\pi\rangle + |\Xi_c^0 D^-\rangle + |\Sigma_c^0 D_s^-\rangle]$ and $|\pi^-\rangle = Z'\,[\,|\pi_0^0\rangle + |\rho\,\pi\rangle + |D^{0*}D^-\rangle]$, where Z and Z' are normalization constants and $|\Sigma_0^-\rangle$ and $|\pi_0^0\rangle$ are the "bare" sigma and pion. The relative normalization of these states is fixed once the cloud parameters are fixed. We shall first study the Σ^-.

With a Σ^- beam there are three possible reaction mechanisms[3-5] for D^- meson production at large x_F and small p_T (the soft regime) in the MCM: a) the baryon in the cloud just "flies through", whereas the corresponding meson interacts inelastically producing a D^- in the final state, b) the meson in the cloud just "flies through", whereas the corresponding baryon interacts inelastically producing a D^- in the final state and c) the meson in the cloud is already a D^- (or D_s^-) which escapes (similar considerations hold for D^- production with a π^- beam). This last mechanism is responsible for generating asymmetries. We shall refer to the first two processes as "indirect production" (I) and to the last one as "direct production" (D). The first two are calculated with convolution formulas whereas the last one is given basically by the meson momentum distribution in the cloud initial $|MB\rangle$ state.

Inside the baryon, in the $|MB\rangle$ state, the meson and baryon have fractional momentum y_M and y_B with distributions called $f_{M/MB}(y_M)$ and $f_{B/MB}(y_B)$ respectively (we shall use for them the short notation f_M and f_B). Of course $y_M + y_B = 1$ and these distributions are related by $f_M(y) = f_B(1-y)$. The "splitting function" $f_M(y)$ represents the probability density to find a meson with momentum fraction y of the total cloud state $|MB\rangle$. With f_M and f_B we can compute the differential cross section for production of D mesons, which, in the reaction $\Sigma^- p \to DX$, is given by:

$$\frac{d\sigma^{\Sigma^- p \to DX}}{dx_F} = \Phi_M + \Phi_B + \Phi_D \tag{1}$$

$$\Phi_{M(B)} = \sum_{MB} \int_{x_F}^1 \frac{dy}{y} f_{M(B)}(y)\, \frac{d\sigma^{M(B)+p\to D+X}(x_F/y)}{d(x_F/y)} \tag{2}$$

$\Phi_{M(B)}$ refers to the indirect meson (baryon) initiated reactions and x_F is the fractional longitudinal momentum of the outgoing meson. Φ_D represents the direct process and is given by:

$$\Phi_D = \frac{\pi}{x_F} f_D(x_F)\, \sigma^{\Xi} \tag{3}$$

where $f_D \equiv f_{D^-/\Xi_c^0 D^-}$ and σ^{Ξ} is the total $p\Xi_c^0$ cross section. An analogous expression can be written for the reaction $\pi^- p \to DX$. For the differential "elementary cross sections" appearing in (2), we shall use the parametrization:

$$\frac{d\sigma^{M(B)+p\to D+X}(x_F)}{dx_F} = \sigma_0 (1-x_F)^n \tag{4}$$

where $n \simeq 4$ and $\sigma_0 \simeq 7\,\mu b$ as suggested by the WA89 data analysis.[1]

In our analysis we use the following light cone form for the splitting functions[6]:

$$f_M(y) = \int_0^{\infty} \frac{d\mathbf{k}_\perp^2}{16\pi^2} |A \exp(-\frac{\mathcal{M}_M^2}{8\alpha^2})|^2 \tag{5}$$

where $\mathcal{M}_M$ is the invariant mass of the meson(M)-baryon(B) system, $\mathbf{k}_\perp$ and y are respectively the tranverse and (fractional) longitudinal momentum of the meson and A is a normalization constant.

Assuming $\Phi_M^{D^-} = \Phi_M^{D^+} = \Phi_M^D$ and $\Phi_B^{D^-} = \Phi_B^{D^+} = \Phi_B^D$, we can write our final expression for the asymmetry:

$$A(x_F) = \frac{F_D(x_F)}{F_D(x_F) + N\, F_I(x_F)} \quad ; \quad N = \frac{2\, A_I^2\, \alpha_I^2\, \sigma_0}{\pi\, A_D^2\, \alpha_D^2\, \sigma^{\Xi}} \tag{6}$$

$$F_D(x_F) = (1-x_F) \exp\left(-\frac{\frac{m_D^2}{x_F} + \frac{m_\Xi^2}{1-x_F}}{4\alpha_D^2} \right) \tag{7}$$

$$\begin{aligned} F_I(x_F) &= \int_{x_F}^1 dy\, (1-y) \left[\exp\left(-\frac{\frac{m_\pi^2}{y} + \frac{m_\Sigma^2}{1-y}}{4\alpha_I^2} \right) + \exp\left(-\frac{\frac{m_\Sigma^2}{y} \frac{m_\pi^2}{1-y}}{4\alpha_I^2} \right) \right] \\ &\times \quad (1 - \frac{x_F}{y})^n \end{aligned} \tag{8}$$

where A_I and α_I (A_D and α_D) are respectively the normalization constant and width of the light (heavy) meson-baryon state.

We are now ready for numerical evaluations. Before presenting them we emphazise that i) our calculation is based on quite general and well established ideas, namely that hadron projectiles fluctuate into hadron-hadron (cloud) states and that these states interact with the target; ii) our results only depend on three parameters: α_D, α_I and N. Whereas α_D (α_I) determines the width of the momentum distribution of the leading (light) meson in the cloud, N depends essentially on the relative weigths of the states $|\Sigma^-\pi^0\rangle$ and $|\Xi_c^0 D^-\rangle$ (or $|\Sigma_c^0 D_s^-\rangle$).

Previous experience with data analysis indicates[6] that $\alpha_I = 0.45\, GeV$. We will keep this number fixed and vary α_D and N. We observe that (6) is much more sensitive to α_D than to N. Indeed, a numerical investigation of (6) reveals that for a wide range of acceptable values of N, the behavior of the asymmetry at large x_F is dictated by α_D (which controls the width of the D meson momentum distribution in the cloud). It may be broad enough to be larger than the indirect contribution (8) making (6) go to unity at large x_F. This would be the case if we would use for f_M (and consequently for f_D) the traditional MCM formula[2,7] and this is also the conclusion of all the models addressing the asymmetry problem. Expression (5) admits this limit for large α_D.

The D_s^-/D_s^+ asymmetry can be calculated following the steps mentioned above and replacing the $|\Xi_c^0 D^-\rangle$ state by $|\Sigma_c^0 D_s^-\rangle$. This implies different values for α_D and N. We show in Figs. 2a and 2b, respectively, our results

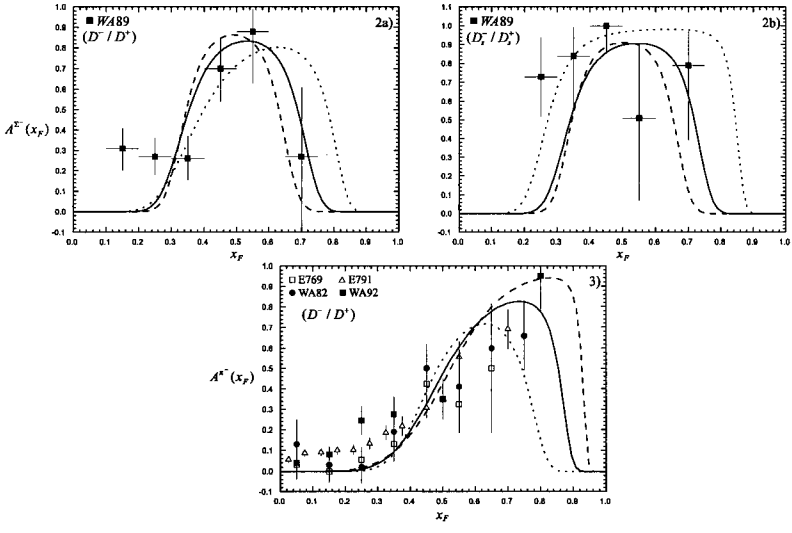

Figure 1:

for the asymmetries D^-/D^+ and D_s^-/D_s^+ (for a Σ^- beam). In 2a we choose $\alpha_D = 0.45\,GeV$ and $N = 4.0\,10^{-8}$ (dashed curve), $\alpha_D = 0.57\,GeV$ and $N = 4.0\,10^{-4}$ (solid) and $\alpha_D = 0.77\,GeV$ and $N = 6.0\,10^{-1}$ (dotted). In 2b we choose $\alpha_D = 0.45\,GeV$ and $N = 1.2\,10^{-8}$ (dashed curve), $\alpha_D = 0.57\,GeV$ and $N = 1.4\,10^{-4}$ (solid) and $\alpha_D = 0.77\,GeV$ and $N = 4.0\,10^{-2}$ (dotted).

It is straightforward to extend our formulas to the pion and compute (6) for a π^- beam. The results are shown in Fig. 3. Again we fix $\alpha_l = 0.45\,GeV$ and choose $\alpha_D = 0.57\,GeV$ and $N = 1.0\,10^{-2}$ (dotted curve), $\alpha_D = 0.77\,GeV$ and $N = 2.5$ (solid), $\alpha_D = 1.00\,GeV$ and $N = 40.0$ (dashed). As it can be seen in Figs. 2 and 3 the agreement between the MCM and data is very good.

In conclusion, we believe that the MCM provides a good understanding of the charm asymmetries in terms of a simple physical picture. Moreover it connects the behavior of the asymmetries at large x_F with the width of the charm meson momentum distribution within the cloud state. Sufficiently narrow distributions lead to decreasing asymmetries at large x_F.

Acknowledgments

This work has been supported by CNPq and FAPESP.

REFERENCES

[1] M. I. Adamovich *et al.*, (WA89 Coll.), *Eur. Phys. J.* C **8**, 593 (1999); *Eur. Phys. J.* C **13**, 247 (2000).

[2] for a review see J. Speth and A. W. Thomas, *Adv. Nucl. Phys.* **24**, 83 (1998); *Phys. Rep.* **303**, 183 (1998).

[3] F. S. Navarra, M. Nielsen and S. Paiva, *Phys. Rev.* D **56**, 3041 (1997).

[4] F. Carvalho, F. O. Durães, F. S. Navarra and M. Nielsen, *Phys. Rev.* D **60**, 094015 (1999).

[5] F. Carvalho, F. O. Durães, F. S. Navarra and M. Nielsen, and F. M. Steffens, *hep-ph/9912378*, to appear in *Eur. Phys. J.* C, (2000).

[6] S. J. Brodsky and B.-Q. Ma, *Phys. Lett.* B **381**, 317 (1996).

[7] S. Paiva, M. Nielsen, F. S. Navarra, F. O. Durães and L. L. Barz, *Mod. Phys. Lett.* A **13**, 2715 (1998).

Crossing Symmetry Violation in Unitarity Corrected ChPT Pion-Pion Amplitude

Isabela P. Cavalcante and J. Sá Borges

Universidade do Estado do Rio de Janeiro
Rio de Janeiro, Brazil

Abstract

Crossing symmetry implies that there is just one amplitude describing the three total isospin channels of pion-pion scattering. One-loop Chiral Perturbation Theory total amplitude fulfills this condition, however the corresponding partial wave amplitudes do not respect exact unitarity relation. The inverse amplitude method (IAM) is usually employed to get unitarized results from ChPT, while violating crossing symmetry.

Using the Roskies relations we measure the amount of crossing symmetry violation when IAM is applied to ChPT in order to fit pion-pion phase-shifts to experimental results in the resonance region.

1 Introduction

The method of Chiral Perturbation Theory [1] aims to explore the low energy structure of Quantum Chromodynamics (QCD). By this method, starting from an effective chiral Lagrangian, the non-linear sigma model, one can describe meson-meson scattering. Working at the one loop level for pion-pion scattering it results a total amplitude that respects exact crossing symmetry. However, the corresponding partial waves satisfy only approximate elastic unitarity.

At low energies, the leading amplitude is of second order in the momenta of the external pions and coincides with the Weinberg soft-pion result obtained in the early days of the applications of current algebra and PCAC hypothesis [2]. The corrections include loop diagrams whose vertices are $\mathcal{O}(p^2)$ and a free-parameter polynomial part coming from tree diagrams of $\mathcal{O}(p^4)$. From the very beginning of the applications of ChPT it was clear that the free parameters have to be obtained phenomenologically. By fitting these parameters from a few low energy experiments it is then possible to obtain successful predictions for other processes.

Nevertheless, there are some *intrinsic limitations* when applying ChPT, namely the fact that the amplitudes calculated within the chiral approach are only unitary in the perturbative sense, that is, up to the next order in the external momenta. As a result it is not possible to reproduce resonant states, which are one of the most relevant features of the strong interacting regime.

Many different methods have been proposed to improve this behaviour and thus to extend the applicability of ChPT at higher energies. One of these methods uses the crossing symmetric result, and strongly violates unitarity [3]. Here we will focus on the Inverse Amplitude Method (IAM) [4], that violates crossing symmetry, but allows one to access the resonance region for pion-pion scattering by adjusting two parameters. In this exercise we quantify the violation of crossing symmetry by computing the Roskies relations between **S**- and **P**-waves [5].

2 Inverse Amplitude Method

In the case of pion-pion scattering, crossing symmetry implies that there is just one amplitude describing the three total isospin channels of the process, $T_I(s,t)$, with $I = 0, 1$ and 2, which are expanded in partial wave amplitudes $t_{I\ell}$, as

$$t_{I\ell}(s) = \frac{1}{2}\int_{-1}^{1} P_\ell(\cos\theta)\, T_I(s,t)\, d(\cos\theta),$$

where P_ℓ are the Legendre polynomials.

Elastic unitarity implies that

$$\mathrm{Im} t_{I\,\ell}(s) = \rho(s)|t_{I\,\ell}(s)|^2, \quad \text{so that} \quad \mathrm{Im}\; t_{I\ell}^{-1} = -\rho(s),$$

where $\rho(s) = 1/(32\pi)\sqrt{(s-4m_\pi^2)/s}$ is the phase space factor for pion-pion scattering.

At one loop level, that is, up to order p^4 in the chiral expansion, the resulting ChPT amplitudes for isospin $I = 0, 2$ ($\ell = 0$, S-wave) and $I = 1$ ($\ell = 1$, P-wave) can be expanded as:

$$t_I(s) = t_I^{ca}(s) + t_I^{ca\ 2}(s)\bar{J}(s) + t_I^{left}(s) + p_I(s),$$

where t_I^{ca} is the (real) Weinberg amplitude, t_I^{left} is the part that bears the left-hand cut and $p_I(s)$ are two-free-parameter polynomials, for instance, $p_1(s) = s\,(s-4m_\pi^2)\,(\lambda_2 - \lambda_1)/(3f_\pi^4)$, and $\mathrm{Im}\ \bar{J}(s) = \rho(s)$.

In order to unitarize ChPT we work with the inverse of the partial-wave. Thus, instead of the exact ChPT result t_I, we use a modified amplitude

$$\tilde{t}_I(s) = \frac{t_I^{ca}}{1 - \left(t_I^{ca\ 2}\bar{J}(s) + t_I^{left} + p_I(s)\right)/t_I^{ca}} \quad I = 0, 1 \text{ and } 2. \tag{1}$$

The main difficulty to work with this formula for S-wave is that at some sub-threshold value for s, the correction is equal to t^{ca} so that the S-wave amplitude is singular. Singularities occur in S-wave sub-threshold amplitudes at $s \simeq 0.7m_\pi^2$, for $I = 0$, and at $s \simeq 2\,m_\pi^2$, for $I = 2$. Those values correspond to points close to the ones where t_0^{ca} and t_2^{ca} vanish.

In order to get rid of those singularities, we performed an extra correction. We have changed the numerator of eq. (1) in such a way that it becomes zero were singularities occurred. The new formula violates unitarity but at a maximum rate of 4 and 0.9 %, at threshold, for I=0 and I=2 S-waves, respectively, and violation tends rapidly to zero as energy increases.

i	r_i^0	r_i^1	α	β	γ	V_i
0	1	0	2	-5		7.535
1	$3s-4m_\pi^2$	0	1	2		0.187
2	$3s-4m_\pi^2$	1	1	0	-2	0.619
3	$10s^2-32sm_\pi^2+16m_\pi^4$	$5s-4m_\pi^2$	2	-5	6	13.61
4	$35s^3-180s^2m_\pi^2+240sm_\pi^4-64m_\pi^6$	$21s^2-48sm_\pi^2+16m_\pi^4$	2	-5	-15	35.79

Table 1: Parameters of Roskies relations and percentage deviations V.

3 Crossing symmetry violation

As explained in the introduction, IAM allows one to access the resonance region for pion-pion scattering. The resulting fits to phase-shifts correspond to the parameters $\lambda_1 = -0.00345$ and $\lambda_2 = 0.01125$; the fits are not shown here. On the other hand, the corresponding partial waves do not respect crossing symmetry and we would like to quantify that violation.

Crossing symmetry imposes constraints between the integrals of some combination of partial-wave amplitudes, known as Roskies relations [5]. Let us define

$$A_i(\alpha,\beta,\gamma) = \int_0^{4m_\pi^2} (s-4m_\pi^2)\left\{r_i^0\ (\alpha\ t_0(s) + \beta\ t_2(s)) + \gamma\ (s-4m_\pi^2)\ r_i^1\ t_1(s)\right\} ds\,,$$

where α, β, γ are integers and r_i^ℓ are polynomials in energy, whose values are given in the Table. Crossing symmetric amplitude must satisfy $A_i(\alpha,\beta,\gamma) = 0$. In the case of IAM amplitudes, we evaluated the relative deviation from these relations as

$$V_i = A_i(\alpha,\beta,\gamma)/A_i(\alpha,\beta,-\gamma)\ ,$$

and $V_i = A_i(\alpha,\beta,0)/A_i(\alpha,-\beta,0)$, when $r_i^1 = 0$. The values obtained are given in the Table.

4 Conclusion

The $\mathcal{O}(\mathrm{p}^4)$ ChPT pion-pion amplitude is crossing symmetric but does not respect exact elastic unitarity. There are several attempts to extrapolate the domain of validity of ChPT and to access the resonance region for meson-meson scattering. One of these methods uses the inverse of the amplitude and fits the two-parameter amplitude to the experimental data.

In the present exercise we were interested in quantifying the crossing violation that this procedure implies. In this way we have used the Roskies relations and we quantified the violation of crossing symmetry. On the other hand we have shown how to get rid of sub-threshold singularities by constructing a quasi-unitarized singularity corrected IAM amplitude.

References

[1] J. Gasser and H. Leutwyler, Nucl. Phys. B 250 (1985) 465.

[2] S. Weinberg, Phys. Rev. Lett. 17 (1966) 616.

[3] J. Sá Borges, J. Soares Barbosa and V. Oguri, Phys. Lett. B 393 (1997) 413.

[4] A. Dobado and J. R. Peláez, Phys. Rev. D 56 (1997) 3057; J. A. Oller and E. Oset, Phys. Rev. D 60 (1999) 074023.

[5] R. Roskies, Nuovo Cimento 65A (1970) 467.

NUCLEAR MATTER PROPERTIES DETERMINED BY RELATIVISTIC MEAN FIELD MODEL WITH σ-ω COUPLING

K.C. Chung[a], C.S. Wang[a,b], A.J. Santiago[a], and J.W. Zhang[b]

(a) Instituto de Física, Universidade do Estado do Rio de Janeiro, Rio de Janeiro-RJ 20559-900, Brazil
(b) Department of Technical Physics, Peking University, Beijing 100871, China

The purpose of this work is to explore the possibility of extending the linear σ-ω model[1] by introducing a σ-ω coupling phenomenologically, and to investigate whether this coupling alone is able to reduce the nuclear incompressibility K_0 and in the same time to increase the effective nucleon mass M^*. The model Lagrangian density is

$$\begin{aligned}\mathcal{L} &= \overline{\psi}[\gamma_\mu(i\partial^\mu - g_\omega\omega^\mu) - (M - g_\sigma\phi)]\psi \\ &+\frac{1}{2}[(\partial_\mu - \eta g'_\omega\omega_\mu)\phi(\partial^\mu + \eta g'_\omega\omega^\mu)\phi - m_\sigma^2\phi^2] \\ &-\frac{1}{4}F_{\mu\nu}F^{\mu\nu} + \frac{1}{2}m_\omega^2\omega_\mu\omega^\mu, \quad \eta = i \text{ and } 1, \end{aligned} \tag{1}$$

where $F^{\mu\nu} = \partial^\mu\omega^\nu - \partial^\nu\omega^\mu$, ψ, ϕ and ω are the nucleon, σ and ω meson fields with masses M, m_σ and m_ω, respectively, while g_σ, g_ω are the respective coupling constants, and g'_ω is the σ-ω coupling constant. $\eta = i$ gives a σ-ω coupling similar to that introduced by usual covariant derivatives, while $\eta = 1$ gives a gauge-like virtual coupling similar to the imaginary coupling[2]. Mathematically, it is equivalent to add a term $\eta^2 g'^2_\omega\omega_\mu\omega^\mu$ to m_σ^2, which is the same as the η_2 term introduced in the nuclear effective field theory[3]. The present model reduces to the original Walecka model when the σ-ω coupling constant is zero, $g'_\omega = 0$.

For static nuclear matter, the field equations derived from this Lagrangian are reduced to the following equations in the mean field approximation:

$$(i\gamma^\mu\partial_\mu - g_\omega\gamma^0\omega_0 - M^*)\psi = 0, \quad m_\sigma^{*2}\phi = g_\sigma\rho_s, \quad m_\omega^{*2}\omega_0 = g_\omega\rho_N, \tag{2}$$

where the effective nucleon mass M^*, effective σ meson mass m_σ^* and effective ω meson mass m_ω^* are defined respectively as

$$M^* = M - g_\sigma\phi, \quad m_\sigma^{*2} = m_\sigma^2 + \eta^2 g'^2_\omega\omega_0^2, \quad m_\omega^{*2} = m_\omega^2 - \eta^2 g'^2_\omega\phi^2, \tag{3}$$

and $\rho_s = \langle\overline{\psi}\psi\rangle$ is the scalar density, $\rho_N = \langle\overline{\psi}\gamma^0\psi\rangle$ the baryon density. For calculating these effective masses, the above three equations can be rewritten as the following self-consistent equations:

$$\xi = \frac{M^*}{M} = 1 - \frac{\alpha}{s}\frac{\rho_s}{\rho_0}, \quad s = \xi_\sigma^2 = \frac{m_\sigma^{*2}}{m_\sigma^2} = 1 + \frac{\alpha_\sigma}{v^2}\frac{\rho_N^2}{\rho_0^2}, \quad v = \xi_\omega^2 = \frac{m_\omega^{*2}}{m_\omega^2} = 1 - \frac{\alpha_\omega}{s^2}\frac{\rho_s^2}{\rho_0^2}, \tag{4}$$

where ρ_0 is the standard nucleon number density, α, α_σ and α_ω are the dimensionless composite parameters defined respectively as

$$\alpha = \frac{g_\sigma^2\rho_0}{m_\sigma^2 M}, \quad \alpha_\sigma = \frac{\eta^2 g'^2_\omega g_\omega^2\rho_0^2}{m_\omega^4 m_\sigma^2}, \quad \alpha_\omega = \frac{\eta^2 g'^2_\omega g_\sigma^2\rho_0^2}{m_\sigma^4 m_\omega^2}. \tag{5}$$

It should be noted that α_σ and α_ω are positive for $\eta = 1$ while negative for $\eta = i$.

The nuclear matter equation of state derived from Lagrangian density (1) can be expressed in terms of the nuclear energy density $\mathcal{E}$ as $e = \mathcal{E}/\rho_N - M$, and

$$\mathcal{E} = \mathcal{E}_k + \mathcal{E}_\sigma + \mathcal{E}_\omega, \tag{6}$$

$$\mathcal{E}_k = \frac{M^4\xi^4}{\pi^2}\sum_{i=p,n} F_1(k_i/\xi M), \quad \mathcal{E}_\sigma = \frac{1}{2}(1-\xi)M\rho_s, \quad \mathcal{E}_\omega = \frac{1}{2}(1-\xi)yM\rho_s, \tag{7}$$

where $y = (s-1)(2v-1)/s(1-v)$, k_p and k_n are the proton and neutron Fermi momenta respectively, and $F_m(x) = \int_0^x dx\, x^{2m}\sqrt{1+x^2}$. The baryon density ρ_N and scalar density ρ_s can be expressed as

$$\rho_N = \frac{1}{3\pi^2}\sum_{i=p,n} k_i^3, \quad \rho_s = \frac{M^3\xi^3}{\pi^2}\sum_{i=p,n} f_1(k_i/\xi M), \tag{8}$$

where $f_m(x) = \int_0^x dx x^{2m}/\sqrt{1+x^2}$.

Having the equation of state, the pressure p can be derived as

$$p = -\mathcal{E} + \rho_N\frac{\partial\mathcal{E}}{\partial\rho_N} = \frac{1}{3}(\mathcal{E}_k - \mathcal{E}_\sigma - M\rho_s) + \mathcal{E}_\omega - \frac{2(1-s)}{s}\mathcal{E}_\sigma. \tag{9}$$

Instead of Fermi momenta k_p and k_n, we will use the nucleon density $\rho_N = \rho_n + \rho_p$ and relative neutron excess $\delta = (\rho_n - \rho_p)/\rho_N$ as independent variables for describing the nuclear matter. At the standard state $\rho_N = \rho_0$, $\delta = 0$, the pressure should be zero,

$$p(\rho_0, 0) = 0. \tag{10}$$

In addition, the depth of the equation of state is related to the nuclear volume energy a_1 as

$$e(\rho_0, 0) = -a_1. \tag{11}$$

At the standard state, the nuclear incompressibility K_0, the symmetry energy J, the density symmetry L and symmetry incompressibility K_s can be calculated:

$$K_0 = 9\Big(\rho_N^2\frac{\partial^2 e}{\partial\rho_N^2}\Big)_0, \quad J = \frac{1}{2}\frac{\partial^2 e}{\partial\delta^2}\Big|_0, \quad L = \frac{3}{2}\Big(\rho_N\frac{\partial^3 e}{\partial\rho_N\partial\delta^2}\Big)_0, \quad K_s = \frac{9}{2}\Big(\rho_N^2\frac{\partial^4 e}{\partial\rho_N^2\partial\delta^2}\Big)_0. \tag{12}$$

For the description of nuclear matter, there are three independent parameters α, α_σ and α_ω in the present model. The saturation point of nuclear matter (ρ_0,a_1) defined by Eqs.(10) and (11) can be used as input to determine α_σ and α_ω as function of α. In our calculation, the nuclear radius constant $r_0 = 1.14$fm which corresponds to the standard nucleon number density $\rho_0 = 0.161\text{fm}^{-3}$, the nuclear volume energy $a_1 = 16.0$MeV, nucleon mass $M = 938.9$MeV and constant $\hbar c = 197.327053$MeV·fm are used.

Fig.1 plots α_σ and α_ω as function of α. At the point $\alpha = \alpha_W = 0.4908$ (indicated by an arrow), we have $\alpha_\sigma = \alpha_\omega = 0$, and the present model reduces to Walecka model. For $\alpha > \alpha_W$, α_σ and α_ω are negative, which corresponds to $\eta = i$. For $\alpha < \alpha_W$, α_σ and α_ω are positive, which corresponds to $\eta = 1$. There is a lower limit $\alpha_{min} = 0.1037$, below this point there is no physical solution, as

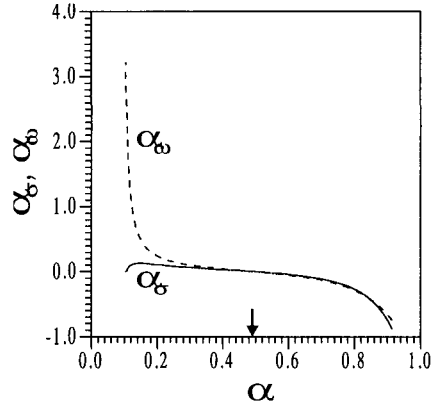

Figure 1:

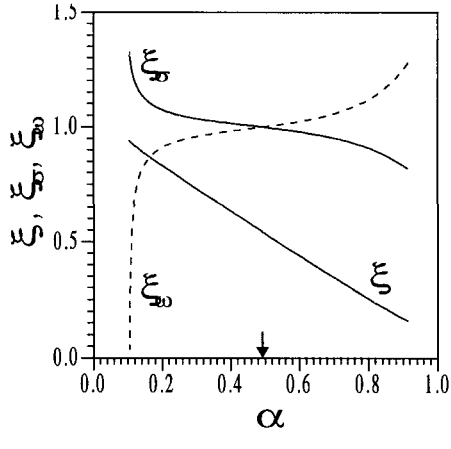

Figure 2:

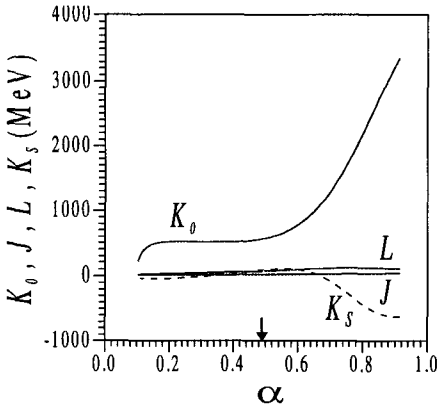

Figure 3:

the effective ω meson mass becomes imaginary, $\xi_\omega^2 < 0$. Fig.2 shows the dimensionless effective nucleon mass ξ, the dimensionless effective σ meson mass ξ_σ and the dimensionless effective ω meson mass ξ_ω as function of α. At the point α_W, $\xi = 0.5437$ and $\xi_\sigma = \xi_\omega = 1$. From α_W to the right, ξ decreases as α increases, and we have $\xi_\sigma < 1$ and $\xi_\omega > 1$. >From α_W to the left, ξ increases as α decreases, and we have $\xi_\sigma > 1$ and $\xi_\omega < 1$. Fig.3 gives K_0, J, L, and K_s as function of α. At α_W, $K_0 = 553$MeV, $J = 20.2$MeV, $L = 70.6$MeV, and $K_s = 88$MeV. As α decreases, K_0 decreases at first and then increases slowly, passing through a very flat plateau, and finally decreases rapidly to a lower limit 227MeV. J and L as well as K_s decrease slowly as α decreases. It is worthwhile to note that K_s is negative in the low α side, in opposition to what is obtained in the usual σ-ω model. Experimentally, K_s obtained from the isoscalar giant monopole resonance energy is[4] between -566 ± 1350 to 34 ± 159MeV. On the other hand, K_0 increases to very high values rapidly as α increases. In this aspect, the case of $\eta = i$ is not acceptable.

The dimensionless effective nucleon mass ξ at the saturation point can be used as the third input to fix the parameter α. For example, if $\xi = 0.85$ at the saturation point, we have $\alpha = 0.1822$. Correspondingly we have $\alpha_\sigma = 0.1134$, $\alpha_\omega = 0.2938$, $\xi_\sigma = 1.085$, $\xi_\omega = 0.895$, $K_0 = 501$MeV, $J = 13.8$MeV, $L = 30.1$MeV, and $K_s = -38$MeV, where the values of ξ_σ and ξ_ω are those at the saturation point. Instead of ξ, the nuclear incompressibility K_0 could be also used to fix α. If $K_0 = 250$MeV is chosen, it yields $\alpha = 0.1050$, $\alpha_\sigma = 0.00783$, $\alpha_\omega = 2.642$, $\xi = 0.939$, $\xi_\sigma = 1.295$, $\xi_\omega = 0.328$, and $K_s = -31.2$MeV, where the values of ξ, ξ_σ and ξ_ω are those at the saturation point.

The symmetry energy J can be increased by including the ρ meson field in the present model. It is easy to prove that, the inclusion of ρ meson produces no change in nuclear energy density $\mathcal{E}$ and pressure p at the standard state. Therefore, the parameters α, α_σ and α_ω have no change, and thus the dimensionless effective masses ξ, ξ_σ and ξ_ω are the same even the ρ meson field is included. In addition, there is no contribution to K_s from the ρ meson field.

In conclusion, the possibility of extending the linear σ-ω model by introducing a σ-ω coupling phenomenologically is explored. It is shown that, in contrast to the usual Walecka model, not only the effective nucleon mass M^* but also the effective σ meson mass m_σ^* and the effective ω meson mass m_ω^* are nucleon density dependent. When the model parameters are fitted to the nuclear radius constant $r_0 = 1.14$fm and volume energy $a_1 = 16.0$MeV as well as to the effective nucleon mass $M^* = 0.85M$, the model yields $m_\sigma^* = 1.09m_\sigma$ and $m_\omega^* = 0.90m_\omega$ at the same nuclear saturation point, and the nuclear incompressibility $K_0 = 501$MeV. This incompressibility seems too high. On the other hand, if the model parameters are fitted to $K_0 = 250$MeV, in addition to $r_0 = 1.14$fm and $a_1 = 16.0$MeV, it yields $M^* = 0.938M$, $m_\sigma^* = 1.295m_\sigma$ and $m_\omega^* = 0.328m_\omega$ at the nuclear saturation point. This effective ω meson mass seems too low. In addition, the lower limit of incompressibility $K_0 = 227$MeV is not low enough. Therefore, even this model is able to reduce the nuclear incompressibility and also to increase the effective nucleon mass simultaneously, there is still not enough degrees of freedom to adjust the parameters in order to give more reasonable result. In this aspect, additional physics should be included in order to improve this model.

References

1. B.D. Serot and J.D. Walecka, *Int. J. Mod. Phys.* **E6** (1997) 515.

2. H.B. Ai, L.S. Celenza, S-F. Gao, and C.M. Shakin, *Phys. Rev.* **C35** (1988) 236.

3. R.J. Furnstahl, Brian D. Serot, and Hua-Bin Tang, *Nucl. Phys.* **A615** (1997) 441.

4. S. Shlomo and D.H. Youngblood, *Phys. Rev.* **C47**, (1993) 529.

The Relativistic Quasi-Particle Random Phase Approximation

C. De Conti, E. F. Batista, B.V. Carlson, and T. Frederico.
Departamento de Física, Instituto Tecnológico de Aeronáutica,
Centro Técnico Aeroespacial,
12228-900 São José dos Campos, SP, Brazil

Abstract

Our aim in this work is to derive the relativistic quasi-particle random phase approximation equations in the ring approximation. We derive the equations in the particle-particle, particle-hole and hole-hole subspaces. We use Green's functions techniques to develop these equations, based on the Dirac-Hartree-Fock-Bogoliubov approximation [1] to the single-particle motion.

1 Introduction

The random-phase approximation (RPA) is the simplest theory of excited states of a nucleus which admits the possibility that the ground state is not of a purely independent particle character but may contain correlations. The nonrelativistic RPA furnishes a microscopic treatment of nuclear excitation in terms of the particle-hole modes of the system. It successfully describes many of the low-energy collective excitations of the nucleus. The ring diagrams of the RPA also modify the effective nucleon-nucleon interaction in the nucleus. In particular, their modification of the interaction has been found to greatly reduce the magnitude of $^1S_0$ pairing.[2]

When it is based on the Dirac-Hartree-Fock-Bogoliubov approximation (DHFB) to the single-particle motion, rather than the Hartree-Fock one, the RPA becomes the quasi-particle RPA (QRPA). It then also includes particle-particle and hole-hole contributions to the excited states and ground state correlations. The particle-particle ground state correlations, in particular, are important for the correct description of β^+ decay and double β decay in medium to heavy nuclei.[3]

In the first section of this work derive the QRPA equations. We then expand the particle-hole response including particle-particle and hole-hole excitations. Finally in the last section we summarize and conclude this poster.

2 Relativistic QRPA

The linear response for the bilinear density

$$A(x) = \overline{\psi}(x)\Gamma_A\psi(x) \tag{1}$$

due to an external perturbation coupled to the density

$$B(x) = \overline{\psi}(x)\Gamma_B\psi(x) \tag{2}$$

can be obtained from the polarization propagator

$$\begin{aligned} i\Pi[A(x),B(y)] &= \langle\Psi \mid T[A(x)B(y)] \mid \Psi\rangle \\ &\simeq \langle\tilde{\Psi} \mid T[\tilde{S}\tilde{A}(x)\tilde{B}(y)] \mid \tilde{\Psi}\rangle_{con.} \end{aligned} \tag{3}$$

where Γ_A and Γ_B are arbitrary 4×4 matrices and $\tilde{S}$, $\tilde{A}$ and $\tilde{B}$ are the S-matrix and the bilinear densities in the Hartree-Fock-Bogoliubov approximation.

The relativistic QRPA is obtained by retaining only the ring diagrams in the expansion of the polarization propagator in (3), including the exchange diagrams. This allows us write the Dyson equation for the polarization propagator, as shown in the Fig. 1, which can be written analytically as

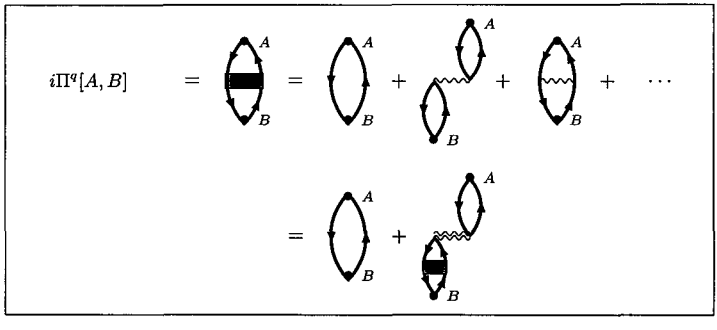

Figure 1: Dyson equation for polarization propagator Π^q. The double line in the meson propagators is introduced to include the direct and exchange diagrams.

$$\begin{aligned} i\Pi[A(x),B(y)] &\simeq i\Pi^q[A(x),B(y)] \\ &= \bar{\mathbb{U}}_s(\boldsymbol{x})\mathbb{\Gamma}_A\mathbb{U}_n(\boldsymbol{x})i\Pi^q_{ns;rm}(x_0-y_0,y_0-x_0)\times\bar{\mathbb{U}}_r(\boldsymbol{y})\mathbb{\Gamma}_B\mathbb{U}_m(\boldsymbol{y}) \end{aligned} \tag{4}$$

where

$$\mathbb{U}_r(\boldsymbol{x}) = \begin{bmatrix} U_r(\boldsymbol{x}) \\ V_r(\boldsymbol{x}) \end{bmatrix} \quad \text{and} \quad \mathbb{\Gamma}_A = \begin{pmatrix} \Gamma_A & 0 \\ 0 & -\tilde{\Gamma}_A \end{pmatrix},$$

and $\tilde{\Gamma}_A = A\Gamma_A^T A^\dagger$. The components $U_{r,s}$ and $V_{r,s}$ are Dirac spinors correspond to the normal and time-reversed components, respectively, of the positive-frequency (ϵ_r) and negative-frequency (ϵ_s) solution to the self-consistency equation of Dirac-Hartree-Fock-Bogoliubov (DHFB) approximation. An alternative, more detailed account can be found in [1]. Taking the static limit for meson propagators and performing a Fourier transformation in temporal variables allows us to write the temporal part of the polarization propagator in the QRPA, $\Pi^q_{ns;rm}$ as

$$\begin{aligned} \Pi^q_{ns;rm}(\omega) &= \tilde{\Pi}_{ns;rm}(\omega) + \sum_{r's'n'm'} \tilde{\Pi}_{ns;r'm'}(\omega)K_{r'm';n's'} \\ &\quad \times\Pi^q_{n's';rm}(\omega), \end{aligned} \tag{5}$$

$K_{rm;ns}$ is the kernel of the QRPA defined as

$$\begin{aligned} K_{rm;ns} &= \frac{1}{2}\sum_j i\int d^3x_1 d^3x_2 \bar{\mathbb{U}}_r(\boldsymbol{x}_1) i\mathbb{\Gamma}_{j\alpha'} \mathbb{U}_m(\boldsymbol{x}_1) iD_j^{0\alpha'\beta'}(\boldsymbol{x}_1-\boldsymbol{x}_2) \\ &\quad \times \bar{\mathbb{U}}_s(\boldsymbol{x}_2) i\mathbb{\Gamma}_{j\beta'} \mathbb{U}_n(\boldsymbol{x}_2) \\ &- \frac{1}{2}\sum_j i\int d^3x_1 d^3x_2 \bar{\mathbb{U}}_r(\boldsymbol{x}_1) i\mathbb{\Gamma}_{j\alpha'} \mathbb{U}_n(\boldsymbol{x}_1) iD_j^{0\alpha'\beta'}(\boldsymbol{x}_1-\boldsymbol{x}_2) \\ &\quad \times \bar{\mathbb{U}}_s(\boldsymbol{x}_2) i\mathbb{\Gamma}_{j\beta'} \mathbb{U}_m(\boldsymbol{x}_2) \end{aligned} \tag{6}$$

The first term in the series is the Hartree-Fock-Bogoliubov polarization propagator. We see in Fig. 2

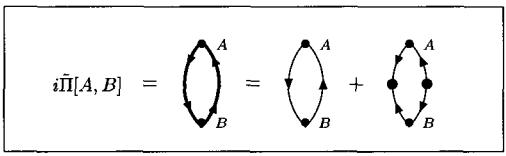

Figure 2: Diagram of zero order for the quasi-particle polarization propagator.

that this propagator contains both the propagation of baryons and nucleon pairs. If we examine the spectral representation for $\tilde{\Pi}(\omega)$, from (5) we can obtain $\Pi^q(\omega)^{-1}$ and write it as

$$\begin{bmatrix} A & B \\ B^* & A^* \end{bmatrix} \begin{bmatrix} X \\ Y \end{bmatrix} = \omega \begin{bmatrix} X \\ -Y \end{bmatrix} \tag{7}$$

where

$$\begin{aligned} A_{n\bar{s};r\bar{m}} &= (\epsilon_r + \epsilon_{\bar{s}})\delta_{rn}\delta_{\bar{s}\bar{m}} + K_{n\bar{s};r\bar{m}} \\ B_{n\bar{s};m\bar{r}} &= K_{n\bar{s};\bar{r}m}. \end{aligned} \tag{8}$$

Here we introduce the notation, $\epsilon_r > 0 \rightarrow r$ and $\epsilon_r \leq 0 \rightarrow \bar{r}$

Equation (7) is the matricial form of the QRPA equations.

3 Extending the Particle-Hole Response

The generalized linear response for the bilinear density

$$A(x) = \begin{cases} \bar{\psi}(x)\Gamma_A\bar{\psi}(x) & \text{particle-particle} \\ \bar{\psi}(x)\Gamma_A\psi(x) & \text{particle-hole} \\ \psi(x)\Gamma_A\psi(x) & \text{hole-hole} \end{cases}, \tag{9}$$

due to an external perturbation coupled to the density

$$B(x) = \begin{cases} \bar{\psi}(x)\Gamma_B\bar{\psi}(x) & \text{hole-hole} \\ \bar{\psi}(x)\Gamma_B\psi(x) & \text{particle-hole} \\ \psi(x)\Gamma_B\psi(x) & \text{particle-particle} \end{cases}, \tag{10}$$

can be obtained from the polarization propagator in (3). For each excitation, we can expand this propagator, retaining only the ring diagrams as in the previous section

Following the same steps as in the previous section we obtain

$$
\begin{aligned}
i\mathbb{\Pi}^q[A(x),B(y)] &= \bar{\mathbb{U}}_s(x)\mathbf{M}_A\mathbb{U}_n(x)i\Pi^q_{ns;rm}(x_0-y_0,y_0-x_0) \\
&\quad \times\bar{\mathbb{U}}_r(y)\mathbf{M}_B\mathbb{U}_m(y)
\end{aligned} \tag{11}
$$

with

$$
i\mathbb{\Pi}^q = \begin{pmatrix} i\Pi^q_{pp;pp} & i\Pi^q_{pp;ph} & i\Pi^q_{pp;hh} \\ i\Pi^q_{ph;pp} & i\Pi^q_{ph;ph} & i\Pi^q_{ph;hh} \\ i\Pi^q_{hh;pp} & i\Pi^q_{hh;ph} & i\Pi^q_{hh;hh} \end{pmatrix}. \tag{12}
$$

The subindices in the matrix elements of $i\mathbb{\Pi}^q$ and $i\tilde{\mathbb{\Pi}}$ denote the type of excitation (pp for particle-particle, ph for particle-hole and hh for hole-hole). The matrices $\mathbf{M}_B$ and $\mathbf{M}_A$ are respectively, the matrices corresponding the excitations $B(y)$ and observable $A(x)$. The polarization propagator $i\Pi^q_{ns;rm}$ is the exactly the same as that we obtained in the previous section. Thus, again, the problem reduces to solving the equation (5).

4 Conclusions

Our aim here has been to show the procedure utilized to obtain the relativistic QRPA equations, starting from the model QHD. We have obtainded the QRPA in matrix form and extended the particle-hole response, including particle-particle and hole-hole excitations.

We intend to continue this work in order to solve the QRPA equations numerically to apply to the β decay of exotic nuclei.

5 Acknowledgments

C. D. C. and E. F. B. acknowledge the support of the FAPESP (Brazil). B.V.C. and T.F. acknowledge the partial support of the FAPESP and CNPq (Brazil).

References

[1] B. V. Carlson, D. Hirata, nucl-th/0006006, to appear in Phys. Rev. C.

[2] T.L. Ainsworth, J. Wambach and D. Pines, Phys. Lett. **222B** (1989) 173; J. Wambach, T.L. Ainsworth and D. Pines, Nucl. Phys. **A555** (1993) 128; H.-J. Schulze, J. Cugnon, A. Lejeune, M. Baldo and U. Lombardo, Phys. Lett. **375B** (1996) 1.

[3] D. Cha, Phys. Rev. C **27** (1983) 2269; J. Engel, P. Vogel and M.R. Zirnbauer, Phys. Rev. C **37** (1988) 731.

A Comparison Between the Relativistic BCS and Hartree-Bogoliubov Approximations to Nuclear Ground States

A.C. De Conti, B.V. Carlson.

Departamento de Física, Instituto Tecnológico de Aeronáutica,

Centro Técnico Aeroespacial,

12228-900 São José dos Campos, SP, Brazil

Abstract

We compare nuclear binding energies and deformations obtained using the Dirac-Hartree-Bogoliubov (DHB) approximation to those obtained using a simplification of the DHB that we call the relativistic BCS approximation.

1-Properties of Static Solutions in the DHFB Approximation

We know that The Dirac-Gorkov equation can be written in Hamiltonian form as a Hermitian eignequation like,

$$\int d^3y \begin{pmatrix} (\omega+\mu)\delta(\vec{x}-\vec{y}) - h(\vec{x},\vec{y}) & \overline{\Delta}^{\dagger}(\vec{x},\vec{y}) \\ \overline{\Delta}(\vec{x},\vec{y}) & (\omega-\mu)\delta(\vec{x}-\vec{y}) + h_T(\vec{x},\vec{y}) \end{pmatrix} \begin{pmatrix} U(\vec{y}) \\ \gamma_0 V(\vec{y}) \end{pmatrix} = 0, \tag{1}$$

where we introduce the single-particle hamiltonian, $h(\vec{x},\vec{y})$, given by

$$h(\vec{x},\vec{y}) = (-i\vec{\alpha}\cdot\vec{\nabla} + \beta M)\delta(\vec{x}-\vec{y}) + \beta\Sigma(\vec{x},\vec{y}) \tag{2}$$

with $h_T(\vec{x},\vec{y}) = Ah^T(\vec{x}\vec{y})A^{\dagger}$ and $h(\vec{x},\vec{y}) = h^{\dagger}(\vec{x},\vec{y})$.

In the case of pure proton-proton or neutron-neutron pairing, the solutions to the Dirac-Gorkov equation will be either purely proton particle-holes ones or neutron particle-hole ones of the form

$$\Psi_p = \begin{pmatrix} U_p \\ 0 \\ 0 \\ V_p \end{pmatrix} \qquad \text{and} \qquad \Psi_n = \begin{pmatrix} 0 \\ U_n \\ V_n \\ 0 \end{pmatrix}, \tag{3}$$

where each of the elements in the column vectors are themselves 4-component Dirac spinors.

The Hamiltonian form of the pairing field is, in this case,

$$\begin{aligned} \overline{\Delta}_t^{\dagger}(\vec{x},\vec{y}) &= \gamma_0\Delta_t(\vec{x},\vec{y})\gamma_0 \\ &= \delta(\vec{x}-\vec{y})c_{pair}\left(\frac{g_\sigma^2}{m_\sigma^2}\gamma_0\kappa_t(\vec{x})\gamma_0 - (\frac{g_\omega^2}{m_\omega^2} + \frac{(g_\rho/2)^2}{m_\rho^2})\gamma_0\gamma^\mu\kappa_t(\vec{x})\gamma_\mu\gamma_0\right), \end{aligned} \tag{4}$$

where the anamalous density $\kappa_t(\vec{x})$ can be written as

$$\begin{aligned}\kappa_t(\vec{x}) &= \frac{1}{2}\sum_{\omega_{t\gamma}<0,\Omega_\gamma>0}(U_{t\gamma}(\vec{x})V^\dagger_{t\gamma}(\vec{x})\gamma_0 + BU^*_{t\gamma}(\vec{x})V^T_{t\gamma}(\vec{x})B^\dagger\gamma_0 \\ &+\gamma_0 V_{t\gamma}(\vec{x})U^\dagger_{t\gamma}(\vec{x}) + \gamma_0 BV^*_{t\gamma}(\vec{x})U^T_{t\gamma}(\vec{x})B^\dagger). \end{aligned} \tag{5}$$

2- Relativistic BCS approximation

To further approximate the DHB equations and put them into a form that resembles more closely the nonrelativistic BCS equations, we first make use of the Hamiltonian form of the Dirac-Gorkov equation. This is

$$W = \int d^3x d^3y \sum_{t\gamma}(U^\dagger_{t\gamma}(\vec{x}), V^\dagger_{t\gamma}(\vec{x})\gamma_0)\begin{pmatrix}(\omega_{t\gamma}+\mu_t)\delta(\vec{x}-\vec{y}) - h_t(\vec{x},\vec{y}) & \overline{\Delta}^\dagger_t(\vec{x},\vec{y}) \\ \overline{\Delta}_t(\vec{x},\vec{y}) & (\omega_{t\gamma}-\mu_t)\delta(\vec{x}-\vec{y}) - h_t(\vec{x},\vec{y}).\end{pmatrix}\begin{pmatrix}U_{t\gamma}\\ \gamma_0 V_{t\gamma}\end{pmatrix}, \tag{6}$$

We then approximate the wave functions as

$$\begin{pmatrix}U_{t\gamma}(\vec{x})\\ \gamma_0 V_{t\gamma}(\vec{x})\end{pmatrix} \longrightarrow \begin{pmatrix}u_{t\gamma}\psi_{t\gamma}(\vec{x})\\ v_{t\gamma}\psi_{t\gamma}(\vec{x})\end{pmatrix} \tag{7}$$

where $u_{t\gamma}$ and $v_{t\gamma}$ are scalar quantities and $\psi_{t\gamma}(\vec{x})$ is a Hartree mean field wave function. When the approximate wave function is substituted in the variational functional, the latter can be reduced to

$$W(\{u_{t\gamma}, v_{t\gamma}\}) = \sum_{t\gamma}(u^*_{t\gamma}, v^*_{t\gamma})\begin{pmatrix}\omega_{t\gamma}+\mu_t-\varepsilon_{t\gamma} & \overline{\Delta}^\dagger_{t\gamma}\\ \Delta_{t\gamma} & \omega_{t\gamma}-\mu_t+\varepsilon_{t\gamma}\end{pmatrix}\begin{pmatrix}u_{t\gamma}\\ v_{t\gamma}\end{pmatrix}, \tag{8}$$

where $\Delta_{t\gamma}$ is the expectation value of the pairing field in the state $t\gamma$

$$\Delta_{t\gamma} = \int d^3x\, d^3y \psi^\dagger_{t\gamma}(\vec{x})\overline{\Delta}_t(\vec{x},\vec{y})\psi_{t\gamma}(\vec{y}). \tag{9}$$

We assume that the $\Delta_{t\gamma}$ are real so that the Bogoliubov coefficients, $u_{t\gamma}$ and $v_{t\gamma}$, can also be taken to be real. We also assume that the Hartree mean field wave functions are normalized, so that $u^2_{t\gamma} + v^2_{t\gamma} = 1$.

Requiring that the variation with respect to each of the coefficients $u_{t\gamma}$ be extremal, and using the normalization condition to relate the variation of $v_{t\gamma}$ to that of $u_{t\gamma}$, we define $\omega_{t\gamma}$ so as to annul the functional W completely,

$$\omega_{t\gamma} = -(\mu_t - \varepsilon_{t\gamma})(u^2_{t\gamma} - v^2_{t\gamma}) - 2\Delta_{t\gamma}u_{t\gamma}v_{t\gamma} = -\sqrt{(\mu_t-\varepsilon_{t\gamma})^2 + \Delta^2_{t\gamma}} \tag{10}$$

The positive-frequency solution, $\omega_{t\gamma} = \sqrt{(\mu_t-\varepsilon_{t\gamma})^2+\Delta^2_{t\gamma}}$, can be obtained with the substitution $u_{t\gamma} \longrightarrow v_{t\gamma}$ and $v_{t\gamma} \longrightarrow -u_{t\gamma}$ However, only the negative-frequency solutions enter the self-consistency equations.

The BCS approximation consists in solving the self-consistency equations using the appoximate BCS wavefunction described here rather than the complete DHFB one.

3-Comparison between DHB and BCS approximation

We compare the binding enegy as a function of the quadrupole deformation in the two approximations. The deformation is constrained by an addicional potential term quadratic in the difference between the calculated quadrupole moment of the desired value. The contribution of this term to the binding energy is then substracted out.

The magnitude of the pairing field is adjusted by varying a parameter f_{pair} that multiplies the pairing interaction. Such a multiplicative factor can be justified on the grounds of renormalization of the interaction due to the truncation of the space in which it acts. The use of different values of f_{pair} for the BCS of DHB calculations are also just frable with this reasoning here, we find due best agreemente for the expected ground state deformations using $f_{pair} = 0.81$ in the relativistic BCS approximation and $f_{pair} = 1.00$ in the DHB one. Form the figures shown here, it would appear that the BCS approximation povides better agreement with the data than the DHB approximation, which in principle, is more exact. We are currently conducting further sudies to try do undestand why this is the case.

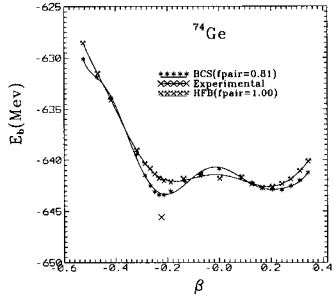

Figure 1: Energia de ligação contra a deformação β para o núcleo de ^{74}Ge na aproximação o BCS

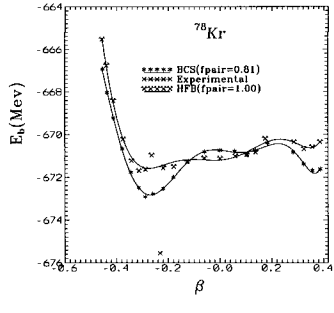

Figure 2: Energia de ligação contra a deformação β para o núcleo de ^{78}Ge na aproximação BCS

References

[1] B.D.Serot and J.D.Walecka, *ADv.Nucl.Phys.* **16**,(1986)1.

[2] P.G.Reinhard, *Rep.Prog.Phys.* **52**, (1989)439.

[3] B.D.Serot, *Rep.Prog.Phys.* **55**, (1992)1855.

[4] B.V.Carlson, T.Frederico and F.B.Guimarães *Phys.Rev.C* **56**, (1997)3097.

CHIRAL PHASE TRANSITION IN A COVARIANT NONLOCAL NJL MODEL

I. GENERAL[a], D. GOMEZ DUMM[b,c] and N. N. SCOCCOLA[a,c,d]

[a] *Physics Dept., Com. Nac. de Energía Atómica, (1429) Buenos Aires, Argentina.*
[b] *Physics Dept., Univ. La Plata, (1900) La Plata, Argentina.*
[c] *CONICET, (1033) Buenos Aires, Argentina,*
[d] *Universidad Favaloro, (1078) Buenos Aires, Argentina.*

ABSTRACT

The properties of the chiral phase transition at finite temperature and chemical potential are investigated within a nonlocal covariant extension of the NJL model based on a separable quark-quark interaction. We find that for low values of T the chiral transition is always of first order and, for finite quark masses, at certain "end point" the transition turns into a smooth crossover. Our predictions for the position of this point is similar, although somewhat smaller, than previous estimates.

The behaviour of hot dense hadronic matter and its transition to a plasma of quarks and gluons has received considerable attention in recent years. To a great extent this is motivated by the advent of facilities like e.g. RHIC at Brookhaven which are expected to provide some empirical information about such transition. The interest in this topic has been further increased by the recent suggestions that the QCD phase diagram could be richer than previously expected (see Ref.[1] for some recent review articles). In this contribution we investigate this problem using a covariant nonlocal generalization of the Nambu-Jona-Lasinio model defined by the effective action

$$\begin{aligned} S &= \int d^4x\ \bar{\psi}(x)\,(i\partial\!\!\!/ - m_c)\,\psi(x) + \int d^4x_1 ... d^4x_4\ V(x_1,x_2,x_3,x_4) \\ &\quad \times \left(\bar{\psi}(x_1)\psi(x_3)\bar{\psi}(x_2)\psi(x_4) + \bar{\psi}(x_1)i\gamma_5\tau^a\psi(x_3)\bar{\psi}(x_2)i\gamma_5\tau^a\psi(x_4)\right)\,, \quad (1) \end{aligned}$$

where, m_c is the (small) current quark mass responsible for the explicit chiral symmetry breaking. The interaction kernel in Euclidean momentum space is given by

$$V(q_1,q_2,q_3,q_4) = \frac{(2\pi)^4}{2}\ G\ r(q_1^2)r(q_2^2)r(q_3^2)r(q_4^2)\ \delta(q_1+q_2-q_3-q_4)\,, \quad (2)$$

where $r(q^2)$ is a regulator normalized in such a way that $r(0) = 1$. Some general forms for this regulator like Lorentzian or Gaussian functions have been used in the literature. Like in the local version of the NJL model, the chiral symmetry is spontaneously broken in this nonlocal scheme for large enough values of the coupling G. In the Hartree approximation the momentum dependent self-energy $\Sigma(q^2)$ at vanishing temperature and chemical potential is given by $\Sigma(q^2) = m_c + (\Sigma(0) - m_c)r^2(q^2)$, where the $\Sigma(0)$ can be obtained as solution of a gap equation. In general, the quark propagator might have a rather complicate structure of poles and cuts in the complex plane. In what follows we will assume that the regulator is such that it only has an arbitrary but numerable set of poles, as it is the case for e.g. the step function regulator, Gaussian regulator, etc.

To introduce finite temperature and chemical potential we follow the imaginary time formalism. Thus, we replace the fourth component of the Euclidean quark momentum by $\omega_n - i\mu$, where $\omega_n = (2n+1)\pi T$ are the discrete Matsubara frequencies and μ is the chemical potential. In what follows we will assume that the model parameters G and m_c, as well as the shape of the regulator, do not change with T or μ. Performing this replacement in the gap equation we obtain after some calculation[3]

$$\frac{\pi^4}{G\,N_c}\,(\Sigma(0) - m_c) = \int d^4q \quad \frac{\Sigma(q^2)r^2(q^2)}{q^2 + \Sigma^2(q^2)} \quad - \\ - \int d^3\vec{q} \sum_{\alpha_p}{}' \gamma_p \, Re\left[\frac{\Sigma(z)r^2(z)}{1 + 2\,\partial_z\Sigma^2(z)}\bigg|_{z=\alpha_p^2} \frac{\epsilon_p}{\epsilon_p^2 + iR_pI_p}\,(n_+ + n_-) \right], \qquad (3)$$

where we have expressed the sum over the Matsubara frequencies in terms of a sum over the quark propagator poles $\alpha_p = R_p + iI_p$ by introducing the auxiliary function $f(z) = 1/(1 + \exp(z/T))$ and using standard finite temperature field theory techniques. In Eq.(3) ϵ_p is given by

$$\epsilon_p = \sqrt{\frac{I_p^2 - R_p^2 + \vec{q}^{\,2} + \sqrt{(I_p^2 - R_p^2 + \vec{q}^{\,2})^2 + 4R_p^2I_p^2}}{2}}, \qquad (4)$$

and the prime implies that the sum runs over all the poles $\alpha_p = R_p + iI_p$ with $R_p \geq 0$ and $I_p > 0$. Moreover, $\gamma_p = 1/2$ for $R_p = 0$ and $\gamma_p = 1$ otherwise and the generalized occupation numbers $n_\pm$ are

$$n_\pm = \left[1 + \exp\left(\frac{\epsilon_p \pm \mu + iR_pI_p/\epsilon_p}{T}\right)\right]^{-1}. \qquad (5)$$

Having introduced the formalism needed to extend the model to finite temperature and chemical potential we turn now to our numerical calculations. In this work we take the nonlocal regulator to be of the Gaussian form $r(q^2) = \exp(-q^2/2\Lambda^2)$ and consider two sets of values for the parameters of the model. Set I corresponds to $G = 50\ \mathrm{GeV}^{-2}$, $m_c = 10.5$ MeV and $\Lambda = 627$ MeV, while for Set II the respective values are

$G = 30$ GeV^{-2}, $m_c = 7.7$ MeV and $\Lambda = 760$ MeV. Both sets of parameters lead to the physical values of the pion mass and decay constant. For Set I the calculated value of the chiral quark condensate at zero temperature and chemical potential is $-(200\ \text{MeV})^3$ while for Set II it is $-(220\ \text{MeV})^3$. These values are similar in size to those determined from lattice gauge theory or QCD sum rules. The corresponding results for the self-energy at zero momentum are $\Sigma(0) = 350$ MeV for Set I and $\Sigma(0) = 300$ MeV for Set II. It is possible to check that Set I corresponds to a situation in which there are no purely imaginary poles of the Euclidean quark propagator and Set II to the case in which there are two pairs of them. Following Ref.[2], Set I might be interpreted as a confinement one since quarks cannot materialize on-shell in Minkowski space.

The behaviour of the zero-momentum self-energy $\Sigma(0)$ as function of the chemical potential for some values of the temperature is shown in Fig. 1. There, we observe

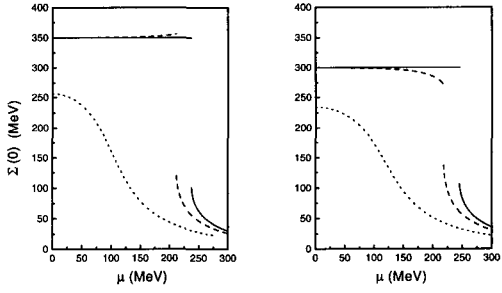

Figure 1: *Behaviour of the self-energy as a function of the chemical potential for three representative values of the temperature. Full line corresponds to T=0, dashed line to $T = 50$ MeV and dotted line to $T = 100$ MeV. The left panels display the results for Set I and the right panels those for Set II.*

that at $T = 0$ there is a first order phase transition for both the confining and the non-confining sets of parameters. As the temperature increases, the value of the chemical potential at which the transition shows up decreases. Finally, above a certain value of the temperature the first order phase transition does not longer exist and, instead, there is a smooth crossover. This phenomenon is clearly shown in the right panel of Fig. 2, where we display the critical temperature at which the phase transition occurs as a function of the chemical potential. The point at which the first order phase transition ceases to exist is usually called "end point". In the chiral limit the latter turns into the so-called "tricritical point", which is the point at which the second order phase transition expected to happen in QCD with two massless quarks becomes a first order one. In fact, this is also what happens within the present model in the chiral limit, as it is shown in the left

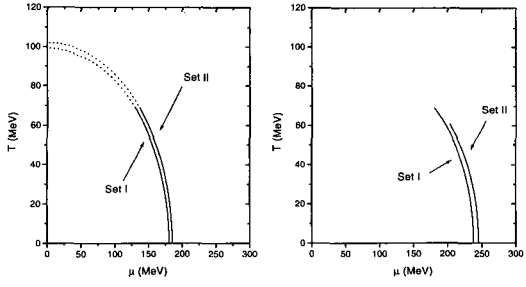

Figure 2: *Critical temperatures as a function of the chemical potential. The left panel corresponds to the chiral limit and the right panel to the case of finite quark masses.*

panel of Fig. 2. Some predictions about both the position of this point and its possible experimental signatures exist in the literature[4]. In our case the "tricritical point" is located at (T_P, μ_P) =(70 MeV, 130 MeV) for Set I and (68 MeV, 138 MeV) for Set II, while the "end points" are placed at (T_E, μ_E) =(69 MeV, 180 MeV) and (61 MeV, 203 MeV), respectively. As we see the predicted values are very similar for both sets of parameters and slightly smaller than the values in Refs.[4], $T_P \approx 100$ MeV and $\mu_P \approx 200 - 230$ MeV. In this sense, we should remark that our model predicts a critical temperature at $\mu = 0$ of about 100 MeV, somewhat below the values obtained in modern lattice simulations which suggest $T_c \approx 140 - 190$ MeV. In any case, our calculation seems to indicate that μ_P might be smaller than previously expected even in the absence of strangeness degrees of freedom.

This work was supported in part by PICT 03-00000-00133 from ANPCYT, Argentina.

References

[1] F. Wilczek, *hep-ph/0003183*; K. Rajagopal, *hep-ph/0009058*.

[2] R.D. Bowler and M.C. Birse, Nucl. Phys. **A582** (1995) 655; R.S. Plant and M.C. Birse, Nucl. Phys. **A628** (1998) 607.

[3] I. General, D. Gomez Dumm and N.N. Scoccola, *hep-ph/0010034*.

[4] J. Berges and K. Rajagopal, Nucl.Phys.**B538** (1999) 215; M.A. Halasz *et al* Phys.Rev.**D58** (1998) 096007; M. Stephanov, K. Rajagopal and E. Shuryak, Phys. Rev. Lett. **81** (1998) 4816; Phys. Rev. **D60** (1999) 114028.

High Density Effects in eA Processes

Victor Gonçalves
Universidade Federal de Pelotas

The high density effects should be manifest at small x and/or large nuclei. In this contribution we consider the behavior of the nuclear structure function F_2^A slope as a search of these effects. We demonstrate that a turnover is predicted in this observable. We verify that the high density implies that the maximum value of the slope occurs at large values of the photon virtuality and is dependent of the number of nucleons and energy. Our conclusion is that the measurement of this observable will allow to explicit the presence of the high density effects, as well as the saturation.

The physics of high-density QCD (hdQCD) has become an increasingly active subject of research, both from experimental and theoretical points of view. Presently, and in the near future, the collider facilities such as the DESY collider HERA (ep, eA), Fermilab Tevatron ($p\overline{p}$, pA), BNL Relativistic Heavy Ion Collider (RHIC) (eA, AA), and CERN Large Hadron Collider (LHC) ($p\overline{p}$, AA) will be able to probe new regimes of dense quark gluon matter at very small Bjorken x or/and at large A, with rather different dynamical properties. In these experiments, be it because of high energies in ep collisions or because of intrinsically higher numbers of partons in eA and AA collisions, QCD effects are dominated by the large number of gluons involved. The description of these processes is directly associated with a correct gluonic dynamics in this kinematical region.

Theoretically, at small x and/or large A we expect the transition of the regime described by the linear dynamics (DGLAP, BFKL), where only the parton emissions are considered, for a new regime where the physical process of recombination of partons become important in the parton cascade and the evolution is given by a nonlinear evolution equation. This regime is characterized by the limitation on the maximum phase-space parton density that can be reached in the hadron wavefunction (parton saturation) and very high values of the QCD field strength $F_{\mu\nu} \approx 1/g$. In general the description of the gluon distribution in high density limit is given by evolution equations which resum powers of the function $\kappa(x,Q^2) \equiv \frac{3\pi^2\alpha_s A}{2Q^2}\frac{xg(x,Q^2)}{\pi R_A^2}$, which represents the probability of gluon-gluon interaction inside the parton cascade. The condition $\kappa = 1$ specifies the critical line, which separates between the linear regime $\kappa \ll 1$ and the high density regime $\kappa \gg 1$, and define the saturation momentum scale Q_s

given by

$$\kappa = 1 \Rightarrow Q_s^2(x;A) = \frac{3\pi^2 \alpha_s A}{2} \frac{x g(x, Q_s^2(x;A))}{\pi R_A^2} \quad , \tag{1}$$

below which the gluon densities reach their maximum value (saturates). At any value of x there is a value of $Q^2 = Q_s^2(x)$ in which the gluonic density reaches a sufficiently high value that the number of partons stops the growth. This scale depends on the energy of the process and the atomic number of the colliding nuclei, determining the typical intrinsic momenta associated with quanta in the nuclear wavefuntion. These quanta go on shell in a collision, and eventually produce a large multiplicity of particles. At very high energies, the saturation scale is the only scale in the problem, and one can estimate that the typical momenta of the particles produced in the collision is at this scale. If this momenta is large enough, one can approach the saturation regime using perturbation theory.

Here we analyze the high density effects in eA processes (For a full discussion see Ref. [3]), where we can study the dynamics of QCD at high densities and at zero temperature, raising questions complementary to those addressed in the search for a quark-gluon plasma in high-energy heavy ion collisions. The nucleus in this process serves as an amplifier for nonlinear phenomena expected in QCD at small x, obtaining at the assessable energies at HERA and RHIC with an eA collider the parton densities which would be probed only at energies comparable to LHC energies with an ep collider. Our goal is to address the boundary region between the linear and nonlinear dynamics and identify possible signatures in the behavior of the nuclear structure function slope. This study is motivated by our results in Ref. [4], where we show that the deep inelastic scattering on nuclear targets is a very good place to look for saturation if we consider the behavior of the nuclear structure function slope, and demonstrate the distinct predictions from DGLAP and high density approaches. Here we extend the previous analyses for the energies of eA processes at RHIC and at HERA, as well as for the possible colliding nuclei in these experiments, analyzing the x and A dependence of the saturation scale.

The deep inelastic scattering $eA \to e + X$ is usually interpreted in a frame where the nucleus is going very fast. In this case the high density effects are the result of an overlap in the longitudinal direction of the parton clouds originated from different bound nucleons [1]. It corresponds to the fact that small x partons cannot be localized longitudinally to better than the size of the nucleus. Thus low x partons from different nucleons overlap spatially creating much larger parton densities than in the free nucleon case. This leads to a large amplification of the nonlinear effects expected in QCD at small x.

In the target rest frame, the electron-nucleus scattering can be visualized in terms of the propagation of a small $q\bar{q}$ pair in high density gluon fields through much larger distances than it is possible with free nucleons. In this frame the nuclear structure function reads

$$F_2^A(x,Q^2) = \frac{Q^2}{4\pi\alpha_{em}} \int dz \int \frac{d^2\vec{r}_t}{\pi} |\Psi(z,\vec{r}_t)|^2 \, \sigma^{q\bar{q}+A}(z,\vec{r}_t) \; , \qquad (2)$$

where $\Psi(z,\vec{r}_t)$ is the light-cone wavefunction for the transition $\gamma^* \to q\bar{q}$ and we have assumed the dominance of the transverse photon polarization. The cross section for scattering a $q\bar{q}$ - dipole off the nucleus is denoted by $\sigma^{q\bar{q}+A}(z,\vec{r}_t)$. In the pure perturbative regime the reaction is mediated by single gluon exchange which changes into multi-gluon exchange when the saturation region is approached. We estimate the high density effects considering the Glauber multiple scattering theory, which was probed in QCD[5]. The nuclear collision is analyzed as a succession of independent collisions of the probe with individual nucleons within the nucleus, which implies that

$$F_2^A(x,Q^2) = \frac{Q^2}{4\pi\alpha_{em}} \int dz \int \frac{d^2\vec{r}_t}{\pi} |\Psi(z,\vec{r}_t)|^2 \int \frac{d^2\vec{b}_t}{\pi} \, 2\,[1 - e^{-\sigma^{q\bar{q}+N}(z,\vec{r}_t) S(\vec{b}_t)}] \qquad (3)$$

where $\vec{b}_t$ is the impact parameter, $S(\vec{b}_t)$ is the profile function and $\sigma^{q\bar{q}+N}$ is the dipole cross section off the nucleons inside the nucleus, which is proportional to the pair separation squared r_t^2 and the nucleon gluon distribution $xg(x,1/r_t^2)$. The expression (3) represents is the Glauber-Mueller formula for the nuclear structure function (see [2] for details). The main characteristic of the Glauber-Mueller formula is that for a large Q^2 it reduces to the standard small x DGLAP expression, while at small Q^2 it goes to zero as $Q^2 log Q^2$, predicting a transition in the behavior of F_2^A at an intermediate value of Q^2. Using a gaussian profile function, we can derive the slope of the nuclear structure function directly from the expression (3), resulting [4]

$$\frac{dF_2^A(x,Q^2)}{d log Q^2} = \frac{R_A^2 Q^2}{2\pi^2} \sum_1^{n_f} \epsilon_i^2 \{C + ln(\kappa_q(x,Q^2)) + E_1(\kappa_q(x,Q^2))\} \; , \qquad (4)$$

where $\kappa_q = (2\alpha_s \, A/3R_A^2)\, \pi \, r_t^2 \, xg(x, \frac{1}{r_t^2})$, A is the number of nucleons, R_A^2 is the mean nuclear radius, C is the Euler constant and E_1 is the exponential function (see [4] for details). The expression (4) predicts the x, Q^2 and A dependence of the high density effects for the F_2^A slope. Similarly to the F_2^A we expect that a turnover, in the behavior of the F_2^A slope, should occur for the saturation scale.

	W = 50 GeV		W = 75 GeV		W = 115 GeV	
	x	Q^2	x	Q^2	x	Q^2
$A = 12$	0.620×10^{-3}	1.55	0.382×10^{-3}	2.15	0.231×10^{-3}	3.05
$A = 32$	0.740×10^{-3}	1.85	0.462×10^{-3}	2.6	0.287×10^{-3}	3.8
$A = 197$	0.11×10^{-2}	2.75	0.649×10^{-3}	3.65	0.389×10^{-3}	5.15

Table 1: The A and W dependence of the turnover predicted in the F_2^A slope.

We consider that the Bjorken variable x and the photon virtuality Q^2 are related by the expression $x = Q^2/W^2$, where W is the $\gamma^* p$ c.m. energy, and calculate the x and Q^2 dependences for W and A fixed. In Table 1 we present explicitly the A and W dependences of the turnover in F_2^A slope. The remarkable property of our results is the presence of a distinct maximum for each slope, dependent of the energy and the number of nucleons considered. We can see that at fixed A, if we increase the value of the energy, the maximum value of the slope occur at larger values of Q^2 and smaller values of x. Moreover, at fixed W, the turnover is displaced at larger values of x and Q^2 if we increase the number of nucleons A. These behaviors can be understood intuitively. The turnover is associated with the regime in which the partons in the nucleus form a dense system with mutual interactions and recombinations, with a transition between the linear and nonlinear regime at the saturation scale [Eq. (1)]. As the partonic density growth at larger values of the number of nucleons A and smaller values of x we have that, at fixed A, the saturation scale Q_s^2 will increase at small values of x, since this is directly proportional to the gluon distribution. Moreover, at fixed energy W, the same density at $A = 12, 32, 197$ will be obtained at larger values of x and Q^2. These properties of the high density effects are verified in the F_2^A slope. The main result of our analysis is that the saturation should occur already at rather small distances (large Q_s^2) well below where soft dynamics is supposed to set in, justifying the use of perturbative QCD to approach a highly dense system.

References

1. L. V. Gribov, E. M. Levin, M. G. Ryskin. *Phys. Rep.* **100** (1983) 1; A. H. Mueller, J. Qiu. *Nucl. Phys.* **B268** (1986) 427.
2. A. L. Ayala, M. B. Gay Ducati and E. M. Levin. *Nucl. Phys.* **B493** (1997) 305.
3. V. P. Gonçalves, *Phys. Lett.* (in press), hep-ph/0010060.
4. M. B. Gay Ducati, V. P. Gonçalves, *Phys. Lett.* **B466** (1999) 375.
5. A. H. Mueller. Nucl. Phys. **B335** (1990) 335.

Quasi-Deuteron Pairing and Isospin Asymmetry

B. Funke Haas[1], B. V. Carlson[2] and T. Frederico[2]
Departamento de Física - Instituto Tecnológico de Aeronáutica - São José dos Campos - SP- Brazil
CEP 12.228-901 - e-mail: barbara@fis.ita.br

We describe how asymmetry may be introduced in the self-consistent-field-equations of the Dirac-Hartree-Fock-Bogoliubov (DHFB) approximation to nuclear matter and the difficulties related with this question. As is done in the HF approximation to asymmetric nuclear matter, we introduce two Lagrange multipliers, μ_p and μ_n, describing the neutron and the proton chemical potentials. In contrast with the HF approximation, we must also introduce Lagrange multipliers to maintain the mean value of the off-diagonal, mixed proton-neutron density equal to zero. This is because of the pairing field, which mixes the particle-hole wave functions.

The DHFB approximation to nuclear matter [1] is a self-consistent model, which describes the average effects of the interaction between nucleons in terms of a self-energy and a pairing field. The self-energy field describes the average effect of the nuclear medium on the propagation of each nucleon. The pairing field takes into account the correlations betweeen nucleons due to their binding into pairs.

The DHFB approximation is most easily studied in symmetric nuclear matter. However, most real nuclear systems are not symmetric in isospin. The isospin asymmetry is of particular importance when studying proton-neutron pairing (either isoscalar or isovector), as the formation of pairs, which predominantly occurs close to the Fermi energy, will be suppressed if the neutron and proton Fermi energies are distant from each other. Here we will develop the formalism necessary to treat the general case of asymmetric nuclear matter.

We start by comparing the contributions to the equations of motion of the expectation value of the full interaction Lagrangian and that of the effective Lagrangian. After performing a little algebra, we obtain equations relating the two, that become self-consistency equations when the expectation val-

[1]Supported by FAPESP
[2]Partially supported by FAPESP and the CNPq

ues are evaluated using the relation between the fields and the generalized propagator. [1]

The next step in developing the DHFB approximation is to introduce the Lorentz and the isospin structure of the fields. The general form of the self-energy field is

$$\Sigma(k) = -[\Sigma_s - \gamma_0\Sigma_0 + \gamma^i k_i \Sigma_v] \otimes 1 + [\Sigma_s^j - \gamma_0\Sigma_0^j + \gamma^i k_i \Sigma_v^j] \otimes \tau_j.$$

Note that the self-energy field possesses isoscalar and both diagonal and off-diagonal isovector components. The off-diagonal components are a result of the pairing field.

We take the pairing field to have the form

$$\begin{aligned}\Delta(k) &= [\Delta_s^j - \gamma_0\Delta_0^j - i\gamma_0\gamma^i k_i \Delta_T^j] \otimes \tau_j \\ &\quad + [\Delta_1 \gamma^i \gamma^5 \xi_i + \Delta_2 k^i \gamma^5 \xi_i + \Delta_3 k^i \not{k}\gamma^5 \xi_i + \Delta_4 P_0 \sigma^{i0}\gamma^5 \xi_i] \otimes 1\end{aligned}$$

where ξ_i represents the deuteron polarization, and Δ_α represents the components of the fields projected into the space of the operator α. The components on the first line of the above expression represent the usual scalar-isovector pairing, in its most general form, while those on the second line account for the vector-isoscalar (quasi-deuteron) pairing. Substituting the above expressions into the self-consistency equations and taking the approriate traces, we can reduce these equations to a set of equations for their components.

The mean fields we have introduced can describe symmetric as well as asymmetric nuclear matter. Indeed, if we provide a symmmetric baryon density, the resulting fields are also symmetric under isospin rotations. To produce asymmetry, we must provide an asymmetric baryon density as an initial condition. The isospin decomposition of the baryon density takes the form $\rho = \rho_0 \otimes 1 + \rho_j \otimes \tau_j$, where

$$\rho_0 = \int d^4q Tr\left[\gamma_0 G(q)\right] e^{iq^0 0+\%}$$

and

$$\rho_j = \int d^4q Tr\left[\tau_j \gamma_0 G(q)\right] e^{iq^0 0^+}$$

The neutron and proton densities are given by

$$\rho_n = \rho_0 + \rho_3$$

and

$$\rho_p = \rho_0 - \rho_3$$

The neutron and proton densities are fixed at the appropriate values by using two Lagrange multipliers, μ_n and μ_p, with

$$\mu_n = \mu_0 + \mu_3$$

and

$$\mu_p = \mu_0 - \mu_3$$

In general, we could also find mixed neutron-proton densities,

$$\rho_1 = Tr\left[\bar{\psi}_p \psi_n\right]$$

and

$$\rho_2 = Tr\left[\bar{\psi}_n \psi_p\right]$$

which are not observed in nature.To ensure that the expectation values of the latter are zero, we must introduce two additional Lagrange multipliers, μ_1 and μ_2, which are fixed so as to annul these components of the density. We thus have

$$\mu = \mu_0 \otimes 1 + \mu_j \otimes \tau_j,$$

which permitss us a completely general description of isoscalar and isovector pairing in nuclear matter.

We are currently modifying our nuclear matter DHFB code in order to study numerically the model we have developed here.

References

[1] F.B. Guimarães, B.V. Carlson and T. Frederico, *PRC* **54** (1996) 2385.

Einstein Equations and Fermion Degrees of Freedom

E. F. Lütz and C. A. Z. Vasconcellos
Instituto de Física, UFRGS, Porto Alegre, Brazil

Abstract:

When Dirac derived the special relativistic quantum equation which brings his name, it became evident that the spin is a consequence of the space-time geometry. However, taking gravity into account (as for, for instance, in the study of neutron stars), most authors do not take into account the relation between hyperbolic geometry and spin and derive an Einstein equation which implicitly takes into account only boson degrees of freedom. In this work we introduce a consistent quantum general relativistic formalism which allows us to study the effects of the existence of fermion degrees of freedom.

1 Introduction

The first source of problems that emerge when we try to build a consistent quantum general relativistic formalism is the heavy dependence upon special coordinate systems possessed by usual quantum formalisms.

On the other hand, general relativistic formalisms usually completely ignore non-integer spin degrees of freedom, that is, they usually deal only with integer rank tensors.

In order to deal properly with gravity and non-integer spin at the same time it is advisable to start by deriving Dirac's equation covariantly. Such a derivation holds the key to unveil the relationship between spin and geometry.

Essentially, we start out by a linearization

$$g^{\alpha\beta}p_\alpha p_\beta = m^2 \Longrightarrow \gamma^\alpha p_\alpha = m\,, \quad g^{\alpha\beta} = \frac{1}{2}\{\gamma^\alpha, \gamma^\beta\}\,; \tag{1}$$

the quantities γ^α are the generalized Dirac matrices.

In General Relativity, all the relevant information about space-time properties is contained in the metric tensor. But, according to relation (1), all the information contained in the metric tensor is also contained in the quantities γ^α, though not vice-versa. Therefore, Dirac's matrices must contain information even about space-time curvature.

Considering the loss of information implied by the application $\gamma^\alpha \mapsto g^{\alpha\beta}$ expressed by (1), we should use Dirac's matrices as field components instead of the metric tensor. On the other hand, if we do not adopt such a procedure or an equivalent one, we are implicitly ignoring (at least in part) the existence of fermions in the system under study.

The gravity field is represented by the metric tensor (usual approach) or by generalized Dirac's matrices (our approach). In order to derive the equation for

gravity (Einstein's) by the usual approach, we split the Lagrange scalar $\mathcal{L}$ into two parts, one for gravity alone ($\mathcal{L}_g$) and one for the other fields: $\mathcal{L} = \mathcal{L}_m + \mathcal{L}_g$. We then obtain the generalized Euler-Lagrange equations for non-gravity fields (q_j) [1]

$$\frac{\partial(\sqrt{-g}\mathcal{L})}{\partial q_j} - \nabla_\alpha \left(\frac{\partial(\sqrt{-g}\mathcal{L})}{\partial q_{j;\alpha}} \right) = 0 , \tag{2}$$

and

$$G_{\alpha\beta} \equiv R_{\alpha\beta} - \frac{1}{2} g_{\alpha\beta} R = \kappa T_{\alpha\beta} , \tag{3}$$

where $T_{\alpha\beta}$, the energy-momentum tensor, may be expressed by the formula

$$T_{\alpha\beta} = \frac{1}{\sqrt{-g}} \frac{\partial(\sqrt{-g}\mathcal{L}_m)}{\partial g^{\alpha\beta}} , \tag{4}$$

and κ is a universal constant.

2 Adding Fermionic Matter

In order to add fermion fields to our approach, we break $\mathcal{L}_m$ into a fermion-dependent part plus a fermion-independend part (essencially for bosons):

$$\mathcal{L}_m = \mathcal{L}_f + \mathcal{L}_b . \tag{5}$$

The variation of $\mathcal{L}_m$ is expressed by

$$\delta(\sqrt{-g}\mathcal{L}_m) = \left(\frac{\partial(\sqrt{-g}\mathcal{L}_f)}{\partial \gamma^\alpha} + \frac{\partial(\sqrt{-g}\mathcal{L}_b)}{\partial g^{\alpha\beta}} \mathcal{R}_S(\gamma^\beta) \right) \delta\gamma^\alpha , \tag{6}$$

with $\mathcal{R}_S$ such that

$$\mathcal{R}_S(A)B \equiv [A + \mathcal{R}(A)]B = \{A, B\} , \quad \mathcal{R}(A)B \equiv BA . \tag{7}$$

We can then apply these ideia to Hamilton's principle:

$$\mathcal{L} = \mathcal{L}_m + \chi_g R = \mathcal{L}_f + \mathcal{L}_b + \chi_g R , \tag{8}$$

$$\mathcal{A} = \mathcal{A}_m + \mathcal{A}_g = \int d\Omega \sqrt{-g}(\mathcal{L}_m + \chi_g R) ; \quad \delta\mathcal{A} = 0 . \tag{9}$$

Taking this equation to (9), we obtain

$$\delta\mathcal{A} = \int d\Omega \sqrt{-g} \left[\mathcal{B}_{\alpha\beta} \mathcal{R}_S(\gamma^\beta) + \frac{\partial \mathcal{L}_f}{\partial \gamma^\alpha} \right] \delta\gamma^\alpha , \tag{10}$$

[1] The symbol ∇_α stands for the directional covariant derivative in the direction ∂_α,

$$q_{j;\alpha} \equiv \nabla_\alpha q_j .$$

where we have defined

$$\mathcal{B}_{\alpha\beta} \equiv \chi_g G_{\alpha\beta} - \frac{1}{2} g_{\alpha\beta}\mathcal{L}_m + \frac{\partial \mathcal{L}_b}{\partial g^{\alpha\beta}} \,. \tag{11}$$

Since the variation of each γ^α is independent, we conclude imediately that

$$\mathcal{B}_{\alpha\epsilon}\mathcal{R}_S(\gamma^\epsilon) + \frac{\partial \mathcal{L}_f}{\partial \gamma^\alpha} = 0 \,. \tag{12}$$

This is the Euler-Lagrange equation for the gravitational field, which could be regarded as our definition of Einstein's equation. Note that we have used implicitly the simmetry of $\mathcal{B}_{\alpha\beta}$, that is, $\mathcal{B}_{\alpha\beta} = \mathcal{B}_{\beta\alpha}$.

In order to restore an equation as much similar to Einstein's as possible, we apply both sides of (12) on γ^β, which yields

$$2\mathcal{B}_{\alpha\epsilon} g^{\beta\epsilon} + \frac{\partial \mathcal{L}_f}{\partial \gamma^\alpha}\gamma^\beta = 0 \,, \quad \text{or} \quad 2\chi_g G_\alpha{}^\beta = \mathcal{L}_m \delta_\alpha{}^\beta - 2g^{\beta\epsilon}\frac{\partial \mathcal{L}_b}{\partial g^{\alpha\epsilon}} - \frac{\partial \mathcal{L}_f}{\partial \gamma^\alpha}\gamma^\beta \,, \tag{13}$$

and we define

$$T_{\alpha\beta} \equiv \frac{\partial \mathcal{L}_b}{\partial g^{\alpha\beta}} - \frac{1}{2} g_{\alpha\beta}\mathcal{L}_m + \frac{1}{2}\frac{\partial \mathcal{L}_f}{\partial \gamma^\alpha}\gamma_\beta \,, \tag{14}$$

whence $G_{\alpha\beta} = \kappa\, T_{\alpha\beta}$, which is equivalent to (3).

But what happens when we use (4) directly with (3)? Obviously, the bosonic part is not affected. Thus, we should verify what happens in this case to the fermionic part of the energy-momentum tensor.

In order to avoid confusion, we shall use the symbol N for the energy-momentum tensor computed *naively* from (4). The symbol T will be used to denote the energy-momentum tensor computed through (14). Thus,

$$N_{\alpha\beta} \equiv \frac{\partial \mathcal{L}_m}{\partial g^{\alpha\beta}} - \frac{1}{2} g_{\alpha\beta}\mathcal{L}_m \,. \tag{15}$$

We are interested in the difference

$$\begin{aligned} d_{\alpha\beta} \;&\equiv\; T_{\alpha\beta} - N_{\alpha\beta} = \frac{\partial \mathcal{L}_b}{\partial g^{\alpha\beta}} - \frac{1}{2} g_{\alpha\beta}\mathcal{L}_m + \frac{1}{2}\frac{\partial \mathcal{L}_f}{\partial \gamma^\alpha}\gamma_\beta - \frac{\partial \mathcal{L}_m}{\partial g^{\alpha\beta}} + \frac{1}{2} g_{\alpha\beta}\mathcal{L}_m \\ &=\; \frac{\partial}{\partial g^{\alpha\beta}}(\mathcal{L}_m - \mathcal{L}_b) + \frac{1}{2}\frac{\partial \mathcal{L}_f}{\partial \gamma^\alpha}\gamma_\beta = \frac{\partial \mathcal{L}_f}{\partial g^{\alpha\beta}} + \frac{1}{2}\frac{\partial \mathcal{L}_f}{\partial \gamma^\alpha}\gamma_\beta \,. \end{aligned} \tag{16}$$

It is important to note that the partial derivative with respect to $g^{\alpha\beta}$ is computed only with respect to explicit dependence upon $g^{\alpha\beta}$, not indirect dependence through γ^α. This expression is, in general, nonzero if there are fermions present in the system.

As an example, let us consider the case of a nucleon field (ψ) interacting with a vector meson field (V_α) and a scalar meson field (σ). In this example, the fermion part of the Lagrangian will be (m is the effective mass and $\tilde{\mathcal{D}}_\alpha$ is the directional covariant derivative, including, but not limited to, geometric covariance)

$$\mathcal{L}_f = \bar{\psi}[\gamma^\alpha \tilde{\mathcal{D}}_\alpha - m(\sigma)]\psi \,. \tag{17}$$

In this case, the difference term is

$$d_{\alpha\beta} = \frac{1}{2}\bar{\psi}\gamma_\beta\tilde{\mathcal{D}}_\alpha\psi\,. \tag{18}$$

This corresponds to an additional term that should be included in the energy-momentum tensor in order to properly consider fermion degrees of freedom in the physical system. In other words, most of the authors underestimate the contribution of fermions to the energy-momentum of physical systems.

3 Conclusions

We have seen that, if we derive the Einstein equation in a conventional way, we are implicitly discarding some information about fermions in the system under study.

There are qualitative differences in the formal treatments required by nuclear matter restricted to Minkowski space (that is, without gravity) and by nuclear matter in a more general space, as is the case for neutron stars.

Besides that, all the relevant information about space-time curvature (gravity) is contained in the generalized Dirac's matrices. Furthermore, using Dirac's matrices as the representation of the gravity field enables us to compute the energy-momentum tensor in a more consistent way, taking properly into account the existence of fermions.

What is new here is that our considerations show that the fermion contribution to energy-momentum has been underestimated in usual approaches; they show also a possible solution for such a problem.

It is possible (even likely), however, that in some limiting cases many usual models might still be accurate enough to provide acceptable results.

4 References

1. I. M. Benn, R. W. Tucker, *An Introduction to Spinors and Geometry with Applications in Physics*, IOP Publishing Ltd., New York, 1987.

2. N. D. Birrel, P. C. W. Davies, *Quantum Fields in Curved Space*, Cambridge University, New York, 1982.

HADRONIC MODEL INDEPENDENCE OF THE HADRON-QGP PHASE TRANSITION AT VERY LOW DENSITY

M. MALHEIRO, A. DELFINO, AND J. B. SILVA
Instituto de Física, Universidade Federal Fluminense, 24210-340, Niterói, Brazil

Using many different relativistic mean field models (RMF) for the hadronic phase and a perturbative QCD equation of state for the QGP , with α_s as a function of the temperature, we study the hadron-QGP phase transition at zero density and high temperature. We show that the critical temperature T_c for this transition is hadronic model independent. We have traced back the reason for this and conclude that it comes from that, QGP entropy (the slope of the Pressure versus T) is much larger than the hadronic entropy obtained in all the RMF models. This finding is quite independent whether the hadronic models have or not a hadronic phase transition at high temperature (related to the strong $N - \bar{N}$ scalar condensate).

1 Introduction

The understanding of nuclear matter under extreme conditions is a crucial and indispensable aim of nuclear and stellar physics, especially with much more experimental information to come with RHIC and Alice/LHC accelerators. It is now widely believed that at sufficiently high energy, in heavy-ion collisions, a central hot region is formed. This region is commonly associated with the existence of a Quark-Gluon Plasma (QGP). This hot region expands, cools down and freezes out into hadrons, exhibiting a hadron-gas phase transition. To observe this transition to the deconfined phase, some observable signatures have been proposed as electromagnetic radiation, strangeness enhancement and J/ψ suppression. In this contribution we show that at very low density, the enhancement of the entropy may become a strong signature of QGP formation, in agreement with some previous work [1]. Thus, we see as a good challenge , from the experimental side, the measurement of the entropy through sophisticated calorimeters.

At the hadronic level, mean-field theory is able to describe well a number of nuclear phenomena through different conceptions of meson-nucleon and meson-meson couplings. It is known that hadronic models may present phase transitions at higher temperatures. For example, in reference [2], hot nuclear matter was extensively studied using the Walecka model regarding the finite temperature behavior for zero density and concluded that, depending on the values taken by those constants, the Walecka model may or may not generate a phase transition into a nucleon-antinucleon plasma.

The question we pose in this contribution is whether the phase transition for the hadronic sector itself , described from hadronic models, may or not have importance to the QGP phase transition. To answer this question we bring to this discussion a representative class of state-of-the-art hadronic models [3]. Most of these models were successfully employed to calculate nuclear matter bulk properties as well as the spectra of finite nuclei. We will present a systematic comparative study of a set of hadronic models at extreme temperatures and its plasma (QGP) phase transition.The QGP phase is represented by a perturbative QCD derivation.

2 The phase transition calculation at high T and zero density

In order to see the hadronic-quark-gluon phase transition we need distinct models for the two different phases of the baryonic matter. We describe the hadronic (meson-baryon) phase (H) by the models of Ref. [3], in the Hartree approximation extended to finite temperature. For the quark-gluon plasma phase, the equation of state is given given by [4]. The Gibbs criteria used in the analysis of the phase transition for zero density is given by $\mu_H(T_c) = \mu_{QGP}(T_c) = 0$ and $p_H(T_c) = p_{QGP}(T_c)$.

The functional, used for the hadronic phase, originates from an effective Lagrangian, with additional physical constraints ensuring QCD symmetries [3]. The pressure is

$$
\begin{aligned}
p(M^*,\rho_B) = & -\frac{m_s^2}{g_s^2}\Phi^2\left(\frac{1}{2}+\frac{\kappa_3}{3!}\frac{\Phi}{M}+\frac{\kappa_4}{4!}\frac{\Phi^2}{M^2}\right) \\
& -\frac{1}{2g_v^2}\left(1+\eta_1\frac{\Phi}{M}+\frac{\eta_2}{2}\frac{\Phi^2}{M^2}+\frac{\eta_3}{3!}\frac{\Phi^3}{M^3}\right)m_v^2W^2 \\
& -\frac{1}{4!g_v^2}\left(\zeta_o+\zeta_1\frac{\Phi}{M}\right)W^4+W\rho_B \\
& +\frac{1}{3}\frac{\gamma}{(2\pi)^3}\int d^3k\frac{k^2}{E^*(k)}\left(f_+(k,T)+f_-(k,T)\right), \qquad (1)
\end{aligned}
$$

where Φ and W are the scalar and vector meson fields respectively , $E^*(k) = (\mathbf{k}^2+M^{*2})^{1/2}$ and $f_\pm(k,T)$ stand for the Fermi-Dirac distribution for baryons (antibaryons). The baryon density ρ_B is defined by $\rho_B = \frac{\gamma}{(2\pi)^3}\int d^3k\ [f_+(k,T)-f_-(k,T)]$. Thus, in the zero density regime we have the same number of baryons and anti-baryons.

The constants (see Table I) are already adjusted to reproduce some of the bulk properties of the nuclear matter ground state [3]. Here $W1$ stands for the usual Walecka model. $C1$ and $Q1$ are nonlinear σ models, having scalar

field self-interaction added to the $W1$ model in order to improve some nuclear matter bulk properties of $W1$. Most of the developed hadronic models has the $C1$ structure, given by cubic and quartic scalar field self-interaction . In this aspect it is a very representative model category. The scalar cubic and quartic self-interaction are usually claimed to simulate three-body and four-body forces effects respectively. The others as $Q2$, $G1$ and $G2$ are models representing further improvements by including different scalar-scalar, vector-vector and scalar-vector fields couplings. We have also considered for the hadronic phase different parametrizations of the non-linear Walecka model, NL1, NL2, NL3 and NLSH models very known in the literature[5].

Table 1: Model parameters, taken from Ref. [3].

Model	$W1$	$C1$	$Q1$	$Q2$	$G1$	$G2$
m_s/M	0.60305	0.53874	0.53735	0.54268	0.53963	0.55410
$g_s/4\pi$	0.93797	0.77756	0.81024	0.78661	0.78532	0.83522
$g_v/4\pi$	1.13652	0.98486	1.02125	0.97202	0.96512	1.01560
η_1		0.29577			0.07060	0.64992
η_2					-0.96161	0.10975
κ_3		1.6698	1.6582	1.7424	2.2067	3.2467
κ_4			-6.6045	-8.4836	-10.090	0.63152
ζ_o				-1.7750	3.5249	2.6416

For the quark-gluon plasma phase, the pressure is given by[4]

$$p_{QGP}(\mu_q, T_q) = \frac{8\pi^2 T_q^4}{45}\left(1 - \frac{15\alpha_s}{4\pi}\right) + N_f\left[\frac{7\pi^2 T_q^4}{60}\left(1 - \frac{50\alpha_s}{21\pi}\right) + \left(\frac{\mu_q^2 T_q^2}{2} + \frac{\mu_q^4}{4\pi^2}\right)\left(1 - \frac{2\alpha_s}{\pi}\right)\right] - B\,, \tag{2}$$

where B is the bag constant, N_f is the number of flavors, α_s is the QCD coupling constant at first order, and for zero density $\mu_q = 0$.

The model for the QGP phase which we use in this work has some parameters such as Λ, B and N_f. As a first approximation, we examine the simplest case with $N_f = 2$ (quarks u and d only). The QCD scale parameter Λ is fixed at 200 MeV, consistent with the current data set. We will use two different bag constants in our analysis: $B^{1/4} = 174$ MeV and $B^{1/4} = 238$ MeV, corresponding to $B = 119$ MeV fm^{-3} and $B = 418$ MeV fm^{-3} respectively. These are the limiting values of the broad range of values used in the literature.

3 Results and Conclusions

Figure 1 shows that not all of hadronic models (twelve in total) have the hot nucleon-antinucleon phase transition in the hadronic sector, manifested by the large decrease of the effective nucleon mass M^*.

Fig.1:EFFECTIVE NUCLEON MASS vs. TEMPERATURE

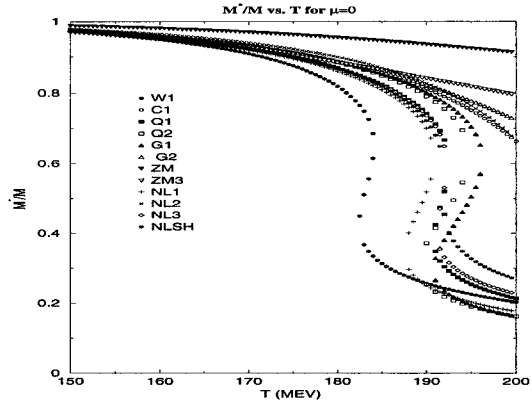

We present in figure 2 the pressure for hadronic-QGP phases (in units of the Stefan-Boltzmann pressure) as a function of T. In this figure we have used the extreme values $B^{1/4} = 174$ MeV and $B^{1/4} = 238$ MeV. It is to remark how the QGP critical temperatures are close for all the hadronic models. The reason lies in the slope for the QGP pressure. This slope is nothing but the entropy, we show in figure 3. Notice how far, by a factor around five, the entropy amounts are different in both phases. It causes the hadronic model independence for the QGP. When the hadronic model itself presents the nucleon-antinucleon phase transition it increases substantially the entropy as can be seen in this figure. However, this enhancement is not enough to be compared with the QGP entropy. Let us also note that the entropy quantity is completely independent of the bag constant B since it is given by $(\mathcal{E}_{QGP} + p_{QGP})/\mathrm{T}$.

In summary, when we have only nucleons in the hadronic phase, the hadronic-QGP phase transition at very low density takes place for approximately the same value of T_c in all the studied hadronic models. The models that show a pure hadronic phase transition seen by the decreasing of the effective baryon masses have an abrupt increasing of the entropy per baryon in the hadronic phase. However, this enhancement is not enough to be compared with the QGP entropy and implies a large latent heat at the phase transition. The increasing of the entropy is so high that a signature for hadronic-QGP could be obtained for zero baryonic density even if the contributions of the

Fig.2:HADRON–QGP PHASE TRANSITION

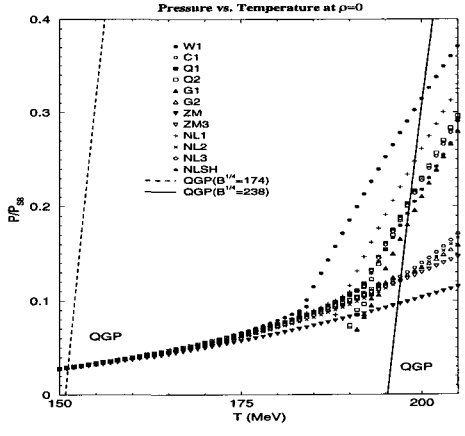

Fig.3: Entropy Density

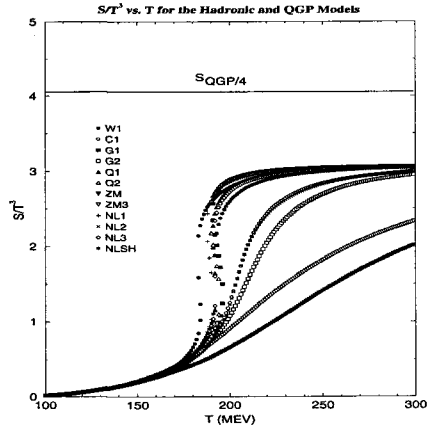

strangeness enhancement is small. In this contribution, we rescue the entropy per baryon enhancement as a real signature for the hadronic-QGP phase transition as suggested before[1]. Moreover the measure of this quantity with good accuracy is for sure a challenge to the experimentalists.

References

1. J. Letessier, A. Tounsi, U. Heinz, J. Sollfrank, and J. Rafelski, Phys. Rev. Lett.**23**, 3530 (1993)
2. J.Theis, G.F.Graebner, G.Bucchwald, J.A.Maruhn, W.Greiner, H.Stoecker and J.Polony, Phys. Rev. **D28**, 2286 (1983)
3. R.J.Furnstahl, B.D. Serot and Hua-Bin Tang, Nucl.Phys.**A615**, 441 (1997)
4. U. Heinz, P.R. Subramanian, H. Stöker and W. Greiner, J. Phys. **G12**, 1237 (1986); Bo-Qiang Ma, Qi-Ren Zhang, D.H. Rischke and W. Greiner, Phys. Lett. **B315**, 29 (1993)
5. P.G. Reinhard, Rep. Prog. Phys. **52**, 439 (1989); G.A. Lalazissis, J.Koening and P.Ring, Phys. Rev. **C55**, 540 (1997); M.M. Sharma, M.A. Nagarajan and P. Ring, Phys. Lett. **B312**, 377 (1993).

Quark degrees of freedom in compact stars.

Marranghello, G. F.[1]; Vasconcellos, C. A. Z.[1]; Hadjimichef, D.[2]
[1] *Departamento de Física, Instituto de Física*
Universidade Federal do Rio Grande do Sul.
[2] *Departamento de Física, Instituto de Física e Matemática*
Universidade Federal de Pelotas.

Abstract

Nuclear matter may show a phase transition at high densities, where quarks and gluons are set free, forming a so called quark-gluon plasma. At the same range of densities, neutron stars are formed. In this work we have grouped both ideas in the study of the quark-gluon plasma formation inside compact stars, here treated as pure neutron star, hybrid star and pure quark matter star.

1 Introduction

Compact stars are grouped as high density stellar objects on which we may include neutron stars, strange stars and many other different faces that can show at $\rho \geq 10^{15} g/cm^3$.

The conception of the structure of compact stars, first studied as pure neutron matter stars, *evolved,* being in many other configurations where we may include the solid iron crust and the quark-gluon plasma core, the superfluid neutrons and superconducting protons, the presence of hyperons and boson condensates (Kaons and Pions), trapped neutrinos and even the pure strange matter stars.

In this work we analize the role of quarks degrees of freedom in the structure of strange stars and hybrid stars.

We describe the internal structure of compact stars by making use of effective nuclear models, based on the quantum field theory of many-particle systems. The quarks degrees of freedom are incorporated into the formalism by using the MIT bag model and the Gibbs criteria for phase transitions.

2 Nuclear Matter

Nuclear matter studies have been developed in the framework of effective hadron models. We discuss three different versions of these models including the Walecka [1], the non-linear [2] and the ZM [3] models. In the following we present the unified version of the equation of state described by the energy density

$$\begin{aligned} \epsilon &= \frac{b}{3}(M-M^*)^3 + \frac{c}{4}(M-M^*)^4 + \frac{C_v^2}{2M^2}\rho^2 \\ &+ \frac{M^4}{2C_s^2}\left(\frac{1-m^*}{m^{*\beta}}\right)^2 + \frac{\gamma}{(2\pi)^3}\int_0^{k_F} d^3k\sqrt{k^2+M^{*2}} \end{aligned} \tag{1}$$

and by the pressure

$$\begin{aligned} p &= -\frac{b}{3}(M-M^*)^3 - \frac{c}{4}(M-M^*)^4 + \frac{C_v^2}{2M^2}\rho^2 \\ &- \frac{M^4}{2C_s^2}\left(\frac{1-m^*}{m^{*\beta}}\right)^2 + \frac{1}{3}\frac{\gamma}{(2\pi)^3}\int_0^{k_F} d^3k\frac{k^2}{\sqrt{k^2+M^{*2}}}, \end{aligned} \tag{2}$$

for these three models. The constants b and c are zero for the Walecka and ZM models and fitted in the non-linear model to give an effective nucleon mass ratio $M^*/M = 0.7$ and a compression modulus $K^{-1} = 250MeV$ in the nuclear matter. β is zero for Walecka and non-linear models and one for the ZM model.

3 Quark-Gluon Plasma

The quark-gluon plasma is described by the MIT bag model [4]. We will not discuss here about the model structure except by the freely choice of the bag constant. The bag constant is a very important parameter to determine the phase transition point, as we can see in the following expressions for the equation of state

$$\epsilon = B + \sum_f \frac{3}{4\pi^2}[E_f k_f (E_f^2 - \frac{1}{2}m_f^2) - \frac{1}{2}m_f^4 ln(\frac{E_f + k_f}{m_f})]; \tag{3}$$

$$p = -B + \sum_f \frac{1}{4\pi^2}[E_f k_f (E_f^2 - \frac{5}{2}m_f^2) + \frac{3}{2}m_f^4 ln(\frac{E_f + k_f}{m_f})]; \tag{4}$$

where f denotes the flavors up, down and strange; and the transition conditions described in the next section.

4 Phase Transition

The phase transition is described by the Gibbs criteria which determine the transition point that occurs when the pressure and chemical potential are equal for both, hadron and quark-gluon plasma (QGP) phases, at constant temperature:

$$\begin{aligned} P_{hadron} &= P_{QGP}; \\ \mu_{hadron} &= \mu_{QGP}; \\ T &= constant, \end{aligned} \tag{5}$$

represented in figure 1 in case of the Walecka and MIT bag models.

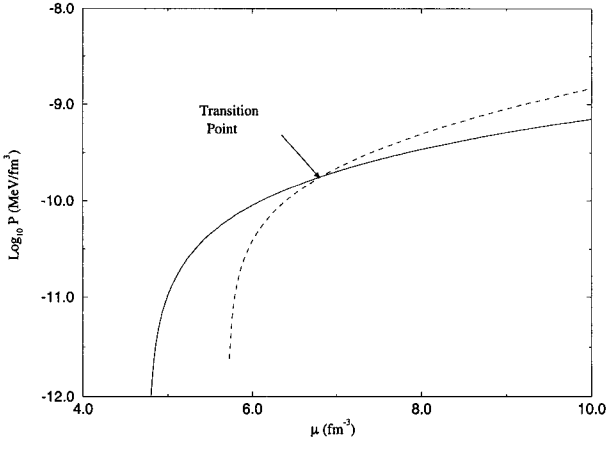

Figure 1: The Gibbs criteria is represented for the Walecka model (solid line) and the MIT bag model (dashed line), determining the two different phases, hadron matter and QGP.

5 Compact Star

Tolman, Oppenheimer and Volkoff (TOV) solved the Einstein's equation of general relativity for the Schwarschild metric [5, 6]. The TOV equations describe a static, uniform and isotropic star in which the gravity is supported against collapse by the degeneracy pressure of the particles inside it.

We describe compact stars by an equation of state that includes both phases of nuclear and quark matter, and we analyse the possibility of a quark core to be formed inside the star. The following table sumarizes the results obtained.

Models	$M/M_{\odot}^{a}$	$M/M_{\odot}^{b}$	$M/M_{\odot}^{c}$	$M/M_{\odot}^{d}$
W	2.11	2.36	2.43	**2.57**
NL	2.26	**2.29**	**2.29**	**2.29**
ZM	**1.70**	**1.70**	**1.70**	**1.70**

Table 1: Neutron (boldfaced numbers) and hybrid star masses. The quark matter equation of state that composes the full equation of state was evaluated for ${}^{a}B^{1/4}$=100 MeV, ${}^{b}B^{1/4}$=131 MeV, ${}^{c}B^{1/4}$=150 MeV and was not taken into account in the last column^{d}, forming the original pure neutron matter stars.

6 Conclusion

We have described the phase transition between the nuclear matter and the quark-gluon plasma. Applying our results to the TOV equations we determined the possible existence of a quark core inside a compact star. We also describe the structure of a strange quark star. The results are shown in figure 2.

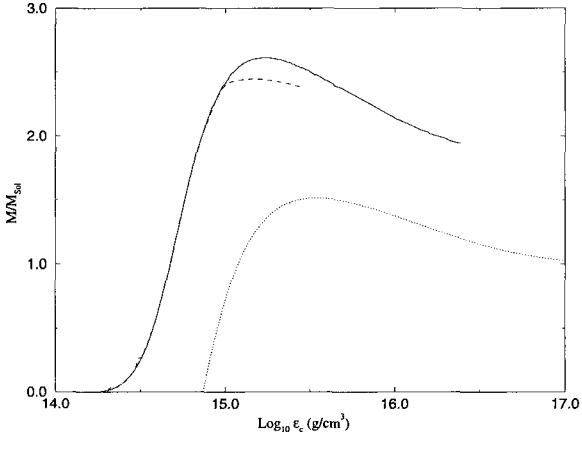

Figure 2: The figure describes the mass of three families of compact stars, where the solid line represents the neutron star, the dashed line describes the hybrid star and the dotted line stands for the strange quark star, as a function of the central density.

The Walecka model has shown the largest quark core inside the star, 2.5Km, while the Zimanyi-Moszkowski model did not show it. We can relate these results to any model property such as nucleon effective mass and compression modulus of nuclear matter, observing that the stiffer equations of state correspond to a largest quark core formed inside the star.

One important point that determines the formation of a QGP inside the star is the central density of the star. The ZM model does not show a quark core because its low maximum mass is not enough to generate a central density high enough to deconfine the quarks and form a QGP core.

Another important point to notice is the relevance of the choice of the MIT bag constant. The B constant is directly related to the pressure and chemical potential of the quark matter equation of state, indicating the phase transition point. The smaller is the bag constant, lower is the density in which the phase transition point occurs and more extensive is the quark core inside the hybrid star.

References

[1] WALECKA, J. D. A theory of high condensed matter. *Annals of Physics*, New York, v. 83, n. 2, p. 491-529, Apr. 1974.

[2] BOGUTA, J., BODMER, A. R. Relativistic calculation on nuclear matter and the nuclear surface. *Nuclear Physics A*, Amsterdam, v. 292, n. 3, p. 413-428, Dec. 1977.

[3] ZIMANYI, J., MOSZKOWSKI, S. A. Nuclear equation of state with derivative scalar coupling. *Phys. Rev. C*, Woodbury, v. 42, n. 4, p. 1416-1421, Oct. 1990.

[4] CHODOS, A., JAFFE, R. L., JOHNSON, K., THORN, C. B., WEISSKOPF, V., *Phys. Rev. D*, v. 9, p. 3471, 1974.

[5] TOLMAN, R. C. Static solutions of Einstein's field equations for spheres of fluid. *Phys. Rev*, New York, v. 55, n. 4, p. 364-373, Feb. 1939.

[6] OPPENHEIMER, J. R., VOLKOFF, G. M. On massive neutron cores. *Physic. Rev.*, New York, v.55, n. 4, p. 374-381, Feb. 1939

Finite temperature nucleon mass in QMC Model

P. K. PANDA and G. KREIN
Instituto de Física Teórica, Universidade Estadual Paulista,
Rua Pamplona 145, 01405-900 São Paulo - SP, Brazil

Abstract

The back-to-back correlation function of nucleon and antinucleon pairs is sensitive to the in-medium effective mass of the nucleons. We use the quark-meson coupling model to calculate the temperature dependent effective nucleon mass. The short-distance repulsion between the nucleons is included through an excluded volume approach which is thermodynamically consistent. The temperature dependence of the nucleon mass is significant and might be observable through the measurement of the back-to-back correlation function at the Relativistic Heavy Ion Collider.

The determination of modifications of hadron properties at high density and temperature is of central interest in heavy ion physics. In this communication we report on a calculation of the temperature dependence of the nucleon mass in the quark meson coupling (QMC) [1] at finite temperature and its possible experimental determination through the measurement of the back-to-back correlation function of nucleon-antinucleon pairs.

The QMC model is a simple extension of the Walecka model incorporating quark degrees of freedom. This model describes nuclear matter as nonoverlapping MIT bags, with effective scalar and vector meson fields coupling directly to the quarks in the bag. In a mean field approximation, the scalar (σ) and vector (ω) fields are treated as classical. At finite temperatures, the quarks inside the bag can be thermally excited to higher angular momentum states. For simplicity, we shall assume the bag describing the nucleon to be still spherical with a radius R which is now temperature dependent [2].

The grand canonical potential in the QMC model is given by [2]

$$\Omega = -P(T,\mu_B) = -\frac{1}{3}\frac{\gamma}{(2\pi)^3}\int d^3k \frac{\mathbf{k}^2}{E^*(k)}(f_B + \bar{f}_B) - \frac{1}{2}m_\omega^2\omega^2 + \frac{1}{2}m_\sigma^2\sigma^2, \quad (1)$$

where f_B and $\bar{f}_B$ are the thermal distribution functions for the baryons and antibaryons, given by

$$f_B = \frac{1}{e^{[E^*(\vec{k})-\tilde{\mu}_B^*]/T}+1} \quad \text{and} \quad \bar{f}_B = \frac{1}{e^{[E^*(\vec{k})+\tilde{\mu}_B^*]/T}+1}, \quad (2)$$

where $\tilde{\mu}_B^* = \mu'_B - g_\omega \omega$, which determine the total baryon density of the system

$$\rho(T, \mu_B) = \frac{\gamma}{(2\pi)^3} \int d^3k \; (f_B + \bar{f}_B). \tag{3}$$

In these, $E^*(\vec{k}) = (\vec{k}^2 + M^{*2})^{1/2}$ is the effective nucleon energy, where the nucleon mass is given by

$$M^* = E_{q\bar{q}} - \frac{Z}{R} + \frac{4\pi}{3} R^3 B, \tag{4}$$

with

$$E_{q\bar{q}} = \sum_{n,\kappa} \frac{3\Omega^{n\kappa}}{R} \left[\frac{1}{e^{(\epsilon_+^{n\kappa}/R - \mu_q)/T} + 1} + \frac{1}{e^{(\epsilon_-^{n\kappa}/R + \mu_q)/T} + 1} \right], \tag{5}$$

where μ_q, quark chemical potential, is determined from

$$n_q = 3 = 3 \sum_{n,\kappa} \left[\frac{1}{e^{(\epsilon_+^{n\kappa}/R - \mu_q)/T} + 1} - \frac{1}{e^{(\epsilon_-^{n\kappa}/R + \mu_q)/T} + 1} \right]. \tag{6}$$

Here, the single-particle quark and antiquark energies in units of R^{-1} are given as

$$\epsilon_\pm^{n\kappa} = \Omega^{n\kappa} \pm g_\omega^q \omega R \;, \quad \text{where} \quad \Omega^{n\kappa} = (x_{n\kappa}^{*2} + R^2 m_q^{*2})^{1/2}. \tag{7}$$

where $x_{n\kappa}^*$ is the temperature-dependent bag eigenvalue for given n and κ, $m_q^* = m_q^0 - g_\sigma^q \sigma$ is the effective quark mass, m_q^0 is the current quark mass and g_σ^q and g_ω^q are the quark couplings with the σ and ω mesons. The bag radius R is determined by the stability condition $\partial M^*/\partial R = 0$.

The main feature of hadronic interactions at high densities is the short distance repulsion between the nucleons. Here we mock up this repulsion through an excluded volume (EVE) approach which is thermodynamically consistent[3]. This approach consists in recognizing that the volume V for a system of N particles is reduced to an effective volume, $V - \mathcal{V}_n N$, due to the intrinsic size of the nucleon bags. In this ansatz, the EVE is considered only for baryons. The *true* baryon pressure and density are given by[3]

$$P_B(T, \mu_B) = P'_B(T, \mu'_B), \qquad \rho_B(T, \mu_B) = \frac{\rho'_B(T, \mu'_B)}{1 + \mathcal{V}_n \rho'_B(T, \mu'_B)}, \tag{8}$$

where $\mu'_B = \mu_B - \mathcal{V}_n P(T, \mu_B)$ is the chemical potential. The prime denotes the corresponding expressions without EVE. The aproach is thermodynamically consistent because $\mu_B = \partial\epsilon/\partial\rho_B$, where the energy and entropy densities

$$\epsilon(T, \mu_B) \equiv \frac{\epsilon'(T, \mu'_B)}{1 + \mathcal{V}_n \rho'_B(T, \mu'_B)}, \quad S(T, \mu_B) = \frac{S'(T, \mu'_B)}{1 + \mathcal{V}_n \rho'_B(T, \mu'_B)}, \tag{9}$$

satisfy the thermodynamic expression

$$\epsilon(T,\mu_B) = T\,S(T,\mu_B) - P(T,\mu_B) + \mu_B\,\rho_B(T,\mu_B). \tag{10}$$

The final step consists in determining the mean field σ and ω through the minimization of the thermodynamic potential.

One possible way to access experimentally medium modifications is through measurement of the back-to-back correlation function of nucleon-antinucleon pairs in a heavy-ion collision [4,5]. The single-particle and the two-particle invariant momentum distributions are defined as

$$N_1(\mathbf{k}) = E_{\mathbf{k}}\langle a^\dagger_{\mathbf{k}} a_{\mathbf{k}}\rangle, \quad N_2(\mathbf{k}_1,\mathbf{k}_2) = E_{\mathbf{k}_1}E_{\mathbf{k}_2}\langle a^\dagger_{\mathbf{k}_1}\tilde{a}^\dagger_{\mathbf{k}_2}\tilde{a}_{\mathbf{k}_2}a_{\mathbf{k}_1}\rangle, \tag{11}$$

$$\langle a^\dagger_{\mathbf{k}_1}\tilde{a}^\dagger_{\mathbf{k}_2}\tilde{a}_{\mathbf{k}_2}a_{\mathbf{k}_1}\rangle = \langle a^\dagger_{\mathbf{k}_1}a_{\mathbf{k}_1}\rangle\langle\tilde{a}^\dagger_{\mathbf{k}_2}\tilde{a}_{\mathbf{k}_2}\rangle - \langle a^\dagger_{\mathbf{k}_1}\tilde{a}_{\mathbf{k}_2}\rangle\langle\tilde{a}^\dagger_{\mathbf{k}_2}a_{\mathbf{k}_1}\rangle + \langle a^\dagger_{\mathbf{k}_1}\tilde{a}^\dagger_{\mathbf{k}_2}\rangle\langle\tilde{a}_{\mathbf{k}_2}a_{\mathbf{k}_1}\rangle.$$

In the above, $\langle\hat{O}\rangle$ denotes the expectation value of operator $\hat{O}$ in the thermalized medium and $E_{\mathbf{k}} = \sqrt{M_N^2 + |\mathbf{k}|^2}$.

The two-particle correlation function is defined as

$$C_2(\mathbf{k}_1,\mathbf{k}_2) = \frac{N_2(\mathbf{k}_1,\mathbf{k}_2)}{N_1(\mathbf{k}_1)\tilde{N}_1(\mathbf{k}_2)}\,. \tag{12}$$

If a thermal gas of b fermions freezes out suddenly at temperature T, the observed single a-particle spectrum is given by

$$N_1(\mathbf{k}) = \frac{V}{(2\pi)^3}\,E_{\mathbf{k}}\,[\cos r_{\mathbf{k}}{}^2\,f_B + \sin r_{\mathbf{k}}{}^2(1-\bar{f}_B)], \tag{13}$$

where $r_{\mathbf{k}}$, $\tan 2r_{\mathbf{k}} = -|\mathbf{k}|\;\Delta M(\mathbf{k})/[E(\mathbf{k})^2 - M_N\;\Delta M(\mathbf{k})]$, is the squeezing function and $M^*(\mathbf{k}) = M_N - \Delta M(\mathbf{k})$. The BBC for fermion – anti-fermion pairs reads as

$$C_2(\mathbf{k},-\mathbf{k}) = 1 + \frac{(1-f_B-\bar{f}_B)^2(\cos r_{\mathbf{k}}\sin r_{\mathbf{k}})^2}{\left[\cos r_{\mathbf{k}}{}^2 f_B + \sin r_{\mathbf{k}}{}^2(1-\bar{f}_B)\right]\left[\cos r_{\mathbf{k}}{}^2\bar{f}_B + \sin r_{\mathbf{k}}{}^2(1-f_B)\right]}. \tag{14}$$

We use $m_q = 0$ and $R = 0.6$ fm and determine B and z_0 to give the nucleon mass in vacuum at zero temperature. We find $B^{1/4} = 211.3$ MeV and $z_0 = 3.987$. We take the sigma and omega meson masses as 550 and 783 MeV. We fit the scalar and vector couplings to the binding energy per nucleon at zero temperature -16 MeV at the saturation point $\rho_B = 0.17$ fm^{-3}, obtaining $g^q_\sigma = 5.399$ and $g_\omega (= 3g^q_\omega) = 7.655$.

The temperature dependence of the nucleon effective mass for fixed chemical potential $\mu = 200$ MeV (small baryon densities) is shown on the left panel of

the Figure. The value of M^* increases monotonically with temperature. This is in contrast to the calculation of hot nuclear matter using Walecka model where, as the temperature is increased, M^* first rises and then falls rapidly. We do not encounter any change in the trend here. Using this QMC model, we then estimate the back-to-back correlation function for different M^*. On the right panel of the Figure we plot the same as a function of effective nucleon mass for different momenta.

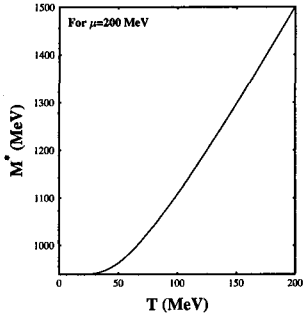

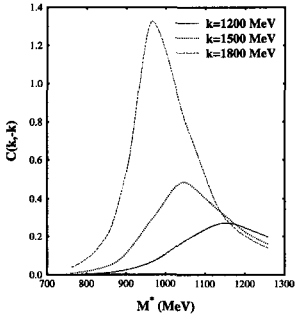

Figures: Left: The effective mass of the nuclear matter as a function of temperature for fixed chemical potential $\mu = 200$ MeV. Note that, effective mass increases with temperature. Right: Correlation function versus effective nucleon mass for $\mathbf{k} =$ 1200, 1500, 1800 MeV.

We have studied quark meson coupling model (QMC) for finite temperature including the excluded volume effects. We then calculated the back-to-back correlation using the QMC model. This may be an observable effect at the Relativistic Heavy Ion Collider.

One of the author (PKP) would like to acknowledge FAPESP (Processo-99/08544-0) for financial support and the IFT, Sao Paulo, for kind hospitality.

References

1. P. A. M. Guichon, *Phys. Lett.* B **200**, 235 (1988); K. Saito and A. W. Thomas, *Phys. Lett.* B **327**, 9 (1994).
2. P.K. Panda, A. Mishra, J.M. Eisenberg, W. Greiner, *Phys. Rev.* C **56**, 3134 (1997).
3. D.H. Rischke, M.I. Gorenstein, H. Stöcker and W. Greiner, *Z. Phys.* C **51**, 485 (1991)
4. M. Asakawa, T. Csörgő and M. Gyulassy, *Phys. Rev. Lett.* **83**, 4013 (1999).
5. P.K. Panda, T. Csörgo, Y. Hama, G. Krein, Sandra S. Padula, hep-ph/0006048.

The Fuzzy Bag Model Revisited

F. Pilotto, C. A. Z. Vasconcellos
Instituto de Física, Universidade Federal do Rio Grande do Sul

H. T. Coelho
Departamento de Física, Universidade Federal de Pernambuco

1 Introduction

In this work we develop a new version of the fuzzy bag model. The main idea is to include the conservation of energy and momentum in the model. This feature is not included in the

original formulation of the fuzzy bag model [1], but is of paramount importance to interpret the model as being a bag model — that is, a model in which the outward pressure of the quarks inside the bag is balanced by the inward pressure of the non-perturbative vacuum outside the bag — as opposed to a relativistic

potential model, in which there is no energy-momentum conservation. In the MIT bag model [2], as well as in the original version of the fuzzy bag model, the non-perturbative QCD vacuum is parametrized by a constant B in the Lagrangian density. One immediate consequence of including energy-momentum conservation in the fuzzy bag model is that the bag constant B will acquire a radial dependence, $B = B(r)$.

2 The fuzzy bag model

In this section we give a short description of the fuzzy bag model [1]. For a more extended introduction, see also Ref. [3]. The fuzzy bag model is a variant of the MIT bag model in which the surface of the bag is not sharp, but rather extended ("fuzzy"). Starting with the Lagrangian density of the MIT bag, we substitute $\theta(R-r)$ and $\delta(R-r)$ by smooth functions $F(r)$ and $G(r)$. In analogy with a similar equation satisfied by $\theta(R-r)$ and $\delta(R-r)$, the function $G(r)$ is defined by $G(r) = -dF(r)/dr$. In the next step we redefine the quark field as $\psi(x)$

$$\psi(t,\vec{r}) = \sqrt{F(r)}\, q(t,\vec{r})\,. \tag{1}$$

In order to better reproduce hadronic properties, we have added a constant scalar potential, $V_0/2$, and a vector potential, $\gamma^0\,[V_0/2 + V_c(r)]$ to the model. The final Lagrangian density is then

$$\mathcal{L}_{FBM} = \frac{i}{2}\left[\overline{\psi}\gamma^\mu\partial_\mu\psi - \partial_\mu\overline{\psi}\gamma^\mu\psi\right] - B(r)F(r) - \overline{\psi}\left[m_q + (1+\gamma^0)V(r)\right]\psi \tag{2}$$

with $V(r) = \frac{1}{2} V_0 + V_c(r)$. The scalar confining potential, $V_c(r)$, is related to $F(r)$ and $G(r)$ through

$$V_c(r) = \frac{G(r)}{2\,F(r)} = -\frac{1}{2\,F(r)} \frac{dF(r)}{dr} \,. \tag{3}$$

In the Lagrangian density (2) we have additionally included a radial dependence in the "bag constant", $B \to B(r)$, which will be justified in the next section.

Following the ideas in [3], we postulate for $F(r)$ and $V_c(r)$ the form

$$F(r) = \begin{cases} 1 & , r < R_0 \\ \mathcal{F}(r) & , R_0 \le r \le R_1 \\ 0 & , r > R_1 \end{cases} \qquad V_c(r) = \begin{cases} 0 & , r < R_0 \\ \mathcal{V}_c(r) & , R_0 \le r \le R_1 \\ \infty & , r > R_1 \end{cases} \tag{4}$$

The above parameterization of $F(r)$ and $V_c(r)$ separates clearly the bag into its interior region, $r < R_0$, where the quarks are free; a surface region, $R_0 \le r \le R_1$, where the quark wave function is suppressed until it vanishes; and the exterior region, $r > R_1$, where the quark field is null.

Notice that the shape of the surface is determined by the functions $\mathcal{F}(r)$ and of $\mathcal{V}_c(r)$. We have chosen them in such a way as to obtain analytic solutions for the quark wave functions, requiring also that $\mathcal{F}(r)$ and $\mathcal{V}_c(r)$ be continuous. We will give here only the expression for $\mathcal{V}_c(r)$,

$$\mathcal{V}_c(r) = \begin{cases} \dfrac{r - R_0}{R_q - R_0} \dfrac{\alpha}{(R_1 - R_q)^2} & , R_0 \le r \le R_q \\ \dfrac{\alpha}{(R_1 - r)^2} & , R_q \le r \le R_1 \end{cases} \tag{5}$$

where $R_q = (R_1 + 2\,R_0)/3$ due to continuity of the derivative of $V_c(r)$. By integrating (3) the form of $\mathcal{F}(r)$ can be determined.

3 Determination of $B(r)$

We have seen that the Lagrangian density of the fuzzy bag model can be more easily interpreted when written in terms of $\psi(x)$ instead of $q(x)$. In the same way, the energy-momentum tensor also turns out to be simpler, and it is furthermore desirable to have it expressed as a functional of $\psi(x)$.

Its divergence can then be readily calculated. We find

$$\partial_\mu T^{\mu\nu} = \partial_\mu \left[B(r)\, F(r)\right] + \sum_q \overline{\psi}\,(1 + \gamma^0)\,\psi\,\partial_\mu V(r) \,. \tag{6}$$

For the ground state, $\overline{\psi}\,(1+\gamma^0)\,\psi$ is independent of the angular variables, and the criterion of energy-momentum conservation, $\partial_\mu T^{\mu\nu} = 0$, implies

$$\partial_r\,[B(r)\,F(r)] + \sum_q \overline{\psi}\,(1+\gamma^0)\,\psi\,\partial_r V_c(r) = 0\,. \tag{7}$$

Notice that the above equation can not be satisfied if B is a constant, so we are forced to consider a radial dependence for B, and thus $B = B(r)$. This radial dependence is not only natural, but also necessary in our version of the fuzzy bag model. In contrast, some authors [4] have put in a somewhat arbitrary manner a radial dependence of B in the bag model when investigating neutron star properties.

¿From the equation above it is possible to determine completely the form of $B(r)$. We integrate equation (7) from zero up to some value r of the radial variable. In the interior region of the bag we have $B(r) = B_0$, where B_0 is a constant, since $dV_c(r)/dr = 0$ for $r < R_0$. In the surface region $(R_0 < r < R_1)$, $B(r)$ satisfies

$$B(r) = \frac{1}{\mathcal{F}(r)}\left[B_0 - \frac{1}{2\,\pi}\sum_q \int_{R_0}^{r} \mathrm{d}r\,\frac{u(r)^2}{r^2}\,\frac{d\mathcal{V}_c(r)}{dr}\right] \tag{8}$$

Due to the continuity of $B(r)$, we see that $B_0 = B(R_0)$. At $r = R_1$ we want the product $B(r)\,F(r)$ to be finite. Since $\mathcal{F}(R_1) = 0$, we obtain

$$B_0 = \frac{1}{2\,\pi}\sum_q \int_{R_0}^{R_1} \mathrm{d}r\,\frac{u(r)^2}{r^2}\,\frac{d\mathcal{V}_c(r)}{dr}\,. \tag{9}$$

In this way $B(r)$ is completely determined.

4 Calculation of baryon masses

The mass of a hadron is given by

$$M = \sum_q E_q + \int \mathrm{d}^3 r\,B(r)\,F(r) = \sum_q E_q + \frac{2}{3}\sum_q \int_{R_0}^{R_1} \mathrm{d}r\,r\,u(r)^2\,\frac{d\mathcal{V}_c(r)}{dr}\,. \tag{10}$$

where E_q is the energy eigenvalue of the quark wave function. This expression should be compared with the corresponding one of the MIT bag model. We see that in our model the volume energy reduces to an expression which involves only the surface of the bag.

In order to calculate the masses of the ground state baryons, we have also added to (10) some standard corrections: center of mass, one-gluon exchange and one-pion exchange corrections. The details of these calculations are to appear in a future publication.

In the table below we give the results for the fit. In addition the separate

baryon	N	Δ	Λ	Σ	Σ^*	Ξ	Ξ^*	Ω^-
experim.	940	1232	1116	1193	1385	1318	1533	1672
theory	942	1199	1153	1172	1400	1306	1534	1700
E_B	1348	1348	1384	1384	1384	1420	1420	1456
E_{BF}	454	454	445	445	445	437	437	429
$(\Delta E_B)_{cm}$	-698	-698	-530	-530	-530	-400	-400	-293
$(\Delta E_B)_g^M$	-120	120	-120	-112	115	-115	112	108
$(\Delta E_B)_\pi$	-43	-26	-28	-16	-16	-35	-35	0

contributions which build up each baryon mass are shown: E_B is the sum of the energy eigenvalues of each quark, E_{BF} is the volume energy, $(\Delta E_B)_{cm}$ is the center of mass correction, $(\Delta E_B)_g^M$ is the color magnetic energy, and $(\Delta E_B)_\pi$ self-energy due to pion-quark interaction.

Notice that there is a mean deviation of only $\sim 18MeV$ between the experimental and the theoretical results. In a future work we will investigate properties of neutron stars using this model.

Acknowledgments

This work was funded by CNPq.

References

[1] Y. Nogami, A. Suzuki and N. Yamanishi, *Can. J. Phys.* **62** 554 (1984).

[2] A. Chodos, R. L. Jaffe, C. B. Thorn and V. Weisskopf, *Phys. Rev.* **D9** 3471 (1974).

[3] C. A. Z. Vasconcellos, H. T. Coelho, F. G. Pilotto, B. E. J. Bodmann, M. Dillig and M. Razeira, *Eur. Phys. J.* **C4** 115 (1998).

[4] X. Jin and B. K. Jennings, *Phys. Rev.* **C54** 1427 (1996).

Neutron Star Properties in the Relativistic Mean Field Theory

Scheilla Maria Ramos and Maria Luiza Cescato

Departamento de Física - CCEN - UFPB
Caixa Postal 5008
58051-970 João Pessoa - PB, Brazil

1 Introduction

In recent years, the Relativistic Mean Field (RMF) theory has been applied to a large number of problems in nuclear structure. It has turned out to provide a very simple way to describe nuclear matter and finite nuclei ground state properties in the entire periodic table[1]. In fact, the model is very successful around the experimentally available regions (at saturation density, small neutron-proton asymmetry and zero temperature). Nevertheless this does not assure that the same is true at extreme conditions, namely very low and very high densities or high asymmetries. It is then very interesting to apply this approach in the description of neutron stars properties, which depend on the neutron matter equation of state at densities and asymmetries much greater than those observed in ordinary nuclei.

In the present work, the neutron matter equation of state is obtained using the Walecka σ-ω-ρ-model[1, 2] in the mean field approach. Linear, non-linear[3] and density dependent(DDRMF) [4, 5] parametrizations, which were successful for the description of nuclear global properties and finite nuclei, are used. With this equation of state, the neutron star limiting mass, M, is obtained by numerically integrating the Oppenheimer-Volkoff equations[6, 7] for hydrostatic equilibrium from the star center, for each value of central density, until the pressure vanishes.

The next section presents the results for several parametrizations of the nuclear force, comparing the results from each other and with the observational estimates. An analysis of star density profiles is performed, allowing to settle typical density profiles and to define appropriate criteria for determining the star radii. It is shown that with a density dependent approach it is possible to achieve a neutron star limiting mass closer to the observational one.

2 Results

In the present work, we use the force parameter sets for the Lagrangian model proposed by Serot and Walecka (WS)[8], Horowitz and Serot (HS)[9], Lalazissis and Ring (NL3)[10] and Haddad and Weigel (DDRMF)[11]. For each of these parametrizations, the equation of state was obtained.

For the WS and DDRMF parametrizations, we observe in Fig.1a a minimum that has no physical meaning. More recent parametrizations like NL3 does not show this problem. In the problematic cases, we adopt the usual procedure of performing a Maxwell construction, determining the equilibrium curve in the "phase transition" region. This can be seen in Fig. 1(b).

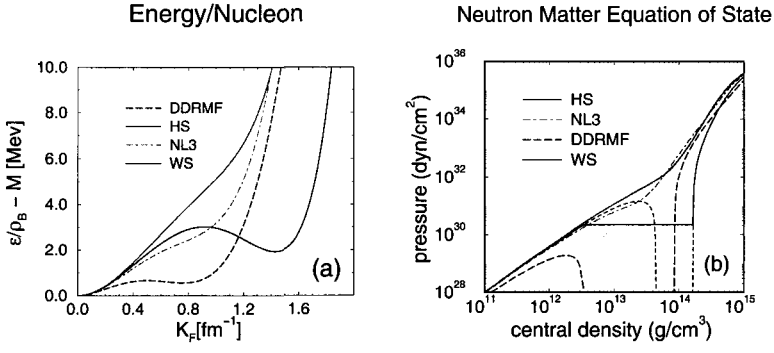

Figure 1: Neutron matter equation of state for some RMF-parametrizations.

With the equation of state obtained from each parametrization, we integrated numerically the Oppenheimer-Volkoff equations, using the Runge-Kutta method. The integration was performed up to the r-value at which the mass does not change anymore within the precision of nearly 10^{-4} %. The result is shown in Fig. 2, which gives the resulting mass as a function of the central density.

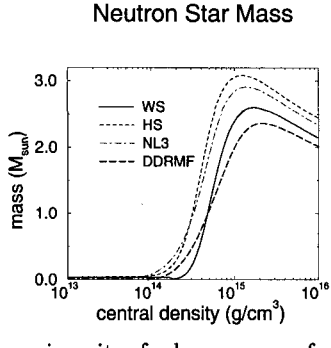

Figure 2: Neutron star masses in units of solar mass as a function of the central density.

The WS and HS parametrizations are linear. HS differs from WS only in the inclusion of the ρ-meson, which makes the equation of state for HS harder than for WS parametrization. For this reason, the limiting mass for HS, $M \approx 3.0 M_{\odot}$, is larger than for WS, $M \approx 2.5 M_{\odot}$. The NL3 parametrization also includes the ρ-meson, but the presence of non-linear terms reduces the limiting mass to $M \approx 2.8 M_{\odot}$. Using the DDRMF approach, we get $M \approx 2.0 M_{\odot}$, the closest prediction to the present observational estimates, which are of the order of $1.5 M_{\odot}$.

Solving the Oppenheimer-Volkoff equations, the star density as a function of the radial coordinate is also obtained. From the analysis of these density profiles, we could observe that, independent of the used parametrization, typical profiles could be determined for different ranges of the central density, ε_c, as can be seen in Fig.3(a). It then becomes clear that the criteria for the definition of the star radius, R, must be different for each region. In first region, $\varepsilon_c < 1 \times 10^{14} g/cm^3$, the profiles are nearly Gaussian. In this case, we assumed that the radius of the star is given by the r-value at which the density is nearly $\varepsilon_c/8$. In the second region, $1 \times 10^{14} < \varepsilon_c < 5 \times 10^{14} g/cm^3$, the profiles have a slightly linear behavior for higher r-values. Here, we made a linear extrapolation of the density profiles and take R as the value at which the density becomes zero in this way. For the two last regions, $5 \times 10^{14} < \varepsilon_c < 2 \times 10^{15} g/cm^3$ and $\varepsilon_c > 2 \times 10^{15}$, an abrupt fall of the density is observed. We could then simply take R as the value at which the integration was stopped. The resulting radii as a function of the central density are shown in Fig. 3(b).

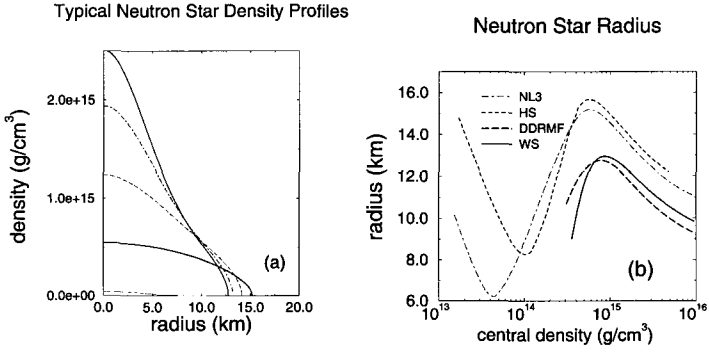

Figure 3: Neutron star properties:(a)typical neutron star density profiles. (b)neutron star radius as a function of the central density.

We observe the appearance of a minimum radius around $10^{14} g/cm^3$ for NL3 and HS. This minimum is associated with the fact that at lower central densities the system has always the same minimum mass and needs to be more extended for produce a lower central density. In the case of DDRMF and WS, this region is not achieved in our calculations because we have avoided the low density region of the corresponding equations of state, which present the already mentioned unphysical "phase transition".

3 Conclusion

We have performed RMF calculations for neutron star properties using several successful parametrizations available in the literature. The results are quite reasonable but show clearly that a lot of work remains to be done for obtaining a reliable description of the equation of state for high densities and asymmetries in this framework, mainly because the different models are adjusted to reproduce saturation properties far away from these extreme conditions.

The DDRMF approach was the only model, including the ρ-meson degree of freedom (expected to be relevant in such a high asymmetric system like neutron star) that could predict a not so big value for the neutron star limiting mass. Nevertheless the model still presents difficulties for reproducing the saturation properties of nuclear and neutron matter.

Our results show then that it is worthwhile to investigate a better dependence of the coupling constants. As a next step in this direction, we are investigating other recent proposed dependences for the coupling constants[12, 13].

References

[1] P.Ring; Progr. Part. Nucl. Phys. **37** (1996) 193

[2] J.D. Walecka; Ann. Phys. (N.Y.) **83** (1974) 491

[3] J. Boguta and A.R. Bodmer; Nucl. Phys. **A292** (1977) 413

[4] R. Brockmann and H. Toki; Phys. Rev. Lett. **68** (1992) 3408

[5] C. Fuchs, H. Lenske, and H.H. Wolter; Phys. Rev. **C52** (1995) 3043

[6] S. S.L. Shapiro and S.A. Teukosky; *The Physics of Compact Objects* (John Wily & Sons, New York,1983).

[7] N.K. Glendenning; *Compact Stars* (Springer-Verlag,New York,1997).

[8] B.D. Serot and J.D. Walecka; Adv. Nucl. Phys. **16** (1986) 1

[9] C.J. Horowitz and B.D. Serot; Nucl. Phys. **A464** (1987) 613

[10] G.A. Lalazissis and P. Ring; Phys. Rev. **C55** (1997) 540

[11] S. Haddad and M. Weigel; Phys. Rev. **C48** (1993) 2740.

[12] S. Typel and H.H. Wolter; Nucl. Phys. **A656** (1999) 331

[13] F. Hofmann,C.M. Keil and H. Lenske; preprint(nucl-th/0008038)

Relativistic Description of Asymmetric Nuclear Matter in a σ–ω–δ–ρ Model

R. Menezes da Silva and M.L. Cescato

Departamento de Física, Universidade Federal da Paraíba
Caixa Postal 5008, 58051-970 João Pessoa - PB, Brazil

1. Introduction

The Relativistic Mean Field Theory (RMF) has proven to be very successful for describing ground state properties of nuclei on the entire range of the periodic table [1, 2]. With a relatively small number of parameters that are adjusted to ground state properties of a few spherical nuclei this phenomenological tool gives a reliable and accurate description of binding energies, radii, deformation parameters in a rather simple and clean framework[3].

The extrapolation of this theory to regions of high proton-neutron asymmetries and densities is of considerable interest for the description of finite nuclei near the proton or neutron drip line and for astrophysical calculations of compact stellar objects (neutron stars, supernova explosions, ...). Since up to recent years the data on asymmetric systems was limited by the available stable nuclei, that are concentrated around Z=N, the isovector part of the nuclear interaction is still not enough studied and the extrapolation of the framework to higher asymmetries is not obvious. Recently, from calculations within the relativistic Brueckner Hartree Fock framework for asymmetric nuclear matter, it was pointed out that an important strength in the isovector scalar channel was found, which can be interpreted as an effective δ–meson[4, 5]. Since the strength in the isovector channel predicted in this way is equal in both scalar and vector channel, this result suggests that a δ–meson of nearly the same coupling strength to that of the ρ–meson should be included as an additional degree of freedom to the usual σ–ω–ρ model. The relevance of this additional degree of freedom must therefore be investigated.

In the present contribution we construct a σ–ω–ρ–δ model and investigate the consequences of the inclusion of the isovector scalar meson in the RMF predictions for nuclear matter properties. It is shown that the inclusion of the isovector meson for small asymmetries, with appropriate fits of the coupling constants, can reproduce the same results of a theory without this degree of freedom. For higher asymmetries however both theories diverge, indicating that the decision between the two approaches should be performed for high asymmetric systems, since experimental data are available.

We write the model Lagrangian in the usual form [2], but include the additional contribution of the δ-degree of freedom as:

$$\mathcal{L}' = \frac{1}{2}\partial^\mu \vec{\delta}\,\partial_\mu \vec{\delta} + \frac{1}{2}m_\delta^2 \vec{\delta}^2 - g_\delta \bar{\psi}\vec{\tau}\vec{\delta}\psi \qquad (1)$$

where $\vec{\delta}$ is the scalar isovector field, ψ is the nucleon field and m_δ and g_δ are the mass and coupling constant for the δ-meson.

From the so constructed Lagrangian the equations of motion for the fields are obtained in the mean field approach. For static, uniform and asymmetric nuclear matter, the equations of the motion are obtained as usual. Due to the presence of the δ-meson the proton and neutron effective masses are now different

$$M_p^* = M - g_\sigma \sigma + g_\delta \delta, \tag{2}$$
$$M_n^* = M - g_\sigma \sigma - g_\delta \delta, \tag{3}$$

where M is the nucleon mass, σ is the scalar field and g_σ its coupling constant. The scalar densities are given by

$$\rho_s = \rho_{sp} + \rho_{sn}, \tag{4}$$
$$\rho_{3s} = \rho_{sp} - \rho_{sn}, \tag{5}$$

where, ρ_{sp} and ρ_{sn}, are the proton and neutron scalar densities

$$\rho_{sp} = \frac{\gamma}{(2\pi)^3} \int_0^{k_{Fp}} \frac{M_p^*}{(M_p^{*2} + k_p^2)^{\frac{1}{2}}} d^3k_p, \tag{6}$$

$$\rho_{sn} = \frac{\gamma}{(2\pi)^3} \int_0^{k_{Fn}} \frac{M_n^*}{(M_n^{*2} + k_n^2)^{\frac{1}{2}}} d^3k_n. \tag{7}$$

The degeneracy $\gamma = 2$ takes into account the two possible spin states. The proton and neutron Fermi moments are represented by k_{Fp} and k_{Fn}. The energy density found from momentum-energy tensor is

$$\varepsilon = \frac{\gamma}{(2\pi)^3} \left(\int_0^{k_{Fp}} d^3k_p \sqrt{M_p^{*2} + k_p^2} + \int_0^{k_{Fn}} d^3k_p \sqrt{M_n^{*2} + k_n^2} \right) + \overbrace{\frac{1}{2} \frac{g_\omega^2}{m_\omega^2} \rho_b^2}^{m_\omega^2 \omega^2}$$
$$+ \overbrace{\frac{1}{2} \frac{g_\rho^2}{m_\rho^2} \rho_3^2}^{m_\rho \rho^2} + \underbrace{\frac{1}{2} \frac{m_\sigma^2}{g_\sigma^2} \left(M + \frac{M_p^* - M_n^*}{2} \right)^2}_{m_\sigma^2 \sigma^2} + \underbrace{\frac{1}{2} \frac{m_\delta^2}{g_\delta^2} \left(\frac{M_p^* - M_n^*}{2} \right)^2}_{m_\delta^2 \delta^2}. \tag{8}$$

In the following we analyze the behavior of the asymmetric system in the proposed model as a function of the barion density, ρ_B, and of the asymmetry parameter, $\Delta = (Z - N)/A$, which for uniform matter is equivalent to $\Delta = (\rho_p - \rho_n)/\rho_B$.

2. Results

The model discussed in the previous section was applied, using the parametrizations proposed by Horowitz and Serot[6]. For the δ-meson, when it is included, we take $g_\delta = g_\rho$, since the predicted strength of both mesons is nearly the same[4, 5].

The analysis of the fields behavior as a function of the barion density shows that they are all linear at low densities, but, while the vector fields remain linear, both scalar fields saturate for high densities.

As a function of the asymmetry, Δ, the ω-field is a constant, while the sigma field behaves like a parabola with minimum at $\Delta = 0$. The inclusion of the δ-meson makes the σ-field more attractive as asymmetry grows. The ρ-field is also linear with Δ, while the δ-field is slightly linear dependent on Δ, but there is, a matter of fact, a very smooth decrease in the slope in direction of saturation.

The nucleon effective mass can also be analyzed s a function of ρ_B and Δ. In Fig. 1. we observe its behavior as an function of ρ_B for $|\Delta| = 1$ and $\Delta = 0$. For $\Delta \neq 0$ we have different neutron and proton effective masses, as we have already pointed out in the last section. The effective masses are always shifted to lower values (relative to the symmetric system) for the major component.

Also in Fig.1 we present the effective mass a function of the asymmetry at saturation density of the symmetric system. We can see that two minima arise, one at $\Delta \simeq -0.65$ for neutron and other at $\Delta \simeq 0.65$ for proton effective mass. This minimum arises from the maximization of the quantity $(g_\sigma \sigma \pm g_\delta \delta)$ during the auto-consistent solution of the effective mass equation.

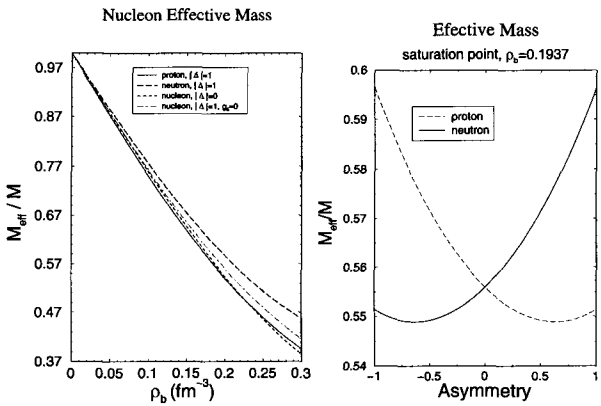

Figure 1: Nucleon Effective Mass as function of ρ_B, for $|\Delta|$=1 an $\Delta = 0$ as a function of asymmetry at saturation point Δ.

Fig. 2 shows the equation of state of nuclear matter for several fixed asymmetries. As the asymmetry grows the system becomes less bounded. The presence of the δ-meson has the effect of increasing the attraction in the system and shifts the equation of the direction of saturation.

In the same figure we observe the binding energy as a function of asymmetry at saturation density of symmetric nuclear matter. We note the expected minimum at $\Delta = 0$. We can see that the presence of the δ increases the binding for high asymmetries.

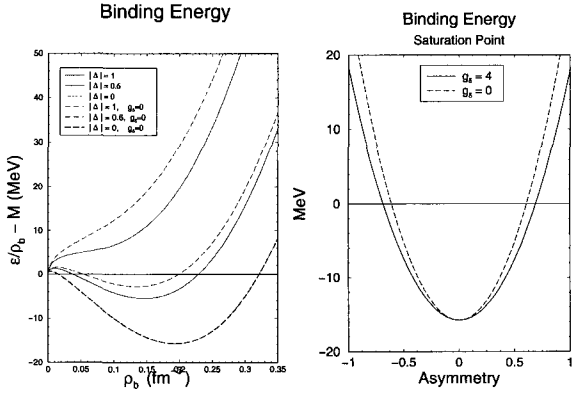

Figure 2: Binding energy per nucleon as a function of barion density

4. Conclusion

We have performed RMF calculations in the Walecka Model including an isovector scalar degree of the freedom, the δ-meson. In this model, the behavior of the fields, effective masses and the nuclear matter equation of state were analyzed as a function of barion density and asymmetry.

We have shown that the presence of the δ-meson influence the behavior of the system specially at high densities and asymmetries. This proves the relevance of the inclusion of this meson in the description of hadronic interaction for systems under extreme conditions (high asymmetries and densities), as is the case, for example, in neutron stars.

References

[1] J.D. Walecka; Ann. Phys. (N.Y.) **83** (1974) 491

[2] B.D. Serot and J.D. Walecka; Adv. Nucl. Phys. **16** (1986) 1

[3] P. Ring; *Relativistic Mean Field Theory in Finite Nuclei*, Progr. Part. Nucl. Phys. **37** (1996) 193

[4] S. Ulrych and H. Müther; Phys. Rev. **C56** (1997) 1788

[5] F. de Jong and H. Lenske; Phys. Rev **C57** (1997) 3099

[6] C.J. Horowitz and B.D. Serot; Nucl. Phys. **A464** (1987) 613

Simplifying Relativistic Density Limits for Nuclear Surface Properties in Walecka Model

Rômulo Rodrigues da Silva and Maria Luiza Cescato
Departamento de Física - CCEN - UFPB
Caixa Postal 5008 58051-970 João Pessoa - PB, Brazil

1 Introduction

In the present work we consider the Walecka Model for studying the semi-infinite nuclear matter problem, the simplest spatially non-uniform nuclear problem, and analyze the reliability of simplifying relativistic limits in the calculation of surface properties. The solution of the mean field equations with the boundary condition at the surface is a somehow elaborate numerical problem, even using the Thomas-Fermi approach used in this work. We propose a simplifying relativistic density limit (SRDL) making more simple the solution of the integral equations of the surface problem. The approach was initially tested in the calculation of infinite nuclear matter, where the saturation properties were well reproduced, and then applied to the semi-infinite problem.

2 Infinite Nuclear Matter

With the Walecka Model[1,2] we first consider infinite nuclear matter, a static uniform system, at zero temperature. In this case we have

$$\rho_s =< F|\bar{\psi}\psi|F >= \frac{\gamma}{6\pi^2}\int_0^{k_F}\frac{m^{*2}}{\sqrt{k^2+m^{*2}}}dk, \tag{1}$$

$$\rho_B =< F|\psi^\dagger\psi|F >= \frac{\gamma}{6\pi^2}k_F^3, \tag{2}$$

whose the mesonic fields gives the simple formula

$$\sigma = \frac{g_\sigma}{{m_\sigma}^2}\rho_s, \tag{3}$$

$$\omega = \frac{g_\omega}{{m_\omega}^2}\rho_B, \tag{4}$$

$$m^* = M + g_\sigma\sigma. \tag{5}$$

For notation, see Ref..[3]

From the calculation of the Hamilton operator of the system in the framework of second quantization we obtain the binding energy per nucleon, u, defined by

$$u = \frac{< F|H|F > - AM}{A}.$$

The energy of the occupied level k is deduced from the Hamiltonian, giving

$$\mathcal{E}(k) = g_\omega \omega + \sqrt{k^2 + m^{*2}}. \tag{6}$$

From this equation the value of the Fermi momentum is obtained, by making $E(k_F) = \mu(T = 0)$, where μ is the chemical potential. The simplifying relativistic density limit (SRDL), which we propose here, consists in consider low and high barion density limits for the integral appearing in Eq.(6),

$$\int_0^{k_F} \frac{k^2}{\sqrt{k^2 + m^{*2}}} dk = \begin{cases} \frac{1}{3}\frac{{k_F}^3}{m^*}, & \frac{k_F}{m^*} << 1, \\ \frac{1}{2}{k_F}^2, & 1 << \frac{k_F}{m^*}. \end{cases} \tag{7}$$

We can then construct the effective mass function $m^*(k_F)$ from two pieces,

$$m^*(k_F) = \begin{cases} M - \frac{4}{3} R \pi k_F^3, & k_F < k_L, \\ \frac{M}{1 + 2R\pi k_F^3}, & k_F > k_L, \end{cases} \tag{8}$$

where the value of the limiting k_F value, k_L, is given by;

$$-3\,M + 2\,k_L + 4\,R\,\pi\,{k_L}^3 = 0, \tag{9}$$

with R,

$$R = \gamma g_\sigma^2 / 8\pi^3 m_\sigma^2.$$

3 The Surface Problem

For the solution of the semi-infinite problem we use the Thomas-Fermi (TF) approximation, which assumes local infinite matter behavior for the barionic density. This approach combined with the SRDL proposal gives

$$\rho_s(z) = \begin{cases} \frac{\gamma}{6\pi^2} k_F^3(z), & k_F < k_L, \\ \frac{\gamma}{4\pi^2} m^*(z) k_F^2(z), & k_F > k_L, \end{cases} \tag{10}$$

$$\rho_B(z) =< F|\psi^\dagger \psi|F >= \frac{1}{6\pi^2}\,\gamma k_F^3(z). \tag{11}$$

Note that for low densities $\rho_s = \rho_B$.

The problem is now non-uniform with a boundary condition at the surface,[2] which gives for the mesonic fields

$$\sigma(z) = -\frac{g_\sigma}{2m_\sigma} \int_{-\infty}^{\infty} e^{-m_\sigma |z - z'|} \rho_s(z') dz', \tag{12}$$

$$\omega(z) = -\frac{g_\omega}{2m_\omega} \int_{-\infty}^{\infty} e^{-m_\omega |z - z'|} \rho_B(z') dz'. \tag{13}$$

The numerical procedure performed to solve these equations was: we begin with a trial $k_F(z)$ profile and $m^*(z) = M$ in Eqs. (11), (12) and insert the resulting densities in Eqs. (13) and (14). These equations are then integrated using a Gaussian quadrature method and spline interpolation. The resulting new σ-field gives, through Eq.(5), the new effective mass profile. The new ω-field gives the new $k_F(z)$ profile through the chemical potential condition

$$k_F(z) = \sqrt{[\mu - g_\omega \omega(z)]^2 - m^{*2}(z)}, \tag{14}$$

which comes from Eq.(6). The chemical potential is taken as that of infinite nuclear matter at $T = 0$. The procedure is then repeated until convergence of the fields.

4 Results

We have performed the calculations for infinite nuclear matter using the parameters presented in Table.1, where the values of the saturation properties are also given. The Fermi momentum at the nuclear matter saturation point is $k_{F,0}$ and E_0 is the corresponding saturation energy. The constants C_v and C_s are the constants defined by Walecka.[1]

Table.1 Force parameters sets used in the present work. For notation see text.

	C_s	C_v	$k_{F,0}$	E_0
SRDL	13.99	16.34	1.41	-15.3
Exact	13.99	16.34	1.42	-14.9

In the Fig.1 we show the effective mass as a function of the Fermi momentum and the nuclear matter equation of state obtained from the exact calculation and with the SRDL approach. For the effective mass we observe a good reproduction of the exact result except for a slight kink in the intermediate k_F region, where the low an high density limits must be connected continuously.

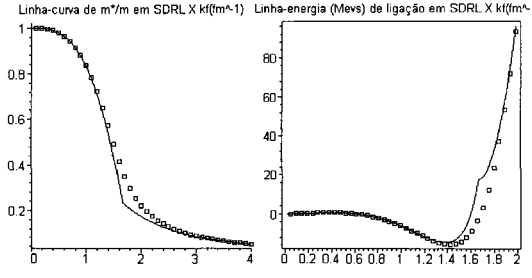

Figure 1: Effective mass and energy per nucleon versus k_F

The semi-infinite nuclear matter problem was considered with the parametrizations presented in Table 2. In proposing parametrizations A1 and A2 we have adopted the same procedure as Boguta and Bodmer,[2] taking small values for the constants C_v and C_s, in order to avoid convergence problems that arise for the usual Walecka parameters. In doing that we are performing only a qualitative study of the problem, leaving a more quantitative description for later studies.

Table 2 - Relativistic mean field parameters used for semi-infinite nuclear matter.

	C_s^2	C_v^2	m_σ(MeV)	m_ω(MeV)	$k_0(fm^{-1})$	$k_{F,0}(fm^{-1})$	t(fm)
A1	18	25	500	780	1	1.972	1.235
A2	19	40.7	500	780	0	1.525	1.5

In Fig.2 the resulting $k_F(z)$ profile obtained for the A1 parametrization is shown. Analogous results are achieved with the A2 parametrization. We emphasize that all the calculations were made with the SRDL approximation. We can observe, in this figure, the natural formation of a surface region, characterized, in the fields profiles, by a well defined surface thickness, t, which is given by the z-distance between the points at which the mesonic fields achieve values equal to 0.9 and 0.1 times its maximum value. The surface thickness obtained with the two parametrizations are also presented in Table 2. Clearly we do not expect here the reproduction of the empirical value $t \approx 2$fm, since we are not using a realistic parametrization.

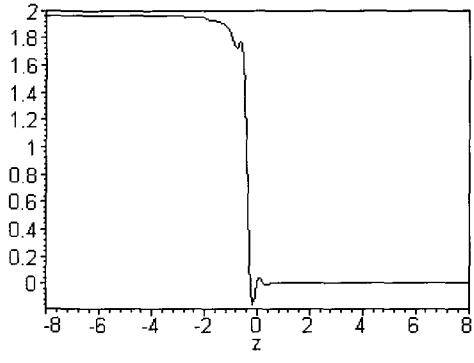

Figure 2: $k_F(z)(fm^{-1})$ versus z(fm)

5 Conclusion

We have performed Relativistic Mean Field calculations for the infinite and semi-infinite nuclear matter in the SRDL approximation. We have shown that the approximation was successful in describing qualitatively both infinite and semi-infinite systems. The SRDL approach then can be useful as a simple tool in obtaining rapid estimates of global nuclear properties for a given parametrization of the Walecka model. For realistic parametrizations it is necessary the introduction of a relaxation parameter to control the convergence in the iterative solution of the integral equations for the mesonic fields. This is presently under work.

6 REFERENCES

[1] B.D. Serot and J.D. Walecka;Adv. Nucl. Phys. 16 (1986) 1

[2] J. Boguta and A.R. Bodmer; Nucl. Phys. A292 (1977) 413

[3] P. Ring; Relativistic Mean Field Theory in Finite Nuclei, Progr. Part. Nucl. Phys. 37 (1996) 193

HYPERONS AND HEAVY BARYONS DECAYS IN THE LIGHT-FRONT MODEL

E.F. Suisso, T. Frederico
Departamento de Física, Instituto Tecnológico da Aeronáutica
Centro Técnico Aeroespacial, 12.228-901, São José dos Campos
São Paulo, Brazil

M. Beyer
Fachbereich Physik, Universität Rostock
18051 Rostock, Germany

H.J. Weber
Dept. of Physics, University of Virginia, Charlottesville
VA 22091, U.S.A.

Abstract

The aim of this work is to study the semileptonic decay rates of the process $\Lambda_b \to \Lambda_c l\overline{\nu}$. We are using the light-front model once the four-dimensional integrations in the two-loop Feynman diagrams are reduced to the null-plane such that the light-front wave function is introduced in the computation of the form-factor.

1 LIGHT-FRONT MODEL

The null-plane [2] is defined by $x^+ = x^0 + x^3 = 0$ and the coordinates and momenta canonically conjugated are

$$x^+ = x^0 + x^3,\ k^- = k^0 - k^3, x^- = x^0 - x^3, \quad (1)$$

$$k^+ = k^0 + k^3, \overrightarrow{x_\perp} = \left(x^1, x^2\right),\ \overrightarrow{k_\perp} = \left(k^1, k^2\right), \quad (2)$$

where x^+ is recognized as the time in the null-plane and k^- (energy) is the coordinate canonically conjugated.

2 MATRIX ELEMENTS OF THE DECAY PROCESS $\Lambda_b \rightarrow \Lambda_c l\overline{\nu}$

We start with the effective Lagrangian for the $\Lambda - 3q$ coupling

$$\mathcal{L}_{\Lambda-3q} = \frac{\alpha}{2}\overline{\Lambda}Q_{b,c}\overline{q_c}\gamma^5 i\tau_2 q + \frac{(1-\alpha)}{2}\overline{\Lambda}\left(i\partial^\mu\overline{\Lambda}\right)Q_{b,c}\overline{q_c}\gamma^\mu\gamma^5 i\tau_2 q + H.C. \quad (3)$$

where: τ_2 is the isospin matrix and $M_{\Lambda_b} \rightarrow M_{udb} = 5.624GeV$, with charges $Q_{\Lambda_b} \rightarrow Q_{udb} = Q_{\frac{2}{3},\frac{-1}{3},\frac{-1}{3}} = 0$ and $Q_{\Lambda_c} \rightarrow Q_{udc} = Q_{\frac{2}{3},\frac{-1}{3},\frac{2}{3}} = 1$.

The macroscopic matrix element $J^+_\Lambda(q^2)$=$\langle\Lambda_b|\overline{b}\gamma^\mu b|\Lambda_c\rangle$ in the Breit-frame and in the light-front spinor basis is given by:

$$\langle s'|J^+_\Lambda(q^2)|s\rangle = \frac{p^+}{m_\Lambda}\langle s'|F_1(q^2) + \iota\frac{F_2(q^2)}{2m_\Lambda}\vec{n}\cdot(\vec{q}_\perp \times \vec{\sigma})|s\rangle \ , \quad (4)$$

where F_1 and F_2 are the Dirac and Pauli form factors.

The microscopic elements of the electromagnetic current for the transition $\Lambda_b \rightarrow \Lambda_c + l\overline{\nu}_l$, in the Breit frame are given by:

$$\begin{aligned} j^+_\Lambda(q^2) &= j^+_{aN}(q^2) \\ &= 2p^{+2}\langle N|\hat{Q}_q|N\rangle \int \frac{d^2k_{1\perp}dk_1^+ d^2k_{2\perp}dk_2^+}{k_1^+ k_2^+ k_3^{+\,2}}\theta(p^+ - k_1^+)\theta(p^+ - k_1^+ - k_2^+) \\ &\quad \mathrm{Tr}\left[(\not{k}_2 + m)\left(\alpha m_N + (1-\alpha)\not{p}\right)(\not{k}_1 + m)\left(\alpha m_N + (1-\alpha)\not{p}'\right)\right] \\ &\quad \bar{u}(p',s')(\not{k}'_3 + m))\gamma^+(\not{k}_3 + m)u(p,s)\Psi(M_0'^2)\Psi(M_0^2) \ , \end{aligned} \quad (5)$$

3 ISGUR-WISE FORM FACTORS

In order to calculate the decay rates of the process $\Lambda_b \rightarrow \Lambda_c l\overline{\nu}$, we have to find out the best fit to the Isgur-Wise form factors [3]. These form factors have three different limits given below [4]:

1. - ISGUR-WISE FORM FACTORS IN THE HEAVY QUARK LIMIT $(m_Q \rightarrow \infty)$:

In this limit, where $(m_Q \rightarrow \infty)$, is obtained by increasing the value of the heavy-quark mass until full convergence of the calculated form factors is reached:

$$F_1^V = F_1^A = \xi(\omega), F_{2,3}^V = F_{2,3}^A = 0. \quad (6)$$

2 - ISGUR-WISE FORM FACTORS INCLUDING FIRST-ORDER $(1/m_Q)$ CORRECTIONS TO THE HEAVY QUARK LIMIT $(m_Q \rightarrow \infty)$:

In this limit, the Isgur-Wise form factors are given by [4]:

$$F_1^V(\omega) = \xi(\omega) + \left(\frac{1}{2m_c} + \frac{1}{2m_b}\right)[2\chi(\omega) + \xi(\omega)], \quad (7)$$

$$F_2^V(\omega) = -\frac{\Lambda}{m_c}\frac{\xi(\omega)}{1+\omega}, F_3^V(\omega) = -\frac{\Lambda}{m_b}\frac{\xi(\omega)}{1+\omega}, \quad (8)$$

for the electromagnetic case, and for the axial-vector:

$$F_1^A(\omega) = \xi(\omega) + \left(\frac{1}{2m_c} + \frac{1}{2m_b}\right)\left[2\chi(\omega) + \xi(\omega)\frac{\omega-1}{\omega+1}\right], \quad (9)$$

$$F_2^A(\omega) = -\frac{\Lambda}{m_c}\frac{\xi(\omega)}{1+\omega}, F_3^A(\omega) = \frac{\Lambda}{m_b}\frac{\xi(\omega)}{1+\omega}. \quad (10)$$

Here $\Lambda \equiv M_{\Lambda_Q} - m_Q + O(1/m_Q)$, is the binding energy of the baryon in the limit of heavy quark limit and $\chi(\omega)$ is an unknown function satisfying the condition $\chi(1) = 0$.

3. - RADIATIVE CORRECTIONS ON THE HEAVY QUARK LIMIT OF THE ISGUR-WISE FORM FACTORS:

The effect of radiative corrections on the heavy quark limit relations is to relate the vector and axial-vector form factors (renormalized) $\xi(\omega)$ as follows [4]:

$$F_i^V(\omega) = C_i^V(\varpi)\,\xi(\omega), F_i^A(\omega) = C_i^A(\varpi)\,\xi(\omega), \quad (11)$$

where $C_i^{V,A}(\varpi)$, with $i = 1,2,3$ are the renormalization-group invariant coefficients [4], taking into account that,

$$\varpi \equiv \omega + \left(\frac{\Lambda}{2m_c} + \frac{\Lambda}{2m_b}\right)(\omega - 1). \quad (12)$$

4 DECAY RATES OF THE PROCESS $\Lambda_b \to \Lambda_c l\overline{\nu}$

The semileptonic decay rate for the process $\Lambda_b \to \Lambda_c + l\overline{\nu}_l$ is defined as follows:

$$Br_{\Lambda_b \to \Lambda_c + l\overline{\nu}_l}(\omega_{\max}) \equiv \tau_{\Lambda_b} \int_1^{\omega_{\max}} d\omega \frac{d\Gamma}{d\omega}(\Lambda_b \to \Lambda_c + l\overline{\nu}_l), \quad (13)$$

where τ_{Λ_b} is the Λ_b mean lifetime ($\tau_{\Lambda_b} = 1.24ps$) and $d\Gamma/d\omega$ is the differential decay rate for the $\Lambda_b \to \Lambda_c + l\overline{\nu}_l$ process and ω-range is given by:

$$\omega_{\max} = \omega_{th} = \frac{\left(M_{\Lambda_b}^2 + M_{\Lambda_c}^2\right)}{2M_{\Lambda_b}M_{\Lambda_c}} \cong 1.44. \tag{14}$$

We can write down the decay rate equation as a function of the longitudinal (L) and transversal (T) decay rates as follows [4]:

$$\begin{aligned}\frac{d\Gamma}{d\omega}\left(\Lambda_b \to \Lambda_c + l\overline{\nu}_l\right) &= \frac{d\Gamma_L}{d\omega}\left(\Lambda_b \to \Lambda_c + l\overline{\nu}_l\right) + \frac{d\Gamma_T}{d\omega}\left(\Lambda_b \to \Lambda_c + l\overline{\nu}_l\right), \\ &= \frac{G_F^2}{(2\pi)^3}\left|V_{cb}\right|^2 \frac{q^2 p_{\Lambda_c} M_{\Lambda_c}}{12 p_{\Lambda_b}} \times \\ &\quad \left[\left|H_{\frac{1}{2},0}\right|^2 + \left|H_{-\frac{1}{2},0}\right|^2 + \left|H_{\frac{1}{2},1}\right|^2 + \left|H_{-\frac{1}{2},-1}\right|^2\right], \end{aligned} \tag{15}$$

where G_F is the Fermi coupling constant, V_{cb} is the Cabibbo-Kobayashy-Maskawa matrix element and, $p_{\Lambda_c} = M_{\Lambda_c}\sqrt{\omega^2 - 1}$ is the moment in the rest frame of the daughter baryon Λ_c.

The helicity amplitudes are given by $H_{\lambda_c,\lambda_W} = H^V_{\lambda_c,\lambda_W} - H^A_{\lambda_c,\lambda_W}$, where H^V and H^A are the helicity amplitudes for the vectorial and axial-vector cases, respectively. λ_c and λ_W indicate the helicity os the daughter baryon and the one of the $W-$boson, respectively. Also, where $H^V_{-\lambda_c,-\lambda_W} = +H^V_{\lambda_c,\lambda_W}$, and $H^A_{-\lambda_c,-\lambda_W} = -H^A_{\lambda_c,\lambda_W}$.

The vector and axial-vector helicity amplitudes can be expressed in terms of the vector and axial-vector form factors as follows [4]:

$$H^{V(A)}_{\frac{1}{2},1} = -2\sqrt{M_{\Lambda_b}M_{\Lambda_c}(\omega \mp 1)}F_1^{V(A)}(\omega), \tag{16}$$

$$\begin{aligned} H^{V(A)}_{\frac{1}{2},0} &= \frac{1}{\sqrt{q^2}}\sqrt{2M_{\Lambda_b}M_{\Lambda_c}(\omega \mp 1)}\left[\left(M_{\Lambda_b} \pm M_{\Lambda_c}\right)F_1^V(\omega) \pm \right. \qquad (17) \\ &\quad \left. M_{\Lambda_c}(\omega \pm 1)F_2^V(\omega) \pm M_{\Lambda_b}(\omega \pm 1)F_3^V(\omega)\right], \qquad (18) \end{aligned}$$

where the upper and lower signs stand for the vector (V) and the axial-vector (A) case, respectively.

5 ASYMMETRIES AND LOGITUDINAL POLARIZATION TO THE $\Lambda_b \to \Lambda_c l\overline{\nu}$ PROCESS

The logitudinal (L) and transversal (T) asymmetries of the $\Lambda_b \to \Lambda_c l\overline{\nu}$ process are defined as follows:

$$a_L(\omega_{\max}) = \frac{\int_1^{\omega_{\max}} d\omega K(\omega) \left[\left| H_{\frac{1}{2},0} \right|^2 - \left| H_{-\frac{1}{2},0} \right|^2 \right]}{\int_1^{\omega_{\max}} d\omega K(\omega) \left[\left| H_{\frac{1}{2},0} \right|^2 + \left| H_{-\frac{1}{2},0} \right|^2 \right]}, \quad (19)$$

$$a_T(\omega_{\max}) = \frac{\int_1^{\omega_{\max}} d\omega K(\omega) \left[\left| H_{\frac{1}{2},1} \right|^2 - \left| H_{-\frac{1}{2},-1} \right|^2 \right]}{\int_1^{\omega_{\max}} d\omega K(\omega) \left[\left| H_{\frac{1}{2},1} \right|^2 + \left| H_{-\frac{1}{2},-1} \right|^2 \right]}, \quad (20)$$

where

$$K(\omega) = \frac{G_F^2}{(2\pi)^3} |V_{cb}|^2 \frac{q^2 p_{\Lambda_c} M_{\Lambda_c}}{12 p_{\Lambda_b}}. \quad (21)$$

The ratio of the longitudinal to transversal decay rates and the the (partially integrated) longitudinal Λ_c polarization can be obtained using the following relationship:

$$R_{L/T}(\omega_{\max}) = \frac{\int_1^{\omega_{\max}} d\omega \frac{d\Gamma_L}{d\omega} (\Lambda_b \to \Lambda_c + l\overline{\nu}_l)}{\int_1^{\omega_{\max}} d\omega \frac{d\Gamma_T}{d\omega} (\Lambda_b \to \Lambda_c + l\overline{\nu}_l)}., \quad (22)$$

$$P_L(\omega_{\max}) = \frac{a_T(\omega_{\max}) + a_L(\omega_{\max}) R_{L/T}(\omega_{\max})}{1 + R_{L/T}(\omega_{\max})}. \quad (23)$$

6 CONCLUSIONS AND PERSPECTIVES

We have calculated in this work the semileptonic decay rates [1], a_L (longitudinal asymmetry), a_T (transversal asymmetry), p_L (longitudinal polarization) and $R_{L/T}$ (ratio of the longitudinal to transversal decay rates) of the $\Lambda_b \to \Lambda_c l\overline{\nu}$ process taking into account simultaneously first order correction and radiative effects to the heavy quark limit ($m_Q \to \infty$).

Using the Isgur-Wise form factor given by the Eqs. (6, 7 - 10, and 11), we have the table below showing the results obtained is this work and the reference [5], for the semileptonic decay rate limits.

$$
\begin{bmatrix}
 & Br & a_L & a_T & p_L & R_{L/T} \\
\text{This Work (HQS)} & 6.88 & -0.934 & -0.4398 & -0.539 & 0.25 \\
\text{Ref.[5]} & 6.65 & -0.931 & -0.488 & -0.763 & 1.63 \\
\text{This Work (FOC)} & 7.47 & -0.944 & -0.551 & -0.631 & 0.26 \\
\text{Ref.[5]} & 7.35 & -0.946 & -0.651 & -0.830 & 1.55 \\
\text{This Work (RC)} & 6.67 & -0.948 & -0.6 & -0.666 & 0.235 \\
\text{Ref.[5]} & 6.28 & -0.946 & -0.651 & -0.830 & 1.548
\end{bmatrix},
$$

where the labels HQS, FOC and RC, stand for Heavy-Quark limit, $(1/m_Q)$ First Order Corrections to the HQS and Radiative Corrections to the HQS, respectively.

The desagreement existing between our calculations and the reference [5] for the a_T, p_L and $R_{L/T}$, stand in the vector and axial-vector helicities.

To finish this work we have to include our calculations for the microscopic matrix elements of the vector and axial-vector currents to the Isgur-Wise form factors in the light-front model and to calculate the longitudinal and transversal asymmetries and the longitudinal polarization of the $\Lambda_b \to \Lambda_c l\overline{\nu}$ process.

References

[1] E.F. Suisso and T. Frederico, **"DECAY RATES OF THE $\Lambda_b \to \Lambda_c l\overline{\nu}$ IN THE LIGHT-FRONT MODEL"**, presented at the 5TH HEAVY QUARK EFFECTIVE THEORY (http://www.lafex.cbpf.br/ ~hq2k), October 2000.

[2] W.R.B. de Araújo, M. Beyer, T. Frederico and H.J. Weber, J. Phys. G 25 (1999) 158.W.R.B. de Araújo, E.F. Suisso, T.Frederico, M.Beyer and H.J. Weber, Phys. Lett. B478 (2000) 86.

[3] N. Isgur and M.B. Wise, Nucl. Phys. **B348**, 276 (1991).

[4] M. Neubert, Phys. Rep. **245**, 259 (1994); J.G. Korner *et al.*, Prog. Part. Nucl. Phys. **33**, 787 (1994).

[5] F. Cardarelli and S. Simula, Phys. Lett. **B421**, 295 (1998), F. Cardarelli and S. Simula, Phys. Rev. **D60**, 074018 (1999).

Neutron Stars in Non-Linear Coupling Models

Andre R. Taurines, Cesar A. Z. Vasconcellos
Universidade Federal do Rio Grande do Sul.

Manuel Malheiro
Universidade Federal Fluminense.

Marcelo Chiapparini
Universidade do Estado do Rio de Janeiro

We present a class of relativistic models for nuclear matter and neutron stars which exhibits a parameterization, through mathematical constants, of the non-linear meson-baryon couplings. For appropriate choices of the parameters, it recovers current QHD models found in the literature: Walecka, ZM and ZM3 models. We have found that the ZM3 model predicts a very small maximum neutron star mass, $\sim 0.72 M_{\odot}$. A strong similarity between the results of ZM-like models and those with exponential couplings is noted. Finally, we discuss the very intense scalar condensates found in the interior of neutron stars which may lead to negative effective masses.

1 Introduction

We still do not have sufficient information about the behaviour of quantum chromodynamics (QCD) in hadronic scales of energy, a knowledge that is very important on the description of neutron stars and relativistic heavy ions collisions. Alternatively, the theoretical physicists use phenomenological lagrangians as those appearing in the MIT bag model and in quantum hadrodynamics (QHD) [1]. The latter method is the basic tool in most of the recent neutron star studies [2]. The present work applies well known QHD models found in the literature in the analysis of neutron star matter. In achieving our goal we introduce a class of non-linear couplings which enable us to relate quantities at saturation density to neutron star properties.

2 A class of non-linear models

The original Walecka model predicts a compression modulus too high ($K \sim 550$ MeV) and some models were proposed in order to get round this problem: *i)* Boguta-Bodmer (BB) model [3]: cubic and quartic scalar self-interactions are introduced in the Lagrangian; *ii)* Zimanyi-Moszkowski (ZM) model [4] : replaces the Yukawa coupling between the scalar and spinor fields by a derivative one;

the authors also presented a version which couples the scalar and vector fields; it is known as the ZM3 model.

We introduce [5] a general Lagrangian which can reproduce the Walecka, ZM and ZM3 results after a suitable choice of mathematical parameters:

$$\mathcal{L} = \sum_B \bar{\psi}_B[i\gamma_\mu\partial^\mu - (M_B - g^\star_{\sigma B}\sigma) - g^\star_{\omega B}\gamma_\mu\omega^\mu - \frac{1}{2}g^\star_{\varrho B}\gamma_\mu\boldsymbol{\tau}\cdot\boldsymbol{\varrho}^\mu]\psi_B$$
$$+ \frac{1}{2}(\partial_\mu\sigma\partial^\mu\sigma - {m_\sigma}^2\sigma^2) - \frac{1}{4}\omega_{\mu\nu}\omega^{\mu\nu} + \frac{1}{2}{m_\omega}^2\omega_\mu\omega^\mu - \frac{1}{4}\boldsymbol{\varrho}_{\mu\nu}\cdot\boldsymbol{\varrho}^{\mu\nu} + \frac{1}{2}m^2_\varrho\boldsymbol{\varrho}_\mu\cdot\boldsymbol{\varrho}^\mu$$
$$+ \sum_\lambda \bar{\psi}_\lambda[i\gamma_\mu\partial^\mu - m_\lambda]\psi_\lambda, \qquad (1)$$

where $g^\star_{(\sigma,\omega,\varrho)B} \equiv m^\star_{(\lambda,\beta,\gamma)B}g_{(\sigma,\omega,\varrho)}$ and $m^\star_{nB} \equiv (1 + g_\sigma\sigma/nM_B)^{-n}$. In these expressions, we assume λ, β and γ as real and positive numbers. ψ denotes the baryon field and $\sigma, \omega^\mu, \boldsymbol{\varrho}$ the scalar, vector and isovector mesons, respectively. Label B corresponds to the fundamental baryon octet (n, p, Λ, Σ^-, Σ^0, Σ^+, Ξ^-, Ξ^0) and l to the leptons (e^-, μ^-). For the sake of simplicity, we are assuming *universal coupling.*

The correspondence between this and other Lagrangian models discussed in the literature is: Walecka with $\lambda, \beta, \gamma \to 0$; ZM with $\lambda = 1$ and $\beta, \gamma \to 0$; ZM3 with $\lambda, \beta, \gamma = 1$. We also define the scalar and vector mean field potentials S and V as $S = -m^\star_{\lambda N}(\sigma)g_\sigma\sigma$; $\quad V = m^\star_{\beta N}(\sigma)g_\omega\omega_0$.

In order to restrict the range of possible combinations for the mathematical parameters, we consider in this work two cases: *i)*Scalar (S): we consider in this case variations of λ with $\beta = \gamma = 0$; this case contains the results of the Walecka and ZM models. *ii)*Scalar-Vector (S-V): here we allow variations of λ, β and γ, with $\gamma = \beta = \lambda$. Walecka and ZM3 models belong to this category. *The models we are considering may be uniquely specified by the λ parameter.*

Notice that, due to the form in our coupling, there occurs a rapid convergence of the coupling to an exponential form, *e.g.* taking $\lambda \to \infty$, we have $g^\star_{\sigma B} \to e^{\frac{-g_\sigma\sigma}{M_B}}g_\sigma$. In the following, we refer to these asymptotic models in the S and S-V cases as EXP/S and EXP/S-V, respectively.

3 Neutron star properties

We determine the coupling constants in order to reproduce the binding energy of nuclear matter $B = -16.0\,MeV$, at saturation density, $\rho_0 = 0.15\,fm^{-3}$, as well as the symmetry energy coefficient, $a_4 = 32.5\,MeV$. As a consequence, the effective nucleon mass and the compression modulus can be determined.

We have found, as expected, that to higher values of the nucleon effective mass corresponds a lower compression modulus (see table 1).

We have obtained values for static properties of neutron stars as a function of the central density, by taking into account hyperon and lepton degrees of freedom. Note that for each value of the λ parameter we have a sequence of neutron stars.

Comparing table 1 we see that some models corresponding to the S-V case (including the ZM3 model) predict very small neutron star masses. The ZM model predicts a maximum mass of approximately $1.6M_{\odot}$, while the ZM3 model leads to just $0.72M_{\odot}$. We observe the similarity of the predictions associated to the ZM and ZM3 models compared to those with exponential couplings, EXP/S and $EXP/S-V$.

Figure *a* shows the maximum neutron star mass for a given value of the λ parameter as a function of the scalar potential S in the center of the neutron star. For $\lambda < 0.5$ in the S-V case, we have obtained regions for which the scalar condensate exceeds the free mass of the nucleon, $\mid S \mid > M$. Negative effective mass manifests itself dramatically also in figure *b* for the Walecka model. These negative values appear in the system due to mass differences among the baryons (even neutron-proton mass difference). In practice, it occurs only with the addition of hyperon degrees of freedom. See [5] for details.

We could wonder if negative effective mass may serve as a signal of a transition to a quark-gluon plasma phase, but we must remember that our Lagrangian model does not know about these partonic degrees of freedom. Besides that we should inquire if the mean field approximation is reaching the limits of its applicability. In fact, as showed in [6], at such high densities and strong meson fields we have already reached the critical density where the production of baryon-antibaryon pairs is favored and we should have considered also contributions from negative energy states.

4 Conclusions

We have studied the influence of a parameterized meson coupling on nuclear and neutron star matter properties. ZM3 model leads to a maximum neutron star mass too small ($\sim 0.72M_{\odot}$), while ZM and Walecka model predict $1.59M_{\odot}$ and $2.77M_{\odot}$, respectively. We have also analysed the negative values for the nucleon effective mass which appear in the interior region of the neutron stars for some values of λ.

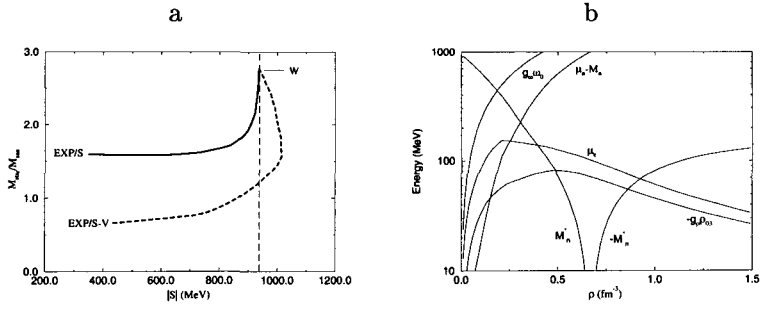

Figure 1: *a)* Maximum mass of a sequence versus scalar potential (S) at $r = 0$. *b)* Field strengths and chemical potentials for the Walecka model.

References

1. Walecka, J. D., Serot, B., *Advances in Nuclear Physics vol. 16*, Plenum Press, 1986.
2. Glendenning, N. K., *Compact stars*, Springer-Verlag, 1997.
3. Boguta, J., Bodmer, A.R., *Nucl. Phys. A*, 292, 413, 1977.
4. Zimanyi, J., Moszkowski, S. A. , *Phys. Rev. C*, 42, 1416-1421, 1990.
5. Taurines, A.R., Vasconcellos, C.A.Z., Malheiro, M., Chiapparini, Mod. Phys. Let. A, 15, 1789, (2000).
6. Mishustin, I.N., Satarov, L.M., Schaffner, J., Stöcker, H., Greiner, W., *J. Phys. G*, 19, 1303, 1993.

Table 1:

	S case			S-V case		
λ	$M_{star}/M_\odot$	K (MeV)	M^*/M	$M_{star}/M_\odot$	K (MeV)	M^*/M
0	2.77	566	0.537	2.77	566	0.537
0.05	2.35	310	0.650	2.63	458	0.554
0.09	2.02	235	0.725	2.50	387	0.567
0.13	1.83	217	0.766	2.37	339	0.579
0.17	1.72	213	0.789	2.24	293	0.594
0.20	1.68	212	0.798	2.17	276	0.600
0.30	1.59	214	0.822	1.83	218	0.630
0.40	1.58	218	0.833	1.57	195	0.649
0.50	1.58	222	0.841	1.31	180	0.667
1.00	1.59	224	0.850	0.72	159	0.710
1.50	1.59	226	0.854	0.67	156	0.728
∞ (EXP)	1.59	228	0.856	0.66	155	0.738

FOUR-WEDGE PRODUCT FOR RELATIVISTIC TREATMENT IN QUANTUM MECHANICS

E. VEITENHEIMER

Instituto de Física, Universidade Federal do Rio Grande do Sul, CP 15051, 91501-970, Porto Alegre, RS, Brazil. E-mail: veitenhe@if.ufrgs.br

In this work is obtained a quantum relativistic approach that arises from a four-dimensional (4D) differential geometry operation named Wedge product. We get a four-dimensional force through the Wedge product applied to 4D potential. The 4D *momentum* maybe also come from this 4D force, generating a complete set of quantum relativistic equations.

Let us recall the way the magnetic force $\overrightarrow{F_B}$ is obtained from the potential vector $\overrightarrow{A}$, *i. e.*

$$\overrightarrow{F_B} = k_q \overrightarrow{v} \times \overrightarrow{\nabla} \times \overrightarrow{A} \tag{1}$$

where $\overrightarrow{v}$ is the vectorial velocity of the charge q over which the force $\overrightarrow{F_B}$ acts and k_q is an electro-magnetic constant.

As we see this formula uses a vectorial product working over three dimensional vectors. By getting a four-dimensional version for this operation, generate we a complete four-dimensional force from a given four potential vector ? In the search for this answer, actually we find there is a four-dimensional version of this vectorial product. This operation come from differential geometry and it is named "Wedge product" denoted by the symbol "$\wedge$". Additionally we introduce the "$*$" operator and the exact correspondence to the vectorial product become

$$\overrightarrow{B} \times \overrightarrow{C} = * \left(\overrightarrow{B} \wedge \overrightarrow{C} \right) \tag{2}$$

where $\overrightarrow{B}$ and $\overrightarrow{C} \in \Re^3$. So, we may rewrite (1) as

$$\overrightarrow{F_B} = k_q * \left[\overrightarrow{v} \wedge * \left(\overrightarrow{\nabla} \wedge \overrightarrow{A} \right) \right] . \tag{3}$$

Expanding our view, we can try a four dimensional version of (3) getting a four dimensional force, as follows

$$\overrightarrow{F_{4D}} = k * \left[\overrightarrow{v_{4D}} \wedge * \left(\overrightarrow{\nabla_{4D}} \wedge \overrightarrow{A_{4D}} \right) \right] \tag{4}$$

where $\overrightarrow{v_{4D}}$ is the four velocity of the receiver of the force $\overrightarrow{F_{4D}}$ and k is a scalar constant characterizing the interaction whose the potential is given by $\overrightarrow{A_{4D}}$. Here we have $\overrightarrow{\nabla_{4D}} = \mathbf{i}\frac{\partial}{\partial x} + \mathbf{j}\frac{\partial}{\partial y} + \mathbf{k}\frac{\partial}{\partial z} + \mathbf{x}_0\frac{\partial}{\partial x_0}$ in Euclidean four-dimensional coordinates, so $x_0 = ict$ and $\overrightarrow{v_{4D}} = v_x\mathbf{i} + v_y\mathbf{j} + v_z\mathbf{k} + v_0\mathbf{x}_0$ with $v_0 = ic$.

By adequate applying of this operations we get the following for $\overrightarrow{F_{4D}} = F_x\mathbf{i} + F_y\mathbf{j} + F_z\mathbf{k} + F_0\mathbf{x}_0$:

$$F_x = kv_0\left(\partial_0 A_x - \partial_x A_0\right) - kv_y\left(\partial_x A_y - \partial_y A_x\right) + kv_z\left(\partial_z A_x - \partial_x A_z\right) \tag{5}$$

$$F_y = kv_0\left(\partial_0 A_y - \partial_y A_0\right) + kv_x\left(\partial_x A_y - \partial_y A_x\right) - kv_z\left(\partial_y A_z - \partial_z A_y\right) \tag{6}$$

$$F_z = kv_0\left(\partial_0 A_z - \partial_z A_0\right) - kv_x\left(\partial_z A_x - \partial_x A_z\right) + kv_y\left(\partial_y A_z - \partial_z A_y\right) \tag{7}$$

$$F_0 = -kv_x\left(\partial_0 A_x - \partial_x A_0\right) - kv_y\left(\partial_0 A_y - \partial_y A_0\right) - kv_z\left(\partial_0 A_z - \partial_z A_0\right) \tag{8}$$

with $\overrightarrow{A_{4D}} = A_x\mathbf{i} + A_y\mathbf{j} + A_z\mathbf{k} + A_0\mathbf{x}_0$ and $\overrightarrow{\nabla_{4D}} = \mathbf{i}\partial_x + \mathbf{j}\partial_y + \mathbf{k}\partial_z + \mathbf{x}_0\partial_0$.

Multiplying (5), (6), (7) and (8) by γm we get

$$\gamma m\overrightarrow{F_{4D}} = k * \left[\gamma m\overrightarrow{v_{4D}} \wedge * \left(\overrightarrow{\nabla_{4D}} \wedge \overrightarrow{A_{4D}}\right)\right] . \tag{9}$$

Putting $p_j = \gamma m v_j$, $\overrightarrow{p}_{4D} = \gamma m\overrightarrow{v_{4D}}$ and $\overrightarrow{F_{4D}} = v_0\frac{d}{dx_0}\overrightarrow{p}_{4D}$, we introduce the 4D *momentum* in (10)

$$p_0\frac{d}{dx_0}\overrightarrow{p}_{4D} = k * \left[\overrightarrow{p}_{4D} \wedge * \left(\overrightarrow{\nabla_{4D}} \wedge \overrightarrow{A_{4D}}\right)\right] . \tag{10}$$

Turning the above total derivative to partial derivatives, we get

$$\frac{d}{dt} = \frac{dx}{dt}\frac{\partial}{\partial x} + \frac{dy}{dt}\frac{\partial}{\partial y} + \frac{dz}{dt}\frac{\partial}{\partial z} + v_0\frac{\partial}{\partial x_0} \tag{11}$$

over that we'll develop the next steps:

$$\frac{\partial}{\partial x_0}\frac{d}{dx_0} = \frac{\partial}{\partial x_0}\left\{\frac{dx}{v_0 dt}\frac{\partial}{\partial x} + \frac{dy}{v_0 dt}\frac{\partial}{\partial y} + \frac{dz}{v_0 dt}\frac{\partial}{\partial z}\right\} + \frac{\partial^2}{\partial x_0^2} ; \tag{12}$$

on the other hand for a free-wave we have

$$k_x \frac{dx}{dt} + k_y \frac{dy}{dt} + k_z \frac{dz}{dt} + k_0 \frac{dx_0}{dt} = 0 \tag{13}$$

$$p_0 \hbar \left\{ \frac{dx}{v_0 dt} k_x + \frac{dy}{v_0 dt} k_y + \frac{dz}{v_0 dt} k_z \right\} = -p_0^2 = p_x^2 + p_y^2 + p_z^2 + c^2 m^2 \tag{14}$$

$$k_0 \left\{ \frac{dx}{v_0 dt} k_x + \frac{dy}{v_0 dt} k_y + \frac{dz}{v_0 dt} k_z \right\} = k_x^2 + k_y^2 + k_z^2 + \frac{c^2 m^2}{\hbar^2} ; \tag{15}$$

doing the association for the operators[a]

$$\frac{\partial}{i \partial x_0} \left\{ \widehat{\frac{dx}{v_0 dt}} \frac{\partial}{i \partial x} + \widehat{\frac{dy}{v_0 dt}} \frac{\partial}{i \partial y} + \widehat{\frac{dz}{v_0 dt}} \frac{\partial}{i \partial z} \right\} = -\frac{\partial^2}{\partial x^2} - \frac{\partial^2}{\partial y^2} - \frac{\partial^2}{\partial z^2} + \frac{c^2 m^2}{\hbar^2} ; \tag{16}$$

and putting[b] (16) into the right-hand side of (12) we finally derive an operatorial representation involving the total derivative in x_0, *i. e.*

$$\widehat{p_0} \frac{\hbar}{i} \frac{\widehat{d}}{dx_0} = \widehat{p_x}^2 + \widehat{p_y}^2 + \widehat{p_z}^2 + c^2 m^2 + \widehat{p_0}^2 ; \tag{17}$$

and from (10) is obtained a complete set of equations in operatorial form with[c] $\widehat{p_j} = \frac{\hbar}{i} \frac{\partial}{\partial x_j}$. On these equations four shifted wave functions ψ will be applied, then we find[d]

$$\widehat{p_0} \frac{\hbar}{i} \frac{\widehat{d}}{dx_0} \widehat{\overrightarrow{p}}_{4D} \overrightarrow{\psi} = -k * \left[\widehat{\overrightarrow{p}}_{4D} \wedge * \left(\widehat{\overrightarrow{A}}_{4D} \wedge \widehat{\overrightarrow{p}}_{4D} \overrightarrow{\psi} \right) \right] \tag{18}$$

as a complete set of quantum relativistic equations, where $\overrightarrow{\psi}$ has the meaning

$$\overrightarrow{\psi} = \psi_1 \mathbf{i} + \psi_2 \mathbf{j} + \psi_3 \mathbf{k} + \psi_0 \mathbf{x}_0 \tag{19}$$

and

---

[a] This step in analogy to the following: $\hbar k_x = p_x \Rightarrow \hbar \frac{\partial}{i \partial x} = \widehat{p_x}$. Thus, at the inverse step, instead of $\widehat{p_x} \Psi_{free} \equiv p_x \Psi_{free}$ we have $\widehat{\frac{dx}{dt}} \Psi_{free} \equiv \frac{dx}{dt} \Psi_{free}$ and $\frac{\partial}{i \partial x} \Psi_{free} = k_x \Psi_{free}$ holds.

[b] m is the rest mass.

[c] We have $x_1 = x$, $x_2 = y$, $x_3 = z$, $x_0 = ict$.

[d] *In Euclidean four-dimensional coordinates* $\widehat{\overrightarrow{O}} \overrightarrow{\psi} \equiv \widehat{O}_x \psi_x \mathbf{i} + \widehat{O}_y \psi_y \mathbf{j} + \widehat{O}_z \psi_z \mathbf{k} + \widehat{O}_0 \psi_0 \mathbf{x}_0$.

$$\widehat{\overrightarrow{p}}_{4D} = \sum_{j=0}^{3} \widehat{p}_j \mathbf{x_j} \,. \tag{20}$$

We express the final relativistic wave function as

$$\Psi = \widehat{\overrightarrow{p}}_{4D} \bullet \widehat{\overrightarrow{p}}_{4D} \overrightarrow{\psi} \tag{21}$$

where "$\bullet$" denotes a scalar product, and, in this way, Ψ naturally will satisfy the equation for the relativistic *momenta*

$$\widehat{p}_{4D}^2 \Psi = -c^2 m^2 \Psi \tag{22}$$

with

$$\widehat{p}_{4D}^2 = \widehat{p}_x^2 + \widehat{p}_y^2 + \widehat{p}_z^2 + \widehat{p}_0^2 \,. \tag{23}$$

If we now write

$$\overrightarrow{\chi} = \widehat{\overrightarrow{p}}_{4D} \overrightarrow{\psi} = \chi_1 \mathbf{i} + \chi_2 \mathbf{j} + \chi_3 \mathbf{k} + \chi_0 \mathbf{x}_0 \tag{24}$$

then we get a final set of quantum relativistic equations, *i. e.*

$$\begin{cases} \widehat{p}_0 \frac{\hbar}{i} \frac{\widehat{d}}{dx_0} \overrightarrow{\chi} + k * \left[\widehat{\overrightarrow{p}}_{4D} \wedge * \left(\widehat{\overrightarrow{A}}_{4D} \wedge \overrightarrow{\chi} \right) \right] = 0 \\ \Psi = \widehat{\overrightarrow{p}}_{4D} \bullet \overrightarrow{\chi} \,. \end{cases} \tag{25}$$

To conclude, we observe in the present quantum relativistic proposed approach the final wave function Ψ results scalar. But, nevertheless, I can't show further details in terms of applications because the present approach is too late for myself. So, in fact, this work is just a hint to make a procedure perform in this way.

Acknowledgments

This work is partially supported by the Brazilian agency **CNPq**.

References

1. Boothby, W., An Introduction to Differentiable Manifolds and Riemannian Geometry. Academic Press, 1986.
2. Nicolaescu, L., Lectures on the Geometry of Manifolds. World Scientific, 1996.
3. Loomis, L., and Sternberg, S., Advanced Calculus. Addison-Wesley, 1968.

Multiplicity of pions from a heated interacting gas

O.K. Vorov and M.S. Hussein
Instituto de Física, Universidade de São Paulo
C.Postal 66318, 05315-970, São Paulo, Brazil

Abstract

We consider a toy model to mimic the properties of the hot self-interacting pion system created in high-energy collisions. We show that the distribution of the multiplicities is similar to the negative binomial distribution that is typical for the squeezed states.

It is well known, that the total multiplicity distribution $P(N)$ of the secondary pions produced in various high energy collisions (pp, $p\bar{p}$ and heavy ion collisions) can be approximately described by the negative binomial distribution[1,2,3]. This feature which persists in a wide energy region, attracted much attention in the literature.

In Ref.[4], it has been shown, within a simple analytically soluble model, that the negative binomial distribution (NBD) can be obtained from the pion-nucleon interaction at the expense of intensity-dependent coupling. For this purpose, the authors of Ref.[4] have used a schematic pion-nucleon Hamiltonian in the form

$$H = \omega(a^\dagger a + 1/2) + [g(N)(a + a^\dagger) + Herm.Conj.], \qquad (1)$$

where $g(N)$ is the intensity dependent pion-nucleon coupling constant, $N = a^\dagger a$, the boson operators $a^\dagger$ (a) create (annihilate) the pion (single mode). Special choice of $g(N)$ leads to a soluble model that reveals the effect of squeezing and the NBD for the pion multiplicities[4].

Since the negative binomial distribution is rather generic feature of the pion multiplicities observed in various collisions, it seems reasonable to think of NBD as a result of interactions in the heated pion system. Contributions from resonances resulting from such interactions have been considered in Ref.[5].

We consider here a toy model of self-interacting bosons which could mimic some properties of the heated pion gas. This schematic nonlinear model (in spirit of soft pion effective theory[6]) can be solved analytically, up to a good accuracy, by the same method that has been applied in Refs.[7,8] to the rotationally-invariant multidimensional anharmonic oscillator. The method is based on algebraic properties of boson operator combinations forming algebra SU(1,1). The effects of "squeezing" and non-Poissonian distribution arise here as a result of self-interaction.

Instead of the Hamiltonian (1), we use the effective Hamiltonian in the form

$$H = \omega(\vec{a}^\dagger \vec{a} + 3/2) + \lambda_c(\vec{a} + \vec{a}^\dagger)^4, \tag{2}$$

which describes the system of self-interacting bosons. The vector $\vec{a}^\dagger = (a_0^\dagger, a_1^\dagger, a_2^\dagger)$ creates the bosons (single-mode pions) distinguished by an additional quantum number ("isospin"). The last term describes the self-interaction controlled by a "coupling constant" λ_c. Such anharmonic term can stem, e.g., from the effective contributions to Lagrangean of type[6]

$$L_{\pi\pi} = m_\pi^2 \left[F_\pi^2 - \frac{1}{2}\vec{\pi}\cdot\vec{\pi} - \frac{1}{4!F_\pi^2}(\vec{\pi}\cdot\vec{\pi})^2 + O(\pi^6) \right], \tag{3}$$

which have been used to study low-energy pion dynamics and their self-interactions[6]. Here $\vec{\pi}$ is the pion field, m_π the pion mass (assumed to be triply degenerate) and $F_\pi = 92MeV$.

Within the thermal-density operator approach[4], the pion multiplicities can be extracted from the distributions $P(N)$ that stem from the thermal density operator

$$\rho = Z^{-1}e^{-\beta H}, \quad \beta = 1/T, \tag{4}$$

For the noninteracting bosons, $H = \omega(a^\dagger a + \alpha)$ and the partition function Z is given by

$$\ln(Z) = -\beta\alpha\omega - ln[1 - exp(-\beta\omega)],$$

the quantity $\alpha\omega$ is the vacuum energy of the pion system. The pion multiplicity distribution, $P(N)$, can be derived from the density operator ρ by evaluating the expectation value

$$P(N) = \langle N|\rho|N\rangle, \tag{5}$$

in the states $|N\rangle$ with definite number of pions, N.

We turn now to the system described by Eq.(2). The Hamiltonian (2) is rotationally invariant in the "isospin" space, so it preserves the "isospin" which is given by

$$I(I+1) = \frac{1}{2}\sum_{i,j}(a_i^\dagger a_j - a_j^\dagger a_i)^2 \equiv C_{O(3)}, \tag{6}$$

i.e., the Casimir operator of the group O(3). In fact, the Hamiltonian (2) describes merely the isotropic three-dimensional anharmonic oscillator, so the technique of Refs.[8] can be applied to obtain approximate solution at low energy in each isospin sector. For this purpose, it is useful to introduce the operator of pair creation $A^\dagger$ and destruction A,

$$A^\dagger = \frac{1}{2}\sum_i a_i^\dagger a_i^\dagger, \quad A = \frac{1}{2}\sum_i a_i a_i, \tag{7}$$

which create (destruct) meson pairs with isospin $I = 0$. The operators $A^\dagger$ and A, together with the operator A^0 that is related to the boson number,

$$A^0 = \frac{1}{4}\sum_i \left(a_i^\dagger a_i + a_i a_i^\dagger\right), \tag{8}$$

are closed under commutation algebra. One has:

$$[A, A^\dagger] = 2A^0, \qquad [A^\dagger, A^0] = -A^\dagger, \quad [A, A^0] = A, \tag{9}$$

and form the algebra SU(1,1). The Hamiltonian of the self-interacting bosons can be expressed in terms of the generators of the SU(1,1) algebra:

$$H = \omega\left[A^0 + \lambda(2A^0 + A + A^\dagger)^2\right], \quad \lambda \equiv \lambda_c/\omega. \tag{10}$$

The Casimir invariant of the algebra SU(1,1),

$$C_{SU(1,1)} = (A^0)^2 - (1/2)(AA^\dagger - A^\dagger A) \tag{11}$$

coincides, up to a c-number, with the Casimir operator of the O(3) group (6),

$$I(I+1) = 1/4 C_{SU(1,1)} + c, \tag{12}$$

This allows one to use the conserved "isospin" quantity in the Holstein-Primakoff representation for the pair operator SU(1,1)-algebra:

$$\begin{aligned} A &= \sqrt{3/2 + I + n}\, b, \\ A^\dagger &= b^\dagger \sqrt{3/2 + I + n}, \\ n &\equiv b^\dagger b, \\ N &\equiv 2A^0 - 3/2 = I + 2n. \end{aligned} \tag{13}$$

where boson operators $b^\dagger$ and b rise and lower the number of isospin zero meson pairs in the system by one, $[b, b^\dagger] = 1$. The total number of mesons N is the sum of the number of mesons with the stretched "isospin" and the doubled number of the isospin-zero pairs [cf. the last eq. (13)]. While the first quantity is conserved by the interaction in (2), (10), the total effect of the interaction is the mixing of the states of different isospin-zero pairs within the same total isospin sector I.

Approximate elimination of the interaction can be done via unitary transformation[8]. One can introduce the new operators $\tilde{A}^\dagger$, $\tilde{A}$ and $\tilde{A}^0$ according to

$$\begin{aligned} A^0 &= (1/4)\left[2(\tilde{\omega} + \tilde{\omega}^{-1})\tilde{A}^0 - (\tilde{\omega} - \tilde{\omega}^{-1})\left(\tilde{A} + \tilde{A}^\dagger\right)\right], \\ A &= (1/4)\left[(\tilde{\omega}^{1/2} + \tilde{\omega}^{-1/2})^2 \tilde{A} + (\tilde{\omega}^{1/2} - \tilde{\omega}^{-1/2})^2 \tilde{A}^\dagger - 2(\tilde{\omega} - \tilde{\omega}^{-1})\tilde{A}^0\right], \end{aligned} \tag{14}$$

with $A = (A^\dagger)^\dagger$. The tilded operators form the same SU(1,1) algebra (9) with the properties (13), the transformation (14) is in fact the finite rotation for the SU(1,1) group that is generated by the unitary operator U

$$U^\dagger A^i U, \qquad U = e^{\theta(A^\dagger - A)}, \qquad \theta = (1/2) ln\tilde{\omega}. \tag{15}$$

If the constant (spin independent) value of the "rotation" parameter $\tilde{\omega}$ is used in (14), the transformation (14) can be interpreted as a Bogolyubov transformation for the meson operators of type $a = u\tilde{a} + v\tilde{a}^\dagger$. The O(3)

invariance in the "isospin" space allows one to employ broader class of transformations (14) using different values of $\tilde{\omega} = \tilde{\omega}_I$ in different isospin sectors. The optimal choice for the $\tilde{\omega}_I$ is given by the solutions of the equation

$$\tilde{\omega}_I^3 - \tilde{\omega}_I = 4(5/2 + I)\lambda, \qquad \tilde{\omega}_I \geq 1, \tag{16}$$

in each isospin sector, which allows one to reduce the Hamiltonian to the form

$$\begin{aligned} \tilde{H} &= \tilde{H}_{diag} + \Delta\tilde{H}_{int}, \\ \tilde{H}_{diag} &= \omega\left\{(1/4)\left(3\tilde{\omega}_I + \tilde{\omega}_I^{-1}\right)(I + 3/2) + \right. \\ &\quad \left. + 2\tilde{\omega}_I\tilde{n}\left[1 + \tilde{\lambda}_I\left[3(\tilde{n} - 1) + I + 5/2\right]\right]\right\} \end{aligned} \tag{17}$$

and $\Delta\tilde{H}_{int}$ is the off-diagonal correction (interaction between the new degrees of freedom)

$$\Delta\tilde{H}_{int} = \omega\tilde{\omega}_I\tilde{\lambda}_I\left[4(\tilde{n}\tilde{A} + \tilde{A}^\dagger\tilde{n}) + (\tilde{A}^\dagger)^2 + (\tilde{A})^2\right], \tag{18}$$

which turns out to be suppressed, due to inequality

$$\tilde{\lambda}_I = \frac{\lambda}{\tilde{\omega}_I^3} = \frac{1 - \tilde{\omega}_I^{-2}}{4(I + 5/2)} < \frac{1}{10 + 4I}, \tag{19}$$

which follows from Eq.(16). Even for the case of the strong coupling, the resulting transformed Hamiltonian $\tilde{H}$ is nearly linear, $\tilde{H} \approx \tilde{H}_{diag} \approx const(I) + \Omega(I)\tilde{A}^0$, while the residual interaction is suppressed due to inequality (19).

We demonstrate the appearance of the NBD for the boson multiplicities, starting from the case of zero temperature, $T = 0$. In this case, the density operator is reduced to

$$\rho \to U^\dagger|0\rangle\langle 0|U, \tag{20}$$

where U is the unitary transformation (15) that is used to diagonalize the Hamiltonian (2),(10). Neglecting the residual interaction $\Delta\tilde{H}_{int}$, we obtain, using Eqs.(15),(16) and (20) in Eq.(5) the following expression for the pion multiplicity distribution in a sector with given isospin I:

$$\begin{aligned} P_I(N) &= \left[\frac{2\tilde{\omega}_I^{1/2}}{1 + \tilde{\omega}_I}\right]^{I+3/2} \frac{\Gamma(n + I + 3/2)}{\Gamma(n + 1)\Gamma(I + 3/2)}\left[\frac{1 - \tilde{\omega}_I}{1 + \tilde{\omega}_I}\right]^{2n} = \\ &= \left[\frac{2\tilde{\omega}_I^{1/2}}{1 + \tilde{\omega}_I}\right]^{I+3/2} \frac{\Gamma(N/2 + I/2 + 3/2)}{\Gamma(N/2 - I/2 + 1)\Gamma(I + 3/2)}\left[\frac{1 - \tilde{\omega}_I}{1 + \tilde{\omega}_I}\right]^{N-I}. \end{aligned} \tag{21}$$

This expression has the form of negative binomial distribution. Extension of Eq.(21) to the case of finite temperature is straightforward, and the result is given by a bit more complicated expression with similar properties.

In fact, the negative binomial distribution is a typical property of the squeezing effect that arise in systems with dynamics governed by the semisimple noncompact groups, such as SU(1,1) and SU(2,1)[9].

One of us (O.V.) is grateful to E.V. Shuryak for discussion. The work has been supported by the FAPESP and by the CNPq.

1. Z.Koba, H.Nielsen, and P.Olesen, Nucl. Phys. **B40**, 317 (1972).

2. G.J.Alner et al.,Phys.Lett. **B138**, 304 (1984);G.J.Alner et al., *ibid.* **160**, 193, 199 (1985);G.J.Alner et al., ibid. **167**, 476 (1986); Phys. Rep. **154**, 247 (1987).

3. R.E.Angsorge et al.,Z. Phys. **C37**, 191 (1988).

4. J. Crnugelj, M. Martinis and V. Mikutamartinis, Phys. Lett. **B318**, 227 (1993), M. Martinis and V. Mikuta-Martinis, Fizika **B5**, 269 (1996).

5. M.Stephanov, K. Rajagopal and E.Shuryak, Phys.Rev. **D60**, 114028 (1999).

6. S.Weinberg, *The Quantum Theory of Fields*, Cambridge University Press, 1996.

7. V.G. Zelevinsky, Sov. Phys. JETP **19**, 1247 (1964).

8. O.K.Vorov and V.G.Zelevinsky, Sov. Journ. of Nucl. Phys. **37**, 1392 (1983); Nucl. Phys. **A439**, 207 (1985).

9. M. S. Hussein, A. F. R. de Toledo Piza and O. K.Vorov, Ann. Phys. (N.Y.) **284**,167(2000); Phys. Rev. **C59**,R1242 (1999).

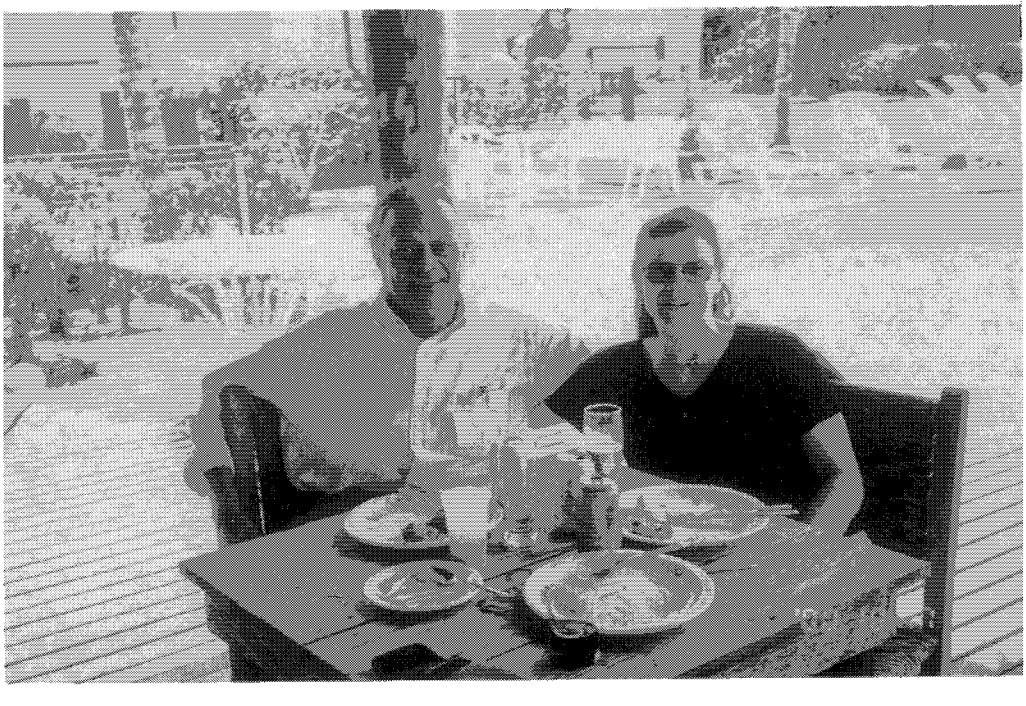


VENICE

SCIENTIFIC PROGRAM

Tuesday, October 17

8:00	Opening	Welcome Address - Yogiro Hama
	Session 1	Chairperson H-Thomas Elze
8:30	John Harris	First Physics Results from STAR
9:30	Grazyna Odyniec	Strangeness as a Signal of Phase Transition
10:30		Coffee Break
	Session 2	Chairperson Frédérique Grassi
11:00	Angela Olinto	The Origin of the Highest Energy Cosmic Rays
12:00		LUNCH
	Session 3	Chairperson Carlos E. Aguiar
14:30	Gustavo Tanco	Ultra-high energy cosmic rays: current data and propagation scenarios
15:30	Grzegorz Wilk	Imprints of Nonextensitivity in Multiparticle Production
16:00		Coffee Break
	Session 4	Chairperson Cezar Z. Vasconcello
17:00	Bikash Sinha	Quark Hadron Phase Transition in the Early Universe
18:00	Marcelo Chiapparini	Hadronic Mean-Field Models at Extreme Temperatures and Densities
19:00		DINNER

Wednesday, October 18

	Session 1	Chairperson Erasmo Ferreira
8:30	Edward Shuryak	Phases of QCD and Heavy Ion Collisions
9:30	Jean-Paul Blaizot	Hard thermal loops and QCD thermodynamics
10:30		Coffee Break
	Session 2	Chairperson Alejandro Szanto de Toledo
11:00	Marcus B. Pinto	Optimized Perturbation Theory: finite temperature applications
12:00		LUNCH
		Excursion
19:00		Churrasco Dinner
21:30	Colloquium	Chairperson Jorge Horvath
	José A. Freitas Pacheco	Potential Gravitational Wave Sources and Laser Beam Interferometers

Thursday, October 19

	Session 1	Chairperson Sergio B. Duarte
8:30	Takeshi Osada	Event-by-event Analysis of Ultrarelativistic Heavy-Ion Collisions in Smoothed Particle Hydrodynamics
9:30	Wolfgang Bauer	Flow Signals of the Phase Transition
10:30		Coffee Break
	Session 2	Chairperson Chung K. Cheong
11:00	Marina Nielsen	Hadronic form factors from QCD sum rules
12:00		LUNCH
	Session 3	Chairperson Tobias Frederico
14:00	Robert Thews	Quarkonium Production in High Energy Heavy Ion Collisions
15:00	Fernando S. Navarra	On the J/psi – nucleon cross section
16:00		Coffee Break
	Colloquium	Chairperson Francisco Krmpotic
16:30	Constantino Tsallis	Nonextensive thermostatistical and thermodynamical anomalies – Microscopic interpretation
		Round Table Discussion
18:00	QGP – Observed ?	J-P. Blaizot, J. Harris, G. Odyniec, J. Rafelski, E. Shuryak, H. Stöcker, K.Werner, F. Navarra, Y. Hama, T.Kodama, Alex S. de Toledo (coordinator)
20:00		DINNER

Friday, October 20

	Session 1	Chairperson Carlos Bertulani
8:30	Gerald A. Miller	Light front nuclear QCD physics
9:30	Klaus Werner	Parton Based Gribov-Regge Theory
10:30		Coffee Break
	Session 2	Chairperson Gastão Krein
11:00	Horst Stöcker	Critical review of quark gluon plasma signatures and latest results
12:00	Johann Rafelski	Strange Quark-Gluon Plasma
13:00	Yogiro Hama	Closing Remarks
		DEPARTURE

List of Participants

Name		E-MAIL
Carlos Eduardo	Aguiar	carlos@if.ufrj.br
Gino	Ananos	gino@lafex.cbpf.br
Wilson Roberto B. de	Araújo	wbaraujo@axpfep1.if.usp.br
Álvaro Leonardi	Ayala Filho	ayala@ufpel.tche.br
Celso Carmargo de	Barros Jr.	barros@fma.if.usp.br
Marta	Barroso	marta@if.ufrj.br
Edilson Ferreira	Batista	edilson@fis.ita.br
Eduardo	Bauer	Bauer@venus.fisica.unlp.edu.ar
Woflgang	Bauer	Bauer@pa.msu.edu
Marcus Emmanuel	Benghi	Fsc1mep@fsc.ufsc.br
Carlos A.	Bertulani	Bertu@if.ufrj.br
Jean-Paul	Blaizot	Blaizot@wasa.saclay.cea.fr
José de Sá	Borges Filho	Saborges@uerj.br
Mirian Enriqueta	Bracco	Bracco@uerj.br
Fabio	Braghin	Braghin@axpfep1.if.usp.br
Rogério Gregorio	Burgugi	Rogerio@wslip2.if.usp.br
Brett	Carlson	Brett@fis.ita.br
Raquel Santos Marques de	Carvalho	raquel@if.usp.br
Isabela P.	Cavalcante	ipca@uerj.br

Maria Luiza	Cescato	Mcescato@fisica.ufpb.br
Marcelo	Chiapparini	chiappa@uerj.br
K. Cheong	Chung	Chung@uerj.br
Eduardo Veitenheimer	Costa	Veitenhe@if.ufrgs.br
Sérgo B.	Duarte	Sbd@cbpf.br
Francisco de Oliveira	Durães	Fduraes@if.usp.br
Hans-Thomas	Elze	Thomas@if.ufrj.br
Erasmo Madureira	Ferreira	Erasmo@if.ufrj.br
Tobias	Frederico	tobias@fis.ita.cta.br
Victor Paulo Barros	Gonçalves	Victor@inf.uri.br
Frederique	Grassi	Grassi@if.usp.br
Barbara F.	Haas	Barbara@fis.ita.br
Yogiro	Hama	Hama@if.usp.br
John W.	Harris	Harris@star.physics.yale.edu
Jorge	Horvath	foton@orion.iagusp.usp.br
Antares	Kleber	Anta@on.br
Takeshi	Kodama	tkodama@if.ufrj.br
Gastão	Krein	GKREIN@AXP.IFT.UNESP.BR
Francisco	Krmpotic	Krmpotic@venus.fisica.unlp.edu.ar
Joaquim	Lopes Neto	Jlneto@if.ufrj.br
Eduardo Ferreira	Lutz	Lutz@if.ufrgs.br
Guilherme Frederico	Marranghelo	Gfm@if.ufrgs.br
Alexandre	Mesquita	Falcon@if.ufrgs.br
Gerhard. A.	Miller	Miller@phys.washington.edu
Fernando	Navarra	Navarra@if.usp.br

Marina	Nielsen	Mnielsen@if.usp.br
Grazyna	Odyniec	G_Odyniec@lbl.gov
Angela	Olinto	Olinto@oddjob.uchicago.edu
Manuel Malheiro. B. de	Oliveira	Mane@if.uff.br
Takeshi	Osada	Osada@fma.if.usp.br
José A Freitas	Pacheco	Pacheco@obs-nice.fr
Prafulla	Panda	panda@ift.unesp.br
Fernando Gonçalves	Pilotto	Pilotto@if.ufrgs.br
Johann	Rafelski	Rafelski@physics.arizona.edu
Moisés	Razeira	Razeira@if.ufrgs.br
Cleide Matheus	Rizzatto	Cleide@ift.unesp.br
Alberto Sperotto S.	Rocha	Sperotto@if.ufrgs.br
Sergio Souto	Rocha	Ssrocha@if.ufrgs.br
Carlos Javier Solano	Salinas	javier@lafex.cbpf.br
Norberto	Scoccola	Scoccola@tandar.cnea.gov.ar
Edward	Shuryak	Shuryak@dau.physics.sunysb.edu
Cesar Luiz da	Silva	slash@fge.if.usp.br
Roberto Menezes da	Silva	Rms@fisica.ufpb.br
Romulo Rodrigue da	Silva	Romulo@fisica.ufpb.br
Scheilla Maria Ramos da	Silva	Smr@fisica.ufpb.br
Bikash	Sinha	Bikash@veccal.ernet.in
Frederico Firmo de	Souza Cruz	fred@fsc.ufsc.br
Horst	Stöcker	Stoecker@th.physik.uni-frankfurt.de
Edson	Suisso	Suisso@fis.ita.br

Gustavo	Tanco	Gustavo@iagusp.usp.br
André Ribeiro	Taurines	Taurines@if.ufrgs.br
Robert	Thews	Thews@physics.arizona.edu
Alejandro Szanto de	Toledo	Szanto@dfn.if.usp.br
Lauro	Tomio	Tomio@ift.unesp.br
Luis Augusto	Trevisan	Latrevis@uepg.br
Constantino	Tsallis	Tsallis@cbpf.br
Cesar A. Z.	Vasconcellos	Cesarzen@if.ufrgs.br
Oleg	Vorov	Vorov@fma.if.usp.br
Klaus	Werner	Wener@subatec.in2p3.fr
Grezgorz	Wilk	Grzegorz.Wilk@fuw.edu.pl
Clovis Jose	Wotzasek	Clovis@if.ufrj.br

Brazilian Institutions:

- UFRJ: Univ. Fed. Rio de Janeiro
- CBPF: Centro Brasileiro de Pesquisas Físicas, Rio de Janeiro
- UFF: Univ. Fed. Fluminense, Niterói, Rio de Janeiro
- UERJ: Univ. Estadual do Rio de Janeiro
- USP: Univ. São Paulo
- UNESP: Univ. Estadual Pauista
- UFPEL: Univ. Fed. Pelotas, Rio Grande do Sul
- ITA: Instituto Tecnológico da Aeronáutica, São José dos Campos, S.Paulo
- UFSC: Univ. Fed. Santa Catarina, Florianópolis
- UFPb: Univ. Fed. Paraíba, João Pessoa
- UFRGS: Univ. Fed. Rio Grande do Sul, Porto Alegre
- IAGUSP: Instituto Astronomico e Geofísico, USP, São Paulo
- ON: Observatório Nacional, Rio de Janeiro
- UFRN: Univ. Fed. Rio Grande do Norte
- UEPG: Univ. Estadual de Ponta Grossa, Paraná

ISBN 981-02-4715-X

www.worldscientific.com
4779 hc